Rapid label-free separation of stromal cell populations for autologous cell therapy in musculoskeletal diseases

Africa Sara Smith de Diego

Submitted in accordance with the requirements for the degree of
Doctor of Philosophy in Tissue Engineering and Regenerative Medicine –
Innovation in Medical and Biological Engineering

The University of Leeds
School of Mechanical Engineering

March 2021

The candidate confirms that the work submitted is her own and that appropriate credit has been given where reference has been made to the work of others.

Acknowledgements

First and foremost, I would like to thank all of my supervisors Prof. Jennifer Kirkham, Dr Chris Wood, Prof. Christoph Wälti, and Dr Xuebin Yang for their guidance and continuous support throughout this thesis until its completion. These four years have been hard, but I have really enjoyed working alongside you and I cannot express my gratitude for all the patience and support that you have shown me every step of the way in and outside the lab.

I would also like to thank Dr Michal Szymonik and Dr Akshay Kale for their help and support in the early days of this PhD in both the lab and the modelling aspect of this project.

I would like to extend my thanks to every member of the bioelectronics lab and the Oral biology department that I had the pleasure to meet during these years for making me feel at home in the lab and the office. In particular, I would like to thank Dr Alice Phillipson, for all the shared moments in and outside the office throughout the years and Samuel Confederat, for encouraging me to finish writing in these difficult circumstances.

I would also like to thank my friends outside the lab for keeping me sane in the most difficult moments, with special thanks to Jackie for being an incredible support throughout this entire journey (occasionally sacrificing weekends), I am forever grateful.

Finally, I would like to thank my wonderful family for always believing in me and supporting me in my endeavours, wherever they take me.

Abstract

The combination of autologous mesenchymal stromal cells (MSCs) with biomimetic scaffolds for tissue repair is a promising treatment strategy for musculoskeletal diseases. For this, the patients' cells need to be harvested and concentrated intra-operatively. Current cell enrichment technologies are either limited by low selectivity, low throughput or by their intrinsic requirement for manipulation of the separated cells.

By using surface acoustic waves dielectrophoresis (SAW-DEP), where virtual electrodes are created within a microfluidic channel using shear-horizontal surface acoustic waves generated on a piezoelectric material, cells can be separated with minimal manipulation. This technology has been previously shown to separate dead from alive dental pulp stromal cells in high conductivity fluids without the need for cell-labelling, and without heating or electrochemical reactions occurring.

The aim of this thesis was to further the understanding of the SAW-DEP technology to increase the device's throughput and determine its suitability to separate MSCs from other cell types found in bone marrow whilst maintaining their osteogenic potential.

In order to understand better the underlying physics of SAW-DEP, the effect of parameters such as input power and channel height on the dielectrophoretic response of the system were investigated. These experiments showed that the throughput could be increased twenty-fold by exploiting the vertical dielectrophoretic forces in the channel using a multi-layered channel approach.

The dielectric properties of MSCs and other white blood cells present in bone marrow were characterised and the differences found between the cell populations suggested that SAW-DEP has the potential to enrich MSC populations from bone marrow samples.

The osteogenic potential of MSCs after exposure to SAW-DEP was assessed first *in vitro* and then *in vivo* by implanting human stem cell-seeded scaffolds into athymic rats with calvarial defects. The results showed the SAW-DEP exposure did not negatively affect the ability of MSCs to repair bone defects.

Table of Contents

List of Figures

List of Tables

List of Abbreviations

ABM	Anorganic bone mineral
APC	Allophycocyanine
BM-MSC	Bone marrow mesenchymal stem cell
BMNC	Bone mononuclear cell
BSA	Bovine serum albumin
CM	Clausius Mossotti
CT	Computer tomography
Cy	Cyanine
DEP	Dielectrophoresis
iDEP	Insulator dielectrophoresis
nDEP	Negative dielectrophoresis
pDEP	Positive dielectrophoresis
DLD	Deterministic lateral displacement
DMSO	Dimethyl sulfoxide
DPSC	Dental pulp stromal cell
DPX	Dibutylphthalate Polystyrene Xylene
EDTA	Ethylenediaminetetraacetic acid
EIS	Electrical impedance spectroscopy
EPC	Endothelial progenitor cells
FACS	Fluorescence-activated cell sorting
FE	Finite element
FFF	Flow field fractionation
FITC	Fluorescein isothiocyanate
FMO	Fluorescence minus one
FRET	Förster resonance energy transfer
FSC	Forward scatter
H&E	Haematoxylin & Eosin
HSC	Hematopoietic stem cells

IDT	Interdigitated transducers
IHC	Immunohistochemistry
iPSC	Induced pluripotent stem cell
MACS	Magnetic activated cell sorting
MSC	Mesenchymal stem cell
MSK	Musculoskeletal
NK	Natural killer
$LiTaO_3$	Lithium tantalate
PBS	Phosphate buffered saline
PCB	Printed circuit board
PCR	Polymerase chain reaction
PDMS	Polydimethylsiloxane
PE	Phycoerythrin
PEG	Polyethylene glycol
PMMA	Polymethyl methacrylate
PMN	Polymorphonuclear
PTFE	Polytetrafluoroethylene
RBC	Red blood cell
RSAW	Rayleigh surface acoustic wave
SAW	Surface acoustic wave
SAW-DEP	Surface acoustic waves dielectrophoresis
SH-SAW	Shear horizontal surface acoustic wave
SH-SSAW	Shear horizontal standing surface acoustic wave
SMA	Surface-mount assembly
SSC	Side scatter
UV	Ultra-violet
VSEL	Very small embryogenic-like cells
WBC	White blood cell

Chapter 1
Introduction and literature review

1.1 Project rationale

Musculoskeletal (MSK) diseases are a major cause of morbidity and are the second greatest cause of disability worldwide [1]. These diseases result in pain and reduced mobility which impacts on the quality of life of the patient. The economic cost of MSK diseases, through increased healthcare expenditure and lost days of work has been estimated to be $213 billion per annum in the USA alone over the past ten years [2]. Population aging is a major challenge in developed countries, and the number of MSK diseases cases is steadily increasing, with the associated healthcare costs increasing by 25% globally in the last ten years [3].

Some MSK disorders affect bones, which often need replacement in advanced disease states. In 2005, 2.2 million bone grafting procedures involving the implantation of bone tissue into a defect were performed throughout the world [4]. These grafts or replacements can be used to fill defects arising from genetic conditions, trauma and tumours, but also debilitating diseases such as osteoporosis [5]. Some of the current bone replacements are conducted in combination with cell therapies, which have been flagged as “one of the UK’s *Great Technologies*” [6]. These combinatorial therapies use cells, along with bone replacements, to accelerate the repair of fracture non-unions, where endogenous bone repair cannot be achieved.

Such therapies require stem cells which can be found in numerous tissues such as bone marrow, dental pulp (obtained after the extraction of teeth) or adipose tissue [7]. Stem cells are multipotent, which means that they can multiply and differentiate into multiple specific lineages via induction of differentiation factors. Mesenchymal stromal cells (MSCs) are a stem cell subset that can differentiate into bone cells (osteoblasts), cartilage cells (chondrocytes), muscle cells (myocytes) and fat cells (adipocytes). They can be obtained from the patient directly (autologous) or from a donor (allogeneic). Allogeneic cells are available in high quantities from donor tissue but can elicit an immune response in the patient [8]. Therefore, in order to

limit the complications, most current clinical trials use autologous stem cells extracted directly from the patient. Another promising solution is the use of induced pluripotent stem cells (iPSCs) and embryonic stem cells, but further research is required to validate the safety of these sources [9].

Typically, bone marrow is extracted from the iliac crest of the pelvis. However, extraction from vertebral bodies, humeral heads, proximal tibia and distal femur have also been reported [10]–[12]. MSC yield has been found to be higher in iliac crest extractions, where 30 to 120 mL of bone marrow can be extracted, making it the preferred option for one-step treatment procedures where high cell concentrations are needed [13]. However, iliac crest extraction of bone marrow is associated with pain and a high rate of complications that could cause chronic pain. Extraction from the tibia or femur could be a safer alternative to obtain bone marrow in cases where only reduced concentrations of MSCs are required.

Extracted bone marrow is composed of a range of cell types which includes red blood cells, mononuclear cells (lymphocytes, monocytes, MSCs and macrophages) and polymorphonuclear cells (neutrophils, basophils and eosinophils). The proportion of the different cells found in bone marrow varies from patient to patient and is dependent on gender, age and health [14]. Studies showed that the estimated frequency of MSCs within the mononuclear fraction of bone marrow ranges from 0.01% to 0.001% (corresponding to 10^2 to 10^3 MSCs/mL) [13], [15], [16]. The proportion of stem cells in bone marrow is very small, so methods are needed to concentrate them for therapeutic applications while discarding the cell types that could hinder regeneration of the target tissue.

It has been hypothesised that use of whole bone marrow could cause hypoxia (oxygen deprivation) in the implanted area due to the high metabolic requirements of the numerous cells present [7]. Additionally, cell apopotosis during the extraction process can lead to detrimental inflammatory responses at the wound site due to the release of intracellular contents [17]. Bone marrow extracts also contain a range of cytokines, fat, extracellular matrix components and bone debris which could hinder bone repair. Fat clots and bone debris are usually removed by filtering, but cellular debris have been shown to remain in solution.

Current treatments involving stem cells require three steps: tissue harvesting, tissue processing and implantation (Figure 1.1). Tissue harvesting and

implantation are often done in two separate operations, as stem cell selection and amplification can take days. This increases the cost and wait time of the treatment which as a consequence becomes a higher risk procedure. Processing steps can include the culturing of cells to increase the population numbers for downstream procedures. However, this also adds to the cost, as cell culture procedures have to comply with good manufacturing practices guidelines, requiring expensive facilities and personnel that have been adequately trained [7]. Moreover, cell culturing in flasks could also irreversibly alter the phenotype of the stem cells after a certain number of passages (removal of the medium and cell transfer from a previous culture into fresh medium to expand them), so the cells used for tissue repair need to be strictly regulated [18]. Cells expanded through tissue culture are classified as advanced therapeutic medicinal products by the European Medicines Agency, which require extensive clinical trials to prove the safety and benefits of the procedure (Regulation No 1394/2007) [19]. In contrast, when the procedure used to obtain the cells does not affect their activity and function, the cells may be considered as “minimally manipulated”. Devices enabling minimally manipulated cell separation are categorised as class III medical devices [20]. This significantly reduces the development cost of the technology and could also accelerate the translation of autologous cell therapies from the bench to the bedside.

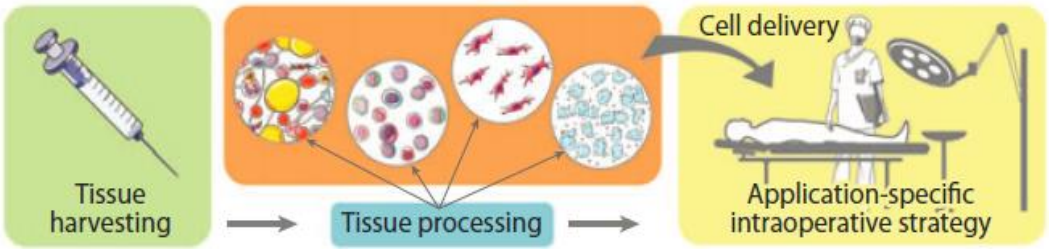

Figure 1.1: Steps involved in tissue engineering constructs requiring stem cells: harvesting of tissue from the same patient or from donor, tissue processing (expansion, addition of cytokines, isolation of MSCs, cell seeding of scaffolds) and cell delivery to the patient. Adapted from [7].

Currently, state of the art intraoperative technologies are limited by the extractable bone marrow quantities (30-120 mL) and the ability to isolate sufficient numbers of stem cells to elicit therapeutic benefit (typically in the range of 10^4 cells) [7], [16]. An additional factor that is lacking in current intraoperative technologies is standardisation. Stem cell technologies have been shown to be dose dependent but stem cell count is variable from patient

to patient, and current intraoperative technologies are unable to determine the dose of cells administered [7]. If an intraoperative separation method could give information about the number and purity of the recovered cells, this could help surgeons standardise their procedures in order to administer the same dose to each patient or to tailor it so that treatment is patient specific. This would lead to more controlled procedures for stem cells therapies [7]. Moreover, MSC variability between patients may have an impact upon the procedures' success rate [21]. The concentration and proliferation potential of MSCs in elder patients is smaller, so more bone marrow aspirate is required to achieve a comparable result to that of a younger patient [22]. Hence, the ability to determine the concentration of MSCs within an intraoperative timeframe (less than 1h) is required, which is currently not achievable with current label-free separation technologies due to the lack of cell purity.

The aim of this thesis was to address these challenges by developing a separation technique to concentrate MSCs from bone marrow in intraoperative timeframes with minimal manipulation. In Chapter 4 the concentration throughput of the technology was increased to make it closer to the time required for intraoperative timeframes. In Chapter 5, the properties of BM-MSCs and other white blood cell populations were characterised and the differences observed suggested that the technology has the potential to enrich MSC populations from bone marrow samples. Finally, in chapter 5, the minimal-manipulation aspect of the technology was investigated using preliminary *in vitro* and *in vivo* experiments of bone repair in rat calvarial defects.

1.2 Currently available cell separation technologies

1.2.1 Adherence-based separation technologies

Mammalian cells such as macrophages, mesenchymal cells or lymphocytes can be characterised by their varying degrees of adhesion to certain surface chemistries and peptides such as RGD (arginine-glycine-aspartic acid) when left to incubate for up to a day [23]. Differential cell adhesion is well established as a method for cell capture from complex mixtures. For example, it has been demonstrated that when culturing the mononuclear fraction of bone marrow in a tissue culture flask, MSCs will adhere to the tissue culture

plastic while the other cell types will remain in solution and can be removed by discarding the supernatant [24]. This form of broad fractioning is minimally manipulative as it does not require the use of cell labels such as antibodies and preserves cell phenotype if they are not in long term culture. It also demonstrates reasonable specificity, as the surfaces can be treated to promote attachment of different cell types, but it can be very time consuming.

1.2.1.1 Selective cell retention separation

To date, the primary clinical method used involving adhesion onto a substrate is selective cell retention, due to the ease of handling. This technology consists of flooding a porous scaffold with freshly harvested bone marrow just before implantation (Figure 1.2). The surface properties of the scaffold increase the preferential adherence of stem cells, while other cells are excluded in the flow-through [25]. The adherence of cells can be controlled by tuning the porosity of the scaffold or by coating it with platelet-rich plasma [26].

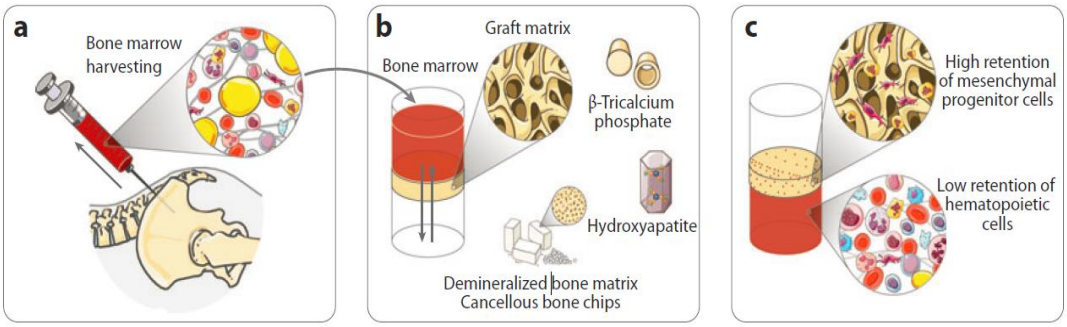

Figure 1.2: A schematic diagram depicting the selective cell retention process: a) Bone marrow is harvested from the iliac crest of the patient. b) Bone marrow is flushed through a syringe containing the matrix. c) After a few cycles, MSCs stay inside the matrix while the other cell types are collected in the fluid phase. Reproduced from [7].

Many regenerative medicine approaches involve the use of matrices that are seeded with cells, so this technology enables cell seeding directly from bone marrow without need for additional separation steps, which speeds up the process considerably. Muschler et al. (2005) reported that enriched matrix grafts delivered 5.6 times more MSCs than matrix supplemented with bone marrow [27]. Although this showed increased repair in some clinical settings, the yield remains low for situations in which large cell concentrations are

required. Furthermore, this technique cannot be considered specific as other cell types are also retained.

1.2.2 Density and size-based separation technologies

1.2.2.1 Centrifugation separation

Centrifugation techniques utilise centrifugal force to accelerate the sedimentation of particles within mixed suspensions. Sedimentation rates described in equation (1.1) depend on specific particle densities and hence differential sedimentation rates are used as the specific separation mechanism.

$$\boldsymbol{Sedimentation\ rate}: \boldsymbol{v_t} = \frac{\boldsymbol{mr\omega^2}}{\boldsymbol{6\pi\eta r_0}} \quad (1.1)$$

Where m is the particle mass, r is the distance between the particle and the rotor axis, ω is the angular velocity of the rotor, η is the viscosity of the fluid and r_0 is the particle radius. As seen in equation (1.1), sedimentation rate increases linearly with particle mass and results in an increased migration within a separation vessel under applied centrifugal force. The sedimentation rate is also dependent upon the viscosity of the medium and hence the separation resolution can be tuned through the creation of density gradients through which the sample is passed (Figure 1.3) [28].

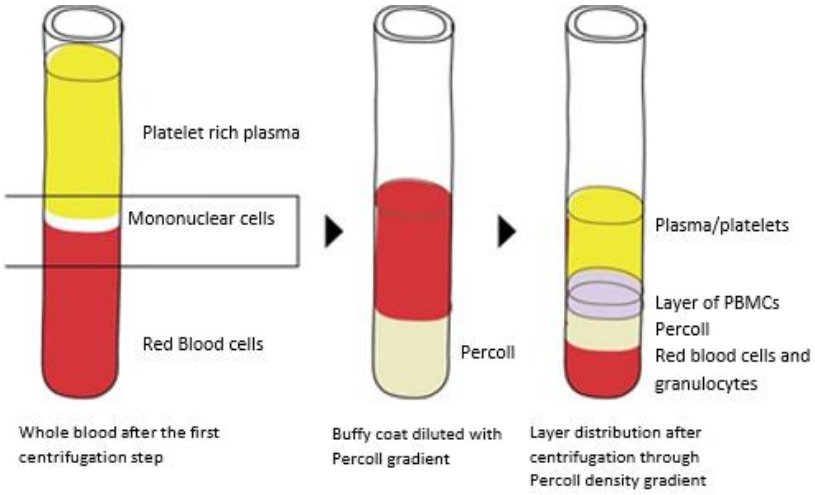

Figure 1.3: Centrifugation of blood with and without a density gradient. The first step of centrifugation without a density gradient enables separation of the white blood cells (WBCs) fraction from red blood cells and plasma. The WBCs fraction is then further separated in a second step by using a Percoll gradient, which gives a finer separation resolution. Adapted from [29].

Density gradient centrifugation is typically used to concentrate the white blood cell fraction and obtain bone mononuclear cells (BMNCs). BMNCs are a mixture of monocytes, T cells, B cells, hematopoietic stem cells (HSCs), MSCs, very small embryogenic-like cells (VSEL) and endothelial progenitor cells (EPC) [30]. Mononuclear cells are found at the interface between the red blood cell fraction and the plasma (Figure 1.3). Once separated, the white cell fraction is extracted and the platelet and red blood cell contamination is minimised through a lysis step using a hypotonic buffer. Limiting red blood cell contamination is crucial, as cell therapy success using BMNCs has been shown to be adversely affected by red blood cell content because the high blood cell count results in hypoxia and necrosis of the tissue [31].

The most common density gradients used for BMNCs retrieval are Percoll and Ficoll. Percoll is a density gradient composed of particles of colloidal silica of different diameters [32]. Due to its composition, it has low viscosity and osmolarity, which results in low cell death. Ficoll on the other hand is composed of high-mass sugars with different sized branches. A study by Posel et al. (2012) showed that when used at the same density, Percoll yields significantly more BMNCs than a Ficoll gradient (75% loss of BMNCs for Ficoll versus 50% for Percoll), and it has been suggested that Ficoll could be cytotoxic [4]. This would explain the significant loss of MSCs and their impaired osteogenic potential downstream [33]. However, contamination with polymorphonuclear cells (PMNs) was greater when using Percoll compared to Ficoll [30]. Even when using a Percoll gradient, the authors only managed to recover 50% of the BMNCs and the amount of stem cells discarded was >60%. It is thought that stem cells are discarded when using centrifugation in conjunction with Percoll due to their tendency to form aggregates [34]. These aggregates migrate further down the tube than the other cells and are discarded with the density gradient media following removal of the individual MSCs fraction.

A wide range of centrifugation protocols that have yielded similar percentages of BMNCs in clinical trials have been described by different groups [35]. As a result, to date, there is no standard procedure designated to recover stem cells using centrifugation. The published procedures differ in the number of washing steps, centrifugation speed or density gradient concentration and this lack of standardisation is a likely factor that contributes to the observed differences between clinical trials using BMNCs [35]. Such

protocol variation is likely to lead to altered BMNC population compositions which would in turn alter their osteogenic potential and hence may be the source of the many conflicting published results [7]. It is possible to standardise centrifugation by using automated cell processors. These processors can also be used in clinical settings to wash the tissue before concentrating the BMNCs with or without the use of density gradients [7]. This makes them more reliable and efficient, however the yield obtained remains low.

1.2.2.2 Surface Acoustic Waves separation

A surface acoustic wave (SAW) is a mechanical wave confined within a few wavelengths of the surface of a piezoelectric material [36]. SAWs can be generated by applying high-frequency signals to metallic interdigitated transducers (IDTs), patterned on a piezoelectric material (Figure 1.4) [37]. When an alternating electric field is applied to the IDTs, the potential difference creates compression and expansion in the lattice of the underlying piezoelectric material which launches a travelling mechanical wave along the material surface (away from the IDTs). The wavelength of this wave is determined by the spacing between electrode finger pairs. When two waves of equal frequency and travelling in opposite directions interfere with each other, a standing wave is formed, comprised of periodic zones of maximum wave amplitude (antinodes) and minimum amplitude (nodes), which alternate at a pitch corresponding to a quarter of the wavelength of the corresponding SAW. These standing waves can be exploited for the separation of different sized particles in a fluid. When the piezoelectric material is placed in contact with a fluid, the standing waves induce periodic pressure nodes within the fluid. The pressure gradient formed across these nodes induces acoustic radiation forces on particles suspended within the fluid. The magnitude of those acoustic forces is dependent on the particle size, density and compressibility [36]. The forces are sufficiently large to overcome gravitational forces which would otherwise result in particle sedimentation (a common problem in microfluidic devices) [37]. In mixtures of particles with different size but the same density, larger particles are found to align within the pressure nodes generated in the liquid whereas smaller particles are found to be trapped at the antinodes (Figure 1.4) [38]. The location of the pressure nodes and antinodes can be modified by changing

the frequency of the wave, thus enabling the placement of the particle alignment to be changed.

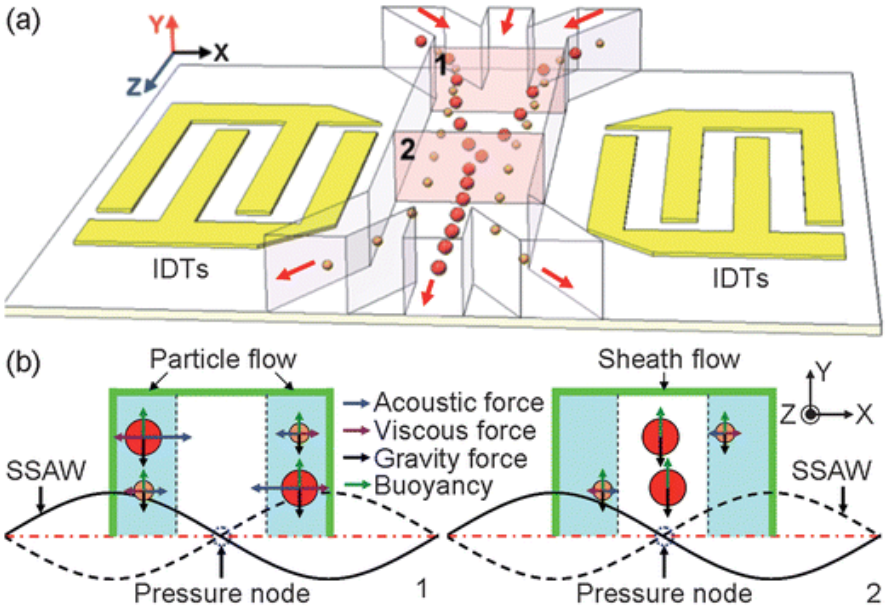

Figure 1.4: A schematic diagram depicting the setup required to use standing SAWs for cell separation. a) Two opposing interdigitated transducers (IDTs) generate a standing wave. A mixture of particles is injected into the channel and upon reaching the standing SAWs, they align depending on their volume, density and compressibility. b) Depiction of the buoyancy, acoustic, viscous and gravity forces applied to the particles within the different regions of the standing waves. Reproduced from [38].

Potentially, this type of technology could be used to separate a mixed population of cells by exploiting their alignment at different regions of the standing SAW based on their inherent mechanical properties, allowing their collection at different channels downstream. However, targeted separation of cells remains difficult, particularly for cell types with either similar mechanical properties, or whose differences in size and density are negated by differences in compressibility.

This separation method is successful when the cells have very different sizes and densities such as platelets and red blood cells. Nam et al. (2011) demonstrated the use of standing SAWs to separate platelets from blood with a yield of 97% and a purity of 98% [39]. However, the low throughput (10^5 cells/h) has thus far relegated this approach to a laboratory based technology, as an intraoperative time separation would require a throughput of at least 3.10^8 cells/h to ensure 10 mL of concentrated bone marrow are processed within 1h.

1.2.2.3 Deterministic lateral displacement separation

Deterministic lateral displacement (DLD) was first described by Huang et al in 2004, who used pillar arrays to generate streamlines in the fluid and sort particles based on their size [40]. The particle trajectory depends on its size and the pillar parameters and can follow two different modes: zig-zag mode and displacement mode (Figure 1.5). If the particle radius is smaller than the width of the streamline it is flowing in, the particle crosses between the pillars in a zig-zag mode. If the particle radius is larger than the streamline width, the particle collides with the pillars and keeps displacing laterally towards the next streamline (displacement mode). The DLD critical diameter at which a particle shifts from zigzag mode to displacement mode can be tailored by altering the pillar diameter, and the lateral and horizontal gaps [41].

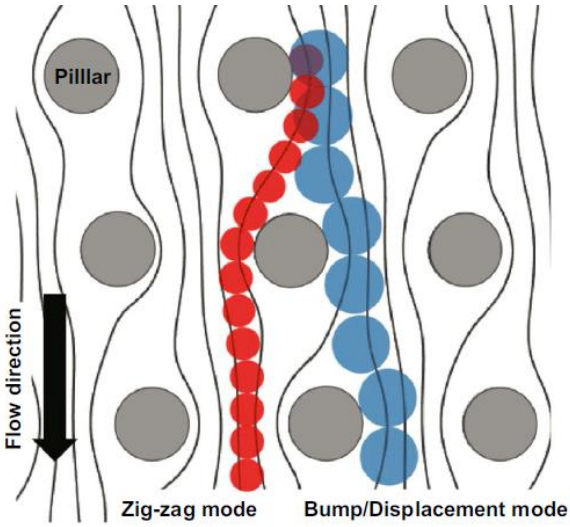

Figure 1.5: Displacement modes observed in DLD. Small particles zig-zag between the pillars while large particles collide with the pillars and show a lateral displacement mode. Figure reproduced from [41].

The separation of non-deformable particles is independent of the flow rate, but this is not the case for deformable particles such as cells. The shear stress generated when high flow rates are employed can alter the cells shapes and reduce their effective diameter, altering their behaviour in the DLD system and switching from lateral displacement mode to zigzag mode (Figure 1.6) [42]. Other parameters that influence the deformability of cells are the fluid viscosity and the capillary number [43]–[45]. Red blood cells have been shown to exhibit both zig-zag and lateral displacement in the same DLD array for different fluid viscosity ratios [46]. The use of different pillar shapes such as triangle, diamond, airfoil shape and I shape has also been

shown to improve the separation of cells based on their deformability [47]. For example, the use of airfoil-shaped pillars has been used to reduce the deformation of cells, whilst I-shaped pillars were used to propel blood cells causing them to rotate and displace laterally following the pillar's angle [47], [48].

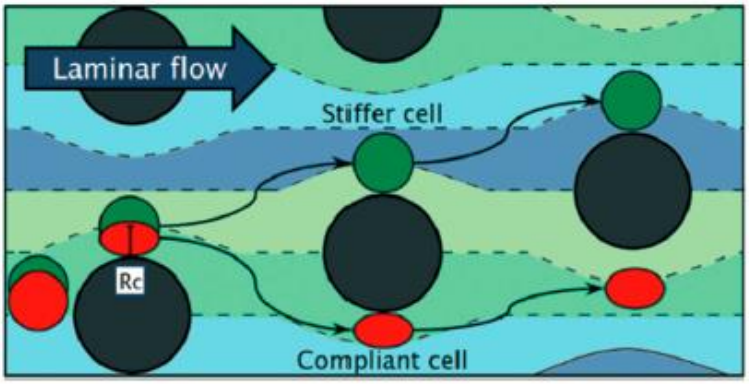

Figure 1.6: Particle sorting by deformation using deterministic lateral displacement. The effective particle radius of the deformable cell (shown in red) decreases due to the shear stress and becomes smaller than the critical diameter of the DLD system and follows a zig-zag displacement. The diameter of the stiffer cell (shown in green) remains unchanged and follows a lateral displacement. Image reproduced from [49].

Deformability-based DLD has been widely used to sort and concentrate cells such as circulating tumour cells, red blood cells and white blood cells [50]–[52]. Civin and colleagues (2016) showed the separation of leukocytes using an inexpensive DLD microchip with a recovery rate of 88% of the input leukocytes [51]. In a recent paper, Xavier and colleagues (2018) investigated the use of DLD to concentrate circulating tumour cells and skeletal stem cells [49]. They achieved the separation of human osteosarcoma cell lines (MG-63) from HL-60 with a 98% purity for flow rates >30 µL/min. However, when they tried to purify skeletal stem cells from white blood cells, the purity of the stem cells was only 73% and decreased at flow rates higher than 15 µL/min, so the separation of MSCs from white blood cells remains a challenge despite the differences in size and deformability.

The separation resolution of DLD is considerably better than that observed for other size-based separation techniques such as cell straining or density gradient centrifugation [49]. Moreover, the cost of fabrication is low, and since the devices do not contain any biological markers, they have a long shelf-life and are easily transportable, which makes it a very promising method for the separation of MSCs from bone marrow. However, there are still some

limitations of using DLD such as low throughput or pillar clogging. The use of pillar structures in DLD arrays increases the fluid resistance compared to other microfluidic techniques, which limits the overall throughput. DLD is commonly operated with flow rates in the range of the tens of µL/min. At higher flow rates, the formation of micro-vortices behind the pillars change the fluid streamlines and the device performance [53]. Moreover, to avoid particle crowding and clogging of the devices, most DLD separation studies use diluted samples, further decreasing the overall cell separation throughput [41]. Another challenge of DLD is that despite the use of surface treatments such as passivation of the pillars using surfactants such as PEG or tween-20, particle clogging still remains an issue due to the small gap between the pillars [54].

1.2.2.4 Limits of density and size-based separation technologies

To date, the main limit of density and size-based technologies is their low selectivity. The difference in cell size and density (as shown in Table 1.1) is typically not big enough to achieve a high throughput separation with high selectivity. However, density based technologies can be used as a first step in a multiphase separation, when the volume of bone marrow available is substantial or when the number of cells required is limited.

Cell type	Diameter (range) (µm)
Neutrophil	8.4 (7.3-9.7)
Eosinophils	10-12
Basophils	8-10
Lymphocyte	7.3 (6.8-7.8)
Monocyte	8.79 (7.72-9.99)
Erythrocytes	7.81 (+-0.63)
Megakaryocytes	19.4 +/- 3.0
Mesenchymal stem cell	15-16

Table 1.1: Bone marrow cells' diameter [55].

1.2.3 Antibody-based separation technologies

As an alternative approach, antibody-based technologies exploit the interaction between antigens present at the surface of cells and antibodies. Monoclonal antibodies bind to a single epitope so if the selected epitope is only present on one cell type, they are very specific. This makes them ideal for applications where selectivity is key and the aim is to isolate a specific cell type. Antibodies can be used in cell separation by tagging them to fluorophores or beads, as a means of non-covalent coupling that can be then analysed. However, it is known that antigen-antibody binding can trigger intracellular responses which could in turn result in a change in phenotype and gene expression of the cell. Moreover, once selection has occurred the tagged antibody has to be removed which can often be difficult. This will be discussed in more detail in the proceeding text (section 1.2.3.5). The different antigen markers used to tag the different types of cells found in bone marrow can be found in Table 1.2.

One of the challenges of antibody based separation of MSCs is that there is not any MSC specific marker that can be used to separate them from other cells. The MSC detection panel as described by the International Society for Cellular Therapy is: $VEGF^+$, $CD90^+$, $CD105^+$, $CD271^+$, $CD73^+$, $CD71^+$, $CD14^-$, $CD19^-$, $CD117^-$, $CD133^-$, HLA^-DR^-, $CD34^-$ and $CD45^-$ [42]. These markers are also present in other cell types so this makes it harder to count accurately the number of MSCs present in a bone marrow and to isolate them from other cell types.

Cell type	Markers
B cells	CD2, CD11b, CD19 (not plasma cells), CD24, CD32, CD35, CD40, CD317 CD307, CD305, CD279, CD275, CD274, CD269, CD268, CD267, CD257, CD256, CD253, CD252, CD229, CD218a, CD213a2, CD213a1, CD210, CD200, CD196, CD192, CD186, CD185, CD184, CD183, CD180, CD179a, CD173, CD171, CD166, CD157, CD153, CD152, CD150, CD148, CD139, CD137, CD135, CD131, CD130, CD127, CD126, CD125, CD124, CD122, CDw121b, CD100, CD89, CD86, CD84, CD83, CD81, CD80, CD79b, CD79a, CD78, CD77, CDw75, CD74, CD72, CD71, CD70, CD69, CD62L, CD50, CD49f Activated: CD26, CD28, CD30, CD39
T cells	CD314, CD305, CD304, CD299, CD295, CD279, CD278, CD274, CD268, CD267, CD261, CD258, CD257, CD256, CD254, CD253, CD247, CD244, CD229, CD226, CD223, CD218B, CD210, CD200, CD198, CD197, CD196, CD195, CD193, CD192, CD186, CD185, CD184, CD183, CD182, CD181, CD178, CD177, CD171, CD169, CD166, CD162, CD161, CD159c, CD159a, CD158, CD157, CD154, CD153, CD152, CD150, CD148, CD147, CD146, CD137, CD134, CD130, CD128, CD127, CD126, CD124, CD122, CDw121b, CD109, CDw108, CD107b, CD107a, CD106, CD102, CD101, CD100, CD99, CD98, CD94, CD90, CD89, CD87, CD86, CD84, CD83, CD81, CD80, CDw75, CD74, CD71, CD70, CD69, CD62L, CDw60, CD57, CD56, CD54, CD51, CD50, CD49f, CD2, CD7, CD11b, CDw17, CD27
Dendritic cells	CD317, CD304, CD275, CD274, CD273, CD265, CD257, CD209, CD207, CD206, CD205, CD197, CD196, CD192, CD180, CD172, CD170, CD97, CD80, CD1e, CD8a, CD11b, CDw17, CD39
Leukocytes	CD288, CD167, CD162, CD124, CD106, CD99, CD82, CD71, CD62P, CD62L, CD62E, CD54, CD11a, CD18, CD29, CD43
Lymphocytes	CD322, CD229, CD227, CD169, CD165, CD123, CD103, CD77, CD72, CD52, CD31, CD11a
NK Killers	CD314, CD305, CD274, CD253, CD247, CD244, CD226, CD223, CD218B, CD218a, CD210, CD186, CD183, CD182, CD181, CD177, CD166, CD161, CD159c, CD159a, CD158, CD122, CDW119, CD99, CD98, CD94, CD87, CD81, CD70, CD69, CD62L, CD57, CD56, CD2, CD7, CD8a, CD11b, CD16, CD26, CD27, CD28, CD39, CD30
Monocytic cells	CD312, CD305, CD284, CD273, CD265, CD258, CD244, CD227, CD226, CD213a2, CD213a1, CD210, CD206, CD198, CD195, CD191, CD184, CD171, CD163, CD162, CD154, CD135, CD127, CD122, CD115, CD101, CD100, CD93, CD91, CD87, CD74, CD68, CD65, CD64, CDw60, CD57, CD50, CD4, CD11a, CD11b, CD11c, CD13, CD14, CD15, CDw17, CD24, CD30, CD31, CD32, CD33, CD35, CD36, CD40
Macrophages	CD305, CD210, CD204, CD169, CD163, CD155, CD143, CDw121b, CD105, CD93, CD74, CD70, CD69, CD68, CD64, CD4, CD11a, CD11c, CD14, CD16, CD26, CD36, CD39, CD40, CD23
HSCs	CD318, CD133, CD131, CD117, CD34, CD7
Granulocytic cells	CD182, CD156a, CD107a, CD101, CD88, CD66c, CD66b, CD63, CD52, CD11a, CD11b, CD11c, CD13, CD14, CD15, CDw17, CD24, CD31, CD32, CD33
Neutrophils	CD312, CD282, CD281, CD181, CD170, CD112, CD97, CD93, CD89, CD66d, CD66b, CD66a, CD66, CD15, CD16, CDw17, CD35
Erythroid cells	CD240, CD239, CD238, CD236, CD235, CD173, CD139, CDw108, CDw75, CD55, CD35
Eosinophils	CD294, CD116, CD66, CD64, CD9, CD15, CD23, CD35
Megakaryocytes	CD41, CD42a, CD42b, CD42d, CD51, CD61
Basophils	CD294, CD154, CD125, CD114, CD66, CD64, CD9

Table 1.2: Currently available antigen markers of bone marrow cells as specified in [56]**. HSC = Pluripotent Haematopoietic stem cells.**

1.2.3.1 Fluorescence-Activated Cell Sorting (FACS)

FACS is an antibody-based sorting method requiring cell labelling with fluorophores that is mostly used in laboratory settings for research purposes. Cells must be first incubated with fluorescently tagged antibodies to identify the cell types of interest [57]. For this, if the aim is to purify a specific population, it is important to use monoclonal antibodies specific to a given cell marker and the marker of choice should not be expressed in other cell populations. Alternatively, if the aim is to perform a negative selection, antigens that are not expressed on the cell of interest but present on the remaining cell populations are targeted.

Cell sorting is then performed using a flow cytometer, in which the cells are focussed into a stream of single-cell-containing buffer droplets (Figure 1.7). A laser detects the forward and side scatter fluorescence of each droplet to identify the encapsulated cell. Sorting takes place by deflecting the droplets into collection tubes through the differential application of charge by a wire coil, prior to the droplet passing between a pair of charged plates (Figure 1.7). Each droplet can be charged with a graduated positive or negative potential enabling multiple targets to be separated successfully [58]. FACS requires skilled technicians to operate, as multiple parameters need optimisation for correct cell separation, especially when separating between multiple cell types [57]. Optimisation parameters include the laser power, incidence angle of the forward (FSC) and side scatter (SSC) detectors, gating and compensation.

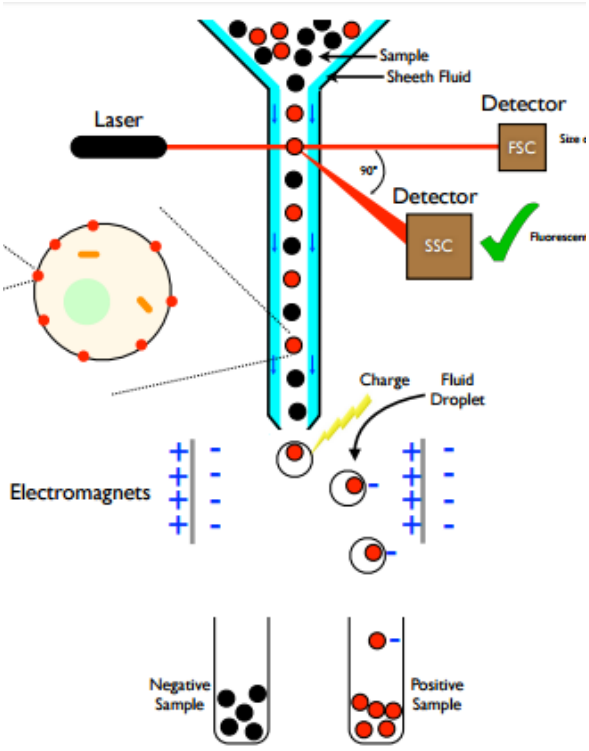

Figure 1.7 : A schematic diagram depicting the separation of a mixture of two cell types using FACS. The mixture of cells is focussed to obtain a single cell stream. The stream is exposed to a laser and the forward and side scatter of the light are detected. Each droplet is charged depending on its identity and attracted to the corresponding electromagnet, falling in the collection tube. Reproduced from [59].

FACS can be used if there is a well-identified marker for the cell in question. Because the separation relies on fluorescence, it is also possible to isolate cells that have low expression of the marker of interest by using a more intense fluorophore. FACS enables high purity separation (95-100%) of the targeted population and can even separate subpopulations [57]. This technique is limited by the same issues observed for other antibody based techniques, as discussed previously (section 1.2.3). In order to circumvent the problems arising from cell labelling of the target cells, these can be purified using a negative selection approach. However, this this would require all the other cell types to be tagged with a fluorescent marker, which requires expensive labelling steps.

Sterilisation and cell viability are key if the aim of the study is to culture the cells after sorting or to implant them into a patient. Sterile FACS can be achieved but cell viability can be affected by the electrostatic fields used for sorting (sometimes reaching 200 V/cm), which compromise the membrane integrity and can result in cell death [60]. Instead, other less destructive

methods of focussing can been used, such as hydrodynamic forces or gravity, but these decrease the collection speed and are only used in research settings [61]. Viability can be further increased by controlling the temperature and by limiting the time the cells remain in the collection tubes [57]. Moreover, by collecting the cells in medium containing serum and mixing the tubes regularly, yield can be enhanced.

Finally, it is important to consider the speed of separation and cost of the technology. FACS is usually used for low volume separation for research. However, the emergence of ultra-high speed FACS has increased the range of applications for this technology, where current spectrophotometers can sort 3.5 10^7 cells/h raising the potential for therapeutic applications [62]. FACS systems are often expensive and bulky, and require a large volume of reagent and sample which can limit their affordability. The current cost of FACS sorters can range from $30,000 to $60,000 depending on the features included. This has prompted the development of more affordable lab-on chip FACS (μFACS), such as the work by Cho et al (2010) [63]. In this work they demonstrated a μFACS disposable system with a throughput of 3.6 10^6 cells/h), low voltage (10 V), high sensitivity and an affordable price [63]. These characteristics would make this kind of device ideal for diagnostic use in hospitals, but would not be optimal for therapeutic procedures requiring a high number of stem cells present in high concentration. Moreover, even if the microfluidics device is inexpensive and can be mass produced, this technique still requires the presence of expensive antibody labels.

1.2.3.2 Magnetic Activated Cell Sorting (MACS)

An alternative, but related approach to FACS, is magnetic activated cell sorting. MACS is based on the use of antibody-labelled magnetic beads and is the current gold standard for clinical cell separation. The surface of the beads is rosetted with antibodies specific to surface antigens on the required cell type. When incubated, the antibodies bind to the antigens and the cell becomes magnetically labelled. The cell mixture is then run through a column surrounded by magnets, where any unlabelled cells are excluded in the flow-through while the labelled cells are retained within the column. The enriched cell population is eluted from the column upon the removal of the magnetic field (Figure 1.8). MACS enables both positive and negative selection through collection of either magnetically labelled cells or unlabelled cells,

respectively, depending on the antibodies utilised. Positive separation has been successfully demonstrated on cell types such as epidermal stem cells, astrocytes, microglia and spermatogonial stem cells [64], [65].

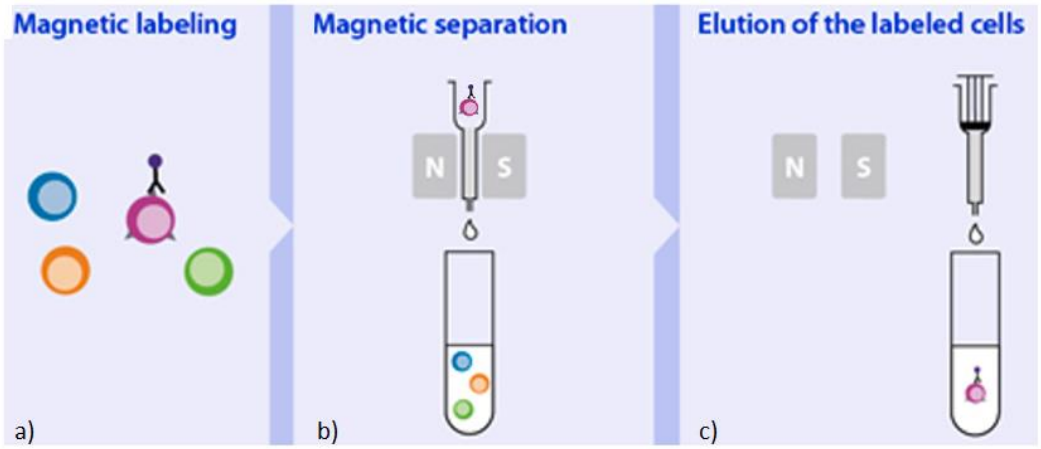

Figure 1.8: A schematic diagram showing positive MACS separation. a) The cells of interest are labelled with antibodies attached to magnetic beads. The mixture of cells is then injected in the column. b) The unlabelled cells are eluted from the column whilst the target cells remain trapped in the column due to the magnets. c) The magnets are removed and labelled cells are collected. Reproduced from [66].

A further application of MACS is immunodepletion, which consists of tagging an unwanted cell type and removing it from the rest of the solution by trapping it in the magnetic column. The use of immunodepletion for purification of samples from erythrocyte contamination has been shown to be more efficient than lysis [30]. When compared to density gradient centrifugation, immunomagnetic depletion has been demonstrated to yield a higher recovery of BMNCs in rats (72% recovery) compared to Percoll (50% recovery) and Ficoll (25% recovery) gradients [30].

One of the limits of this technique is that it is not possible to separate multiple targets in one step. To do this, cells have to be sequentially labelled and separated. Two successive positive selections can be achieved by using a release agent that enzymatically removes the beads from the cells, however the antibody remains attached to the cell [67]. Another way of isolating a particular cell type is by labelling all the other cell types contained in the solution (negative selection). However, this increases the separation time, and requires multiple antibodies and beads which will increase the cost of the separation.

When MACS is used in a single step, 10^9 cells can be separated within 1h, which makes it suitable for separation in intraoperative times. This throughput can be increased further by using multiple columns in parallel or by using quadrupole magnets for continuous cell sorting [68]. In this application, the cells attached to the beads are deflected in a specific direction whereas the rest are collected in another direction. However, it must be considered that the cell labelling can sometimes be time consuming.

All separations can be performed under sterile conditions without major inconvenience. As far as cell manipulation is concerned, currently used magnetic beads are 50 nm biodegradable beads consisting of iron oxide and sugar designed to supress the need to remove them after cell sorting. However, some reports state endocytosis of iron oxide beads can have an adverse effect on cells and lead to cytoxicity [69], [70].

The cost of this technology is relatively cheap and does not require large equipment like in FACS. Beads are available from £50 to £450 (Miltenyi Biotec) and the columns £150 to £550 (25 column packs) and magnets £400 to £1000 but these are reusable. However, cost can sometimes be increased by the need for high quality antibodies for every marker involved in the separation. This is particularly true for negative selection applications which would be required to concentrate MSCs.

1.2.3.3 Pluribeads

Pluribeads is a similar technique to MACS which uses different size beads enabling multiple cell types to be separated at the same time. Each size of bead can be coated with different antibodies so that, once the antibody-antigen recognition takes place, the different cell populations can be retrieved separately using different sized filters (Figure 1.9).

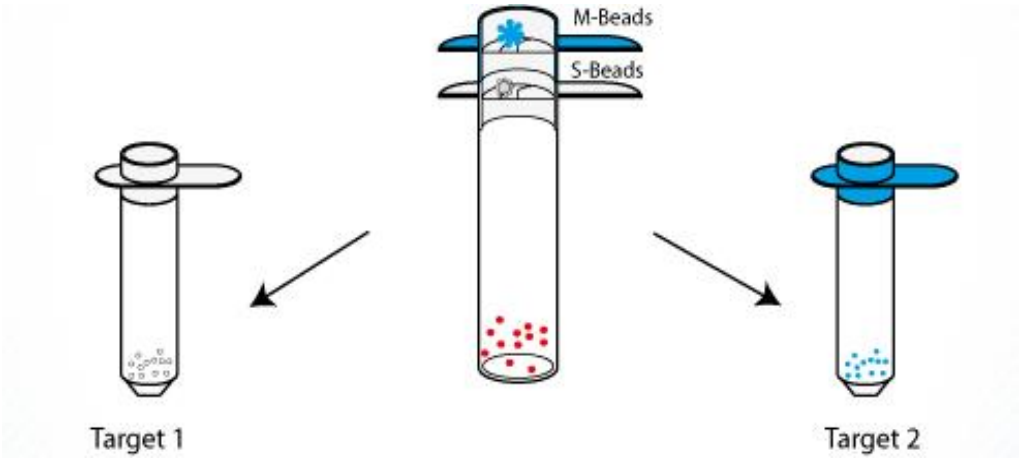

Figure 1.9: A schematic diagram depicting pluribeads separation of multiple targets attached to difference sized beads. Cells tagged with medium beads (M-beads) are retained by the medium filter. Cells tagged with small beads (S-beads) go through the medium filter and are retained by the small filter. Non-labelled cells flow through both strainers. Reproduced from [71].

By using pluribeads it is possible to separate multiple cell types such as PMNs and erythrocytes in one step using different bead sizes [30]. This would result in a one-step approach whereas MACS would require a two-step approach. Pluribeads perform better than centrifugation, producing a purer BMNCs fraction with a yield of up to 70% in rats [30]. However, even though the proportion of MSCs increased, the yields achieved remained low. Where human BMNCs have been separated with pluribeads, BMNCs can be recovered to 60% yields, but the recovery yield of MSCs from those extracted BMNCs was only 45% [30].

1.2.3.4 Affinity chromatography

Cell affinity chromatography is a laboratory based technique which exploits the interaction between receptors present at the cell membrane surface and receptor-specific ligands. The ligands are trapped in a stationary matrix and when the target cell is flushed through the matrix, it attaches non-covalently to the ligands. The cells that do not possess the ligand will elute. One example of this is the use of cells labelled with an antibody and a matrix containing protein A (Figure 1.10). The tagged cells attached to the matrix via antibody-protein A interactions are eluted by adding an excess of immunoglobulin solution.

Affinity chromatography columns can be found in two main configurations: bead packed or monolithic. Bead-packed columns have been reported to induce high shear stress on the separated cells and are time consuming [72]. The other type of columns available are monolithic, i.e. they are made of a continuous and porous matrix. Kumar et al. (2010) developed a protocol to create macroporous monolithic cryogels containing protein A ligands. The technique consists of freezing most of the solvent in order to concentrate the dissolved monomers into the small liquid regions. Once the polymerisation is complete, the solvent is melted leaving a highly porous hydrogel [72]. This gives the cryogel higher mechanical properties and pores of up to 100 µm, which increases the flow rate capabilities of the column. It also enables separation of cells, as the pores are big enough for the cells to flow without getting trapped and experiencing high shear forces. Thanks to these properties, the gel can be compressed to optimise cell recovery.

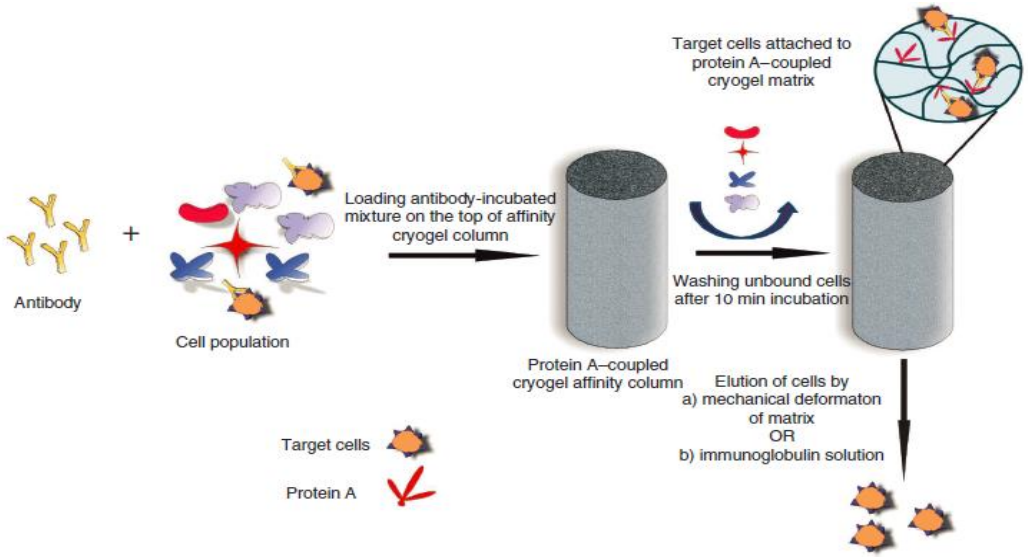

Figure 1.10: A schematic diagram depicting affinity chromatography separation of cells using antibodies and protein A. The cell mixture is first incubated with specific antibodies targeting the cells of interest. The mixture is then loaded onto a column containing protein A motifs. The constant fraction of the antibodies attach to the cryogel thus retaining the target cells while the other cells are eluted. The attached cells are then eluted by displacement with an immunoglobulin solution or by compression of the gel. Reproduced from [72].

Kumar et al. (2010) used this column to separate lymphocytes from other white blood cells and reported a 90% yield and 90% purity for a throughput of 10^5 cells/mL. Moreover, they reported that after mechanically compressing the gel, most of the antibodies remained fixed to the column, so most of the cells collected are not labelled. However, this technology requires the use of

antibody solutions to displace the tagged cells, and the columns can only be reused three times until they lose their properties, which could increase the cost of the technology. It also requires a prior step of concentration using centrifugation, so the overall yield is low.

1.2.3.5 Limits of antibody-based technologies

As discussed previously (section 1.2.3) cell sorting technologies using antibodies are limited by the fact that they can only sort homogeneous cell subpopulations that have a well-defined panel of markers. Antibody-based technologies followed by laboratory amplification lead to highly purified stem cell cultures, unlike other techniques that offer an enrichment rather than a pure population. However, it is not yet known whether high purity of stem cells will lead to a higher rate of healing of bone defects, since the mechanisms of repair are not well understood. It has been argued that other cell types may help increase repair rates by secreting growth factors [7]. Some experiments suggest B cells could have a high impact on bone regeneration within the BMNCs [73]. The presence of other cell types promoting angiogenesis might also be of use when considering osteogenesis, as it is important that blood vessels are also formed to carry nutrients and oxygen to the cells to prevent hypoxia [7]. In order to compensate for this lack of growth factors when using highly purified cells, some approaches include growth factors embedded into the scaffolds [74]. However, this could also lead to negative side effects such as uncontrolled growth, so it is difficult to determine whether this would have an overall positive impact since the mechanisms have not yet been fully elucidated.

1.2.4 Dielectrophoresis

Dielectrophoresis (DEP) is a technique based on the movement of particles in a non-uniform electric field that was first used for the manipulation of cells in 1966 by Herbert Pohl and Ira Hawk [75]. They showed that when particles are in the presence of a non-uniform field, charges accumulate at the interface between the surrounding liquid and the particle, which induces a dipole along the direction of the electric field [76], [77]. If the polarizability of the particle is higher than that of the surrounding medium, the particle moves towards the zones of higher electric field gradient, referred to as positive

dielectrophoresis (pDEP). In contrast, if the cell is less polarizable than the medium, it migrates towards the zones of lower electric field gradient (Figure 1.11), referred to as negative dielectrophoresis (nDEP).

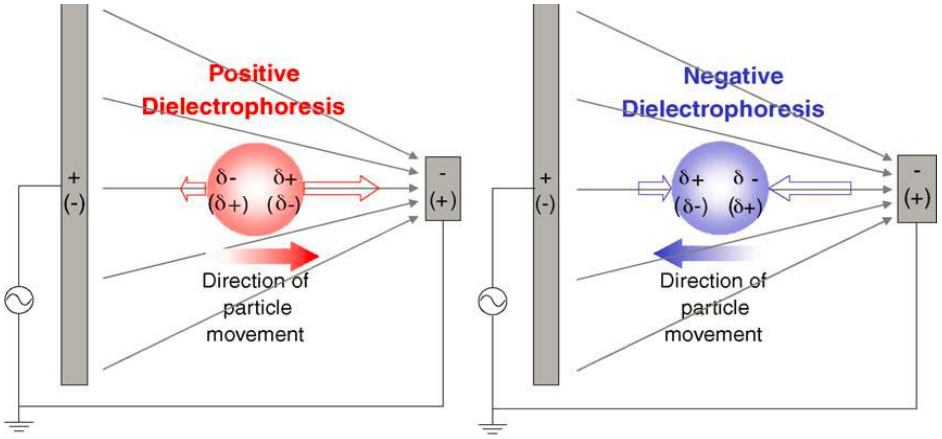

Figure 1.11: A schematic diagram depicting DEP behaviour of cells in a non-uniform electric field generated by a pin and plate electrode pair. When the particle experiences positive dielectrophoresis, it migrates towards the zones of higher electric field gradient. When the particle experiences negative dielectrophoresis, it migrates towards the zones of lower electric field gradient. Reproduced from [76].

The DEP behaviour of a certain cell type depends on the cell's radius and dielectric properties, the voltage applied to the electrodes, the frequency of the AC field used and the conductivity of the medium. The dielectric properties of the cell depend strongly on the cell's structure (including the thickness, protein content, capacitance and conductivity of the membrane) and content (in terms of electrolytes, proteins, organelles and nuclei). This will be further detailed in Chapter 2 section 2.2.1. This allows for different cell types to be separated from each other using this principle. The same cell can experience both negative and positive DEP for a different set of parameters, such as frequency and the medium conductivity and permittivity, which can be optimised for each separation application (Figure 1.12). DEP does not require any labelling, which decreases the cost of the technology, and is able to separate cells depending on their dielectric properties alone. Hence, this approach overcomes two limiting factors of antibody-based separation technologies; one, it is label free, and two, it can separate cells for which there is no specific antibody identified.

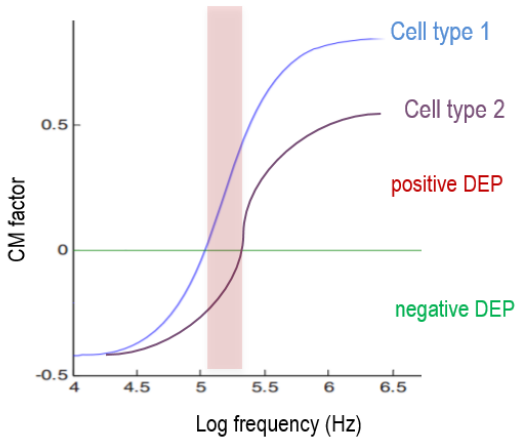

Figure 1.12: Dielectrophoretic behaviour of two different cell types for a range of frequencies. The differences in DEP polarity (positive or negative) can be used to separate both cell types for the range of frequencies highlighted in the red area.

The first experiments of DEP described by Herbert Pohl used pin and plate electrodes and required high voltages to generate DEP forces. The use of photolithographic fabrication allowed to create the first planar castellated and interdigitated electrodes which were designed to create areas of low and high electric field (Figure 1.13). With the miniaturisation of the electrodes, the voltages needed to produce the DEP force were greatly reduced, allowing for higher field non-uniformities without the need for high voltages [78].

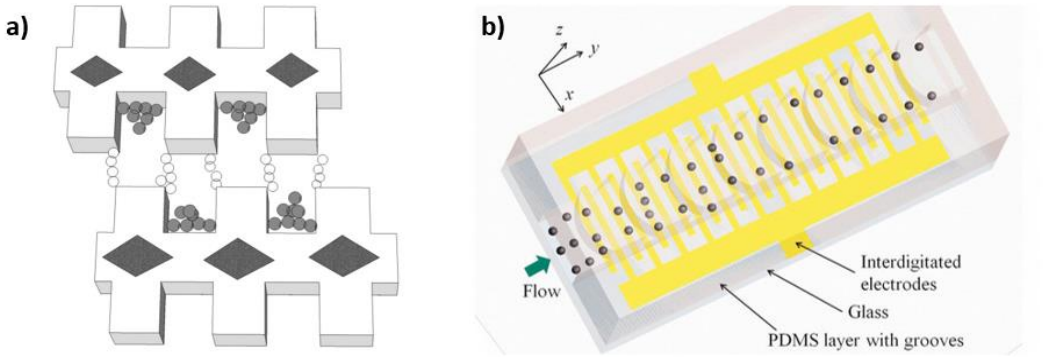

Figure 1.13: a) Schematic diagram depicting castellated electrodes. Cells experiencing pDEP cells (represented in dark) collect at the regions of higher electric field between the electrode edges whereas the ones experiencing nDEP (represented in white) collect at the edges. b) Schematic diagram depicting interdigitated electrodes used for dynamic separation of two cell types. The cells experiencing pDEP are trapped at the electrode edges whilst the cells experiencing nDEP are repelled from the electrodes. Figures reproduced from [79] and [80].

Since the first paper in 1992 showing the first separation of cancer cells using interdigitated castellated electrodes, this field has greatly evolved into different approaches to generate non-uniform electric fields to separate cells

based on their dielectric properties [81]. In this section, the main areas of research involving cell separation using DEP are described.

1.2.4.1 Hydrodynamic DEP

Hydrodynamic DEP requires the use of two inlets filled with liquid surrounding a central channel where the mixture of cells is injected. The sheath flow generated by the surrounding inlets focuses the cells onto the centre of the channel. In the model developed by Doh et al. (2005), the electrodes present at the bottom of the channel have a unique asymmetrical geometry which generates a non-uniform electric field allowing for separation of dead and alive yeast cells [76]. Living cells subjected to pDEP were attracted to the zones of higher electric fields, thus moving towards the edges of the channel while dead cells experienced nDEP and remained in the central streamline (Figure 1.14).

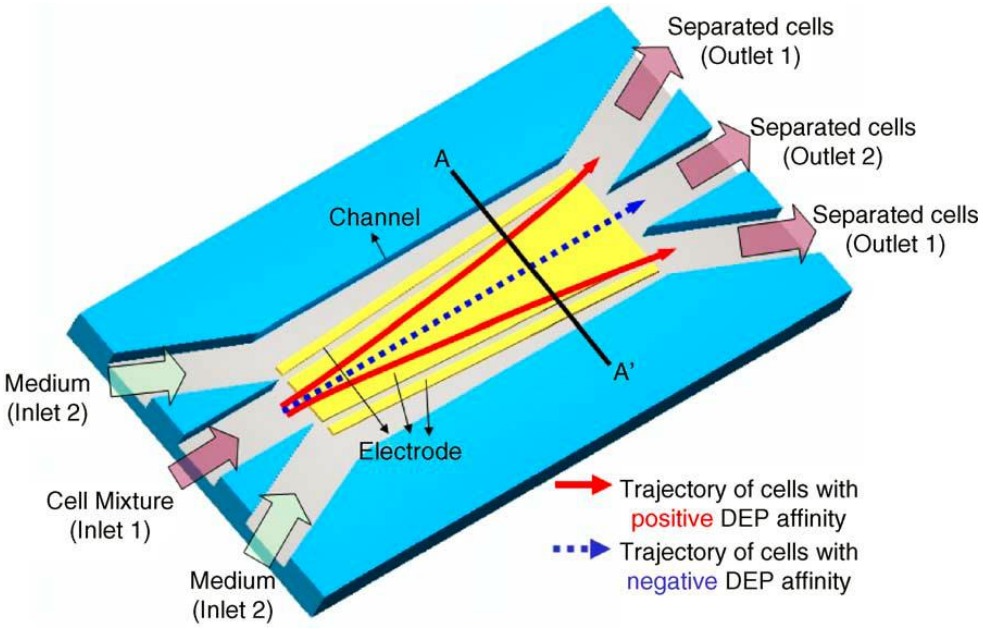

Figure 1.14: A schematic diagram depicting hydrodynamic DEP in a 400 µm wide centre channel. Cells are injected via inlet 1 and focused as a result of the medium coming from the surrounding inlets. The trajectory of the cells in the central stream is modified by the non-uniform electric field generated by the electrodes. Positive and Negative DEP cells are collected in three different outlets. Figure reproduced from [76].

This type of device allows for continuous flow separation, as cells align at different places and are collected via separated outlets, which increases cell throughput. This device was used to separate dead from living cells achieving a purity of 95 % and 70 % of living and dead yeast cells respectively with flow

rates of up to 1 µL/min (2 x 10^6 cells/hour). However, this throughput remains too slow to be considered as a future solution for intraoperative cell separation.

Moreover, for hydrodynamic DEP, the electrodes are in contact with the liquid where the cells are suspended, which can result in Joule heating that can compromise cell viability, as well as electro-chemical effects and bubble formation [82]. In order to limit this, the conductivity of the medium must remain low, which could affect viability. Moreover, there is a risk of electrode fouling (accumulation of cells on the electrodes) when in direct contact with the cells.

1.2.4.2 Flow field fractionation DEP

Field flow fractionation (FFF) was first used by Giddings (1966) to separate blood cells based on density [83]. The separation was based on the fact that denser particles experience a higher sedimentation rate, so they can be separated at different heights inside a channel or column [84]–[86].

To increase the selectivity of the method, DEP was added to the FFF method creating DEP flow field fractionation (FFF DEP), which combined the DEP levitation and gravitational sedimentation forces [87]–[89]. The DEP force depends on the cell's properties, frequency of applied AC voltage and conductivity of the buffer as explained in section 1.2.4. On the other hand, the sedimentation force depends on the density and size of cells as well as the viscosity of the suspending medium. The cells are typically flown at the bottom of the chamber and then repelled by negative DEP until they reach a height where the DEP and sedimentation forces annul each other [90]. The nature of the laminar flow profile then causes cells to move at different velocities depending on their heights. The flow is faster at the centre of the channel whereas it is slower on the sides so the cells can be separated at different speeds (Figure 1.15). The cells experiencing pDEP are found closer to the electrodes (at the bottom of the channel) whereas the ones experiencing nDEP hover at different heights depending on their properties. The height at which the cells align can be modulated by changing the frequency of the field to optimise collection and increase the difference in properties between the cells. It is also possible to switch the frequency for sequential collection of cells. When changing the frequency, some of the cells

that were experiencing pDEP will shift to experiencing negative DEP, enabling separation of cells that exhibit similar parameters.

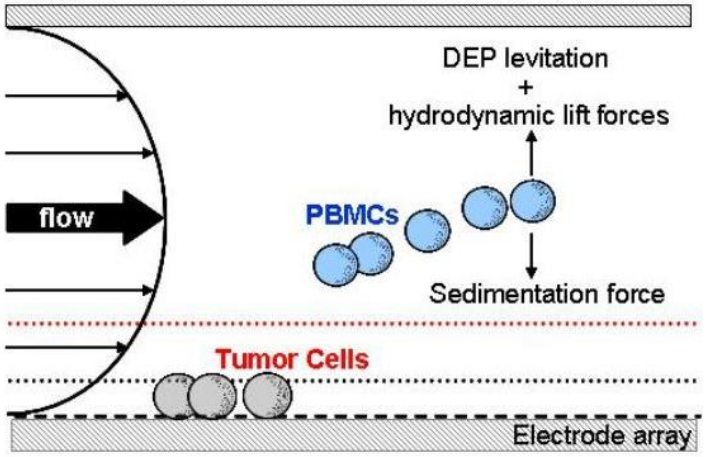

Figure 1.15: A schematic diagram depicting cell behaviour in FFF DEP. In this example, tumour cells experiencing pDEP are found closer to the electrode array. PBMCs are found to levitate due to the nDEP force and are also subjected to the sedimentation force in the opposite direction. The flow profile will then push the cells at different speeds. Reproduced from [91].

DEP FFF of white cell fraction samples has been shown to achieve high purity separation of B cells and T cells with 94% and 92% purities, respectively. Moreover, this technique can be scaled up in order to increase throughput and it does not require big machinery [90]. The limiting factor of this technology is that stabilisation of the cells at the different levels requires ten minutes which lowers throughput. High exposure to electric fields could also have an impact on cell viability.

1.2.4.3 3D electrodes

The throughput of DEP devices using planar electrodes is limited because the electric field gradient generated can only be found at a short distance from the surface of the electrode, which limits the height of the channels used (typically < 50 μm high). To overcome these limitations, different approaches have been taken to revert to the use of 3D electrodes, so that the field generated can penetrate the bulk of the fluid. To generate 3D electrodes, electroplating techniques have been used to generate gold electrode pillars [92], [93]. Gold electroplating techniques are expensive and have low yield so to reduce the costs, the use of 3D carbon electrodes has been proposed. The

3D structures are fabricated by carbonization of pillar structures formed from photoresist SU-8 at high temperatures in an inert atmosphere (Figure 1.16) [94]. These carbon electrodes are low cost, biocompatible and electrochemically stable [95]. An array of carbon electrodes was used to concentrate yeast cells at a flow rate of 5mL/min which is a significantly higher throughput than that obtained for planar electrodes.

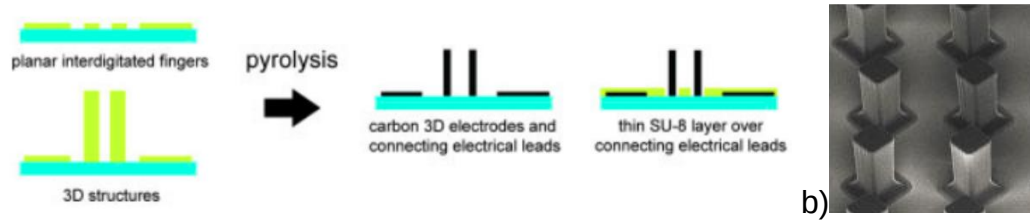

a) b)

Figure 1.16: a) Fabrication process of 3D carbon electrodes using pyrolysis. The fused silica substrate is shown in blue, the SU8 structures are represented in yellow and the carbon structures are represented in black. b) Scanning electron microscopy images of 100 µm high DEP carbon electrodes. Images reproduced from [94].

Another approach to 3D electrode fabrication described by Fatoyinbo et al consisted of drilling holes through alternating layers of conducting and insulating sheets to create “DEP-wells” [96], [97]. The consecutive metal layers are connected to opposite phases of a signal generator to create a non-uniform electric field across the entire channel walls that can be exploited for dielectrophoresis. In this configuration, the cells experiencing nDEP are pushed away from the electrodes towards the centre of the wells where the lowest electric fields are found and can be collected in the flow through. The cells experiencing pDEP are retained on the walls where the highest electric fields can be found (Figure 1.17) and can be eluted in fresh media when the power is turned off.

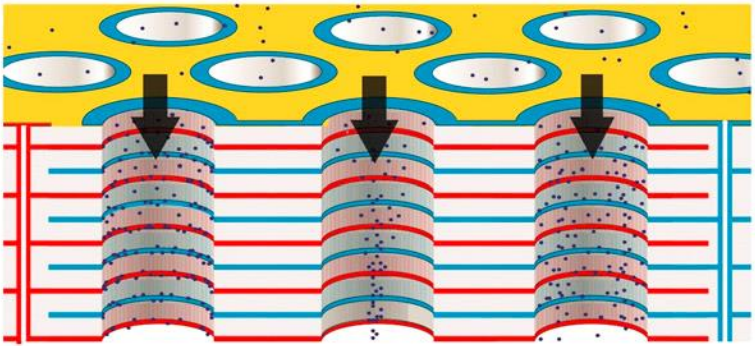

Figure 1.17: Schematic showing cell separation in a DEP-well device. The cells experiencing positive DEP are attracted to the electrode walls while the cells experiencing negative DEP are repelled into the centre of the well and collected in the flow through. Image reproduced from [96].

To achieve high throughput separation, Faraghat et al proposed a chip containing 397 DEP wells of 400 µm diameter and twelve conducting layers. The device was used to separate fibroblasts from RBCs at a flow rate of 1 mL/min and showed a mean recovery of 75.6% for RBCs and 86.4% for fibroblasts with cell losses below 4%. Owing to the low losses, a second pass was performed and showed an increase in purity of RBCs reaching 94%, but the recovery was reduced to 81%, due to the cell loss associated with the volume of the device. This highly parallelised device allowed for a throughput of 10^9 cells/h, which corresponds to a 30-fold increase in throughput compared to other DEP devices [98]. A new iteration of this device is currently commercially available under the name DEParator [99].

1.2.4.4 Contactless DEP and liquid electrodes

Contactless DEP relies on the use of electrodes separated from the channel by polydimethylsiloxane (PDMS) barriers. This technique enables DEP without direct contact between the electrodes and the fluid, thus avoiding electrolysis and electrode fouling [100]. The cells experiencing nDEP are washed through the system, while those experiencing pDEP remain trapped on the surface until the applied power is switched off and they can be collected (Figure 1.18).

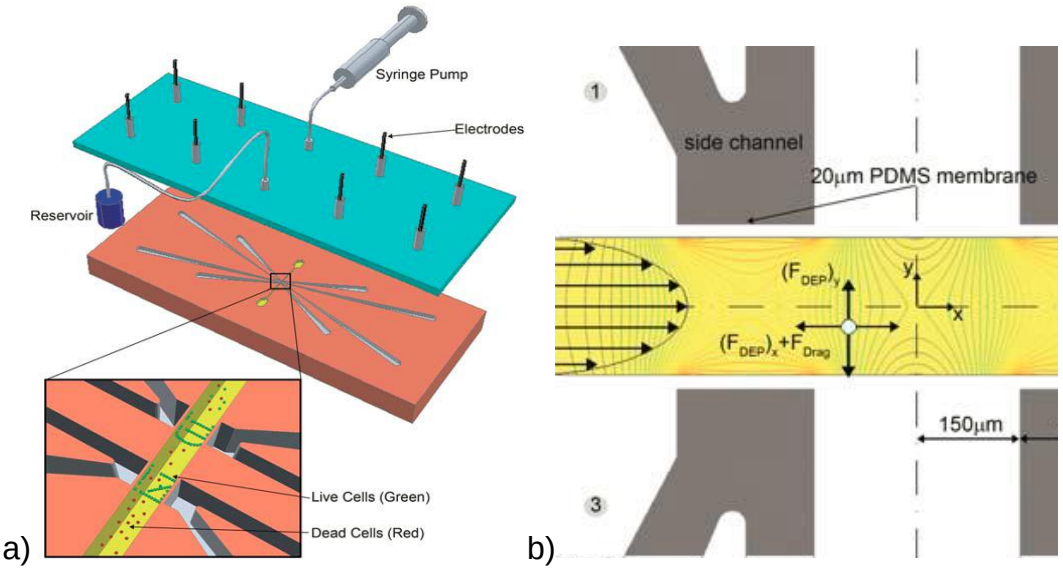

Figure 1.18: a) A schematic diagram depicting a contactless DEP device. The electrodes are arranged inside the side channels of the device. Cells are injected by a syringe pump into a central microfluidics channel insulated from the side channels via a PDMS membrane. The cells experiencing pDEP remain in the channel while the cells experiencing nDEP are collected in a reservoir. b) Forces exerted on the cells: DEP force and drag force caused by the fluid's viscosity. Reproduced from [100].

In this work, a trapping efficiency of 90 % at 0.02 mL/h (18,000 cells/h) was reported. However, the efficiency decreased to 45 % at 0.8 mL/h (i.e. 5.10^5 cells/h) which limits the throughput speed well below that required for intraoperative times scales (~10^8 cells/h). Moreover, when high voltages were used (more than 50 V_{rms}) to increase separation speed, cells began to lyse and the PDMS broke down which indicated a significant transfer of heat to the sample. The authors proposed that this occurred due to the lack of uniformity of the channel, as peak voltages of 350 V were possible in some of the regions, which could cause electroporation.

Another approach to contactless DEP proposed by Demierre et al consisted in using large metal electrodes on the bottom of chamber positioned perpendicularly to the main channel to create "liquid electrodes" [101]. The chambers containing the electrodes are connected to the main channel through access channels and produce a non-uniform electric field in the main channel that can be exploited for DEP separation (Figure 1.19). The vertical plane at the boundary of the access and the main channel is an equipotential surface. This "liquid electrode" plane is equivalent to a vertical metal electrode on the sidewall of the main channel. As for conventional electrodes,

the particles experiencing nDEP will be pushed away from the liquid electrodes and those experiencing pDEP will be attracted towards the electrodes. The hydrodynamic force generated for strong flow rates overcomes the attraction from the pDEP and the particles are simply deviated and collected downstream.

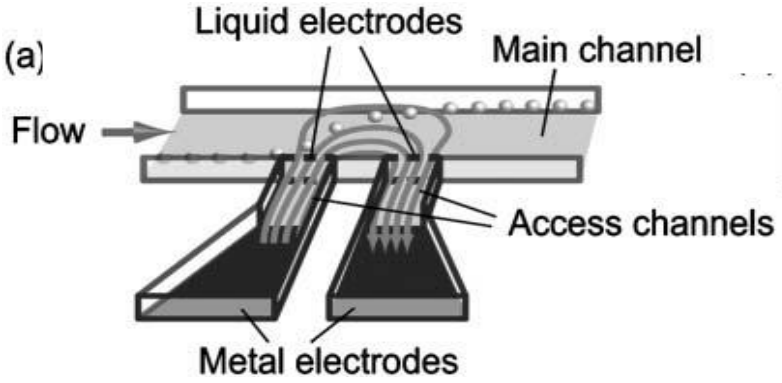

Figure 1.19: Schematic showing the concept of liquid electrodes. Metal electrodes present on chambers connected to the main channel by access channels generate a non-uniform electric field that can be exploited for DEP separation. The liquid electrodes refer to the equipotential surface at the cross-section of the access channels. Image reproduced from [101].

This method was used to generate a combination of DEP forces at multiple frequencies to discriminate between cells based on their dielectric properties [102], [103]. The cells were first focused into a stream by using two low frequency signals from each side to generate nDEP. Then a high frequency DEP signal was chosen to shift the equilibrium position of the particles based on their dielectric responses at the given frequency and the sorted particles were collected in different channels (Figure 1.20). This device was used to separate dead from alive yeast with 100% purity and to enrich a solution of red blood cells infected with *Bavesia bovis*, showing an 8-fold enrichment in continuous flow separation [104].

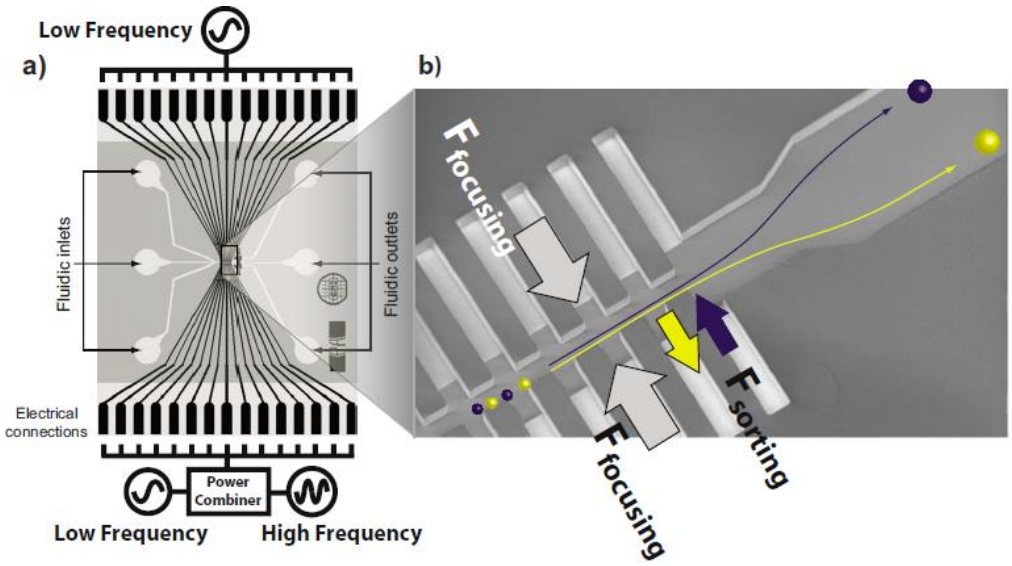

Figure 1.20: Schematic of the cell sorting device using liquid electrodes. The cells are first focused towards the centre of the channel using two low frequency signals and then sorted using a high frequency signal to deviate the cells depending on their dielectric properties, allowing them to be collected in different outlets. Image reproduced from [105].

The use of large metal electrodes results in lower impedance, which allows for operation at lower frequencies. Other problems encountered in conventional DEP such as electrode fouling and hydrolysis are bypassed by the use of separate chambers, because the cells are never in direct contact with the electrodes. Moreover, since the liquid electrodes can be considered as vertical electrodes, the height of the channel can be increased without losing the electric field strength, thus increasing the particle throughput while maintaining the DEP force efficacy.

1.2.4.5 Insulator DEP

The first account of insulator DEP (iDEP) was described by Masuda and Washizu in 1989 and consisted of trapping cells using DEP generated by an electric field constriction between two insulators [106]. Cummings et al later proposed the use of an array of insulating posts in order to increase the throughput [107]. Instead of using electrodes to generate non-uniform electric fields, iDEP relies on the use of insulators to distort the direct-current (DC) electric field generated by electrodes present at either end of the channel (Figure 1.21) [106], [108]. The zones of higher electric fields are found between two opposing insulators, trapping the cells experiencing pDEP. The

zones of lower electric field are found at the centre of four insulators, where the cells experiencing nDEP are trapped.

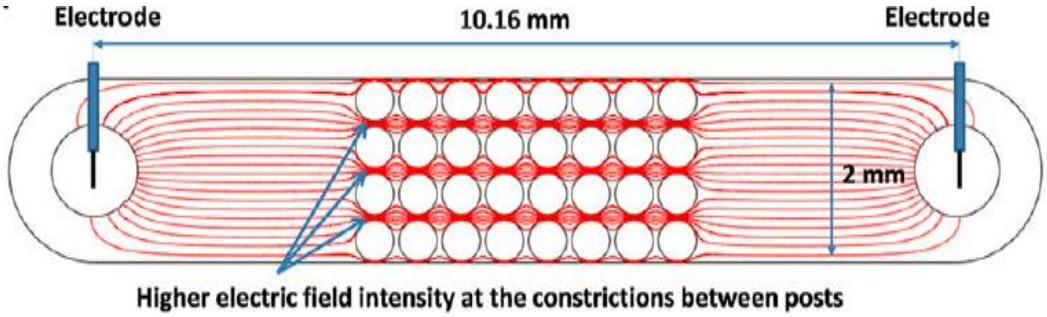

Figure 1.21: A schematic diagram depicting an insulator based-DEP device using insulator rods. A uniform electric field is generated by electrodes at both sides of the channel. The field is then distorted, creating zones of higher and lower electric field that can be exploited for DEP separation. This image was reproduced from [109].

This technology has been widely used to separate different bacteria and yeast cells [110], [111]. The cells were first injected separately to determine which electric field intensity was required in order to trap the cells in the zones of negative DEP. Different cell types required increasing electric forces so by using the highest electric force, all cells were trapped and could be eluted sequentially by decreasing the force, thus achieving concentration of the different cell types [110].

To increase the throughput, Jen et al. (2010), combined iDEP with hydrodynamic separation forces to sort cells continuously [112]. In this case, some cells were trapped in the pDEP regions while the others were trapped in the nDEP regions. The cells experiencing pDEP remained trapped while the ones experiencing nDEP were flushed out and collected. However, this approach required additional steps to get rid of the cells accumulating on the pDEP regions. This means that the trapped cells are exposed to high fields for longer periods in an iDEP device than is generally the case with an electrode-based device, which could affect their viability. Another approach to continuous cell concentration using iDEP was proposed by Barret et al, who used ridge-like insulators of different heights to selectively confine some of the particles to a specific channel while the rest of the particles were free to flow in all directions [113].

Despite the use of continuous cell sorting, the throughput of 2D iDEP devices remained low, and to generate the electric fields, the use of high voltages was necessary, so research moved towards the exploitation of three

dimensional iDEP. Agah et al proposed a device consisting of PDMS micro-posts and electrodes passivated with a thin glass slide (Figure 1.22) [114]. The use of high micro-posts generated high electric field gradients without the need of high voltage requirements and the device showed a 100% trapping efficiency of *Staphylococcus aureus* between the micro-posts at throughputs up to 740 µL/h.

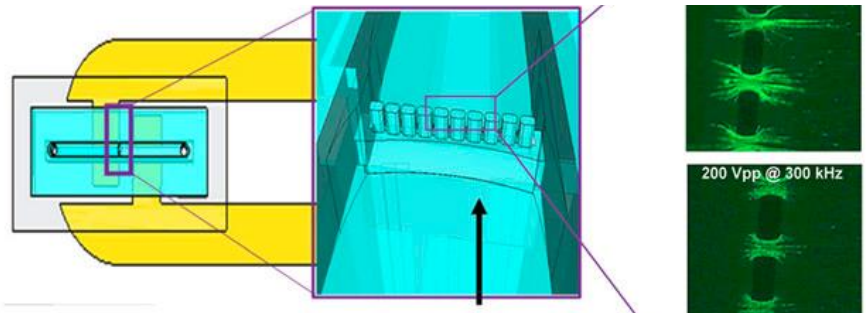

Figure 1.22: Illustration of a 3D iDEP device used to trap *Staphylococcus aureus* cells (stained in green in the fluorescence microscopy images) in a 2.2 mm wide channel. The electric field is generated by the passivated electrodes (represented in yellow) and is distorted by the PDMS micro-posts. The arrow represents the fluid flow. Reproduced from [114].

Another approach to 3D iDEP is the use of chambers packed with beads made from an insulating material such as glass, which was first reported by Suehiro et al [115]. The device consisted of two parallel plate electrodes encasing a reservoir containing the insulating beads. In this system, the electric field gradients were generated at the constrictions between adjacent beads. A similar system was reported in 2007 by Iliescu et al, showing a trapping efficiency of up to 75% with flow rates in the ranges of 1 mL/min and potentials of 220 V showing great promise for high throughput separation (Figure 1.23) [116].

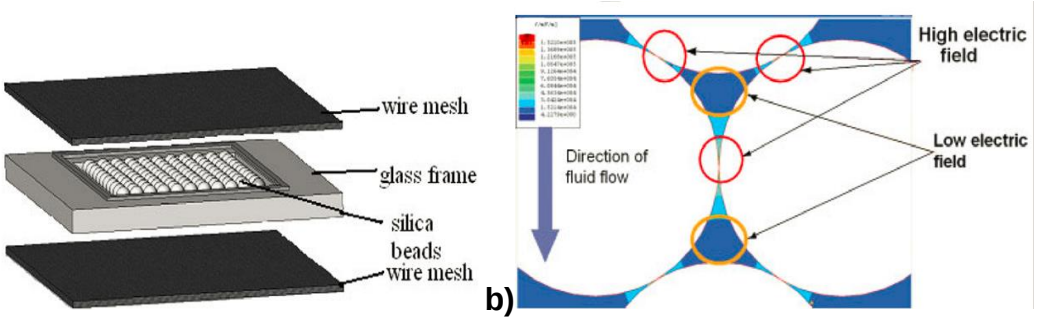

Figure 1.23: a) Schematic of a 3D iDEP device made of two plate electrodes and a chamber packed with insulating beads. b) schematic showing the low and high electric field regions between the insulating beads. Reproduced from [116].

Insulator DEP offers a solution to avoid some of the major limitations of DEP applications requiring the use of microelectrodes, such as fouling, sample hydrolysis or delamination of electrodes due to large current densities [101]. Moreover, iDEP devices are cheap to fabricate as they can be mass-produced using fabrications like injection moulding and no metal microelectrodes are required [117]. However, iDEP has also limitations such as the use of very high voltages needed to create the electric field gradients necessary for DEP, which can be dangerous to manipulate and also result in costly equipment. Despite improvements such as the use of 3D designs, the voltages needed remain high. These high voltages are associated with Joule heating, which can affect cell viability and also create electrothermally induced fluid motion affecting the electroosmotic flow [118]. Recent studies of joule heating showed that fluid temperatures in iDEP devices can result in a temperature rise of 37°C or more, which could significantly impact the viability of the collected cells [118], [119].

1.2.5 Impedance flow cytometry

Impedance is defined as the complex ratio between the voltage and the current in an alternating or direct current circuit. Impedance flow cytometry is the measurement of the impedance of single or multiple cells suspended in a medium or adhered to a surface [120]–[122].

The first instance of use of impedance flow cytometry to characterise cells was in 1956, when Coulter developed a cell counter relying on the measurement of cell impedance at zero frequency (direct current) to determine the cell's volume [123]. Since then, improvements to the original coulter counter involving the use of alternating electrical current (AC) of high frequencies and the miniaturisation of the electrodes and their integration into microfluidics walls were made. The coulter counter is now a standard method for cell volume determination and is used routinely for blood analysis [124], [125]. In 2001, Gawad and colleagues determined the impedance of cells in suspension using two pairs of electrodes energised with a voltage at a certain frequency (Figure 1.24) [126]. One pair of electrodes is used to sense the changes in electric current caused by the cell passing through the electrodes, and the other is used as a reference.

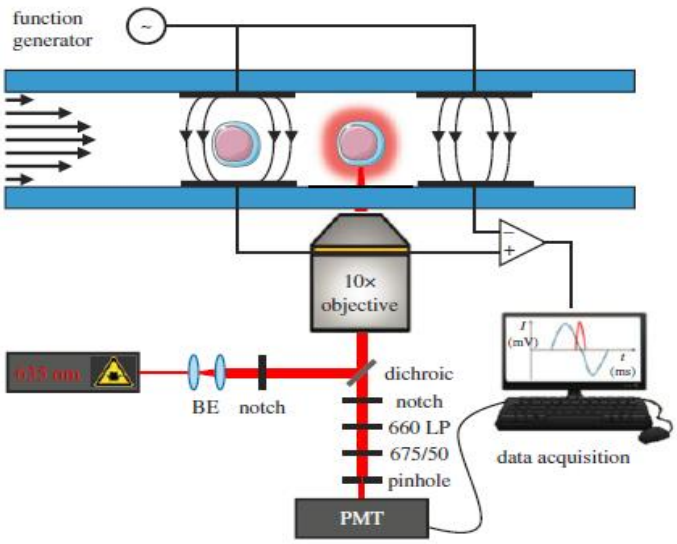

Figure 1.24: Schematic diagram of an impedance flow cytometry set-up described in [127]. When the cells flow through the first pair of electrodes in the microchannel, the electric current fluctuates and the change in impedance caused by the passing cell compared to the reference electrode gives an impedance spectrum that can be used to identify the cell based on its size and dielectric properties.

Different cell types can be identified based on their size and intracellular dielectric properties, which affect the impedance measured between the sensing electrodes [128], [129]. This technique has applications in cell biology, cancer research, drug screening, cell counting and sorting but the most common application is the discrimination of white blood cells for blood cells counting [128], [130]–[132]. In 2001, Holmes and colleagues used a microfluidic impedance flow cytometer to count the different white blood cells populations based on their impedance for two frequencies [128]. The double frequency analysis allowed for determination of differences between the cell types (monocytes, T and B lymphocytes, neutrophils, eosinophils and basophils) in terms of cell size and also membrane capacitance. Separation of lymphocytes from the other white blood cell populations was easy due to the differences in cell size, but to differentiate monocytes from neutrophils, a preliminary treatment of whole blood using saponin (routinely used for cell lysis) was necessary to increase the differences in membrane capacitance between the two populations. Following red blood cell lysis, the impedance cytometer was able to discriminate between the different white blood cell populations with a 95% correlation between the impedance analysis and the standard haematological analysis. However, this analysis was done at very

low flow rates (25 μL /min) and is better suited for cell counting and analysis of low volumes of blood rather than a cell separation method [133].

Aside from blood cells, impedance cytometry has been shown to successfully identify changes in dielectric properties such as membrane capacitance and cytoplasmic conductivity associated with cell differentiation and expression of TRP channel protein in stem cells, making it a potential label – free alternative method to FACS for the identification of stem cells in their earlier undifferentiated state [134]–[136].

1.3 Surface Acoustic Wave-induced Dielectrophoresis (SAW-DEP)

DEP generated by SAWs (described in section 1.2.2.2) on a piezoelectric substrate has previously been observed when aligning multi-walled carbon nanotubes [137]–[139]. The SAWs were generated by applying an alternating potential on a piezoelectric material. This causes the material to compress and expand alternatively following the potential applied.

In these experiments, the force of the pressure wave generated was found to be stronger than the DEP force and therefore drove the alignment of the tubes. The tubes aligned along the SAWs antinodes but also oriented following the electric field generated by the SAWs travelling along the surface of the piezoelectric material. However, the force generated by DEP in this case is magnitudes smaller than the pressure force so it could not be exploited for cell alignment.

In order to use the DEP force to drive alignment, it is crucial to eliminate the acoustic pressure generated by the SAW. Smith et al. (2017) proposed a technique in which the surface acoustic wave generated was on the horizontal surface plane [140]. This eliminated the acoustic pressure wave generated in the vertical direction. By using IDTs patterned on a piezoelectric material, the horizontal surface acoustic waves induced a vertical evanescent electric field (described in more detail in Chapter 2 section 2.3). The two IDTs generated opposing shear-horizontal waves thus creating a standing wave which in turn gave rise to a periodic, non-uniform electric field enabling DEP separation. The result was a separation via DEP, as described previously (section 1.2.4) generated in a similar way to the previously described SAW setups (section 1.2.2.2). Cells experiencing positive DEP align in the

antinodes of the electric field, while cells experiencing negative DEP align in the nodes (Figure 1.25).

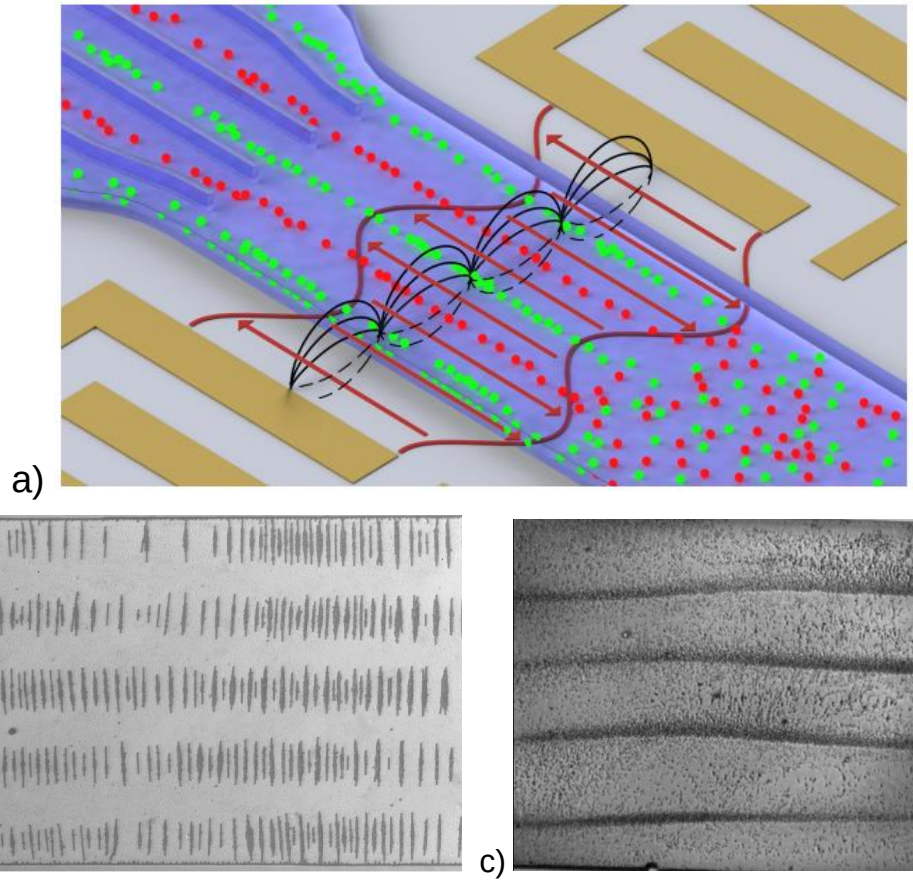

Figure 1.25: a) A schematic diagram depicting the SAW-DEP device designed by Smith and colleagues. The SAW (in dark red) generated by the gold IDTs induces a vertical electric field (in black). Cell type 1 (in red) experiences positive DEP and aligns at the nodes. Cell type 2 (in green) aligns at the antinodes. Figure reproduced from [141]. b) Alignment of alive horse red blood cells experiencing pDEP at the antinodes. c) Alignment of latex beads experiencing nDEP at the nodes.

This example of remote DEP does not require the electrodes to be in contact with the liquid, so high conductivity buffers can be used with negligible Joule heating as demonstrated by simulations [140]. This arrangement also eliminates the fouling of the electrodes which was a considerable issue with previous designs. The authors demonstrated the applicability of the SAW-DEP approach by separating dead from live dental pulp stromal cells (DPSCs). The cells were separated in sterile conditions using a buffer with a conductivity of 0.15 S/m and at a frequency of 10 MHz. Viable cells were shown to align in the positive DEP regions generating a collected enriched population of 98% purity. Separation was carried out under a continuous flow of 2.10^6 cells/h, which offers a promising throughput but which still falls short

of the current gold standard of MACS separation (section 1.2.3.2). Optimisation of this throughput is one of the key aims of this PhD project in order to process clinically-relevant numbers of cells required.

Viability of the SAW-DEP sorted cells was investigated and was not found to be significantly lower than the control sample containing unseparated alive cells. The osteogenic potential of the DPSCs was then compared to that of non-sorted controls. An alkaline phosphatase assay showed that both the control and SAW-DEP separated DPSCs demonstrated the same osteogenic potential. In order to widen the applications of this method to select for specific cell types, it would be necessary to determine the dielectric properties of the cells that need to be separated. Approaches to achieve this are discussed in the following section.

1.4 Determination of cells' dielectric properties

As discussed in section 1.2.4, the DEP force depends on the medium conductivity, electric field, frequency used and the dielectric properties of the cell. In order to exploit the differences in DEP force between cell types it is important to determine the dielectric properties of a specific cell type to tailor the frequencies and conductivities best suited for cell separation. The dielectric properties of a cell can be extracted from DEP spectra showing the dielectrophoretic behaviour of cells for different frequencies and medium conductivities. The different methods available for the characterisation of cells properties are discussed in this section and an in-depth review of the theory behind the determination of dielectric properties from DEP spectra can be found in chapter 2 section 2.2.2.3.

1.4.1 Standard dielectrophoresis

The simplest method to determine the DEP spectra for particles in suspension consists of counting the number of cells collected at either the surface of the electrodes (positive DEP) or between the electrodes (negative DEP) for different frequencies (Figure 1.26). The determination of the frequencies at which the cells switch from experiencing positive DEP to negative DEP (crossover frequencies) for different conductivities is essential for the determination of the cells dielectric properties such as the membrane

capacitance and cytoplasm conductivity [142], [143]. Details on the relationship between the crossover frequencies and the dielectric properties are discussed in more detail in Chapter 2 section 2.2.3.

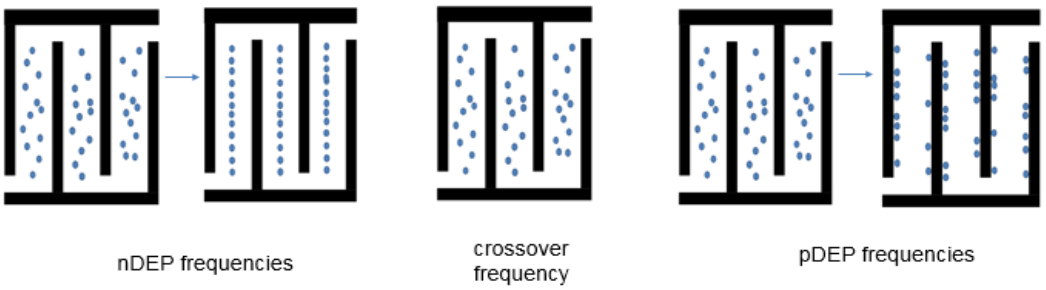

Figure 1.26: Schematic showing DEP behaviour of particles for different frequencies. For low frequencies, the cells experience negative DEP (nDEP) and align between the electrodes. At the crossover frequency, no DEP force is exerted on the particles and they remain immobile. At higher frequencies, the polarity is reversed, cells experience positive DEP (pDEP) and they align at the edge of the electrodes.

This technique can be further improved by monitoring the displacement of the particles using a camera and a tracking algorithm [81], [102], [144]. However, it is important to consider that co-planar electrodes create fields that are localised within a short distance from the plane of the electrodes, so if the cells are too far from the electrodes, they will be unaffected by the DEP force while the ones present in the electrode vicinity will align very fast. This means that the determination of the higher DEP forces based on the particle movement is often difficult, due to the limitations in the camera resolution and frame-rate and the tracking algorithm [145].

Moreover, due to the variation between individual cells, in order to determine the dielectric properties of a given cell type, multiple cells need to be studied to obtain statistically significant results. Since each the behaviour of the cells needs to be determined at different frequencies, this can be very time consuming, and can take up to an hour. Moreover, if cells are left in low conductivity media for a hours, the risk of ion exchange between the highly ionic cytoplasm and the suspending medium increases, resulting in a decrease of cytoplasm conductivity and creating artefacts that can affect the measurements [145].

1.4.2 Electrical impedance spectroscopy

Electrical impedance spectroscopy (EIS) is a multiple frequency sweeping technique that can be used to determine the dielectric properties of cells [146]–[151]. As shown in section 1.2.5 for impedance flow cytometry, two pairs of electrodes are used; one pair senses the changes in electric current caused by the cell passing through the electrodes, and the other pair is used as a reference.

The impedance of cells in suspension is measured for different excitation signal frequencies and the resulting spectrum is used to provide information about the membrane capacitance and resistance, as well as the conductivity and permittivity of the cytoplasm (Figure 1.27) [129].

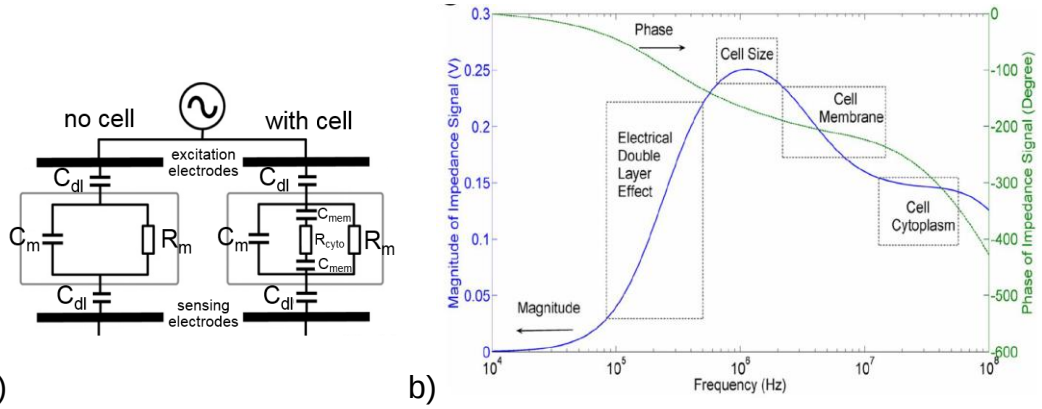

a) b)

Figure 1.27: a) Schematic of a cell impedance detection system consisting of two pairs of electrodes, reproduced from [129]**. The cell is represented by an equivalent circuit model of membrane capacitance C_{mem} and cytoplasm resistance R_{cyto} and the medium is represented as having a resistance R_m and a capacitance C_m. C_{dl} is the electrical double layer capacitance at the interface between the media and the electrode. When a cell goes through a pair of electrodes, the impedance of the system changes and can be compared to the reference electrode. b) Impedance spectrum of a single cell for different frequencies and the influence of the different cell properties on the shape of the curve. Image reproduced from [134].**

In order to extract the dielectric properties from the impedance spectra, an equivalent circuit model of the cells is used (Figure 1.27) [152]–[154]. In the model described by Forster and Schwan, the cell can be modelled as a capacitor (representing the cell membrane) and a resistance (representing the cytoplasm) in series [150]. The values of impedance obtained for low frequency input signals (below 1 MHz) give information about cell volume [155]. The impedance obtained for intermediate frequencies (1 to 20 MHz) is mostly dependent on the membrane capacitance while the higher

frequencies (above 100 MHz) are used to characterise the resistance of the cytoplasm [156].

Electrical impedance spectroscopy has been used to study the dielectric properties of white and red blood cells, human breast cancer cell lines, dendritic cells, fibroblasts, adipocytes and stem cells [86], [128], [89], [94], [95]. In 2017, Xavier and colleagues characterised the size and dielectric properties of skeletal stem cells in bone marrow before and after cell expansion using a high-throughput microfluidic impedance cytometry device and showed that there were differences associated with cell expansion [127]. EIS can discriminate cells based on dielectric properties and can be used to determine the best conditions for separation in an impedance flow cytometer. However, the measurements are strongly influenced by the electrode size and the cell volume, so it is difficult to obtain precise values of the dielectric properties for the design of DEP electrodes for separation [157]. Moreover, even if this technique is faster than conventional DEP, multiple cells need to be measured to obtain statistically significant results and each set of measurements can take up to 30 minutes to record [128].

1.4.3 Electrorotation

Electrorotation was developed in 1988 by Arnold and Zimmermann to trap a single cell and then determine its rotation speed in response to different frequencies of rotating electric field [158]. Moreover, since electrorotation is a single cell measurement technique, by imaging the cell, information about its morphology such as radius, surface area and roughness can be obtained at the same time [159]. Numerous electrorotation devices have been used to determine the dielectric properties of cells [157], [160]–[166]. In the method proposed by Han et al. (2013), a 3D octode consisting of two sets of identical quadrupoles (Figure 1.28) layered on top of each other and connected in parallel was used [161]. In order to trap and levitate a single cell, two sets of out of phase signals with equal amplitude are applied to the quadrupoles (Figure 1.28, orange and green). This creates a repulsive force that pushes adjacent cells away, trapping the cell in the middle where the field is smaller. This levitation is important to reduce surface-drag on the cell during subsequent measurements. The cell is then rotated using four signals with a 90° phase difference which are generated in each one of the electrode pairs (Figure 1.28, 1 – 4), creating a torque on the cell causing it to rotate.

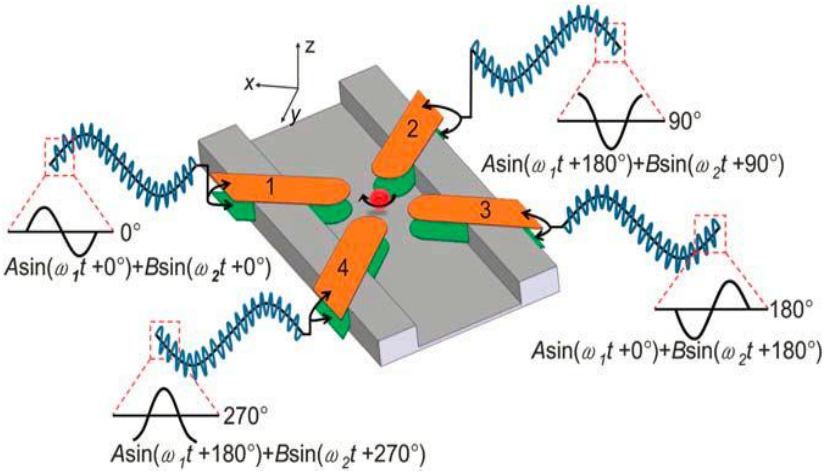

Figure 1.28: A schematic diagram depicting the octopole design described by Han et al. (2013). A cell (red) is trapped in the centre due to two out of phase signals: A sin ($\omega_1 t$ + 180°) and A sin ($\omega_2 t$ + 180°). This waveform is represented in black. The cell is then subjected to a torque created by 4 electrorotation signals: B sin ($\omega_1 t$ + 0°), B sin ($\omega_2 t$ + 90°), B sin ($\omega_3 t$ + 180°), B sin ($\omega_4 t$ + 270°) (waveform represented in blue). Rotational direction of the cell is represented with a black thick arrow. Reproduced from [129].

The expression of the DEP torque generated described by Morgan and Green is [167]:

$$\Gamma\,(\omega) = -4\,\pi\,\varepsilon_m^*\,r^3 Im(f_{CM}) \text{ and } \varepsilon^* = \varepsilon - j\frac{\sigma}{\omega} \quad (1.2)$$

Where ε_m^* is the complex medium permittivity, r the radius of the particle, σ represents the conductivity, ω is the electric field frequency of the alternating electric current (AC) and $Im(f_{CM})$ is the imaginary part of the Clausius Mossotti factor (f_{CM}), described in more detail in Chapter 2 section 2.2.1.

The rotation rate (R) of a particle in an electrorotation device composed of four electrodes is:

$$R = -\frac{\varepsilon_m k^2 V^2}{2\,\eta} Im(f_{CM}) \quad (1.3)$$

Where η is the viscosity of the media, k is the constant related to the position of the particle within the specific electrode geometry and V is amplitude of the signal. The rotation speed depends on the frequency of the applied signal, electrode geometry, the viscosity of the media and the cell's intrinsic properties. From the above equation (1.3) the dielectric properties of a single cell type can be determined without interference from other cells [161]. The rotation speed of the cell is recorded for specific time intervals at various frequencies to determine a rotation spectrum (Figure 1.29).

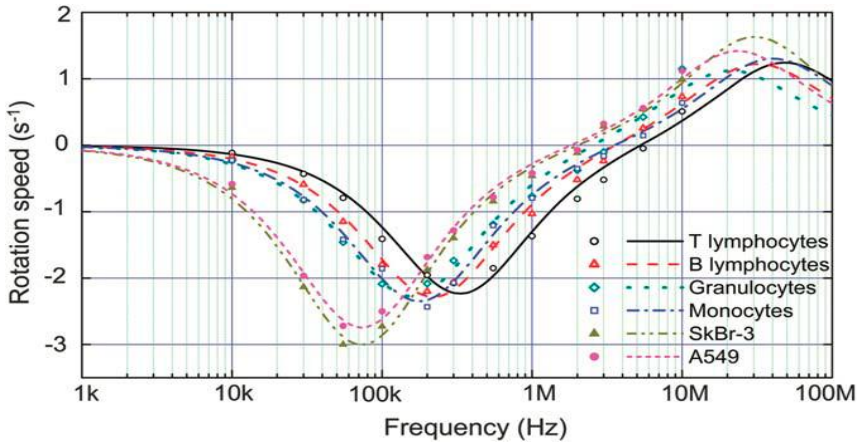

Figure 1.29: Rotation speed of different cell types for different frequencies on a logarithmic scale. The experimental data points are fitted by the theoretical rotation spectra (bold lines) and the dielectric properties can be extracted by determining the best fit. Graph reproduced from [125].

The experimental points obtained are fitted to the equation describing the rotational speed and the intrinsic dielectric properties of the cell are extracted by determining the values that give the best fit between experimental data and the theoretical rotation spectrum. Values such as the cytoplasm permittivity and the cell's membrane conductance can be determined accurately but the capacitance of the membrane and the cytoplasm conductivity cannot be easily determined with this method. Huang et al (2018) showed that electrorotation was not suitable to determine precisely the value of the membrane conductivity, as it made a negligible difference to the rotational speed of the cells for all frequencies studied [157]. The value of the cytoplasm permittivity is also difficult to determine by electrorotation, because this parameter only affects the rotational spectrum for frequencies above 100 MHz and most commercially available AC signal generators have an upper frequency limit of 100 MHz [157].

Another limit of electrorotation is the hydrolysis observed for low AC frequencies or when the voltage used is high [157]. To limit this effect, voltages must be kept low (typically under 14 V) and frequencies must be kept above 10 kHz [168]. Recent experiments have shown that by using microelectrode chambers, electrorotation can be used in physiological ionic strengths [169], [170]. However, this can result in joule heating and this increase in temperature can affect the cell viability as well as the viscosity of the medium. An increase in the viscosity of the medium will affect the measurements of the rotation spectra and can lead to errors in the

determination of the dielectric properties of the analyte. Moreover, as explained previously for electrical impedance spectroscopy, due to the intra-population variation, the rotational spectrum of multiple cells from a population must be determined to obtain statistically significant values. Even though automated electrorotation and motion tracking algorithm have been proposed, this technique is still very time consuming when a high number of cells are analysed [165], [171].

1.4.4 3D DEP-well dielectrophoresis

This technique is based on the 3D DEP device described in section 1.2.4.3, where electrode wells are fabricated by stacking alternating thin layers of conductive laminate copper and insulating polyimide and drilling holes through, creating evenly spaced thin electrode rings around the walls of the well [172]. The low electric fields are the furthest away from the electrodes, at the centre of the wells, whist the high electric fields are at the walls [173]. For low frequencies or very high frequencies for which the cells experience negative DEP, the cells are pushed away from the electrodes and towards the centre of the well. For the frequencies for which the cells experience positive DEP, they are attracted towards the electrode walls (Figure 1.30). To quantify the movement of multiple cells at the same time, a light source is used to illuminate the well and images of the light transmitted through the well are taken every five seconds to observe the redistribution of particles over time [173]. When the cells experiencing nDEP are pushed towards the centre of the well, the light transmission decreases and when the cells are pushed towards the edges of the well due to pDEP the transmission increases. The changes in light intensity can be used to determine the magnitude and polarity of the DEP forces exerted on the cells.

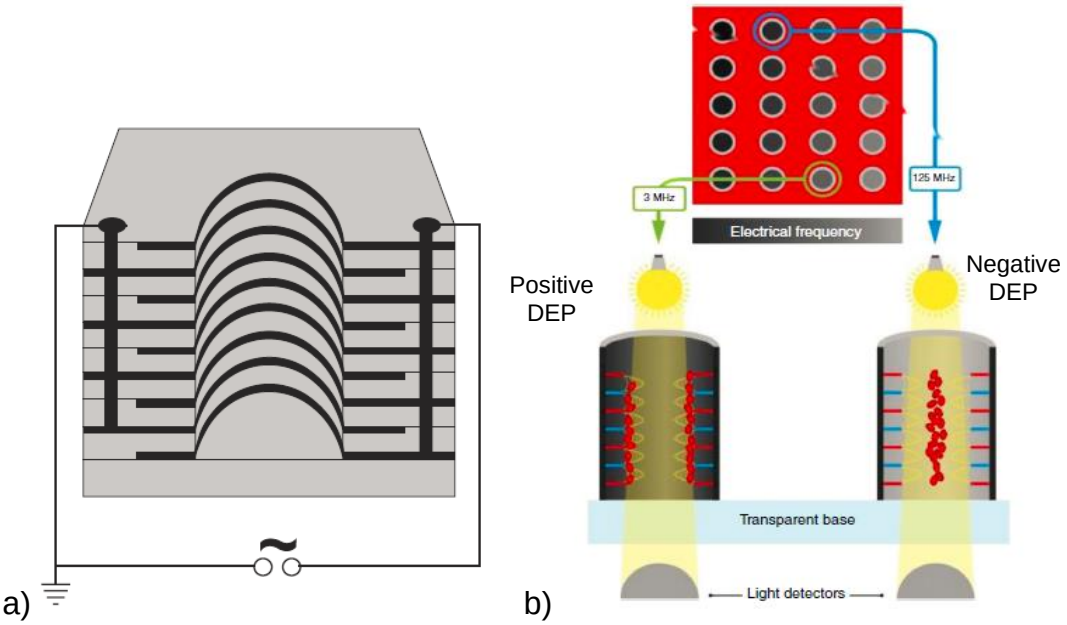

Figure 1.30: a) Schematic diagram of the 3D well electrodes. Holes are drilled through layers of alternating thick conductive copper tape and insulating polyimide so that the 3D electrode walls have electrodes of alternating potential separated by insulating layers. Image reproduced from [174]**. b) Schematic of the commercial 3DEP system consisting of 20 wells energised at different frequencies. For the lower frequencies, the cells experience positive DEP and are attracted towards the electrode walls, letting the light through. For the higher frequencies, the cells experience negative DEP and are pushed away from the electrodes, towards the centre of the well, obstructing the path of the light. Image reproduced from [175].**

This technique is currently available commercially under the name of DEPtech and has been used to determine the effect of different drugs on the dielectric properties of red blood cells and antibiotic resistance in *E. Coli* [172],[174]. The commercial instrument uses disposable chips containing twenty parallel 3D electrodes to determine the dielectric properties of cells for twenty difference frequencies up to 45 MHz (Figure 1.30). The relative DEP force obtained for each frequency is plotted on a graph and a single-shell model (chapter 2 section 2.2.2.3) is used to determine the dielectric properties based on the best fit of the experimental data (Figure 1.31).

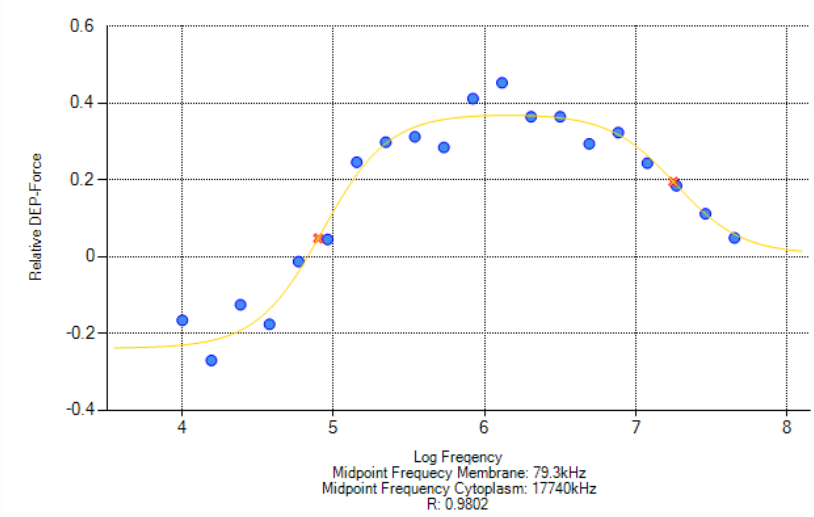

Figure 1.31: DEP spectrum of B cells obtained using 3DEP. The experimental data showing the relative DEP behaviour for each frequency well is represented by a blue dot. The best fit model used to determine the cells' dielectric properties is represented by a solid yellow line.

The use of wells instead of planar electrodes or single cell measurements allows for a greater number of cells (in the order of thousands of cells) to be measured per experiment, which makes the measurements more statistically significant, as they are less likely to be influenced by intra-cell variability. Moreover, due to the use of multiple wells energised with different frequencies at the same time, a full DEP spectra of a cell can be determined via 3DEP in under a minute, unlike other time consuming methods described in this chapter. The time the cells are exposed to the electric field is greatly reduced compared to electrorotation, so there is less risk of the cells undergoing hydrolysis or a reduction in cell viability.

Chapter 2

Theory of surface acoustic waves and dielectrophoresis

2.1 Acoustic waves

2.1.1 Types of mechanical waves

Acoustic waves are mechanical waves resulting from a periodic oscillation of pressure in a solid, liquid or gas that is exhibited by a temporary change to the relative positions of the atoms within the material.

Depending on the movement direction of the atoms within the substrate, the waves can be categorised as either longitudinal or transverse (shear) waves (Figure 2.1). Longitudinal waves are characterised by a displacement of the atoms parallel to the propagation direction. In transverse waves, the atoms within the substrate move in a direction perpendicular to that of the wave propagation.

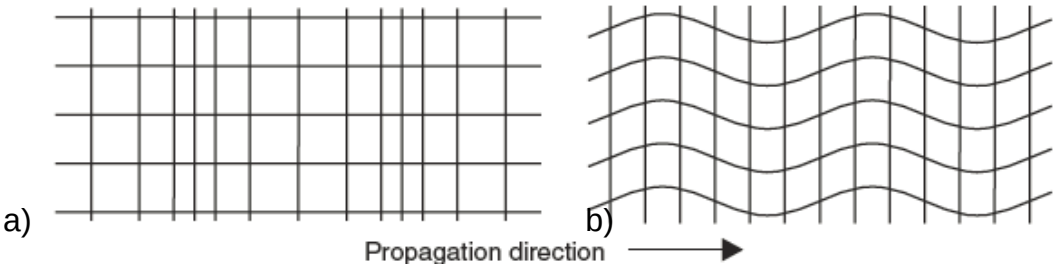

Figure 2.1: Schematic of the displacement of a rectangular grid caused by propagation of bulk waves within an isotropic material (viewed from the top-down). The intersections of the grid represent the individual atoms within the substrate. The direction of propagation is indicated by the arrow. (a) In a longitudinal wave, the atoms are displaced in a surface plane parallel to the propagation direction. (b) In a transverse (shear) wave, the atoms are displaced in a plane perpendicular to the direction propagation.

Acoustic waves can be further divided into bulk waves and surface acoustic waves (SAWs). Whilst longitudinal and transverse bulk waves affect the entire substrate, the mechanical oscillation of SAWs is confined to the surface of the material and their amplitude decays exponentially with increasing distance from the surface (Figure 2.2).

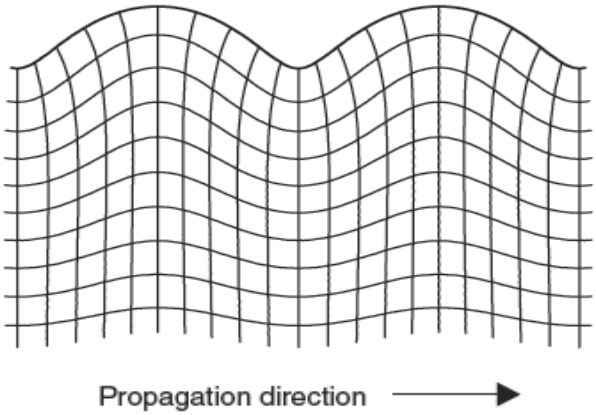

Figure 2.2 Schematic of the displacement of a rectangular grid caused by propagation of a surface acoustic wave (viewed from the side). The intersections of the grid represent the individual atoms within the substrate. The wave propagates at the surface of the material and the propagation is attenuated as the distance from the surface increases. The direction of propagation is indicated by the arrow.

The two most common types of SAW used in microfluidics and RF/microwave filtering applications are the shear horizontal SAW and the Rayleigh wave. Similarly to transversal waves, in shear horizontal SAWs the mechanical displacement is perpendicular to the propagation of the wave, within the plane of the substrate surface (i.e. with no surface-normal component). Rayleigh waves are more complex, as the mechanical displacement occurs in directions both parallel and perpendicular to that of the wave propagation. Here, the perpendicular component is out-of-plane (i.e. normal to the substrate surface), allowing Rayleigh waves to be used for particle trapping using acoustophoresis (Chapter 2, section 1.2.2.2).

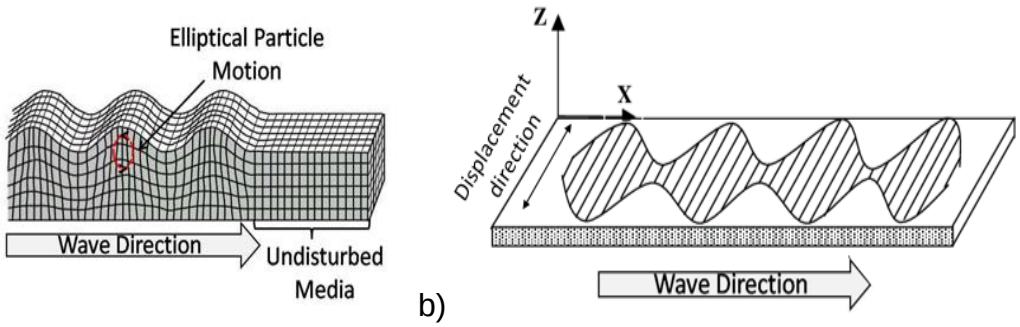

Figure 2.3: a) Rayleigh SAW showing displacement parallel to the propagation direction. The points in the lattice move in an elliptical path, where the direction is with the propagation within the substrate, and against the propagation direction above the surface. b) Shear horizontal SAW showing displacement perpendicular to the wave displacement. The surface of the material moves side to side. Adapted from [176].

2.1.2 Generation of SAWs on piezoelectric substrates

Piezoelectric materials are key for generating SAWs for microfluidics applications, as they can transform electric inputs into mechanical deformation and vice versa. When an alternating electric potential is applied to a piezoelectric material via a set of interdigitated transducers (IDTs), an expansion or compression of the crystal proportional to the applied voltage is induced which launches a SAW that travels away from the excited area. When the wave propagates, the mechanical deformation alters the distribution of charges within the crystal lattice creating a dipole and therefore generating an electrostatic field above the substrate surface [177].

SAW device manufacturing requires the use of piezoelectric materials such as lithium niobate, lithium tantalate ($LiTaO_3$) and on some occasions quartz (principally for electronics applications). The nature of the material and its crystallographic cut determines the type of SAW (Rayleigh or Shear Horizontal) that can be generated and the wave propagation velocity in the material. For microfluidics applications, the substrate should ideally combine a high wave propagation velocity with good temperature stability. Further criteria depend on the final application. For example, the surface-normal component of Rayleigh SAWs allows pressure waves to be generated within an overlaid fluid, useful for e.g. acoustophoresis (Chapter 1, section 1.2.2.2) or micropumps. However, in situations where fluid movement should be either minimised or independent of the SAW, such as sensing or dielectrophoresis, shear-SAWs are preferred as these do not induce pressure waves in an overlaid fluid. To meet these criteria, 42° rotated Y-cut lithium tantalate substrates were used to create shear-horizontal waves in the devices described in this thesis.

Surface acoustic waves (SAWs) can be generated by applying high-frequency electrical signals to metallic interdigitated transducers (IDTs), patterned on the surface of a piezoelectric material (Figure 2.4) [37]. These transducers were first used as a source of SAWs by White and Voltmer in 1965 and consist of a set of metal electrodes (generally gold or aluminium), alternately connected to two bus bars [178]. One bus bar is grounded, while an AC voltage is applied to the other. When the alternating electric field is applied to the IDTs, the potential difference creates compression and expansion in the lattice of the underlying piezoelectric material which launches a travelling mechanical wave along the material surface (away from the IDTs).

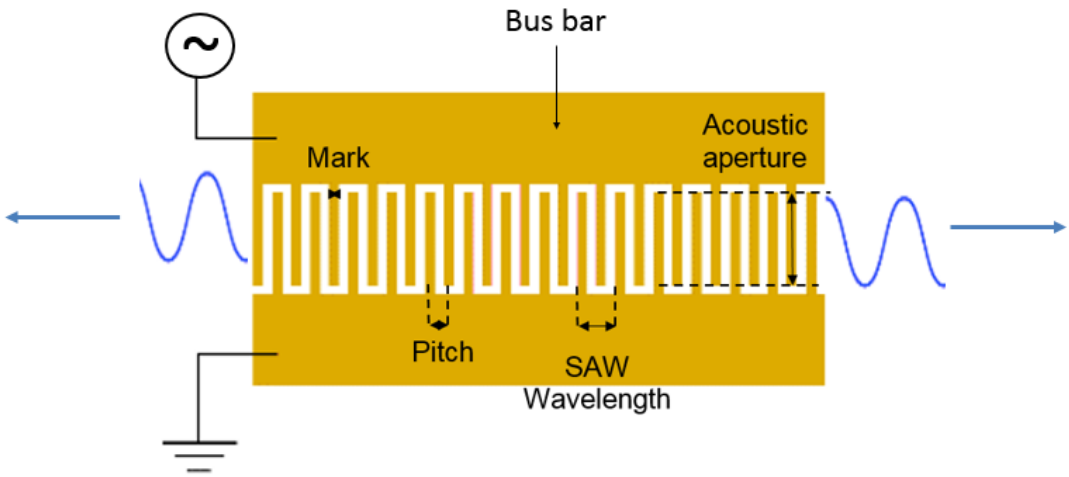

Figure 2.4: Schematic of an interdigitated transducer indicating the key design parameters. An AC signal is applied to the top set of transducers whilst the bottom set is grounded, generating a SAW (blue) that propagates along the substrate's surface. The electrode width (mark) and gap (space) define the pitch and are key design parameters to determine the wavelength of the SAW generated. The acoustic aperture is formed by the overlap of opposing transducer fingers, and defines the length over which the SAW will be generated. The arrows indicate the direction of SAW travel.

The frequency of the SAWs generated by the IDTs is determined by the pitch between electrode finger pairs as described in the following equation:

$$f_0 = \frac{v}{\lambda} \qquad with\ \lambda = 2\,p \quad (2.1)$$

Where f_0 is the resonant SAW frequency, v is the wave speed in the substrate, λ is the SAW wavelength and is the p electrode pitch.

One of the limiting factors when it comes to the maximum achievable operating frequency is the minimum finger width that can be patterned. As explained in the above equation, the wavelength should be twice as big as the electrode pitch and therefore (assuming a 1:1 mark:space ratio) four times the electrode width. As SAW frequency increases the electrode width correspondingly decreases, introducing fabrication limitations at frequencies higher than ~3 GHz [179]. For example, a 3 GHz filter formed on 42°Y-X $LiTaO_3$ and assuming a wave propagation velocity of 4000 m/s, corresponds to a wavelength of 1.3 µm, a pitch of 0.65 µm, and an individual electrode width of 0.325 µm. The further miniaturisation of the electrode can also decrease the filter's durability as its resistance increases [179].

2.1.3 Generation of standing SAWs on piezoelectric substrates

When identical AC signals are applied to two identical, opposing IDTs, two waves are generated of equal frequency and amplitude, and travelling in opposite directions. When these two counter-propagating SAWs interfere a standing wave is formed, comprised of periodic zones of maximum displacement (antinodes) and minimum displacement (nodes), which alternate at a pitch corresponding to a quarter of the wavelength of the corresponding standing SAW (Figure 2.5).

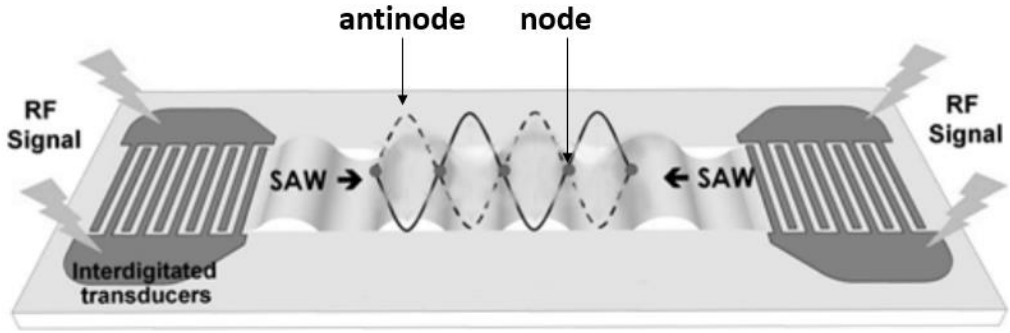

Figure 2.5: Generation of a Rayleigh standing SAW by two sets of IDTs on a piezoelectric material. A signal is applied to each of the opposing IDTs, each of which generates a mechanical displacement within the piezoelectric substrate. The generated SAWs are of the same amplitude and combine to form a standing wave presenting zones of maximum (antinodes) and minimum (nodes) displacement. Image adapted from [180].

Generating SAWs using the IDT geometry introduces losses that arise from each IDT's symmetrical nature. When excited using an AC voltage, each IDT generates not one, but two SAWs from its two ends, both equal in amplitude but propagating in opposite directions. One portion (50% of the total power) enters the acoustic cavity (defined as the area enclosed between the opposing IDTs) and constitutes 'useful' signal. However, an equal proportion travels away from the acoustic cavity and is lost, corresponding to a 3 dB reduction in power (Figure 2.6). Since this occurs at both sets of IDTs, a theoretical best-case minimum loss of 6 dB, called the insertion loss, is imposed on this design. Although additional device modifications (e.g. reflectors) can be added to reflect a portion of the lost energy back into the acoustic cavity, this is beyond the scope of this thesis.

a)

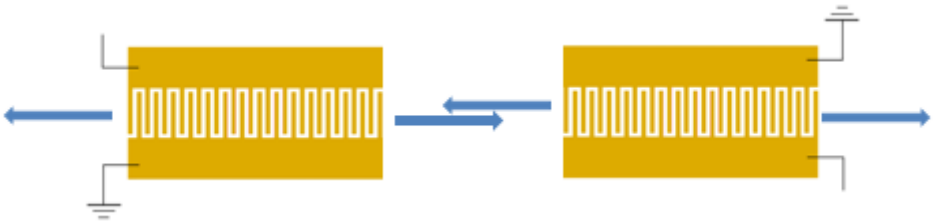

b)

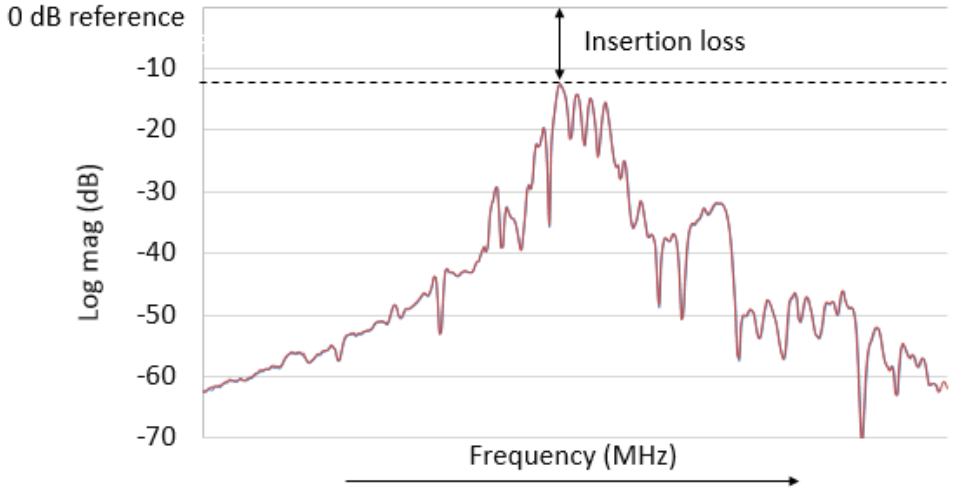

Figure 2.6: a) Schematic of a two-port device consisting of two sets of IDTs. The propagation direction of the SAWs generated from each set of IDTs is indicated by blue arrows. The SAWs generated between the two IDTs generate a standing SAW whilst the SAWs generated at the ends of the electrodes is lost power, corresponding to 3dB. b) Frequency domain response of a SAW filter and determination of insertion loss in an experimental device. The highest transmission peak frequency is determined by the electrode geometry and size and the insertion loss corresponds to the power lost in the device. A larger insertion loss indicates that less power is being coupled into the SAW.

When the impedance of the electrodes is matched to the output resistance of the signal generator, the efficiency of the two-port device is maximized and the total power loss is close to the minimal theoretical insertion loss of 6 dB. The impedance of the devices can be matched to the output resistance of the signal generator using a matching network consisting of a series of capacitors and inductors. Alternatively, the IDTs can be designed to match the output impedance without the need for marching networks. The IDT impedance can be controlled through four variables, namely H_w, R_{in}, f_0 and N_p. These correspond respectively to the acoustic aperture width (the overlap length between signal and ground IDT fingers), the desired input resistance (which is assumed to be real and purely resistive), the SAW centre frequency and the finger pair count.

These variables are related through the following equation:

$$H_w = \frac{1}{R_{in}2}\frac{1}{f_0 C_s N_p}\frac{4k^2 N_p}{\left(4k^2 N_p\right)^2 + \pi^2} \qquad (2.2)$$

The majority of microwave and radio frequency signal generators have an output impedance of 50 Ω, so the input resistance R_{in} was fixed to 50 Ω to match the output impedance. The acoustic aperture H_w was fixed to 1 mm in order to allow for visualisation of the particle separation under the microscope. The propagation velocity, static capacitance and coupling coefficient are material properties that were obtained from datasheets for 42°Y cut lithium tantalate ($LiTaO_3$) [181] [182].

This equation was used to determine the appropriate number of finger pairs needed for a given SAW frequency, with the fixed parameters described in Table 2.1

Property	Symbol	Value
Acoustic aperture	H_w	3 mm
Wave propagation speed in 42°Y cut $LiTaO_3$	v	4022 m/s[181]
SAW centre frequency	f_0	10 MHz
Finger pair number	N_p	50
Input resistance	R_{in}	50 Ω
Coupling coefficient of 42°Y cut $LiTaO_3$	k^2	7.6 (%) [181]
Static capacitance	C_s	4.4 pF/cm [182]

Table 2.1: Summary of the electrode geometry and properties of 42°Y cut lithium tantalate ($LiTaO_3$).

2.2 Dielectrophoresis

A general overview of dielectrophoresis (DEP) and its use for particle separation is described in Chapter 1 section 1.2.4. Here, the theory will be discussed further in order to identify key concepts that govern the response of a particle to non-uniform electric fields applied in a particular environment.

2.2.1 DEP force main equation derivation

The time-averaged DEP force exerted on a spherical particle in a surrounding dielectric medium was defined by Washizu as [183]:

$$< F_{DEP} > = 2\pi\varepsilon_{med}R^3Re\left[\frac{\varepsilon_p^* - \varepsilon_{med}^*}{\varepsilon_p^* + 2\,\varepsilon_{med}^*}\right]\nabla E^2 + \frac{2\pi}{3}\varepsilon_{med}R^5\,Re\left[\frac{\varepsilon_p^* - \varepsilon_{med}^*}{2\varepsilon_p^* + 3\,\varepsilon_{med}^*}\right]\nabla.\nabla E^2 \quad (2.3)$$

Where R is the radius of the particle and E is the applied electric field. The terms ε_{med}^* and ε_p^* are the medium and particle complex permittivity, respectively, and take the general form:

$$\varepsilon^* = \varepsilon_0\varepsilon_r - i\frac{\sigma}{\omega} \quad (2.4)$$

Where $\varepsilon_0 = 8.85 \times 10^{-12}$ F/m is the permittivity of free space, ε_r is the relative permittivity of the medium/particle, σ is the conductivity of the medium/particle, ω is the angular frequency (in rad/sec) of the applied alternating electric field and $i = \sqrt{-1}$.

The cells studied in this this thesis had a particle diameter of ≤10 μm, and were used in devices operating at frequencies of 10 – 20 MHz (wavelengths of ~400 – 200 μm, respectively). In cases such as this, where the particle diameter is less-than-or-equal-to one tenth of the electrode pitch, the quadrupole term in equation (2.3) tends to zero and the DEP force equation can therefore can be simplified to:

$$< F_{DEP} > = 2\pi\varepsilon_{med}R^3Re[CM]\nabla E^2 \quad (2.5)$$

As discussed in Chapter 1 section 1.2.4, a particle subjected to a DEP force will propagate in one of two directions: either towards, or away from, areas of high electric-field density. The term that describes this behaviour is called the Clausius Mossotti (CM) factor. In the case of a spherical particle of permittivity ε_p^* suspended in a medium of permittivity ε_{med}^* the Clausius Mossotti (CM) factor can be written as:

$$CM^* = \frac{\varepsilon_p^* - \varepsilon_{med}^*}{\varepsilon_p^* + 2\,\varepsilon_{med}^*} \quad (2.6)$$

According to Wagner, the complex conductivity σ^* and complex permittivity ε^* of a material are linked by the relationship [184]:

$$\sigma^* = i\omega\varepsilon_0\varepsilon^* \quad (2.7)$$

By combining (2.6) and (2.7) the particle and medium conductivities (respectively σ_p^* and σ_{med}^*) give:

$$CM^* = \frac{\sigma_p^* - \sigma_{med}^*}{\sigma_p^* + \sigma\,\varepsilon_{med}^*} \quad (2.8)$$

This complex form of the CM factor accounts for the dielectric and conduction losses of the particle in the suspending medium and is required when time dependent (i.e. AC) electric fields are used.

The real part of the CM factor is given by [185], [186]:

$$Re[CM^*] = \left[\left(\frac{\omega^2\tau^2}{1+\omega^2\tau^2}\right)\left(\frac{\varepsilon_p^* - \varepsilon_{med}^*}{\varepsilon_p^* + 2\,\varepsilon_{med}^*}\right) + \left(\frac{1}{1+\omega^2\tau^2}\right)\left(\frac{\sigma_p^* - \sigma_{med}^*}{\sigma_p^* + 2\,\sigma_{med}^*}\right)\right] \quad (2.9)$$

in which the general form of the relaxation time for interfacial polarization τ is given by:

$$\tau = \varepsilon_0 \frac{\varepsilon_p + 2\varepsilon_{med}}{\sigma_p + 2\sigma_{med}} \quad (2.10)$$

At low frequencies, i.e. when $\omega \to 0$, this equation can be approximated to:

$$Re[CM^*] \approx \frac{\sigma_p - \sigma_{med}}{\sigma_p + 2\sigma_{med}} \quad (2.11)$$

This indicates that at low frequencies (typically below 10 kHz), the conductive properties of the medium and the particle determine the DEP force experienced by the particle. When the conductivity of the particle is higher than that of the medium, the real part of the CM factor is positive and so is the DEP force exerted on the particle, causing it to move toward areas of highest field gradient. When the opposite scenario occurs, the CM factor is negative and the direction of DEP force is reversed. At high frequencies (above 500MHz), i.e. when $\omega \to \infty$, equation (2.9) instead becomes:

$$Re[CM^*] \approx \frac{\varepsilon_p - \varepsilon_{med}}{\varepsilon_p + 2\varepsilon_{med}} \quad (2.12)$$

In this case the DEP force depends on the permittivity values of the particle and the medium.

The maximum value of the real part of the CM factor is obtained when $\sigma_p \gg \sigma_{med}$ and $\varepsilon_p \gg \varepsilon_{med}$, which is the case for a homogeneous metallic particle suspended in distilled water. For this condition, Re[CM] ≈ 1. The minimum value is obtained when $\sigma_{med} \gg \sigma_p$ and $\varepsilon_{med} \gg \varepsilon_p$, for example in the case of an air bubble suspended in water. This condition gives a minimum value of Re[CM] ≈ -0.5.

The small range of values for Re [CM*] (-0.5 ≤ Re[CM*] ≤1) indicate that distinguishing particles based on small differences in their dielectric properties could be difficult. In order to maximize the differences in DEP

response between particles in order to separate them, it is important to focus on the conditions that cause the DEP force to change polarity. The frequencies at which this occurs are called DEP crossover frequencies.

2.2.1.1 Crossover frequencies

In low conductivity media (typically < 0.2 S/m), cells can experience two DEP crossovers: a first transition from negative to positive DEP at lower frequency, and a second, higher-frequency transition from positive to negative DEP [187]. These are called first and second DEP crossover frequencies, respectively (Figure 2.7).

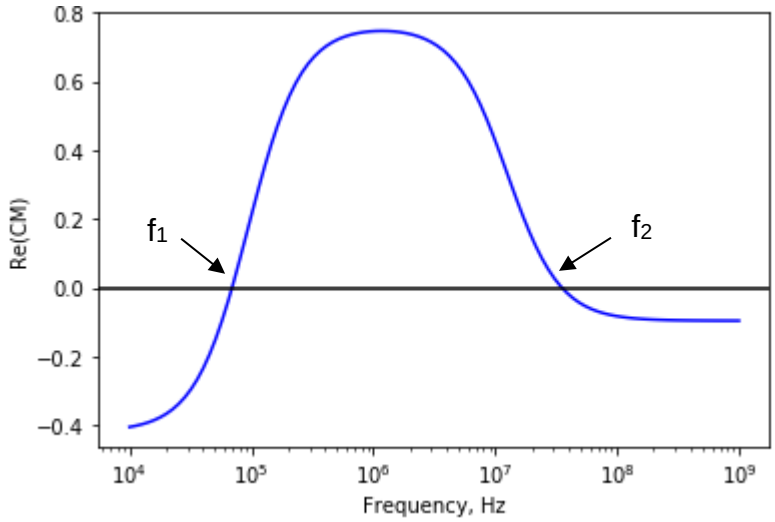

Figure 2.7: Real part of the Clausius Mossotti factor of a cell for different frequencies; f_1 and f_2 represent the first and second crossover frequencies respectively.

The first crossover frequency (f_1) typically occurs between 10 kHz and 1 MHz but has been reported as high as 4 MHz [188]. The value of this first crossover frequency is driven by polarization occurring at the interface between the suspending liquid and the cell membrane (or mobile charges at the surface of a solid particle). When the radius of a specific cell type is known, this cross-over frequency can therefore give information about its membrane conductance and capacitance. At frequencies higher than the first crossover frequency, the cell membrane has no further effect on the electric field, and the cell can be therefore treated as a ball of cytoplasm suspended in the medium.

These findings were demonstrated by Höber in 1910, who showed that for cells treated with saponin (a detergent that can permeabilise the cell membrane) the conduction current remained unchanged at high frequencies whereas the low frequency conduction increased significantly [189].

If the permittivity of the suspending medium is higher than that of the cytoplasm, the interfacial polarization between the cytoplasm and the medium can give rise to a second frequency crossover (f_2). This crossover depends on the cytoplasm permittivity and is typically observed at frequencies higher than 200 MHz although this reduces in low-conductivity media and can be as low as 10 MHz.

2.2.1.2 First crossover frequency

At low frequencies, a cell's dielectric properties are dominated by the cell membrane and the relaxation time described in equation

(2.10) becomes:

$$\tau_1 = \varepsilon_0 \frac{\varepsilon_{mem}+2\varepsilon_{med}}{\sigma_{mem}+2\sigma_{med}} \quad (2.13)$$

Where σ_{mem} and ε_{mem} are the cell membrane conductivity and permittivity respectively.

By setting $Re[CM^*] = 0$ in Equation

(2.9) and with the relaxation time τ given above, the equation obtained for the crossover angular frequency is :

$$\omega_{x01} = \frac{1}{\varepsilon_0}\sqrt{\frac{(\sigma_{med}-\sigma_{mem})(\sigma_{mem}+2\sigma_{med})}{(\varepsilon_{mem}-\varepsilon_{med})(\varepsilon_{mem}+2\varepsilon_{med})}} \quad (2.14)$$

At low frequencies, the conductivity of a typical cell is significantly lower than that of the medium, whereas the effective permittivity of a cell largely exceeds that of a typical suspension medium [187]. Equation (2.14) can therefore be reduced to:

$$\omega_{x01} \cong \frac{1}{\varepsilon_0}\frac{\sqrt{2}\sigma_{med}}{\varepsilon_{mem}} \quad (2.15)$$

From this equation, the first crossover frequency can be given as:

$$f_{x01} = \frac{\omega_{x01}}{2\pi} \approx \frac{\sigma_{med}}{\sqrt{2}\pi\varepsilon_0\varepsilon_{mem}} \quad (2.16)$$

This crossover frequency can also be expressed in terms of membrane capacitance, C_{mem}, and conductance, G_{mem} by using the equivalences between "classical" and "electrical" models as described in more detail in section 2.2.2.1:

$$G_{mem} = \frac{\sigma_{mem}}{d_{mem}} \qquad C_{mem} = \frac{Re[\varepsilon^*_{mem}]}{d} = \frac{\varepsilon_0\,\varepsilon_{mem}}{d_{mem}} \quad (2.17)$$

Where d_{mem} is the cell membrane thickness. Substituting C_{mem} for ε_{mem}into equation (2.16), the following expression for the crossover frequency can be obtained:

$$f_{x01} \approx \frac{\sigma_{med}}{\sqrt{2}\pi d_{mem} C_{mem}} \quad (2.18)$$

An improvement to the approximate nature of equation (2.18) can be made by including the membrane's specific conductance G_{mem} [190]:

$$f_{x01} \approx \frac{\sigma_{med}}{\sqrt{2}\pi R C_{mem}} \sqrt{1 - \frac{R G_{mem}}{2\sigma_m} - 2\left(\frac{R G_{mem}}{2\sigma_{med}}\right)^2} \quad (2.19)$$

Where R is the radius of the particle.

2.2.1.3 Second crossover frequency

The second, high frequency crossover (f_{x02}) is typically above 10MHz in low conductivity media and is dominated by the properties of the cell's cytoplasm [191].

At high frequencies, the membrane becomes "invisible" to the applied electric field, and the field penetrates directly into the cytoplasm, allowing the cell to be considered as a ball of cytoplasm suspended in medium.

The mismatch between the cytoplasm conductivity and that of the suspending medium gives rise to a second relaxation time τ_2, given by:

$$\tau_2 = \varepsilon_0 \frac{\varepsilon_{cyt} + 2\varepsilon_{med}}{\sigma_{cyt} + 2\sigma_{med}} \quad (2.20)$$

Where σ_{cyt} and ε_{cyt} are the cytoplasm conductivity and permittivity respectively.

By setting $Re[CM^*] = 0$ in equation

(2.9) (corresponding to the point at which the CM factor changes polarity) and combining with equation (2.20), the crossover angular frequency is given by:

$$\omega_{x02} = \frac{1}{\varepsilon_0}\sqrt{\frac{(\sigma_{med} - \sigma_{cyt})(\sigma_{cyt} + 2\sigma_{med})}{(\varepsilon_{cyt} - \varepsilon_{med})(\varepsilon_{cyt} + 2\varepsilon_{med})}} \quad (2.21)$$

This equation, first derived by Giemsa and colleagues has real solutions for the following condition [192] :

$$\frac{\sigma_{med} - \sigma_{cyt}}{\varepsilon_{cyt} - \varepsilon_{med}} > 0 \quad (2.22)$$

For an aqueous medium, the permittivity ($\varepsilon_{med} = 79$) is often greater than that of the cells suspended, therefore to fulfil the condition given by equation (2.22), the conductivity of the cytoplasm must be higher than that of the medium. Typical cytoplasm conductivities reported in the literature (Table 5.2) have been found to be between 1 and 0.1 S/m so this condition can be satisfied when using medium conductivities lower than 0.1 S/m. For cases where the cytoplasm conductivity is much larger than that of the surrounding media, such as in all DEP characterization protocols, equation (2.21) can be simplified to give [91], [193]–[196]:

$$f_{x02} = \frac{\omega_{x02}}{2\pi} = \frac{\sigma_{cyt}}{2\pi\varepsilon_0}\sqrt{\frac{(\sigma_{med}-\sigma_{cyt})(\sigma_{cyt}+2\sigma_{med})}{(\varepsilon_{cyt}-\varepsilon_{med})(\varepsilon_{cyt}+2\varepsilon_{med})}} \quad (2.23)$$

Equation

(2.23) shows that the high-frequency crossover is mostly influenced by the cytoplasm conductivity and the permittivity only contributes to its value minimally [143], [197].

2.2.2 Cell modelling for the determination of dielectric properties

Eukaryotic cells are comprised of a nucleus and organelles suspended in an aqueous solution (called cytosol) surrounded by a semi-porous membrane (Figure 2.8). The presence of organelles and internal membranes, such as the nuclear envelope or endoplasmic reticulum, contribute to the internal

dielectric properties of the cell, including the cytoplasm permittivity and conductivity.

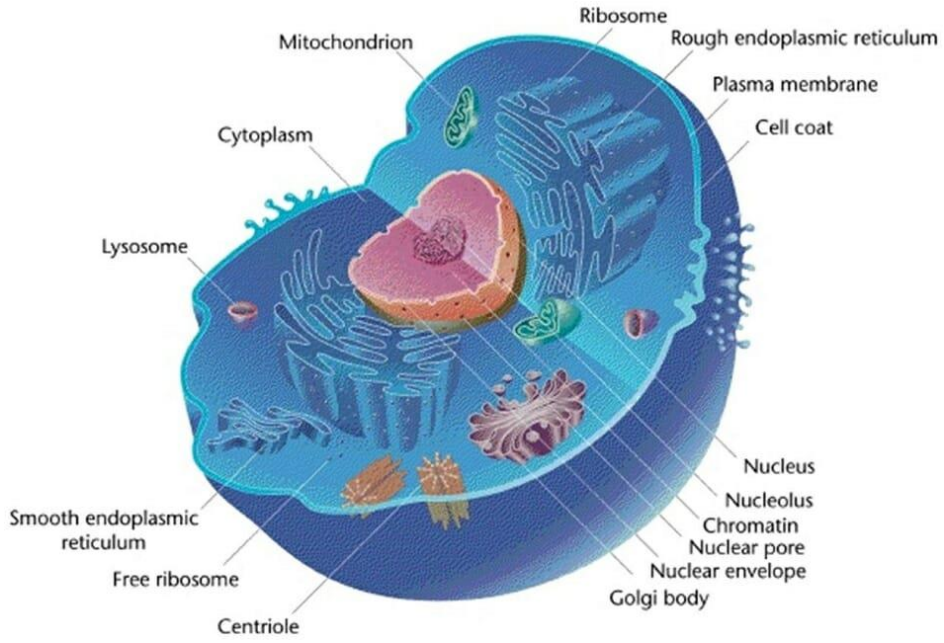

Figure 2.8: Eukaryotic cell components: organelles and membranes. Image reproduced from [198].

In order to simplify the complexity of cell structure and predict the behavior of cells in DEP fields, several mathematical models have been developed and are discussed in the next sections.

2.2.2.1 Electrical model of a cell membrane

The “external” dielectric properties of the cells, such as the membrane capacitance and conductance, are dictated by the cell membrane. The membrane is semi-permeable; it allows for the passage of small molecules, including gases and certain lipophilic molecules, but is impermeable to ions, water and large molecules (such as sugars and amino acids) which can only pass through tightly regulated channels [187]. Due their impermeability to ions and their extremely thin nature (7 nm), cell membranes can be approximated as a capacitor in which the lipid bilayer acts as a thin dielectric sandwiched between two conductors (the suspending medium and the cytoplasm) [199].

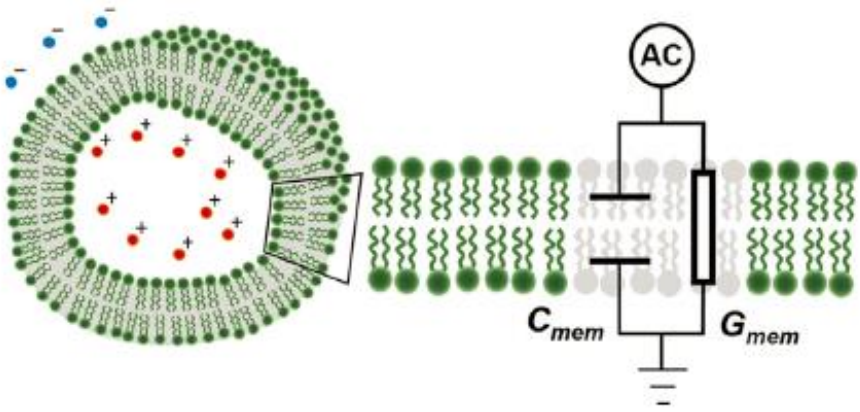

Figure 2.9: Electrical model of a cell membrane. The lipid bilayer can be modelled as a dielectric with a capacitance and a conductance. Image reproduced from [199].

Wang and colleagues described membrane capacitance as *"a measure of the area of the membrane that can accumulate ionic charges in the suspending medium in response to the applied electrical field"* whilst membrane conductance *"reflects the net transport of ionic species across the membrane and through pores and ion channels"* [200].

For eukaryotic cells, the total cell radius R is always much greater than the membrane thickness, d, so the membrane capacitance can be calculated using Wang's model and expressed as a simple parallel-plate capacitor, comprised of two electrodes of area *A* separated by a distance *d*:

$$C_{mem} = \frac{A\varepsilon_0\varepsilon_r}{d} \quad (2.24)$$

The above equation is valid when the membrane surface is smooth, which is the case for erythrocytes but is not the case for most other cell types. To quantify this "surface roughness" a membrane topography parameter (ϕ) can be introduced [63]. This parameter represents the ratio of the rough membrane area to that of the area obtained if the surface of the cell was stretched and smooth.

$$C_m = \frac{\phi A_0\varepsilon_0\varepsilon_r}{d} \quad (2.25)$$

This equation shows that the main factors affecting the capacitance of the membrane are the membrane thickness d, the surface area A_0, the membrane topography and the composition of the cell membrane (defined by the membrane relative permittivity ε_r).

2.2.2.2 Effective medium theory

Effective medium theory states that a heterogenous material can be represented as a homogenous material for a sufficiently large observation scale. Using this approximation it is possible to determine the effective permittivity of a very dilute suspension of cells, as long as the average distance between cells is much bigger than the cell radius, and assuming that the applied field is not influenced by local field distortions caused by dipoles induced within or across the cell.

The discussion begins by considering a spherical region of radius R_m within the medium, which contains n total cells. The volume fraction (V_C) of suspended cells within this spherical region is given by:

$$V_C = \frac{nR_{Cell}^3}{R_m^3} \quad (2.26)$$

The potential ϕ_1 at a point located outside the sphere at a distance r from its centre, will comprise the summation of the induced dipole fields of all n cells, plus a directional component of the applied field, E, and is of the form:

$$\phi_1 = \left(\frac{nA}{r^2} - Br\right) Ecos\theta, \quad with\, A = \frac{\varepsilon_{cell} - \varepsilon_{med}}{\varepsilon_{cell} + 2\varepsilon_{med}} R_{Cell}^3 \quad (2.27)$$

Where E is the applied field applied at an angle θ, B is the magnetic field, ε_{med} is the permittivity of the medium containing the cell suspension, R_{cell} is the cell radius and ε_{cell} is the permittivity of the cell.

Using the volume fraction, the potential described in (2.27) can be rewritten as:

$$\phi_1 = \left(\frac{V_C R_m^3}{r^2} \frac{\varepsilon_{cell} - \varepsilon_{med}}{\varepsilon_{cell} + 2\varepsilon_{med}} - Br\right) Ecos\theta \quad (2.28)$$

If we now replace the spherical volume containing n discrete cells, with an equivalent spherical volume formed from a homogeneous material of permittivity ε_{eff}, the potential is instead described as:

$$\phi_2 = \left(\frac{R_m^3}{r^2} \frac{\varepsilon_{eff} - \varepsilon_{med}}{\varepsilon_{eff} + 2\varepsilon_{med}} - Br\right) Ecos\theta \quad (2.29)$$

For very dilute solutions ($V_C < 0.1$), the heterogenous cell suspension can be assumed to be homogenous and, equating $\phi 2 = \phi 1$, we obtain the Maxwell-Garnett mixing equation:

$$\frac{\varepsilon_{eff}^* - \varepsilon_{med}^*}{\varepsilon_{eff}^* + 2\varepsilon_{med}^*} = V_C \frac{\varepsilon_{cell}^* - \varepsilon_{med}^*}{\varepsilon_{cell}^* + 2\varepsilon_{med}^*} \quad (2.30)$$

which can be rearranged to give the effective permittivity of the cell-containing medium:

$$\varepsilon_{eff}^{*} = \frac{2\varepsilon_{med}^{*} + \varepsilon_{cell}^{*} + 2V_C(\varepsilon_{cell}^{*} - \varepsilon_{med}^{*})}{2\varepsilon_{med}^{*} + \varepsilon_{cell}^{*} - V_C(\varepsilon_{cell}^{*} - \varepsilon_{med}^{*})}\varepsilon_{med}^{*} \quad (2.31)$$

This expression is used to develop the single shell model of a cell and is used to determine the cell's dielectric properties from experimental data.

2.2.2.3 Single and double shell models of a cell

The single shell model is the most broadly used model for analysing the experimental dielectric properties of cells [79], [161], [162]. This model accounts for the presence of the cell's external lipid membrane in addition to its cytoplasm and therefore, the conductivity and permittivity of both must be determined.

The single shell model approximates a cell as two concentric spheres; a spherical shell representing the membrane and an inner shell filled with an homogenous cytoplasm. For one cell (n=1) the volume fraction given by equation

(2.30) is:

$$V_C = \frac{R_{Cell}^3}{(R_{cell} - d)^3} \quad (2.32)$$

The two concentric spheres are equivalent to an homogeneous single sphere whose complex permittivity (ε_{cell}^{*}) can be expressed in terms of the cell radius and the complex permittivities of both the cytoplasm (ε_{cyt}^{*}) and membrane (ε_{mem}^{*}) in a similar way to equation (2.31).

$$\varepsilon_{cell}^{*} = \frac{2\varepsilon_{mem}^{*} + \varepsilon_{cyt}^{*} + 2V_C(\varepsilon_{cyt}^{*} - \varepsilon_{mem}^{*})}{2\varepsilon_{mem}^{*} + \varepsilon_{cyt}^{*} - V_C(\varepsilon_{cyt}^{*} - \varepsilon_{mem}^{*})}\varepsilon_{mem}^{*} \quad (2.33)$$

Where the complex permittivity of the cytoplasm and the membrane (respectively ε_{cyt}^{*} and ε_{mem}^{*}) follow the general form given in equation $\frac{\sigma}{\omega}$

(2.4):

$$\varepsilon_{cyt}^{*} = \varepsilon_0\, \varepsilon_{cyt} - j\frac{\sigma_{cyt}}{\omega} \quad (2.34)$$

$$\varepsilon_{mem}^{*} = \varepsilon_0\, \varepsilon_{mem} - j\frac{\sigma_{mem}}{\omega} \quad (2.35)$$

As shown in section 2.2.2.1, we have the following equivalences between the "classical" and "electrical" models:

$$G_{mem} = \frac{\sigma_{mem}}{d_{mem}} \qquad C_{mem} = \frac{\varepsilon_{mem}}{d_{mem}} \qquad (2.36)$$

Using those equivalences, ε^*_{mem} can be written in terms of the membrane capacitance and conductance:

$$\varepsilon^*_{mem} = \varepsilon_0 \, d \, C_{mem} - j \frac{G_{mem} \, d}{\omega}$$

The complex permittivity of the cell (2.36) can therefore be written in terms of the membrane capacitance, membrane conductance, cytoplasm conductivity and cytoplasm permittivity. The effective permittivity ε^*_{cell} of the cell can finally be used to calculate the Clausius Mossotti factor described in (2.6) and repeated here for convenience:

$$CM^* = \frac{\varepsilon^*_{cell} - \varepsilon^*_{med}}{\varepsilon^*_{cell} + 2\varepsilon^*_{med}} \quad \text{with} \quad \varepsilon^*_{med} = \varepsilon_0 \, \varepsilon_{med} - j \, \frac{\sigma_{med}}{\omega} \quad (2.37)$$

The single shell model gives a good first approximation for the dielectric properties of a cell, however it assumes a perfectly spherical shell and is found to be less applicable to mammalian cells which contain additional internal membranes, such as the nuclear envelope, mitochondria and endoplasmic reticulum. Moreover, this simplified model does not account for variations in intracellular membrane area which occur as a consequence of various intracellular processes, such as molecular trafficking.

In order to account for these heterogeneities, a double-shell model including an external membrane and nuclear membrane was developed by Irimajiri et al. (1979) [201]. The same procedure used to derive equation (2.33) was used in the double shell model to derive the equivalent homogeneous permittivity of an additional sphere (representing the nucleus) that is inserted into the larger sphere that represents the cytoplasm. In this model, additional parameters were considered including the conductivity and permittivity of the inner nuclear membrane, the outer cell membrane and the cytoplasm (see Figure 2.10) [202].

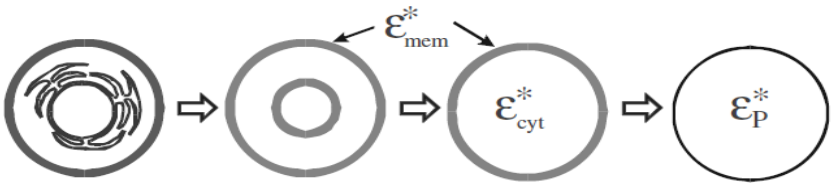

Figure 2.10: A schematic diagram depicting the models available for cell representation. From left to right: cell, double shell model, single cell model and uniform particle. For each model, the permittivity and conductivity of each of the regions and membranes has to be determined in order to calculate the complex permittivities (ε*). Reproduced from [203].

The differences between cell models produced using the single and double shell approaches are exacerbated for cell types in which the volume of the nucleus is more than 60% of the cell's total volume, which includes T cells and B cells [201]. For those cells, the accuracy of the modelling using a single shell model drops [204]. However, the increased complexity of the double-shell model requires an increase in the number of parameters that need to be determined, alongside a detailed knowledge of the volume occupied by the nucleus and the thickness of the nuclear envelope. With all factors considered, the single shell model remains the most commonly used model and was therefore the one used in this thesis.

2.2.3 Influence of dielectric properties on frequency crossovers

The primary factors that influence the first (lower-frequency) crossover frequency, as explained in section 2.2.1.2, are the capacitance of the membrane and, to a lesser extent, the membrane conductance. The membrane capacitance depends on parameters such as the surface area, the surface roughness or the composition of the membrane (section 2.2.2.1). As seen in (Figure 2.11), with increasing capacitance the first crossover increases in frequency whilst the maximum value of the Clausius Mossotti factor decreases. The minimum values of the CM factor remain unchanged.

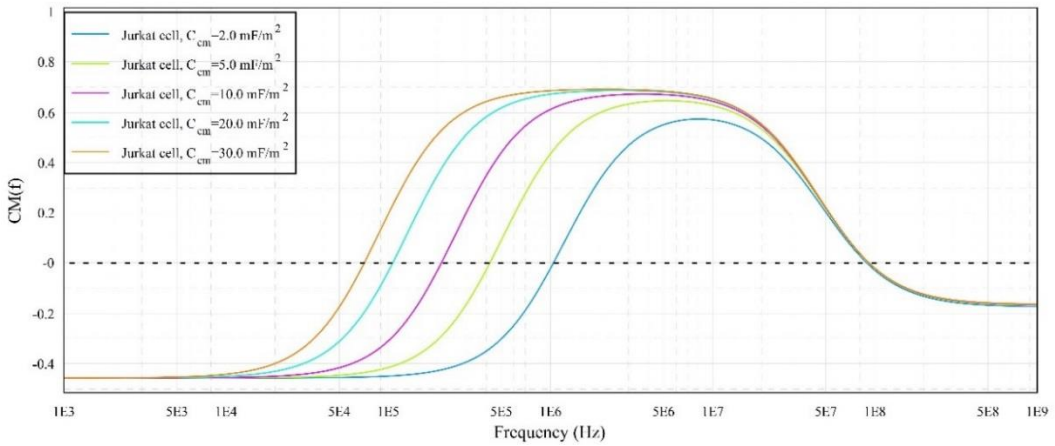

Figure 2.11: Influence of membrane capacitance on Clausius Mossotti factor. The single shell cell model used was based on the values of a Jurkat T cell line. All parameters, other than the cytoplasm conductivity, were fixed at the following values: cell radius 5µm, medium conductivity $\sigma_m = 0.05\ S/m$, cytoplasm conductivity $\sigma_{cp} = 0.4\ \mathrm{S/m}$, cytoplasm permittivity $\varepsilon_{cp} = 45$, membrane conductance $G_{cm} = 600\ S/m^2$.

As seen in (Figure 2.12), the membrane conductance has a negligible influence on the first crossover frequency. With increasing conductance, the minimum value of the CM factor (observed at frequencies lower than the first crossover) is seen to increase.

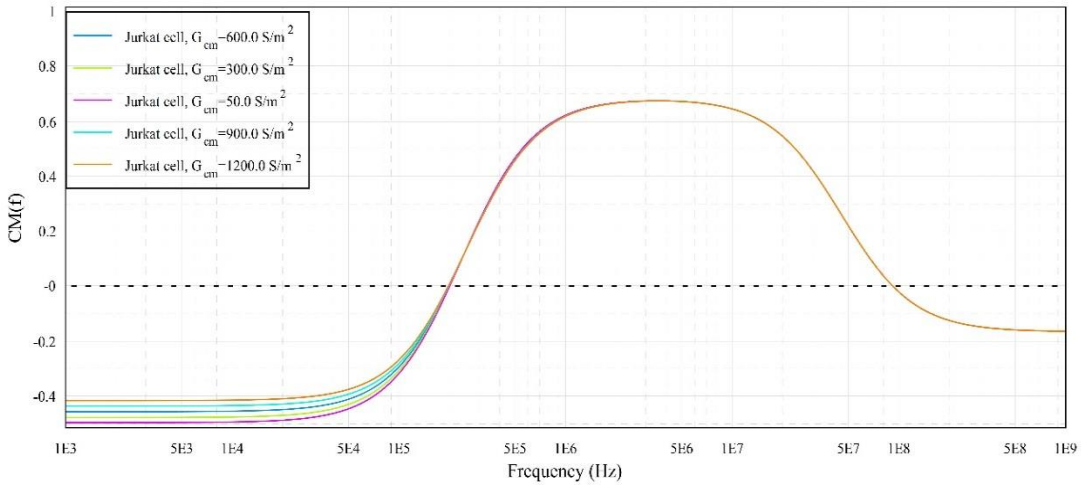

Figure 2.12: Influence of membrane conductance on Clausius Mossotti factor. The single shell cell model used was based on the values of a Jurkat cell (T cell line). All parameters other than the cytoplasm conductivity were fixed for all plots at the following values: cell radius 5µm, medium conductivity $\sigma_m = 0.05\ S/m$, cytoplasm conductivity $\sigma_{cp} = 0.4\ \mathrm{S/m}$, cytoplasm permittivity $\varepsilon_{cp} = 45$, membrane capacitance $C_{cm} = 10.61\ mF/m^2$.

On the other hand, the high-frequency crossover is influenced by the dielectric properties of the cytoplasm. Figure 2.13 shows that by increasing

the cytoplasm conductivity, the second crossover increases in frequency and the maximum value of the Clausius Mossotti factor increases in magnitude. The low-frequency values of the CM factor remain unchanged.

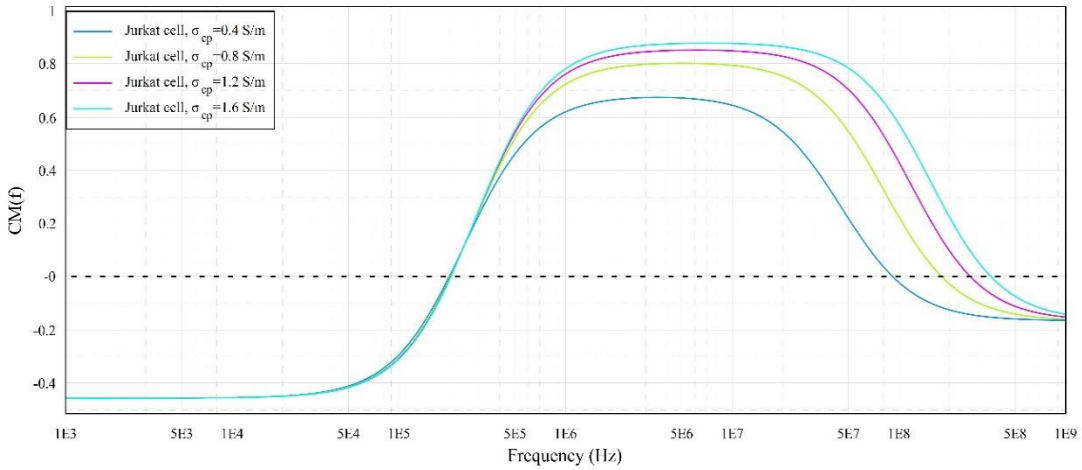

Figure 2.13: Influence of cytoplasm conductivity on Clausius Mossotti factor. The single shell cell model used was based on the values of a Jurkat cell (T cell line). All parameters other than the cytoplasm conductivity remained fixed for all plots at the following values: cell radius 5μm, medium conductivity $\sigma_m = 0.05\,S/m$, cytoplasm permittivity $\varepsilon_{cp} = 45$, membrane capacitance $C_{cm} = 10.61\,mF/m^2$, membrane conductance $G_{cm} = 600\,S/m^2$.

The second crossover frequency also increases with increasing cytoplasm permittivity, as shown in Figure 2.14, however the maximum value of the Clausius Mossotti factor remains unchanged whilst the minimum values increase to the extent that, eventually, the high-frequency crossover is lost.

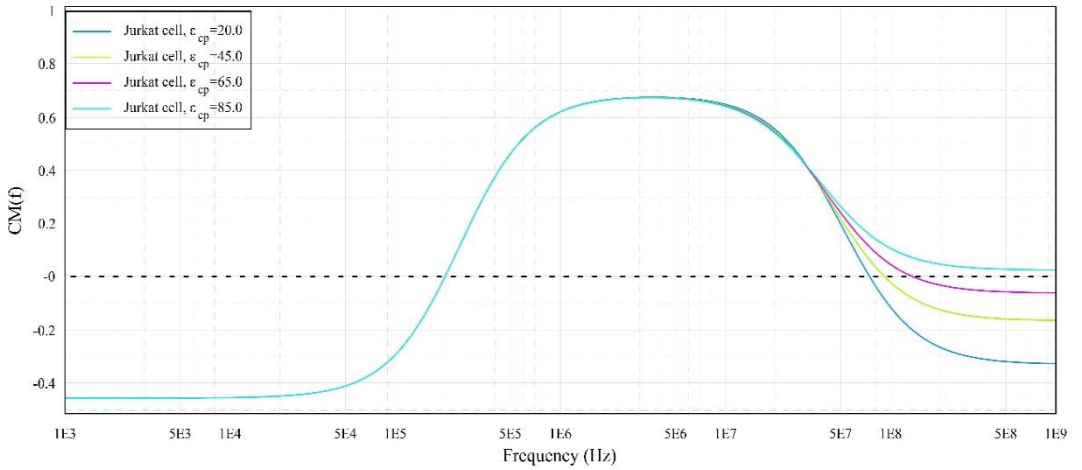

Figure 2.14: Influence of cytoplasm permittivity on Clausius Mossotti factor. The single shell cell model used was based on the values of a Jurkat cell (T cell line). All parameters other than the cytoplasm conductivity remained fixed for all plots at the following values: cell radius 5μm, medium conductivity $\sigma_m = 0.05\ S/m$, cytoplasm conductivity $\sigma_{cp} = 0.4\ \mathrm{S/m}$, membrane capacitance $C_{cm} = 10.61\ mF/m^2$ and membrane conductance $G_{cm} = 600\ S/m^2$.

The influences of all parameters on each frequency crossover are summarized in the following table:

Parameter	Influence			
	f_{01}	f_{02}	CM max	CM min
Membrane capacitance	***	-	*	-
Membrane conductance	-	-	-	*
Cytoplasm conductivity	-	***	**	-
Cytoplasm permittivity	-	***	-	***

Table 2.2: Summary table of influence of dielectric properties on first and second crossover frequencies (f_{01}, f_{02}) and maximum and minimum Clausius Mossotti factor values (CM max and CM min). Influence is determined as none (-), low (*), moderate (**), high (***).

2.2.4 Theoretical modelling of DEP force generated by IDTs

An analytical expression of the electric field generated by a set of interdigitated electrodes was first derived by Morgan et al (2001) [205], [206]:

$$\nabla|E^2| = \nabla\left(E_y^2 + E_z^2\right) = 2\hat{y}\left(E_y\frac{\partial E_y}{\partial y} + E_z\frac{\partial E_z}{\partial y}\right) + 2\hat{z}\left(E_y\frac{\partial E_z}{\partial z} + E_z\frac{\partial E_z}{\partial z}\right) \quad (2.38)$$

Where $\hat{y}$ and $\hat{z}$ are the unit vectors in the y and z direction, respectively, and the derivatives of the electric field components $\frac{\partial E_y}{\partial y}$ and $\frac{\partial E_y}{\partial z}$ are:

$$\frac{\partial E_y}{\partial y} = \frac{V_0}{d^2}\left(\frac{\sinh(\bar{z})\cos(\bar{y})}{\cosh(2\bar{z}) - \cos(2\bar{y})} + \frac{\sinh(\bar{z})\sin(\bar{y})}{\cosh(2\bar{z}) + \cos(2\bar{y})}\right)$$

$$\frac{\partial E_y}{\partial z} = \frac{V_0}{\pi d^2}\left(\frac{\cosh(\bar{z})\cos(\bar{y})}{\cosh(2\bar{z}) - \cos(2\bar{y})} - \frac{\cosh(\bar{z})\sin(\bar{y})}{\cosh(2\bar{z}) - \cos(2\bar{y})}\right)$$

Where d is the electrode width and $\bar{y}$, $\bar{z}$ are the normalised coordinates given by:

$$\bar{y} = \frac{\pi y}{2d} + \frac{\pi}{4} \qquad \text{and} \qquad \bar{z} = \frac{\pi z}{2d}$$

Equation (2.38) assumes that the acoustic aperture of the electrodes is infinitely wide and that there is an infinitely thick layer of water above the electrodes. This expression can be used to calculate the amplitude of the vertical and horizontal components of the negative DEP force exerted on a 5 µm latex bead (Figure 2.15).

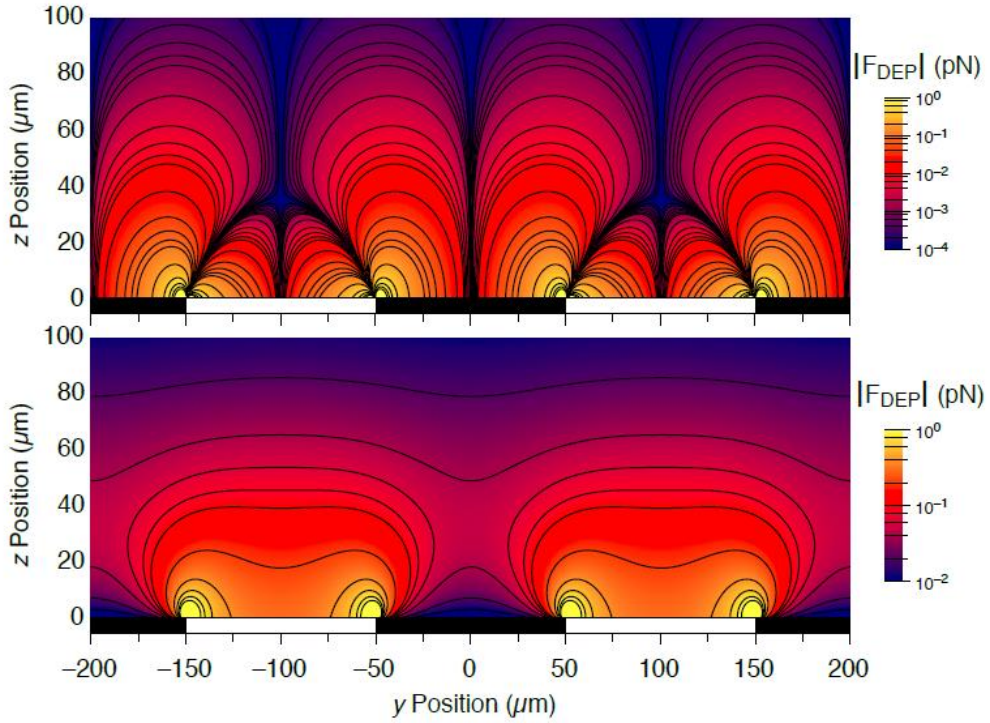

Figure 2.15: Plots showing the amplitude of the horizontal (top graph) and vertical (bottom graph) components of the negative DEP force experienced by a 5 µm latex bead for different positions along the channel height (z) and across the channel width (y). The position of the virtual electrodes is indicated by black rectangles. Reproduced from [141].

The analytical expression shows that the amplitude of both components of the DEP force decreases with increasing distance from the electrodes. The horizontal component of the DEP force (along the channel width) is maximal above the edge of the electrodes and minimal between the electrodes and at the electrode centre. The vertical component of the DEP force (along the channel height) is highest at the edge of the electrodes and lowest between

the electrodes but remains approximately constant across the channel width at a given height.

In addition, this analytical expression shows that the component of the DEP force acting along the channel height (i.e. away from the substrate surface) is an order of magnitude higher than the horizontal component across the channel width. This suggests that, upon reaching the virtual electrodes, the beads experiencing negative DEP are pushed rapidly towards the top of the channel until they reach a height in which the DEP forces and gravitational forces are balanced. Then, the beads align across the channel width owing to the weaker lateral DEP force, toward the zones of lowest electric field gradient.

Conversely, particles experiencing positive DEP are pushed towards the electrode surface by the stronger, vertical component of the DEP force and then align towards the zones of highest electric field gradient according to the horizontal component of the DEP force. This suggests that by exploiting the vertical alignment force rather than the horizontal alignment force, the throughput of a DEP separation device could be significantly increased, so this was investigated in Chapter 4.

2.3 Surface Acoustic Waves Dielectrophoresis (SAW-DEP)

Now that we understand the mechanisms behind both surface acoustic wave generation, and the application of dielectrophoretic forces to cells in suspension, we have the necessary tools to understand surface acoustic waves induced dielectrophoresis (SAW-DEP). This technique, proposed by Smith et al (2017) uses surface acoustic waves on a piezoelectric material to generate virtual electrodes that can be used for dielectrophoresis (Chapter 2 section 1.3) [140]. As explained in section 2.1.2, a standing SAW can be generated on a piezoelectric material when equivalent AC signals are applied to two opposing interdigitated transducers (IDTs). For SAW-DEP, a 42° cut lithium tantalate substrate is used, in which a shear horizontal standing SAW (SH-SSAW) is generated at the surface of the material. Due to the piezoelectric effect, the SH-SSAW induces an evanescent electric field in a plane normal to the substrate surface, with regions of low and high electric field density located above the nodes and antinodes of the standing wave (Figure 2.16). These fields play the role of “virtual electrodes” with a pitch and periodicity equivalent to those of the IDTs used to generate them.

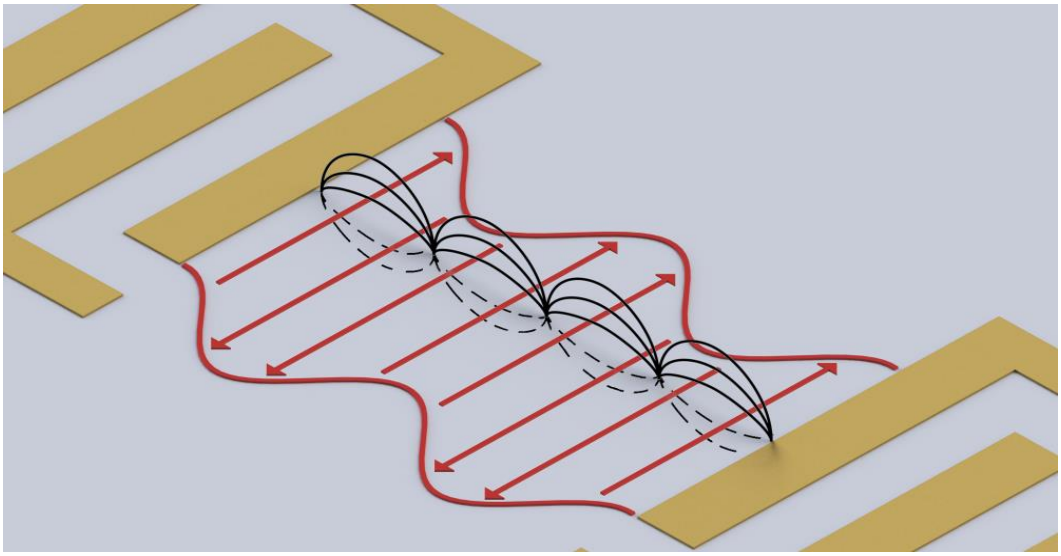

Figure 2.16: A schematic diagram depicting the SAW-DEP device designed by Smith et al. The gold IDTs generate a shear horizontal SAW (represented in dark red) contained within the piezoelectric substrate that induces a non-uniform vertical electric field (represented in black) that contains nodes and antinodes. Adapted from [140]**.**

Smith et al (2017) showed experimentally that, unlike a standing Rayleigh SAW which would produce a combined DEP and mechanically-induced alignment of target species, the influence of mechanical energy on an overlaid material from a shear SAW-DEP device is negligible [207]. This was further confirmed by a finite element modelling study performed by Dr Akshay Kale. A Comprehensive 3D model of the SAW-DEP setup used by Smith et al was used to generate plots of the SAW-induced mechanical displacement components on the surface of the piezoelectric chip (Figure 2.17).

As seen in Figure 2.17, the contribution of the longitudinal and surface normal displacements to the effective SAW displacement (which are the ones involved in acoustophoresis) is small compared to the shear normal displacement.

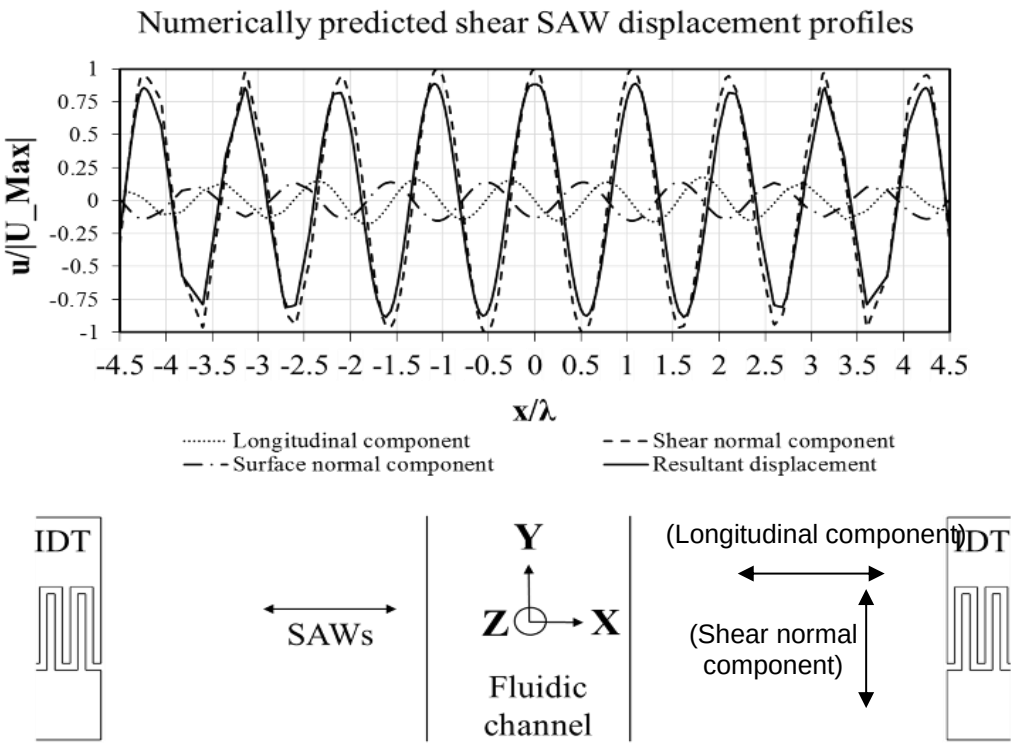

Figure 2.17: Numerically predicted mechanical displacement normalized by the maximum magnitude plotted at the chip-channel interface along the coordinate in the direction of the SAW propagation (X axis). The profiles are normalised by the maximum magnitude of the displacement for comparing the relative strengths of each component. λ represents the SAW wavelength.

Chapter 3
General material and methods

This chapter will focus on the general material and methods used in the results chapters. First, the general techniques used to fabricate SAW-DEP devices and microfluidic channels as well as the general setup used for the SAW-DEP experiments is outlined. Then, the techniques used for tissue cell culture used in chapters 4 and 5 are described to give a general understanding of how the DPSCs and MSCs were cultured. For a detailed description of the specific techniques used in each individual results chapter, a materials and methods section in included at the beginning of each chapter.

3.1 SAW-DEP devices fabrication

This section includes details on the fabrication of SAW-DEP chips in cleanroom facilities as well as the fabrication of moulds used for microfluidics channels and the general set up used for all SAW-DEP experiments.

3.1.1 Fabrication of SAW-DEP chips

SAW-DEP devices were fabricated using a standard photolithographic technique in a cleanroom environment (Figure 3.1). A cleanroom is a specialised laboratory designed to reduce the level of particulates suspended in the air (such as dust) to a minimum. This environment is essential for semiconductor manufacturing, as dust particles present on the substrate during the processing reduces the adherence of the metal electrodes to the wafer and results in poor electrical connections.

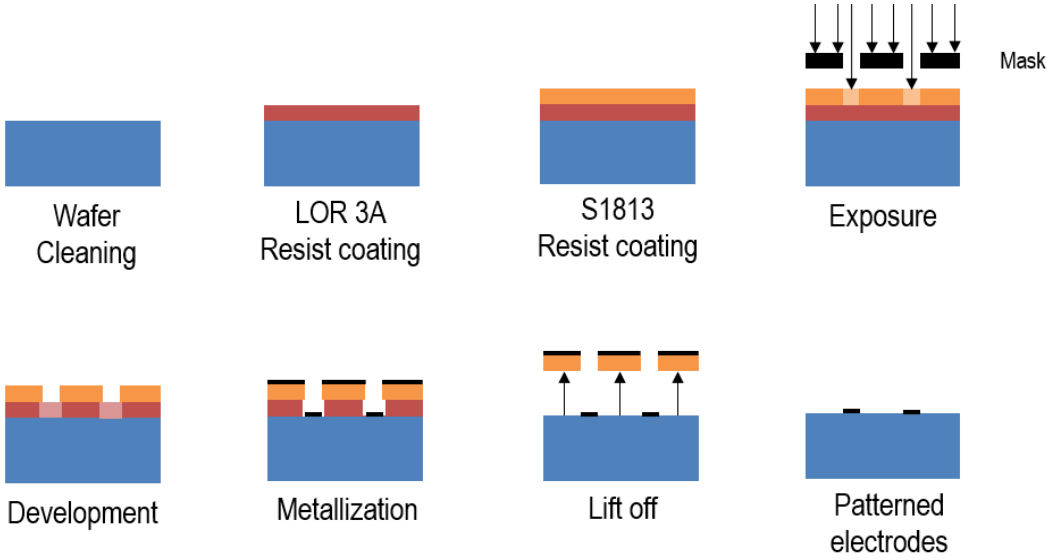

Figure 3.1: Interdigitated electrodes fabrication process. Two layers of photoresist are spun onto a clean lithium tantalate wafer and exposed through a chrome mask that serves as a stencil of the electrode geometry. A developer is used to etch the resists, creating an undercut. The E-beam evaporator is then used to deposit titanium and gold on the wafer. Following lift off, the resist is dissolved and only the metallic layer directly deposited on the wafer remains.

Photolithography requires the use of a photomask or a direct laser writer machine. In both cases, a photomask containing the electrode design was drawn using L-edit software (Figure 3.2). The electrode geometry was based on the design described by Smith et al (2017) [141]. A 1:1 mark to space ratio was used and the finger width was chosen depending on the operating frequency (a finger pitch of 100 µm was used to generate devices of 10MHz working frequency) as described in chapter 2 section 2.1.2.

In initial experiments, 15 finger pairs were used but these devices required matching networks, so 50 finger pairs were used in subsequent experiments to bypass the need of matching networks. The acoustic aperture was chosen to be 1 mm, as it was a good range to be imaged on the microscope with a 5x magnification. The gap between the two sets of IDTs was chosen to be 3 mm to allow space for a 1 mm fluidic channel and avoid contact of the electrodes with the liquid. Bond pads were also included to allow for bonding of gold wires for electrical connection.

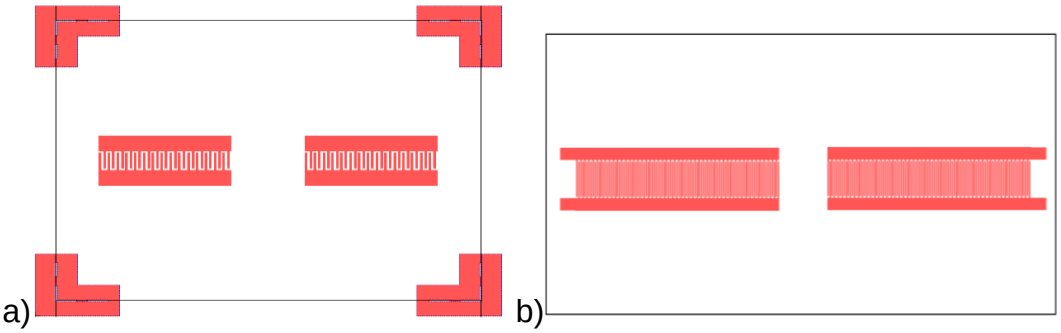

Figure 3.2: a) Example of one of the initial mask designs used for SAW-DEP electrode fabrication consisting of two sets of interdigitated electrodes with 15 finger pairs, 100 μm finger width and spacing. The alignment marks at the corners were used to align the designs to the flat of the wafers using the mask aligners. In the mask, the red areas were transparent while the white areas were opaque and covered with a layer of chrome. b) Schematic of the latest mask designs used for SAW-DEP fabrication using maskless lithography. The IDTs contained 50 finger pairs.

For initial experiments, a 10'' x 12'' chrome photomask was ordered from JD photodata (Hitchin, UK) and a mask aligner was used to expose the resists. For later experiments, an MLA-150 direct-write laser system (Heidelberg Instruments, Heidelberg, Germany) was available so no masks were necessary and the file with the design was directly uploaded onto the machine.

Electrodes fabrication protocol

Firstly, a thin layer of S1813 photoresist (Shipley, UK) was spun at 3000 rpm onto the $LiTaO_3$ wafers and baked for one minute at 105°C in order to limit the particle deposition on the wafer before cutting it. The wafer was then cut into 20 mm x 38 mm rectangles using a Microace 66 wafer saw (Loadpoint ltd, Swindon, UK). The cut substrate was then cleaned for ten minutes using a piranha etch made from a 3:7 ratio of dihydrogen peroxide:sulphuric acid. The chips were then washed in deionised (DI) water, blow dried using nitrogen (N_2) and oxygen plasma ashed for five minutes at 50 W. The samples were then baked at 185°C for ten minutes to remove any moisture. The temperature was ramped slowly to avoid stresses.

After the cleaning steps, a thin layer of LOR 3B (Kayaku advanced materials, MA, USA) was spun on the wafer at 4000 rpm for 40 seconds and baked for four minutes by ramping the temperature up to 185°C. Then, S1813 positive

photoresist was spun on the wafer at 4000 rpm for forty seconds and baked for three minutes by ramping the temperature to 115°C. Chips were UV exposed at ~ 90 mJ/cm^2 through a photoresist mask using a mask aligner. For later experiments where the MLA-510 was used, the dose used was 130 mJ/cm^2.

Following exposure, chips were developed in MF-319 (Shipley, UK) for 67 s, rinsed using DI water, then blow dried with nitrogen gas. Chips were then oxygen plasma ashed at 50 W for forty seconds. A Leybold L560 E-beam evaporator (Leybold, Cologne, Germany) was used to first evaporate a 5 nm thick layer of titanium followed by a 50 nm layer of gold at < 2 x 10^{-6} mbar. To lift off, the S1813 was stripped by leaving the chips in 1165 remover at 65°C for one hour and thirty minutes, then rinsed with isopropanol and blow dried with nitrogen. For storage, the chips were protected by spinning a thin layer of S1813 at 4000 rpm for forty seconds.

3.1.2 PDMS microfluidic channels fabrication

The microfluidic channel moulds were designed in L-edit software and then fabricated using SU 8 50 resist on a silicon oxide wafer. The surface of the wafers was first cleaned with isopropanol, blow dried and plasma ashed for five minutes at 50 W. The wafers were then baked for five minutes on a hot plate at 200°C to achieve dehydration. The substrate was left to cool, before spinning on a layer of SU8 50 resist (Kayaku advanced materials, MA, USA). To create different sized channels, SU8 50 was spun at different speeds, baked and UV exposed using the MLA-510 for different amounts of time. The specific settings used for each thickness are described in Table 3.1.

SU-8 50 Thickness	Speed (rpm)	Soft bake at 65°C	Soft bake at 95°C	UV exposure (mJ/cm^2)	Post exposure bake at 95°C
30 µm	3570	4 minutes	12 minutes	175	3 minutes
40 µm	3000	5 minutes	16 minutes	190	4 minutes
50 µm	2000	6 minutes	20 minutes	215	5 minutes
60 µm	1850	6 minutes	23 minutes	250	6 minutes
80 µm	1375	9 minutes	28 minutes	320	8 minutes

Table 3.1: Spinning speed, baking times and UV exposure times necessary to obtain all SU8 50 thickness moulds created. Data obtained following SU8 50 data sheet [208].

SU 8 50 was first spun at 500 rpm for 10 seconds to spread evenly then at the speed was chosen to achieve the desired thickness. Following spin

coating, the wafers were baked at 65°C followed by a 95°C soft bake. The coated wafers were then UV exposed from the back. After exposure, the wafers were baked at 65°C for one minute and then baked at 95°C as specified in Table 3.1. The resist was then developed in two consecutive baths of EC solvent (Shipley, UK) first for three minutes and then for one minute and thirty seconds in a clean new beaker. The wafers were then washed in IPA and blow dried. This concluded the SU8 patterning step.
To define the outer dimensions of the microfluidics layer, 12 x 40 x 3 mm gaskets were cut out of 3 mm perspex using a laser cutter. These were stuck onto the silicon wafers (around the SU8 mould) with double-sided sticky tape to create a mould. Polydimethylsiloxane (PDMS) was made by mixing Sylgard™ 180 base and elastomer (DOW Chemical Company, MI, USA) at a 10:1 ratio of base:crosslinker and degassed in a desiccator connected to a vacuum pump for 20 minutes. PDMS was then poured into the moulds and cured by heating in an oven at 70°C for an hour. The PDMS was then peeled off the mould after cutting the sides with a scalpel. Finally, holes for tubing to be connected were made using a 1.5 mm diameter biopsy punch. The height of the channels was measured using an alpha step surface profiler to ensure the correct channel height was obtained.

3.1.3 SAW-DEP device assembly

Following fabrication of the SAW-DEP chips and the PDMS microfluidic channels, the devices were assembled. Prior to bonding, the PDMS channel was sonicated at 50% power in isopropanol for five minutes. The chip was then cleaned in acetone for five minutes followed by five minutes in isopropanol. After cleaning, the PDMS was plasma bonded to the chip using a PDC-32G-2 plasma cleaner (Harrick plasma, NY, USA) equipped with an IDP-3 vacuum pump (Agilent Technologies, CA, USA) for one minute with special care taken to obtain a good alignment between the IDTs and the channel. The bonded chip was stuck to a printed circuit board (PCB) using Apiezon black wax that had been previously heated to 120^0C. The IDTs of the chip were then electrically connected to the PCB copper tracks by gold wires via ball bonding and silver epoxy glue (cured at 70°C for fifteen minutes). Finally, two SMA connectors were soldered onto the PCB.

3.1.4 General set up for SAW-DEP experiments

The experimental set up used for all the SAW-DEP experiments is illustrated in Figure 3.3. A Marconi 2022E signal generator (SGLabs, Perugia, Italy) was connected to a ZHL-1-2W amplifier (Mini-Circuits, NY, USA) with a 24 V DC power supply (Agilent Technologies, CA, US). The signal was split via a 2APD-30-s signal splitter (Mini-circuits, NY, USA) to provide each IDT with the same signal. The total input power applied to each set of interdigitated electrodes was calculated considering the amplification (29 dB gain) and the 3 dB loss corresponding to the signal being halved by the signal splitter.

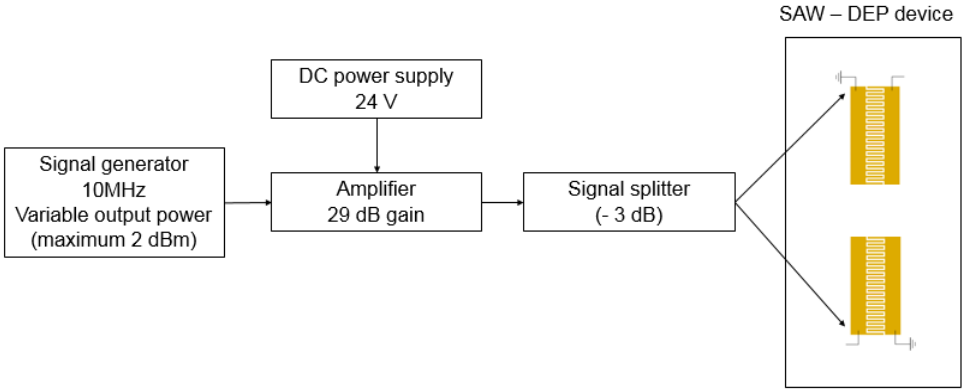

Figure 3.3: General SAW-DEP setup. A signal generator is used to generate a sinusoidal signal of 10 MHz. The signal is amplified using an amplifier powered by a DC power supply, and split into two signals using a signal splitter to power both electrodes.

The liquid suspensions were injected in the microfluidics channel via a syringe connected to PTFE tubing of 2 mm outer diameter and 0.5 mm inner diameter. The fluid was dispensed at a controlled flow rate using a PHD 2000 syringe pump (Harvard apparatus, MA, USA).

3.2 Tissue culture general procedures

For the results chapters 5 and 6, dental pulp stromal cells (DPSCs) and bone marrow mesenchymal stem cells (BM-MSCs) were cultured and expanded in a tissue culture lab following standard procedures described in this section and maintaining sterility. All the procedures described in this section were performed in a sterile tissue culture hood where the air flow provided positive pressure, such that microparticles were not brought in from the outside and all materials were sprayed with a 70 % ethanol solution to limit the risk of contamination.

DPSCs were harvested from the dental pulp of extracted molars obtained with informed consent from donors via the Leeds School of Dentistry Tissue bank. This work was authorised by the Dental Research Ethics Committee (280716/ASD/210). Following digestion of the dental pulp with collagenase I (3 mg/mL) and dispase (4 mg/mL), the primary dental stem cells were selected via plastic adherence (Chapter 1 section 1.2.1).

Proliferating human BM-MSCs were purchased from Promocell (UK) at passage 2 and cultured up to passage 6.

3.2.1 Growth conditions

Both DPSCs and BM-MSCs were cultured in T175 polystyrene cell culture flasks containing 25 mL of stem cell basal media consisting of alpha MEM supplemented with 10 % foetal calf serum, 1 % of 100 g/mL penicillin-streptomycin solution and 1 % of 200 mM L-glutamine solution, all obtained from Sigma-Aldrich (UK). The flasks were left in an incubator at 37 °C, with 5 % CO_2 and the medium was changed every three days. The confluence of the cells (ie the percentage of surface covered by the growing cells) was checked regularly, to avoid a confluence higher than 80%, as this can trigger early differentiation of cells. For DPSCs, typical doubling times of 2-4 days depending on the passage were observed whereas BM – MSCs grew slower, with doubling times of 4-7 days depending on the passage.

3.2.2 Passaging of BM-MSCs and DPSCS cultures

Once the cells reached 80% confluence, the cells were detached from the flask and either used, frozen or reseeded into multiple cell culture flasks. When the cells were detached from the flask or thawed from a frozen aliquot and sub-cultured, this represented one passage. Stem cells were used until passage 6, as their growth decreased significantly after this passage and they started showing signs of differentiation.

To detach the cells from the flask, the basal media was first aspirated and the cells were washed with 10 mL of warm PBS to remove all traces of foetal calf serum. The PBS was then aspirated, and 5 mL of trypsin solution were added to break down the cellular anchors attaching the cells to the flask's surface. After a seven-minutes incubation in at 37 °C, the cells detached from the flask

and 5 mL of basal media were added. The cells were resuspended using a stripette, collected in a Falcon tube and centrifuged at 800g for five minutes. The supernatant was discarded and the cells were resuspended in 10 mL of basal media.

To split the cells, 2 mL of cell suspension was added two one flask containing 20 mL of basal media and left in the incubator. Four hours later, the cells were attached to the bottom of the flask.

3.2.3 Freezing of BM-MSCs and DPSCS for long term storage

In order to preserve the cells long term for later experiments, the expanded cells were frozen and kept in a freezer until needed. After detaching the cells from the flask using trypsin, as described in section 3.2.2, the cells were counted using a haemocytometer and the cell suspension was centrifuged at 800g for five minutes. The pellet was then resuspended in freezing medium consisting of alpha MEM supplemented with 30 % foetal calf serum and 10 % dimethyl sulfoxide (DMSO) at a concentration of 1 million cells/mL and transferred to a 1.5 mL cryovial. The cryovials were transferred to a Nalgene® Mr Frosty freezing container (Sigma Aldrich, UK) and stored in a freezer at - 80 °C. The freezing box contained isopropanol, which controls the cooling rate of the temperature for the vials (- 1°C/minute) to limit thermal shocks that could reduce cell viability. Once the vials were frozen, they were left in - 80 °C, for short term storage (less than 3 months) or transferred to a - 196 °C liquid nitrogen freezer for long term storage.

3.2.4 Thawing of BM-MSCs and DPSCS

To thaw the cells after long periods of storage, the cryovials were submerged in a water bath at 37 °C until completely thawed. The liquid suspension was then transferred to a Falcon containing 4 mL of media and centrifuged at 800 g for five minutes. The supernatant was aspirated, and the pellet was resuspended in 5 mL of basal medium. The suspended cells were then seeded onto a T175 flask containing 20 mL of basal media and kept in the incubator at 37 °C and 5 % CO_2.

Chapter 4
Characterisation of SAW-DEP devices and optimisation of channel design for increased throughput

4.1 Introduction

In this chapter, a detailed characterisation of the physics governing the SAW-DEP device is presented. Smith and colleagues used an analytical model (Chapter 2 section 2.2.4) to describe the DEP force generated by virtual electrodes established by a standing SH-SAW. This model suggested that the vertical component of the DEP force (i.e. normal to the substrate surface) was an order of magnitude higher than the horizontal component across the channel. Here, it was hypothesised that the vertical alignment force could be exploited to separate particles based on their DEP properties at a higher throughput than previously reported using a horizontal separation [140]. While Smith and colleagues reported that the DEP force calculated using the analytical model described in Chapter 2 section 2.2.4 showed good agreement with proof of concept experiments [141], the assumptions made were not an accurate description of the actual experimental situation. The analytical model assumed the virtual electrodes generated by the standing SH-SAW to be equivalent to physical electrodes with an infinitely wide acoustic aperture and submerged in an infinitely thick layer of water. A detailed understanding of the underlying physics involved in SAW-DEP remains crucial for establishing guidelines when designing SAW-DEP devices with increased throughput.

COMSOL Multiphysics is a finite element (FE) analysis tool that can be used to simulate devices involving coupled physics such as acoustics, mechanics, electromagnetic or fluid flow in multiple dimensions. 3D and 2D finite element models of cell separation devices relying on conventional DEP, insulator DEP and electroosmotic flow have been extensively described in the literature [209]–[213]. These models are used to simulate different electrode and channel geometries and input voltages to achieve optimal separation before testing experimentally [214], [215]. However, these models cannot be used to describe SAW-DEP, which relies on the use of SH-SAWs to generate the virtual electrodes used for DEP separation. While FE models of surface acoustic waves have been reported, these often focus on Rayleigh SAWs (RSAWs), which are often used for electronic signal filtering, sensing and

acoustophoresis (Chapter 2 section 1.2.2.2) [216]–[219]. For RSAWs, a 2D model along the half-way cut across the channel suffices for describing the behaviour of the system, because there are no SAW components perpendicular to this plane. However, the structure of SH-SAWs as exploited in SAW-DEP technology necessitates the use of a comprehensive 3D model to account for all components of the shear wave being perpendicular to the direction of wave propagation, and to therefore avoid possibly unrealistic assumptions. In order to better understand the underlying physics of SAW-DEP, Dr Akshay Kale proposed a comprehensive 3D finite element model of the entire SAW-DEP device (Figure 4.1). This model included the IDTs patterned on the lithium tantalate substrate, the supporting printed circuit board and the microfluidics channel. To reduce computational time, the geometry width was set to 5 mm and the device symmetry was exploited by imposing a symmetry plane equidistant between opposing IDTs, normal to the direction of the SAW propagation. A more detailed description of the parameters and equations used in the FE model can be found in [140].

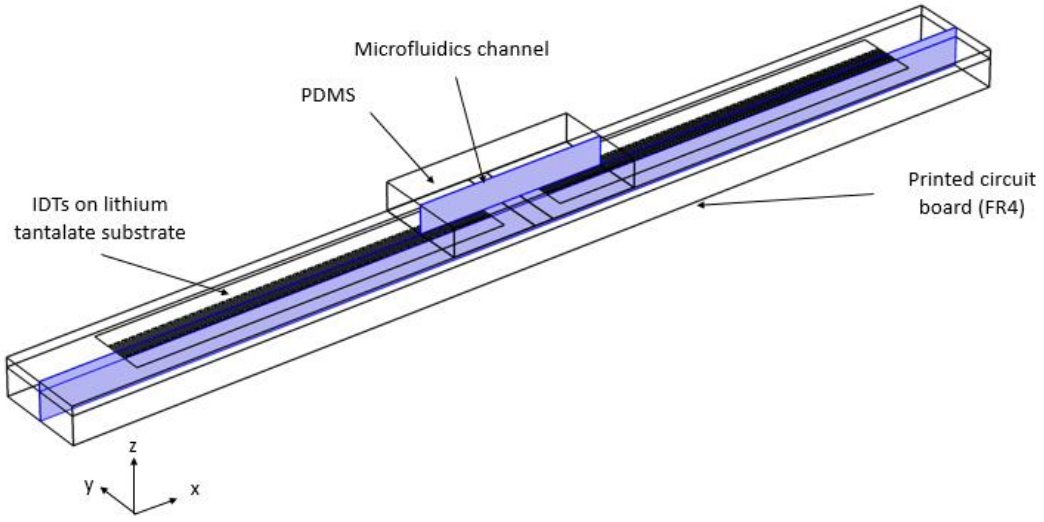

Figure 4.1: 3D geometry of the FE model generated by Dr Akshay Kale on COMSOL Multiphysics 5.2a on the high performance computing platform provided by Amazon Web Services. The generated SAW wave propagates in the x direction whereas the fluid flow is in the y direction.

4.1.1 Research questions

In this chapter, two main objectives were addressed. The first objective consisted of characterising the factors affecting the DEP force amplitude through the validation of a FE model. The second objective was the

optimisation of the device to maximise the DEP forces acting on the particles and to design and implement a fluidic setup to demonstrate enhanced separation throughput. These objectives were addressed via the following research questions:

1. Can the finite element model describe accurately the experimental data?

The first section of this chapter focuses on the experimental validation of the FE model developed by Dr Akshay Kale. A range of SAW-DEP devices were fabricated with different channel heights and evaluated experimentally for different input powers. The effect of these two parameters on the alignment velocity of latex beads, and therefore the magnitude of generated negative DEP force, were recorded and analysed. These experimental results were then compared to the numerical data generated by the FE element model.

2. What flow conditions and channel geometries allow for increased throughput?

The experimental characterisation of the forces obtained for different channel heights was used to inform the subsequent design of multi-layered microfluidics channels to exploit the vertical force separation and increase the throughput of the device 20-fold. COMSOL Multiphysics was used as a tool to simulate the flow conditions and particle tracking in different channel geometries to determine the best design exploiting the vertical force separation for increased throughput. Following the computational data, the best performing designs were fabricated and tested experimentally with latex beads at different flow rates to demonstrate the increase in throughput achieved by the new designs.

4.2 Materials and Methods

4.2.1 SAW-DEP device assembly for determination of DEP forces for different channel heights.

The SAW-DEP device electrodes were fabricated via lithography (as explained in chapter 3 section 3.1.1) with 50 finger pairs for an operating frequency of 10.275 MHz, which approximately corresponds to a SAW wavelength of 400 µm. The device was then stuck to a printed circuit board

(PCB) using Apiezon black wax heated to 120°C and the IDTs of the chip were electrically connected to the PCB copper tracks by gold wires via ball bonding and silver epoxy cured at 70°C for fifteen minutes. Finally, two SMA connectors were soldered onto the PCB. The insertion loss was characterised in an Agilent network analyser and determined to be -11.5 dB.

For the validation of the COMSOL model, five different channels with heights of 24, 44, 50, 64 and 84 µm were fabricated by casting PDMS on SU-8 moulds (as shown in chapter 3, section 3.1.2). Each channel was assembled in turn onto the same SAW-DEP device using M4 screws to clamp the device between a perspex lid and support as shown in Figure 4.2. This clamping system allowed the same SAW-DEP device to be used for all the channel conditions tested to avoid confounding factors related to the SAW-DEP device fabrication during data collection.

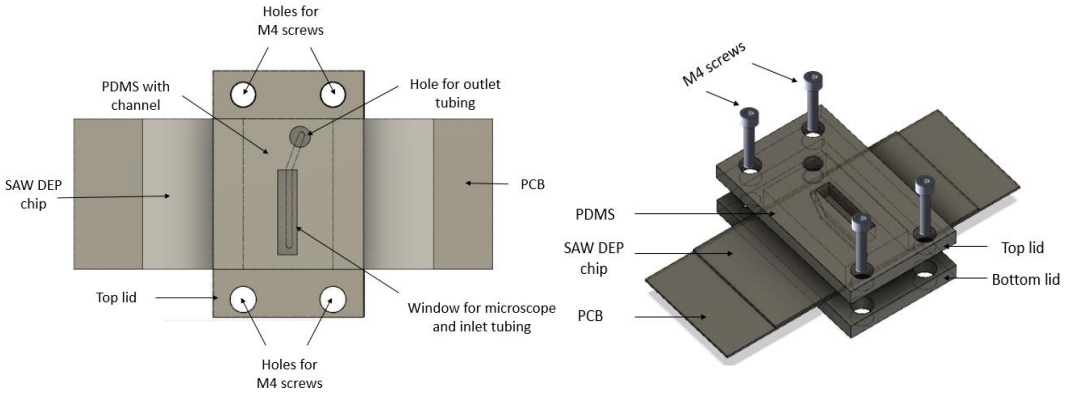

Figure 4.2: Top and side view of the clamping system used to keep the PDMS channels in place.

4.2.2 Experimental validation of FE model using latex beads

Fluoro-Max green-dyed latex beads with a mean diameter of 5 µm (ThermoFisher, MA, USA) were used in these experiments. Latex beads were used because they are known to experience negative DEP in the test conditions used (SAW operating frequency = 10 MHz, medium conductivity = 0.01 S/cm) (Figure 4.3).

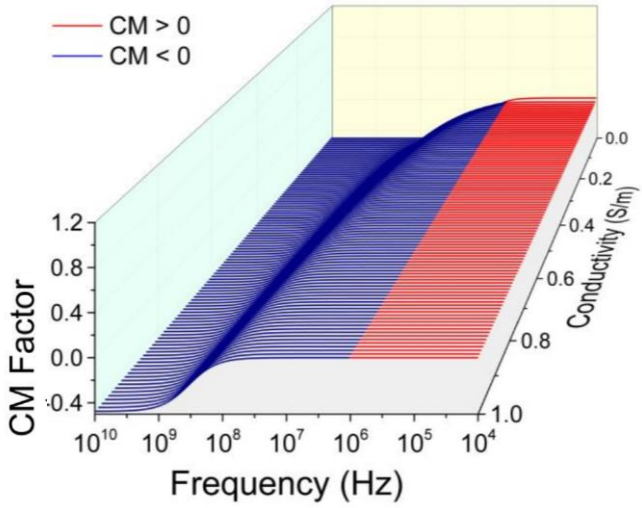

Figure 4.3: Numerical calculations of Clausius Mossotti (CM) factor of latex beads for different frequencies and conductivities. For a positive CM factor (red), latex beads experience positive DEP. For a negative CM factor (blue), latex beads experience negative DEP. Image reproduced from [141].

For each PDMS channel height, the beads were diluted 20 times in 0.1% triton solution and injected into the fluidic channels to generate a homogeneously distributed suspension. Once the flow had stopped, the SAW-DEP device was activated by applying power to both IDTs simultaneously, using a signal generator connected to a 29 dB amplifier and a signal splitter as described in Chapter 3 section 3.1.4. For each channel height, the signal generator output power was varied as shown in Table 4.1. The total power delivered to each set of interdigitated electrodes was the linear sum of the signal generator output power, the amplifier gain of 29 dB and a loss of 3 dB owing to the signal being split into two at the signal splitter (Table 4.1). The formula used to convert the power in decibel-milliwatts (dBm) to milliwatts (mW) was:

$$P_{mW} = 10^{P_{dBm}/10}$$

Where P_{mW} is the power in milliwatts and P_{dBm} is the power in dBm.

The liquid containing the beads was injected in the microfluidics channel via a syringe connected to PTFE tubing (2 mm outer diameter and 0.5 mm inner diameter). Experiments were performed under a non-inverted Olympus BX60 fluorescent microscope (Olympus, Tokyo, Japan) with a mercury lamp, using a 10x objective. Alignment videos were recorded using a Photometrics prime

4 MP camera (Teledyne Photometrics, TZ, USA) connected to the microscope.

Channel height (µm)	Signal generator output powers (dBm)	Power applied to each IDT	
		dBm	mW
24	-4, -6, -8, -10, -12	22, 20, 18, 16, 14	158, 100, 63, 40, 25
44	-2, -4, -6, -8, -10	24, 22, 20, 18, 16	251, 158, 100, 63, 40, 25
50	-2, -4, -6, -8, -10	24, 22, 20, 18, 16	251, 158, 100, 63, 40, 25
64	-2, -4, -6, -8, -10	24, 22, 20, 18, 16	251, 158, 100, 63, 40, 25
84	-2, -4, -6, -8, -10	24, 22, 20, 18, 16	251, 158, 100, 63, 40, 25

Table 4.1: Power applied to each IDT in the SAW-DEP device for each of the microfluidic channels with different channel heights. The power applied to each IDT accounts for 29 dB amplification and 3 dB loss from the signal splitter (half the generated power is delivered to each IDT).

Particle path-lines were generated from the recorded videos (Trackmate, Fiji) [220]. The data was then analysed using a custom-built Java program, the output of which yielded a graph of the DEP alignment force against the position in the channel along the direction of SAW propagation (as explained in section 4.2.3). The average DEP force was calculated by averaging the absolute value of the peak amplitudes of the DEP sinusoidal curves without taking into account the edge of the channels to avoid anomalies, as shown in Figure 4.4.

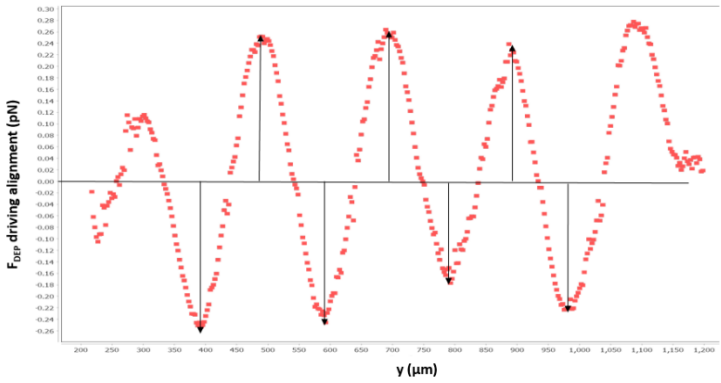

Figure 4.4: DEP force profile along the y axis (direction of propagation of the SAW). The arrows show the amplitudes considered when calculating the average DEP force.

4.2.3 Determination of DEP force from beads alignment

This section provides a detailed explanation of the particle tracking program used for generating the experimentally obtained DEP alignment force profiles (Figure 4.4). Particle tracks were generated from the bead alignment videos recorded using the Trackmate plugin (Fiji) and the position co-ordinates of the particles for the different time instants were exported into a program to process the data (Figure 4.5).

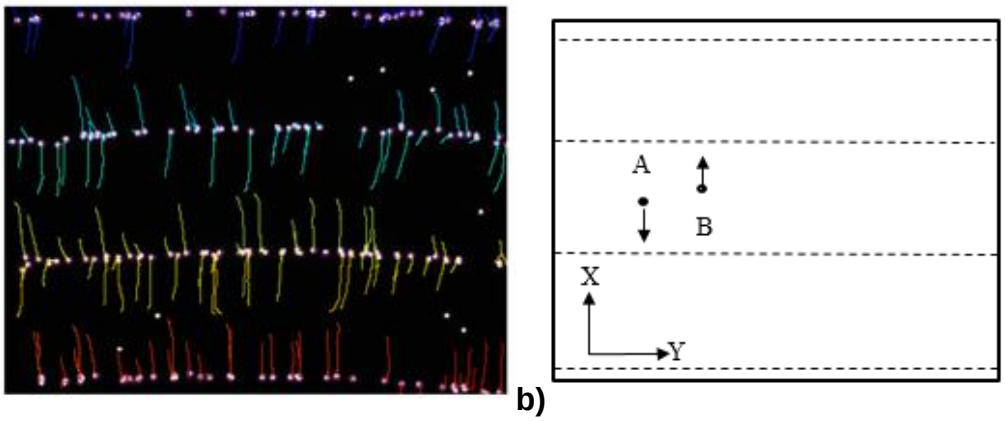

Figure 4.5: a) Particle alignment and track generation as seen in the top view of the channel. b) Schematic of particle alignment directions.

First, the program plots the x coordinate for each particle in the channel against time and fits a polynomial to the curve to reduce the scatter. The lateral velocity component of the bead, u_p, is deduced as a function of x from the polynomial fit by differentiation.

The total force (F_{tot}) exerted on the particle can be described using Newton's Second Law:

$$F_{tot} = m_p \frac{du_p}{dt} \quad (4.1)$$

Where m_p is the particle's mass, and $\frac{du_p}{dt}$ is the lateral component of the bead's acceleration. In this system, it is assumed that the total force exerted on the particle in the vertical direction is comprised of the DEP force (F_{DEP}) and the drag force (F_{drag}) that can be written as:

$$F_{drag} = 6\pi\eta_m r(u_p - u_m) \quad (4.2)$$

where η_m is the medium density r is the particle radius and $u_p - u_m$ is the speed of the particle relative to the fluid.

Using (4.1) and (4.2), the correlation between the DEP alignment force and the velocity shown below can be found:

$$m_p \frac{du_p}{dt} = F_{DEP} + 6\pi\eta_m r(u_p - u_m) \quad (4.3)$$

The instantaneous rate of change of velocity for a micron-sized bead (given by the LHS of Equation (4.3)) is negligible, so the equation simplifies to:

$$F_x(x) + 6\pi\eta_m r u_p(x) = 0 \quad (4.4)$$

where F_x is the alignment component of F_{DEP} along the channel. F_x can therefore be obtained as a function of x for each particle using equation (4.4), with the corresponding value of u_p taken from the previous polynomial fit. In order to limit the scatter, a mean value of DEP force is calculated for all particles in a small portion along the x direction. The average DEP force for each portion is then plotted against x to generate the final force profiles shown in Figure 4.4. These values were later compared with the finite element predictions, as outlined in the following sections.

4.2.4 Fluid flow and particle tracing modelling using COMSOL Multiphysics

The commercial finite element simulation software COMSOL Multiphysics version 5.2a (COMSOL Ltd, Cambridge, UK) was used to generate a 3D model of fluid flow and the trajectories of particles in the liquid. The “laminar flow” and “particle tracing for fluid flow” interfaces of the software were used to simulate the fluid flow and the trajectories of particles in each of the different channel geometries shown in Figure 4.6.

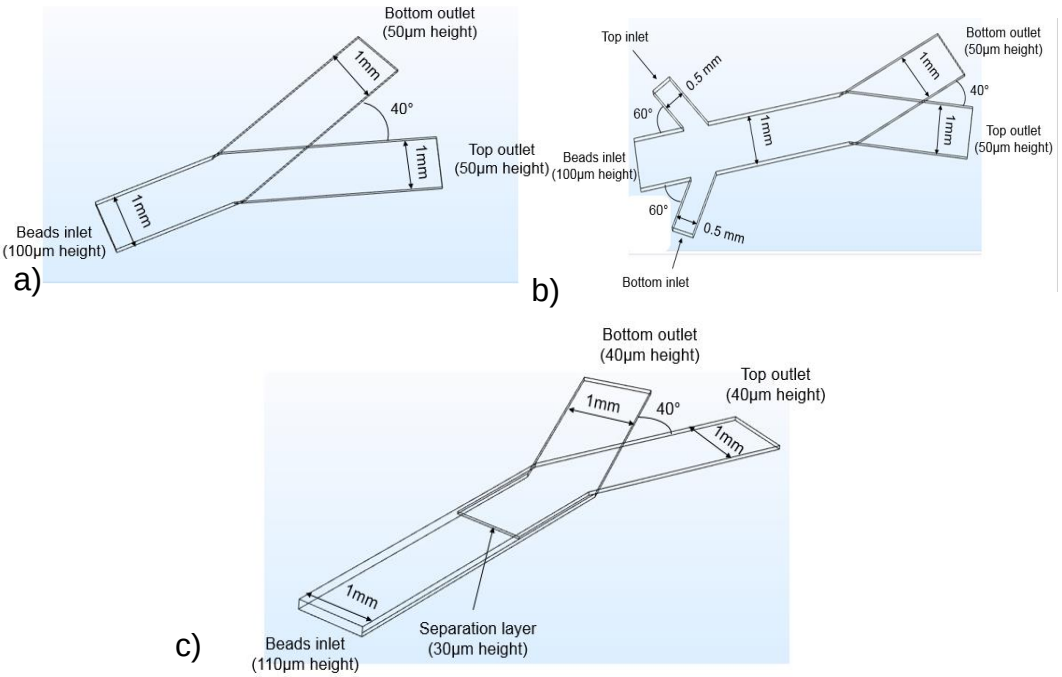

Figure 4.6: Multichannel geometries used for modelling in COMSOL Multiphysics. a) Double layer channel with 40° forked outlet. b) Fluid focusing model. c) Triple layer channel with separation layer.

The channels were modelled as a single domain containing water. The free surfaces of the fluid in the inlets and outlets were assumed to be exposed to the atmosphere. A first stationary study was used to model the fluid flow. The flow was modelled to be laminar since, for the microchannels and flow rates tested, the Reynolds number (characterising the relative influences of the inertial terms to the viscous terms in the Navier-Stokes equations) was found to be very small (~ 0.001). The beads inlet flow was modelled to be 5 µL/min for all the geometries tested whilst the flow at the side inlets of the flow focusing models was varied as shown in Table 4.2.

Name	Top Inlet flow rate	Bottom inlet flow rate
Flow focusing 1	5 µL/min	5 µL/min
Flow focusing 2	2.5 µL/min	2.5 µL/min
Flow focusing 3	10 µL/min	10 µL/min
Flow focusing 4	10 µL/min	10 µL/min
Flow focusing 5	5 µL/min	2.5 µL/min

Table 4.2: Differences in geometry and fluid dynamics between the different double layer models tested.

A second time dependent study with a time step of 250 ms was used to simulate the particle trajectories using the “Particle Tracing” module. The boundary condition “bounce” was applied to the side walls. The particles were

released at time 0 with a null velocity and simulated as an array of 12 lines across the beads inlet channel with an 85 µm separation to assess the trajectories at different places across the channel width. The particles were modelled at different heights from the bottom of the channel depending on the conditions of DEP that were studied. To simulate the lifting effect of positive dielectrophoresis, the particles were modelled at a distance of 10 µm from the bottom of the channel. To simulate lifting effect of negative dielectrophoresis, the particles were modelled at a distance of 80 µm from the bottom of the channel, which was calculated to be the distance at which the DEP force and the gravitational force were equal (see section 4.3.1.3). The gravitational and drag forces were considered when modelling the particles' trajectories. The relevant properties of the particles and fluid used to calculate the forces and particle trajectories in the model are shown in Table 4.3.

Symbol	Value	Unit	Description
ρ	1000	kg/m^3	Fluid density (of water)
ρ_p	1055	kg/m^3	Particle density
d_p	5	µm	Particle diameter

Table 4.3: Summary of the material properties used in all the fluid flow models.

A fine physics-controlled mesh was used to ensure a precise solution whilst minimizing the computational memory and therefore simulation time. The obtained solutions were postprocessed in COMSOL and exported in the form of fluid flow profiles and particle trajectory images.

4.2.5 Fabrication of multi-layered microfluidic channel SAW-DEP devices and fluid flow testing with latex beads

A multichannel composed of two PDMS layers was first fabricated (Figure 4.7). The top, thick layer of PDMS was cast onto an SU8 mould (as described in Chapter 3, section 3.1.2) to create a 50 µm high channel. Before assembly, an inlet and two outlet holes were punched into the top layer to allow for tubing.

The bottom thin layer was fabricated by spinning PDMS (10:1 ratio of elastomer to crosslinker) on a supporting glass slide at 2500 rpm for 50 seconds with an acceleration of 200 rpm/s, followed by curing for 5 minutes at 95°C on a hot plate. The resulting ~50 µm layer of PDMS was laser cut using a ProtoLaser R cutter (LKPF, Garbsen, Germany) to create the bottom channel. The top and bottom layers were bonded by exposure to oxygen plasma for 40 seconds, and the resulting multilayer stack was peeled off the supporting glass slide. When bonding the multilayer to the SAW-DEP device, care was taken to position the electrodes immediately before the channel fork.

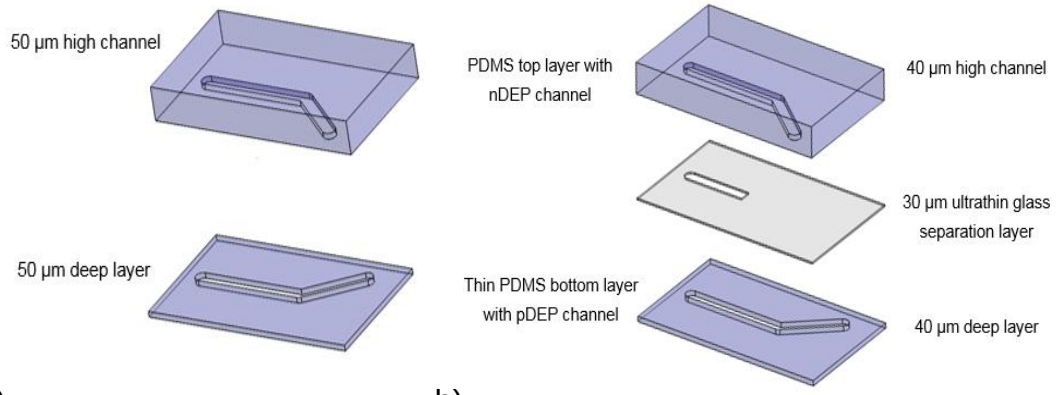

Figure 4.7: Assembly of the double and triple layer channels used in the flow experiments. a) The double layer channel was composed of a thick PDMS layer bonded on top of a thin PDMS layer. b) The triple layer channel was composed of the same layers which were separated by a 30 µm ultrathin glass separation layer with a window at the inlet portion of the channel. NOTE: The angle between the top and bottom channels was 40° to allow for enough separation between the outlets to account for tubing.

A second multichannel design, also composed of two PDMS layers, contained a third layer of ultrathin glass positioned between the upper and lower PDMS layers (Figure 4.7). Additionally, the glass slide supporting the bottom PDMS layer was first coated with a S1813 photoresist ‘release layer’ before spinning the PDMS. This allowed for easier recovery of the multilayer stack after plasma bonding, since the S1813 layer can be selectively dissolved to release the assembled layer stack.

To fabricate the glass separation layer, a laser cutter was used to cut a window into a 30 µm thick layer of AF 32® eco thin glass (SCHOTT AG, Germany). All three layers were assembled as shown in Figure 4.7 using

oxygen plasma, as before. To avoid breakage of the ultrathin glass, the assembled multilayer was left in microposit 351 Developer overnight to dissove the S1813 layer and release the multilayer from the supporting glass slide. When bonding the multilayer stack to the SAW-DEP device, care was taken to position the electrodes immediately before the separation layer window, so that the vertical DEP force remained active on the particles as they passed over the glass, thereby preventing sedimentation back into the lower channel once they exit the active separation region. The multilayer devices were fixed to a printed circuit board (PCB) using Apiezon black wax heated to 120°C and the IDTs of the chip were then electrically connected to the PCB copper tracks by gold wires via ball bonding. To increase device robustness, the bond wire ends were then set in silver epoxy, cured at 70°C for fifteen minutes. Finally, two SMA connectors were soldered onto the PCB to allow connection to external circuitry.

Fluoro-Max green-dyed latex beads with a mean diameter of 5 μm were diluted 20 times in 0.1% triton solution and injected into the fluidic channels at flowrates ranging from 5 to 70 μL/min using a syringe pump. The SAW-DEP devices were activated by applying 631 mW to both IDTs (in total) via a signal generator connected to a 24 V amplifier and a signal splitter as described in Chapter 3 section 3.1.4).

4.3 Results

4.3.1 Characterisation of DEP forces for different powers and channel heights using a FE model and experimental models

4.3.1.1 DEP force profiles in SAW-DEP devices

The experimental alignment of 5 μm latex beads in the SAW-DEP devices was used to determine the DEP force profiles along the length of the channel and was compared to the numerical DEP profile obtained by the FE model. Latex beads were used because they are known to have a Clausius Mossotti factor of -0.476 for the set of conditions tested (10 MHz, 0.01 S/cm) and therefore experience negative DEP, causing them to move upwards from the bottom of the channel and laterally align at the nodes [140]. For both the experiment and the model, the obtained DEP force profiles vary sinusoidally (Figure 4.8), as expected owing to the sinusoidal nature of the driven electric

signal. As explained in equation (2.3), the DEP force is proportional to $\nabla \mathrm{E}^2 = 2E.\nabla \mathrm{E}$ where E is the electric field and $\nabla \mathrm{E}$ is the gradient of the electric field. At the nodes of the electric field profile, where the beads are aligned due to negative DEP, the electric field E is zero, so the DEP force is zero (Figure 4.8). At the antinodes of the electric field profile, the electric field gradient $\nabla \mathrm{E}$ is zero, so the DEP force is also zero (Figure 4.8). The electric field nodes are seen to act as points of stable equilibrium, where any deviation from the node position generates a restoring force toward the node. Conversely, the antinodes represent points of unstable equilibrium for the beads, where even the smallest possible perturbation directs the beads away from the antinode and towards the nearest node. The periodicity of the DEP force is characteristic of the operating frequency (10.4 MHz) and corresponds to half of the SAW wavelength as discussed in Chapter 2 section 2.2.4.

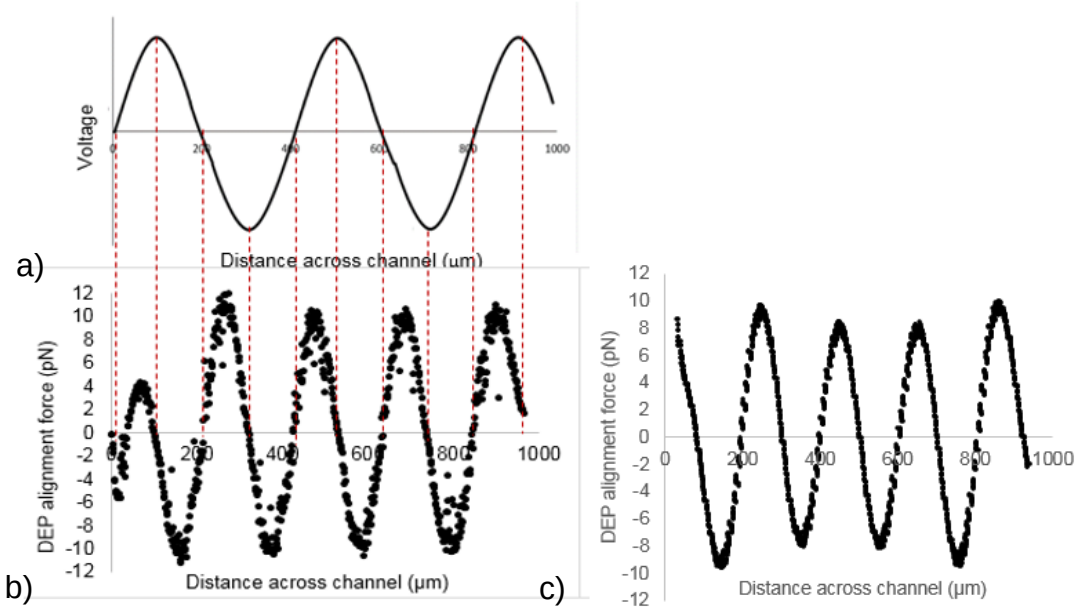

Figure 4.8: a) Potential in the channel as a function of the distance across the channel. The nodes and antinodes of the electric field correspond to the regions where the DEP alignment force is zero. b) DEP alignment force profile obtained experimentally for 5 µm beads, 100 mW input power and a 44 µm channel height. c) Numerical DEP alignment force profile obtained by the FE model for 5 µm beads, 100 mW input power and a 44 µm channel height.

4.3.1.2 Influence of input power on vertical component of the DEP force

The influence on alignment DEP force of increasing the input power was investigated for each channel height (24, 44, 51, 64, 84 µm). As an example, the DEP force profiles obtained for a 51 µm channel are shown in Figure 4.9. The other force profiles can be found in APPENDIX A.

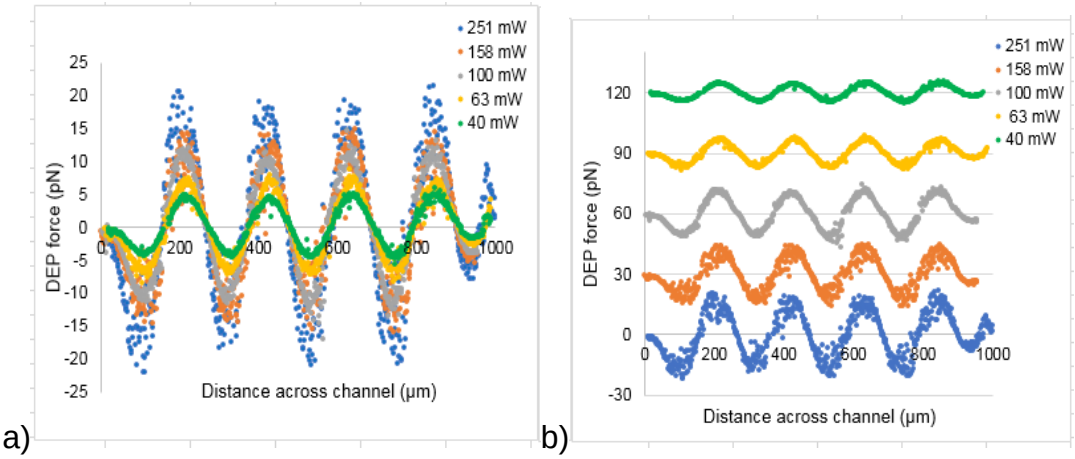

Figure 4.9: Plots of experimentally measured profiles of the DEP force component driving alignment of 5 µm beads for different powers power in 51 µm high channel. In b, data for each power are vertically offset for clarity.

The generated force amplitude is seen to increase with increasing power delivered to the IDTs whilst maintaining the sinusoidal force variation. Herein, the discussion of force therefore refers only the arithmetic mean of the peaks in the corresponding force profile. The peak force versus input power for different channel heights are presented for experimental and simulated devices in Figure 4.10.

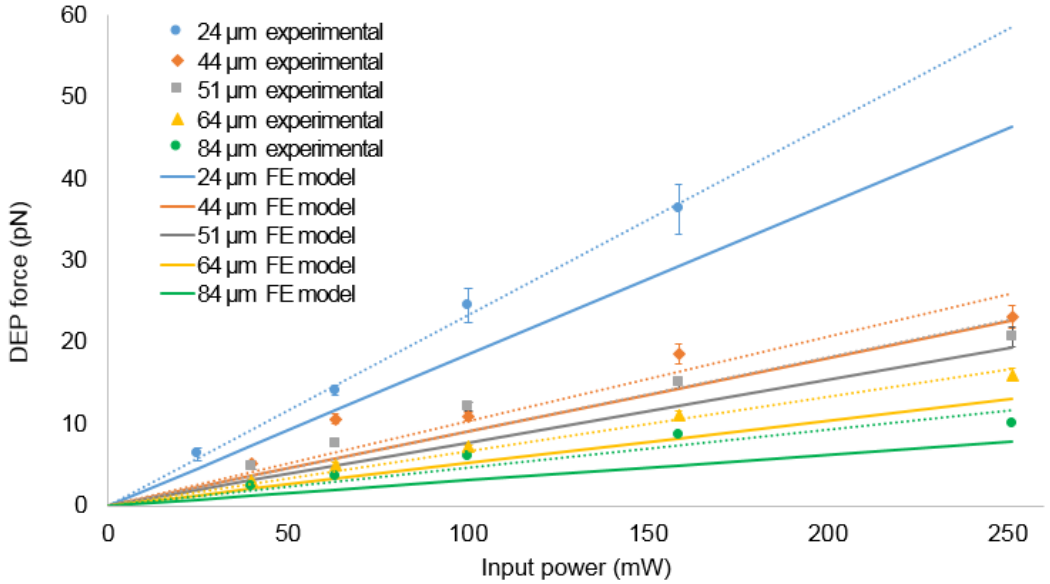

Figure 4.10: Experimental data points, line of best fit through experimental datapoints (dashed) and numerical values obtained by the FE model (solid lines) showing the behaviour of the DEP force driving alignment of 5 µm latex beads as a function of power for different channel heights. Error bars represent the standard deviation of obtained for each experimental applied power point for 4 repeats. The slopes of the linear regressions are detailed in Table 4.4.

For both the experimental and numerical data, a linear relationship was observed between the average DEP force and the applied power and the values obtained were in good agreement within the experimental error. This is in agreement with the expression of the time averaged DEP force acting on a sphere of diameter d in an electric field E described in Chapter 2 section 2.2.1 and repeated here for convenience:

$$\mathrm{F_{DEP}} = \frac{\pi}{4}\mathrm{d}^3\varepsilon_\mathrm{m}\mathrm{Real}(\mathrm{f_{CM}})\nabla\left\|\mathrm{E_{RMS}}^2\right\| \qquad \mathrm{f_{CM}} = \frac{(\varepsilon_\mathrm{p}-\varepsilon_\mathrm{m})+\mathrm{i}\left(\frac{\sigma_\mathrm{p}-\sigma_\mathrm{m}}{2\pi\mathrm{f}}\right)}{(\varepsilon_\mathrm{p}-\varepsilon_\mathrm{m})+2\mathrm{i}\left(\frac{\sigma_\mathrm{p}-\sigma_\mathrm{m}}{2\pi\mathrm{f}}\right)};\mathrm{i} = \sqrt{-1} \quad (4.5)$$

Where $\mathbf{E}_\mathrm{RMS}$ is the root mean square value of the alternating electric field, f is its frequency, and $\mathrm{f_{CM}}$ is the Clausius-Mossotti factor which is a function of the electrical permittivities and conductivities of the particle $(\varepsilon_\mathrm{p}, \sigma_\mathrm{p})$ and the medium$(\varepsilon_\mathrm{m}, \sigma_\mathrm{m})$. Equation (4.2) shows that the DEP force ($\mathbf{F}_\mathrm{DEP}$) changes linearly with $\nabla\left\|\mathrm{E_{RMS}}^2\right\|$ which is proportional to the power (P), for a fixed impedance, therefore equation (4.2) can be can be rewritten as:

$$\mathrm{F_{DEP}} = a\,\mathrm{P} \qquad \text{where } a = \frac{\pi}{4}\mathrm{d}^3\varepsilon_\mathrm{m}\mathrm{Real}(\mathrm{f_{CM}})\, b$$

Here, b is a proportionality constant between power and $\nabla\left\|\mathrm{E_{RMS}}^2\right\|$ which depends on the channel height. The equation of linear fit obtained for the experimental data points was determined for all different channel heights and the results are shown in Table 4.4.

Channel height (µm)	FE model slope	Experimental slope a	Experimental Standard error	Adjusted R-square
24	0.185	0.214	0.00651	0.996
44	0.090	0.124	0.0087	0.981
51	0.077	0.104	0.00865	0.966
64	0.052	0.0652	0.00157	0.997
84	0.031	0.0537	0.00352	0.979

Table 4.4: Linear regression parameter values of the experimental and numerical values obtained by the FE model. The standard errors and adjusted R-square values (determined using OriginPro software) for all the experimental channel heights tested are also presented.

To determine the goodness of fit, the adjusted R-square value, which evaluates the scatter of the data points around the fitted regression line, was used. For all the channel heights, the adjusted R-square value was higher than 0.95, showing good agreement between the experimental data and the linear fit.

4.3.1.3 Influence of channel height on the vertical component of the DEP force

The influence of channel height on the horizontal alignment DEP force was investigated for each input power (251, 158, 100, 63, 40 mW). As an example, the DEP force profiles obtained for 63 mW input power per IDT are shown in Figure 4.11. The force profiles at different applied powers show a similar trend and are detailed in APPENDIX A.

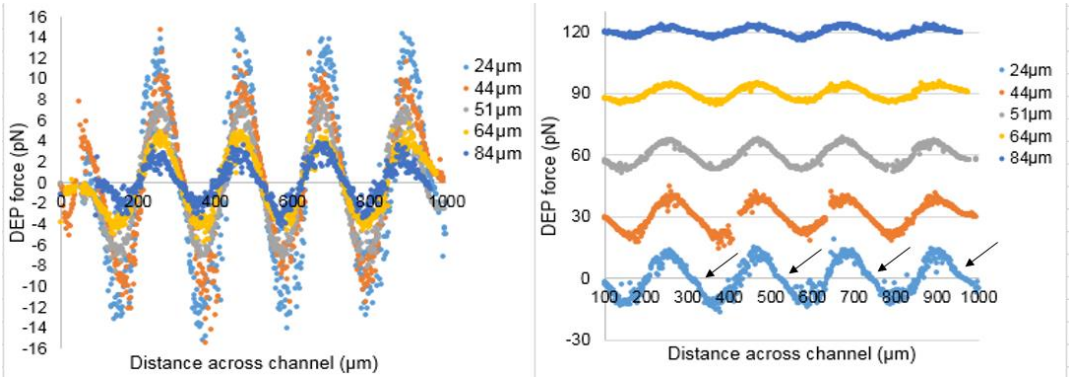

Figure 4.11: Plots of experimentally measured profiles of the DEP force component driving alignment of 5 µm beads for different channel heights and 63 mW input. The right plot shows the forces staggered for clarity. The shoulders observed for the 24 µm high channels are indicated by black arrows.

The experimental profile for the 24 µm channel reveals the presence of a shoulder at the nodes (Figure 4.11), which becomes less prominent with increasing channel height and disappears almost completely for the 51 µm channel. The FE model simulations however, do not predict this shoulder. This is likely to be a result of the way in which COMSOL models the piezoelectric crystal. COMSOL assumes the crystal to be perfectly elastic and therefore with no hysteresis, so the isopotential driving voltage relaxes instantly into a sinusoidal wave in the simulations. However, this is not necessarily true experimentally, which introduces distortions in the actual waveform thereby generating the shoulder in the force profile. The model represents an ideal situation of a perfectly sinusoidal voltage at the bottom of the channel, so any defect in the piezoelectric crystal will not be considered. This is not thought to affect the resultant force amplitude in the simulations and will therefore not affect the analysis.

To assess the influence of channel height on DEP alignment force, simulations were performed at a fixed input power for all experimental channel heights, using the linear relationships shown in Table 4.4 to generate Figure 4.12. For a fixed applied SAW-DEP power, the alignment force across the channel was observed to exhibit a monotonic decrease with increasing channel height for both the experimental and numerical values obtained by the finite element model (Figure 4.12).

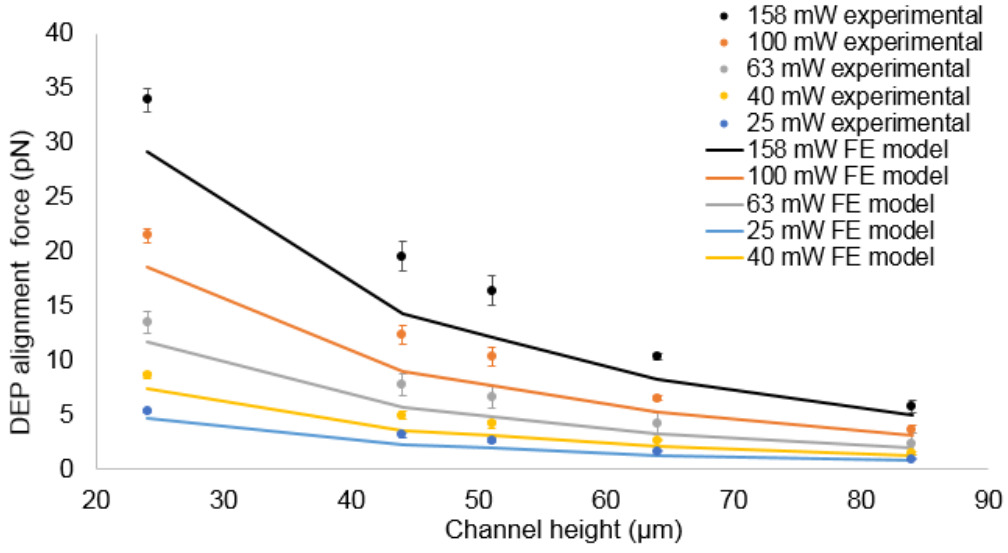

Figure 4.12: Experimental data points and numerical values obtained by the FE model (solid lines) showing the DEP force driving alignment of 5 µm beads as a function of channel height for different SAW powers. The error bars represent the standard deviation obtained for each experimental data point, for n = 4 measurements.

The results observed for both the FE model and the experiments are consistent with those described for the analytical model (Chapter 2 section 2.2.4). The DEP force has components in the horizontal (recording alignment direction) and vertical directions (towards the top of the channel). The DEP force's vertical component is stronger, so the beads move first towards the top of the channel before beginning to align across the channel (Figure 4.13). Once the beads have either reached the top of the channel, or in deeper channels have reached the equilibrium height (at which point the DEP force cancels gravitational forces) they align horizontally to the electric field nodes. As the channel depth exceeds the equilibrium sedimentation height, the beads do not exceed this height and therefore the alignment force reaches a constant value in deeper channels, as is beginning to occur in Figure 4.12. This process is described graphically in Figure 4.13. The equilibrium force further depends on the input power since, at higher powers, the equilibrium height is moved higher with respect to the substrate surface. The equilibrium height, determined experimentally to be at the height for which the force reached a constant value, was used inform the height of the collection channels needed to collect the particles experiencing negative DEP.

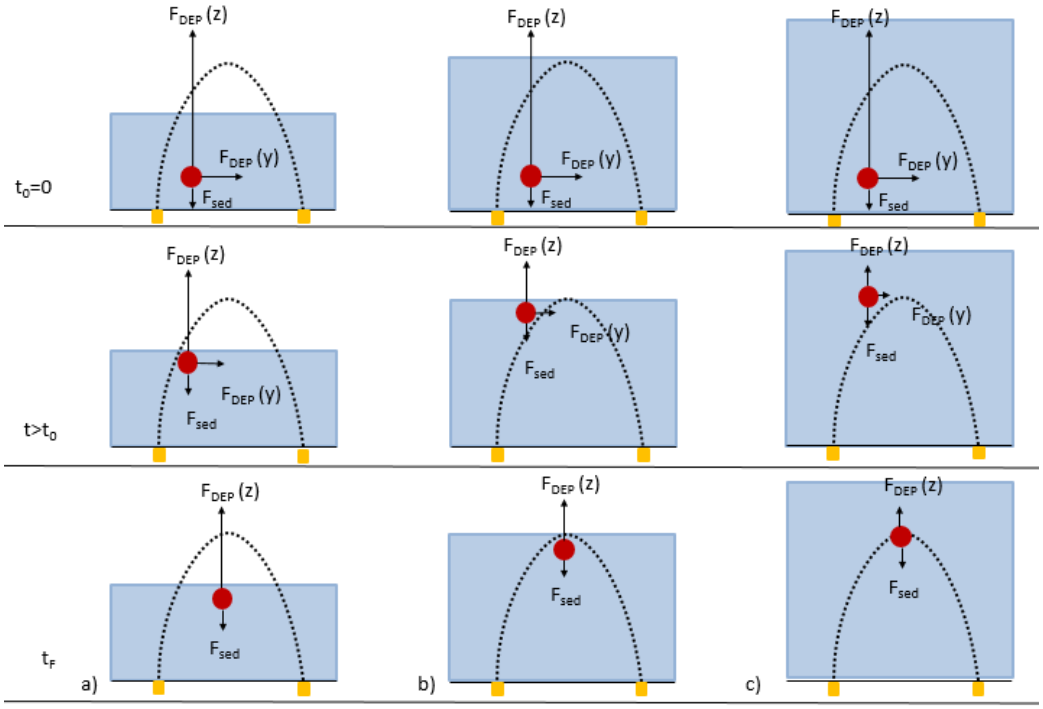

Figure 4.13: Schematic of sedimentation (F_{sed}) and DEP (F_{DEP}) forces applied to particles experiencing negative DEP for different channel heights and timepoints. The virtual electrodes are represented in gold and the SAW-induced AC electric fields are represented in a dashed line. a) For channel heights lower than the equilibrium height, the beads are pushed upwards until they reach the top of the channel and then align following the alignment force across the channel. b) For channel heights equal to the equilibrium height, the beads reach the top of the channel and then align more slowly (owing to a reduced lateral force) following the alignment force across the channel. c) For channels higher than the equilibrium height, the beads are pushed upwards until they reach the equilibrium height between the sedimentation force and the DEP force and then align laterally at the same speed as in b).

4.3.2 Multilayer channel designs for increased throughput

As described in the previous section 4.3.1.3, the DEP force has two components that can be exploited to separate cells experiencing pDEP from those experiencing nDEP: a lateral force, acting along the channel, and a vertical force acting along the channel height. In previous work, Smith et al. (2017) attempted to collect the cells using a design consisting of splitting the separation channel into small horizontal channels to collect cells experiencing pDEP and nDEP separately across the channel (Figure 4.14 a) [141]. This design exploited the fact that positive and negative DEP cells will

align at different regions across the channel width. This design can be easily fabricated in PDMS using a single mask and following the same procedures as the simple channel used for previous experiments. However, this design is limited by the resistance of the liquid within the thin channels due to a mismatch between the tubing and the channels cross sections. This configuration is also not easily scalable, as each forked channel would be further split in a second stage separation and parallelisation would further increase the complexity. Also, due to the channels being thin, the probability of surface fouling and channel clogging increases. Moreover, this would mean that the channel height would have to be kept low, as in deeper channels the lateral force component reduces (as discussed in section 4.3.1.3), which in turn limits the throughput.

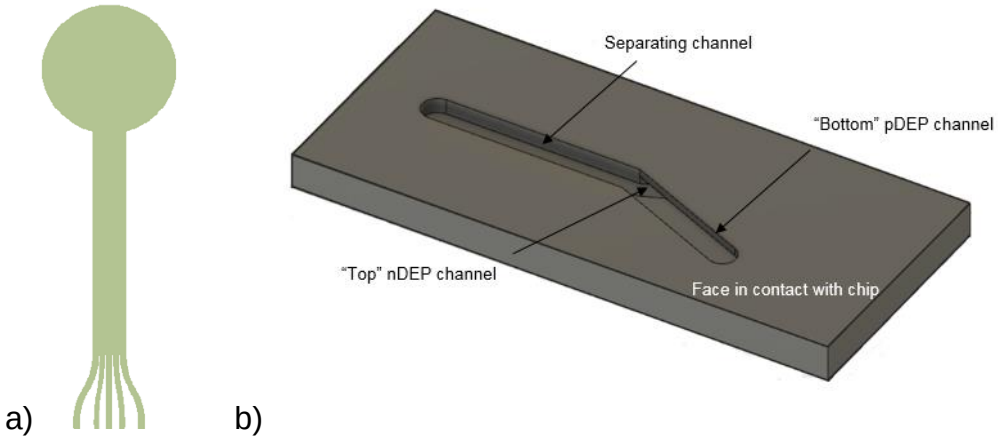

Figure 4.14: Schematic diagrams depicting the different microfluidic channel designs. a) A horizontally split channel design, as used by Smith et al. [141] and b) an example of a staggered height collection channel explored in this section. The channel is presented upside-down for clarity.

In this section, an alternative separation regime that exploits the difference in vertical force exerted on cells experiencing pDEP and nDEP is discussed. As described in chapter 2 section 2.2.4, the component of the DEP force that acts vertically within the channel is an order of magnitude greater than the component that aligns the cells across the channel, and therefore offers potentially faster separation. To exploit this, different designs were proposed consisting of two output channels at staggered heights (Figure 4.14 b). By using the COMSOL model, the optimum heights for both the separation and collection channels can be designed, based on the modelled equilibrium sedimentation height of a given particle. This approach allows for deeper

channels, which translates into higher throughput and reduces the problems associated with fluid resistance.

4.3.2.1 Fluid flow and particle trajectories in double-layered, forked channels

In order to exploit the shooting force to collect nDEP beads, a multilayer fluidic geometry was considered. The first channel geometry that was tested consisted of a double-layer, forked channel (Figure 4.15). The electrodes were placed immediately before the channel fork to minimise sedimentation of the particles under gravity after they exit the acoustic aperture. This ensured that the beads experiencing nDEP were located at their highest point when reaching the fork.

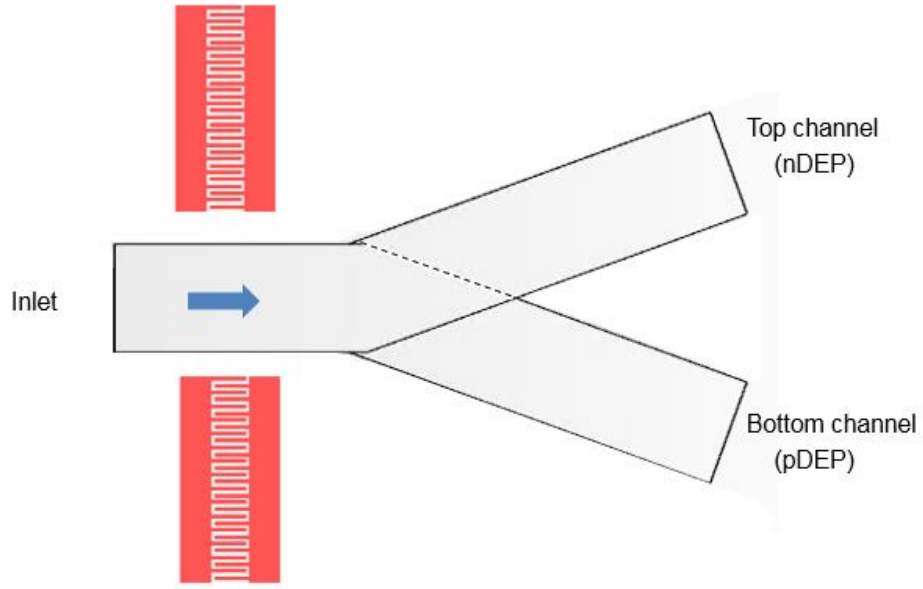

Figure 4.15: Schematic of a double layer channel used in separation experiments on latex beads. The beads were flown through the inlet and the SAW-DEP generated by the electrodes was used to levitate the particles experiencing nDEP and collect them into the top channel. The blue arrow shows the direction of the flow.

When the SAW-DEP power was turned on, the beads aligned and collected in the top channel for flow rates up to 5 µL/min (Figure 4.16). However, when they reached the fork, the beads aligning at the far end of the channel collided with the wall and were dragged by the fluid flow into the bottom channel. This effect was more visible with increasing flow rates, resulting in a loss of nDEP particles.

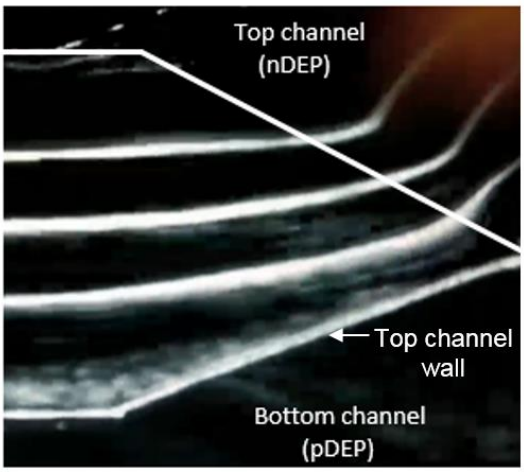

Figure 4.16: Experimental testing of double layer forked channel with latex beads flown at 5 µL/min. The top and bottom channels were both 50 µm high.

To better understand the fluid flow in the forked channels, COMSOL Multiphysics was used to model the fluid velocity (Figure 4.18) and the particle trajectories for particles experiencing either positive or negative DEP in an equivalent channel geometry (Figure 4.17).

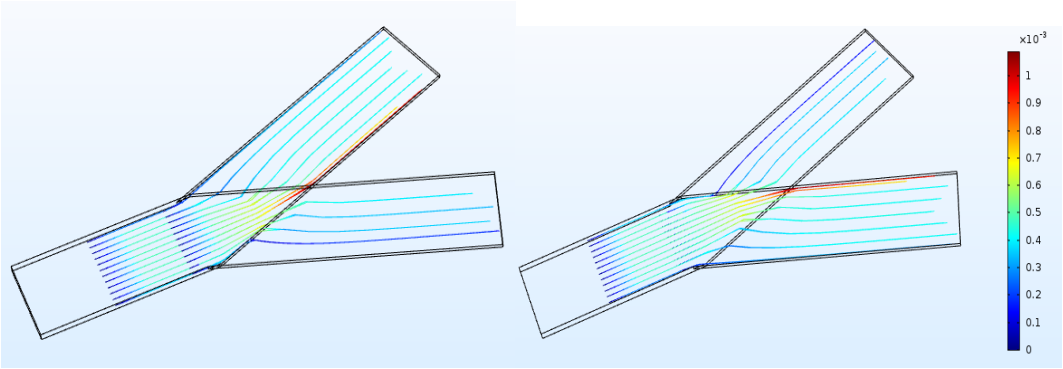

Figure 4.17: Trajectories of particles experiencing pDEP (LEFT) and particles experiencing nDEP (RIGHT) in a 40° forked outlet channel. The colours represent the particles' velocity in m/s.

The particle traces showed that, similarly to what was observed in the experimental set-up, the particles that collided with the walls at the fork were dragged into the opposite channel. The fluid velocity data showed that the fluid velocity was the greatest at the intersection between the outlet channels, explaining the acceleration observed for the particles in that area (Figure 4.18).

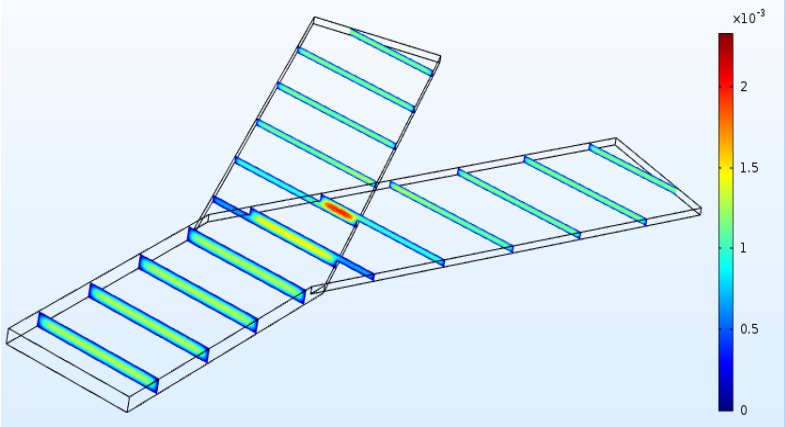

Figure 4.18: Fluid flow velocity in a 40° forked outlet channel for a 5 µL/min inlet flow rate. The colours represent the fluid velocity in m/s.

4.3.2.2 Fluid flow and particle trajectories in a double-layered, forked channel with inlet fluid focusing

In order to increase the recovery rate for each of the outlet channels, flow focusing was investigated as a means of concentrating the particles at the middle of the channel, rather than at the edges. The use of hydrodynamic flow focusing has been widely reported in the literature, in combination with both conventional and insulator-based DEP to focus the particles towards the zones of higher electric field [76], [112]. This technique requires the use of two inlets filled with liquid surrounding a central channel into which the particles are injected. The sheath flow generated by the surrounding inlets focuses the particles into the centre of the channel.

The particle trajectories for the different side inlet flow rates tested are shown in Figure 4.19 to Figure 4.22 and a summary of the performance of the devices can be found in Table 4.5.

a) 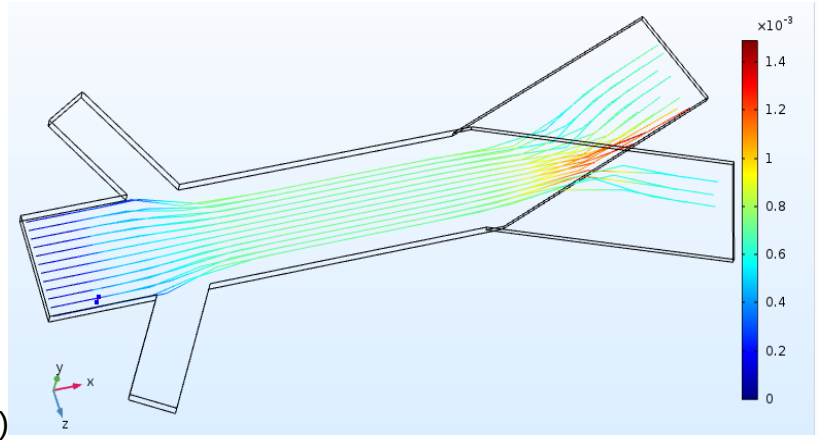

b) 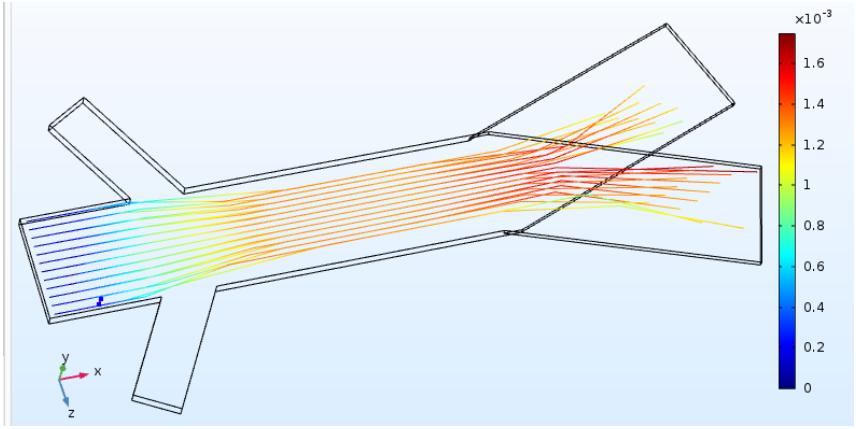

Figure 4.19: Trajectories of particles experiencing pDEP (a) and particles experiencing nDEP (b) in a fluid focusing channel for a side inlet flow rate of 2.5 µL/min. The colours represent the particles' velocity in m/s.

a) 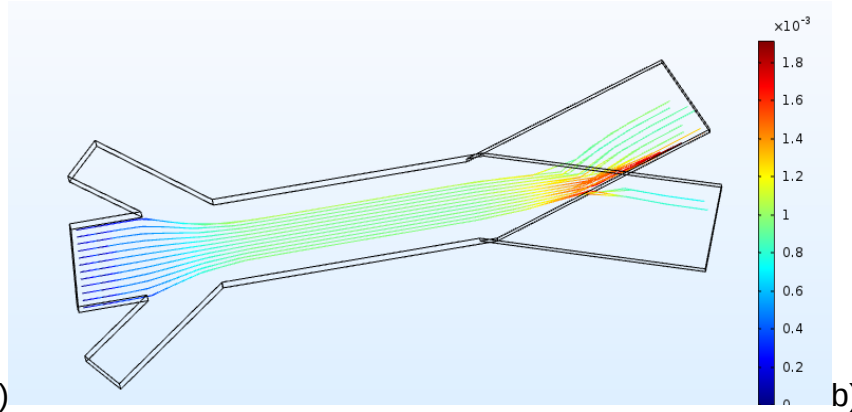

b) 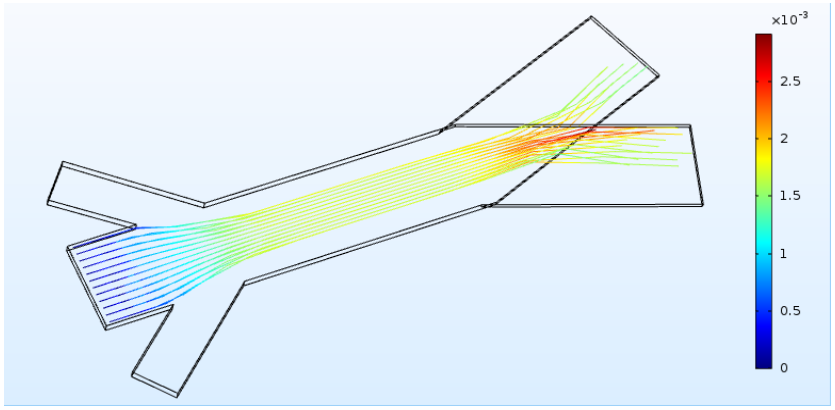

Figure 4.20: Trajectories of particles experiencing pDEP (a) and particles experiencing nDEP (b) in a fluid focusing channel for a side inlet flow rate of 5 µL/min. The colours represent the particles' velocity in m/s.

a) 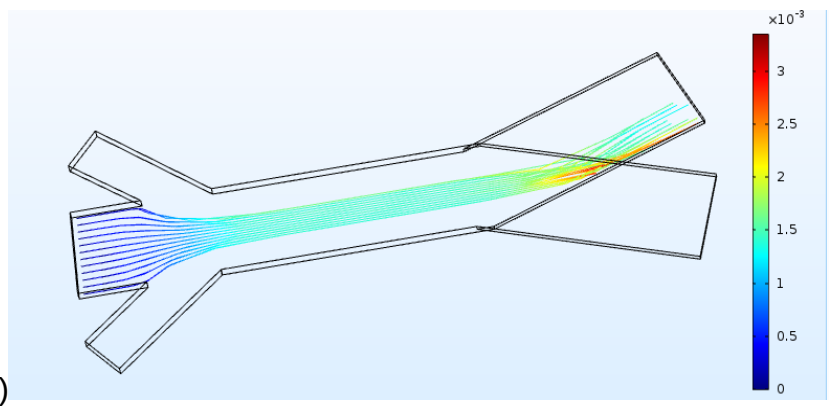

b) 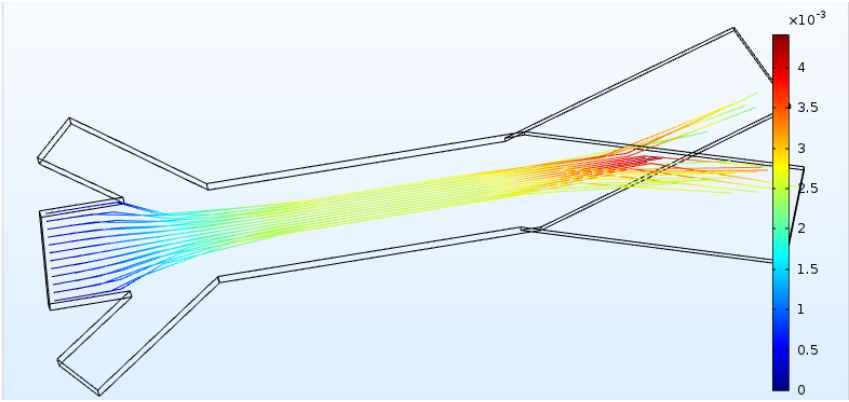

Figure 4.21: Trajectories of particles experiencing pDEP (a) and particles experiencing nDEP (b) in a fluid focusing channel for a side inlet flow rate of 10 µL/min. The colours represent the particles' velocity in m/s.

a) 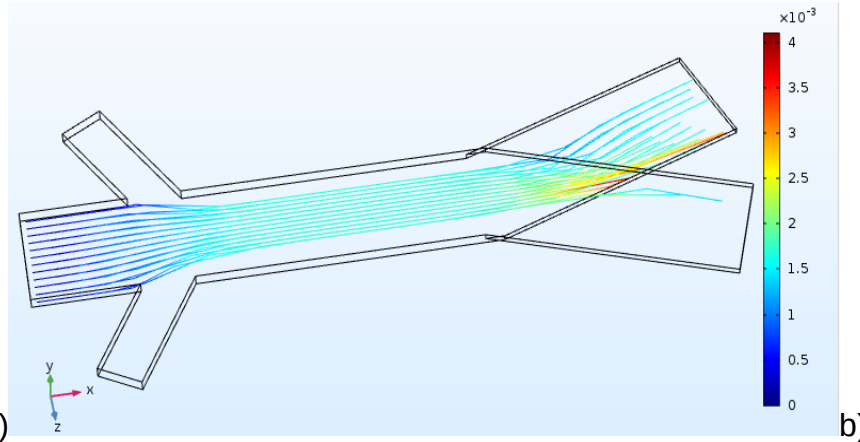

b) 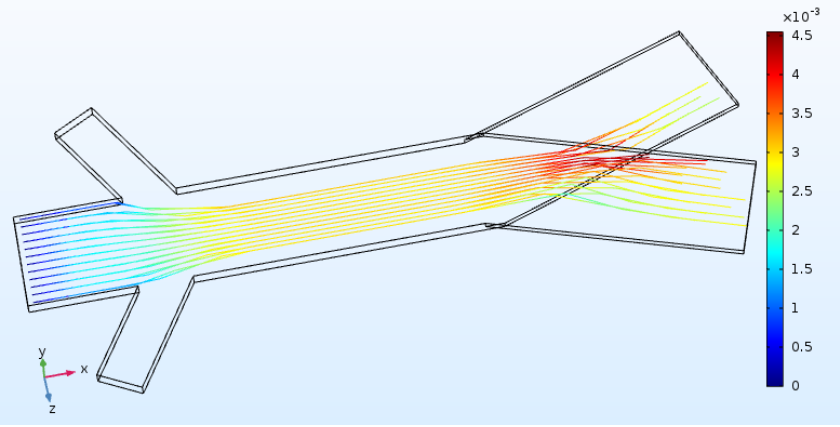

Figure 4.22: Trajectories of particles experiencing pDEP (a) and particles experiencing nDEP (b) in a fluid focusing channel for a top side inlet flow rate of 5 µL/min and a bottom inlet flow rate of 10 µL/min. The colours represent the particles' velocity in m/s.

With increasing flow rates, the beads were focused towards the centre of the channel and the number of particles lost for each DEP condition decreased. For the pDEP particles, 100% capture was achieved for the highest condition of flow focusing tested, but the percentage capture of the nDEP beads in the top outlet was only 75%. This can be explained by the fact that the particles experiencing nDEP do not reach the top of the channel, instead becoming suspended at the equilibrium sedimentation height, 80 µm from the channel bottom (and 20 µm from the channel top) according to the simulations (section 4.3.1.3). Conversely, the particles experiencing pDEP are attracted directly over the virtual electrodes, so they were simulated to be 10 µm above the electrodes, and therefore further from the middle of the channel where the outlets fork out.

In order to account for this bias, an asymmetric flow focusing condition was tested where the top inlet had a higher flow rate than the bottom inlet, thus focussing the beads slightly towards the nDEP outlet. However, this did not increase the recovery of nDEP particles and the recovery of pDEP particles on the bottom outlet decreased slightly.

Name	Top Inlet Flow rate	Bottom inlet Flow rate	Beads location	Bottom outlet	Top outlet
Flow focusing 1	2.5 µL/min	2.5 µL/min	Bottom Top	75% 25%	42% 58%
Flow focusing 2	5 µL/min	5 µL/min	Bottom Top	83% 17%	33% 67%
Flow focusing 3	10 µL/min	10 µL/min	Bottom Top	100% 0%	25% 75%
Flow focusing 4	5 µL/min	2.5 µL/min	Bottom Top	92% 8%	25% 75%

Table 4.5: Summary of performance for all the flow focusing devices tested.

4.3.2.3 Fluid flow and particle trajectories in a three-layered channel with a spacer layer

The final channel geometry consisted of a three-layered, forked channel. In order to bypass the problems arising from the previous forked channel design, a separation layer was introduced between the top and bottom PDMS layers. This layer acts to prevent sedimentation of the nDEP particles to the bottom channel, and also prevents nDEP particles being diverted into the bottom channel after colliding with the channel walls. The fluid flow

simulations showed that 100% of the nDEP and pDEP particles were captured in the corresponding outlet channel (Figure 4.23).

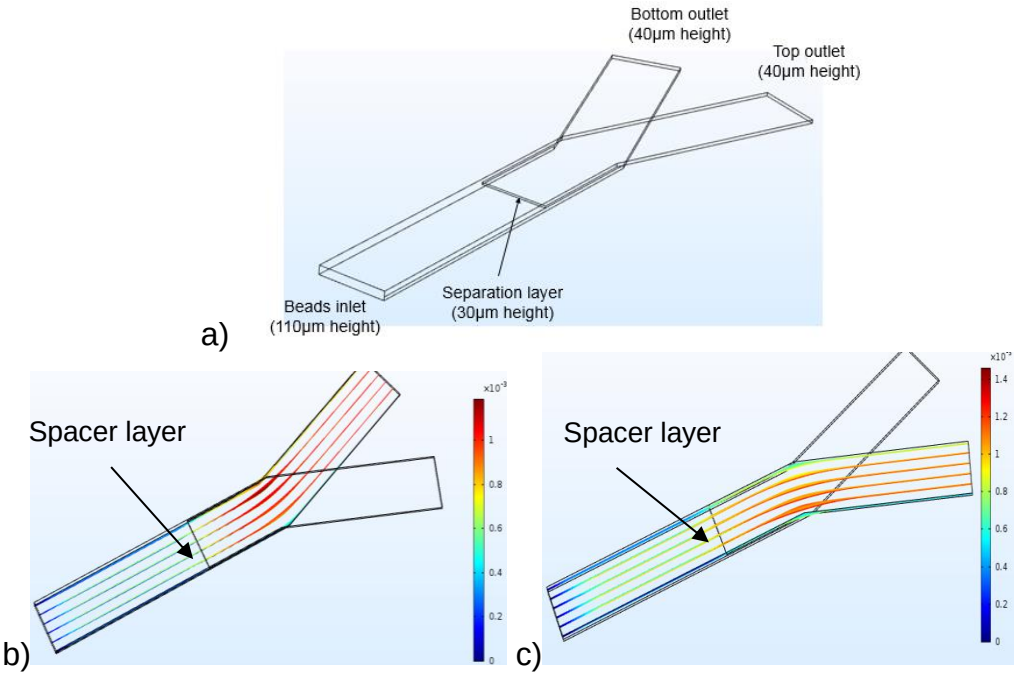

Figure 4.23: a) Schematic showing the layout of the three-layered channel with a spacer layer. b) Trajectories of particles simulated at the bottom of the multilayer channel (10-30 µm height). c) Trajectories of particles simulated at the top of the multilayer channel (80µm height). The colours represent the particle velocity in m/s.

The modelling of fluid flow and particle tracking showed that the presence of a separation layer increased the fluid velocity in the separation channels but did not alter the trajectory of the particles. Only the particles that were modelled at the same height as the separation layer were diverted from their original trajectories.

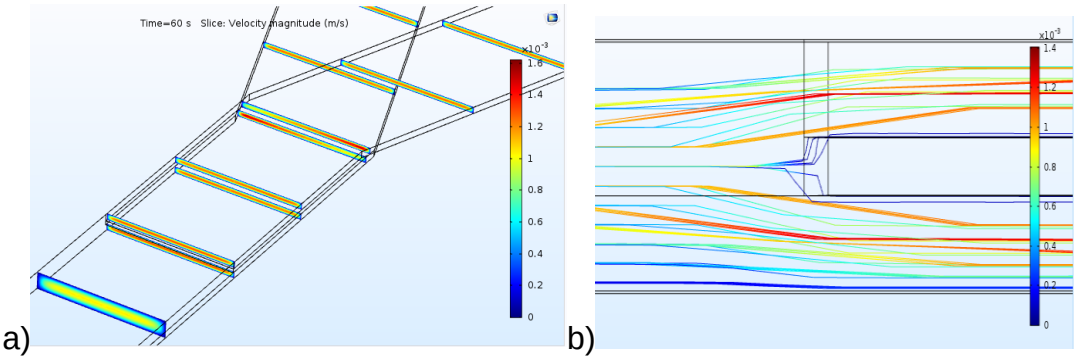

Figure 4.24: a) Fluid flow velocity in triple layer channel. The colours represent the fluid velocity in m/s. b) Trajectories of particles simulated al across all a multilayer sandwich channel the channel. The colours represent the particle velocity in m/s.

Following the promising results obtained *in silico*, a three-layer forked channel was fabricated and tested with latex beads. The SAW-DEP electrodes were placed immediately before the separation layer to fully take advantage of the vertical DEP force (Figure 4.25).

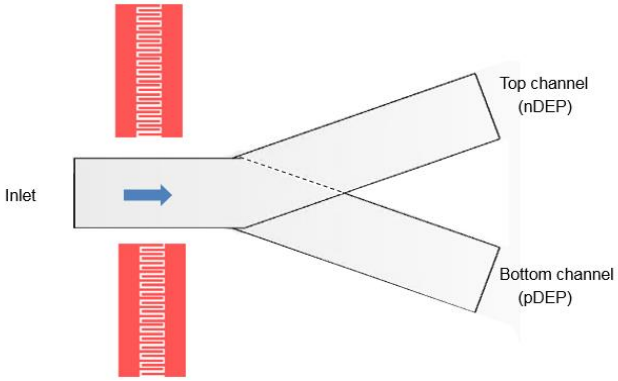

Figure 4.25: Schematic of triple layer channel used in beads experiments. The beads were flown through the inlet and the SAW-DEP generated by the electrodes was used to levitate the particles experiencing nDEP and collect them into the top channel. The separation layer prevents sedimentation / deflection of nDEP particles back into the lower channel. The blue arrow shows the direction of the flow.

The device showed a behaviour as predicted by the simulation with all beads flowing into both top and bottom channel equally when the SAW-DEP power was turned off. When the SAW-DEP power was turned on, the beads were pushed towards the top of the channel and collected in the top channel (Figure 4.26).

Beads were successfully collected in the top chamber with >90% efficiency for flow rates up to 60 µL/min. For higher flow rates, the capture efficiency decreased, and it was hypothesised that for these flow rates the beads did not have the time to move towards the top of the channel before they reached the separation layer in the channel.

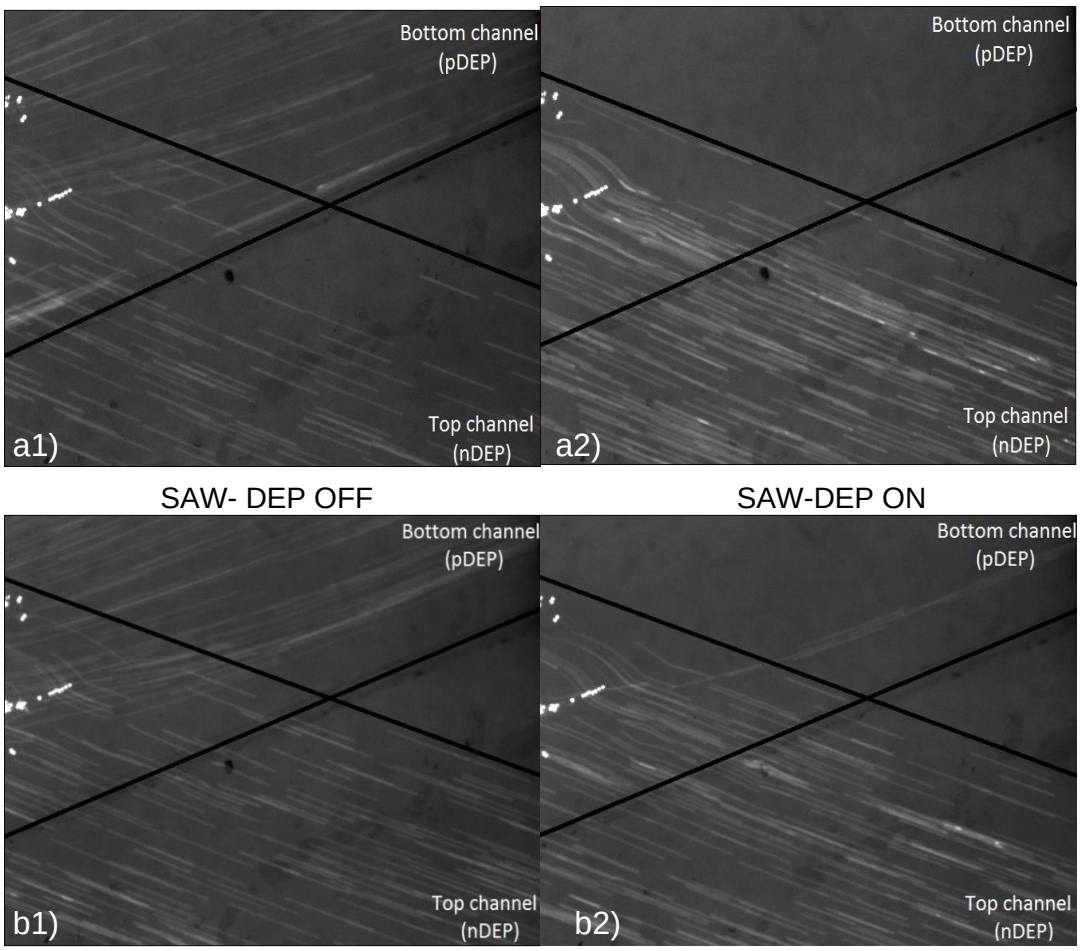

Figure 4.26: Pictures of fluorescent 5 µm beads flown into the triple layer device at 50 µL/min (a1 and a2) and 60 µL/min (b1 and b2). The edges of the top and bottom channels are delimited by a black solid line for clarity. When the SAW-DEP is turned off (a1 and b1), the beads flow equally into both the top and bottom channel. When the SAW-DEP is turned on (a2 and b2), the beads experience nDEP and are collected in the top channel.

4.4 Discussion

4.4.1 Differences between the experimental and computational experiments

In this chapter, we set out to understand better the physics governing SAW-DEP. The alignment forces of latex beads experiencing nDEP for different SAW-DEP powers and channel heights were used to validate the FE model developed by Dr Akshay Kale. The comparison between the experimental and computational data showed that there was a good qualitative agreement between the DEP forces generated by the FE element model and those determined experimentally. However, the magnitude of the DEP forces

calculated by the model were on average slightly lower (around 30%) than those obtained experimentally. This could be due to differences between the FE model and the experimental set-up. A factor that could explain some of the differences observed between the model and the experimental data was the existence of a bulk acoustic wave mode. The FE model showed that 20 % of the acoustic wave force was transferred into a bulk acoustic wave mode. This would suggest that the simulation is diverting energy into bulk modes that are not observed in the experimental setup, and therefore would explain some of the differences observed.

Another factor that could explain the differences between the experimental results and the model results is the fact that the percentage of power that is converted by the IDTs and coupled into a SAW, which in turn generates virtual electrodes in the channel is not known. To assess this, the SAW-DEP device was characterised using a network analyser and the insertion loss was determined (Figure 4.27). The experimental value obtained for the SAW-DEP device was 11 dB, whilst the FE model assumes an ideal insertion loss of 6 dB (as explained in Chapter 2 section 2.1.3). The insertion loss describes the signal loss between the transmission IDT and the receiving IDT. However, the insertion loss is not indicative of the real power present in the middle of the channel at the virtual electrodes and cannot be used to determine any damping of the wave during propagation.

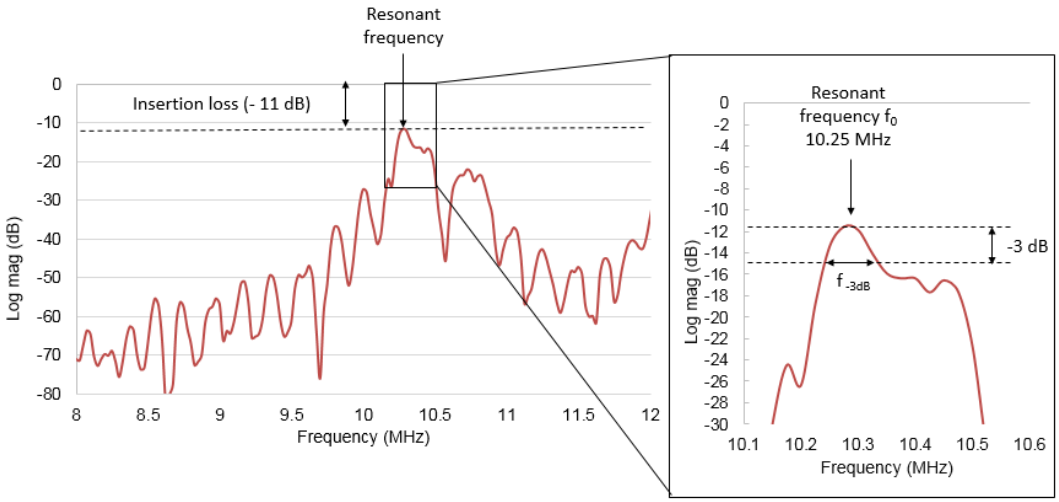

Figure 4.27: Frequency domain response of the experimental SAW-DEP device and determination of insertion loss and quality factor.

The FE model accounts for mechanical losses occurring during the propagation of the wave by adding a damping loss. The quality factor Q is a measure of the strength of the damping of the SAW and can be determined experimentally using the formula:

$$Q = \frac{f_0}{f_{3dB}}$$

Where f_0 is the centre resonance frequency and f_{3dB} is the 3 dB bandwidth as shown in Figure 4.27. In the case shown, for a resonant frequency of 10.25 MHz, the quality factor obtained was 125. The quality factor was measured for different devices and ranged from 50 to 200 depending on the device used. COMSOL uses a damping coefficient of the form $\frac{1}{2Q}$, so any error in the experimental determination of the quality factor will contribute the differences observed between the experimentally observed and simulated DEP forces.

4.4.2 Limits of multilayer channel fabrication

The fabrication techniques described in this chapter to obtain multilayer microfluidic channels had limited yield. This was caused by multiple factors, including: variability of the spun PDMS bottom layer thickness, arising from the viscous nature of the PDMS components; problems with poor adhesion of the PDMS at channels edges, resulting in 'dead' fluid volumes and trapping sites for particles; misalignment between layers during formation of the multi-layer stack, and breakage of the ultrathin glass during fabrication.

The first problem encountered was the variability of the thickness of the bottom PDMS layer. Despite using the same rotation speed to spread the PDMS into a thin layer, the thickness of thin layer obtained varied greatly (with up to 15 µm error). The thickness varied depending on the amount of PDMS that was poured on the glass slide before spinning, and the time spent since the elastomer and crosslinker were mixed. The second problem encountered was the adhesion of the ultrathin glass to the bottom thin layer of PDMS. When the CO_2 laser is used to cut the thin layer of PDMS, the edges of the channel melt and become slightly raised, which hinders subsequent adhesion of the bottom layer to the ultrathin glass layer and can result in glass cracking. These two problems could be solved by using micro-imprinting techniques instead of spin coating and laser cutting. Micro-imprinting consists of pouring uncured PDMS onto a mould (often made of SU8) and pressing it against a stamp to obtain through holes [221]. Once the PDMS sets, the stamp carrying the patterned thin layer is peeled off the mould and can be bonded to the next PDMS layer (Figure 4.28).

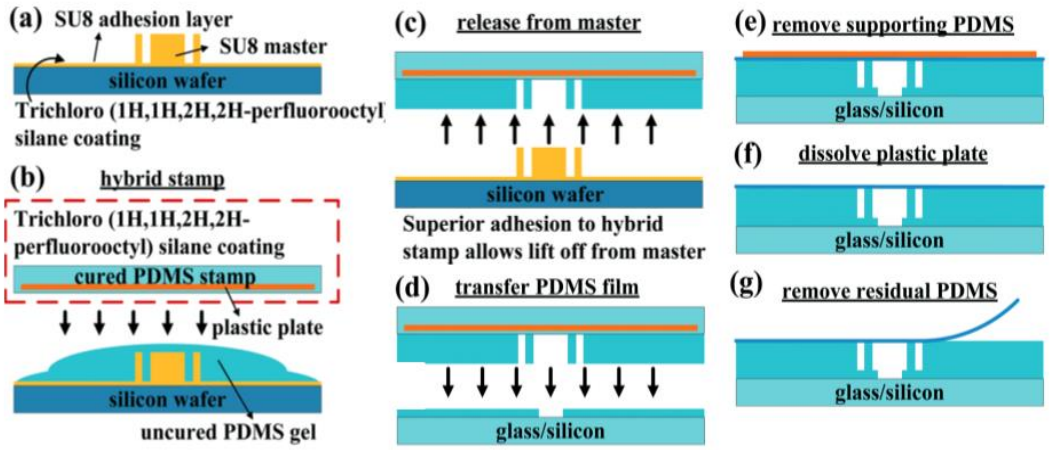

Figure 4.28: Schematic of micro- imprinting fabrication process flow using a plastic plate embedded hybrid stamp. (a) A SU8 mould is coated with Trichloro (1H, 1H, 2H, 2H-perfluorooctyl) silane PFOCTS to facilitate later demoulding. (b) Uncured PDMS is poured onto the mould, and a stamp is used to press the PDMS. (c) The hardened PDMS film adheres to the hybrid stamp and is peeled off from the master. (d) The film is transferred and bonded by oxygen plasma treatment. (e) The support PDMS on the hybrid stamp is removed. (f) The polystyrene plastic plate is dissolved in acetone. (g) The residual PDMS thin film is removed. Image reproduced from [221].

The third problem encountered that reduced the yield of the multilayer fabrication was misalignment between the three layers during assembly. In the method described in section 4.2.5, the layers were aligned manually and bonded immediately after activation with plasma, which resulted in alignment error and limited the reproducibility of the technique. The main difficulty of this technique is to align the layers precisely and quickly on the first try without any further adjustment, because the layers are irreversibly bonded once the two surfaces are in contact. To solve this issue, multiple plasma-free methods have been proposed involving the use of partially cured PDMS layers [222]–[224]. However, these methods might not be ideal for very thin layers of PDMS, as it could result in deformation. Another approach to substitute plasma bonding is the use of γ-ray irradiation, which is commercially used for the sterilisation of medical products [225]. Oyama et al (2020) showed that by applying γ-rays to an already aligned stack of PDMS layers, it was possible to bond the interfaces between the layers [226]. Since the bonding is done after the layers are aligned and pressed together, this allows for sufficient time to align the layers with high resolution. The alignment resolution can be further improved by using a mechanical jig [227], [228]. Xiang et al (2015) described the use of desktop aligner to fabricate multilayer PDMS systems with an accuracy of 50 μm (Figure 4.29) [229].

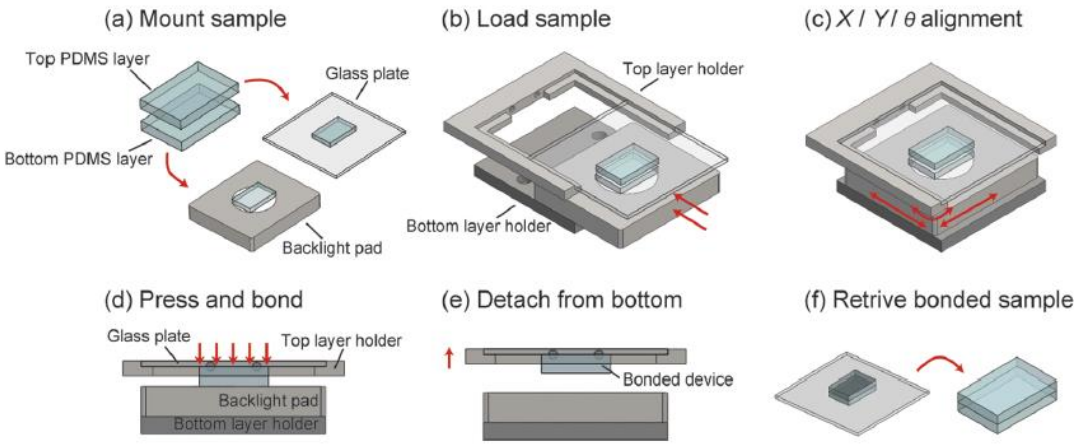

Figure 4.29: Alignment of two PDMS layers using a desktop aligner. (a) The bottom PDMS layer is mounted onto the bottom holder and the top layer is embedded into a glass plate. (b) The holders are inserted into the top and bottom layer holders. (c) Digital microscopes are used to monitor alignment and the bottom layer holder is adjusted to align the two layers. (d) Top and bottom layers are pressed together. (e) The top holder is raised to allow for sample retrieval. (f) The bonded sample is retrieved from the top holder. Image reproduced from [229].

Moreover, γ-ray irradiation has been shown to enhance the mechanical strength of PDMS up to three times by converting the bulk PDMS into a Si–Ox-rich structure (where x is 3 or 4) though crosslinking [226]. This suggests that the ultrathin glass layer could be replaced by a thin layer of PDMS that would be hardened via γ-ray irradiation, allowing for a rigid separation layer without the need of fragile ultrathin glass.

Another technique that could be used to substitute the current PDMS/ultrathin glass hybrid multi-channels is the fabrication of laminated microfluidic chips. Laminated microfluidic channels are created by stacking independently cut layers of polymer layers (commonly polycarbonate, PMMA, and COC) and bonded together [230]. The height of the channels is defined by the thickness of the material used and the channels can be easily patterned by using a knife plotter or a laser cutter. Bonding can be performed by using adhesive tapes, solvent bonding or thermal bonding, but this can sometimes result in warping of the features from the heating [231].

4.5 Summary and future work

4.5.1 Summary

The objective of this chapter was to better understand the physics behind SAW-DEP with the aim to optimise the forces used to separate the particles and increase the throughput. For this, the experimentally determined negative DEP forces exerted on latex beads were used to validate a FE model and to predict the best conditions in terms of channel height and input power to achieve faster separation. Even though the magnitude of the DEP forces generated by the COMSOL model were slightly lower than those observed experimentally, this was still considered a good agreement, as the model was able to predict the same trends observed experimentally. The model was therefore used in combination with the experimental data to inform the design of multi-layer microfluidics separation devices where the stronger vertical component of the DEP force was exploited for alignment. Both the experimental and computational data were used to determine the equilibrium heights that the beads reach when pushed by the negative DEP vertical force. The equilibrium height was used to inform the design of microfluidics channels exploiting the alignment height difference between the cells experiencing pDEP and nDEP. Different multilayer microfluidic designs were proposed consisting of two output channels at staggered heights. The best performing design consisted of a three-layer, forked channel in which an upper and lower PDMS channel were separated using ultrathin glass. These novel devices exploiting the vertical alignment force increased the throughput 20-fold compared with previously used channels relying on the lateral separation of particles across the channel [140].

4.5.2 Future work

A rigorous analysis of the system and the differences between the FE element model and the experimental conditions should be performed to investigate the origin of the 30% difference observed between the model and the experiments. Moreover, the work presented in this chapter concentrated on determining the optimum alignment forces for particles experiencing nDEP for increased separation throughput. However, validation experiments using particles experiencing pDEP (such as live cells) will be necessary for predicting pDEP alignment. Particles experiencing pDEP will be attracted to

the bottom of the channel where the electric field is higher, and any mechanical perturbation of the liquid by the SAW is most likely to have an influence on alignment. Another further improvement to the model would be to combine the model with the multi-layered fluidics model to account for the effect of flow rate on particle alignment times. This dual model would be useful to determine if a longer acoustic aperture needs to be implemented for higher flow rates, thereby increasing the time for which the particles are exposed to the SAW-DEP forces to allow them to reach their equilibrium height.

The typical concentration of cells injected in the SAW-DEP devices is 10^7 cells/mL (as shown in Chapter 6), so the new improved flow rate (3.6 mL/h) corresponds to a throughput of 36 million cells/h, which moves the SAW-DEP cell separation technology significantly closer to throughput needed to achieve separation within intra-operative times. In order to achieve concentration of BM-MSCs from 30 mL of bone marrow (containing a cell concentration of 10^7 cells/mL) in less than an hour, the throughput would need to be further increased by a factor of 10. This could be achieved by using parallelisation to separate a higher volume of cells simultaneously. The multi-layered configuration only has two output channels which is easily scalable, as each forked channel would be further split in a second stage separation and parallelisation could be achieved without too much complexity. This type of approach could take advantage of the SAW generated in both directions from each IDT, as only one direction is currently exploited. Alternatively, the introduction of reflective gratings would increase the DEP forces generated by the SAW within a single channel, thereby decreasing alignment times.

Chapter 5

Characterisation of bone marrow cells' dielectric properties

5.1 Introduction

The bone marrow is a tissue that can be found inside the bone cavities and is the primary site of new blood cell production (also called haematopoiesis) [232]. Haematopoietic stem cells found in bone marrow can differentiate into myeloid progenitors and lymphoid progenitors. The myeloid progenitors can then differentiate into erythrocytes (red blood cells), megakaryocytes (platelets precursors), myeloblasts (granulocyte and monocyte precursors) and mast cells. On the other hand, the lymphoid progenitors can differentiate into natural killer cells and T and B lymphocytes (Figure 5.1) [233].

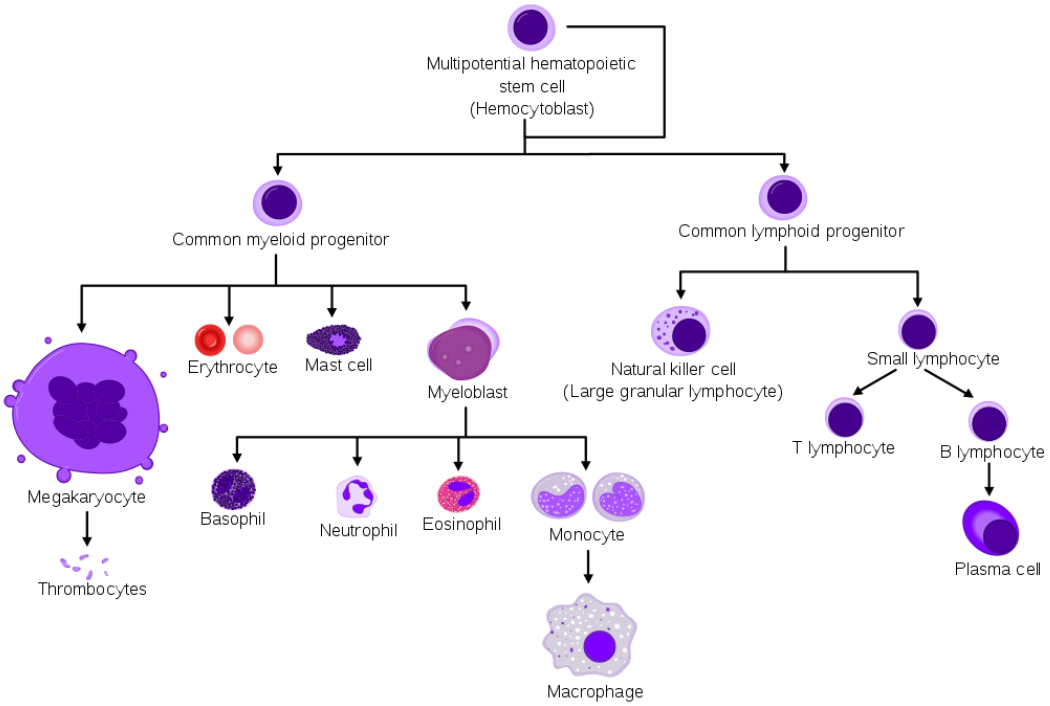

Figure 5.1: Diagram of haematopoiesis showing the differentiation of multipotential haematopoietic stem cells into the mature blood cells. This image was made by A. Rad and M. Häggström (CC-BY-SA 3.0 license).

Since the bone marrow is the place where haematopoiesis occurs, it contains a complex mixture of cell types including hematopoietic cells, leukocytes and a very low percentage of mesenchymal stem cells which we aim to concentrate by using SAW-DEP (Table 5.1).

Cell type	Mean percentage
Promyeloblast	0.3 ± 0.3 %
Myelocyte	2 ± 1.4 %
Metamyelocyte	9.4 ± 4.5 %
Band cell	24 ± 2.1 %
Neutrophils	23.3 ± 3 %
Eosinophils	2.9 ± 1.2 %
Basophils	1.3 ± 0.6 %
Lymphocyte (B and T)	16.3 ± 2.9 %
Monocyte	2.6 ± 1 %
Plasma cell	0.4 ± 0.6 %
Proerythroblast	3.7 ± 1.8 %
Erythroblast	14 ± 3.4%
Mesenchymal Stromal Cells	0.01% to 0.001%

Table 5.1: Distribution of cell types in human bone marrow. The data was taken from [234]. The cell types shown in *italic* are precursors of white blood cells (myelocytes, band cells) and red blood cells (erythroblasts). The cell types shaded will be studied in this chapter.

For the preliminary work shown in this chapter, in order to simplify the system, only the dielectric properties of the main mature cell types found in bone marrow (T and B lymphocytes, monocytes, neutrophils and eosinophils) were characterised. Myelocytes and band cells were not considered in this study, as they are precursors of granulocytes (neutrophils, eosinophils, basophils), can be difficult to isolate and do not constitute a homogenous population, as they consist of cells at different stages of cell maturation [235]. Erythroblasts were not characterised in this chapter either, as they are precursors of red blood cells and red blood cells are lysed during the purification process.

The different cell types found in bone marrow can be identified by their characteristic morphologies (Figure 5.2). Monocytes are the largest type of white blood cell, have an amoeboid shape and an ellipsoidal nucleus. Lymphocytes (T and B cells) can be recognised by their large nucleus and lack of granules. Granulocytes (neutrophils and eosinophils) are characterised by the presence of granules in the cytoplasm and a multilobulated nucleus [236].

	Basophil	Eosinophil	Neutrophil	Lymphocyte	Monocyte
Microscopic image	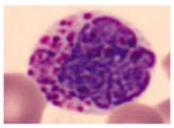	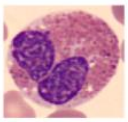	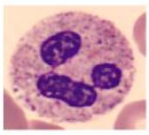	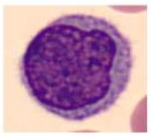	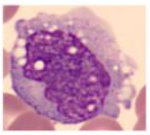
Approx. % in adults	0.4	2.3	62	30	5.3
Diameter (μm)	10–16	9–15	9–15	Small lymphocytes 7–8 Large lymphocytes 12–18	12–20

Figure 5.2: Table showing the morphologies and sizes of different white blood cells. Image reproduced from [236].

The differences in morphologies found between the white blood cells indicate are indicative of differences in dielectric properties that could be exploited for DEP separations [237]. Cell dielectric properties have been proven to depend on morphological factors, such as the cell radius, membrane area, topography, and composition of the cytoplasm and nucleus [79], [237]. The diameter of a cell has an influence on the capacitance of the membrane. With increasing diameter, the total surface area of the membrane increases and with it so does the charge storing capacity of the cell [79]. Another factor influencing the membrane capacitance of a cell is the membrane topography. The presence of membrane folds such as blebs and microvilli increases the effective surface area of the membrane and strongly influences the dielectric properties of the cell [238]. The membrane capacitance could also be dependent on its composition. As described in Chapter 2 section 2.2.2.1, the cell membrane is composed of a lipid bilayer containing cholesterols and membrane proteins surrounded by phospholipids [239]. The protein content of the membrane has been shown to have a minor role in determining its capacitance, which is largely influenced by lipid composition of the membrane and in particular the amount of saturated lipids [193], [240].

Cells dielectric properties have been reported in the literature for different methods such as electrorotation (Chapter 1 section 1.4.3) and impedance spectroscopy (Chapter 1 section 1.4.2). However, as seen in Table 5.2, the dielectric properties obtained differed from one method to another. Since the dielectric properties of all the cell types studied in this chapter have not been determined using the same method in the same conditions, differences in set up between research groups could lead to biases in the determination of the dielectric properties. In this chapter, all cells were characterised using the same method and in the same experimental conditions to reduce any biases arising from the dielectric properties determination experimental conditions.

Cell types	Date	Reference	Model used	Type of measurement	Radius (µm)	Membrane capacitance (mF/m^2)	Membrane conductance	Cytoplasm conductivity (S/m)	Cytoplasm permittivity
Erythrocytes	1995	[241]	Single-shell	Electrorotation	2.8±0.1	9±0.8	-	0.52±0.051	57±5.4
	2018	[242]	-	FM wave DEP	-	31.3±6.7	-	0.17	-
	2004	[243]			3.6	8.72	222.2	0.31	59
	1998	[192]			2.4	9.99	125	0.53	50
	1997	[195]	Single-shell spheroid	Electrorotation	3.10±0.02	12± 1.2	271	0.52±0.05	57±5.4
T lymphocytes	1995	[241]	Single-shell	Electrorotation	3.5±0.2	11±1.1	-	0.76±0.058	64±5.9
	1999	[164]	Single-shell	Electrorotation	3.29±0.35	10.5±3.1	-	0.65±0.15	103.9±24.5
	2013	[161]	Single-shell	Electrorotation	3.6±0.6	7.01±0.91	-	0.53±0.1	100
	2009	[146]	Single-shell	Impedance spec	3.40±0.08	13.29±1.82	-	-	-
	1999	[244]	Double-shell	Dielectric spec	3.4	14.1			
	1986	[245]	Maxwell-Wagner	Line capacitive sensor	-	7.7	-	-	-
	1999	[166]	Single-shell	Electrorotation	3.04±0.26	12.1±1.5	-	1.06±0.14	74.0±5.3
	2012	[246]	-	DEP FFF	3.40±1.29	12.8±2.9	-	-	
B lymphocytes	1999	[164]	Single-shell	Electrorotation	3.29±0.03	12.6±3.5	-	0.73±0.18	154.4±39.9
	2013	[161]	Single-shell	Electrorotation	3.6±0.6	10.33±1.6	-	0.41±0.1	100
	2009	[146]	Single-shell	Impedance spec	3.09±0.22	9.91±0.80	-	-	-
	1999	[244]	Double-shell	Dielectric spec	3.3	16.2		-	-
	2018	[157]	Single-shell	Electrorotation	4.1±0.7	10.14±0.08	-	0.55±0.07	-
Monocytes	1999	[164]	Single-shell	Electrorotation	4.63±0.36	15.3±4.3	-	0.56±0.10	126.8±35.2
	2013	[161]	Single-shell	Electrorotation	4.8±0.55	11.77±2.12	-	0.37±0.15	100
	2009	[146]	Single-shell	Impedance spec	3.09±0.22	14.23±0.81	-	-	-
Granulocytes	1999	[164]	Single-shell	Electrorotation	4.71±0.23	11.0±3.2	-	0.60±0.13	150.9±39.3
	2013	[161]	Single-shell	Electrorotation	4.3±0.55	9.14±1.06	-	0.31±0.06	100
Neutrophils	2009	[146]	Single-shell	Impedance spec	3.09±0.22	9.84±0.07	-	-	-
Eosinophils	2009	[146]	Single-shell	Impedance spec	3.09±0.22	9.39±0.41	-	-	-
MSCs Stro-1+	2016	[247]	Single-shell	3DEP	7.7	10.7±0.13		0.34±0.13	91.6

Table 5.2: Dielectric properties of bone marrow cells as reported in the literature.

5.1.1 Research questions

The objective of this chapter was to determine the best conditions in terms of frequency and conductivity to separate BM-MSCs from the main cell types present in bone marrow using SAW-DEP. This objective was addressed via the following research questions:

1. Can pure populations of white blood cells be obtained from blood samples?

In order to determine the dielectric properties of the most present cell types found in bone marrow (B cells, T cells, Monocytes, neutrophils and eosinophils), the cells had to be isolated and purified. Since bone marrow aspirates are difficult to obtain, the cells were isolated from blood samples obtained from healthy donors, which were more readily available. The white blood cells were isolated from whole blood using a MACS approach (Chapter 1 section 1.2.3.2), and the purity of the samples obtained was determined using a FACS multi-panel approach (Chapter 1 section 1.2.3.2), whilst bone marrow mesenchymal stem cells (BM-MSCs) were obtained from pure commercial samples.

2. Can we determine the dielectric properties of the main cell types present in bone marrow using 3DEP and what are the factors influencing these properties?

Following isolation, the dielectric properties of each purified cell type were determined via 3DEP (Chapter 1 section 1.4.4). The cells' dielectric properties were determined for three different conductivities in order to account for a wide range of conductivities. The use of different fitting programs based on the single shell model (Chapter 2 section 2.2.2.3) to determine the dielectric properties from the DEP spectra obtained was also investigated. The influence of factors such as cell suspension concentration, conductivity and the passage number for BM-MSCs in the determination on the dielectric properties of the cells were studied.

3. What are the ideal conditions to separate BM-MSCs from other cell types present in bone marrow in terms of media conductivity and SAW-DEP frequency?

Once the dielectric properties of the cells were determined via 3DEP, the DEP responses of all the cell types were modelled for different frequencies

and medium conductivities in order to determine the best conditions allowing for separation of BM-MSCs from the rest of the white blood cells studied.

5.2 Materials and Methods

The materials were purchased from Sigma unless otherwise specified.

5.2.1 Buffers

MACS separation buffer: For MACS separation, a solution containing phosphate-buffered saline (PBS), pH 7.2, 0.5% bovine serum albumin (BSA), and 2 mM EDTA was prepared.

FACS separation buffer: For FACS, a solution of PBS containing 0.05% sodium azide was prepared.

3DEP solution: For 3DEP, the solution used consisted of a 5.4% (w/v) mannitol solution pH 7 and the conductivity was adjusted using a 10% NaCl solution. For higher conductivity buffers, the amount of mannitol was decreased so as to maintain the buffer osmolarity between 280 and 300 mosm. In the course of the experiments, three buffers were prepared at 0.01 S/m, 0.05 S/m and 0.1 S/m.

5.2.2 Culture of bone marrow stem cells

For all experiments, BM-MSCs (Promocell) were cultured from passage 2 until passage 6 in T75 flasks filled with 25 mL of MSCs culture medium following the passaging procedure described in Chapter 3 section 3.2.

5.2.3 Blood collection

Cell characterisation was conducted using blood provided by healthy volunteers, the procedure for which ethical approval was sought via the School of Dentistry's Research ethics Committee (DREC ref: 200417/ASD/227). All volunteers signed an approved informed consent form before each blood donation.

Two 10 mL venous blood samples were collected in heparin coated tubes following a standard procedure carried out by a trained phlebotomist [248]. Studies suggest that cryopreservation could have an effect on the cells' dielectric properties, as it can affect the surface morphology and gene expression of the cells, therefore all blood was used within the same day [249].

5.2.4 MACS separations of blood cells for dielectric characterisation

Blood was an ideal test sample for optimisation of methodologies as it was more readily available than bone marrow aspirate and also contained all the desired cell types, although at different proportions as shown in Table 5.3.

Cell type	Adult human blood (% distribution in white blood cells)	Bone marrow (% distribution in white blood cells)
Myelocytes	N/A	8-40 %
T cells	15 – 34%	5 – 23%
B cells	2 – 10%	
Neutrophils	45 – 75%	21 – 46%
Monocytes	4 – 10%	0.3 – 5%
Eosinophils	1 – 7%	0.8 – 7%
Basophils	0 – 2%	0.1 – 0.8%

Table 5.3: Distribution of cell types in human blood and bone marrow. The data was taken from [250]. Note: myelocytes are precursors of granulocytes (neutrophils, eosinophils, basophils).

As mentioned in the Chapter 2 section 1.2.3.2, MACS uses antibody-coated magnetic beads which can have an influence on the cell morphology and properties. Moreover, the presence of magnetic beads in the sample induces signal noise that affects the determination of the cell's dielectric properties. Consequently a negative selection approach was used for all cell purifications. This was done to ensure that the fraction collected was unlabelled to eliminate the influence of the magnetic beads on the dielectric properties of the cells separated. A summary of the workflow used to obtain pure populations of cells from blood is described in Figure 5.3.

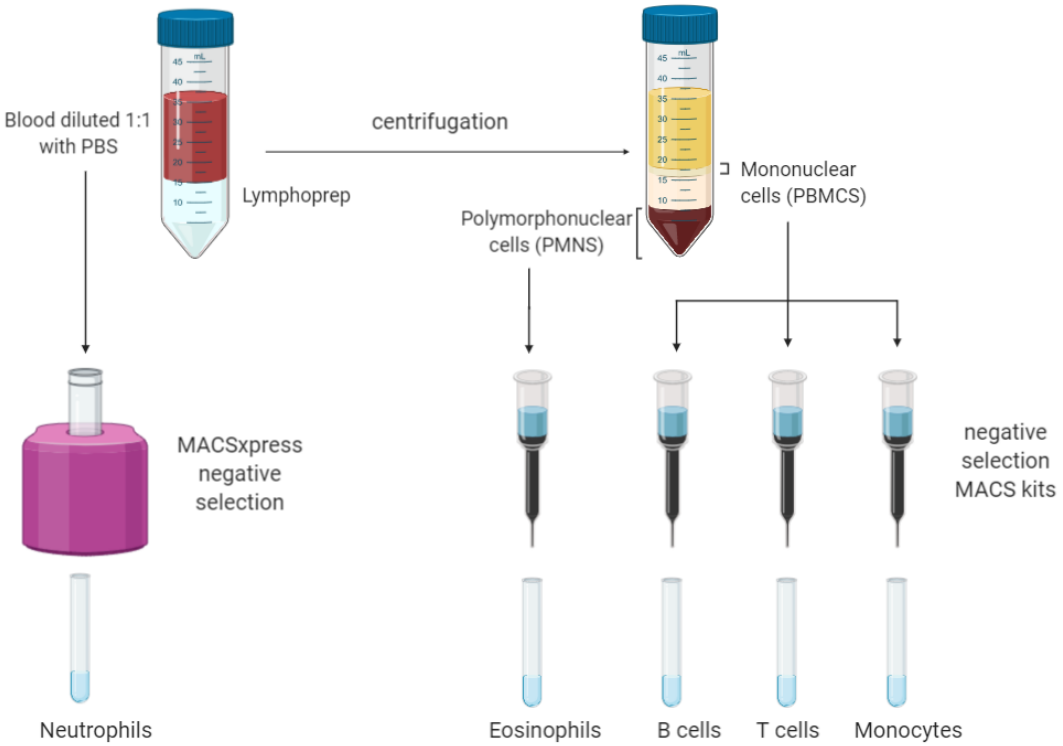

Figure 5.3: Purification of white blood cells from whole blood using density centrifugation and MACS negative selection. Neutrophils were obtained from whole blood using a MACSxpress negative selection kit. A lymphoprep density gradient was used to separate whole blood into mononuclear and polymorphonuclear cells that were later separated into B cells, T cells, monocytes and eosinophils using MACS separation kits and MidiMACS separator magnets. This figure was created using biorender.com.

5.2.4.1 Blood preparation for MACS separation

Each 10 mL sample of blood was first diluted with an equal volume of PBS and carefully layered on top of 10 mL of Lymphoprep™ (Axis-Shield, Alere Technologies, UK) so as to not disturb the surface of the density gradient. The tubes were then centrifuged at 800 g for 20 minutes at 20°C in a swinging bucket rotor without brake. The mononuclear cell fraction (Figure 5.4) was then carefully removed using a pastette and centrifuged at 350 g for 10 minutes. The remaining plasma and Lymphoprep™ solutions were removed to obtain the fraction containing the PMNs and the red blood cells.

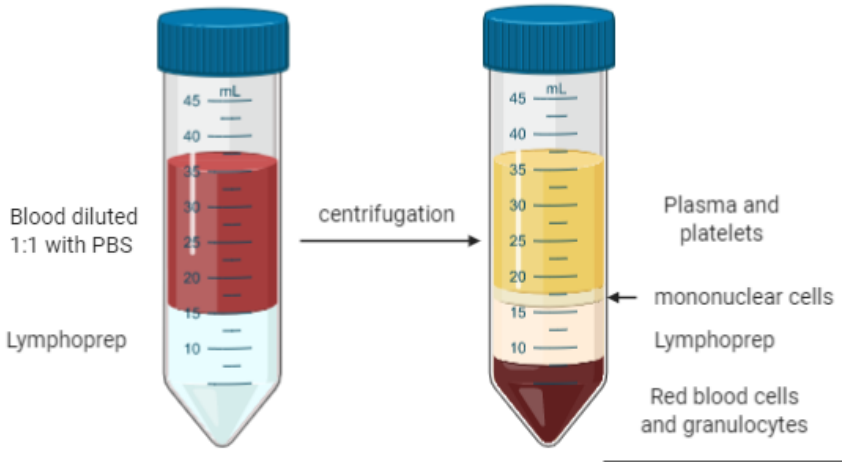

Figure 5.4: Separation of blood into mononuclear and polymorphonuclear cells using a Lymphoprep™ density gradient. The blood sample (represented in red) is diluted with PBS and layered onto the Lymphoprep™ medium (light blue). Following centrifugation, the blood is fractionated into plasma and platelets (yellow), Lymphorep™ medium (light pink) and red blood cells and granulocytes (dark red). The buffy coat containing the mononuclear cells (white) can be found at the interface between the plasma and the Lymphoprep™ medium. This figure was created using biorender.com.

5.2.4.2 Lysis of red blood cells

The red blood cells (RBCs) were lysed using a 10X RBC lysis buffer (Biolegend, USA) diluted ten times with distilled water and warmed to 37°C. The cell pellet was resuspended in 50 mL of lysis buffer and left for 10 minutes. Then, the cells were centrifuged at 350 g for five minutes and the supernatant containing the lysed RBCs was removed. A white pellet indicated that a minimal number of RBCs remained.

5.2.4.3 Isolation of mononuclear white blood cells using MACS

B cells, T cells and monocytes were isolated from the mononuclear fraction using commercially available MACS isolation kits purchased from Miltenyi Biotec: human B cell isolation kit II, human pan T cell isolation kit and human pan monocyte isolation kit.

Cell numbers in the mononuclear fraction were first determined by manual cell count using a haemocytometer and then the fraction was centrifuged at 350 g for 10 minutes. The cell pellet was resuspended in 40 µL of buffer per 10^7 total cells and 10 µL of Biotin-antibody cocktail per 10^7 total cells. After a

5 minutes incubation in the refrigerator (2−8°C) 30 µL of buffer per 10^7 total cells and 20 µL of Anti-Biotin MicroBeads per 10^7 total cells were mixed in. The mixture was then incubated for 10 minutes in the refrigerator (2−8°C) prior to magnetic separation. When the final volume was less than 500 µL, MACS buffer was added. A MACS LS column (Miltenyi Biotec, Germany) was placed in a MidiMACS separator and rinsed with 3 mL of MACS buffer. The cell suspension was then applied onto the column and washed with three sets of 3 mL of MACS buffer. The flow-through containing the unlabelled cells was collected and the cells were counted manually using a haemocytometer. The cells were then pelleted via centrifugation at 400 g for 10 minutes and when the pellet was red, an additional RBC lysis step was added as described in 5.2.4.2.

5.2.4.4 Isolation of eosinophils using MACS

Eosinophils were isolated from the polymorphonuclear (PMN) cells fraction using a human eosinophil isolation kit (Miltenyi Biotec, Germany) following RBC lysis as described in 5.2.4.2. The PMN pellet was first lysed following the RBC lysis protocol and the remaining cells were resuspended in 50 mL of MACS buffer, counted using a haemocytometer and centrifuged at 350 g for 10 minutes. Typical initial cell numbers varied from 20 to 70 million depending on the initial blood volume and RBC contamination. The cell pellet was resuspended in 40 µL of buffer per 10^7 total cells and 10 µL Biotin-antibody cocktail per 10^7 total cells. After a 10 minute incubation in the refrigerator (2−8°C), 30 µL of buffer per 10^7 total cells and 20 µL of Anti-Biotin MicroBeads per 10^7 total cells were mixed in. The mixture was then incubated for 15 minutes in the refrigerator (2−8°C) prior to magnetic separation, washed with 2 mL of MACS buffer and centrifuged at 300 g for 10 minutes. The supernatant was completely removed and the pellet was resuspended in 500 µL of MACS buffer. A MACS LS column (Miltenyi Biotec, Germany) was placed in a magnetic field and rinsed with 3 mL of MACS buffer. The cell suspension was then applied onto the column and washed with three sets of 3 mL of MACS buffer. The flow-through containing the unlabelled cells was collected and the cells were manually counted using a haemocytometer.

5.2.4.5 Isolation of neutrophils using MACS

Neutrophils were isolated from whole blood using a MACSxpress® human Neutrophil Isolation Kit (Miltenyi Biotec, Germany), a MACSmix Tube Rotator (Miltenyi Biotec, Germany) and a MACSxpress® Separator (Miltenyi Biotec, Germany). The antibody cocktail (details of the antibodies not given by manufacturer) was first prepared according to the manufacturer's instructions. Then, 6 mL of blood were processed by adding 0.5 mL volumes of antibody cocktail in a 15 mL Falcon tube and left to incubate for 5 minutes at room temperature using the MACSmix Tube Rotator on permanent run speed of approximately 12 rpm. After mixing, the tube was opened and placed on the MACSxpress Separator for 15 minutes. The magnetically labelled cells adhered to the wall of the tube while the aggregated erythrocytes sedimented to the bottom. While the tube was still inside the MACSxpress Separator, the supernatant containing the target cell fraction was collected. The supernatant was spun at 300 g for 10 minutes and the pellet was resuspended in RBC lysis solution following the RBC lysis protocol (Section 5.2.4.2).

5.2.5 Determination of isolated cell suspensions purity using FACS

FACS (Chapter 2, section 1.2.3.1) was used to assess the purity of the cell suspensions obtained. For this, a simplified multi antibody panel based on the one described by Bocsi *et al*. (2014) was used [251]. This panel was adapted for use with the FACS analyser available in house, a CytoFLEX (Beckman Coulter, USA) that had four lasers (blue 488 nm, violet 405 nm, red 633 nm and UV 355 nm) and 13 filters allowing for detection of up to 13 different fluorophores.

In order to minimise spill over, markers co-expressed by a given cell were labelled using antibody-conjugated fluorochromes with low spectral overlap (APPENDIX B). For this, where possible, fluorophores were spread out across the three available lasers (Table 5.4). This reduced the spill over of one fluorophore onto a second channel, as each laser was used sequentially. The details of the FACS analyser set up and the fluorescent compounds and antibodies used can be found in Table 5.4.

Laser	Filter (wavelength/ bandwidth)	Fluorochrome	Specificity	Target cells
Blue (488 nm)	525/40	FITC	CD8	T cells, NK cells, dendritic cells
	585/42	PE	CD56	T cells, NK cells
	780/60	PE-Cy7	CD16	Neutrophils, NK cells, eosinophils/monocytes
Violet (405 nm)	450/45	Pacific Blue	CD14	Monocytes
	525/40	V500	CD3	T cells
	610/20	BV605	CD45	All white blood cells
Red (633 nm)	660/20	APC	HLA-DR	B cells, monocytes
	712/25	APC R700	CD19	B cells, MSCs, dendritic cells
	780/60	APC Cy7	CD4	T cells, monocytes

Table 5.4: Specifications of lasers and band-pass filters setup of the Cytoflex flow cytometer, antibodies used and cell types targeted. APC = allophycocyanine; PE = phycoerythrin; Cy = cyanine; FITC = fluorescein isothiocyanate; NK = natural killer cells; MSCs = mesenchymal stem cells.

The main factor considered during the panel set up was peak resolution. As a general rule, the brightest antibody conjugated fluorochromes were used to label antigens with predicted lower densities and antibodies conjugated to dim fluorochromes were used to label high density antigens to increase peak resolution (Table 5.5). These antigen densities were provided by BD Biosciences. The densities had been determined by the company using standard curves made with beads expressing different amounts of antigens against which the populations of interest were measured. However, the antigen densities of some cell types were unknown. It is important to note that the expression of a given antigen can vary based on the cell type. For example, monocytes express 110,000 CD14 molecules (high density) per cell whereas neutrophils only express 3,500 CD14 molecules per cell (low density) (Table 5.5). In the panel used here, CD14 was used to gate monocytes so the marker was labelled using an antibody conjugated with a low brightness score fluorophore.

The flow cytometry files were analysed using the Cytexpert software developed by Beckman Coulter.

Cell type	Fluorophores	Fluorophore Brightness score	Markers	Marker molecules per cell
B cells	APC-R700	3	CD19	18,000
	APC	3	HLA-DR	85,000
T cells	V500	1	CD3	123,000
	APC-Cy7	1	CD4	100,000
	FITC	2	CD8	90,000
	PE	1	CD56	
Monocytes	APC-Cy7	1	CD4	
	APC	3	HLA-DR	
	Pacific Blue	1	CD14	110,000
	PE-Cy7	3	CD16[1]	
Neutrophils	Pacific Blue	1	CD14	3,500
	PE-Cy7	3	CD16	225,000

Table 5.5: Fluorophore brightness score and marker density for all the different white blood cells studied.

5.2.5.1 Titration of antibody concentrations for use in FACS

All antibodies (described in Table 5.6) were titrated to optimise their performance and limit background signal.

Antibody Name and target	reference	Lot	Clone	concentration
CD3 V500 mouse	561416	7096601	UCHT1	100 µg/mL
Isotype V500 mouse IgG1, κ	560787	7004583	X40	200 µg/mL
CD4 APC-Cy7 mouse	557871	7075668	RPA-T4	50 µg/mL
Isotype APC-Cy7 mouse IgG1, κ	557873	7079856	MOPC-21	50 µg/mL
CD8 FITC mouse	555366	6190704	RPA-T8	12.5 µg/mL
Isotype FITC mouse IgG1, κ	556649	7072907	MOPC-21	50 µg/mL
CD14 Pacific Blue mouse	558121	6350793	M5E2	200 µg/mL
Isotype Pacific Blue mouse IgG2a, κ	558118	6266867	G155-178	200 µg/mL
CD16 PE-Cy7 mouse	557744	7019721	3G8	100 µg/mL
Isotype PE-Cy 7 Mouse IgG1, κ	557872	7135509	MOPC-21	50 µg/mL
CD19 APC-R700 mouse	564977	7026663	HIB19	25 µg/mL
Isotype APC-R700 mouse IgG1, κ	564974	7062612	X40	200 µg/mL
CD45 BV605 mouse	564047	7129951	HI30	50 µg/mL
Isotype BV605 mouse IgG1, κ	562652	7039790	X40	200 µg/mL
CD56 PE mouse	555516	6054620	B159	6 µg/mL
Isotype PE mouse IgG1, κ	555749	7089770	MOPC-21	50 µg/mL
HLA-DR APC mouse	559866	7012621	G46-6	12 µg/mL
Isotype APC mouse IgG2a, κ	555576	7096625	G155-178	6 µg/mL

Table 5.6: Detail of all antibodies used in the FACS experiments: BD Biosciences reference number, lot number, clone and concentration.

[1] Note: only 20% of the monocytes express CD16 according to [397].

Samples containing 100 µL of blood were lysed by adding 2 mL of warm RBC lysis buffer and incubated for 10 minutes at room temperature, protected from light. The tubes were then centrifuged at 350 g for 5 minutes and the supernatant removed carefully so as to not disturb the pellet. The pellet was resuspended in 2 mL of FACS buffer and centrifuged at 350 g for 5 minutes. The supernatant was discarded again and the pellet was resuspended in 100 µL of FACS buffer with 5% mouse serum and different volumes of antibodies were added to each tube. Each anti-CD antibody solution was tested at three different volumes. For the antibodies where the recommended volume was 5 µL, the volumes tested were 5, 2.5 and 1 µL. For the antibodies where the recommended volume was 20 µL, the volumes tested were 20, 10 and 5 µL. All volumes were tested in different tubes. After incubation with the antibodies on ice for 45 minutes in the dark, 2 mL of FACS buffer were added. After centrifugation at 350 g for 5 minutes at 4°C, the supernatant was removed and the pellet was washed with 1 mL of FACS buffer. The tubes were centrifuged again at 350 g for 5 minutes, the pellet was resuspended in 400 µL of FACS buffer and the tubes were kept on ice until FACS analysis on the Cytoflex.

The isotype controls are antibodies raised against antigens not found in the cell type analysed and are used to account for non-specific binding, so they were not titrated and they were used at the same concentration as their pair. The analysis of the titration results for one of the antibodies tested is presented in section 5.3.1.1 and the titration results for the other antibodies can be found in APPENDIX C.

5.2.5.2 Compensation experiments

Compensation is a mathematical method needed when multiple fluorophores are used to stain the same sample to account for the spill over of the fluorophores in the other detection channels (Figure 5.5).

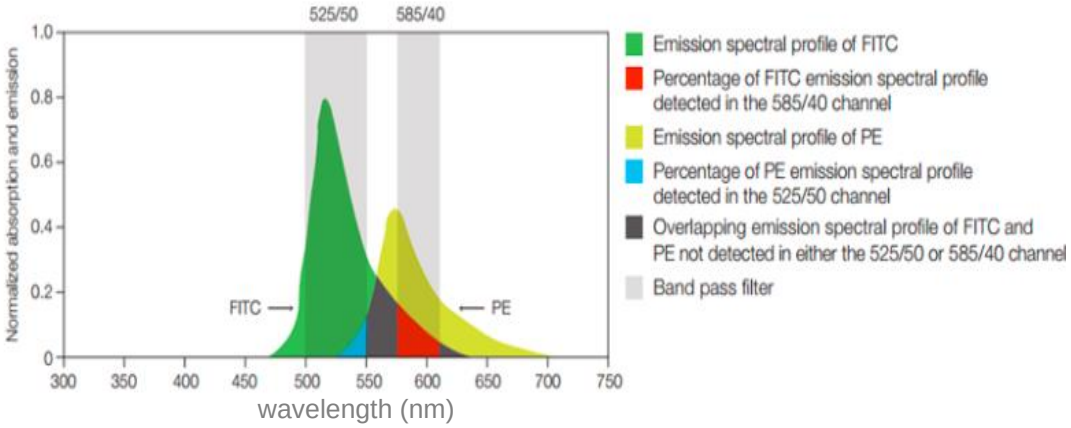

Figure 5.5: Spectral overlap between the emission of FITC and PE. A 525/40 (wavelength/bandwidth) filter is used to detect the FITC signal whilst the PE signal is detected by a 585/40 filter. The blue are of the PE emission spectrum and detected in the FITC channel is must be subtracted from the PE signal. Similarly, the red area of the FITC emission spectra is detected in the PE channel and must be subtracted from the PE signal.

To determine the compensation matrix, the blood samples (treated as explained in section 5.2.5.1) were stained with one fluorophore at a time using the volumes described in Table 5.7 and their fluorescence was recorded for all FACS channels.

Tube	Antibody	Volume / dilution
1	Unstained	
2	Anti-CD3 V500	2.5 µL
3	Anti-CD4 APC-Cy7	1 µL
4	Anti-CD8 FITC	5 µL
5	Anti-CD14 Pacific Blue	10 µL
6	Anti-CD16 PE-Cy7	1 µL of 2X dilution
7	Anti-CD19 APC-R700	1 µL
8	Anti-CD45 BV605	2.5 µL
9	Anti-CD56 PE	20 µL
10	Anti-HLA-DR APC	20 µL of 2X dilution

Table 5.7: Distribution of antibodies volumes and dilutions used in compensation experiments.

The Cytexpert software was used to calculate the spill over values of each fluorophore in each channel, and created a compensation matrix (Table 5.8) that was used for subsequent experiments.

Channel	-FITC%	-PE%	-ECD%	-PC5.5%	-PC7%	-APC%	-APC-A700%	-APC-A750%	-PB450%	-KO525%	-Violet610%
FITC		1.00	0.00	0.00	0.32	0.00	0.00	0.00	0.00	25.00	0.00
PE	23.00		61.30	2.50	2.20	0.00	0.00	0.00	0.00	2.00	10.80
ECD	2.30	13.00		0.56	0.31	0.00	0.00	0.00	0.00	0.00	7.50
PC5.5	0.80	5.00	70.80		0.85	1.00	8.00	0.00	0.00	0.00	7.20
PC7	0.10	0.50	10.50	14.70		0.10	2.00	3.50	0.00	0.00	1.00
APC	0.00	0.00	0.30	32.00	0.00		10.00	7.00	0.00	0.00	0.00
APC-A700	0.00	0.00	0.05	3.80	0.01	7.20		1.00	0.00	0.00	0.00
APC-A750	0.00	0.00	0.00	2.10	3.60	4.10	43.00		0.00	0.00	0.00
PB450	0.00	0.00	0.00	0.00	0.00	0.00	0.00	0.00		20.00	18.00
KO525	0.20	0.00	0.00	0.00	0.00	0.00	0.00	0.00	0.39		0.00
Violet610	0.00	1.00	9.00	0.00	0.00	0.00	0.00	0.00	0.05	46.00	

Table 5.8: Antibody panel compensation matrix. The compensation factors were calculated by accounting for the spill over values of each of the fluorophores (left column) into each of the detection channels (first row).

5.2.5.3 Fluorescence minus one controls experiments

Fluorescence minus one (FMO) controls are necessary when building a multicolour FACS panel to determine where the gates should be set. An FMO control is a tube where cells are stained with all fluorophores used in the panel except for one, and it is used to determine the limit between the background fluorescence and the positive populations in a sample stained with multiple fluorophores (Figure 5.6).

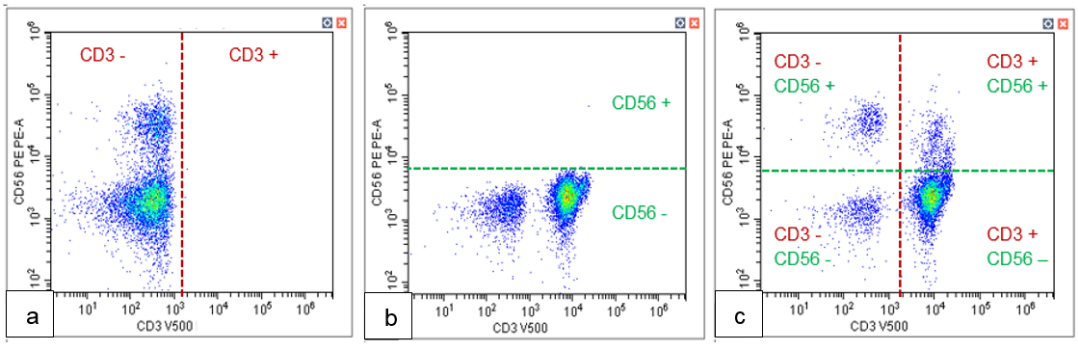

Figure 5.6: Gating of populations using FMO controls. a) Fluorescence of a blood sample containing all antibodies minus CD3 V500. The gate (red) represents the boundary between CD3+ and CD3- cells. b) Fluorescence of a blood sample containing all antibodies minus CD56 PE. The gate (green) represents the boundary between CD56+ and CD56- cells. c) Fluorescence of a blood sample containing all antibodies. The gates established in A and B are used to determine which populations are CD3 positive or negative and CD56 positive or negative.

For the FMO control experiments, the initial treatment of the blood samples was the same as described in the section 5.2.5.1 but in each tube, all of the antibodies were used minus one as shown in Table 5.9. The volumes of antibodies used for these experiments are described in Table 5.10.

Tube	Antibodies								
1	UNSTAINED								
3	**V500**	CD4	CD8	CD14	CD16	CD19	CD45	CD56	HLA-DR
4	CD3	**APC-Cy7**	CD8	CD14	CD16	CD19	CD45	CD56	HLA-DR
5	CD3	CD4	**FITC**	CD14	CD16	CD19	CD45	CD56	HLA-DR
6	CD3	CD4	CD8	**Pac Blue**	CD16	CD19	CD45	CD56	HLA-DR
8	CD3	CD4	CD8	CD14	**PE-Cy7**	CD19	CD45	CD56	HLA-DR
9	CD3	CD4	CD8	CD14	CD16	**APC-R700**	CD45	CD56	HLA-DR
10	CD3	CD4	CD8	CD14	CD16	CD19	**BV605**	CD56	HLA-DR
11	CD3	CD4	CD8	CD14	CD16	CD19	CD45	**PE**	HLA-DR
12	CD3	CD4	CD8	CD14	CD16	CD19	CD45	CD56	**APC**

Table 5.9: Distribution of antibodies in FMO controls experiments. The first tube did not contain any antibodies and the isotype controls are represented in bold.

Antibody	Volume / dilution	Isotype controls	Volume / dilution
Anti-CD3 V500	2.5 µL	Isotype V500	2.5 µL of 2X dilution
Anti-CD4 APC-Cy7	1 µL	Isotype APC-Cy7	1 µL
Anti-CD8 FITC	5 µL	Isotype FITC	5 µL of 4X dilution
Anti-CD14 Pacific Blue	10 µL	Isotype Pacific Blue	10 µL
Anti-CD16 PE-Cy7	1 µL of 2X dilution	Isotype PE-Cy7	1 µL
Anti-CD19 APC-R700	1 µL	Isotype APC-R700	1 µL of 8X dilution
Anti-CD45 BV605	2.5 µL	Isotype BV605	5 µL of 4X dilution
Anti-CD56 PE	20 µL	Isotype PE	20 µL of 8.3X dilution
Anti-HLA-DR APC	20 µL of 2X dilution	Isotype APC	20 µL

Table 5.10: Antibody volumes and dilutions used in FMO controls and multi-panel FACS experiments.

For the FMO control experiments, the incubation time was longer than the recommended 45 minutes, as the addition of all the components in each tube was very time consuming so total incubation time was of 75 minutes. The process after incubation was the same as described in section 5.2.5.1. For each tube, 40,000 events in the intact cellular bodies gate (excluding debris) were acquired and before analysis, the compensation table obtained previously (Table 5.8) was applied to account for fluorochrome spill over. The FMO controls were used to set up all the gates used in subsequent experiments using the principle described in Figure 5.6 and the details are presented in APPENDIX C.

5.2.5.4 Determination of the purity of the MACS-isolated cell fractions using the FACS antibody panel

For all the purified cell suspensions, the MACS flow-through was centrifuged at 350 g for 5 minutes and the supernatant removed carefully so as to not disturb the pellet. The pellet was resuspended in 2 mL of FACS buffer and then centrifuged at 350 g for 5 minutes. The supernatant was discarded again and the pellet was resuspended in 100 µL of FACS buffer with 5% (v/v) mouse serum. For each purified cell sample, two tubes were prepared. One contained all relevant isotype controls and the other all the tagged antibodies in the volumes described in Table 5.10. The process after incubation was the same as that described in section 5.2.5.1. For each cell type, 50,000 events (intact cells) were acquired. The data obtained was then analysed using the compensation matrix (Table 5.8) and the gates set up using the data from the FMO control experiments (Section 5.3.1.2, Figure 5.11) to determine the percentage purities of each fraction using the formula:

$$\%\, purity = \frac{total\ cells - \ number\ of\ target\ cells}{total\ cells}\ x\ 100$$

5.2.6 3DEP measurements the MACS-purified cell suspensions and stem cells

The dielectric properties of BM-MSCs and each MACS-purified cell type were determined using 3DEP (Labtech International Ltd, Heathfield, UK), a commercially available well-based DEP cytometer. The instrument used disposable chips formed of twenty wells that enable simultaneous stimulation of the cells with twenty different frequencies (Chapter 1, section 1.4.4) [173], [174]. For a given medium conductivity and at each frequency, the cells in the well either move towards the channel walls (pDEP) or are pushed towards the centre of the wells (nDEP). The wells are illuminated by the instrument and the changes in light intensity can be used to determine the magnitude and polarity of the DEP forces exerted on the cells (Figure 5.7).

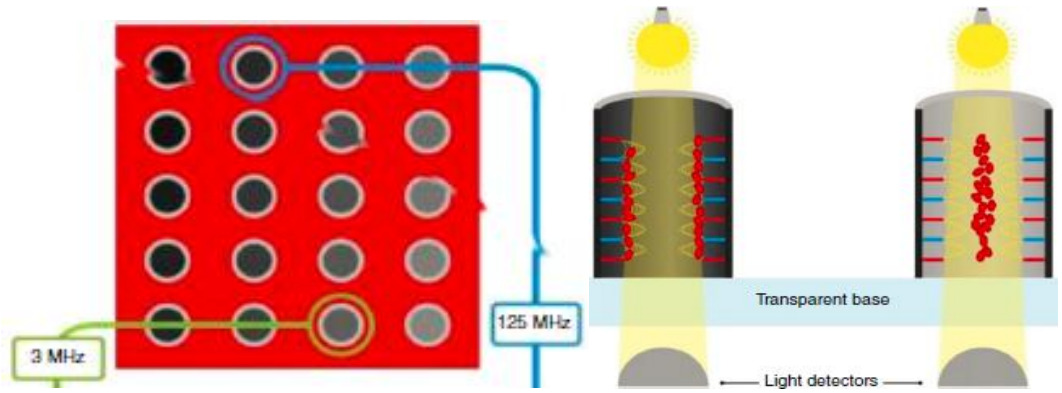

Figure 5.7: Diagram of the commercial 3DEP system consisting of 20 wells energised at different frequencies. For the lower frequencies, the cells experience positive DEP and are attracted towards the electrode walls, allowing for the light to pass through. For the higher frequencies, the cells experience negative DEP and are pushed away from the electrodes, towards the centre of the well, resulting in a decrease in light intensity recorded at the detectors. Image reproduced from [175].

For all cell types, the DEP spectra was determined for three different conductivities: 0.01, 0.05, 0.10 S/m. These conductivities were selected because they covered the range of conductivities for which the cells experienced both positive and negative DEP at the range of frequencies that the 3DEP device operates. Each cell suspension was centrifuged at 350 g and resuspended in 10 mL of 3DEP solution (section 5.2.1) at one of the three conductivities twice to ensure all of the MACS buffer was removed. Finally, the cells were centrifuged at 350 g resuspended in 3DEP solution to obtain a concentration of 1 million cells/mL and loaded onto one of the 3DEP chips. For each cell and conductivity, a full DEP spectrum was generated by applying frequencies ranging from 10 kHz to 40 MHz (maximum supported frequency) for 30 seconds. The lower frequency limit was chosen because it has been shown that for frequencies lower than 4 kHz, heating effects and electro-osmosis can induce fluid motion affecting data acquisition [173].

During data acquisition, the 3DEP instrument divided each of the wells into ten concentric bands that were recorded separately. Hoettges *et al* (2008) noted that the field generated by the 3D electrodes did not reach the inner part of the well, generating noise that could be reduced by limiting the analysis to the region containing the particles nearest to the electrode walls [172], [173]. To limit the data noise, only bands 7 to 9 (corresponding to the 30% outer radius of the well) were used for the analysis.

At least three repeats of these measurements were made for each cell type and conductivity.

5.2.7 Modelling of 3DEP spectra for determination of dielectric properties of each cell type

The frequency spectra obtained by 3DEP were analysed using Python scripts (APPENDIX E) based on the single-shell model to determine dielectric properties (Chapter 2 section 2.2.2.3). To limit the number of variables solved, the assumed value for conductance of the membrane was fixed at 500 S/m^2 for all cells, as this parameter has been shown to have little impact on the overall DEP spectrum (Chapter 2 section 2.2.3) [243]. The value used in the modelling for the radii of the cells was based on values obtained in the literature (Table 1.1) for B cells, T cells, monocytes, neutrophils, BM-MSCs and eosinophils.

Three fits were used to determine the cells' dielectric properties. A first single-conductivity fit was used to determine the dielectric properties for one single conductivity. The single-shell model was fitted to the data using non-linear least-square minimisation with four variable parameters: the cytoplasmic conductivity and permittivity, the membrane capacitance and a scaling factor. This scaling factor was introduced because the 3DEP instrument measures the relative DEP force, rather than a CM factor (Chapter 1 section 1.4.4). The second fit used three conductivities in combination with one single scaling factor and the third fit used the three conductivities in combination with three different scaling factors.

For all fits, the program used a least square fit. To estimate the relative quality of the fit, the reduced χ^2 goodness of fit test was used. The chi-square value is a non-parametric test used to determine how different the experimental value is from the fitting value. In this test, the distance between the experimental points and the value of the fit is squared and divided by the number of points and then normalised by the value of the fit. A lower χ^2 value, indicates a better agreement between the experimental data and the fit. To account for overfitting when multiple fitting parameters were used, the Bayesian information criterion was used to compare the different fitting programs. This criterion introduces a penalty term for the number of parameters in the model and the model with the lowest Bayesian criterion is preferred.

5.2.8 Modelling ideal cell separation conditions

The dielectric properties determined via the 3DEP system were used to calculate the CM factor of the different cells using the equations (2.33), (2.34), (2.35) and (2.37) described in chapter 2 section 2.2.2.3 for different conductivities and frequencies. The python scripts used to calculate the CM factors and generate graphs for different conductivities and frequencies graphs were based on the scripts described by Smith and colleagues (2017) and are presented in APPENDIX E [141].

5.3 Results

5.3.1 Purity of cell suspensions separated by MACS

The first step towards the determination of the cells' dielectric properties was to obtain pure populations of the cell types present in bone marrow. The system was simplified by only considering the cell types that are most prominent in bone marrow (Table 5.11) and where negative selection MACS kits were commercially available. These included lymphocytes (T and B), monocytes, neutrophils and eosinophils. Erythroblasts were excluded as these were depleted from the samples prior to testing using a lysis solution.

	Mean percentage (Observed range)		
	Bone marrow		**Lysed Blood**
Cell type	**Men**	**Women**	
Blast cells	1.4 (0-3.2) %		-
Promyelocytes	7.8 (3.6-13.2) %		
Neutrophil myelocytes	7.6 (4-21.4) %		
Metamyelocytes	4.1 (1-7) %		
Neutrophils	32.1(21-45.6) %	37.4 (29.6-46.6) %	60%
Eosinophils + eosinophils myelocytes	3.5 (0.9-7.4) %		3%
Basophils	0.1 (0-0.8) %		-
Erythroblasts	28.1 (18-39.4) %	22.5 (14-31.8) %	
Lymphocytes	13.1 (4.6-22.6) %		25% T cells 7% B cells
Plasma cells	0.6 (0-1.4) %		-
Monocytes	1.7 (0-4.5) %		5%

Table 5.11: Published values for proportions of different cell types in human bone marrow and lysed blood. Differences for men and women were only reported when there was a significance (P< 0.01). Adapted from [14]. Data on lysed blood without platelets [252].

Due to its availability, blood was used for these experiments as it contains all the desired cell types that are of interest in bone marrow, despite being present in different proportions (Table 5.11). Once the cell types had been initially separated using MACS as described in section 5.2.4, FACS was used to assess the purity of the solutions obtained based upon detection of the relevant cell type-specific markers. The details of the marker expression of each cell type of interest can be found in Table 5.12.

Marker	Cell types expressing marker
CD3	T cell subpopulations
CD4	T cells, monocytes
CD8	T cells, NK cells, dendritic cells
CD14	Monocytes
CD16	Neutrophils, NK cells, eosinophils/monocytes
CD19	B cells, MSCs, dendritic cells
CD45	All leukocytes
CD56	T cells, NK cells
HLA-DR	B cells, monocytes

Table 5.12: Markers used in the FACS multi-panel and marker expression in relevant cell types.

5.3.1.1 Optimisation of antibody concentrations for FACS panel

All antibodies used in the FACS panel were first titrated to determine the minimal concentration needed to achieve a reasonable fluorescence signal to noise ratio with minimal channel spill over at three concentrations (section 5.2.5.1). Two examples of antibody titration are shown Figure 5.8 and Figure 5.9 and the rest of the titrations can be found in APPENDIX C. In the case of CD8-FITC, all concentrations tested yielded a similar fluorescence peak which was clearly distinct from the isotype control peak and so the smallest volume was used.

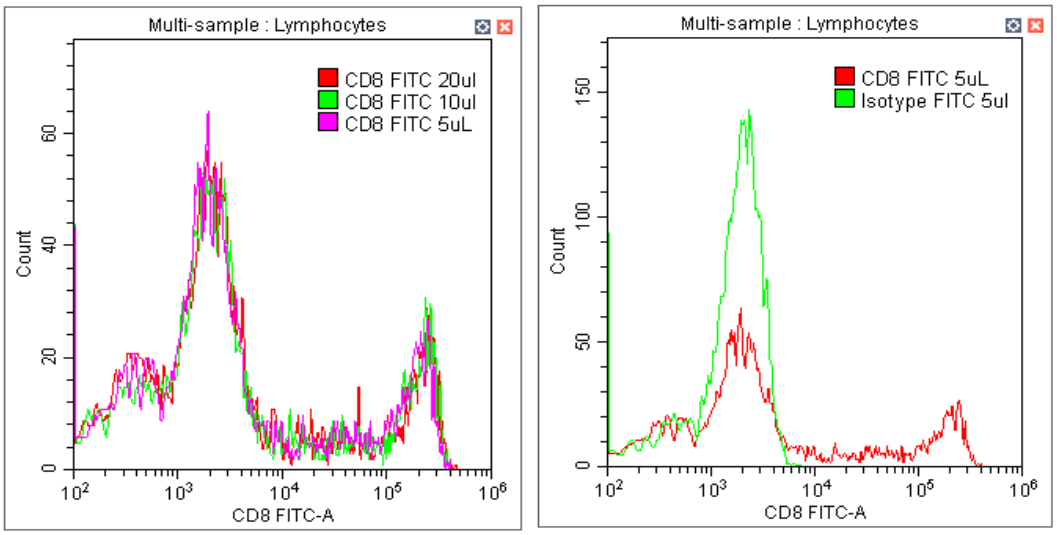

Figure 5.8: Titration of anti-CD8 antibody. a) Fluorescence values obtained when three different volumes of anti-CD8 FITC antibodies were used to label lymphocytes, gated on lymphocytes gate. b) Comparison of anti-CD8 antibody fluorescence with Isotype control. For all volumes of CD8 FITC, the fluorescence intensity (right peak) was similar and distinct from the isotype control.

A contrasting example can be seen in the case of anti-CD56-PE antibodies, where only the highest concentration tested yielded a fluorescence peak distinct from the matching isotype control peak, so the highest concentration was used for all experiments.

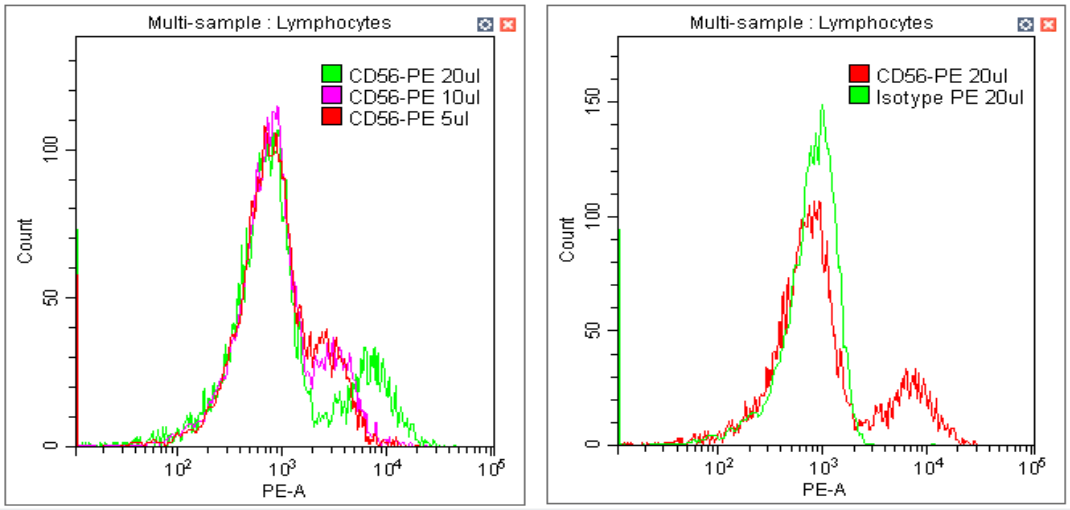

Figure 5.9: Titration of anti-CD56 antibody. a) Fluorescence of three volumes of anti-CD56 PE antibodies gated on lymphocytes gate. b) Comparison of CD4 antibody fluorescence with Isotype control. Note: Intact cells gate comprises Lymphocytes + Monocytes + Granulocytes gates. For 20 µL, the fluorescence peak was distinct from the isotype control peak, whereas for lower volumes, there was no clear separation between the positive and negative (isotype control) peaks.

5.3.1.2 Determination of MACS purified cell suspensions purity using a FACS multi-panel

Once the optimised working concentrations for each antibody had been determined, the FMO controls were used to determine the gates to be used in the final FACS analysis. A simplified version of the gating strategy used to generate the data shown in Figure 5.13 to Figure 5.16 can be found in Figure 5.10.

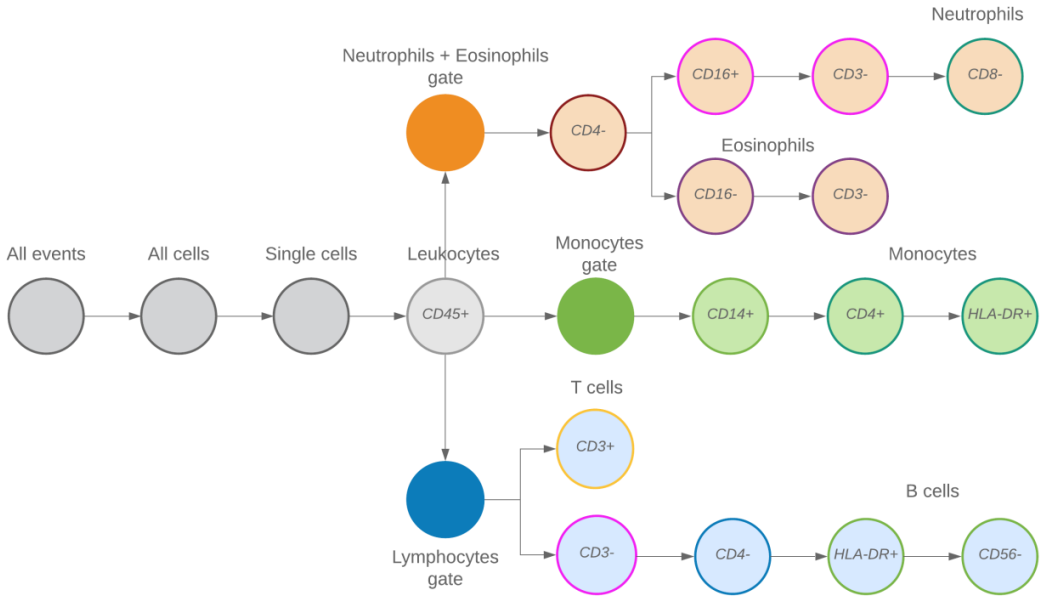

Figure 5.10 : FACS panel population tree and marker expression for the different cell types.

First, single cells were obtained after excluding air bubbles, debris and non-single events. The next step was to obtain the neutrophil / eosinophil, monocyte and lymphocyte gates based on the CD45 marker expression (as all leukocytes are CD45+) against the side scatter (SSC) plot. All $CD45^-$ events including any remaining erythrocytes, debris and thrombocytes were excluded. The combined neutrophil /eosinophil population was then divided into a $CD3^-$ / $CD16^-$ population (representing pure eosinophils) and a $CD3^-$ / $CD16^+$ gate (containing the neutrophil fraction). All $CD4^+$ events (possible monocytes or T cells contamination) were then removed. Finally, $CD8^+$ events (representing possible NK cells contamination) were excluded from the $CD4^-$ $CD16^+$ population to obtain the pure neutrophil fraction. The monocyte population was further purified by selecting only the population that was $CD14^+$. To confirm the purity of the population, any possible contamination by lymphocytes ($CD4^+$ HLA-DR^- events for T cells and $CD4^-$ HLA-DR^+ events for B cells) was excluded and only $CD4^+$ HLA-DR^+ events

(pure monocytes) were considered. The lymphocyte gate was first divided between a $CD3^+$ and a $CD3^-$ population (containing B cells and NK cells). The T cell population was defined as $CD3^+$ $CD16^-$. The $CD3^-$ population was further gated around $CD4^-$ to make sure that there was no remaining contamination from the T cells. Finally, B cells ($HLA\text{-}DR^+$ $CD56^-$) were separated from NK cells ($HLA\text{-}DR^-$ $CD56^+$).

This antibody panel was used to collect the data shown in Figure 5.13 - Figure 5.16. The cell purity results are summarised in Table 5.13.

	Samples					
Cell type	Lysed blood	Purified B cells	Purified T cells	Purified Monocytes	Purified Neutrophils	Purified Eosinophils
B cells	4%	82%	0.9%	0.1%	0%	0%
T cells	30%	2%	94%	0%	0%	0%
Monocytes	4%	1.2%	0.5%	74%	0.1%	0.4%
Neutrophils	27%	0%	0%	0%	98%	0.8%
Eosinophils	3%	0.2%	0%	1%	0.2%	93%
Other[1]	32%	15%	4%	25%	2%	6%

Table 5.13: Summary table showing the presence of mononuclear cells (T cells, B cells, monocytes) and granulocytes (eosinophils, neutrophils) in lysed blood and each of the MACS-purified cell suspensions. The percentages are calculated as percentage of single cells using the FACS multi-panel. [1]Other may refer to debris or remaining RBCs.

The percentages of B cells, T cells monocytes and eosinophils obtained for the lysed blood sample were similar to those expected in a blood sample (Table 5.3). In contrast, the amount of neutrophils was lower than expected, but this could be due to neutrophil activation and clumping that was observed when resuspending the MACS-purified neutrophil cell suspension in FACS media. The results showed that all MACS-purified cell suspensions contained some debris and RBC contamination despite the lysis step but no major contamination from other white blood cells. The debris and RBC contamination could be seen in the CD45 plot represented as $CD45^-$ events, notably in the monocytes and the B cells purified samples, which explains why the percentage purity for these samples was lower.

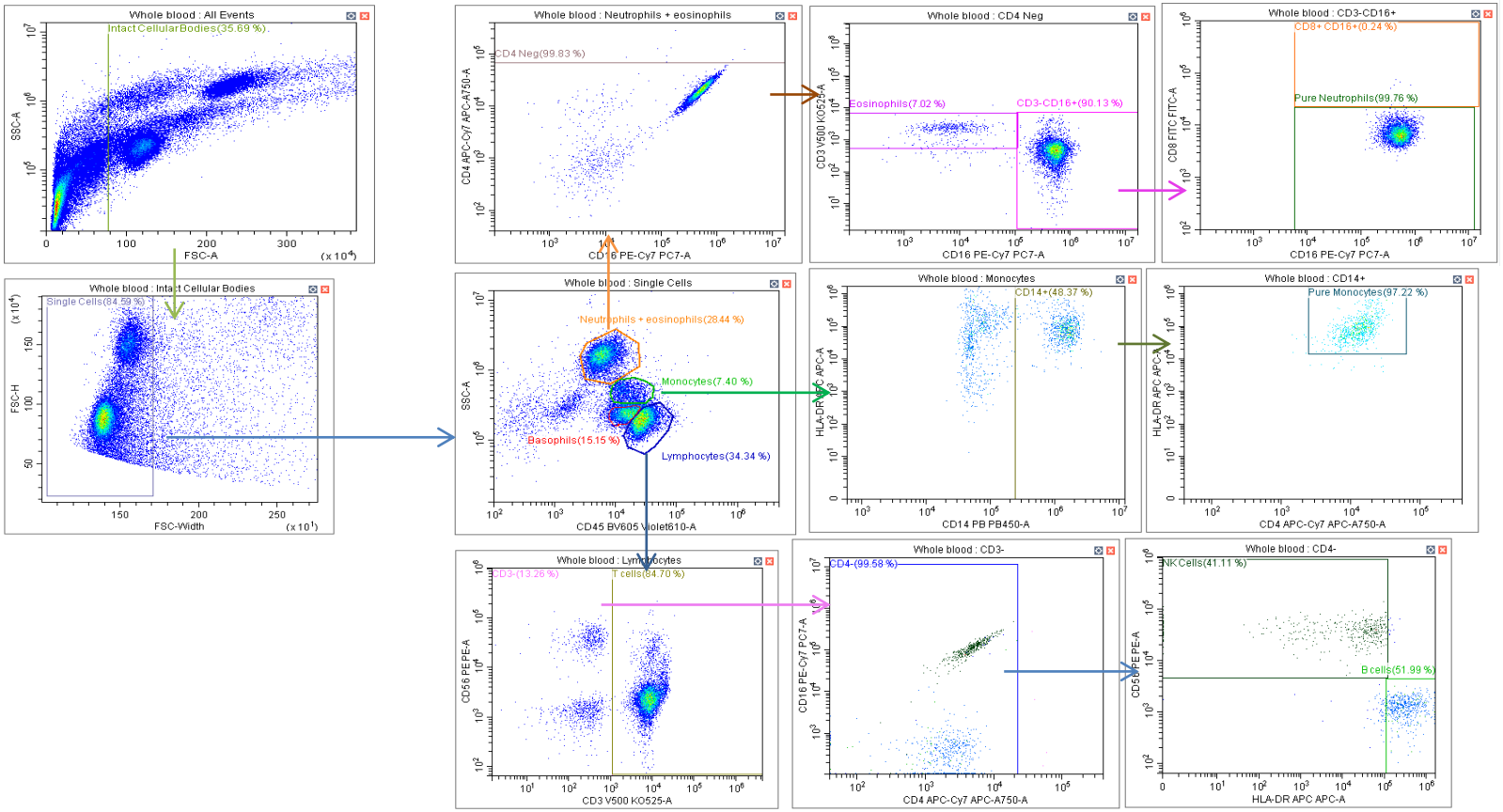

Figure 5.11: FACS panel gating analysis on whole lysed blood. The gates used to define the eosinophils, neutrophils, monocytes, B cells and T cells populations (explained in detail in Figure 5.10) show the proportion of each cell type found in blood. The colour of the plots represents the cell density (blue represents low density whilst red represents high density).

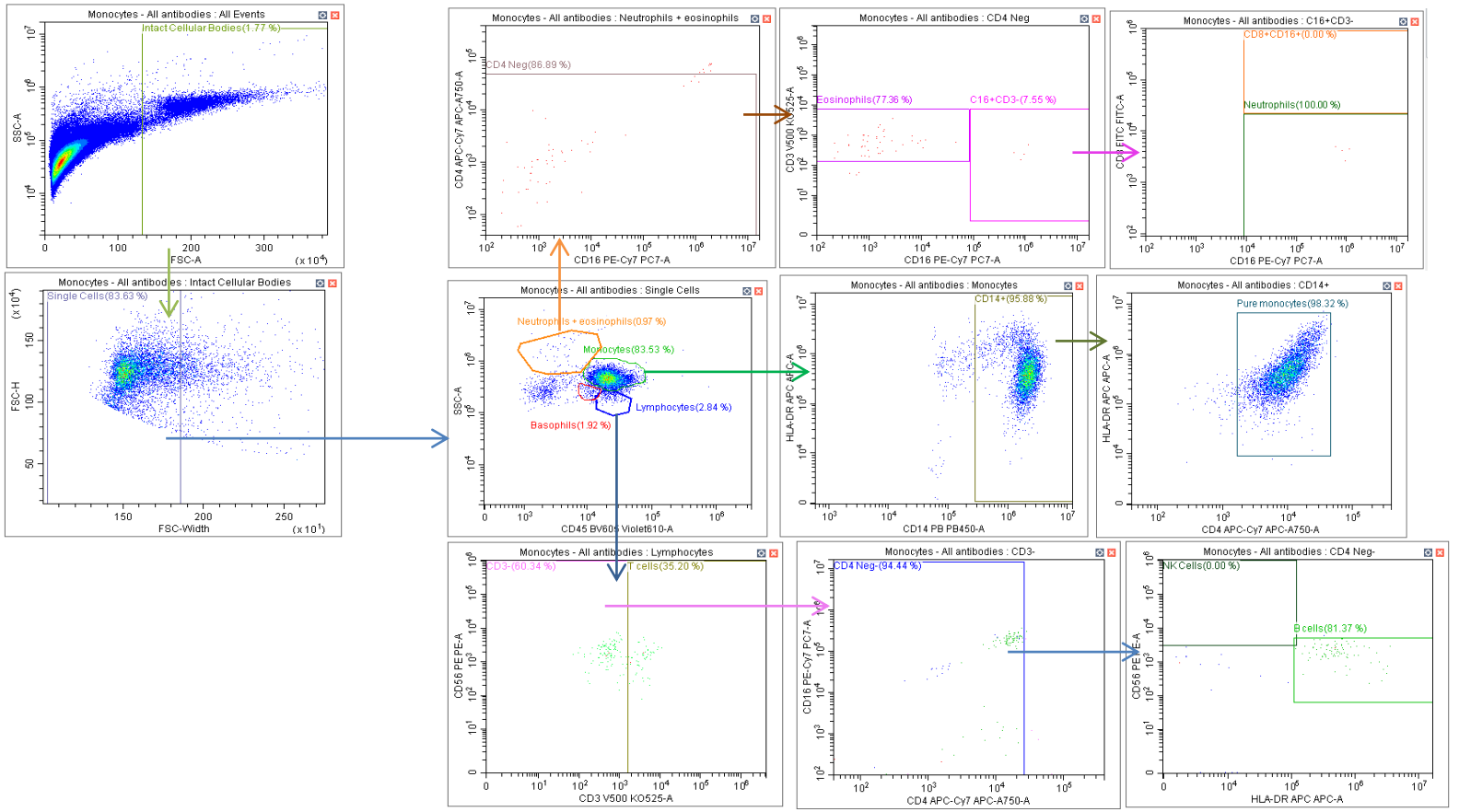

Figure 5.12: FACS panel gating analysis of monocytes isolated from whole blood using MACS kits. The monocytes gate contains 74% of the intact cell events and the other empty gates show there was no contamination from B cells, T cells, neutrophils or eosinophils. The colour of the plots represents the cell density (blue represents low density whilst red represents high density).

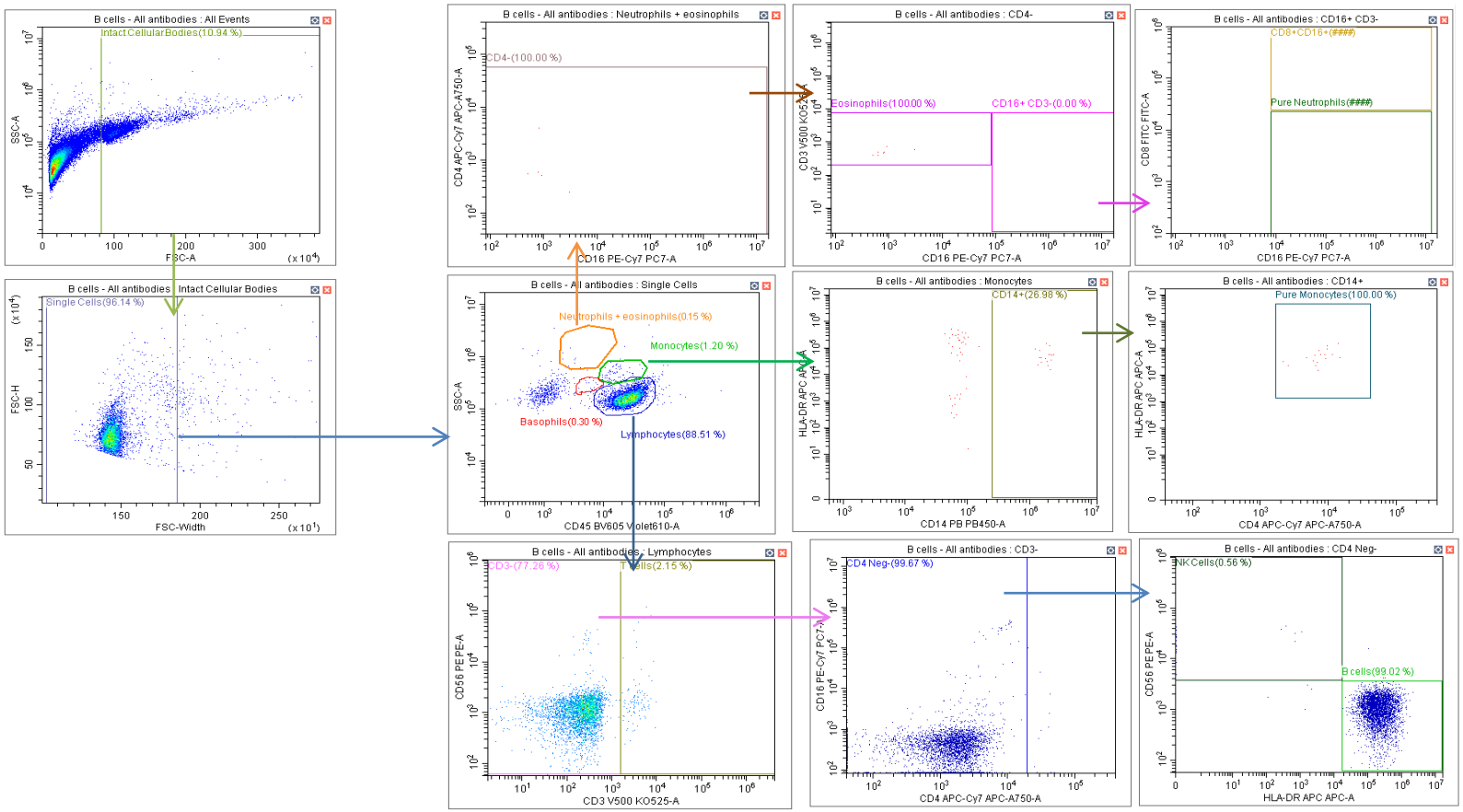

Figure 5.13: FACS panel gating analysis of B cells isolated from whole blood using MACS kits. The B cells gate contains 82% of the intact cells and other empty gates show there was no contamination from monocytes, T cells, neutrophils or eosinophils. The colour of the plots represents the cell density (blue represents low density whilst red represents high density)

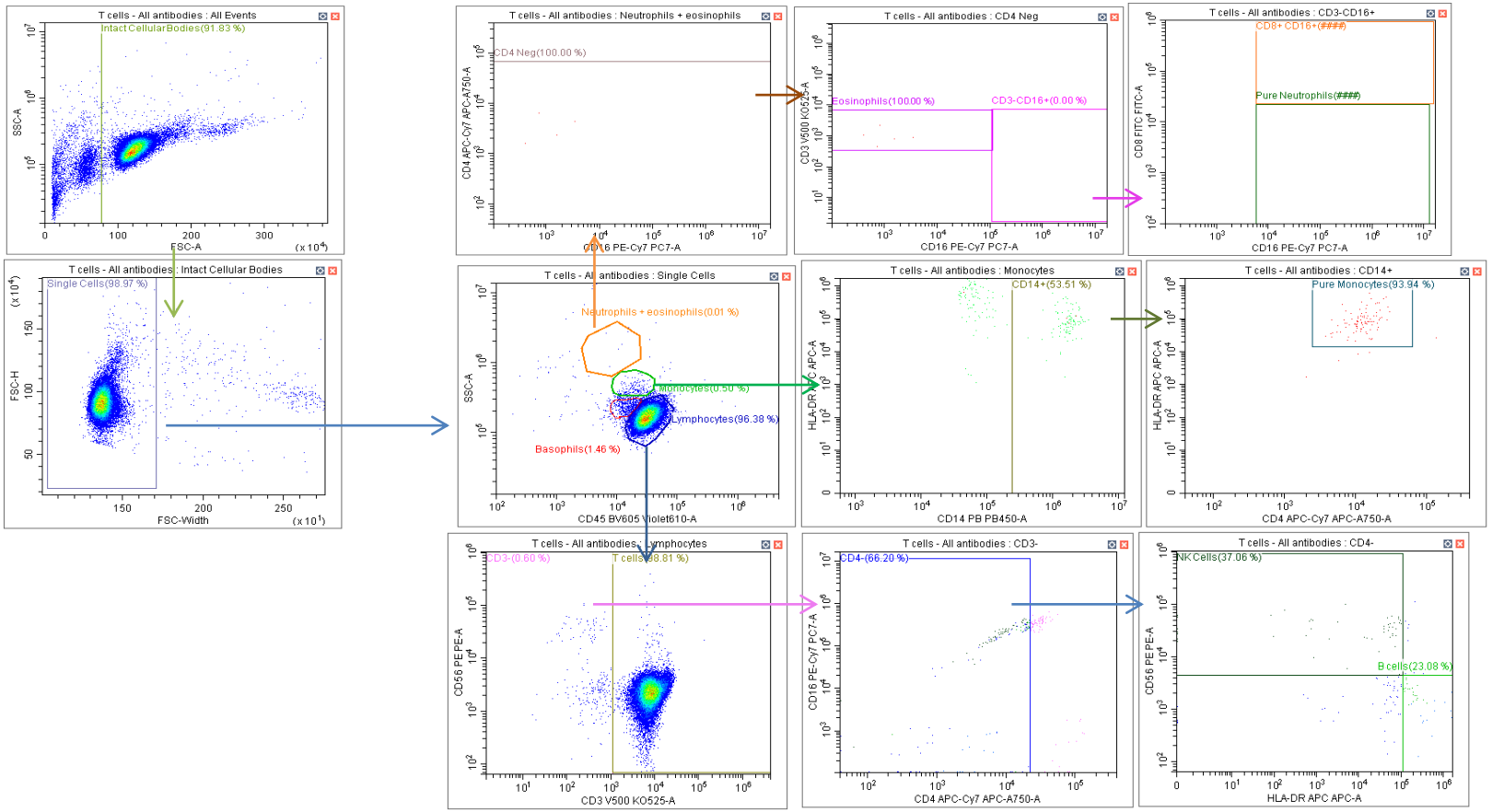

Figure 5.14: FACS panel gating analysis of purified T cells isolated from whole blood using MACS kits. The T cells gate contains 94% of the intact cells and other empty gates show there was no contamination from monocytes, B cells, neutrophils or eosinophils. The colour of the plots represents the cell density (blue represents low density whilst red represents high density).

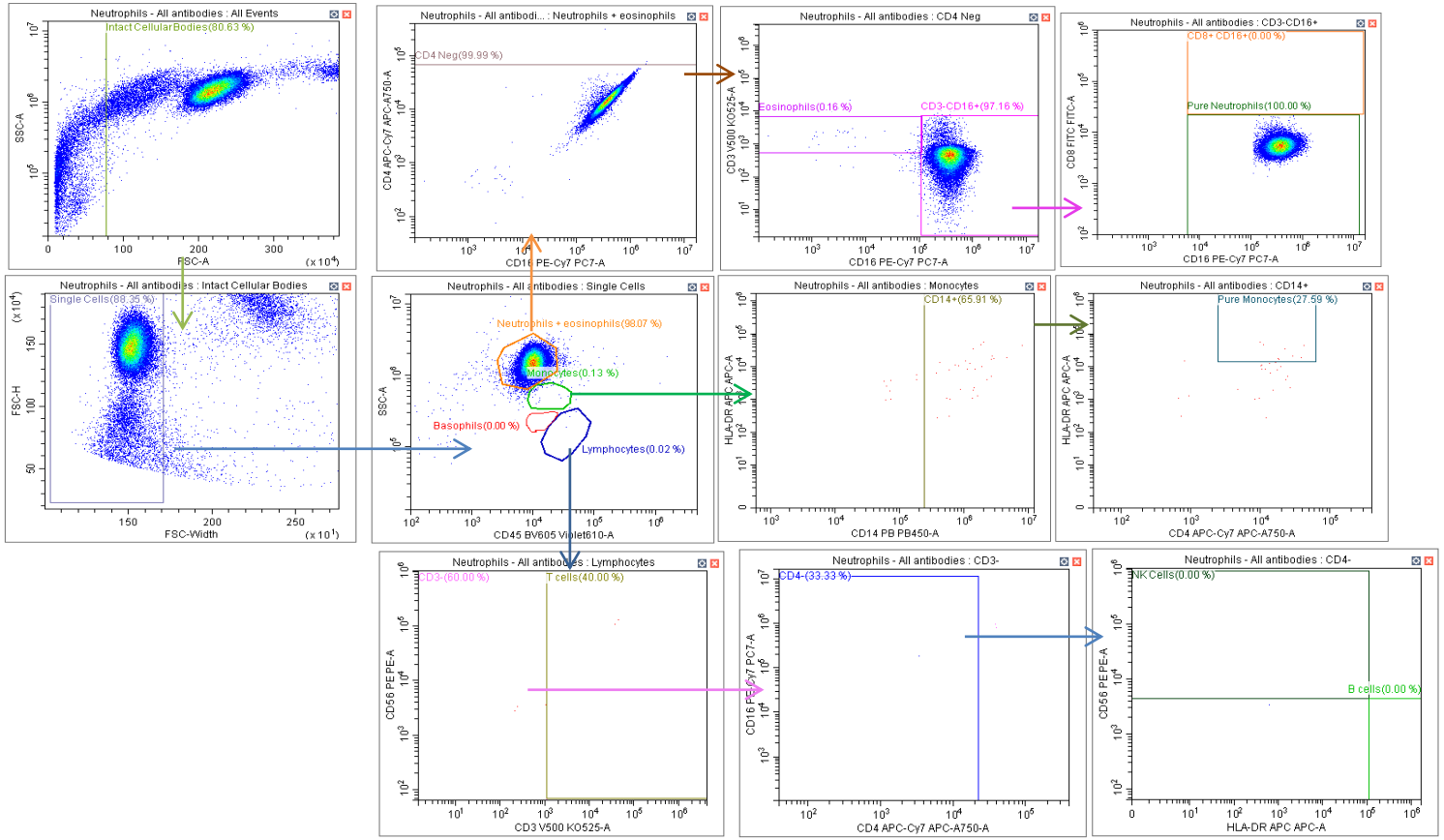

Figure 5.15: FACS panel gating analysis of neutrophils isolated from whole blood using MACS kits. The neutrophils gate contains 98% of the intact cells and other empty gates show there was no contamination from monoctyes, T cells, B cells or eosinophils. The colour of the plots represents the cell density (blue represents low density whilst red represents high density).

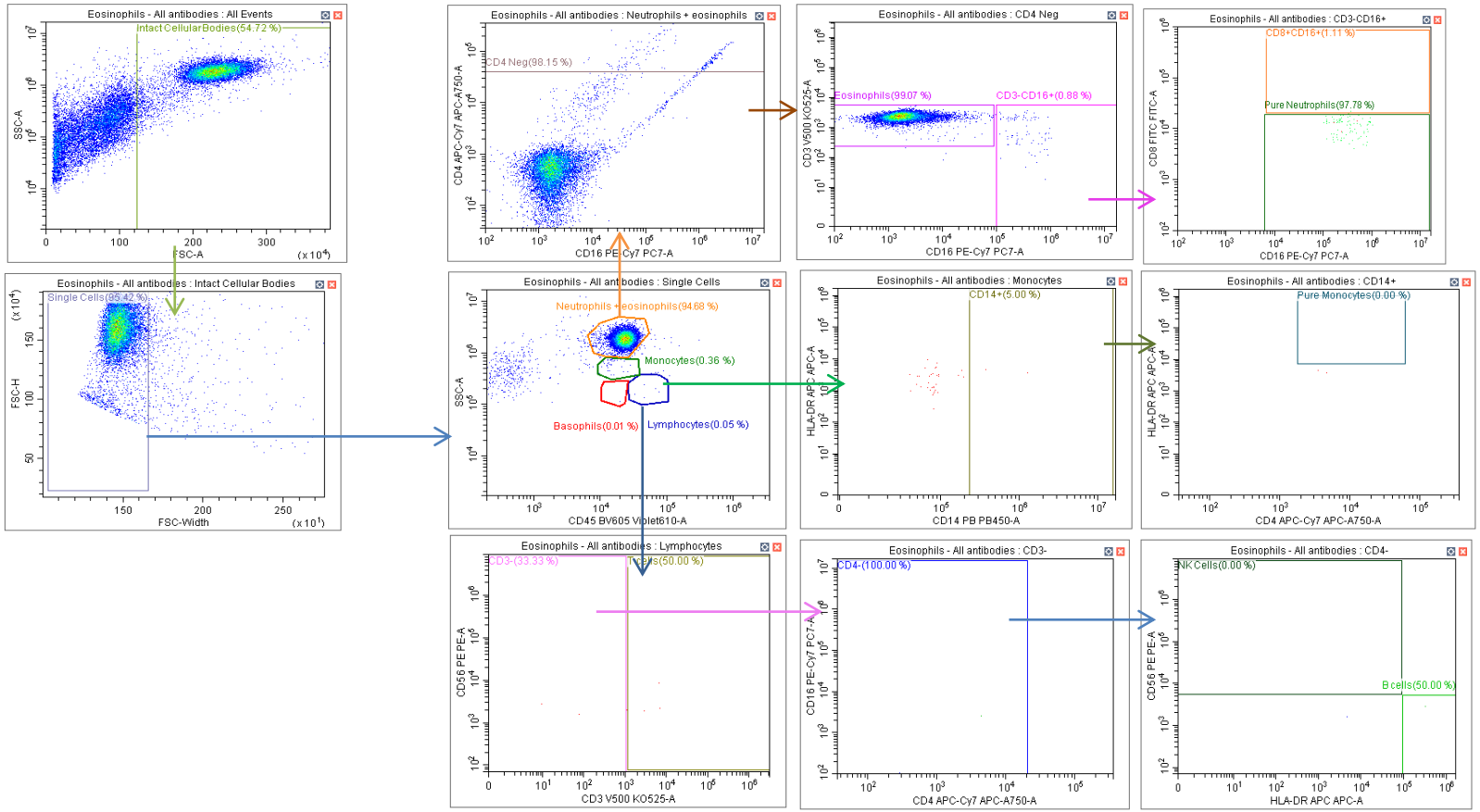

Figure 5.16: FACS panel gating analysis of eosinophils isolated from whole blood using MACS kits. The eosinophils gate contains 82% of the intact cells and other empty gates show there was no contamination from monocytes, B cells, T cells or neutrophils. The colour of the plots represents the cell density (blue represents low density whilst red represents high density).

5.3.2 Dielectric properties of MACS-purified cell suspensions determined using 3DEP

Once the purity of the MACS-purified white blood cell suspensions had been confirmed by FACS (section 5.3.1.2), the dielectric properties of the different cell types were determined using 3DEP. The dielectric properties (membrane conductivity, cytoplasm conductivity and permittivity) were extracted from the 3DEP experimental DEP spectra by using python scripts (APPENDIX E) derived from the single-shell model described in Chapter 2 section 2.2.2.3. To increase the dataset used to determine the dielectric properties and ensure that the values described the behaviour of the cells for a range of conductivities, the 3DEP spectra of each cell type were determined for three different conductivities (0.01, 0.05 and 0.1 S/m). The experimental 3DEP spectra were then fitted using three different fitting approaches: a single conductivity fit for each conductivity studied, a triple conductivity fit with one single scaling factor, and a triple conductivity fit with three different scaling factors.

Since the 3DEP device does not give directly the CM factor values obtained for different frequencies, but instead gives a relative DEP value (Chapter 1 section 1.4.4), a scaling parameter was added to the single-shell fit. For the third fit consisting of triple conductivity fits, the parameters used for fitting were the three dielectric parameters (membrane conductivity, cytoplasm conductivity and cytoplasm permittivity) and one scaling factor for each conductivity studied. The concern was that when fitting models it is possible to increase the likelihood of the fit adhering the data by adding parameters, but doing so may result in overfitting. To account for overfitting, the Bayesian information criterion used to compare the different fitting programs. This criterion introduces a penalty term for the number of parameters in the model and the model with the lowest Bayesian criterion is preferred. To estimate the quality of the fit for each of the different fitting programs, the chi-square (χ^2) goodness of fit test was used. The chi-square value is a non-parametric test used to determine how different the experimental value is from the fitting value. In this test, the distance between the experimental points and the value of the fit is squared and divided by the number of points and then normalised by the value of the fit. A lower χ^2 value, indicates a better agreement between the experimental data and the fit.

5.3.2.1 Dielectric properties of MACS-purified monocytes derived from blood

The dielectric properties of MACS-purified monocytes were determined independently for one single donor using the three conductivity fits described in the above section 5.3.2. The dielectric properties were first determined by fitting the experimental DEP spectra obtained for each of the three conductivities studied (0.01 S/m, 0.05 S/m and 0.1 S/m) using the single-conductivity fit (Figure 5.17).

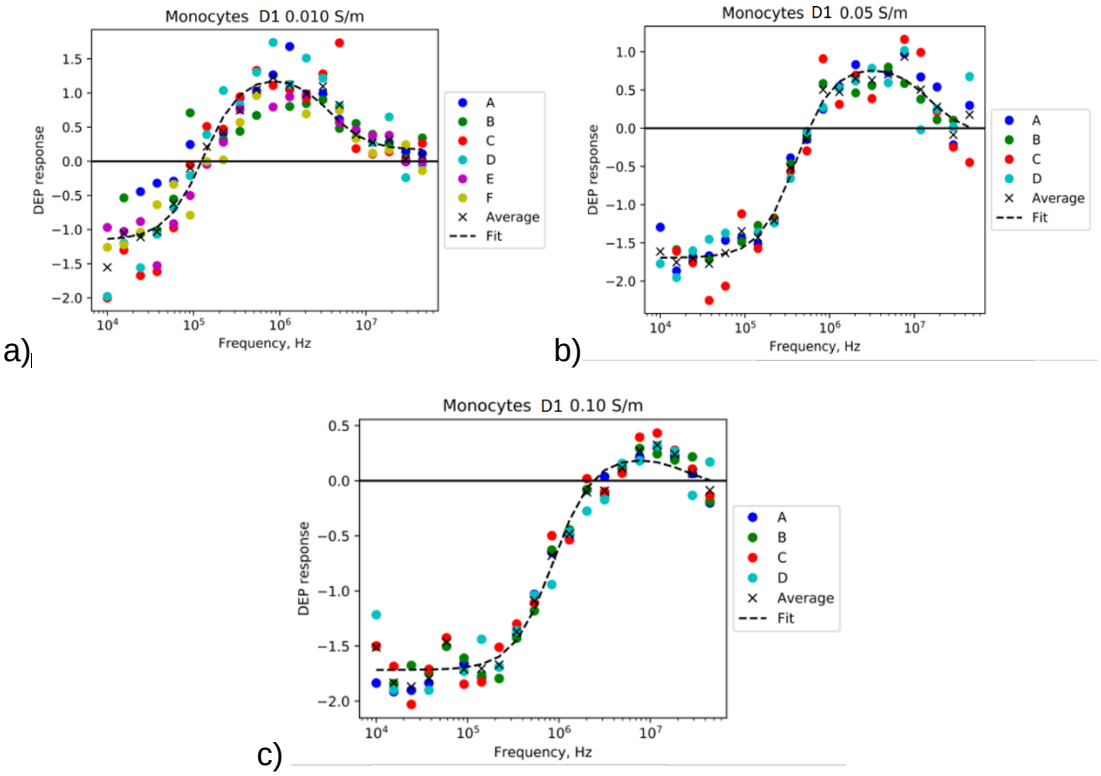

Figure 5.17: DEP spectra of monocytes from donor 1 (D1) at three buffer conductivities: 0.01 S/m (a), 0.05 S/m (b) and 0.1 S/m (c). The dashed line represents the single-conductivity fit and the experimental DEP response obtained by 3DEP is shown by dots. The different replicates (A, B, C, D, E, F) are shown in different colours.

The experimental replicates of all conductivities were very similar and there was a good fit between experimental data and the fitting curve, as shown by the reduced χ^2 values obtained for all the fits and the low standard deviation obtained for each of the dielectric properties determined (Table 5.14).

	Conductivities used for the single conductivity fit		
	0.01 S/m	0.05 S/m	0.1 S/m
Cell radius (μm)	3.7 (fixed)		
Membrane conductance	500 S/m^2 (fixed)		
Reduced χ^2	0.12	0.062	0.026
Bayesian criteria	-220	-196	-268
Membrane capacitance (mF/m^2)	4.5±0.3	5.3±0.3	3.8±0.2
Cytoplasm permittivity	99±7	77±8	80±7
Cytoplasm conductivity (S/m)	0.034±0.004	0.098±0.005	0.127±0.004
Scaling factor	3	3.5	3.5

Table 5.14: Summary of dielectric properties of MACS-purified monocytes from a single donor (D1) derived using a single conductivity fit of DEP spectra obtained for different medium conductivities. The reduced χ^2 values and Bayesian criteria showed that the fits accurately described the experimental data.

Theoretically, the dielectric properties are independent of the conductivity of the solution they are suspended in, so the values obtained should be the same for all conductivities. However, as seen in Table 5.14, the cytoplasm conductivity value obtained for the 0.01 S/m conductivity was four times smaller than that obtained for the 0.1 S/m conductivity.

In order to increase the dataset used to determine the dielectric properties and ensure that the values described the behaviour of the cells for a range of conductivities, a triple conductivity fit including the datasets obtained for 0.01, 0.05 and 0.1 S/m was then used to determine the dielectric properties of monocytes. For the triple conductivity analysis, two fitting methods were considered: one using a common scaling factor for all three conductivity data sets and another with three separate scaling factors (Figure 5.18). The dielectric properties obtained using each fitting method can be found in Table 5.15.

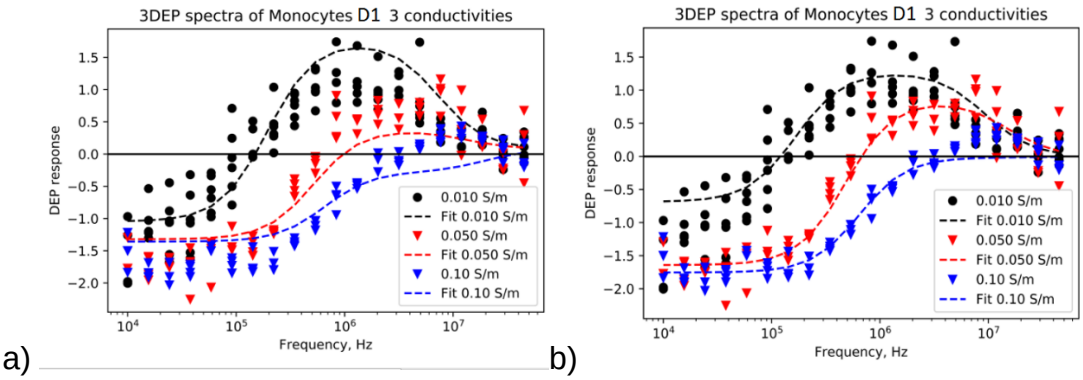

Figure 5.18: 3DEP spectra of monocytes from donor 1 using the three-conductivity model for a single common scaling factor (a) and three different scaling factors (b). The fitting curves are represented as dotted lines while the experimental data is shown by circles and triangles. For each conductivity, at least four replicates were considered.

As seen in Figure 5.18, the triple conductivity analysis did not match all three conductivity datasets when a common scaling factor was used but the goodness of the fit improved when three different scaling factors were used, as shown by a smaller reduced χ^2 value than when the same scaling factors were used. This was further confirmed by a smaller value of Bayesian criteria, which accounts for overfitting.

	Triple conductivity fit (0.01, 0.05, 0.1 S/m)	
	Same scaling factor	Different scaling factor
Cell radius (µm)	3.7 (fixed)	
Membrane conductance	500 S/m^2 (fixed)	
Reduced χ^2	0.17	0.10
Bayesian criteria	-447	-573
Membrane capacitance (mF/m^2)	3.6±0.2	4.5±0.2
Cytoplasm permittivity	92±8	83±7
Cytoplasm conductivity (S/m)	0.078±0.005	0.102±0.005
Scaling factor	2.8	1.8, 3.5, 3.6

Table 5.15: Summary of dielectric properties of MACS-purified monocytes from a single donor (D1) derived using a triple conductivity fit (with the same or different scaling factors) of DEP spectra obtained for different medium conductivities. The reduced χ^2 values and Bayesian criteria showed that the fits accurately described the experimental data.

The differences in dielectric properties between four different donors were investigated next (Table 5.16). The 3DEP spectra and fits obtained for each of the four donors for all conductivities can be found in APPENDIX D.

	Donors			
	D1	D2	D3	D4
Cell radius (µm)	3.74 (fixed)			
Membrane conductance	500 S/m^2 (fixed)			
Reduced χ^2	0.10	0.1	0.076	0.030
Bayesian criteria	-573	-383	-380	-257
Membrane capacitance (mF/m^2)	4.5±0.2	6.3±0.3	10.0±0.5	11.5±0.5
Cytoplasm Permittivity	83±7	90±10	98±9	71±9
Cytoplasm Conductivity (S/m)	0.102±0.005	0.129±0.007	0.133±0.006	0.120±0.009

Table 5.16: Summary of dielectric properties of MACS-purified monocytes derived using a multiple conductivity fit of DEP spectra with different scaling factors obtained for different donors. Note: For donors 2, 3 and 4, only the data for 0.01 S/m and 0.1 S/m was available, so a double conductivity fit was used instead of a triple conductivity fit used to fit the data from donor D1. The reduced χ^2 values and Bayesian criteria showed the quality of the fits.

For all donors studied, there was a good fit between experimental data and the fitting curve, as shown by the low reduced χ^2 values obtained for all the fits and the standard deviation obtained for each of the dielectric properties determined (Table 5.16). The values obtained for cytoplasm permittivity and conductivity were very similar for all donors. However, there were differences in terms of membrane capacitance, where the cells from donor 3 had double the capacitance of that observed for donor 1. Since the Bayesian criterion of the fit for donor 1 was lower than that for donor 3, the values obtained for D1 were considered more accurate.

5.3.2.2 Dielectric properties of MACS-purified B cells derived from blood

As for monocytes, the dielectric properties of MACS-purified B cells were determined independently for the same donor using the three conductivity fits described in the above section 5.3.2. The full DEP spectra and fits obtained for all three fitting methods can be found in APPENDIX D, and the dielectric properties obtained are shown in Table 5.17.

	Single conductivity fit			Triple conductivity fit	
	0.01 S/m	0.05 S/m	0.1S/m	Same scaling factor	Different scaling factor
Cell radius (µm)	3.1 (fixed)				
Membrane conductance	500 S/m^2 (fixed)				
Reduced χ^2	0.12	0.069	0.18	0.17	0.13
Bayesian criteria	-195	-291	-190	-553	-635
Membrane capacitance (mF/m^2)	12.5±1.0	9.2±0.5	4.3±0.5	8.9±0.6	9.8±0.5
Cytoplasm permittivity	117±10	86±9	109±15	99±12	93±10
Cytoplasm conductivity (S/m)	0.04 ±0.006	0.12 ±0.006	0.09 ±0.01	0.131 ±0.009	0.133 ±0.007
Scaling factor	2.7	3	2.6	2.2	1.69, 2.9, 2.65

Table 5.17: Summary of dielectric properties of MACS-purified B cells from a single donor (D7) derived using a single conductivity fit and the triple conductivity fit of DEP spectra obtained for different medium conductivities. The reduced χ^2 values and Bayesian criteria showed that the fits accurately described the experimental data.

Similarly to the monocytes, the dielectric properties (the membrane capacitance and cytoplasm conductivity in particular) obtained using the single conductivity fit varied for the different conductivities studied. The triple conductivity with different scaling factors showed a smaller reduced χ^2 value than when a single scaling factor was used and showed the smallest Bayesian criterion of all the models used, so this was determined to be the best fitting method.

The differences in dielectric properties between four different donors were investigated next (Table 5.18).

	Donors			
	D2	D5	D6	D7
Cell radius (µm)	3.1 (fixed)			
Membrane conductance	500 S/m^2 (fixed)			
Reduced χ^2	0.14	0.044	0.097	0.13
Bayesian criteria	-199	-230	-209	-635
Membrane capacitance (mF/m^2)	10±0.7	11.0±0.6	7.8±0.6	9.8±0.5
Cytoplasm Permittivity	97±7	96±19	85±26	93±10
Cytoplasm Conductivity (S/m)	0.02±0.002	0.19±0.02	0.16±0.03	0.133±0.007

Table 5.18: Summary of dielectric properties of MACS-purified B cells derived using a multiple conductivity fit of DEP spectra with different scaling factors obtained for different donors. Note: For donors 2, 5 and 6, only the data for 0.01 S/m and 0.1 S/m was available, so a double conductivity fit was used instead of a triple conductivity fit used to fit the data from donor 7. The reduced χ^2 values and Bayesian criteria showed the quality of the fits.

The values for membrane capacitance and cytoplasm permittivity obtained were similar for all donors. The value of cytoplasm conductivity obtained for donor JM was seven times lower than that obtained for the other donors, but this was the fit for which the reduced χ^2 and Bayesian criterion values were the highest, so the difference could be due to a higher error in the fit.

5.3.2.3 Dielectric properties of MACS-purified T cells derived from blood

As for the previous cell types , the dielectric properties of MACS-purified T cells were determined independently for the same donor using the three conductivity fits described in the above section 5.3.2. The full DEP spectra and fits obtained for all three fitting methods can be found in APPENDIX D, and the dielectric properties obtained are shown in Table 5.19.

	Single conductivity fit			Triple conductivity fit	
	0.01 S/m	0.05 S/m	0.1 S/m	Same scaling factor	Different scaling factor
Cell radius (μm)	3.1 (fixed)				
Membrane conductance	500 S/m^2 (fixed)				
Reduced χ^2	0.0047	0.049	0.046	0.108	0.052
Bayesian criteria	-322	-225	-282	-616	-812
Membrane capacitance (mF/m^2)	9.45±0.5	12.1±0.7	13.5±0.8	10.2±0.5	11.7±0.4
Cytoplasm permittivity	105±18	56±17	50±16	63±22	57±12
Cytoplasm conductivity (S/m)	0.18 ±0.02	0.21 ±0.01	0.25 ±0.01	0.26 ±0.01	0.237 ±0.008
Scaling factor	1.7	2.5	2.9	1.97	1.6, 2.4, 2.9

Table 5.19: Summary of dielectric properties of MACS-purified T cells from a single donor 7 derived using a single conductivity fit and the triple conductivity fit of DEP spectra obtained for different medium conductivities. The reduced χ^2 values and Bayesian criteria showed that the fits accurately described the experimental data.

The membrane capacitances and cytoplasm conductivities obtained were similar for all conductivities analysed using the single conductivity fit. However, the cytoplasm permittivity varied for the different conductivities studied. The triple conductivity with different scaling factors showed a reduced χ^2 value comparable to that obtained for the single conductivity fits and showed the smallest Bayesian criterion of all the models used, so this was determined to be the best fitting method.

The differences in dielectric properties between four different donors were investigated next (Table 5.20). The 3DEP spectra and fits obtained for each of the four donors for all conductivities can be found in APPENDIX D.

	Donors			
	D6	D2	D5	D7
Cell radius (µm)	3.1 (fixed)			
Membrane conductance	500 S/m^2 (fixed)			
Reduced χ^2	0.034	0.11	0.24	0.052
Bayesian criteria	-254	-201	-97	-812
Membrane capacitance (mF/m^2)	10.4±0.5	8.3±0.7	9±1	11.7±0.4
Cytoplasm Permittivity	39±20	113±38	54±36	57±12
Cytoplasm Conductivity (S/m)	0.24±0.02	0.21±0.04	0.13±0.03	0.237±0.008

Table 5.20: Summary of dielectric properties of MACS-purified T cells derived using a multiple conductivity fit of DEP spectra with different scaling factors obtained for different donors. Note: For donors 2, 5 and 6, only the data for 0.01 S/m a was available, so the single conductivity fit was used instead of a triple conductivity fit used to fit the data from donor 7. The reduced χ^2 values and Bayesian criteria showed the quality of the fits.

The values for membrane capacitance and cytoplasm conductivity were similar for all donors, except for donor 5 that had a lower value of cytoplasm conductivity, but this could be due to the higher error in the fitting as described by a higher reduced χ^2 and Bayesian criterion values than the other donors, which suggests the fitting was worse. The biggest intra-donor differences were observed for the cytoplasm permittivity with values ranging from 39 to 113 S/m. However, the fits with the lowest reduced χ^2 and Bayesian criterion values showed a cytoplasm permittivity of 39 and 54, so these values were considered the most accurate.

5.3.2.4 Dielectric properties of MACS-purified neutrophils derived from blood

As for the previous cell types, the dielectric properties of MACS-purified neutrophils were determined independently for the same donor using the three conductivity fits described in the above section 5.3.2. The full DEP spectra and fits obtained for all three fitting methods can be found in APPENDIX D, and the dielectric properties obtained are shown in Table 5.21 to Table 5.19.

	Single conductivity fit			Triple conductivity fit	
	0.01 S/m	0.05 S/m	0.1 S/m	Same scaling factor	Different scaling factor
Cell radius (μm)	3.5 (fixed)				
Membrane conductance	500 S/m^2 (fixed)				
Reduced χ^2	0.038	0.074	0.061	0.16	0.091
Bayesian criteria	-229	-284	-254	-508	-654
Membrane capacitance (mF/m^2)	9.3±0.4	7.4±0.4	5.1±0.4	6.5±0.4	7.3±0.3
Cytoplasm permittivity	97±3	75±8	79±9	88±8	82±6
Cytoplasm conductivity (S/m)	0.029 ±0.002	0.117 ±0.006	0.127 ±0.006	0.098 ±0.005	0.112 ±0.004
Scaling factor	4	3.4	3.6	3	2, 3.4, 3.7

Table 5.21: Summary of dielectric properties of MACS-purified neutrophils from a single donor (D5) derived using a single conductivity fit and the triple conductivity fit of DEP spectra obtained for different medium conductivities. The reduced χ^2 values and Bayesian criteria showed that the fits accurately described the experimental data.

The membrane cytoplasm conductivities obtained were similar for all conductivities analyses using the single conductivity fit. However, the membrane capacitance and cytoplasm permittivity varied for the different conductivities studied. The triple conductivity with different scaling factors showed a reduced χ^2 value comparable to that obtained for the single conductivity fits and showed the smallest Bayesian criterion of all the models used, so this was determined to be the best fitting method.

The differences in dielectric properties between four different donors were investigated next (Table 5.22). The 3DEP spectra and fits obtained for each of the four donors for all conductivities can be found in APPENDIX D.

	Donors			
	D8	D2	D6	D5
Cell radius (μm)	(fixed)			
Membrane conductance	500 S/m^2 (fixed)			
Reduced χ^2	0.085	0.11	0.098	0.091
Bayesian criteria	-452	-362	-384	-654
Membrane capacitance (mF/m^2)	6.0±0.3	8.0±0.5	5.3±0.3	7.3±0.3
Cytoplasm Permittivity	93±8	93±11	95±10	82±6
Cytoplasm Conductivity (S/m)	0.118±0.006	0.135±0.008	0.12±0.007	0.112±0.004

Table 5.22: Summary of dielectric properties of MACS-purified neutrophils derived using a multiple conductivity fit of DEP spectra with different scaling factors obtained for different donors. Note: For donors 2, 6 and 8, only the data for 0.01 S/m and 0.1 S/m was available, so a double conductivity fit was used instead of a triple conductivity fit used to fit the data from donor 5. The reduced χ^2 values and Bayesian criteria showed the quality of the fits.

The values for all dielectric properties obtained were similar for all donors, and the quality of the fits was good, as shown by the low reduced χ^2 and Bayesian criteria values.

5.3.2.5 Dielectric properties of MACS-purified eosinophils derived from blood

As for the previous cell types, the dielectric properties of MACS-purified eosinophils were determined independently for the same donor using the three conductivity fits described in the above section 5.3.2. The full DEP spectra and fits obtained for all three fitting methods can be found in APPENDIX D, and the dielectric properties obtained are shown in Table 5.23Table 5.19.

	Single conductivity fit			Triple conductivity fit	
	0.01 S/m	0.05 S/m	0.1 S/m	Same scaling factor	Different scaling factor
Cell radius (μm)	3.7 (fixed)				
Membrane conductance	500 S/m^2 (fixed)				
Reduced χ^2	0.09	0.16	0.082	0.21	0.12
Bayesian criteria	-262	-132	-275	-430	-592
Membrane capacitance (mF/m^2)	10.7±0.7	9.2±0.9	10.1±0.6	7.5	9.1±0.4
Cytoplasm permittivity	154±12	88±11	66±10	94	80±8
Cytoplasm conductivity (S/m)	0.05 ±0.007	0.09 ±0.006	0.16 ±0.006	0.13	0.142±0.006
Scaling factor	2.6	3.7	3.7	2.6	1.9, 3, 3.7

Table 5.23: Summary of dielectric properties of MACS-purified eosinophils from a single donor (D1) derived using a single conductivity fit and the triple conductivity fit of DEP spectra obtained for different medium conductivities. The reduced χ^2 values and Bayesian criteria showed that the fits accurately described the experimental data.

The membrane capacitance values obtained were similar for all conductivities analyses using the single conductivity fit. However, the cytoplasm conductivity and permittivity values varied for the different conductivities studied. The triple conductivity with different scaling factors showed a reduced χ^2 value comparable to that obtained for the single conductivity fits and showed the smallest Bayesian criterion of all the models used, so this was determined to be the best fitting method.

The differences in dielectric properties between four different donors were investigated next (Table 5.24). The 3DEP spectra and fits obtained for each of the four donors for all conductivities can be found in APPENDIX D.

	Donors			
	D4	D2	D7	D1
Cell radius (µm)	(fixed)			
Membrane conductance	500 S/m^2 (fixed)			
Reduced χ^2	0.05	0.10	0.16	0.12
Bayesian criteria	-273	-212	-464	-592
Membrane capacitance (mF/m^2)	9.7±0.6	5.5±0.4	9.4±0.7	9.1±0.4
Cytoplasm Permittivity	90±19	166±15	38±32	80±8
Cytoplasm Conductivity (S/m)	0.19±0.02	0.06±0.01	0.26±0.02	0.142±0.006

Table 5.24: Summary of dielectric properties of MACS-purified eosinophils derived using a multiple conductivity fit of DEP spectra with different scaling factors obtained for different donors. Note: For donors 2 and 4, only the data for 0.01 S/m was available, so a single conductivity fit was used instead of a triple conductivity fit used to fit the data from donors 1 and 7. The reduced χ^2 values and Bayesian criteria showed the quality of the fits.

There were intra-donor differences for all the dielectric parameters determined. The dielectric values obtained for donor 1 were considered the most accurate, as the fit had the lowest Bayesian criterion value and a low reduced χ^2.

5.4 Discussion

5.4.1 Establishing a multi-antibody panel for FACS analysis of specific cell types purified from whole blood

FACS is the gold standard for single cell analysis based upon detection of fluorescently tagged antibodies to their respective cell surface marker epitope. FACS was therefore selected to determine the purity of isolated fractions of specific cell types from whole blood using MACS before the determination of their dielectric properties. However, the total number of cells available per donor was necessarily limited due to the low prevalence of some cell types and the volume of blood available for each donor. A panel of multiple antibodies ("multi-panel") was used to reduce the amount of sample needed for FACS analysis but this approach is traditionally associated with loss of resolution due to fluorophores "spill over". Fluorescence spill over introduces spread of the data from one fluorophore (and therefore one antibody) detector into other detectors that cannot be removed with compensation and this results in a systematic underestimation of specific cell populations. Sources of spill over include the use of dyes with similar emission spectra or the use of tandem dyes, also known as Förster resonance energy transfer (FRET) pairs. FRET

dyes are composed of two fluorophores linked together in closed proximity. One of the fluorophores (called donor) is excited by a laser and transfers the excitation energy non-radiatively to the second fluorophore, called the acceptor (Figure 5.19).

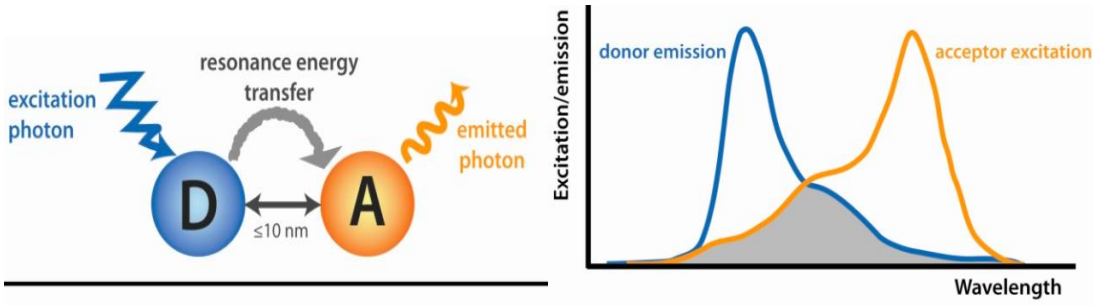

Figure 5.19: Schematic representation of Förster resonance energy transfer (FRET). (a) A laser is used to excite the donor (D) and the energy is transferred to the nearby acceptor (B) by a non-radiative process, causing it to emit fluorescence. (b) The donor emission peak (blue) must overlap with the acceptor excitation spectrum (orange). Image adapted from [253]**.**

In order to achieve FRET, the donor and acceptor fluorophores must be in very close proximity (<10 nm) [253]. The tandem dyes used in the FACS panel are composed of two fluorophores linked together. The linker can be degraded over time due to light exposure, temperature changes or cell interaction [254]. Once the linker is broken, the acceptor is no longer close to the donor and there is no energy transfer, so the only fluorescence recorded is that of the donor instead of that of the acceptor, which results in channel spill over. To minimise this effect, tandems were spread out where possible in different cell types as each cell is analysed individually.

5.4.2 Factors influencing the determination of the cell's dielectric properties

The determination of cells' dielectric properties can be influenced by a number of factors during cell purification and the determination of the properties via 3DEP. A detailed analysis of these factors is presented in this section.

One of the factors that can alter the immune cells' dielectric properties is their activation. For example, human B lymphocytes have a higher dielectrophoretic mobility when secreting antibodies compared to their resting state which might be due to an increase of intracellular protein production with associated shifts in size and volumes of organelles such as rough endoplasmic reticulum [167].

Activation of white blood cells can be triggered by antibody-antigen interactions, so a negative MACS selection approach (Chapter 1 section 1.2.3.2) was used to avoid antigen-antibody interactions during the purification [255], [256]. However, some cells could have been activated before cell isolation if the donor was in contact with a pathogen before the donation, with which could lead to intra-population variations in the dielectric properties. A problem could arise if the differences in dielectric properties between activated and resting cells within a specific population were bigger than the differences between populations of different cells. Hu et al. (1990) showed that even though mature lymphocytes had a higher apparent membrane conductivity than immature ones, the difference between B and T cells was still significantly different for both parameters, despite the intra-population differences due to variations in size and maturity [237]. This would suggest that it would be possible to differentiate T and B cells using their dielectric properties alone.

Another factor that has been shown to affect the cells' dielectric properties is osmolarity. Burt *et al* (1990) reported mammalian cells are sensitive to sugar deprivation in media of low conductivity and required isotonic conditions to ensure membrane integrity [257]. When mammalian cells are suspended in a hypertonic solution, the water flows out of the cell and causes the cell to shrink, which affects surface roughness and cytoplasm conductivity, thus altering the dielectric properties of the cell [160], [258]. Conversely, when mammalian cells are suspended in hypotonic solution, the water enter the cells and the cell membrane stretches increasing the effective radius and reducing the number of microvilli on the surface [238]. Irimajiri et al (1987) studied the dielectric properties of basophil leukaemia cells and found that the specific membrane capacitance value was strongly correlated with the number density of microvilli on the membrane surface, so osmoregulation must be maintained during the determination of the cells' dielectric properties [204]. In the work presented, a lysis step was needed after MACS purification of white blood cells from blood to avoid contamination with RBCs. However, studies have shown that RBC lysis solutions are hypertonic and the ammonium chloride present in the buffers can cause leukocyte swelling and damage [259], [260]. To limit this factor, following MACS purification, the white blood cells were resuspended in isotonic 3DEP medium after lysis for up to 1 h before 3DEP measurements. The 3DEP medium used to suspend the cells during the determination of the dielectric properties was adjusted with different concentrations of mannitol to ensure it was isotonic (280-320 mosmol) and the cells were not deprived of sugar.

Finally, the presence of dead cells and clumped cells in the analysed fraction could cause an inconsistency in the data, increasing the data spreading. Indeed, dead cells have very different properties to living cells. Even at early stages of the apoptotic process, the cell membrane is often compromised and the cells shrink [247], [261]. Big clumps of cells may affect the analysis as cell-cell dipole interactions can alter the DEP force by distorting the field locally [79]. Clumping was particularly observed here for purified neutrophils. In some cases, the cells were activated and started clumping, so the data could not be used. DNAse I has been shown to reduce clumping of mononuclear cells after thawing, so it could be used to prevent clumping of the neutrophils in future experiments.

For BM-MSCs, changes in dielectric properties were observed at different passages, but the behaviour of the MSCs with passage differed greatly between donors. For donor 2, an increase in cell membrane capacitance with passage number was observed. However, for donor 1, all of the dielectric properties at passage 4 and 5 were similar for membrane capacitance but drastically different in terms of cytoplasm permittivity and conductivity. This is in line with recent studies that showed there were intra-donor differences in the impedance profile of undifferentiated adult stem cells [262]. Phenotypic changes at different passages have also been documented in the literature [263]. The differentiation stage of stem cells can be associated with changes in cell radius and membrane morphology and therefore dielectric properties. Cho and colleagues (2008) demonstrated that differences in dielectric properties could be used to distinguish BM-MSCs that were low (lower than P6) and high passage (P12 or higher) [264]. The data analysed in this chapter was taken for low passage BM-MSCs (P2 to P6). In the experiments described here, the models were carried out using a cell radius value of 9.5 µm for cells from all passages, as the average cell diameter reported in the literature for expanded BM-MSCs was 9.1 to 10.5 µm [247], [265]–[268]. However, data from Xavier *et al* (2017) suggested that there could be differences in size and dielectric properties of skeletal stem cells (SSC) from passage 0 [127]. They reported that freshly isolated SSCs had a mean radius of 4.5 µm. After expansion the radius increased significantly up to 9 µm and up to 10.5 µm at passage 3 but did not increase further. The membrane capacitance increased with increasing surface area and osteogenic differentiation. Other research groups have also reported an increase in radius, stiffness and loss of surface markers along with decrease of differentiation potential with increasing passage numbers [265]–[267], [269]–[277]. This meant that the data obtained

for expanded cells used here could not be fully representative of the freshly isolated cells that would be injected in intraoperative timeframes (<1h). For this, freshly isolated cells should be used to determine their properties and to optimise the device. It was however difficult, time consuming and expensive to obtain high enough numbers of BM-MSCs fresh after isolation to carry out the experiments needed to develop the SAW-DEP device so cells had to be used up to passage 4 for later experiments.

5.4.3 Dielectric properties of BM-MSCs

The dielectric properties of BM-MSCs were determined in order to separate them from a mixture containing white blood cells. Although the ultimate objective is to separate primary non cultured BM-MSCS from bone marrow, clinical samples are difficult to obtain, so commercially available isolated BM-MSCs cultured until passage 2 were used instead. As for all purified cells, the dielectric properties of BM-MSCs were determined in three different ways: a single conductivity fit for each conductivity studied, a triple conductivity fit with one single scaling factor, and a triple conductivity fit with three different scaling factors.

The analysis was carried out for two donors and different cell passages to investigate the influence of passage number on the dielectric properties and assess whether passaged cells can be a substitute for primary non cultured BM-MSCs (Figure 5.20 and Figure 5.21). The graphs for the single conductivity fit for each frequency studied, and the triple conductivity fit can be found in APPENDIX D.

The data analysed for the first donor showed there were differences in cell dielectric properties when moving from passage 4 to passage 5 for all solution conductivities used, as the spectra shifted with passage. The factors that could explain the differences observed between passages will be discussed in section 5.4.2.

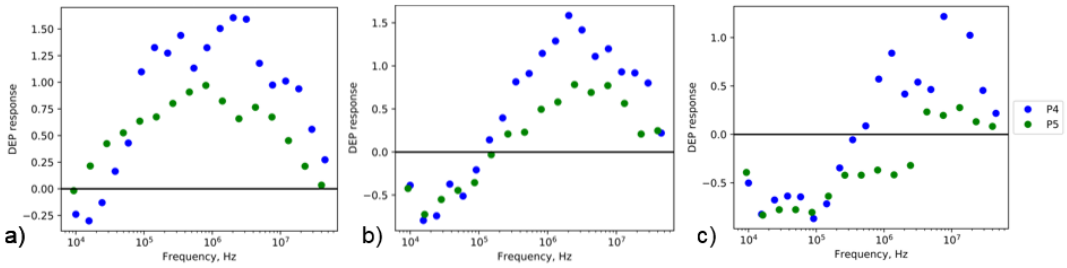

Figure 5.20: DEP spectra of BM-MSCs obtained for donor 1 at two different passages (P4 in blue and P5 in green) for medium conductivities of 0.01 S/m (a), 0.05 S/m (b) and 0.1 S/m (c). Each data point corresponds to the mean value from four replicates.

BM-MSCs from a second donor were analysed at passage 2 (as supplied by the company) to passage 4 (Figure 5.21).

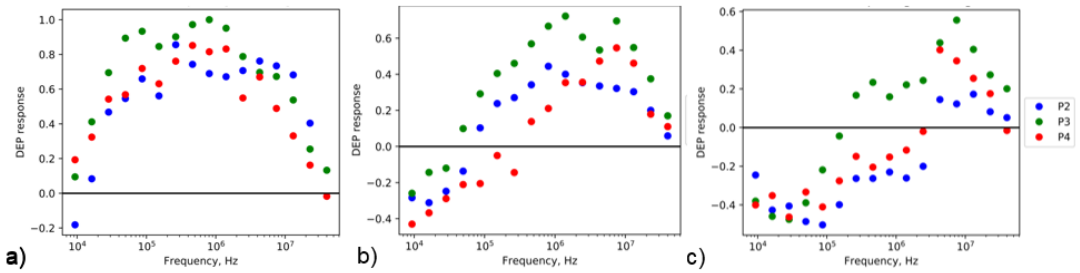

Figure 5.21: DEP spectra of BM-MSCs obtained for donor 2 at three different passages (P2 in blue, P3 in red and P4 in blue) for medium conductivities of 0.01 S/m (a), 0.05 S/m (b) and 0.1 S/m (c). Each data point corresponds to the mean value from four replicates.

For donor 2, there was no differences between the cells at different passages for the 0.01 S/m conductivity solution. However, there was a shift in DEP spectra and hence dielectric properties for solutions with conductivities of 0.05 and 0.1 S/m. This further confirmed the need to use the triple conductivity fit which takes into account the datasets for all three conductivities instead of the single conductivity fits for each medium conductivity (as discussed in the previous section 5.3.2). Since the triple conductivity model with different scaling factors was deemed to be more accurate, only the data obtained using the triple conductivity model is shown in Table 5.25. The data obtained using the single conductivity fits and triple conductivity fit with one single scaling factor can be found in APPENDIX D.

	Donor 2			Donor 1	
	Passage 2	Passage 3	Passage 4	Passage 4	Passage 5
Cell radius	7.5 µm (fixed)				
Membrane Conductance	500 S/m^2 (fixed)				
Reduced χ^2	0.072	0.12	0.27	0.12	0.071
Bayesian criteria	-638	-546	-155	-466	-687
Membrane capacitance (mF/m^2)	17±2	26±1	16±2	9.0±0.6	10.6±0.9
Cytoplasm Permittivity	128±13	99±21	126±21	30±68	121±13
Cytoplasm Conductivity (S/m)	0.112±0.007	0.26±0.02	0.11±0.01	0.38±0.03	0.110±0.007

Table 5.25: Summary of dielectric properties of BM-MSCs derived using a triple conductivity fit of DEP spectra with different scaling factors for different donors and passages. The reduced χ^2 values and Bayesian criteria showed the quality of the fits.

For donor 2, all of the BM-MSC dielectric properties obtained at passage 2 and 4 were similar. However, the values obtained for the membrane capacitance and cytoplasm were doubled for passage 3 when compared to those obtained for passages 2 and 4.

For BM-MSCs derived from donor 1, all the cell dielectric properties at passage 4 and 5 were similar for membrane capacitance but drastically different in terms of cytoplasm permittivity and conductivity. This behaviour is closer to that described in the literature.

5.4.4 Modelling of ideal cell separations

In order to determine the ideal conditions to separate the BM-MSCs from the other white blood cells characterised, the Clausius Mossotti factor of each cell type was modelled using the dielectric properties determined in sections 5.3.2 and 5.4.3 and the script shown in APPENDIX D. As discussed in Chapter 1 section 1.2.4, the Clausius Mossotti factor indicates whether a cell experiences positive or negative dielectrophoresis and depends on the dielectric properties of the cell, the conductivity of the medium and the frequency of the applied signal. The same cell can experience both negative and positive DEP for a different set of frequency and medium conductivity parameters. The best conditions for separation of BM-MSCs from the other cell types are the frequencies and medium conductivities for which BM-MSCs and the other cells are experiencing DEP in different polarities.

For all cell types, the dielectric properties obtained using the triple conductivities model with different scaling factors were used to model the CM factor for different frequencies and medium conductivities. To model BM-MSCs, the dielectric properties values obtained for the lower passage (P2) were used as they were considered to be the closest to the primary non cultured BM-MSCs that would be obtained in any clinical procedure.

	B cells	T cells	Monocytes	Neutrophils	Eosinophils	BM-MSCs Donor 2 P2
Radius (µm)	3.1	3.1	3.74	3.5	3.65	6.5
Membrane Conductance		500 S/m^2				
Membrane capacitance (mF/m^2)	9.8±0.5	11.7±0.4	4.5±0.2	7.1±0.4	9.1±0.4	17±2
Cytoplasm Permittivity	93±10	57±12	83±7	110±8	80±8	128±13
Cytoplasm Conductivity (mS/m)	133±7	237±8	102±5	49±5	142±6	112±7

Table 5.26: Summary table of dielectric properties of all cells investigated. The values were obtained using the triple conductivity fit with three different scaling factors.

The CM factors of all the cell types characterised were first modelled for two medium conductivities and a range of frequencies (Figure 5.22).

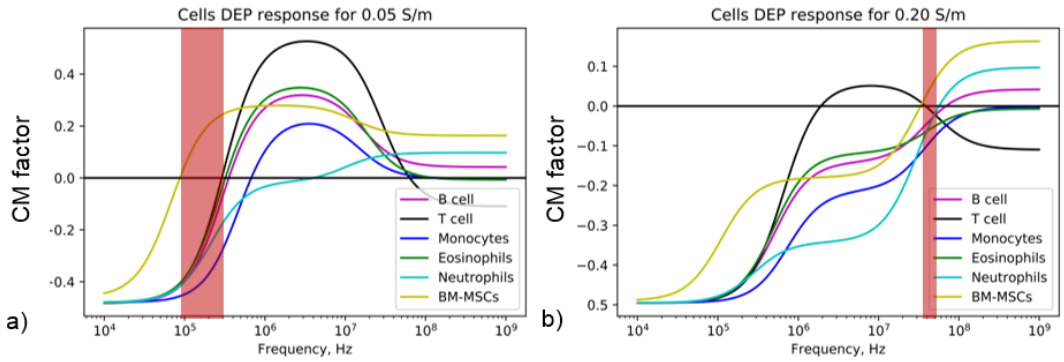

Figure 5.22: Clausius Mossotti (CM) factor of blood cells and BM-MSCs for multiple frequencies for a medium conductivity of 0.05 S/m (a) and 0.2 S/m (b). The regions shaded in red are the zones where BM-MSCs and the rest of the cell types experienced opposing DEP forces.

The DEP response of the blood cells and BM-MSCs described in Figure 5.22 showed that there were two regions in terms of conductivities where the differences in DEP behaviour could be exploited for the separation of BM-MSCs from the other cell types. These two regions corresponded to the two frequency crossovers described in Chapter 2 section 2.2.1.1. The first conductivity crossover was observed for 100 kHz whilst the second frequency crossover was seen at 40 MHz. SAW-DEP technology is limited by the size of

the electrodes. The minimum feature that could be made using the available mask aligner was 1 µm wide and so the maximum frequency was 1 GHz (chapter 2, section 2.1.3). Below 1 MHz, the IDT fingers would be 1 mm wide, which would significantly increase the size of the chip so the frequencies around the first crossover were not considered further. Since all frequencies lower than 1 MHz were disregarded, the region of interest was between 20-100 MHz. The ideal medium conductivities for those ranges were then investigated and the results are shown in Figure 5.23.

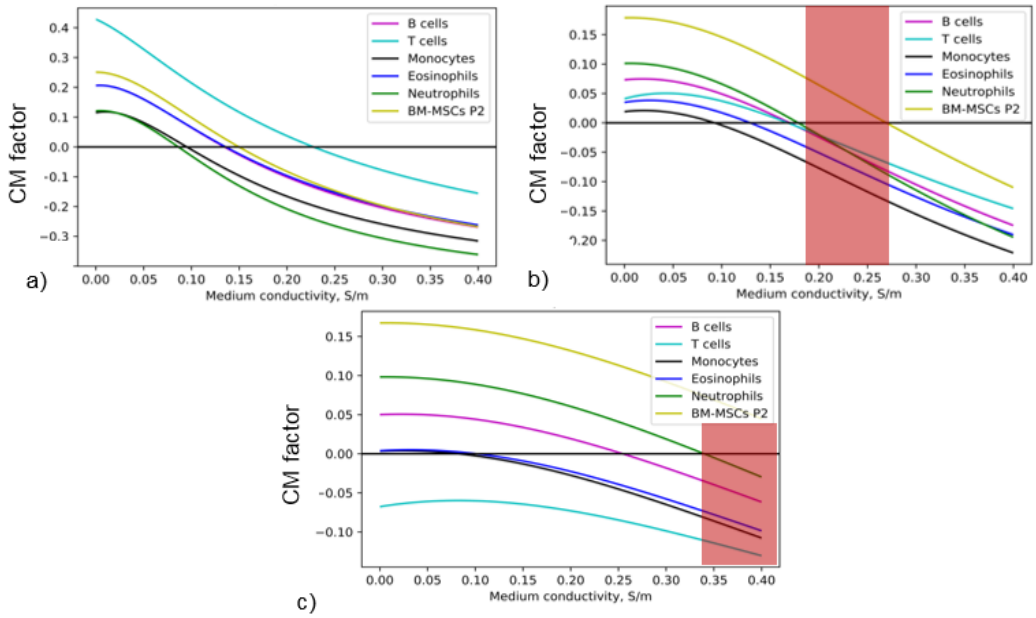

Figure 5.23: Clausius Mossotti (CM) factor of blood cells and BM-MSCs for multiple conductivities for a SAW-DEP frequency of 20 MHz (a), 50 MHz (b) and 100 MHz (c). The regions shaded in red are the zones where BM-MSCs and the rest of the cell types experienced opposing DEP forces.

For the frequencies studied, regions of interest were found between 0.15 and 0.40 S/m solution conductivity. The ideal frequencies for these ranges were then investigated further in Figure 5.24 to obtain a final set of conditions predicted to be ideal for separation of MSCs from the other cell types considered.

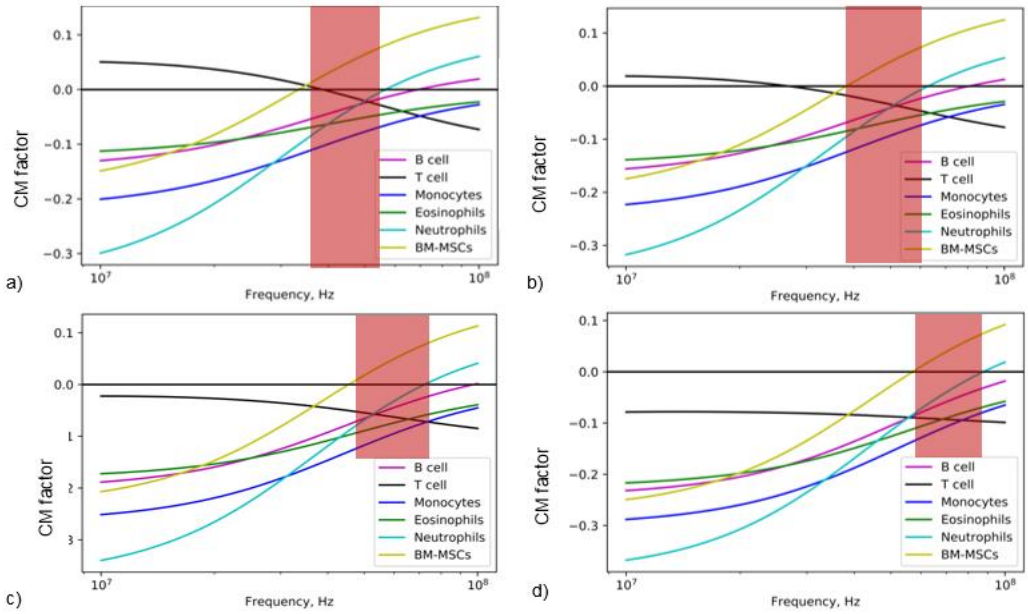

Figure 5.24: Clausius Mossotti (CM) factor of blood cells and BM-MSCs for multiple frequencies for a medium conductivity of 0.2 S/m (a) 0.22 S/m (b), 0.25 S/m (c) and 0.3 S/m (d). The regions shaded in red are the zones where BM-MSCs and the rest of the cell types experienced opposing DEP forces.

The ideal frequency and conductivity pairs for separation of BM-MSCs from the white blood cells were found to be: 50 MHz for 0.22 S/m and 70 MHz for 0.30 S/m. These were the conditions for which BM-MSCs experienced positive DEP whilst the rest of the cells experienced negative DEP. Moreover, since the BM-MSCs experiencing positive DEP are also the biggest cells (12 µm diameter), the sedimentation force will help the cells move to the bottom channel. The best separation of BM-MSCs from other cell types could therefore be potentially achieved by choosing the conditions where the negative DEP force is more prominent as this force will decrease with distance to the electrodes. In this case, the best conditions would be a frequency of 60 MHz and 0.30 S/m solution conductivity.

5.5 Summary and future work

5.5.1 Summary

The objective of this chapter was to determine the best conditions in terms of frequency and conductivity to separate BM-MSCs from the main cell types present in bone marrow (monocytes, T cells, B cells, neutrophils and eosinophils). Each white blood cell type was extracted from blood, which was

more readily available than bone marrow samples, using a MACS negative selection approach whilst BM-MSCs were obtained commercially. The purity of the MACS-isolated cell suspensions was verified using a FACS multi-panel, which showed that the purity of the isolated cell suspensions was higher than 74% for all cell types. The dielectric response of the purified cell suspensions was determined for a range of frequencies using 3DEP and a triple conductivity single-shell model fit was used to extract the dielectric properties from the DEP spectra. The dielectric properties obtained were used to model the DEP responses of all the cell types for a range of frequencies and conductivities. The best conditions for separation were a 50 MHz SAW-DEP frequency and a 0.22 S/m medium conductivity. For that frequency and medium conductivity the BM-MSCs experienced positive DEP whilst the rest of the cells experienced negative DEP.

5.5.2 Future work

Now that the theoretical ideal frequency for separation has been determined, the next step would be to fabricate SAW-DEP devices of 40, 50 and 60 MHz operating frequencies. To test these devices experimentally, each cell type characterised (BM-MSCs, B cells, T cells, monocytes, neutrophils and eosinophils) should be tested individually for a range of conductivities close to 0.22 S/m to determine the experimental conditions for which the white blood cells experience negative DEP while the BM-MSCs experience positive DEP.

If a single set of conditions in terms of frequency and conductivity suggests that the BM-MSCs could be separated from the white blood cells, mixtures of BM-MSCs and each of the other cell types should be tested one at a time in the devices to assess the interactions between cells and see if this would affect the separation efficiency. The concentration of BM-MSCs could be also assessed for decreasing concentrations in order to determine the enrichment percentage for low concentrations.

If the experimental results suggest that the BM-MSCs cannot be separated from all the white blood cells in one set of conditions in terms of frequency and conductivity, a multi-step separation approach could be implemented (**Figure 5.25**). A first SAW-DEP frequency would be used to separate the BM-MSCs and the other white blood cells experiencing positive DEP from all the rest of white blood cells experiencing negative DEP. Then, successive SAW-DEP

steps would be used for different frequencies or conductivities until the BM-MSCs would be concentrated and the other cells discarded into a waste outlet.

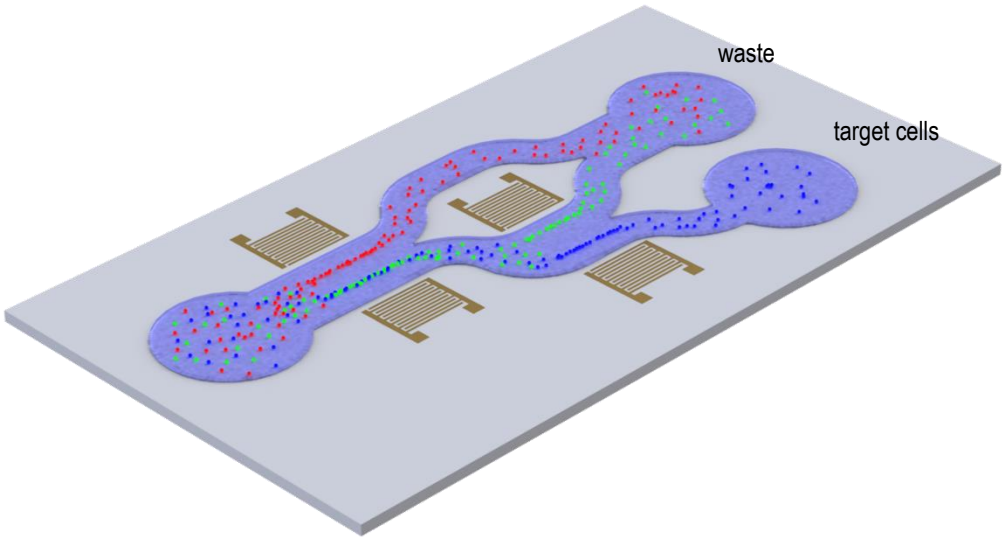

Figure 5.25: Schematic of a SAW-DEP multi-separation approach. In the first step, the a first cell type (represented in red) is discarded at a first SAW-DEP frequency. In the second step, a second SAW-DEP frequency is used to discard the second cell type (represented in green) into a waste outlet whilst the target cells (represented in blue) are collected in a separate reservoir.

Chapter 6

In vitro and in vivo proof of safety of SAW-DEP

6.1 Introduction

In this chapter, the impact of SAW-DEP on the osteogenic potential of MSCs was investigated both *in vitro* and in a preclinical study *in vivo*. In order to better understand how SAW-DEP separation of cells could affect the bone healing process, it is important to know what the architecture of healthy bone looks like and what the steps of fracture healing are.

Bones are formed of a compact shell of cortical bone surrounding a spongy cancellous bone (Figure 6.1). Cortical bone is composed of an array of osteon units consisting of concentric layers of collagen fibrils and hydroxyapatite crystals surrounded by blood vessels and nerves whereas cancellous bone consists of a network of trabeculae [278].

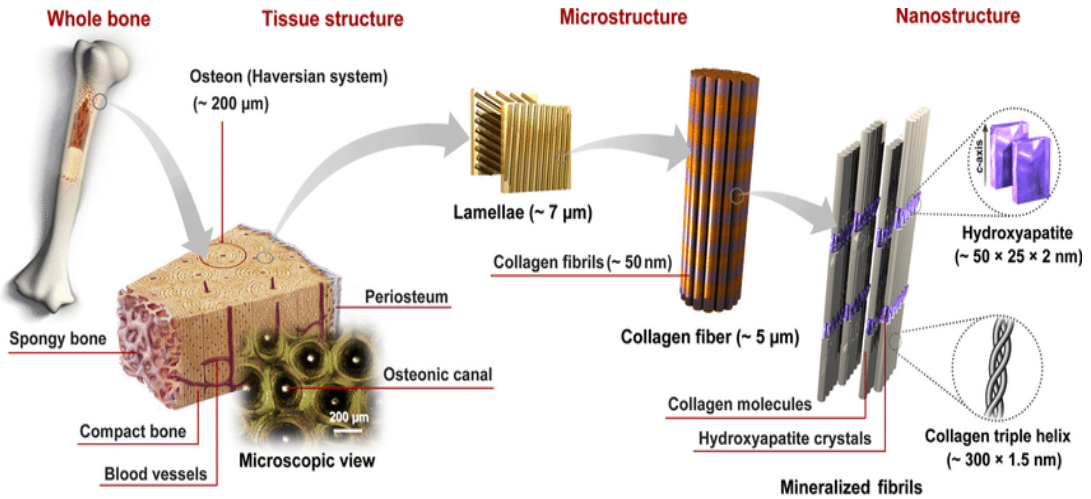

Figure 6.1: Different levels of bone structure: from whole bone to nanostructure. Image adapted from [279].

Fracture healing can be achieved in two different ways. Primary fracture healing occurs when there is only a partial crack in the bone or when two bone fragments are held together by external fixation. This type of healing assumes that the edges of both bone fragments are touching exactly and does not require cartilaginous callus formation (described below). However, most fracture cases result in shattering and multiple bone fragments, which requires a process of secondary fracture healing involving callus formation [280], [281]. Secondary fracture healing is a more complex process that involves the use of multiple cell types and molecules and takes place over several discrete stages: haematoma formation and inflammation, blood vessel formation

(angiogenesis), early stage cartilage formation, cartilage calcification and bone remodelling (see Figure 6.2) [282]–[284].

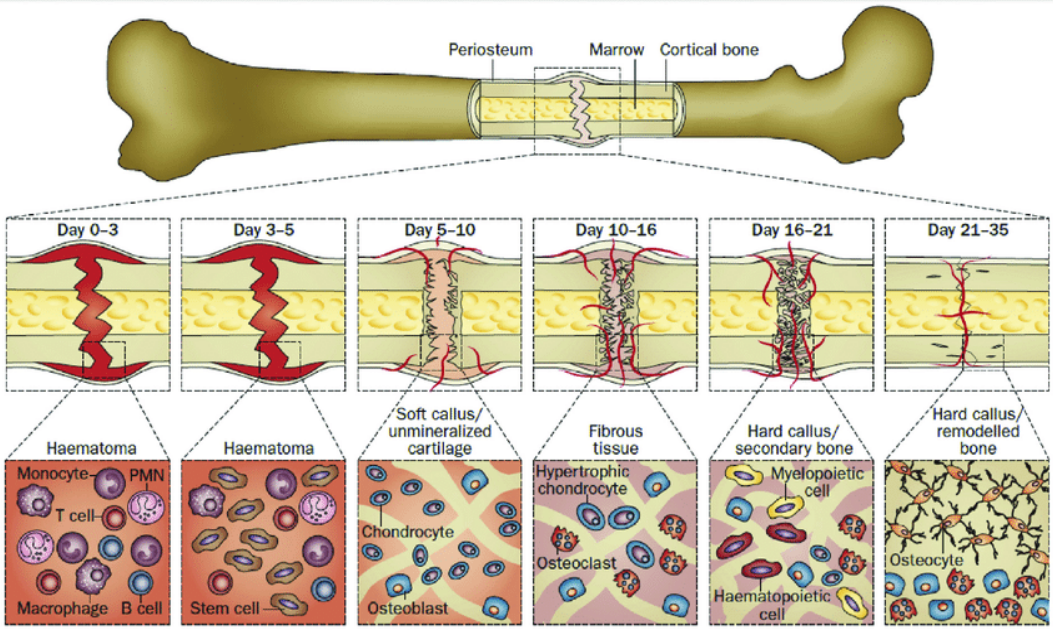

Figure 6.2: Schematic representing the different stages of secondary bone fracture healing and the cells involved in each event. During days 0-5, a haematoma is formed around the edges of the bone fracture and inflammatory cells and stem cells are recruited. During days 5-10, a soft cartilaginous callus is formed and vascularisation begins. Following the differentiation of MSCs into osteoclasts and osteoblasts, the soft callus is progressively replaced by a harder mineralised callus. The final phase involves remodelling of the newly formed bone into a more organised and packed structure orchestrated by osteocytes. Note: *polymorphonuclear leukocyte* is abbreviated as PMN. The image was adapted from [285].

The first stage of secondary bone healing typically takes seven days and involves an acute inflammatory response and the formation of a haematoma that will be used as a template for subsequent callus formation [284], [286]. Within the first 24 h, the haematoma is formed between the ends of the fractured bone and inflammatory cells such as monocytes, macrophages, polymorphonuclear cells and lymphocytes are recruited. These cells secrete growth factors and cytokines necessary to prevent infection, to recruit progenitor mesenchymal stem cells (MSCs) and to initialise angiogenesis [281], [287], [288]. After haematoma formation, the next stage of bone repair is the formation of a cartilaginous callus which is generally observed within 7 to 9 days post trauma in most animal models (rabbit, rat and mouse) [281], [289]. This callus is mainly composed of proteoglycans and collagen type II

and provides a mechanically stable framework to start the mineralisation of the tissue [288].

Another key step of bone regeneration is the revascularisation of the injured site [290]. This involves degradation of the cartilage and extracellular matrices to make space for blood vessels to infiltrate the wound site [291]. As vascularisation progresses, the initial cartilaginous callus is progressively resorbed and replaced by a harder mineralised callus. The recruitment and subsequent differentiation of MSCs into osteogenic cells is instrumental in the production of collagen type I and II necessary for hard callus formation [292]–[294]. The calcified cartilage will be ultimately replaced with a more mechanically rigid woven bone that will allow for weight bearing [280], [295]. In animal models, bony callus formation typically peaks by day 14 and is characterised by an increased number of osteogenic markers such as alkaline phosphatase or osteocalcin [281], [284].

The final stage of bone regeneration is bone remodelling of the hard callus which starts three weeks after bone fracture in humans and animal models and can last between six months and a year [296], [297]. This process consists of a balance between bone resorption and the generation of new lamellar bone infiltrated by blood vessels [283], [286], [288], [294]. Bone remodelling involves two main differentiated cell types: osteoclasts which break down the bony callus and osteoblasts which secrete alkaline phosphatase that encourages mineral deposition onto extracellular matrices [297].

However, in some complex cases spontaneous bone healing does not occur resulting in fracture non-unions. This is often observed in fractures resulting from congenital or degenerative diseases, tumour ablation or complex trauma [282]. When a large amount of bone regeneration is required, the use of biomaterial scaffolds implanted in the site of defect and the injection of autologous bone marrow have been investigated.

Commonly used scaffolds include polymer scaffolds, acellular demineralised bone matrix and porous hydroxyapatite scaffolds, which have a similar composition, structure or mechanical strength as the original bone [298]–[302]. Depending on the biomaterial, the immune response can promote regeneration or lead to a fibrotic foreign body reaction hindering bone repair. The immune response to the biomaterial depends on a range of factors such as particle size, surface properties or substances released from the biomaterial so it is important to test its biocompatibility [303].

In attempts to improve regeneration, the use of bone marrow mesenchymal stem cells (BM-MSCs) in combination with the scaffolds has also been studied. BM-MSCs have a key role in bone regeneration as has been established in clinical models and their ablation can disrupt the healing process [304]–[307]. The use of concentrated bone marrow loaded onto scaffolds has been reported in the literature to treat long bone defects and has been shown to promote angiogenesis and decrease the healing duration [298], [308], [309]. Other approaches have used the amplification of isolated BM-MSCs *ex vivo* cultured onto acellular scaffolds and showed that the combination therapy was successful in increasing bone regeneration [285], [310], [311].

6.1.1 Research questions

In this chapter, the main objective addressed was the initial proof of safety of SAW-DEP. In order to demonstrate that the SAW-DEP technology can separate out BM-MSCs without altering their phenotype, the osteogenic potential of human MSCs exposed to the SAW-DEP device was characterised. This objective was addressed via the following research questions:

1. Does SAW-DEP affect the osteogenic potential of cells *in vitro*?

For this, following *in vitro* culture of BM-MSCs, the expression of alkaline phosphatase (early osteogenic marker) was assessed qualitatively via histological staining. The presence of calcium deposits (and hence a mineralised matrix) was also assessed via Alizarin red staining.

2. Do cells subjected to SAW-DEP induce chronic inflammation *in vivo*?

After successful *in vitro* results, the ability of BM-MSCs undergoing SAW-DEP to regenerate bone was studied *in vivo* using an athymic rat cranial defect model. A preliminary study was first performed to prove that the procedure did not elicit chronic inflammation and to determine the most suitable scaffold for MSCs delivery. A second study with a larger sample size was then carried out at two different time endpoints. Histological staining was performed to find any signs of inflammatory cells characteristic of chronic inflammation.

3. Does SAW-DEP affect bone formation negatively *in vivo*?

The degree of mineralisation of the implants was assessed at two endpoints using micro computed tomography (micro CT) to check for calcified tissue and quantify any newly formed bone. The retrieved explants were also analysed

by histological and immunohistological staining following decalcification to assess the quality and composition of the newly formed bone.

6.2 Materials and Methods

Refer to Chapter 3 section 3.2 for cell source, normal cell culture, passaging and freeze/thaw.

6.2.1 In vitro experiments

Note: All chemicals described in this section were purchased from Sigma Aldrich unless otherwise specified.

6.2.1.1 Buffers and solutions

SAW-DEP Buffer: The buffer used for all SAW-DEP experiments comprised of 8 % sucrose, 0.3 % dextrose, 2 % BSA, 0.02 % EDTA and 0.595 % HEPES and the pH was adjusted to 7.0-7.2 by adding drops of 5 M KOH. The buffer conductivity was adjusted to 0.15 S/m by adding drops of 12 % NaCl solution.

MSCs culture medium: Cells were cultured in Alpha MEM supplemented with 10 % Foetal Calf serum, 1 % Penicillin-streptomycin solution and 1 % L-glutamate.

BM-MSCs osteogenic medium: During osteoinduction, cells were cultured in osteogenic medium supplemented with 1 % (v/v) Penicillin-Streptomycin solution.

6.2.1.2 Preparation of the BM-MSCs suspension

For all experiments, BM-MSCs (Promocell) were cultured from passage 2 until passage 4 in T75 flasks filled with 25 mL of MSCs culture medium following the passaging procedure described in Chapter 3 section 3.2.2.

The cell suspension obtained was then centrifuged at 800 g for 5 minutes. The supernatant was discarded, and the cell pellet was resuspended in 2 mL of SAW-DEP buffer. This step was repeated twice and the last pellet was resuspended in 400 µL of SAW-DEP buffer at a concentration of 10^7 cells/mL.

6.2.1.3 BM-MSCs exposure to SAW-DEP field in device

The set-up used for the experiments was the same as that described in Chapter 3 section 3.1.4. A signal generator was connected to an amplifier powered with a 24 V DC power supply. The signal was split via a signal splitter to provide each interdigitated electrode (IDT) with the same signal. The SAW-DEP device used had an insertion loss of - 8 dB and an operating frequency of 10.125 MHz and a 75 µm height channel.

The fluidic setup was stored overnight in 5 % Decon 90 (Camlab, UK) to dissolve cellular residues from previous experiments. To sterilise the channel and tubing, 70 % ethanol was flowed in the device and left for 10 minutes prior to the start of the experiment. Once sterilised, the device was functionalised by flowing SAW-DEP buffer into the channel for 30 minutes. This allowed for the BSA to coat the surface of the channels in order to reduce cell adhesion.

The cell suspension was injected in the microfluidics channel at a density of 10^7 cells/mL via a 1 mL syringe connected to the tubing (2 mm outer diameter and 0.5 mm inner diameter). The fluid was controlled using a Harvard instruments syringe pump. When the SAW-DEP was turned on, a flow rate of 3 µL/min was used to ensure the cells had the time to experience SAW-DEP. This is the slowest flow rate that allowed 98 % separation of dead from alive DPSCs that had been reported previously by Smith and colleagues (2017) [141]. The two highest possible total input powers per electrode (24 dB and 22 dB) were investigated in order to test the limits of the system. The input powers and conditions used are summarised in Table 6.1. During the exposure to SAW-DEP, the cells were monitored using a non-inverted fluorescent microscope (Olympus BX60) with a mercury lamp, through a 10x objective, to ensure cells were aligning to the field and there were no bubbles. For each condition tested, 100 µL of cell suspension were collected in a sterile 50 mL Falcon tube to ensure enough cell numbers were obtained for the alkaline phosphatase and alizarin red experiments. To preserve sterility as much as possible, the Falcon tube was closed with parafilm and tubing was punched through to limit contamination. The collection tube contained 20 mL of MSCs culture medium to limit the amount of time the cells spent in the SAW-DEP medium and maximise viability. After collection, the BM-MSCs were counted using a haemocytometer, centrifuged at 800 g for 10 minutes and resuspended in 1 mL of BM-MSCs culture medium.

6.2.1.4 Preparation of controls

Microfluidics control: This control was added to assess if the shear stress experienced in the microfluidics set up had any effect on the cells. For this, BM-MSCs resuspended in SAW-DEP buffer were flown into the device at a speed of 3 µL/min with the power turned off.

SAW-DEP buffer control: This control contained cells that had been resuspended in SAW-DEP buffer for 1 h and kept at room temperature (which was the time it took to obtain the samples going through the SAW-DEP device). After incubation for 1 h, cells were counted using a haemocytometer, centrifuged at 800 g and resuspended in BM-MSCs medium.

Positive control: A positive control consisted of BM-MSCs obtained immediately after flask detachment using trypsin.

Negative control: A negative control comprised of fibroblasts which are cells that do not normally express alkaline phosphatase or undergo osteoinduction. This control was added to identify the possibility of false positives.

6.2.1.5 Alkaline phosphatase expression of BM-MSCs after SAW-DEP exposure

To assess the effect of SAW-DEP exposure on the osteogenic potential of BM-MSCs, an alkaline phosphatase staining was performed. Alkaline phosphatase has a key role in the early stages of bone formation and is considered an early marker of osteoblast differentiation [312]–[314].

All cell suspensions shown in Table 6.1 were seeded in duplicates in a 24-well plate at a density of 1.5×10^5 cells/well and cultured for two days until they reached 80 % confluence.

Sample name	Cell type	Medium before seeding	Signal generator power	Total power applied	Flow rate
20 dBm	BM-MSCs	SAW-DEP	2 dBm	20 dBm	3 µL/min
18 dBm	BM-MSCs	SAW-DEP	0 dBm	18 dBm	3 µL/min
Microfluidics control	BM-MSCs	SAW-DEP	N/A	N/A	3 µL/min
SAW-DEP buffer control	BM-MSCs	SAW-DEP	N/A	N/A	N/A
Positive control	BM-MSCs	BM MSCs medium	N/A	N/A	N/A
Negative control	Fibroblasts	Fibroblasts medium	N/A	N/A	N/A

Table 6.1: Details of cell samples included in the Alkaline Phosphatase experiments: cell types used, SAW-DEP powers and flow rates. Total power was calculated by considering the amplification (29 dB), the power halving of the signal splitter (- 3 dB), the device insertion loss (- 8 dB) and the input power of the signal generator. The positive and negative control samples were not flown into the device and were seeded straight after detachment.

Once the cells had reached 80 % confluence, the BM-MSCs culture medium was removed and replaced with osteogenic medium which was changed every three days. Fourteen days after seeding, the medium was removed and the cell monolayers were washed carefully three times using PBS. Then, the cells were fixed using a 98 % ethanol solution and left in the cold room for 20 minutes. The ethanol was then removed and the cells were washed with PBS three times.

The PBS was removed and replaced with a staining solution made up of 0.4 mL of naphtol AS-MX phosphate alkaline solution diluted in 9.4 mL of distilled water and 2.4 mg of fast violet B salt. The cells were incubated with the staining solution in the dark for 45 minutes. The remaining staining solution was then aspirated and the monolayers were rinsed three times with distilled water and left in distilled water to avoid drying until photographed.

6.2.1.6 Alizarin red staining of calcium deposits generated by BM-MSCs

To assess the effect of SAW-DEP exposure on the ability of MSCs to differentiate in to osteoblast-like cells, an alizarin red assay was performed [315]. Alizarin red is commonly used in histology to stain calcium-rich deposits, which are indicative of mineralised matrix and can be used as a biomarker of osteogenic differentiation of MSCs [316]–[318].

All cell suspensions shown in Table 6.1 were seeded in duplicates in a 24-well plate at a density of $1.5x10^5$ cells/well and cultured for two days until they reached 80% confluence (Figure 6.8). Once the cells reached 80% confluence, the BM-MSCs culture medium was removed and replaced with osteogenic medium which was changed every three days. Twenty-eight days after seeding, the medium was removed and the cell monolayers were washed carefully three times using PBS. Then, the cells were fixed using a 98 % ethanol solution and left in the cold room for 15 minutes. After the incubation, the ethanol was removed and the cells were washed with PBS three times.

The PBS was removed and the monolayers incubated with 300 µL of 2 % alizarin red stain (Sciencell, USA) at room temperature for 15 minutes. The staining solution was then aspirated and the monolayers were rinsed three times with distilled water and photographed using a Leica microscope.

6.2.2 *In vivo* experiments

Despite the development of new alternative technologies to animal testing, the use of standardised animal models is still essential to test therapies before their translation into human use [319]. However, strict ethical regulation exists to ensure humane animal research. To ensure this, the principles of the 3Rs (refinement, replacement and reduction) were followed in the experiments described in this chapter [320].

An ideal animal model must be reproducible, relevant to the clinical condition investigated and cause little mortality to the animal to ensure the experimental endpoints can be reached [321]. For investigations of bone healing, multiple animal models exist such as sheep, pigs, goats, dogs, rabbits, rats and mice but due to costs and throughput, rodent models are the most commonly used in the most preliminary stages of translational research [322]–[326].

Depending on the clinical condition investigated, multiple sites of defect have been described including the mandible, vertebrae, femora and calvarium [321], [326]–[328]. Among these defects, the rat calvarial defect is one of the most clinically relevant models for non-union application because regeneration of this area is challenging due to the poor vascularisation [321], [329]–[331]. It has been extensively used for testing biomaterials and does not require external fixation, as there is no load bearing conditions [321], [332], [333]. However, because the calvarium is not load-bearing, it is not clinically relevant to therapies involving long bone repair, as these involve an endochondral bone

formation that is not observed in most skull bones, which are formed by intramembranous bone formation. The term critical is defined as the smallest size of defect that cannot spontaneously heal over the animal's lifetime or by the experimental endpoint fixed [333]. In the literature, sizes ranging from 4 to 8 mm have been considered critical for rat calvarias as there was no healing if left untreated [326], [334], [335]. For this study, this model was chosen because the surgical procedure is short (45 minutes), our laboratory had people that were experienced in performing the surgery and the bone regeneration in rats is quick (2 - 4 months) so data can be generated faster.

Two *in vivo* experiments were carried out to determine if SAW-DEP influenced the viability and osteogenic potential of the stem cells implanted. For both experiments, cell-coated scaffolds were implanted into critical calvarial defects in immunocompromised rats.

A preliminary study with a lower number of animals was first considered in order find the most suitable scaffold for the test and investigate any signs of chronic inflammation caused by the exposure of cells to SAW-DEP. Various types of scaffolds were considered such as chipped bone, demineralised bone matrix, acellular tendon and cancellous bone (provided by the NHS blood and tissue service), ABM/P-15, Bio-Gide® (Geistlich Biomaterials, Switzerland) and BioOss (Geistlich Biomaterials, Switzerland). These scaffolds were first tested *in vitro* by Dr Guillaume Perry. Tests included seeding the scaffolds with DPSCs and testing proliferation, viability, surface adherence and osteogenic potential. Among the scaffolds tested *in vitro*, the two best performing scaffolds (Bio-Gide and ABM/P-15) were investigated here in a preliminary *in vivo* study.

Bio-Gide® is a commercially available scaffold composed of type I and type III collagen fibres. This collagenous scaffold is resorbable and has been used clinically for bone regeneration around periodontal implants [336]. Despite being of porcine origin, the scaffold has been shown not to elicit an immune response in humans after implantation for up to 9 weeks [337].

The second scaffold investigated was ABM/P-15, an anorganic bovine-derived hydroxyapatite matrix (ABM) combined with a 15-amino-acid peptide (P-15). The attached peptide replicates the cell-binding domain of collagen type I and has been shown to significantly improve cell growth when compared to ABM alone [338], [339].This composite material provides a stable matrix for new bone formation and has been shown to release minerals promoting osteoinduction [340]–[342]. ABM/P-15 has been shown to be effective in human clinical studies for over 10 years in dental applications and has gained

CE approval in Europe where it is used in humans with the commercial name i-Factor™. Its use in orthopaedics has also been investigated in pre-clinical studies and one human clinical trial involving tibia repair [343]–[347].

After the preliminary results showed which scaffold was most appropriate and that there was no chronic inflammation or deleterious effect to bone repair, a second formal study was then carried out with a larger number of animals and two time endpoints to obtain more rigorous data.

6.2.2.1 Experimental design of preliminary *in vivo* study

The first *in vivo* study was carried out to determine which scaffold (Bio-Gide® or ABM/P-15) was most suitable for bone repair and check if there were any concerns in terms of safety of the device so a small number of rats was used in order to abide by the reduction and refinement policies in terms of animal trials [320]. This number did not allow for significant comparisons between groups but informed the planning of the second formal *in vivo* study.

Ten two-months-old 300-350 g athymic (immunocompromised with no T cell formation) nude male rats were purchased from Charles River and housed in the CBS facility at the Wellcome Trust Brenner building. The rats were immunocompromised to avoid an immune reaction to the human stem cells implanted. Two animals were allocated to each condition to be tested (Table 6.2) and only one endpoint at 5 weeks was considered. For each animal, two 4 mm defects were performed to reduce the number animals needed. To limit the potential interactions between the two adjacent defects, the same cell conditions (no cells, control or SAW-DEP cells) were used for both defects within the same rat and care was taken to limit spill over of ABM/P-15 onto the adjacent defects.

For this first experiment, DPSCs at passage 5 were used as they were readily available and their doubling times were faster than BM-MSCs. A negative control without treatment (no cells, no scaffold) was used to prove the defects were critical and did not heal over the experimental time. A positive control consisting of a scaffold seeded with cells that did not undergo SAW-DEP was also used as a clinical standard for comparison with the SAW-DEP cells.

The *in vitro* results showed there was no significant difference in terms of viability and osteogenic potential between the cells that had undergone SAW-DEP and the control ones for all powers tested so the highest tested input power (20 dBm) was used for these experiments.

	Defect 1		Defect 2	
Rat 2	Bio-Gide®	No cells	ABM/P-15	No cells
Rat 3	Bio-Gide®	SAW-DEP cells	ABM/P-15	SAW-DEP cells
Rat 4	Bio-Gide®	Control cells	ABM/P-15	Control cells
Rat 5	No scaffold	SAW-DEP cells	Bio-Gide®	SAW-DEP cells
Rat 6	No scaffold	Control cells	ABM/P-15	Control cells
Rat 7	ABM/P-15	SAW-DEP cells	No Scaffold	SAW-DEP cells
Rat 8	No scaffold	No cells	ABM/P-15	No cells
Rat 9	No Scaffold	Control cells	Scaffold	Control cells
Rat 10	Bio-Gide®	No cells	No Scaffold	No cells

Table 6.2: Details of scaffolds and DPSCs implanted into each rat calvarial defect for the preliminary *in vivo*. Control cells were DPSCs that had been cultured and not subjected to SAW-DEP whereas SAW-DEP cells had been flown through the device at 3 µL/min and had been subjected to a SAW-DEP field of 19 dBm. Note: The first rat died during the operation so was excluded from this table.

6.2.2.2 Experimental design of second formal *in vivo* study

After obtaining the preliminary experiment results, ABM/P-15 was deemed the most suitable scaffold (section 6.3.2) and was used in the formal *in vivo* experiment.

Twenty-two 8-weeks old 300-350 g athymic (immunocompromised) nude male rats were purchased from Charles River and housed in the CBS facility at the Wellcome Trust Brenner building. Eight animals were allocated to each condition tested (Table 6.3) and two endpoints were considered in order to see any progression of bone formation over time. The chosen endpoints were 1 and 2 months. The animals were identified by markings on their ears. For each animal, two 4 mm defects were performed as the preliminary experiments showed that there was no spontaneous healing of the defect over the time of the experiment (5 weeks) so this size was considered critical. The operations were done in two separate days due to the length of the surgical procedures.

For this second, larger experiment, BM-MSCs were intended to be used but the cells we obtained from the donor had significantly lower doubling times compared with the cells that had been used for the *in vitro* experiments so due to time constraints DPSCs were finally used in the experiments.

	Defect 1		Defect 2		Endpoint
Rat 1 (3R)	No scaffold	SAW-DEP cells	Scaffold	SAW-DEP cells	1 month
Rat 2 (3N)	No scaffold	No cells	Scaffold	No cells	1 month
Rat 3 (6L)	No scaffold	Control cells	Scaffold	Control cells	1 month
Rat 4 (5L)	No scaffold	SAW-DEP cells	Scaffold	SAW-DEP cells	1 month
Rat 5 (6N)	No scaffold	No cells	Scaffold	No cells	1 month
Rat 6 (7N)	No scaffold	Control cells	Scaffold	Control cells	1 month
Rat 7 (4R)	No scaffold	SAW-DEP cells	Scaffold	SAW-DEP cells	2 months
Rat 8 (6R)	No scaffold	No cells	Scaffold	No cells	1 month
Rat 9 (7R)	No scaffold	Control cells	Scaffold	Control cells	1 month
Rat 10 (4N)	No scaffold	SAW-DEP cells	Scaffold	SAW-DEP cells	2 months
Rat 11 (7L)	No scaffold	No cells	Scaffold	No cells	1 month
Rat 12 (9R)	No scaffold	Control cells	Scaffold	Control cells	2 months
Rat 13 (11R)	Scaffold	SAW-DEP cells	Scaffold	SAW-DEP cells	1 month
Rat 14 (2R)	No scaffold	No cells	Scaffold	No cells	2 months
Rat 15 (2L)	No scaffold	Control cells	Scaffold	Control cells	2 months
Rat 16 (11N)	Scaffold	SAW-DEP cells	Scaffold	SAW-DEP cells	2 months
Rat 17 (8L)	No scaffold	Control cells	Scaffold	Control cells	2 months
Rat 18 (8N)	No scaffold	No cells	Scaffold	No cells	2 months
Rat 19 (9N)	No scaffold	Control cells	Scaffold	Control cells	2 months
Rat 20 (8R)	No scaffold	No cells	Scaffold	No cells	2 months
Rat 21 (9L)	No scaffold	No cells	Scaffold	No cells	2 months

Table 6.3: Details of scaffolds and DPSCs implanted into each rat calvarial defect during the second *in vivo* experiment. Control cells were DPSCs that had been cultured and not subjected to SAW-DEP whereas SAW-DEP cells had been flown through the device at 3 µL/min and had been subjected to a SAW-DEP power of 20 dBm.

6.2.2.3 Preparation of scaffolds for *in vivo* implantation in rat calvarial defects

ABM/P-15 (available in house) scaffolds were sterilised under UV for 30 minutes and then conserved in 1mL Eppendorf® tubes containing small volumes of sterile Alpha MEM medium for ease of handling. Sterilisation using ethanol was avoided as this would damage the structure of P-15. The precise quantity of ABM/P-15 was difficult to establish when dry, so it was packed using a scoop until the defect was filled.

Bio-Gide® (Geistlich Biomaterials, Switzerland) was cut into 1.9 mm radius circles, sterilised under UV for 30 minutes and kept in sterile containers until the time of implantation. Tests on dead rats showed that upon wetting with medium, Bio-Gide® scaffolds expanded to 4 mm and two sheets were sufficient to fill the 12 mm^3 defect. Additionally, two sheets had been shown to perform better than a single layer [348].

6.2.2.4 Preparation of DPSCs suspensions for *in vivo* implantation

The SAW-DEP devices used were sterilised using ethanol 70% and functionalised by flowing DEP media 30 minutes before the separation. For the first *in vivo* study, a device of 50 µm height and 9 dB insertion loss was used whereas for the second *in vivo* study, the device used was the same as the one used for the *in vitro* tests and had a channel of 75 µm height and an insertion loss of 8 dB.

The cells were prepared as described in section 6.2.1.2 but for the *in vivo* experiments, DPSCs at passage 4 were used instead of BM-MSCs. The SAW-DEP procedure was the same as described in section 6.2.1.3. The only difference was that all the cells were injected at 3 µL/min and the SAW-DEP power used was 20 dBm. After collection, the DPSCs were counted using a haemocytometer, centrifuged at 800 g for 10 minutes, resuspended at a concentration of 10 million cells/mL and kept on ice until time of implantation. The seeding concentration (2.10^5 cells/defect) and density was chosen following optimisation by Dr Guillaume Perry in previous scaffold-seeding *in vivo* experiments. The defect volume was small (13 µL) so the cells were highly concentrated to limit cell dispersion during the injection in the scaffold seeding procedure.

6.2.2.5 Surgical procedures

Calvarial defects were created under Home Office project license number 70/8549 by Dr Xuebin Yang, a trained orthopaedic surgeon. Each rat was sedated using 5 % isoflurane (dial 5) in oxygen for 5 minutes until the sedative took effect. The rat was then placed on a heated pad on to the operating table to ensure body temperature was kept at 37°C. The animal was kept under sedation in oxygen supplemented with 3% isoflurane. The head of the animal was then shaved using an electric razor and the fur was aspirated using gentle vacuum. A solution made up of 70 % ethanol was used to sterilise the operating site and sterile drapes were used.

A first incision was made through the skin and then through the periosteum. Where bleeding occurred, cold injection water was used and pressure was applied with a sterile swab. Two 4 mm diameter defects were made at both sides of the calvarium (as shown in Figure 6.3) using a 4 mm trephine drill. The scaffold was then placed into the defect and the cells were administered. Where Bio-Gide® was used, two 3.8 mm sheets of dry scaffold were placed

on the defect and immediately soaked with the cell suspension. In the case of ABM/P-15, the scaffold was wet prior to implantation but was dried using a sterile swab once packed in order to maximise the absorption of the 12 µL of cell mixture (equivalent to $2x10^5$ cells/defect).

a) 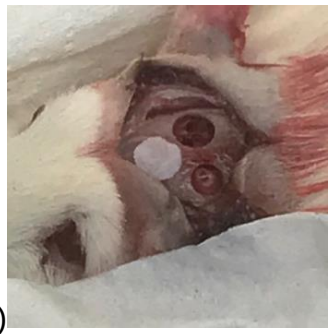 b)  c) 

Figure 6.3: Surgical procedure of rat calvarial defects. a) Two 4 mm calvarial defects were made using a 4 mm trephine drill. These defects were left empty to act as a control. A Bio-Gide® sheet is shown next to the defects for size comparison. b) Defects packed with ABM/P-15. c) Defects packed with two sheets of Bio-Gide®.

Once the cell-seeded scaffolds were in place, the periosteum was sutured using 5.0 Vicryl Ethicon (Ethilon W9105) resorbable sutures and the cranial skin was closed using 5.0 Ehicon sutures (Ethilon W1616T).

Post-surgery, the animals were administered 0.1 mL of 0.3 mg/mL Vetergesic® (Ceva Animal health ltd, UK) and placed in a recovery chamber heated at 37°C until awake and then re-housed. The animals were checked daily for signs of pain and behavioural changes until the day of schedule 1 procedure.

Schedule 1 was performed by placing the rats in a chamber gradually filled with CO_2 and death was further confirmed via cervical dislocation. The top of the cranial vault containing the defects was immediately harvested and placed in 10 % formalin for five days to allow for fixation.

6.2.2.6 Image reconstruction and quantification of new bone formation via micro Computed Tomography (micro CT)

Microcomputed tomography (micro CT) is a non-destructive imaging tool for the production of high resolution three-dimensional (3D) images of a target specimen [349]. Micro CT equipment is essentially composed of an X-ray source, a radiation filter, a collimator used to focus the X-ray beam, a rotating specimen stand and a charge-coupled detector (CCD) [350]. In desktop

systems such as the one used in these experiments, the X-ray source travels through the sample to generate a series of 2D projections that will be converted to a 3D representation by using a computer program (Figure 6.4) [310], [351].

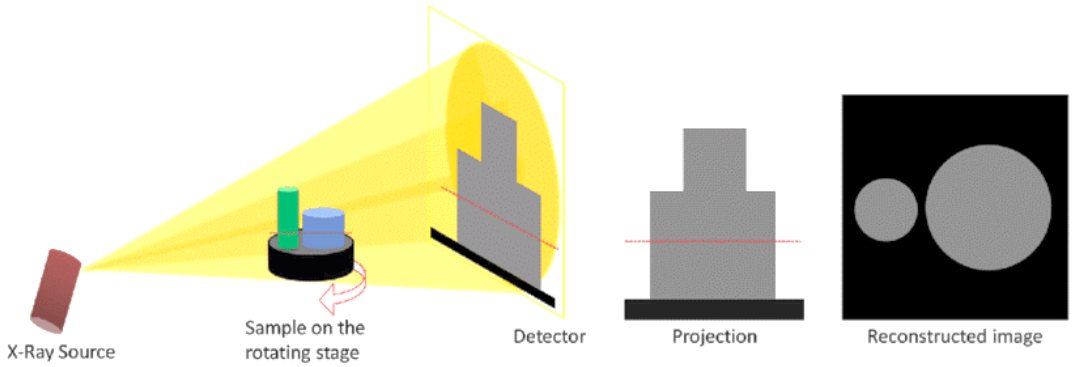

Figure 6.4: Schematic of micro Computed tomography set up and projection analysis. X-rays travel from the source through the sample, reaching the detector with attenuation, and a grayscale projection image is acquired at each rotation angle. The generated projections are reconstructed via a computer program to generate 3D images or slices used to determine material density. The red dashed line indicates the position of the reconstructed cross-sectional image. Image adapted from [350].

Over the past thirty years, micro CT has become a standard tool for the quantification of bone regeneration in preclinical experiments [349]. This technique can be performed on entire defect sites and, using analysis programs, the volume and mineral density of newly formed bone can be quantified reliably [352]–[354].

In the experiments described in this chapter, the explants were imaged using a Skyscan 1172 micro-CT instrument (Bruker, Billerica, MA, USA) in the Wellcome Trust Brenner Building. The bone fragments were tightly lodged in 2 mL Eppendorf tubes filled with 10 % formalin solution to prevent them from moving and drying out during the scan. Scanning was performed using a 0.5 mm Aluminium filter, the X-ray tube voltage used was 53 kV, the image binning was 2000 x 1332 and the images were taken with an isotropic voxel size of 11.19 µm.

Two standards were scanned before each sample to ensure that the X-ray intensity did not change throughout the day. The density of the hydroxyapatite standards was known (0.5 and 0.75 g/cm^3) and used to calibrate the pixel grayscale to the density of the bone (Figure 6.5).

a) 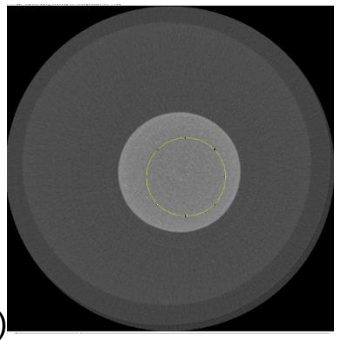 b) 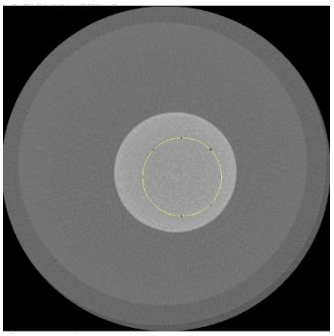

Figure 6.5: X-ray slices of the two hydroxyapatite standards used to calibrate the mineral density. a) Slice through first standard (0.5 g/cm^3) b) Slice through second standard (0.75 g/cm^3). A circle was drawn inside the image of the standard at different slices for each standard and the grayscale obtained was matched to the known density of the hydroxyapatite.

After reconstruction using NRecon Skyscan software (Version: 1.6.6.0; Skyscan Bruker, Billerica, MA, USA) 3D image reconstructions were obtained using the 3D Visualization Software CTvox v. 2.5 (Skyscan Bruker, Billerica, MA, USA).

The datasets obtained after reconstruction were analysed using Image J to obtain a quantitative measurement of the newly formed bone volume. The slices obtained via micro CT were overlaid and a 4 mm circular region of interest (ROI) was drawn around the defect, representing the original defect area (Figure 6.6).

In order to distinguish the newly formed bone from the ABM/P-15 particles, a bone density threshold was used. It was determined that the newly formed bone had a density between 0.5 and 1.5 g/cm^3 whereas (consistent with values observed in the literature) the ABM/P-15 particles were brighter and had a density higher than 1.51 cm^3 [355]. Using a script, the area corresponding to the new bone density threshold within the 4 mm circle of each slice was determined. The area was then multiplied by the number of slices and the depth of each slice (11.19 µm) to obtain the volume of newly formed bone. Similarly, the volume of the ABM/P-15 particles within the defect was determined.

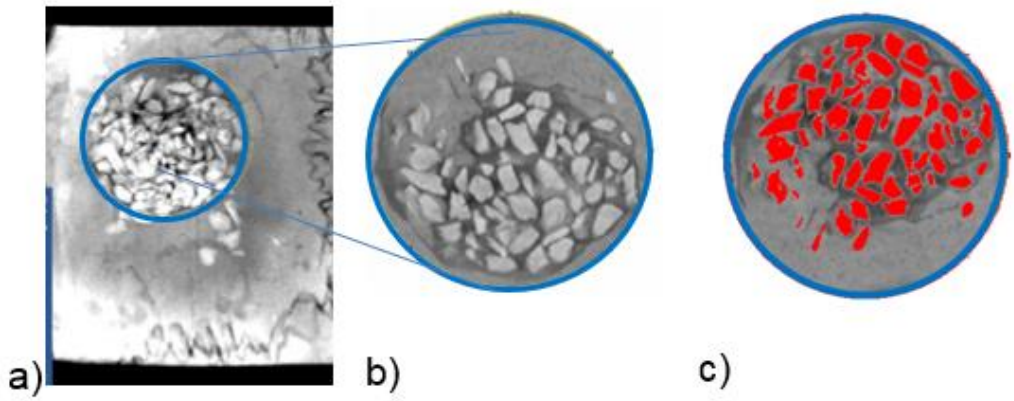

Figure 6.6: Micro CT image reconstruction steps for quantification of new volume formed using Image J. a) Overlay of all slices obtained for the defect using micro CT. A 4 mm region of interest (ROI), represented in blue, was drawn to represent the original defect. b) For each individual slice, only the data inside the ROI was considered. New bone is shown in grey corresponding to a density between 0.5 and 1.5. ABM/P15 particles are shown as white corresponding to a density between 1.51 and 3. c) The area corresponding to ABM/P-15 particles is selected for each slice by using a threshold and the total area is calculated.

The newly formed bone volume was analysed on R using a script written by Professor Robert West. The statistical model used for the comparison between the different conditions tested was a multilevel study [356]. The linear mix regression model accounts for the variability of the rats and considers three fixed effects: the experimental endpoint (1 or 2 months), the scaffold use (no scaffold or ABM+P15) and the type of cells used (no cells, control DPSCs or SAW-DEP DPSCs). The condition consisting of no scaffold, control DPSCs and 1-month endpoint was considered as the intercept (control condition) and the effects of each of the variables was compared to the intercept.

The effect of the rats was modelled as a random effect. A comparison was made between a linear model containing the rat's random effect and a simplified model that did not account for this effect. Although the effect was small compared to the model error it was statistically significant, so it was included in the modelling.

6.2.2.7 Decalcification of bone samples

After micro CT scanning was performed, the fixed samples were decalcified to remove all inorganic material, softening bone tissue and allowing for easier sectioning using a microtome [357]–[359]. This step is routinely performed in histology laboratories by means of acids such as acetic acid, formic acid, nitric

acid and Morse's solution or chelants such as ethylenediaminetetraacetic acid (EDTA) [360]–[363]. An ideal decalcifying solution should be fast, allow for easier tissue slicing, preserve the tissue morphology for histological staining and preserve its antigenicity for immunohistochemical staining. In order to find the most suitable decalcifying approach, Liu and colleagues (2017) evaluated the performance of different solutions [364]. They found that mineral acids were quicker than chelants but the integrity of the histological structures and the antigens was better when chelants were used, which is consistent with previous literature.

Overall, the sections demineralised with a 10 % solution of neutral buffered EDTA had the highest integrity of collagen type I and III as revealed by H&E, Masson's trichrome, Picrosirius red and collagen immunohistochemical staining. Therefore, all explants obtained from the *in vivo* experiments in this study were decalcified for two weeks at 5 °C in a solution made of 10 % EDTA in distilled water buffered to pH 7.0 with sodium hydroxide.

The EDTA solution was changed every week and the decalcification process was followed using X-rays to ensure total decalcification was achieved (Figure 6.7). The radiographs were taken using an Oralix 65 X ray machine (Secondent, Philips, UK) for 7.5 mA, 0.2 seconds, 65 kVp.

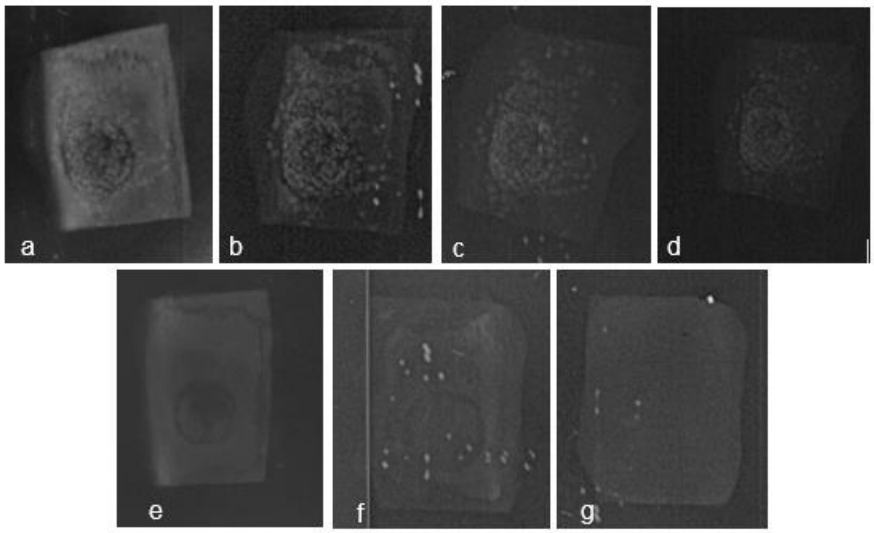

Figure 6.7: Decalcification process of retrieved bone samples followed by X-ray imaging. All images were taken on an Oralix 65 X-ray machine (Secondent, Philips, UK). Pictures a-d show the decalcification of ABM/P-15 filled defects 0, 3, 6 and 12 days after start of decalcification. Pictures e-g show decalcification of Bio-Gide® filled defects 0, 3 and 6 days after start of decalcification. In both cases, by day 6 the original and newly formed bone had been completely decalcified. However, even after day 12 the ABM/P-15 particles are still mineralised.

6.2.2.8 Preparation of histological sections

After demineralisation, the decalcified bone samples were processed using a tissue processor and embedded in paraffin wax. Using a Leitz Wetzlar microtome fitted with MX PREMIER+ microtome blades (Thermo Scientific, UK), the paraffin embedded samples were cut into 5 µm sections. The sections were then mounted onto Superfrost slides, heated at 90°C for 1h and left in a 37 °C for at least 2 days prior to histological staining.

For the second formal *in vivo* study, the bone samples were decalcified and the histological processing, paraffin inclusion, sectioning and mounting was done by Covance Inc.

6.2.2.9 Haematoxylin and Eosin (H&E) staining of histological sections

Haematoxylin and Eosin (H&E) is the most widely used stain combination for medical diagnostics [365]. Haematoxylin stains the cell nuclei in dark blue whilst eosin stains the cytoplasm in pink.

To perform the H&E staining, the paraffin-embedded decalcified bone sections were first deparaffinised. For this, the slides were immersed in two 5-minute baths in xylene followed by two 5-minute baths in absolute ethanol and rehydrated in running tap water for 5 minutes. The sections were then stained with Harris' haematoxylin (Atom scientific, UK) solution for 3 minutes and washed in running tap water for 5 minutes. Nuclear staining was differentiated by dipping the slides quickly in 1 % acid alcohol (1 % HCl in 70 % ethanol solution) three times and washing them in running tap water for 5 minutes. The slides were then "blued" in Scott's tap water (Atom Scientific, UK) for 2 minutes, rinsed in running tap water for 5 minutes and counterstained with eosin (Atom scientific, UK) for 3 minutes. The stained slides were finally washed in tap water for 5 minutes, dehydrated in two 5-minute absolute ethanol baths and cleared in two 5 minute baths of xylene before being mounted using dibutylphthalate polystyrene xylene (DPX) mountant. The stained sections were left to dry and imaged using a Leica microscope.

6.2.2.10 Alcian blue and Picrosirius red staining of histological sections

Picrosirus red and alcian blue are a stain combination commonly used to distinguish bone and cartilage [366]. Collagen is stained in red whilst proteoglycans observed in cartilage are stained blue.

Before staining, the paraffin-embedded decalcified bone sections were deparaffinised in two xylene and ethanol baths and hydrated in tap water as described in the previous section.

After hydration, the sections were first stained in Weigerts Hematoxylin (TCS biosciences, UK) for 8 minutes. After a 5-minute rinse in tap water, the slides were stained with an Alcian blue solution (Merck Milllipore, USA) for 10 minutes and rinsed in tap water for 5 minutes. The slides were then placed in phosphomolybdic acid solution (Polysciences Inc, USA) for 2 minutes, rinsed in distilled water and stained for 60 minutes using a Picrosirius Red solution (Polysciences Inc, USA). After staining, the slides were placed in a 0.1 M HCl solution (Polysciences Inc, USA) for 2 minutes followed by a 45 seconds wash in 70 % ethanol. The stained slides were finally dehydrated in two 5-minute absolute ethanol baths and cleared in two 5-minute baths of xylene before being mounted using DPX and imaged using a Leica microscope.

6.2.2.11 Gomori's trichrome staining of histological sections

Gomori's trichrome is a single step staining used to differentiate between collagen and smooth muscle fibres [367]. It can also be used to differentiate between old mature bone (stained in dark red) and newly formed bone (stained in green or blue).

Before staining, the sections were deparaffinised in two 5-minute baths in xylene followed by two 5-minute baths in absolute ethanol and rehydrated in running tap water for 5 minutes. The sections were then stained for 5 minutes in Harris Hematoxylin solution and washed with tap water until clear. The slides were then immersed in Gomori trichrome stain for 10 minutes and differentiated by quickly dipping in 0.2 % acetic acid three times. The stained slides were finally dehydrated in two 5-minute absolute ethanol baths and cleared in two 5-minute baths of xylene before being mounted using DPX and imaged using a Leica microscope.

6.2.2.12 Collagen type I and osteocalcin immunostaining of histological sections

Immunohistochemistry (IHC) uses antibodies to specifically bind to and therefore permit precise detection of cell /extracellular antigens in tissue sections [368]. The antibodies used can be labelled using either fluorescent tags or enzymes enabling colorimetric visualisation of the antigen-antibody interactions. This technique is commonly used for histological evaluation of sections as it can determine the localisation and level of expression of particular antigens [369]. IHC was used in this study to detect and localise two markers found in bone: collagen type I and osteocalcin. Collagen type I was chosen as it is the main component of the organic matrix of bone (as shown in Section 6.1 Figure 6.1). Osteocalcin was also selected because it is a protein secreted by osteoblasts that is involved in osteogenic differentiation after bone calcification starts [370].

To ensure the immuno-histological staining had been performed correctly, control sections containing osteochondral plugs were also included. In these sections, the bone part acted as a positive control for both collagen type I and osteocalcin whereas the cartilage portion was a negative control for both markers to avoid false positives due to background staining.

The sections were deparaffinised in two 5-minute baths in xylene followed by two 5-minute baths in absolute ethanol and rehydrated in running tap water for 5 minutes followed by a 5-minute PBS bath. The slides were then transferred into a bath of 2 % hydrogen peroxide dissolved in methanol for 20 minutes and washed in a PBS bath for 5 minutes with gentle agitation. Antigen retrieval was achieved by submerging the slides in a chymotrypsin solution for 20 minutes at 37 °C. The solution was made by dissolving 100 mg of calcium chloride and 100 mg of chymotrypsin in 100 mL of distilled water and drops of 0.1 M NaOH were added until the solution reached pH 7.8. The slides were then washed in PBS for 5 minutes and then placed onto Sequenza^{TM} (Fisher Scientific, USA) plates and racks. After a second 5-minute wash with PBS, the sections were incubated for 30 minutes with 100 μL of 1/5 normal goat serum (Dako, Agilent Technologies, USA) in 0.1 % bovine serum albumin solution. The “positive” sections were then incubated with 100 μL of diluted monoclonal antibody solution overnight at 4°C for collagen type I and at room temperature for osteocalcin. For the collagen type I immunostaining, the antibody (ab6308, Abcam UK) was diluted 200 times in 0.1 % BSA solution and for the osteocalcin immunostaining, the antibody (ab13420, Abcam, UK) was diluted

50 times in 0.1 % BSA solution. The optimal dilutions were determined after dosage of both solutions to ensure staining was achieved with minimal non-specific background. Negative control sections were left in the 1/5 normal goat serum solution and were not exposed to the monoclonal antibody solution.

Following the overnight incubation, the slides were washed three times in PBS for 5 minutes and 1 drop of labelled polymer-HRP (Dako Envision® + Dual Link System-HRP (DAB+) Kit, Agilent Technologies, USA) was added in each well and left for 30 minutes. After the incubation with the secondary antibody, the slides were washed three times with PBS for 5 minutes and developed by adding 100 µL of diluted DAB+ solution (Dako Envision® kit) for 10 minutes. The Sequenza™ plates were then removed and the slides were washed well in PBS for 5 minutes and counterstained in Harris' Haematoxylin for 15 seconds, followed by a 1-minute wash in running tap water and a 1-minute incubation in Scott's tap water. The stained slides were finally washed in running tap water for 1 minute and dehydrated in two 5-minute absolute ethanol baths and cleared in two 5-minute baths of xylene before being mounted using DPX and imaged using a Leica microscope.

6.3 Results

6.3.1 Influence of SAW-DEP exposure on BM-MSCs osteogenic potential *in vitro*

Preliminary experiments conducted by Dr Alban Smith demonstrated that DPSCs separated using SAW-DEP showed the same alkaline phosphatase expression levels and same level of osteodifferentiation after 2 weeks of monolayer culture in osteoinductive medium compared to control cells [141]. These results were obtained using DPSCs for SAW-DEP force powers of 12 dBm (16 mW) per IDT. In the present study, after optimisation of the fabrication methods, the insertion loss of the SAW-DEP devices (described in 2.1.3) was found to be considerably lower than previous devices, allowing for SAW-DEP forces four times higher than the ones previously obtained. The aim of the work shown in this section was to test if the higher power SAW-DEP affected the ability of clinically relevant MSCs to differentiate and produce a mineralisable matrix. Alkaline phosphatase expression was first observed qualitatively via staining of BM-MSCs cultures 14 days after osteoinduction

(Figure 6.8). The two highest total powers of SAW-DEP were tested in comparison with a microfluidics control and a SAW-DEP buffer control.

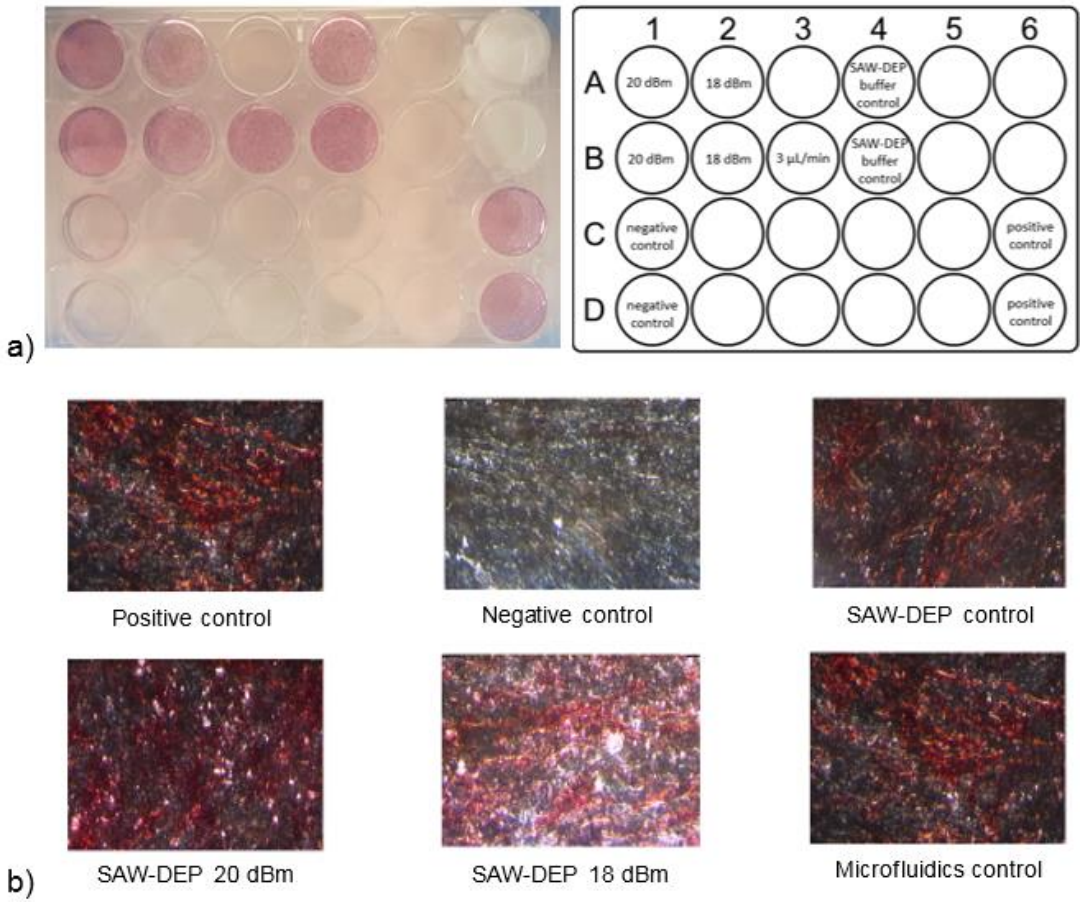

Figure 6.8: Alkaline phosphatase expression by BM-MSCs 14 days after osteoinduction following exposure to different conditions. a) 24-well plate overview image. b) Image of individual wells taken at 10X magnification with a Leica microscope. The 20 dBm and 18 dBm samples contained BM-MSCs subjected to SAW-DEP electric field at a total power of 20 and 18 dBm respectively. The microfluidics control contained BM-MSCs flowed through the SAW-DEP device at 3 µL/min but with no exposure to the electric field. The SAW-DEP control contained BM-MSCs resuspended in SAW-DEP buffer but had not been flown through the device. The positive control contained BM-MSCs obtained straight after culturing with no exposure to the SAW-DEP device and the negative control contained fibroblasts.

For all conditions tested, alkaline phosphatase expression of the experimental samples was similar to the controls. This marker is considered to have a key role in the early stages of bone tissue mineralisation, so the results obtained indicated that SAW-DEP had no influence in BM-MSCs differentiation even at the highest powers [312].

To reveal the presence of calcium deposits at later stages of differentiation, Alizarin red staining of BM-MSCs cultures was performed 28 days after initial

osteoinduction (Figure 6.9). For this test, the same controls as described above for the alkaline phosphatase test were performed. However, the cultures obtained for the microfluidics control and the SAW-DEP at 18 dBm conditions were lost after washes as the monolayer peeled off.

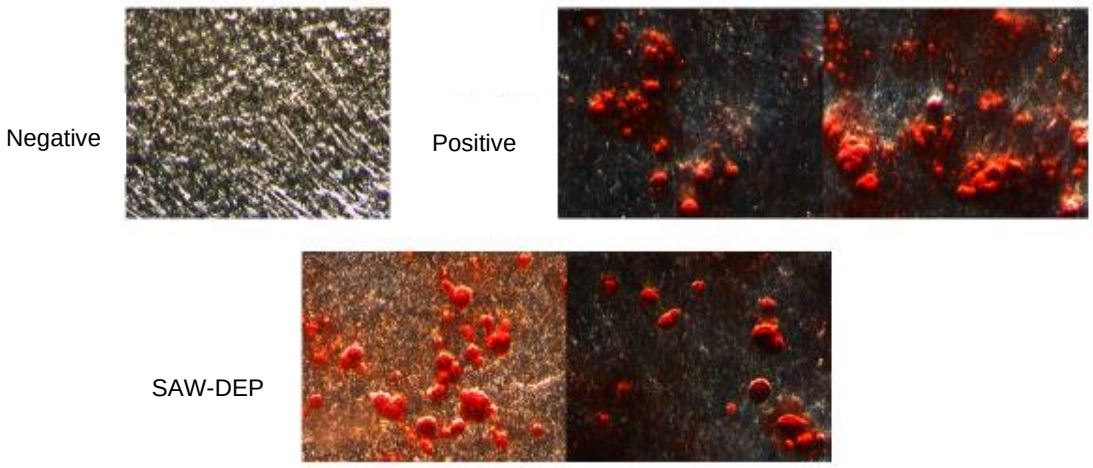

Figure 6.9: Photos of Alizarin red-stained calcified deposits present in cultures of BM-MSCs 28 days after osteoinduction for different conditions of SAW-DEP. All images of individual wells were taken at 10X magnification with a Leica microscope. The 20 dBm sample contained BM-MSCs subjected to SAW-DEP with a total power of 20 dBm per electrode. The positive control contained BM-MSCs obtained straight after culturing with no exposure to the SAW-DEP device, the negative control contained fibroblasts.

For all samples, aside from the negative control, calcified deposits were revealed by Alizarin red staining. The presence of Alizarin red-stained calcium deposits in the wells containing BM-MSCs that experienced the highest SAW-DEP forces showed that the electric fields did not influence their ability to produce calcium salt.

6.3.2 Determination of most appropriate scaffold for bone repair *in vivo*

The first *in vivo* study described here was carried out to determine which scaffold (Bio-Gide® or ABM/P-15) was the most suitable for testing the influence of SAW-DEP on bone regeneration and investigate any signs of chronic inflammation / tissue necrosis that might be associated with the exposure of cells to SAW-DEP. Calvarial explants were retrieved 5 weeks after implantation, sectioned after decalcification and stained using Haematoxylin

and Eosin (Figure 6.10). Only a selection of representative images are shown here. The images of the other replicates can be found in APPENDIX F.

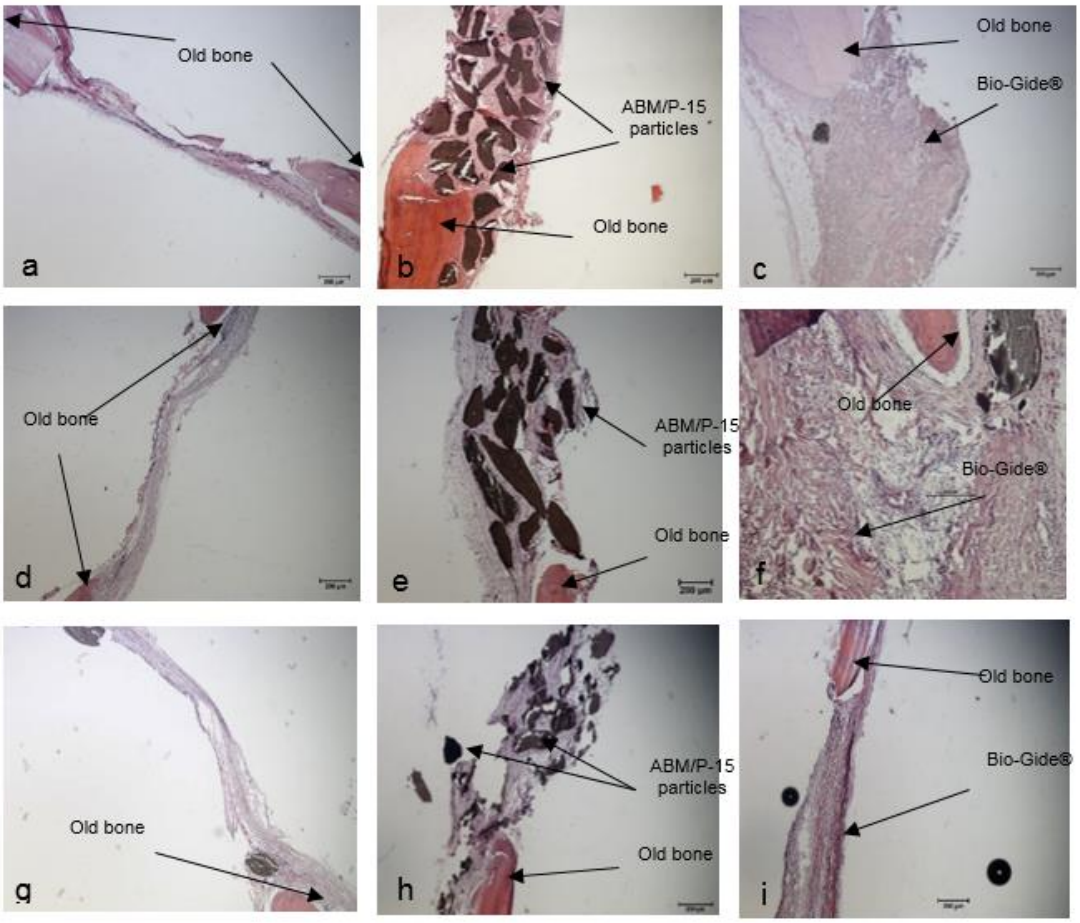

Figure 6.10: Histological staining using H&E of defects from rats sacrificed after 1 month. Nuclei were stained blue by Haematoxylin whereas cytoplasm and collagen were stained pink by eosin. Old bone was stained in a darker shade of pink. The pictures were taken using a 5X objective and the scale bars in the pictures represent 200 µm. a) Control defect left empty. b) Defect filled with ABM/P-15 (no cells). c) Defect filled with Bio-Gide® (no cells). d) Control defect filled with SAW-DEP DPSCs. E) Defect filled with ABM/P-15 and SAW-DEP DPSCs. f) Defect filled with Bio-Gide® and SAW-DEP DPSCs. g) Control defect filled with control DPSCs. Note: A particle of ABM/P-15 had migrated towards the empty defect during the procedure. h) Defect filled with ABM/P-15 and control DPSCs. i) Defect filled with Bio-Gide® and control DPSCs.

The histological sections revealed there was no signs of chronic inflammation or tissue necrosis 5 weeks after implantation as no granulomas were found in any of the samples investigated. These preliminary results suggested that both scaffolds performed better than the negative control (no scaffold). Even if a thin bridging was formed between both sides of the empty 4 mm defects, the

collagen structure was not dense so this defect was still considered critical and the same size defect was used for the formal *in vivo* study.

After 5 weeks, both biomaterials were still clearly identifiable in the defects. Bio-Gide® is a commercially available collagen bilayer membrane and it has been reported to last for 9 months *in vivo* [371]. Both sheets remained in place and did not move during the entire duration of implantation. However, its structure is very similar to that of the newly formed bone after demineralisation so it was difficult to distinguish the collagen fibres belonging to Bio-Gide® from any newly formed collagen even when using higher magnification (Figure 6.11). ABM/P-15 is mainly composed of hydroxyapatite and has been shown to take 1-2 years to be resorbed [372]. Even after demineralisation, the particles were still visible and clearly distinguishable from the newly formed collagen fibres (Figure 6.11). However, some particles migrated during the procedure and were not evenly distributed throughout the defect area so this could affect reproducibility.

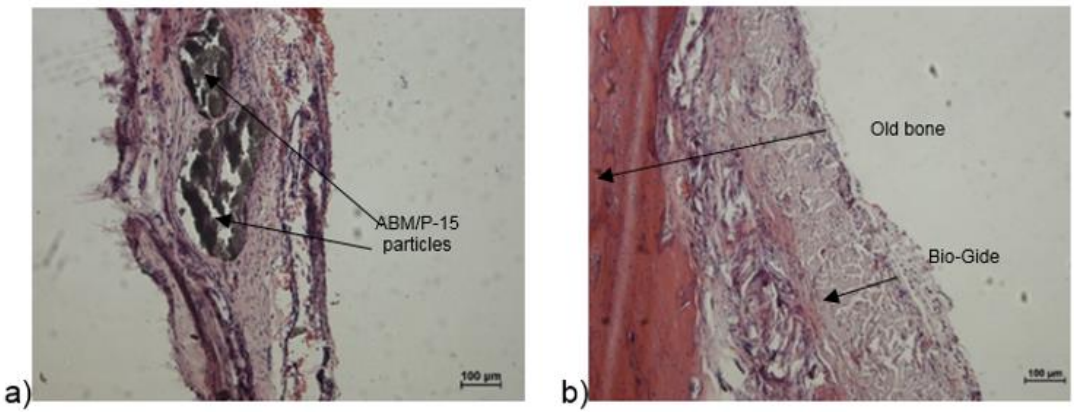

Figure 6.11: H&E Histological staining of defects filled with ABM/P-15 (a) and Bio-Gide® (b) from rats sacrificed after 1 month. The pictures were taken using a 10X objective and the scale bars in the pictures represent 100 µm. In the H&E stained sections, nuclei were stained blue by haematoxylin whereas cytoplasm and collagen were stained pink by eosin. Old bone presents as a darker shade of pink.

In summary, no signs of chronic inflammation or tissue necrosis were observed in any of the animals, so the use of cells subjected to SAW-DEP was considered ready to be tested in a study with a larger sample size. Both scaffolds provided support for the implanted cells and enhanced bone formation when compared to the empty defect controls but ABM/P-15 was chosen for the larger *in vivo* experiment as it was easier to distinguish from the newly formed tissue after histological staining.

6.3.3 Influence of SAW-DEP exposure on DPSCs bone repair *in vivo*

6.3.3.1 Qualitative and quantitative determination of new bone formation using 3D reconstruction of micro CT data

Preliminary results showed ABM/P1-15 was the most appropriate scaffold to facilitate determination of newly formed bone and the presence of any chronic inflammation / necrosis following implantation of cells undergoing SAW-DEP exposure. The objective of the second *in vivo* study was to determine qualitatively but also quantitatively the amount of newly formed bone for all conditions tested to determine whether SAW-DEP exposure affected the osteogenic potential of the cells and their ability to effect bone repair.

For this, the calvaria explants were first analysed using micro CT. Unlike histological examination, micro CT provides information about the entire defect in a non-invasive way by means of reconstructed 3D images (see section 6.2.2.6) [373], [374]. Moreover, micro CT allows for quantification of the volume and mineral density of newly mineralised bone prior to the demineralisation step required for histological analysis. For each rat, two calvarial defects were performed. Each defect was filled with either a scaffold or no scaffold and either no cells, control cells or cells that had gone through the SAW-DEP process ("SAW-DEP cells"). Four rats were allocated to each combination and sacrificed at either one month or two months after the implantation. A summary of the samples and variables analysed can be found in Table 6.4.

Group	Variables			Planned number of defects (experimental number*)
	Time	Scaffold	Cells	
1NN	1 month	No scaffold	No cells	4 (4)
1NC	1 month	No scaffold	Control cells	4 (4)
1NS	1 month	No scaffold	SAW-DEP cells	4 (2)
1AN	1 month	ABM+P15	No cells	4 (4)
1AC	1 month	ABM+P15	Control cells	4 (2)
1AS	1 month	ABM+P15	SAW-DEP cells	4 (4)
2NN	2 months	No scaffold	No cells	4 (3)
2NC	2 months	No scaffold	Control cells	4 (4)
2NS	2 months	No scaffold	SAW-DEP cells	4 (2)
2AN	2 months	ABM+P15	No cells	4 (3)
2AC	2 months	ABM+P15	Control cells	4 (4)
2AS	2 months	ABM+P15	SAW-DEP cells	4 (4)

Table 6.4 Details of variables and number of defects allocated to each group.*Experimental number refers to the actual number of defects available after the experiments. The defects that were damaged during harvest or for which data was not collected were excluded.

Following micro CT scanning, a 3D reconstruction of the samples was used to determine the volume of newly formed bone. The volume of ABM/P-15 scaffold was also calculated to determine if it had an influence in bone repair (section 6.4).

A control group consisting of defects that had not been filled with cells was first analysed (Table 6.5). For all empty defects, the volume of newly formed bone was very low one-month post-surgery and the defect remained empty. This confirmed that the defects were critical as no spontaneous bone formation was observed during the time of the study. The defects containing ABM/P-15 showed a few bony spicules throughout the defect but the newly formed bone volume remained low except for sample 7L where new bony bridging was visible at the sides of the defect.

Sample name	**Micro CT reconstruction Front**	**Micro CT reconstruction Back**	**ABM/P-15 defect**		**No scaffold defect**
			New bone volume	Scaffold volume	New bone volume
3N	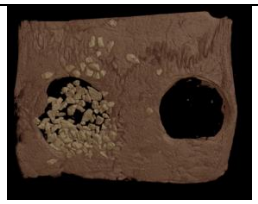	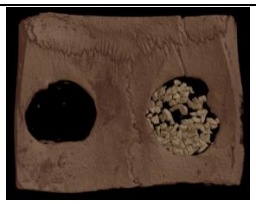	1.04 mm^3	1.5 mm^3	0.59 mm^3
6N	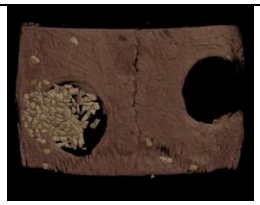	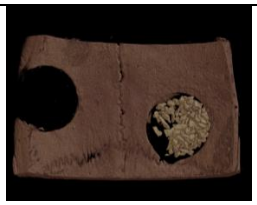	1.68 mm^3	2.36 mm^3	0.35 mm^3
6R	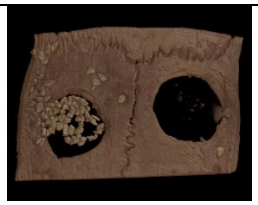	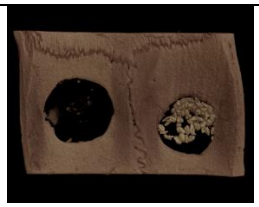	1.69 mm^3	1.17 mm^3	0.15 mm^3
7L			3.32 mm^3	2.76 mm^3	0.35 mm^3

Table 6.5: 3D micro CT reconstructions of explants with no cells 1 month after implantation and determination of newly formed bone volume and scaffold volumes. For all the samples shown, the left defect contained ABM/P-15 particles whilst the right defect was left empty (control). Note: The 6N explant control was damaged whilst being retrieved.

The trend observed for the no cells control one month after implantation was still similar in the two months group (Table 6.6). The amount of newly formed bone increased compared to the one-month group especially in the ABM/P-15 filled defects where bony bridging was visible at the defect borders. In the empty defects, thin bone bridging was observed but the overall new bone volume remained low.

Sample name	Micro CT reconstruction Front	Micro CT reconstruction Back	ABM/P-15 defect		No scaffold defect
			New bone volume	Scaffold volume	New bone volume
2R	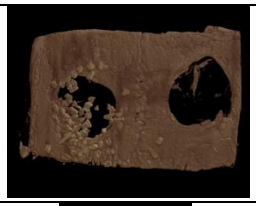	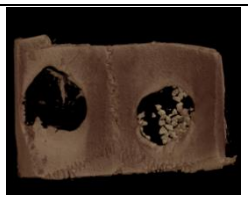	2.13 mm^3	1.07 mm^3	1.45 mm^3
8N	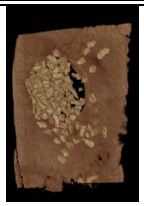		3.98 mm^3	2.88 mm^3	-
8R	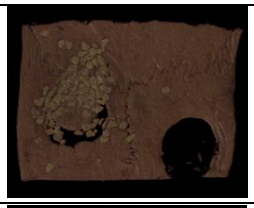	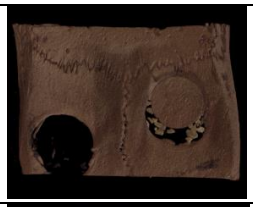	N/A	N/A	1.37 mm^3
9L	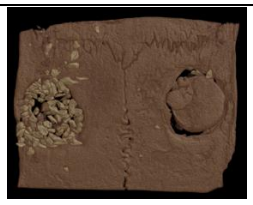	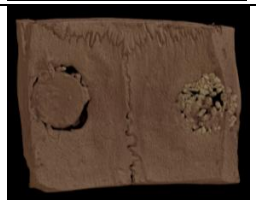	3.25 mm^3	1.65 mm^3	N/A

Table 6.6: 3D micro CT reconstructions of explants with no cells 2 months after implantation and determination of newly formed bone volume and scaffold volumes. For all the samples shown, the left defect contained ABM/P-15 particles whilst the right defect was left empty (control). Note: The 8N explant control was damaged whilst being retrieved. For 8R, the bone disk remained inside the ABM/P-15 defect so the new bone volume for this defect was not considered. Similarly, the control defect was not considered for 9L.

The following group analysed consisted of defects that had been treated with control DPSCs (Table 6.7). Due to the presence of bone disks that remained after the procedure, little information was available for this group. However, the 3D reconstructions showed the presence of bony spicules dispersed

through the empty defects showing an improvement in bone formation compared to the no cell controls.

Sample name	Micro CT reconstruction Front	Micro CT reconstruction Back	ABM/P-15 defect		No scaffold defect
			New bone volume	Scaffold volume	New bone volume
6L	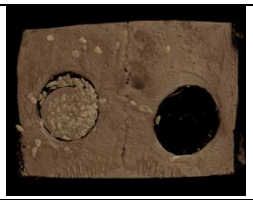	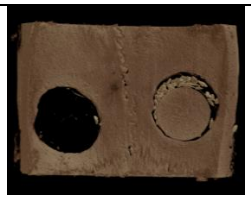	N/A	N/A	0.53 mm^3
7N	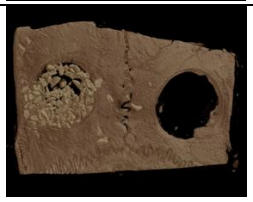		3.21 mm^3	1.99 mm^3	0.76 mm^3
7R	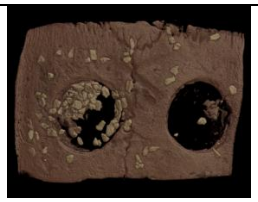	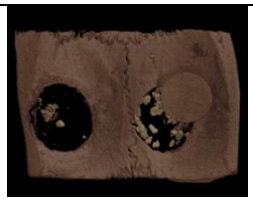	N/A	N/A	1.13 mm^3

Table 6.7: 3D micro CT reconstructions of explants with control DPSCs 1 month after implantation and determination of newly formed bone volume and scaffold volumes. For all the samples shown, the left defect contained ABM/P-15 particles whilst the right defect was left empty (control). Note: For both 6L and 7R the bone disk remained inside the ABM/P-15 defect so the new bone volume for these defects was not considered.

The data obtained for the control cells group two months after implantation is shown in Table 6.8. This data showed mixed results for the samples observed. In samples 9L and 9R, the presence of newly formed bone on the edges of the defect is clear and shows an improvement compared to the previous groups. However, samples 2L and 8L did not show any significant increase in bone volume compared to the one-month group. In terms of ABM/P-15, the reconstructions showed some new bone repair but there was no improvement compared to the no cells samples after two months.

Sample name	Micro CT reconstruction Front	Micro CT reconstruction Back	ABM/P-15 defect		No scaffold defect
			New bone volume	Scaffold volume	New bone volume
2L	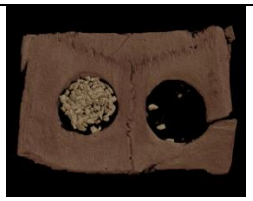	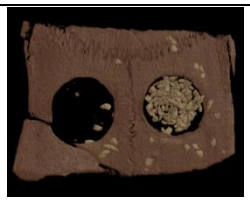	2.05 mm^3	1.92 mm^3	0.44 mm^3
8L	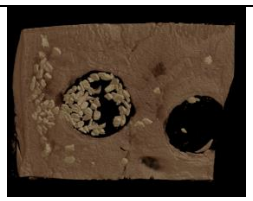	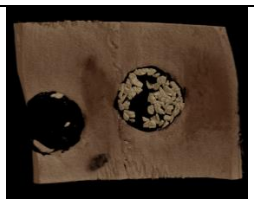	1.11mm^3	1.45 mm^3	1.28 mm^3
9N	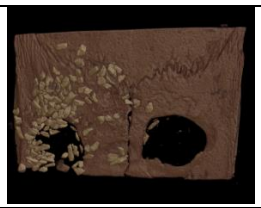	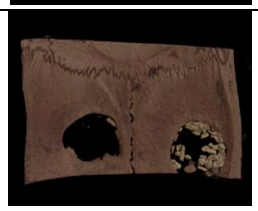	2.41 mm^3	1.07 mm^3	1.53 mm^3
9R	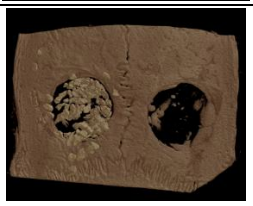		2.08 mm^3	1.98 mm^3	2.73 mm^3

Table 6.8: 3D micro CT reconstructions of explants with control DPSCs 2 months after implantation and determination of newly formed bone volume and scaffold volumes. For all the samples shown, the left defect contained ABM/P-15 particles whilst the right defect was left empty (control). Note: The 8L control and 9N ABM/P-15 defects were damaged during retrieval but were still considered as a whole defect.

The final group analysed consisted of defects that had been treated with DPSCs subjected to SAW-DEP (Table 6.9). For this group, both the controls with no scaffold and the ones containing ABM/P-15 showed the formation of new bone bridging around the edges of the defect and the presence of bony islands.

Sample name	Micro CT reconstruction Front	Micro CT reconstruction Back	ABM/P-15 defect		No scaffold defect	
			New bone volume	Scaffold volume	New bone volume	
3R	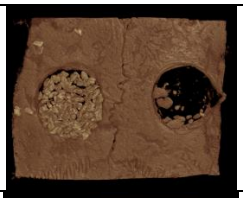	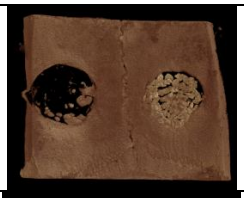	2.63 mm^3	2.17 mm^3	1.76 mm^3	
5L	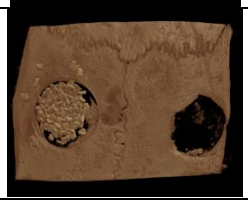	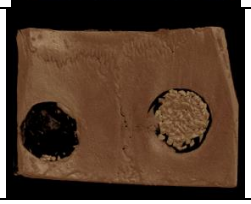	1.89 mm^3	2.08 mm^3	1.46 mm^3	
			ABM/P-15 defect 1		**ABM/P-15 defect 1**	
			New bone volume	Scaffold volume	New bone volume	Scaffold volume
11R	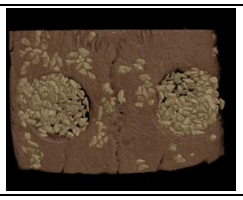	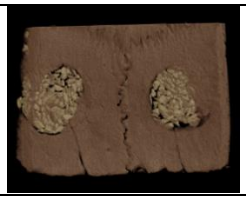	3.92 mm^3	2.52 mm^3	3.41 mm^3	2.97 mm^3

Table 6.9: 3D micro CT reconstructions of explants with DPSCs subjected to SAW-DEP 1 month after implantation and determination of newly formed bone volume and scaffold volumes. For 3R and 5L, the left defect contained ABM/P-15 particles whilst the right defect was left empty (control). For 11R, both defects were filled with ABM/P-15.

In the two-month group, the volume of newly formed bone increased compared to the one-month group for both no scaffold and ABM/P-15 defects (Table 6.10). The 3D reconstructed images and showed integration of the particles into the newly formed bone and bridging between the two sides of the defect. Both ABM/P15 defects filled with SAW-DEP were performed on the same animal so the differences should be minimal. However, there was a big difference in terms of the newly formed bone. The factors influencing this were discussed in section 6.4.

Sample name	Micro CT reconstruction Front	Micro CT reconstruction Back	ABM/P-15 defect		No scaffold defect	
			New bone volume	Scaffold volume	New bone volume	
4R	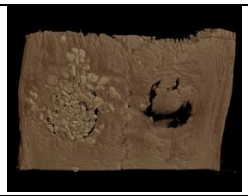	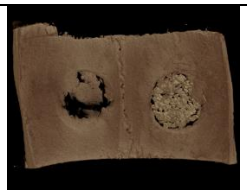	3.49 mm^3	2.4 mm^3	3.07 mm^3	
4N		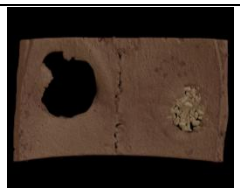	5.44 mm^3	1.66 mm^3	1.17 mm^3	
			ABM/P-15 defect 1		**ABM/P-15 defect 1**	
			New bone volume	Scaffold volume	New bone volume	Scaffold volume
11N	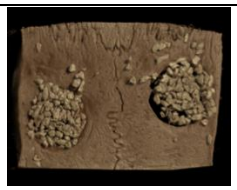	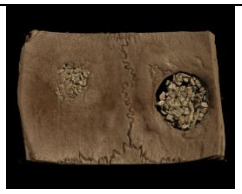	4.37 mm^3	1.83 mm^3	2.93 mm^3	2.47 mm^3

Table 6.10: 3D micro CT reconstructions of explants with DPSCs subjected to SAW-DEP 1 month after implantation and determination of newly formed bone volume and scaffold volumes. For 4R and 4N, the left defect contained ABM/P-15 particles whilst the right defect was left empty (control). For 11N, both defects were filled with ABM/P-15.

An image analysis script was used on the micro CT data to quantify the volume of newly formed bone to allow for comparison of all the conditions tested (Figure 6.12).

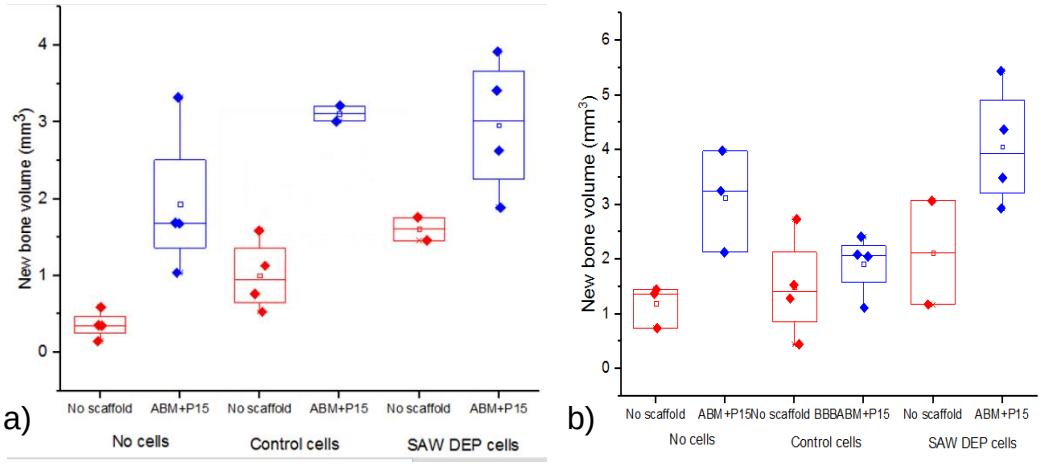

Figure 6.12: Box plots showing new bone volume formed within the original 4 mm calvarial defect using data from micro CT 1 month (a) and 2 months (b) after implantation for different conditions of cells (no cells, control DPSCs and SAW-DEP DPSCs) and scaffold (control with no scaffold and ABM/P-15).

The data obtained showed there was no negative effect of SAW-DEP on new bone formation. The statistical results obtained using the linear mixed effects model (described in section 6.2.2.6) are shown in Table 6.11.

Fixed effects			Estimate change in new bone volume (mm^3)	Standard error	P value
Endpoint	Scaffold	Cells			
1 month	None	Control	1.05	0.27	
2 months	None	Control	0.07	0.30	NS
1 month	**ABM/P-15**	Control	1.59	0.37	<0.001
1 month	None	**None**	-0.29	0.30	NS
1 month	None	**SAW-DEP**	1.23	0.45	<0.001

Table 6.11: Statistical results obtained using a linear mixed effects regression model. The estimated change in volume and P values were obtained when compared to that of the control condition (highlighted in light grey) corresponding to the samples with control cells, no scaffold 1 month after implantation. The number of samples corresponds to the number of experimental samples available for analysis.

The use of ABM+P15 scaffold was shown to significantly increase the new bone volume when compared to the no scaffold control, which has been shown in multiple publications[343], [372], [375]–[377]. The use of SAW-DEP was also shown to significantly increase the new bone volume when compared to the no cells or DPSCs control cells. However, the number of samples used in the statistical analysis was limited but is indicative that SAW-DEP had no deleterious effect on new bone formation.

The analysis also showed that despite an increase in bone volume at 2 months compared to 1 month there was no significant statistical difference between the two endpoints.

6.3.3.2 Characterisation of new bone formed via histological staining

Histological staining is a technique that involves the use of stains to colour the different components of a tissue sample to assist its observation via microscopy [378]. The first histological techniques were derived from experiments carried out in the 17th century [379]. However, the use of histology for pathology and diagnosis did not begin until the 19th century when surgeons started examining patient tissue samples under the microscope to determine the malignancy of tumours [365].

Nowadays, histology is a well-established technique used to study tissue morphology and the microscopic structure of cells [380]. In bone, histological staining is used to highlight the different components of the extracellular matrix (collagen types I and III) and the presence of inflammatory cells or osteocytes involved in bone repair (Figure 6.13).

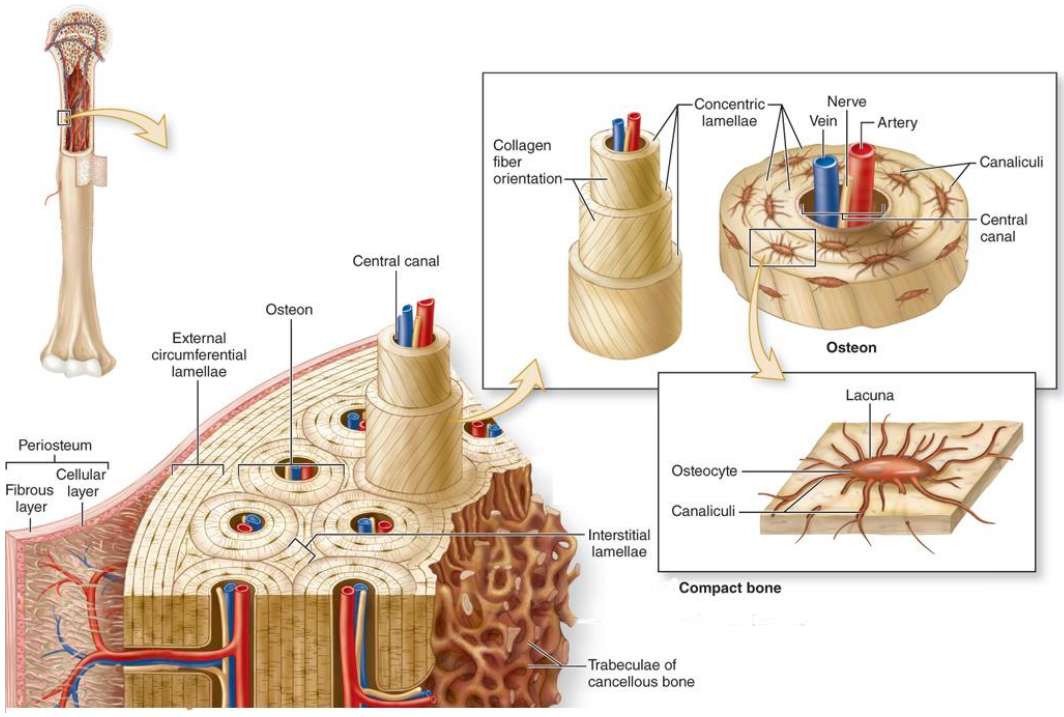

Figure 6.13: Microscopic structure of bone. At the microscopic level, cortical bone is formed of an array of osteon units composed of concentric layers of collagen fibres infiltrated by osteocytes surrounding blood vessels and nerves. Adapted from [381]**.**

The presence of osteocytes and blood vessels in newly formed bone is indicative of bone vitality and maturity and serve as parameters in histopathologic evaluations [382]. Another important parameter is the presence of inflammatory cells indicating chronic inflammation or foreign body reactions (granuloma) [383]. Although inflammation is a necessary step in bone repair (see section 6.1), chronic inflammation can have a negative effect on bone healing and can be indicative of a rejection of the biomaterial or cells implanted [303].

The most commonly used stains are haematoxylin and eosin, which stain nuclei in dark blue and cytoplasm in pink. This stain was used to give an overall idea of the tissue structure and the images can be found in APPENDIX G. In this chapter, only the sections stained with Gomori's trichrome were presented, as the staining shows the difference between mature bone stained in dark red and immature bone made of collagen fibres stained in blue (Table 6.12 to Table 6.23).

In the following tables, the micro CT images corresponding to each histological section stained with Gomori's trichrome were also included (on the left column) to confirm that the newly formed bone observed in the demineralised sections (right column) corresponded to mineralised bone.

Table 6.12 shows the control defects left empty (no scaffold and no cells) from animals sacrificed after 1 month. Samples 3N and 7L showed signs of inflammation corresponding to suture granulomas (Figure 6.14). These suture granulomas are present on the outside of the newly formed bone. Other than the granuloma, little inflammation was found with no presence of neutrophils or multinucleate giant cells. In sample 6R, some brain tissue was also observed in the section, but this might have been as a result from the harvesting rather than a damage to the brain sustained during the operation. Newly formed bone was formed around the edges of the defect, showing a callus formation.

Sample name	Micro CT reconstruction	Gomori's trichrome
3N	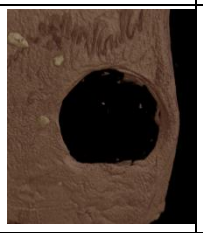	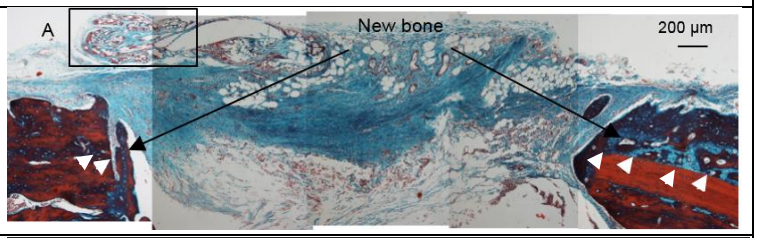
6N	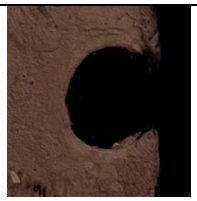	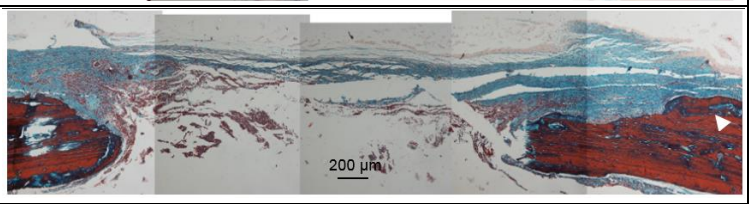
6R	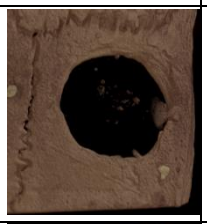	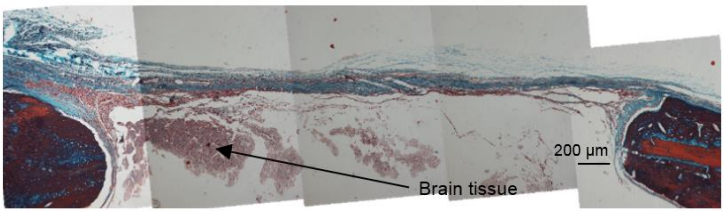
7L	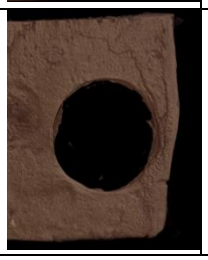	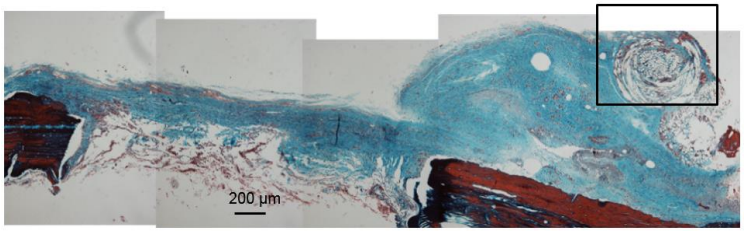

Table 6.12: Control defects (no scaffold and no cells) from rats sacrificed after 1 month. Micro CT 3D reconstruction and histological sections stained with Gomori's trichrome. The limit between the old and new bone is marked by white arrows. Decalcified mature bone sections are stained in red whereas collagen fibres are coloured in blue. The rectangular areas on samples 3N and 7L were studied at further magnification and are shown in Figure 6.14.

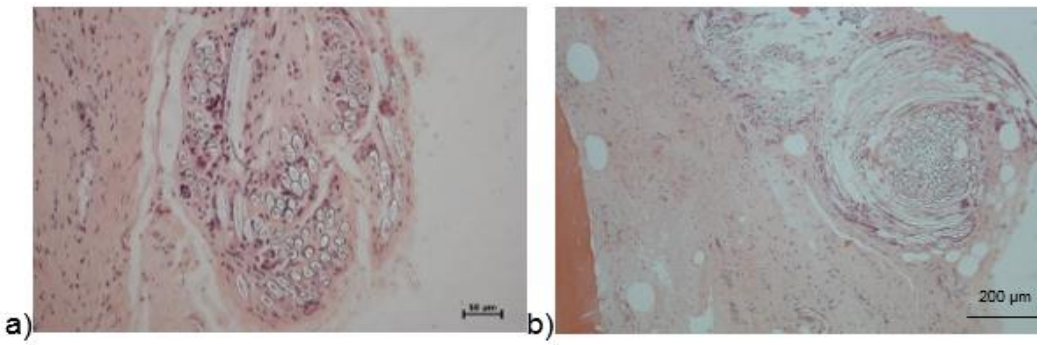

Figure 6.14: Suture granulomas observed in histological samples 3N (a) and 7L (b) stained with H&E. The pictures were taken at 20x and 10x magnification respectively. The round and white circles correspond to suture fibres and are encased in a granuloma.

The data obtained for the control defects left empty (no scaffold and no cells) from animals sacrificed after 2 months is shown in Table 6.13. Two months after implantation, some mature bony islands can be observed in some of the samples and a suture granuloma was also observed, due to the foreign body reaction caused by the sutures used.

Sample name	Micro CT reconstruction	Gomori's trichrome
2R		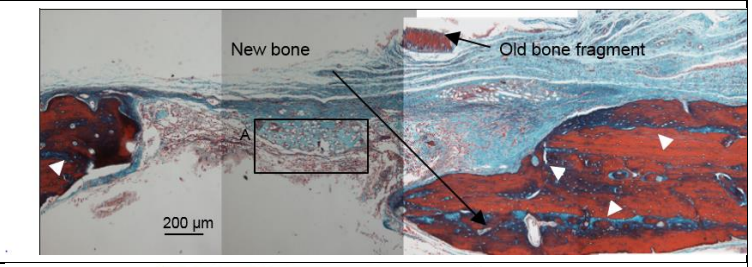
8N	MISSING	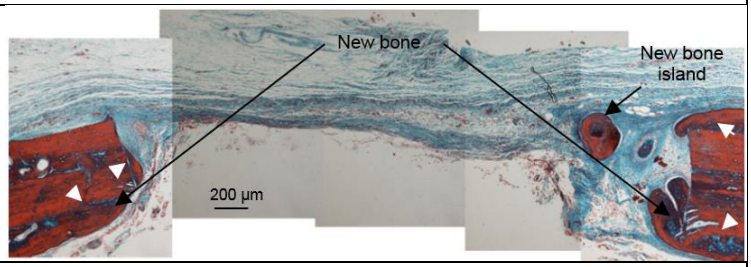
8R	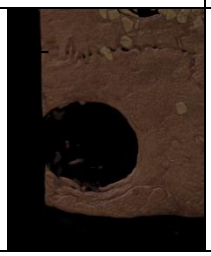	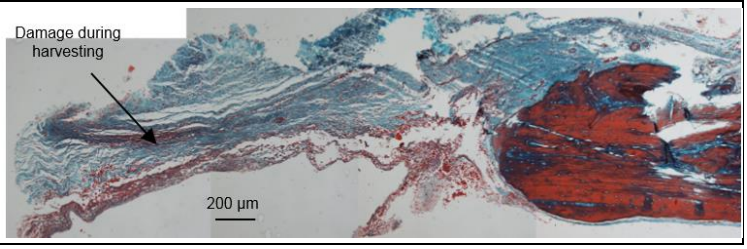

Table 6.13: Control defects (no scaffold and no cells) from rats sacrificed after 2 months. Micro CT 3D reconstruction and histological sections stained with Gomori's trichrome. The limit between the old and new bone are marked by white arrows. Decalcified mature bone sections are stained in red whereas collagen fibres are coloured in blue. Sample 8R was damaged during the harvesting procedure. Note: Sample 9L was not considered for histology because the bone disk was left in during the procedure and this could have affected new bone formation.

Table 6.14 shows the control defects (no cells) left filled with ABM/P-15 particles from animals sacrificed after 1 month. All samples showed no signs of inflammation and good integration of the biomaterial particles as shown by the presence of thick collagen fibres and new mature bone. The newly formed bone found in sample 7L showed signs of maturity with the presence of small blood vessels and lacunae containing osteocytes encasing the ABM/P-15 particles (Figure 6.15).

Sample name	Micro CT reconstruction	Gomori's trichrome
3N	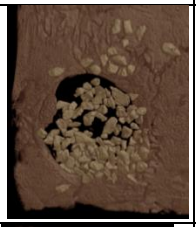	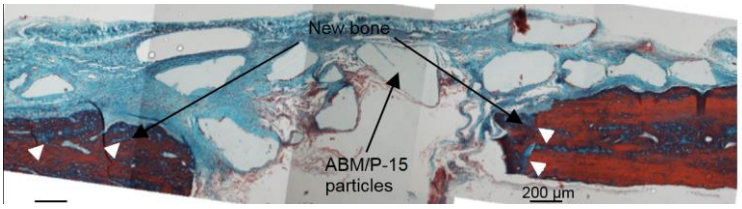
6N	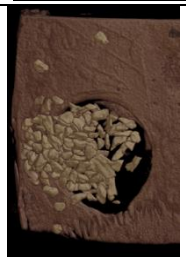	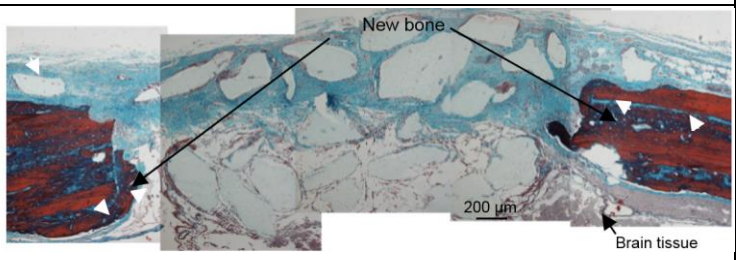
6R	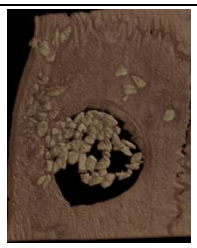	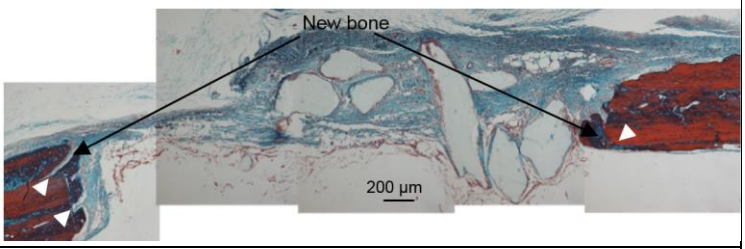
7L	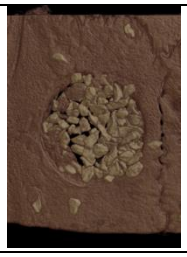	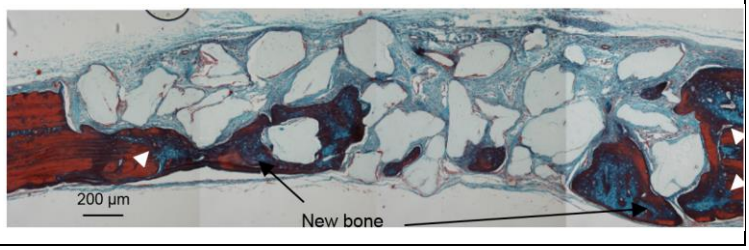

Table 6.14: Defects filled with ABM/P-15 (without cells) from rats sacrificed after 1 month. Micro CT 3D reconstruction and histological sections stained with Gomori's trichrome. The limits between the old and new bone are marked by white arrows. Decalcified mature bone sections are stained in red whereas collagen fibres are coloured in blue.

a) 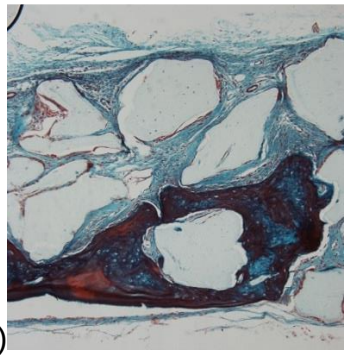 b) 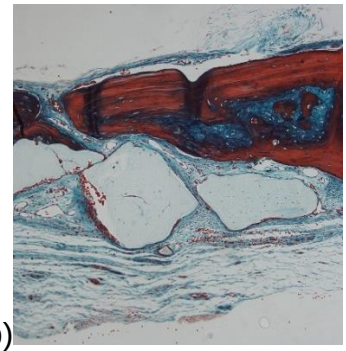

Figure 6.15: Newly formed mature bone in histological samples with no cells and ABM/P-15 scaffold 1 month after implantation (sample 3N on the left) and 2 months after implantation (9L on the right) with Gomori's trichrome. The picture was taken at 20x magnification. An ABM/P-15 particle is seen encased in newly formed bone containing small lacunae.

Two months after implantation, the presence of newly formed bone bridging in the control defects filled with ABM/P-15 (no cells) was more evident, with no signs of inflammation (Figure 6.15). Some mature bony islands can be observed in some of the samples.

Sample name	Micro CT reconstruction	Gomori's trichrome
2R	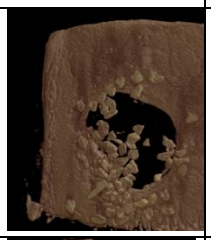	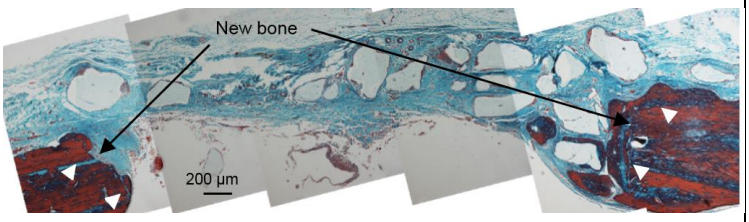
8N		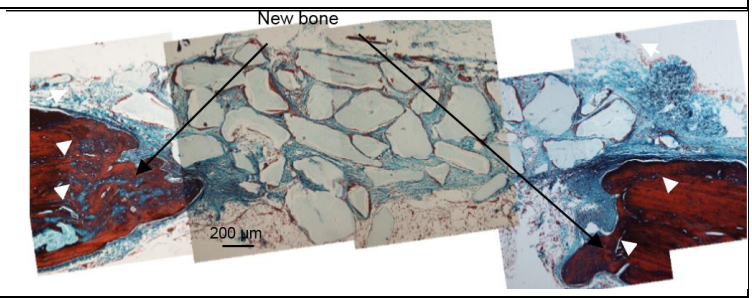
9L	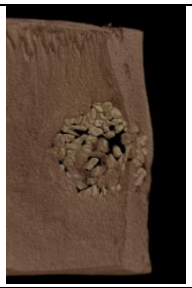	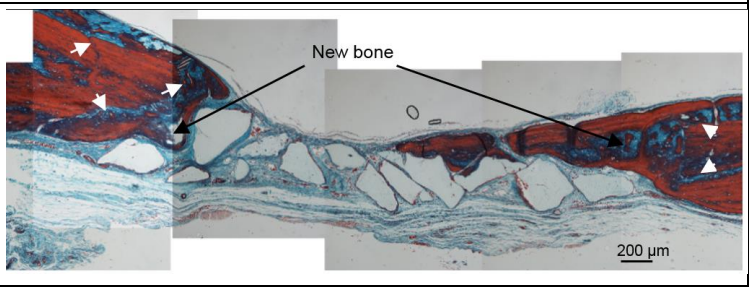

Table 6.15: Defects filled with ABM/P-15 (without cells) from rats sacrificed after 2 months. Micro CT 3D reconstruction and histological sections stained with Gomori's trichrome. The limits between the old and new bone are marked by white arrows. Decalcified mature bone sections are stained in red whereas collagen fibres are coloured in blue. Note: Sample 8R was not considered for histology because the bone disk was left in during the procedure and this could have affected new bone formation.

Table 6.16 shows the control defects filled with control DPSCs from animals sacrificed after 1 month. In sample 6L two suture granulomas were observed at both sides of the defect (inside and outside the skull) (Figure 6.16). This might be explained by the prolapse of the sutured periosteum inside the defect cavity. Other than the granuloma (Figure 6.16), no inflammatory cells were present in any of the defects. Some new bone formation can be observed by the presence of bony islands but predominantly around the edges of defect but

the thin tissue bridging both sides is composed of collagen fibres corresponding to immature bone.

Sample name	Micro CT reconstruction	Gomori's trichrome
6L		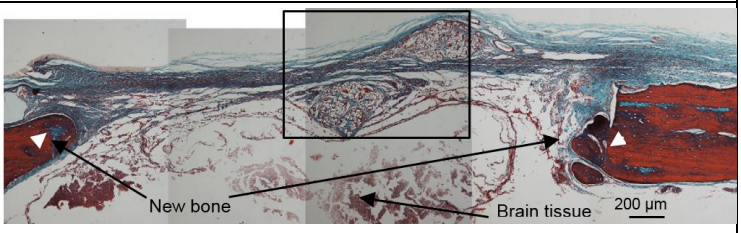
7N	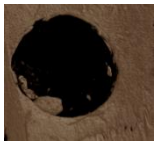	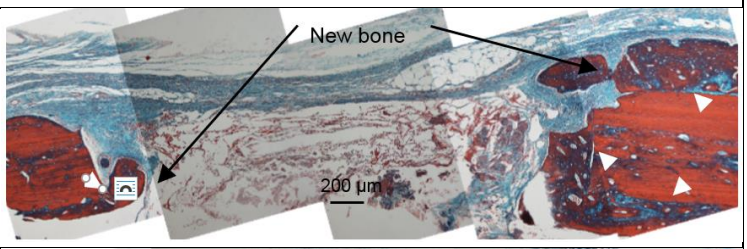
7R	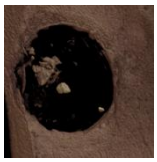	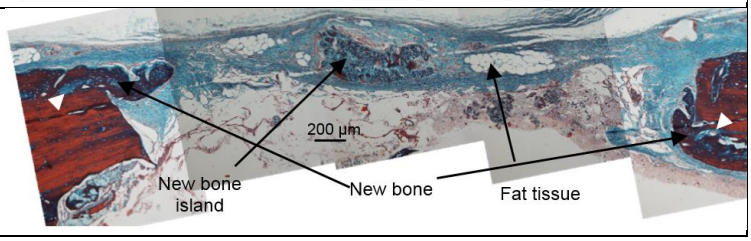

Table 6.16: Defects filled with control DPSCs (no scaffold) from rats sacrificed after 1 month. Micro CT 3D reconstruction and histological sections stained with Gomori's trichrome. The limits between the old and new bone are marked by white arrows. Decalcified mature bone sections are stained in red whereas collagen fibres are coloured in blue.

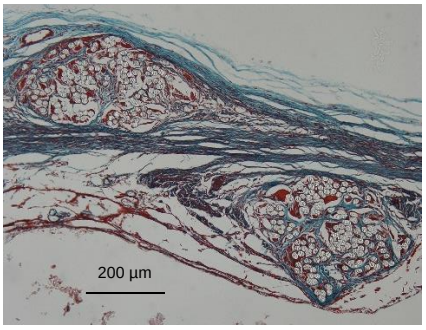

Figure 6.16 Suture granulomas observed in histological sample 6L stained with Gomori's trichrome. The picture was taken at 10x magnification. The round and white circles correspond to suture fibres and are encased in a granuloma.

The trend observed 2 months after implantation for control defects filled with control DPSCs is analogous to that observed in animals sacrificed after 1 month. The tissue connecting the edges of the defect was composed of thin collagen fibres with limited mature bone formation (Table 6.17).

Sample name	Micro CT reconstruction	Gomori's trichrome
2L	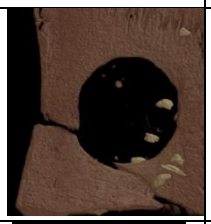	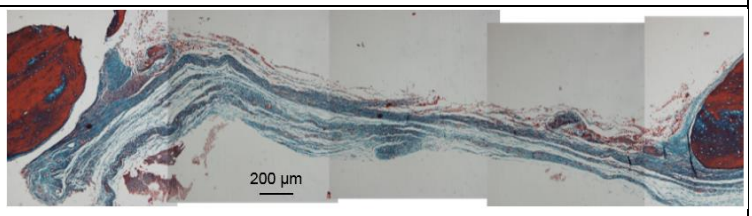
8L	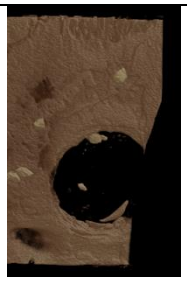	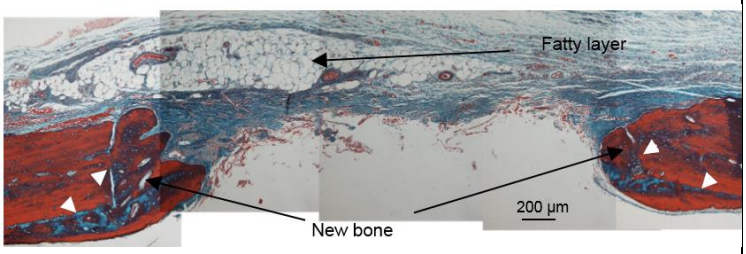
9N	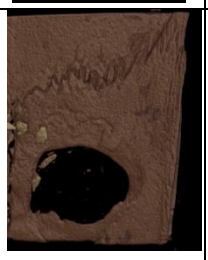	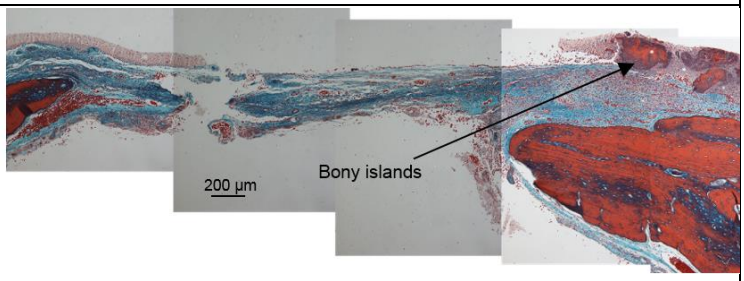
9R	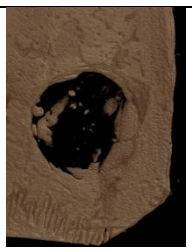	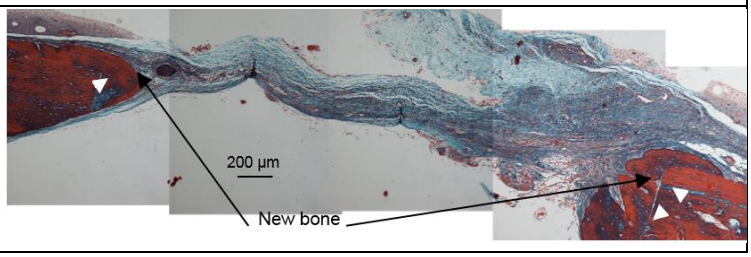

Table 6.17: Defects filled with control DPSCs (no scaffold) from rats sacrificed after 2 months. Micro CT 3D reconstruction and histological sections stained with Gomori's trichrome. The limits between the old and new bone are marked by white arrows. Decalcified mature bone sections are stained in red whereas collagen fibres are coloured in blue.

The data obtained for defects filled with ABM/P-15 and control DPSCs from rats sacrificed after 1 month was limited to one sample (Table 6.18). The other two samples were not considered due to the bone disk remaining in the defect site after the procedure. For this sample, there was evidence of new mature bone formation at the edges of the defect encasing ABM/P-15 particles.

Sample name	Micro CT reconstruction	Gomori's trichrome
7N	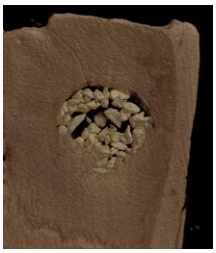	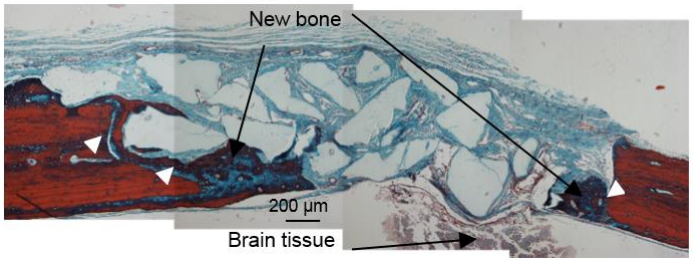

Table 6.18: Defects filled with ABM/P-15 and control DPSCs from rats sacrificed after 1 month. Micro CT 3D reconstruction and histological sections stained with Gomori's trichrome. The limits between the old and new bone are marked by white arrows. Decalcified mature bone sections are stained in red whereas collagen fibres are coloured in blue. Note: Samples 6L and 7R were not considered for histology because the bone disk was left in during the procedure and this could have affected new bone formation.

Two months after implantation, defects filled with ABM/P-15 and control DPSCs showed bony callus formation at the edges (Table 6.19). No inflammatory cells were observed on the defects aside from one suture granuloma observed in sample 8L.

Sample name	Micro CT reconstruction	Gomori's trichrome
2L	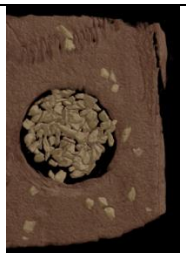	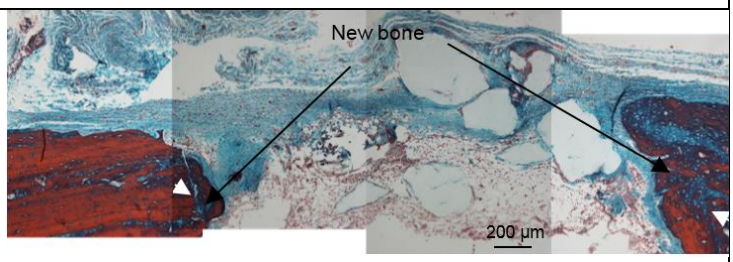
8L	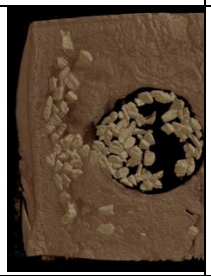	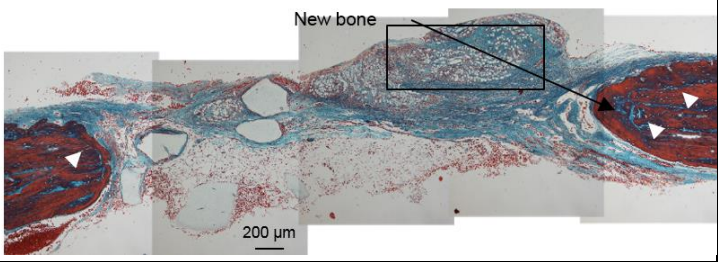
9N	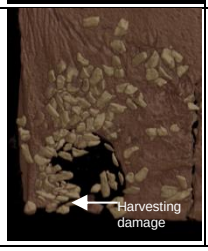	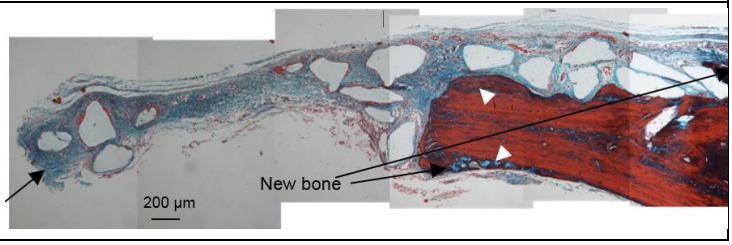

9R	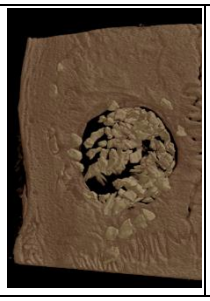	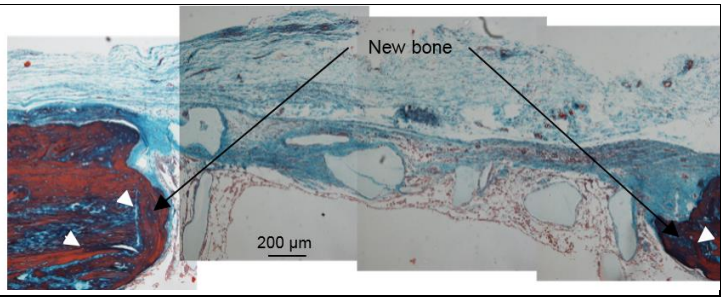

Table 6.19: Defects filled with ABM/P-15 and control DPSCs from rats sacrificed after 2 months. Micro CT 3D reconstruction and histological sections stained with Gomori's trichrome. The limits between the old and new bone are marked by white arrows. Decalcified mature bone sections are stained in red whereas collagen fibres are coloured in blue. Sample 9N was damaged during the harvesting procedure. A suture granuloma observed in 8L is shown by a black rectangle.

Table 6.20 shows the control defects filled with DPSCs that went through the SAW-DEP field from animals sacrificed after 1 month. In sample 3R, new bony islands were observed both in the micro CT reconstruction and in the histological section where lacunas and blood vessels were visible. On the other hand, sample 5L showed only thin and collagen fibres bridging both edges and a suture granuloma on the outside of the defect.

Sample name	Micro CT reconstruction	Gomori's trichrome
3R	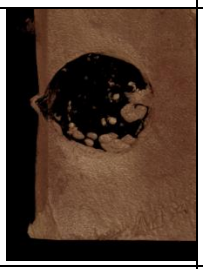	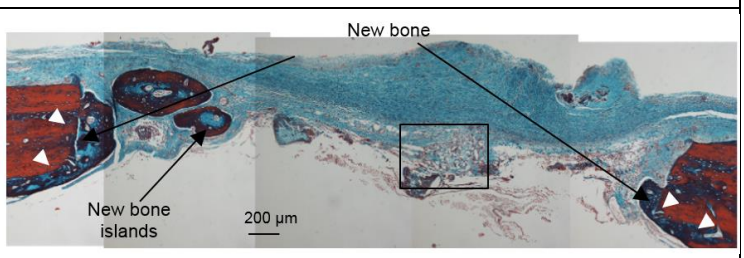
5L	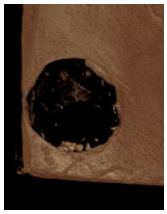	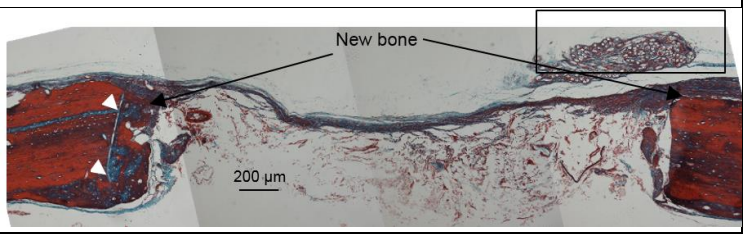

Table 6.20: Defects filled with SAW-DEP DPSCs (no scaffold) from rats sacrificed after 1 month. Micro CT 3D reconstruction and histological sections stained with Gomori's trichrome. The limits between the old and new bone are marked by white arrows. Decalcified mature bone sections are stained in red whereas collagen fibres are coloured in blue. Two regions corresponding to suture granulomas are shown in squares.

The samples of the control defects filled with DPSCs that went through the SAW-DEP field from animals sacrificed after 2 months showed significant bony bridging and no signs of chronic inflammatory response (Table 6.21). For sample 4R, the bridging spanned across the entire defect with lacunae and small blood vessels infiltrating the newly formed bone. The newly formed bone in sample 4N was smaller but this could be explained by the presence of brain tissue that could have been damaged during the procedure.

Sample name	Micro CT reconstruction	Gomori's trichrome
4R		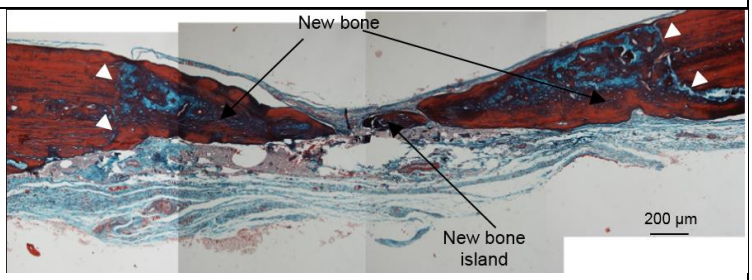
4N	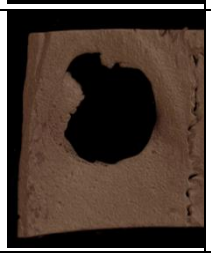	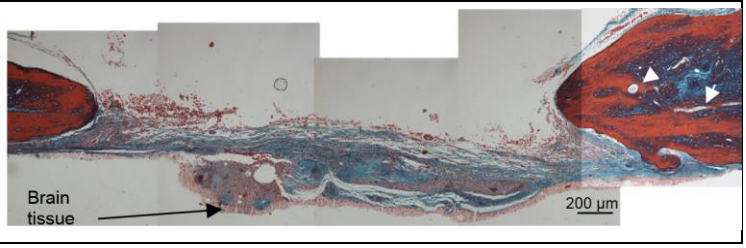

Table 6.21: Defects filled with SAW-DEP DPSCs (no scaffold) from rats sacrificed after 2 months. Micro CT 3D reconstruction and histological sections stained with Gomori's trichrome. The limits between the old and new bone are marked by white arrows. Decalcified mature bone sections are stained in red whereas collagen fibres are coloured in blue.

Table 6.22 shows the defects filled with ABM/P-15 seeded with DPSCs that went through the SAW-DEP field obtained from animals sacrificed after 1 month. All samples showed integration of the particles and the presence of new mature bone islands or callus formation at the edges of the defect. Other than the suture granulomas observed in sample 3R, no immune reaction was observed in the samples.

Sample name	Micro CT reconstruction	Gomori's trichrome
3R		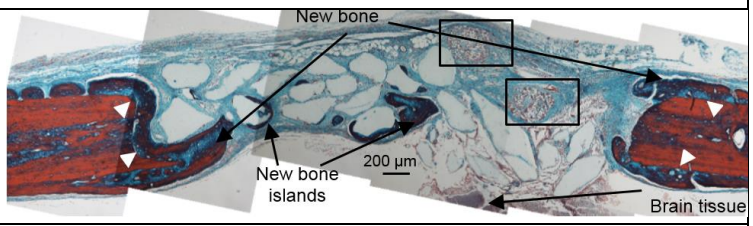
5L	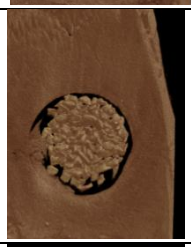	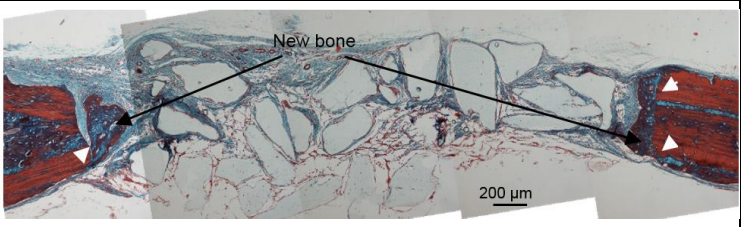
11R	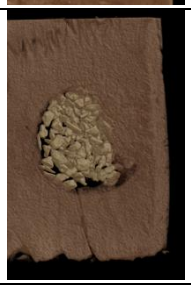	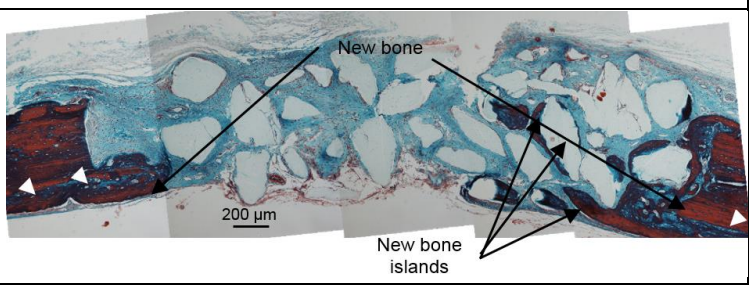
11R 2	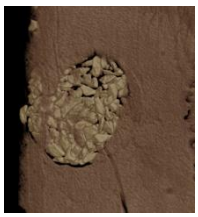	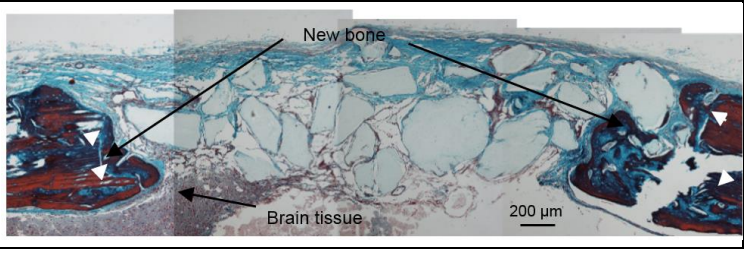

Table 6.22: Defects filled with SAW-DEP DPSCs (no scaffold) from rats sacrificed after 1 month. Micro CT 3D reconstruction and histological sections stained with Gomori's trichrome. The limits between the old and new bone are marked by white arrows. Decalcified mature bone sections are stained in red whereas collagen fibres are coloured in blue. Two suture granulomas (indicated by a rectangle) were observed in sample 3R.

Two months after implantation, the defects filled with ABM/P-15 seeded with DPSCs that went through the SAW-DEP field showed increased bone repair compared to the 1-month samples and no chronic inflammation that might have been expected if the SAW-DEP treated cells had caused a localised tissue reaction resulting in tissue death (Table 6.23).

Sample name	Micro CT reconstruction Back	Gomori's trichrome
4R	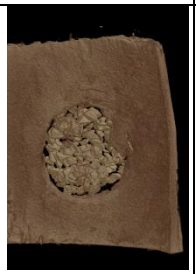	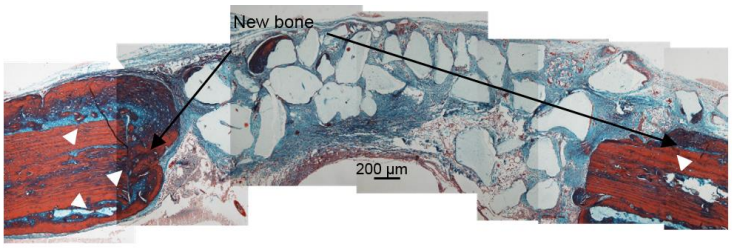
4N		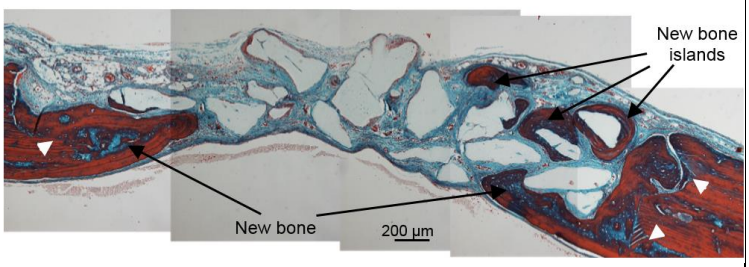
11N	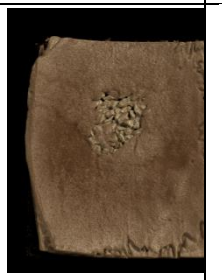	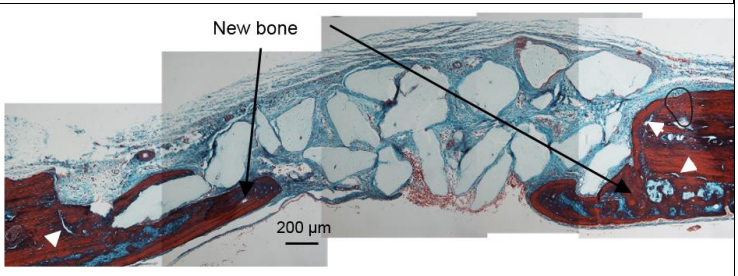
11N 2	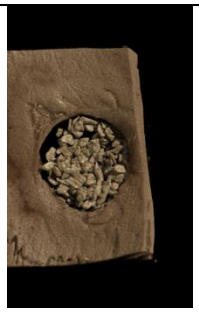	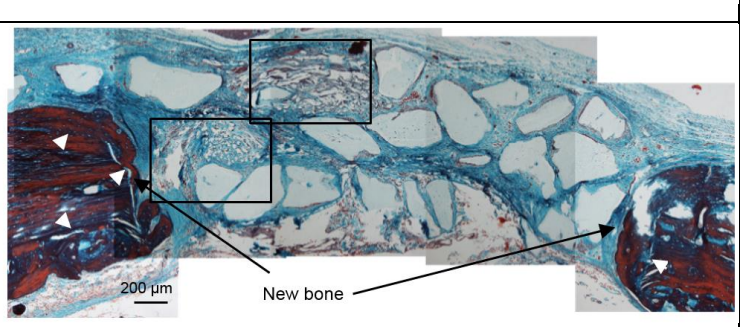

Table 6.23: Defects filled with ABM/P-15 and SAW-DEP DPSCs from rats sacrificed after 2 months. Micro CT 3D reconstruction and histological sections stained with Gomori's trichrome. The limits between the old and new bone are marked by white arrows. Decalcified mature bone sections are stained in red whereas collagen fibres are coloured in blue. One suture granuloma (indicated by a rectangle) was observed in sample 11N (2).

6.3.3.3 Detection of osteocalcin and Collagen type I in decalcified histological bone samples via immunohistochemistry

Immunohistochemistry was used to determine the localisation and level of expression of osteocalcin and collagen type I in the histological sections obtained after demineralisation of the rat calvarial defects. Collagen type I is the main component of bone matrix and was observed in all newly formed tissues bridging the defect. The images of the sections stained with collagen type I can be found in APPENDIX G.

The expression of osteocalcin was also assessed via immunochemistry and the results are shown in Figure 6.17 to Figure 6.20. Osteocalcin is an extracellular matrix protein produced by osteoblasts that can be used as a late marker for bone formation as its production is upregulated during bone maturation [384], [385]. This protein has a key role in bone mineralisation and determines the shape, strength and size of newly formed bone [386]–[388].

In this section, only one sample is shown for each condition tested. The rest of the histological images corresponding to the other defects can be found in APPENDIX G. For all samples analysed, osteocalcin was present throughout the old bone but also within the newly formed bone islands within the defect. A faint staining for osteocalcin was also found in the collagen matrix bridging the defect. This is to be expected, as osteocalcin is a marker of mature bone so the cells within the bony islands should express more of this protein. These findings suggest that the newly formed bone observed in all samples is following normal patterns of development and is mature. A gradual decrease of the osteocalcin staining can be observed in some samples from the edge of the defect (containing the oldest bone) towards the centre of the defect consisting of the newest collagen fibres.

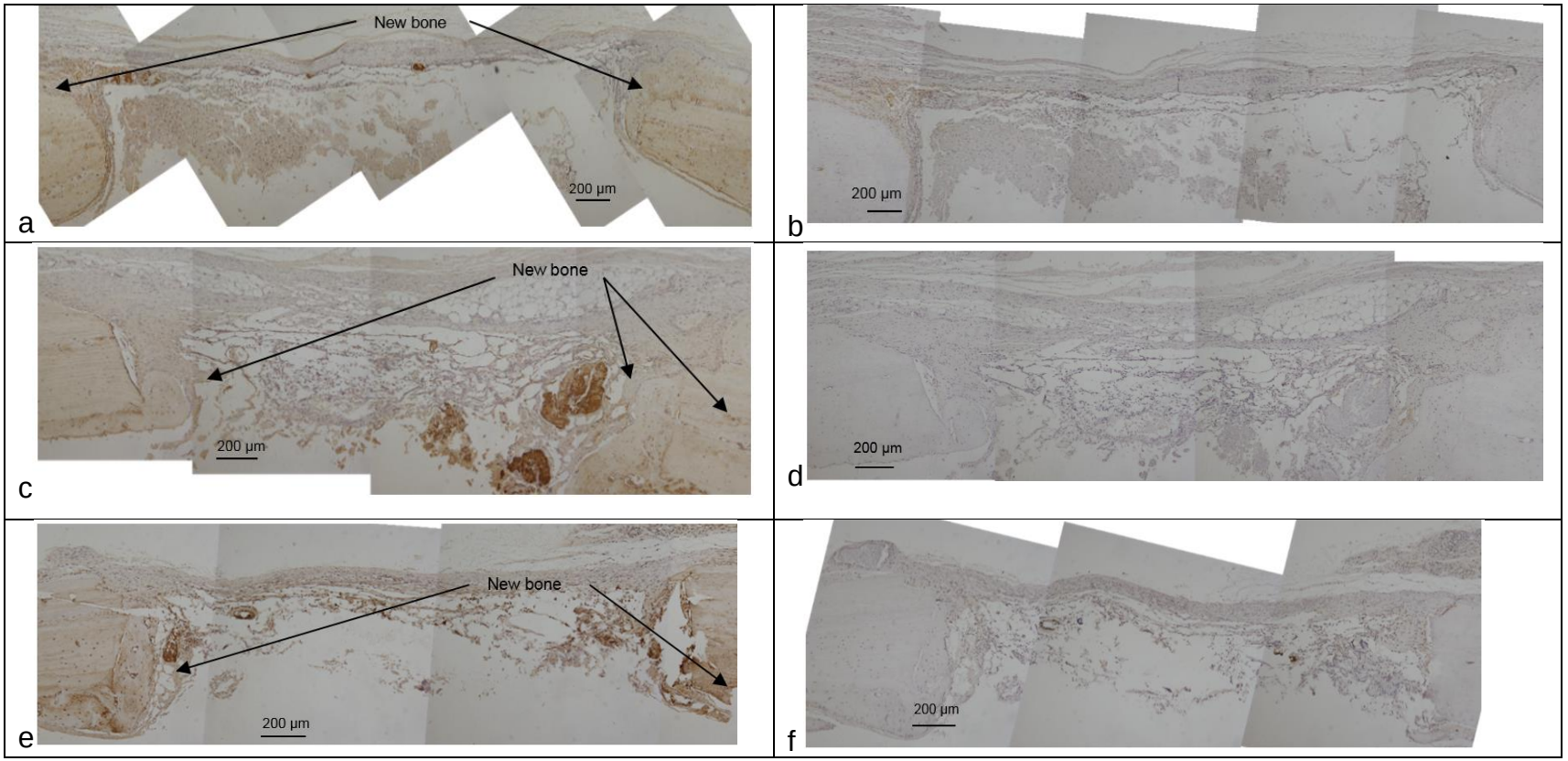

Figure 6.17: Osteocalcin immunohistological staining of defects with no scaffold 1 month after implantation. a) Positive staining for osteocalcin in sample 6R where the defect was not filled with cells. b) Sample 6R negative control. c) Positive staining for osteocalcin in sample 7N where the defect was filled with control DPSCs. d) Sample 7N negative control. e) Positive staining for osteocalcin in sample 5L where the defect was filled with SAW-DEP cells. f) Sample 5L negative control. Scale bars correspond to 200 µm and the magnification used was 10x. Note: Brain tissue also expresses osteocalcin.

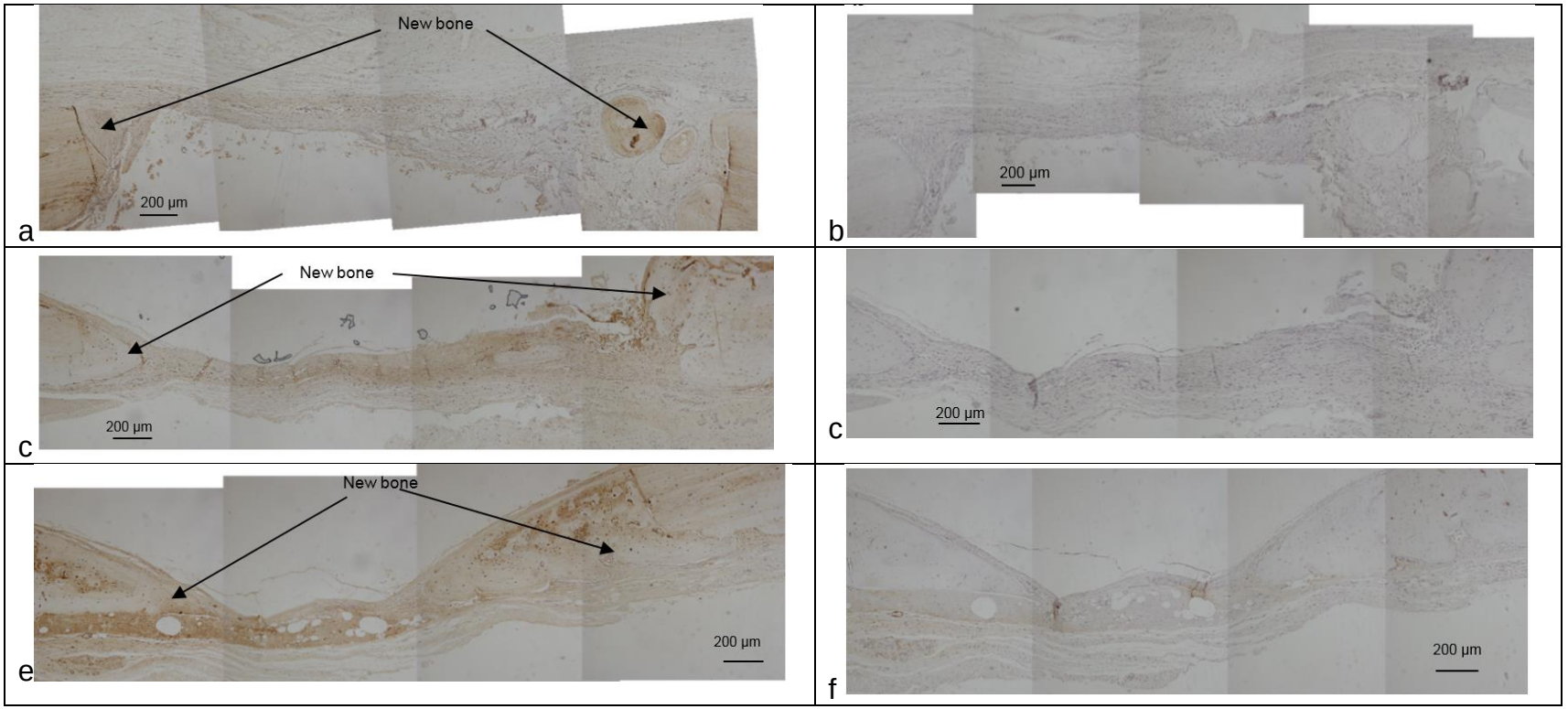

Figure 6.18: Osteocalcin immunohistological staining of defects with no scaffold 2 months after implantation. a) Positive staining for osteocalcin in sample 8N where the defect was not filled with cells. b) Sample 8N negative control. c) Positive staining for osteocalcin in sample 9R where the defect was filled with control DPSCs. d) Sample 9R negative control. e) Positive staining for osteocalcin in sample 4R where the defect was filled with SAW-DEP cells. f) Sample 4R negative control. Scale bars correspond to 200 µm and the magnification used was 10x.

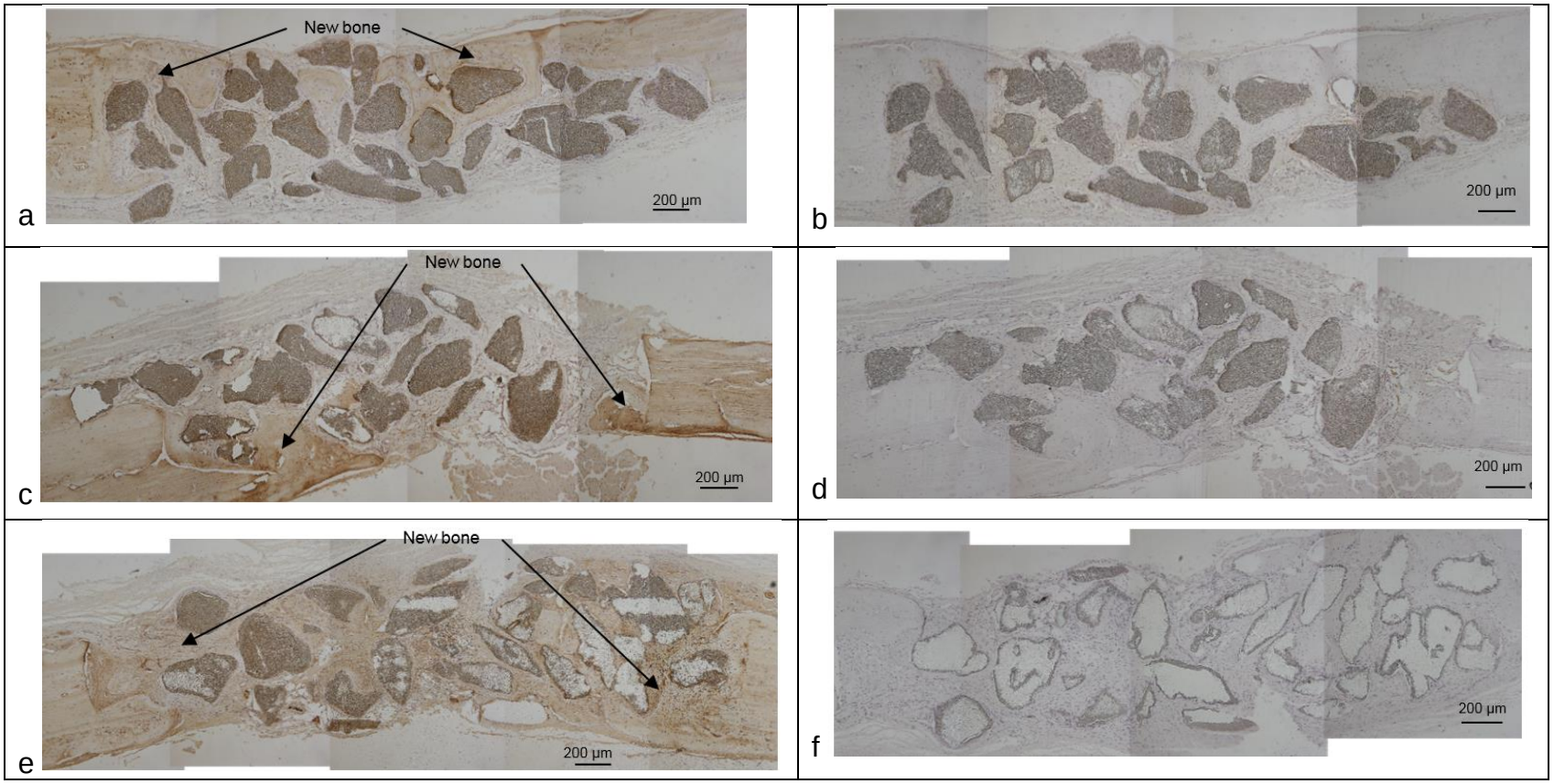

Figure 6.19: Osteocalcin immunohistological staining of defects with ABM/P-15 1 month after implantation. a) Positive staining for osteocalcin in sample 7L where the defect was not filled with cells. b) Sample 7L negative control. a) Positive staining for osteocalcin in sample 7N where the defect was filled with control DPSCs. d) Sample 7N negative control. e) Positive staining for osteocalcin in sample 11R where the defect was filled with SAW-DEP cells. f) Sample 11R negative control. Scale bars correspond to 200 µm and the magnification used was 10x.

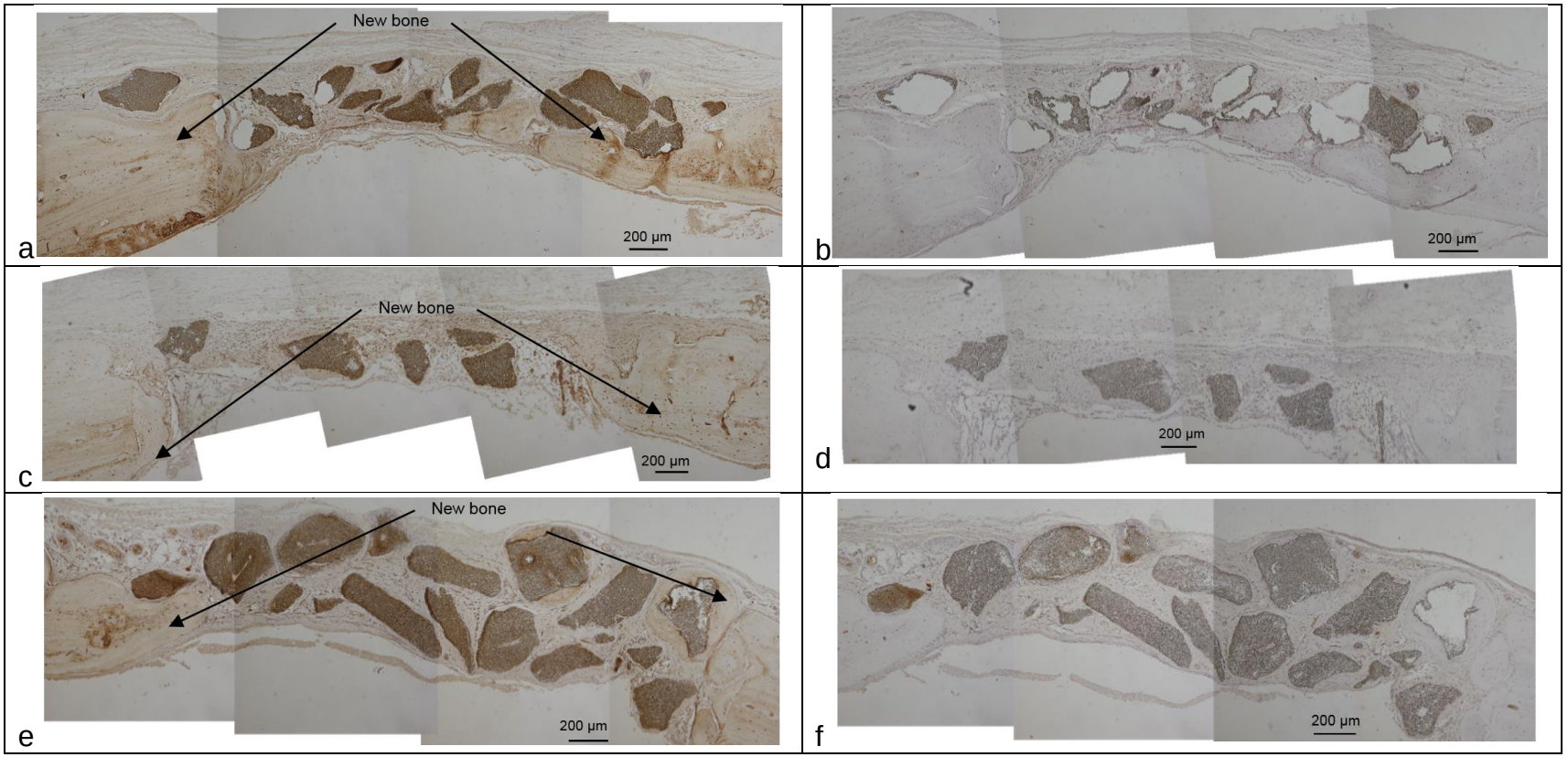

Figure 6.20: Osteocalcin immunohistological staining of defects with ABM/P-15 2 months after implantation. a) Positive staining for osteocalcin in sample 9L where the defect was not filled with cells. b) Sample 9L negative control. c) Positive staining for osteocalcin in sample 9R where the defect was filled with control DPSCs. d) Sample 9R negative control. e) Positive staining for osteocalcin in sample 4N where the defect was filled with SAW-DEP cells. f) Sample 4N negative control. Scale bars correspond to 200 µm and the magnification used was 10x.

6.4 Discussion

When determining the factors influencing the volume of newly formed bone in rat calvaria defects, three variables were considered: the presence or absence of scaffold, the cell type used (no cells, control DPSCs and SAW-DEP DPSCs) and the endpoint (1 or 2 months). However, other confounding factors could affect bone formation and explain the differences between the replicates for each of the conditions considered.

One of the factors that could have influenced the total volume was the placement of the defect (Figure 6.21). O'Reilly and colleagues (2011) measured the parietal bone thickness at four different locations and found that the average skull thickness of adult rats was 0.71 ± 0.03 mm. Although small, there were differences between rats, and it is also important to note that the parietal bone is slightly thicker at the margins than at the central part.

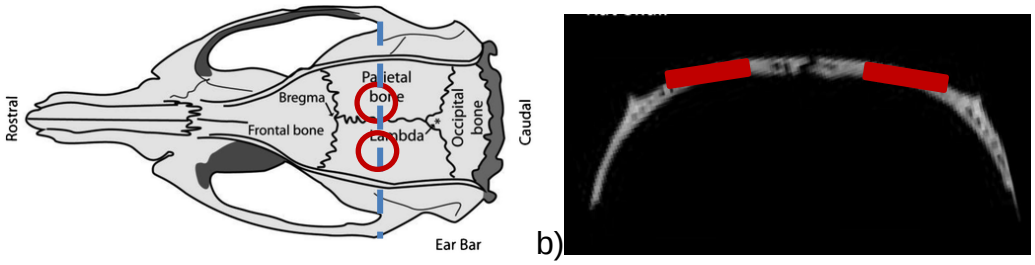

Figure 6.21: a) Anatomy of a rat's skull. The defects are represented by red circles and the location of the cross section shown in b is shown by a blue dashed line. Note: The image was modified from [389]**. b) Micro CT cross section of a rat skull as shown in** [390]**. The defect areas are represented in red.**

During the surgical procedure used in this thesis, the defects were placed symmetrically on the parietal bone when possible in order to limit the differences in thickness but small differences might have remained between rats.

Another factor that could influence the volume of newly formed bone is the volume of ABM/P-15 particles present in each sample. Despite delivering a similar amount in each defect, due to the nature of the biomaterial (small loose particles) it was difficult to obtain a reproducible amount throughout all defects. As shown in section 6.3.3.1, some of the ABM/P-15 particles migrated during the procedure. Moreover, the particle size was not consistent between samples, and different particle volumes and surface areas could result in differences in bone formation. The correlation between the total volume of ABM/P-15 particles and the volume of newly bone formed was investigated in Figure 6.22.

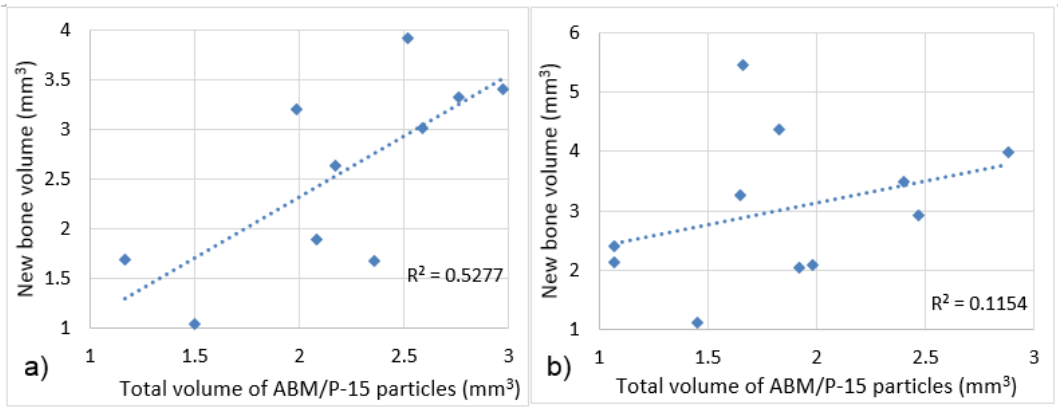

Figure 6.22: Correlation analysis between the volume of newly formed bone and the total volume of ABM/P-15 particles present in the defect determined by image J analysis of the micro CT stacks. a) For all samples harvested 1 month after implantation. b) For all samples harvested 2 months after implantation. R^2 is the Pearson's correlation coefficient.

There was a small correlation between the total volume of ABM/P-15 particles and the volume of newly bone formed for the samples obtained at the 1-month endpoint suggesting that a larger volume of ABM/P-15 resulted in increased bone formation. However, the two-month endpoint showed there was little correlation between the variables. It could be hypothesized that that a smaller volume of particles could result in less support for initial new bone formation. However, the presence of a large volume of ABM+P15 particles could limit the space available for new bone to be formed so both effects could negate each other at the two-month endpoint.

Finally, the presence of brain tissue in some of the histological samples could be indicative of damage during the surgery. Damage to the dural and brain tissues could arise if the trephine penetrated the bone too far during the defect formation. The dura has been shown to play a role in bone healing so a damage in this tissue could result in reduced bone healing [391], [392].

6.5 Summary and future work

6.5.1 Summary

The main objective of this chapter was to investigate whether the SAW-DEP technology was minimally manipulative and that it did not adversely affect bone repair. *In vivo* experiments showed that BM-MSCs exposed to SAW-DEP had the same expression of alkaline phosphatase and ability to form

calcified deposits as unexposed control cells. After successful *in vitro* results and a preliminary *in vivo* study, a second *in vivo* study was carried out using a rat cranial defect model. The bone volume was analysed via micro CT and the data suggested the SAW-DEP exposure did not affect negatively the amount newly formed bone volume compared to control DPSCs. Histological analysis of the explant showed that aside from some suture granulomas, there was no sign of chronic inflammation / tissue necrosis associated with the SAW-DEP exposed cells. The newly formed bone showed signs of maturity as histological stains revealed the presence of lacunae and small vessels as well as osteocalcin expression.

6.5.2 Future work

The *in vitro* analysis could be extended by quantifying the expression of osteogenic markers such as the runx2 gene, and osteocalcin during the osteoinduction process in SAW-DEP MSCs using quantitative PCR. The runx2 gene codes for core-binding factor alpha-1, a transcriptional activator involved in the differentiation of osteoblasts [393], [394]. As explained in section 6.3.3.3, the level of osteocalcin expression increases with osteogenic differentiation of MSCs into osteoblasts [370]. Monitoring osteocalcin expression could further confirm that SAW-DEP does not affect the differentiation process of the MSCs. For this, a commercially available assay (96-well TaqMan® Array Human Osteogenesis, Thermo Fisher Scientific, USA) containing 96 markers involved in osteogenesis could be used to further show that the cells are minimally manipulated.

During the *in vivo* trials, problems due to the slow culturing of BM-MSCs and contaminations resulted in the use of DPSCs as replacement due to time constraints. However, another *in vitro* experiment with BM-MSCs and a higher number of replicates for each variable considered would be needed to obtain more significant results. To keep the number of animals used low, a single time-point at two months could be considered, as the data showed that there was no statistical difference between the volume formed at one and two months. This would increase the number of observations two-fold without increasing the number of animals needed.

In order to have more information at different timepoints, Raman spectroscopy could be used. This technique is a label-free, non-invasive measurement that has been previously used to measure BM-MSCs differentiation *in vitro* and bone repair *in vivo* [395], [396]. This measurement

can be done every two weeks on sedated rats to follow one regeneration without the need for multiple endpoints.

In addition to the staining performed, an immunohistological staining could be used to determine if the human cells implanted remain 2 months after surgery. The cells used were obtained from a human donor, so a simple anti-human antibody could be used to detect the presence of the implanted cells.

Finally, in addition to the histological staining, mechanical testing of the explants could be performed. Push out testing, consists in placing the specimen on a support jig and pushing the centre of the defect with a metal rod until bone failure. This test can be used to assess the strength of newly formed bone bridging the edges of the defect [321]. Even if the calvaria is not a load bearing bone, the integrity of the newly formed bone is still critical to its function, so testing the mechanical strength of the new bone could give an indication of its integrity.

Chapter 7
Conclusion and future work

7.1 Summary of key achievements

The objective of this thesis was to develop the understanding of SAW-DEP technology to determine its suitability to separate MSCs from other cell types found in bone marrow whilst maintaining their osteogenic potential and increase its throughput to achieve separation within intra-operative timeframes.

In Chapter 4, the effect of parameters such as the input power and channel height on the dielectrophoretic forces generated by the SAW-DEP device were investigated in order to better understand the underlying physics behind the remote dielectrophoresis separation. The negative dielectrophoretic forces generated on latex beads for a range of input powers and channel heights were determined by tracking the particles' motion in the SAW-DEP device. These experimental results were compared to the predicted DEP force values generated by a three-dimensional FE model developed by Dr Akshay Kale. The model was able to predict the trends observed experimentally and could therefore be used in combination with the experimental data to inform the design of the separation devices.
The detailed analysis of the DEP forces generated by the SAW-DEP device revealed that the vertical forces (i.e. the forces acting on the particles perpendicular to the SAW plane) are an order of magnitude stronger than the horizontal alignment forces, which had been previously exploited for alignment. To exploit the vertical DEP forces and the alignment height difference between the cells experiencing pDEP and nDEP, different multilayer approaches consisting of two output channels at staggered heights were modelled *in silico* using COMSOL Multiphysics. The best performing design consisted of a three-layered forked channel in which an upper and lower PDMS channel were separated using an ultrathin glass separation layer. The multichannel was realised experimentally and showed a 20-fold increase in throughput (corresponding to 36.10^6 cells/h) compared with previously used channels relying on the lateral separation of particles across the channel.

In chapter 5, the characterisation of the dielectric properties of MSCs and other cell types found in bone marrow was described. BM-MSCs were obtained commercially whilst pure populations of the principal cells found in bone marrow (B cells, T cells, monocytes, neutrophils and eosinophils) were

extracted from blood using a MACS negative selection approach. Before the determination of the cell's dielectric properties, the purity of the MACS-isolated cell suspensions was verified using a bespoke FACS multi-panel and was found to be higher than 74% for all cell types.
The dielectrophoretic response of the purified cell suspensions was then determined using a commercial technology (3DEP), for a range of frequencies and conductivities. The dielectric properties of the cells were determined from the experimental DEP spectra obtained using different fitting approaches based on the single-shell cell model. The dielectric properties determined for each cell type were then used to model the DEP responses of all the cell types for a range of frequencies suitable for SAW-DEP and buffer conductivities compatible with minimal manipulation of cells in order to determine the best conditions for MSC enrichment. The data suggested that for a 50 MHz SAW-DEP frequency and a 0.22 S/m medium conductivity, MSCs experienced positive DEP and could be separated from the other white blood cells experiencing negative DEP, showing that SAW-DEP has the potential to enrich MSC populations from bone marrow samples.

In chapter 6, the minimal-manipulation requirement of the SAW-DEP cell separation technology was assessed in order to investigate whether the exposure of MSCs to SAW-DEP affected their ability to repair bone defects.
Preliminary *in vitro* experiments showed that BM-MSCs exposed to SAW-DEP showed the same alkaline phosphatase expression and ability to form calcified deposits as unexposed control cells following osteoinduction.
After successful *in vitro* results, a two-phase *in vivo* study was performed, where human stem cell-seeded scaffolds were implanted into athymic rats with calvarial defects to assess the impact of cell-seeding and the treatment of the cells prior to seeding. The volume of newly formed bone in the explants was determined using micro CT. The data showed that cell seeding increased the bone formation, and that exposure to SAW-DEP prior to seeding did not affect negatively the amount of newly formed bone volume compared to control cells. To corroborate these findings further, histological analysis of the bone explants was carried out. The newly formed bone showed signs of maturity evidenced by the histological stains which revealed osteocalcin expression and the presence of lacunae and small vessels. Importantly, there was no sign of inflammation or tissue necrosis associated with the exposure to SAW-DEP.

7.2 Future directions of the SAW-DEP technology

The analysis of the dielectric properties of BM-MSCs and other white blood cell types presented in chapter 5 suggests that a single set of conditions in terms of frequency and conductivity could be used to separate BM-MSCs from B cells, T cells, monocytes, neutrophils and eosinophils. To exploit this optimal frequency and conductivity for the separation of BM-MSCs from other white blood cells, the next step would be to fabricate SAW-DEP devices operating at a range of frequencies close to the optimal frequency to test the behaviour of the cells experimentally. To investigate these devices, each characterised cell type (BM-MSCs, B cells, T cells, monocytes, neutrophils and eosinophils) should be tested individually for a range of conductivities close to the optimal conductivity revealed by the model (0.22 S/m). These experiments can then be used to determine the conditions for which the white blood cells experience negative DEP while the BM-MSCs experience positive DEP. Following the single conductivity experiments, mixtures of BM-MSCs and each of the other cell types should be tested one at a time in the devices to assess the interactions between cells and see if this would affect the separation efficiency.

It has to be anticipated that the experimental studies may reveal that BM-MSCs cannot be separated from white blood cells at the same frequency and medium conductivity with the desired yield and purity. In this case, a multi-step separation approach could be implemented. A first SAW-DEP frequency would be used to separate the BM-MSCs and the other white blood cells experiencing positive DEP from all the rest of white blood cells experiencing negative DEP. Then, successive SAW-DEP steps would be used for different frequencies or conductivities until the BM-MSCs are separated and the other cells are discarded into a waste outlet. For this, a potential SAW-DEP cell separation device would contain several different sets of IDTs designed for the specific frequencies to be applied at each stage. Ideally, all steps will be performed in the same medium and at the same conductivity. However, where this is not possible, the buffer may need to be exchanged between steps using pumps and this process will have to be accounted for when designing the fluidic setup.

The multi-step design would then be tested with a mixture of cells including MSCs and other white blood cells. Following enrichment via SAW-DEP, the FACS antibody panel described in chapter 5 could be used to assess the purity of the sample and by comparing it to the initial composition of the mixture, the enrichment factor will be determined. Each of the separation step

could be optimised and fine-tuned to ensure that the stem cell enrichment satisfies the downstream specificity requirements. After these preliminary optimisation steps, the design could be tested with either commercially supplied bone marrow aspirates or clinically relevant aspirates from patients. The clinical samples would be centrifuged prior to SAW-DEP separation in order to eliminate debris and the red blood cells would be removed using either lysis or MACS depletion. The sample could be then concentrated to achieve optimal separation and injected into the microfluidics design to undergo SAW-DEP separation.

In terms of throughput suitable for intra-operative stem cell enrichment, the 20-fold increase achieved by exploiting the vertical SAW-DEP forces is a promising development, which brings the throughput within the reach of what is needed to achieve clinically relevant separation times. One option to increase the separation rate further would be to design a highly parallel multi-channel to separate a higher volume of cells simultaneously. The multi-layered configuration presented in chapter 4 only has two output channels on different layers, which are easily scalable and expandable, as each forked channel could be further split in a second stage separation and parallelisation could be achieved without much complexity. This type of approach could also take advantage of the SAW generated in both directions from each IDT. Alternatively, the introduction of reflective gratings would increase the DEP forces generated by the SAW within a single channel, thereby decreasing alignment times and allowing for a higher throughput.

Bibliography

[1] C. J. L. Murray *et al.*, “UK health performance: Findings of the Global Burden of Disease Study 2010,” *Lancet*, vol. 381, no. 9871, pp. 997–1020, 2013, doi: 10.1016/S0140-6736(13)60355-4.

[2] P. Ignaciuk and A. Bartoszewicz, “BMUS: The Burden of Musculoskeletal Diseases in the United States,” *Communications and Control Engineering*, 2013. .

[3] L. B. Connelly, A. Woolf, and P. Brooks, “Chapter 51. Cost-Effectiveness of Interventions forMusculoskeletal Conditions,” *Dis. Control Priorities Dev. Ctries. (2nd Ed.*, pp. 963–980, 2006, doi: 10.1596/978-0-8213-6179-5/chpt-51.

[4] P. V. Giannoudis, H. Dinopoulos, and E. Tsiridis, “Bone substitutes: An update,” *Injury*, vol. 36, no. 3, pp. S20–S27, Sep. 2005, doi: 10.1016/j.injury.2005.07.029.

[5] C. R. Perry, “Bone repair techniques, bone graft, and bone graft substitutes,” in *Clinical Orthopaedics and Related Research*, 1999, no. 360, pp. 71–86, doi: 10.1097/00003086-199903000-00010.

[6] “Our plan for growth: science and innovation,” *HM Treasury*, 2014. www.gov.uk/government/publications/our-plan-for-growth-science-and-innovation (accessed Apr. 20, 2012).

[7] M. B. Coelho, J. M. S. Cabral, and J. M. Karp, “Intraoperative Stem Cell Therapy,” *Annu. Rev. Biomed. Eng.*, vol. 14, no. 1, pp. 325–349, Aug. 2012, doi: 10.1146/annurev-bioeng-071811-150041.

[8] R. J. Swijnenburg, K. E. van der Bogt, A. Y. Sheikh, F. Cao, and J. C. Wu, “Clinical hurdles for the transplantation of cardiomyocytes derived from human embryonic stem cells: role of molecular imaging,” *Current Opinion in Biotechnology*, vol. 18, no. 1. pp. 38–45, Feb. 2007, doi: 10.1016/j.copbio.2006.12.003.

[9] A. Trounson and N. D. DeWitt, “Pluripotent stem cells progressing to the clinic,” *Nature Reviews Molecular Cell Biology*, vol. 17, no. 3. Nature Publishing Group, pp. 194–200, Mar. 01, 2016, doi: 10.1038/nrm.2016.10.

[10] R. F. Mclain, J. E. Fleming, C. A. Boehm, and G. F. Muschler, “Aspiration of osteoprogenitor cells for augmenting spinal fusion: comparison of progenitor cell concentrations from the vertebral body and iliac crest,” *J Bone Jt. Surg Am* , vol. 87, no. 12, pp. 2655–2661, 2005.

[11] A. D. Mazzocca *et al.*, “Bone marrow-derived mesenchymal stem cells obtained during arthroscopic rotator cuff repair surgery show potential for tendon cell differentiation after treatment with insulin,” *Arthrosc. - J. Arthrosc. Relat. Surg.*, vol. 27, no. 11, pp. 1459–1471, Nov. 2011, doi: 10.1016/j.arthro.2011.06.029.

[12] J. Narbona-Carceles, J. Vaquero, S. B. S. Suárez-Sancho, F. Forriol, and M. E. Fernández-Santos, “Bone marrow mesenchymal stem cell aspirates from alternative sources: Is the knee as good as the iliac crest?,” *Injury*, vol. 45, no. S4, pp. S42–S47, Oct. 2014, doi: 10.1016/S0020-1383(14)70009-9.

[13] J. Chahla, S. Mannava, M. E. Cinque, A. G. Geeslin, D. Codina, and R. F. Laprade, “Bone Marrow Aspirate Concentrate Harvesting and Processing Technique,” *Arthrosc. Tech.*, vol. 6, pp. e441–e445, 2017, doi: 10.1016/j.eats.2016.10.024.

[14] B. J. Bain, “The bone marrow aspirate of healthy subjects,” 1996.

[15] M. F. Pittenger *et al.*, “Multilineage potential of adult human mesenchymal stem cells,” *Science (80-.).*, vol. 284, no. 5411, pp. 143–147, Apr. 1999, doi: 10.1126/science.284.5411.143.

[16] P. Hernigou, A. Poignard, F. Beaujean, and H. Rouard, “Percutaneous autologous bone-marrow grafting for nonunions: Influence of the number and concentration of progenitor cells,” *J. Bone Jt. Surg. - Ser. A*, vol. 87, no. 7, pp. 1430–1437, Jul. 2005, doi: 10.2106/JBJS.D.02215.

[17] F. Mouquet *et al.*, “The presence of apoptotic bone marrow cells impairs the efficacy of cardiac cell therapy,” *Cell Transplant.*, vol. 20, no. 7, pp. 1087–1097, 2011, doi: 10.3727/096368910X544924.

[18] H. J. Sun, Y. Y. Bahk, Y. R. Choi, J. H. Shim, S. H. Han, and J. W. Lee, “A proteomic analysis during serial subculture and osteogenic differentiation of human mesenchymal stem cell,” *J. Orthop. Res.*, vol. 24, no. 11, pp. 2059–2071, Nov. 2006, doi: 10.1002/jor.20273.

[19] European Medicines Agency, “Scientific recommendation on classification of advanced

therapy medicinal products Article 17 - Regulation No 1394/2007," Apr. 2019. Accessed: Mar. 07, 2021. [Online]. Available: https://www.ema.europa.eu/en/documents/report/scientific-recommendation-classification-advanced-therapy-medicinal-products-ex-vivo-expanded_en-3.pdf.

[20] MHRA, "Advanced therapy medicinal products: regulation and licensing," 2015. https://www.gov.uk/guidance/advanced-therapy-medicinal-products-regulation-and-licensing.

[21] A. V. Cuomo, M. Virk, F. Petrigliano, E. F. Morgan, and J. R. Lieberman, "Mesenchymal stem cell concentration and bone repair: Potential pitfalls from bench to bedside," *J. Bone Jt. Surg. - Ser. A*, vol. 91, no. 5, pp. 1073–1083, May 2009, doi: 10.2106/JBJS.H.00303.

[22] V. Dexheimer, S. Mueller, F. Braatz, and W. Richter, "Reduced reactivation from dormancy but maintained lineage choice of human mesenchymal stem cells with donor age," *PLoS One*, vol. 6, no. 8, 2011, doi: 10.1371/journal.pone.0022980.

[23] X. Wang, K. Ye, Z. Li, C. Yan, and J. Ding, "Adhesion, proliferation, and differentiation of mesenchymal stem cells on RGD nanopatterns of varied nanospacings," *Organogenesis*, vol. 9, no. 4, pp. 280–286, Oct. 2013, doi: 10.4161/org.26080.

[24] D. G. Phinney, G. Kopen, R. L. Isaacson, and D. J. Prockop, "Plastic adherent stromal cells from the bone marrow of commonly used strains of inbred mice: Variations in yield, growth, and differentiation," *J. Cell. Biochem.*, vol. 72, no. 4, pp. 570–585, Mar. 1999, doi: 10.1002/(SICI)1097-4644(19990315)72:4<570::AID-JCB12>3.0.CO;2-W.

[25] P. Hernigou, O. Manicom, A. Poignard, A. Nogier, P. Filippini, and L. De Abreu, "Core decompression with marrow stem cells," *Oper. Tech. Orthop.*, vol. 14, no. 2, pp. 68–74, Apr. 2004, doi: 10.1053/j.oto.2004.03.001.

[26] D. Brodke *et al.*, "Bone grafts prepared with selective cell retention technology heal canine segmental defects as effectively as autograft," *J. Orthop. Res.*, vol. 24, no. 5, pp. 857–866, May 2006, doi: 10.1002/jor.20094.

[27] G. F. Muschler *et al.*, "Selective retention of bone marrow-derived cells to enhance spinal fusion," *Clin. Orthop. Relat. Res.*, no. 432, pp. 242–251, 2005, doi: 10.1097/01.blo.0000149812.32857.8b.

[28] G. Oster and M. Yamamoto, "Density gradient techniques," *Chem. Rev.*, vol. 63, no. 3, pp. 257–268, Jun. 1963, doi: 10.1021/cr60223a003.

[29] V. Salunkhe, P. Papadopoulos, and L. Gutiérrez, "Culture of Megakaryocytes from Human Peripheral Blood Mononuclear Cells," 2015. [Online]. Available: http://www.bio-protocol.org/e1639.

[30] C. Pösel, K. Möller, W. Fröhlich, I. Schulz, J. Boltze, and D. C. Wagner, "Density Gradient Centrifugation Compromises Bone Marrow Mononuclear Cell Yield," *PLoS One*, vol. 7, no. 12, Dec. 2012, doi: 10.1371/journal.pone.0050293.

[31] B. Assmus *et al.*, "Red Blood Cell Contamination of the Final Cell Product Impairs the Efficacy of Autologous Bone Marrow Mononuclear Cell Therapy," *J. Am. Coll. Cardiol.*, vol. 55, no. 13, pp. 1385–1394, Mar. 2010, doi: 10.1016/j.jacc.2009.10.059.

[32] H. Pertoft, T. C. Laurent, T. Låås, and L. Kågedal, "Density gradients prepared from colloidal silica particles coated by polyvinylpyrrolidone (Percoll)," *Anal. Biochem.*, vol. 88, no. 1, pp. 271–282, Jul. 1978, doi: 10.1016/0003-2697(78)90419-0.

[33] D. Bhartiya *et al.*, "Very Small Embryonic-Like Stem Cells with Maximum Regenerative Potential Get Discarded During Cord Blood Banking and Bone Marrow Processing for Autologous Stem Cell Therapy," *Stem Cells Dev.*, vol. 21, no. 1, pp. 1–6, Jan. 2011, doi: 10.1089/scd.2011.0311.

[34] N. Ahmadbeigi *et al.*, "The aggregate nature of human mesenchymal stromal cells in native bone marrow," *Cytotherapy*, vol. 14, no. 8, pp. 917–924, 2012, doi: 10.3109/14653249.2012.689426.

[35] F. H. Seeger, T. Tonn, N. Krzossok, A. M. Zeiher, and S. Dimmeler, "Cell isolation procedures matter: a comparison of different isolation protocols of bone marrow mononuclear cells used for cell therapy in patients with acute myocardial infarction," *Eur. Heart J.*, vol. 28, pp. 766–772, 2007, doi: 10.1093/eurheartj/ehm009.

[36] J. Friend and L. Y. Yeo, "Microscale acoustofluidics: Microfluidics driven via acoustics and ultrasonics," *Rev. Mod. Phys.*, vol. 83, no. 2, pp. 647–704, Jun. 2011, doi: 10.1103/RevModPhys.83.647.

[37] L. Y. Yeo and J. R. Friend, "Surface acoustic wave microfluidics," *Annu. Rev. Fluid Mech.*, vol. 46, pp. 379–406, Jan. 2014, doi: 10.1146/annurev-fluid-010313-141418.

[38] J. Shi, H. Huang, Z. Stratton, Y. Huang, and T. J. Huang, “Continuous particle separation in a microfluidic channel via standing surface acoustic waves (SSAW),” *Lab Chip*, vol. 9, pp. 3354–3359, 2009, doi: 10.1039/b915113c.

[39] J. Nam, H. Lim, D. Kim, and S. Shin, “Separation of platelets from whole blood using standing surface acoustic waves in a microchannel,” *Lab Chip*, vol. 11, no. 19, pp. 3361–3364, Oct. 2011, doi: 10.1039/c1lc20346k.

[40] L. R. Huang, E. C. Cox, R. H. Austin, and J. C. Sturm, “Continuous Particle Separation Through Deterministic Lateral Displacement,” *Science (80-.).*, vol. 304, no. 5673, pp. 987–990, 2004, doi: 10.1126/science.1094567.

[41] T. Salafi, Y. Zhang, and Y. Zhang, “A Review on Deterministic Lateral Displacement for Particle Separation and Detection,” *Nano-Micro Letters*, vol. 11, no. 1. SpringerOpen, p. 3, 2019, doi: 10.1007/s40820-019-0308-7.

[42] Z. Zhang, E. Henry, G. Gompper, and D. A. Fedosov, “Behavior of rigid and deformable particles in deterministic lateral displacement devices with different post shapes,” *J. Chem. Phys.*, vol. 143, no. 24, p. 243145, 2015, doi: 10.1063/1.4937171.

[43] S. Ye, X. Shao, Z. Yu, and W. Yu, “Effects of the particle deformability on the critical separation diameter in the deterministic lateral displacement device,” *J. Fluid Mech.*, vol. 743, pp. 60–74, 2014, doi: 10.1017/jfm.2014.22.

[44] G. Kabacaoğlu and G. Biros, “Sorting same-size red blood cells in deep deterministic lateral displacement devices,” *J. Fluid Mech.*, vol. 859, pp. 433–475, 2018, doi: 10.1017/jfm.2018.829.

[45] G. Kabacaoğlu and G. Biros, “Optimal design of deterministic lateral displacement device for viscosity-contrast-based cell sorting,” *Phys. Rev. Fluids*, vol. 3, no. 12, p. 124201, 2018, doi: 10.1103/PhysRevFluids.3.124201.

[46] E. Henry *et al.*, “Sorting cells by their dynamical properties,” *Sci. Rep.*, vol. 6, no. 1, pp. 1–11, 2016, doi: 10.1038/srep34375.

[47] M. Al-Fandi, M. Al-Rousan, M. A. K. Jaradat, and L. Al-Ebbini, “New design for the separation of microorganisms using microfluidic deterministic lateral displacement,” *Robot. Comput. Integr. Manuf.*, vol. 27, no. 2, pp. 237–244, 2011, doi: 10.1016/j.rcim.2010.06.003.

[48] K. K. Zeming, S. Ranjan, and Y. Zhang, “Rotational separation of non-spherical bioparticles using I-shaped pillar arrays in a microfluidic device,” *Nat. Commun.*, vol. 4, no. 1, pp. 1–8, 2013, doi: 10.1038/ncomms2653.

[49] M. Xavier *et al.*, “Label-free enrichment of primary human skeletal progenitor cells using deterministic lateral displacement,” *Lab Chip*, vol. 19, no. 3, pp. 513–523, 2019, doi: 10.1039/c8lc01154k.

[50] H. Okano *et al.*, “Enrichment of circulating tumor cells in tumor-bearing mouse blood by a deterministic lateral displacement microfluidic device,” *Biomed. Microdevices*, vol. 17, no. 3, pp. 1–11, 2015, doi: 10.1007/s10544-015-9964-7.

[51] C. I. Civin *et al.*, “Automated leukocyte processing by microfluidic deterministic lateral displacement,” *Cytom. Part A*, vol. 89, no. 12, pp. 1073–1083, 2016, doi: 10.1002/cyto.a.23019.

[52] J. P. Beech, S. H. Holm, K. Adolfsson, and J. O. Tegenfeldt, “Sorting cells by size, shape and deformability,” *Lab Chip*, vol. 12, no. 6, pp. 1048–1051, 2012, doi: 10.1039/c2lc21083e.

[53] B. M. Dincau, A. Aghilinejad, T. Hammersley, X. Chen, and J. H. Kim, “Deterministic lateral displacement (DLD) in the high Reynolds number regime: high-throughput and dynamic separation characteristics,” *Microfluid. Nanofluidics*, vol. 22, no. 6, p. 59, 2018, doi: 10.1007/s10404-018-2078-9.

[54] J. chul Hyun, J. Hyun, S. Wang, and S. Yang, “Improved pillar shape for deterministic lateral displacement separation method to maintain separation efficiency over a long period of time,” *Sep. Purif. Technol.*, vol. 172, pp. 258–267, Jan. 2017, doi: 10.1016/j.seppur.2016.08.023.

[55] T. Gregory, “Cell size database,” 2005. bionumbers.hms.harvard.edu.

[56] Abcam, “CD Antigens,” 2009. http://docs.abcam.com/pdf/immunology/cdantigen_poster.pdf %0A%0A.

[57] S. Basu, H. M. Campbell, B. N. Dittel, and A. Ray, “Purification of Specific Cell Population by Fluorescence Activated Cell Sorting (FACS),” *J. Vis. Exp.*, no. 41, Jul. 2010, doi: 10.3791/1546.

[58] A. L. Givan, *Flow Cytometry: First Principles*. New York, USA: John Wiley & Sons, Inc., 2001.

[59] S. Sabban, H. Ye, and B. Helm, “Development of an in vitro model system for studying the interaction of Equus caballus IgE with its high-affinity receptor FcεRI,” *J. Vis. Exp*, no. 93, p. 52222, 2014, doi: 10.3791/52222.

[60] M. A. McClain, C. T. Culbertson, S. C. Jacobson, and J. M. Ramsey, “Flow cytometry of Escherichia coli on microfluidic devices,” *Anal. Chem.*, vol. 73, no. 21, pp. 5334–5338, Nov. 2001, doi: 10.1021/ac010504v.

[61] B. Yao, G. A. Luo, X. Feng, W. Wang, L. X. Chen, and Y. M. Wang, “A microfluidic device based on gravity and electric force driving for flow cytometry and fluorescence activated cell sorting,” *Lab Chip*, vol. 4, no. 6, pp. 603–607, 2004, doi: 10.1039/b408422e.

[62] L. Bonetta, “Flow cytometry smaller and better,” *Nat. Methods*, vol. 2, no. 10, pp. 785–794, Oct. 2005, doi: 10.1038/nmeth1005-785.

[63] S. H. Cho, C. H. Chen, F. S. Tsai, J. M. Godin, and Y. H. Lo, “Human mammalian cell sorting using a highly integrated micro-fabricated fluorescence-activated cell sorter (μFACS),” *Lab Chip*, vol. 10, no. 12, pp. 1567–1573, 2010, doi: 10.1039/c000136h.

[64] R. Marek, M. Caruso, A. Rostami, J. B. Grinspan, and J. Das Sarma, “Magnetic cell sorting: A fast and effective method of concurrent isolation of high purity viable astrocytes and microglia from neonatal mouse brain tissue,” *J. Neurosci. Methods*, vol. 175, no. 1, pp. 108–118, Oct. 2008, doi: 10.1016/j.jneumeth.2008.08.016.

[65] H. Valli *et al.*, “Fluorescence- and magnetic-activated cell sorting strategies to isolate and enrich human spermatogonial stem cells,” *Fertil. Steril.*, vol. 102, no. 2, p. 566–580.e7, 2014, doi: 10.1016/j.fertnstert.2014.04.036.

[66] Elveflow, “Commercial magnetic particle separation – MACS,” 2014. http://www.elveflow.com/microfluidic-tutorials/microfluidic-reviews-and-tutorials/magnetic-particle-separation-a-short-review/commercial-magnetic-particle-separation-macs/.

[67] “MACS® MicroBeads,” 2016. http://www.miltenyibiotec.com/en/products-and-services/macs-cell-separation/macs-technology/microbeads_dp.aspx.

[68] M. Zborowski, L. Sun, L. R. Moore, P. Stephen Williams, and J. J. Chalmers, “Continuous cell separation using novel magnetic quadrupole flow sorter,” *J. Magn. Magn. Mater.*, vol. 194, no. 1, pp. 224–230, 1999, doi: 10.1016/S0304-8853(98)00581-2.

[69] M. A. Voinov, J. O. S. Pagán, E. Morrison, T. I. Smirnova, and A. I. Smirnov, “Surface-mediated production of hydroxyl radicals as a mechanism of iron oxide nanoparticle biotoxicity,” *J. Am. Chem. Soc.*, vol. 133, no. 1, pp. 35–41, Jan. 2011, doi: 10.1021/ja104683w.

[70] S. J. H. Soenen, U. Himmelreich, N. Nuytten, and M. De Cuyper, “Cytotoxic effects of iron oxide nanoparticles and implications for safety in cell labelling,” *Biomaterials*, vol. 32, no. 1, pp. 195–205, Jan. 2011, doi: 10.1016/j.biomaterials.2010.08.075.

[71] Pluriselect, “Pluribeads,” 2017, [Online]. Available: https://pluriselect.com/pluribead-cascade.html.

[72] A. Kumar and A. Srivastava, “Cell separation using cryogel-based affinity chromatography,” *Nat. Protoc.*, vol. 5, no. 11, pp. 1737–1747, Oct. 2010, doi: 10.1038/nprot.2010.135.

[73] T. T. Goodchild *et al.*, “Bone Marrow-Derived B Cells Preserve Ventricular Function After Acute Myocardial Infarction,” *JACC Cardiovasc. Interv.*, vol. 2, no. 10, pp. 1005–1016, Oct. 2009, doi: 10.1016/j.jcin.2009.08.010.

[74] H. Takigami *et al.*, “Bone formation following OP-1 implantation is improved by addition of autogenous bone marrow cells in a canine femur defect model,” *J. Orthop. Res.*, vol. 25, no. 10, pp. 1333–1342, Oct. 2007, doi: 10.1002/jor.20411.

[75] H. A. Pohl and I. Hawk, “Separation of Living and Dead Cells by Dielectrophoresis,” 1966. [Online]. Available: http://science.sciencemag.org/.

[76] I. Doh and Y. H. Cho, “A continuous cell separation chip using hydrodynamic dielectrophoresis (DEP) process,” *Sensors Actuators, A Phys.*, vol. 121, no. 1, pp. 59–65, May 2005, doi: 10.1016/j.sna.2005.01.030.

[77] F. Yang, X. Yang, H. Jiang, W. M. Butler, and G. Wang, “Dielectrophoretic Separation of Prostate Cancer Cells,” *Technol. Cancer Res. Treat.*, vol. 12, no. 1, pp. 61–70, Aug. 2012, doi: 10.7785/tcrt.2012.500275.

[78] M. P. Hughes, “Fifty years of dielectrophoretic cell separation technology,” *Biomicrofluidics*, vol. 10, no. 3, 2016, doi: 10.1063/1.4954841.

[79] R. Pethig, “Dielectrophoresis: Status of the theory, technology, and applications,”

Biomicrofluidics, vol. 4, no. 2, Jun. 2010, doi: 10.1063/1.3456626.

[80] S. Yan *et al.*, “On-chip high-throughput manipulation of particles in a dielectrophoresis- active hydrophoretic focuser,” *Sci. Rep.*, vol. 4, May 2014, doi: 10.1038/srep05060.

[81] P. R. C. Gascoyne, Y. Huang, R. Pethig, J. Vykoukal, and F. F. Becker, “Dielectrophoretic separation of mammalian cells studied by computerized image analysis,” *Meas. Sci. Technol.*, vol. 3, no. 5, pp. 439–445, May 1992, doi: 10.1088/0957-0233/3/5/001.

[82] Y. Kang, D. Li, S. A. Kalams, and J. E. Eid, “DC-Dielectrophoretic separation of biological cells by size,” *Biomed. Microdevices*, vol. 10, no. 2, pp. 243–249, Apr. 2008, doi: 10.1007/s10544-007-9130-y.

[83] J. C. Giddings, “A New Separation Concept Based on a Coupling of Concentration and Flow Nonuniformities,” *Sep. Sci.*, vol. 1, no. 1, pp. 123–125, Jan. 1966, doi: 10.1080/01496396608049439.

[84] P. J. P. Cardot, J. Gerota, and M. Martin, “Separation of living red blood cells by gravitational field-flow fractionation,” *J. Chromatogr. B Biomed. Sci. Appl.*, vol. 568, no. 1, pp. 93–103, Jul. 1991, doi: 10.1016/0378-4347(91)80343-B.

[85] B. Barman, E. R. Ashwood, and J. C. Giddings, “Separation and size distribution of red blood cells of diverse size, shape, and origin by flow/hyperlayer field-flow fractionation,” *Anal Biochem*, vol. 212, no. 1, pp. 35–42, 1993.

[86] V. Yue, R. Kowal, L. Neargarder, L. Bond, A. Muetterties, and R. Parsons, “Miniature field-flow fractionation system for analysis of blood cells,” in *Clinical Chemistry*, 1994, vol. 40, no. 9, pp. 1810–1814.

[87] X. B. Wang, J. Yang, Y. Huang, J. Vykoukal, F. F. Becker, and P. R. C. Gascoyne, “Cell separation by dielectrophoretic field-flow-fractionation,” *Anal. Chem.*, vol. 72, no. 4, pp. 832–839, 2000, doi: 10.1021/ac990922o.

[88] G. H. Markx, J. Rousselet, and R. Pethig, “DEP-FFF Field-flow fractionation using non-uniform electric fields,” *J. Liq. Chromatogr. Relat. Technol.*, vol. 20, no. 16–17, pp. 2857–2872, 1997, doi: 10.1080/10826079708005597.

[89] Y. Huang, X.-B. Wang, F. F. Becker, and P. R. C. Gascoyne, “Introducing Dielectrophoresis as a New Force Field for Field-Flow Fractionation,” 1997.

[90] X. B. Wang, J. Vykoukal, F. F. Becker, and P. R. C. Gascoyne, “Separation of polystyrene microbeads using dielectrophoretic/gravitational field-flow-fractionation,” *Biophys. J.*, vol. 74, no. 5, pp. 2689–2701, 1998, doi: 10.1016/S0006-3495(98)77975-5.

[91] V. Gupta *et al.*, “ApoStream™, a new dielectrophoretic device for antibody independent isolation and recovery of viable cancer cells from blood,” *Biomicrofluidics*, vol. 6, no. 2, pp. 1–14, 2012, doi: 10.1063/1.4731647.

[92] L. Wang, L. A. Flanagan, N. L. Jeon, E. Monuki, and A. P. Lee, “Dielectrophoresis switching with vertical sidewall electrodes for microfluidic flow cytometry,” *Lab Chip*, vol. 7, no. 9, pp. 1114–1120, 2007, doi: 10.1039/b705386j.

[93] J. Voldman, M. L. Gray, M. Toner, and M. A. Schmidt, “A microfabrication-based dynamic array cytometer,” *Anal. Chem.*, vol. 74, no. 16, pp. 3984–3990, 2002, doi: 10.1021/ac0256235.

[94] R. Martinez-Duarte, P. Renaud, and M. J. Madou, “A novel approach to dielectrophoresis using carbon electrodes,” *Electrophoresis*, vol. 32, no. 17, p. n/a-n/a, 2011, doi: 10.1002/elps.201100059.

[95] C. Wang, G. Jia, L. H. Taherabadi, and M. J. Madou, “A novel method for the fabrication of high-aspect ratio C-MEMS structures,” *J. Microelectromechanical Syst.*, vol. 14, no. 2, pp. 348–358, 2005, doi: 10.1109/JMEMS.2004.839312.

[96] M. A. A. Razak, K. F. Hoettges, H. O. Fatoyinbo, F. H. Labeed, and M. P. Hughes, “Efficient dielectrophoretic cell enrichment using a dielectrophoresis-well based system,” *Biomicrofluidics*, vol. 7, no. 6, p. 64110, 2013, doi: 10.1063/1.4842395.

[97] H. O. Fatoyinbo, D. Kamchis, R. Whattingham, S. L. Ogin, and M. P. Hughes, “A high-throughput 3-D composite dielectrophoretic separator,” *IEEE Trans. Biomed. Eng.*, vol. 52, no. 7, pp. 1347–1349, 2005, doi: 10.1109/TBME.2005.847553.

[98] S. A. Faraghat *et al.*, “High-Throughput, low-loss, low-cost, and label-free cell separation using electrophysiology-Activated cell enrichment,” *Proc. Natl. Acad. Sci. U. S. A.*, vol. 114, no. 18, pp. 4591–4596, 2017, doi: 10.1073/pnas.1700773114.

[99] “DEParator.” https://deparator.com/elementor-204/.

[100] H. Shafiee, J. L. Caldwell, M. B. Sano, and R. V. Davalos, “Contactless dielectrophoresis: A new technique for cell manipulation,” *Biomed. Microdevices*, vol. 11, no. 5, pp. 997–1006, Oct. 2009, doi: 10.1007/s10544-009-9317-5.

[101] N. Demierre, T. Braschler, P. Linderholm, U. Seger, H. Van Lintel, and P. Renaud, “Characterization and optimization of liquid electrodes for lateral dielectrophoresis,” *Lab Chip*, 2006, doi: 10.1039/b612866a.

[102] R. Pethig, M. S. Talary, and R. S. Lee, “Enhancing Traveling-Wave Dielectrophoresis with Signal Superposition,” *IEEE Eng. Med. Biol. Mag.*, vol. 22, no. 6, pp. 43–50, Nov. 2003, doi: 10.1109/MEMB.2003.1266046.

[103] N. Demierre, T. Braschler, R. Muller, and P. Renaud, “Focusing and continuous separation of cells in a microfluidic device using lateral dielectrophoresis,” *Sensors Actuators, B Chem.*, vol. 132, no. 2, pp. 388–396, Jun. 2008, doi: 10.1016/j.snb.2007.09.078.

[104] T. Braschler, N. Demierre, E. Nascimento, T. Silva, A. G. Oliva, and P. Renaud, “Continuous separation of cells by balanced dielectrophoretic forces at multiple frequencies{,” *Lab Chip*, 2007, doi: 10.1039/b710303d.

[105] A. Valero, T. Braschler, N. Demierre, and P. Renaud, “A miniaturized continuous dielectrophoretic cell sorter and its applications,” *Biomicrofluidics*, vol. 4, no. 2, pp. 1–9, 2010, doi: 10.1063/1.3430542.

[106] S. Masuda, M. Washizu, and T. Nanba, “Novel Method Of Cell Fusion In Field Constriction Area In Fluid Integrated Circuit,” *IEEE Trans. Ind. Appl.*, vol. 25, no. 4, pp. 732–737, 1989, doi: 10.1109/28.31255.

[107] E. B. Cummings and A. K. Singh, “Dielectrophoresis in microchips containing arrays of insulating posts: Theoretical and experimental results,” *Anal. Chem.*, vol. 75, no. 18, pp. 4724–4731, Sep. 2003, doi: 10.1021/ac0340612.

[108] M. Washizu, T. Nanba, and S. Masuda, “Handling Biological Cells Using a Fluid Integrated Circuit,” *IEEE Trans. Ind. Appl.*, vol. 26, no. 2, pp. 352–358, 1990, doi: 10.1109/28.54263.

[109] B. H. Lapizco-Encinas, “On the recent developments of insulator-based dielectrophoresis: A review,” *Electrophoresis*, vol. 40, no. 3, pp. 358–375, 2019, doi: 10.1002/elps.201800285.

[110] B. H. Lapizco-Encinas, B. A. Simmons, E. B. Cummings, and Y. Fintschenko, “Insulator-based dielectrophoresis for the selective concentration and separation of live bacteria in water,” *Electrophoresis*, vol. 25, no. 1011, pp. 1695–1704, Jun. 2004, doi: 10.1002/elps.200405899.

[111] H. Moncada-Hernández and B. H. Lapizco-Encinas, “Simultaneous concentration and separation of microorganisms: insulator-based dielectrophoretic approach,” *Anal. Bioanal. Chem.*, vol. 396, no. 5, pp. 1805–1816, 2010, doi: 10.1007/s00216-009-3422-4.

[112] C. P. Jen, C. Te Huang, and H. Y. Shih, “Hydrodynamic separation of cells utilizing insulator-based dielectrophoresis,” in *Microsystem Technologies*, Jul. 2010, vol. 16, no. 7, pp. 1097–1104, doi: 10.1007/s00542-009-0947-6.

[113] L. M. Barrett, A. J. Skulan, A. K. Singh, E. B. Cummings, and G. J. Fiechtner, “Dielectrophoretic Manipulation of Particles and Cells Using Insulating Ridges in Faceted Prism Microchannels,” *Anal Chem*, vol. 77, no. 1, pp. 6798–6804, 2005, doi: 10.1021/ac0507791.

[114] D. Nakidde *et al.*, “Three dimensional passivated-electrode insulator-based dielectrophoresis,” *Biomicrofluidics*, vol. 9, no. 1, p. 14125, 2015, doi: 10.1063/1.4913497.

[115] J. Suehiro, G. Zhou, M. Imamura, and M. Hara, “Dielectrophoretic filter for separation and recovery of biological cells in water,” *IEEE Trans. Ind. Appl.*, vol. 39, no. 5, pp. 1514–1521, 2003, doi: 10.1109/TIA.2003.816535.

[116] C. Iliescu, G. Xu, F. C. Loe, P. L. Ong, and F. E. H. Tay, “A 3-D dielectrophoretic filter chip,” *Electrophoresis*, vol. 28, no. 7, pp. 1107–1114, 2007, doi: 10.1002/elps.200600431.

[117] B. A. Simmons, G. J. McGraw, R. V. Davalos, G. J. Fiechtner, Y. Fintschenko, and E. B. Cummings, “The development of polymeric devices as dielectrophoretic separators and concentrators,” *MRS Bull.*, vol. 31, no. 2, pp. 120–124, 2006, doi: 10.1557/mrs2006.26.

[118] B. G. Hawkins and B. J. Kirby, “Electrothermal flow effects in insulating (electrodeless) dielectrophoresis systems,” *Electrophoresis*, vol. 31, no. 22, pp. 3622–3633, 2010, doi: 10.1002/elps.201000429.

[119] R. A. Prabhakaran *et al.*, “Joule heating effects on electroosmotic entry flow,” *Electrophoresis*, vol. 38, no. 5, pp. 572–579, Mar. 2017, doi: 10.1002/elps.201600296.

[120] T. A. Nguyen, T. I. Yin, D. Reyes, and G. A. Urban, “Microfluidic chip with integrated electrical cell-impedance sensing for monitoring single cancer cell migration in three-dimensional matrixes,” *Anal. Chem.*, vol. 85, no. 22, pp. 11068–11076, Nov. 2013, doi: 10.1021/ac402761s.

[121] C. R. Keese, J. Wegener, S. R. Walker, and I. Giaever, “Electrical wound-healing assay for cells in vitro,” *Proc. Natl. Acad. Sci. U. S. A.*, vol. 101, no. 6, pp. 1554–1559, Feb. 2004, doi: 10.1073/pnas.0307588100.

[122] M. Evander, A. J. Ricco, J. Morser, G. T. A. Kovacs, L. L. K. Leung, and L. Giovangrandi, “Microfluidic impedance cytometer for platelet analysis,” *Lab Chip*, vol. 13, no. 4, pp. 722–729, Feb. 2013, doi: 10.1039/c2lc40896a.

[123] W. . Coulter, “High speed automatic blood cell counter and cell size analyzer,” *Proc Natl Electron Conf.*, vol. 12, pp. 1034–1040, 1956.

[124] R. A. Hoffman and W. B. Britt, “Flow-system measurement of cell impedance properties,” *J. Histochem. Cytochem.*, vol. 27, no. 1, pp. 234–240, 1979, doi: 10.1177/27.1.374580.

[125] D. Satake *et al.*, “A sensor for blood cell counter using MEMS technology,” in *Sensors and Actuators, B: Chemical*, Mar. 2002, vol. 83, no. 1–3, pp. 77–81, doi: 10.1016/S0925-4005(01)01045-0.

[126] S. Gawad, L. Schild, and P. Renaud, “Micromachined impedance spectroscopy flow cytometer for cell analysis and particle sizing,” *Lab Chip*, vol. 1, no. 1, pp. 76–82, Sep. 2001, doi: 10.1039/b103933b.

[127] M. Xavier, M. C. De Andres, D. Spencer, R. O. C. Oreffo, and H. Morgan, “Size and dielectric properties of skeletal stem cells change critically after enrichment and expansion from human bone marrow: Consequences for microfluidic cell sorting,” *J. R. Soc. Interface*, vol. 14, no. 133, 2017, doi: 10.1098/rsif.2017.0233.

[128] D. Holmes *et al.*, “Leukocyte analysis and differentiation using high speed microfluidic single cell impedance cytometry,” *Lab Chip*, vol. 9, no. 20, pp. 2881–2889, 2009, doi: 10.1039/b910053a.

[129] H. Morgan, T. Sun, D. Holmes, S. Gawad, and N. G. Green, “Single cell dielectric spectroscopy,” *J. Phys. D Appl. Phys*, vol. 40, pp. 61–70, 2007, doi: 10.1088/0022-3727/40/1/S10.

[130] X. Han, C. van Berkel, J. Gwyer, L. Capretto, and H. Morgan, “Microfluidic Lysis of Human Blood for Leukocyte Analysis Using Single Cell Impedance Cytometry,” *Anal. Chem.*, vol. 84, no. 2, pp. 1070–1075, Jan. 2012, doi: 10.1021/ac202700x.

[131] J. Hong, K. Kandasamy, M. Marimuthu, C. S. Choi, and S. Kim, “Electrical cell-substrate impedance sensing as a non-invasive tool for cancer cell study,” *Analyst*, vol. 136, no. 2. Royal Society of Chemistry, pp. 237–245, Jan. 21, 2011, doi: 10.1039/c0an00560f.

[132] H. Pick, S. Terrettaz, O. Baud, O. Laribi, C. Brisken, and H. Vogel, “Monitoring proliferative activities of hormone-like odorants in human breast cancer cells by gene transcription profiling and electrical impedance spectroscopy,” *Biosens. Bioelectron.*, vol. 50, pp. 431–436, Dec. 2013, doi: 10.1016/j.bios.2013.06.052.

[133] V. S. Hollis, J. A. Holloway, S. Harris, D. Spencer, C. van Berkel, and H. Morgan, “Comparison of Venous and Capillary Differential Leukocyte Counts Using a Standard Hematology Analyzer and a Novel Microfluidic Impedance Cytometer,” *PLoS One*, vol. 7, no. 9, p. e43702, Sep. 2012, doi: 10.1371/journal.pone.0043702.

[134] Y. Xu, X. Xie, Y. Duan, L. Wang, Z. Cheng, and J. Cheng, “A review of impedance measurements of whole cells,” *Biosensors and Bioelectronics*, vol. 77. Elsevier Ltd, pp. 824–836, Mar. 15, 2016, doi: 10.1016/j.bios.2015.10.027.

[135] G. Schade-Kampmann, A. Huwiler, M. Hebeisen, T. Hessler, and M. Di Berardino, “On-chip non-invasive and label-free cell discrimination by impedance spectroscopy,” *Cell Prolif.*, vol. 41, no. 5, pp. 830–840, Oct. 2008, doi: 10.1111/j.1365-2184.2008.00548.x.

[136] S. Crocetti *et al.*, “Impedance flow cytometry gauges proliferative capacity by detecting TRPC1 expression,” *Cytom. Part A*, vol. 85, no. 6, pp. 525–536, Jun. 2014, doi: 10.1002/cyto.a.22461.

[137] T. Smorodin, U. Beierlein, J. Ebbecke, and A. Wixforth, “Surface-Acoustic-Wave-Enhanced Alignment of Thiolated Carbon Nanotubes on Gold Electrodes,” *Small*, vol. 1, no. 12, pp. 1188–1190, Dec. 2005, doi: 10.1002/smll.200500208.

[138] K. M. Seemann, J. Ebbecke, and A. Wixforth, “Alignment of carbon nanotubes on pre-structured silicon by surface acoustic waves,” *Nanotechnology*, vol. 17, no. 17, pp. 4529–

4532, Aug. 2006, doi: 10.1088/0957-4484/17/17/040.

[139] X. H. Kong *et al.*, “Surface acoustic wave mediated dielectrophoretic alignment of rolled-up microtubes in microfluidic systems,” *Appl. Phys. Lett.*, vol. 96, no. 13, 2010, doi: 10.1063/1.3371708.

[140] A. J. Smith *et al.*, “Rapid cell separation with minimal manipulation for autologous cell therapies,” *Sci. Rep.*, vol. 7, 2017, doi: 10.1038/srep41872.

[141] A. Smith, “Surface acoustic wave-induced dielectrophoresis: Lab on a Chip cell sorting technology for autologous cell therapies,” 2017.

[142] H. A. Pohl and J. S. Crane, “Dielectrophoresis of Cells,” *Biophys. J.*, vol. 11, no. 9, pp. 711–727, 1971, doi: 10.1016/S0006-3495(71)86249-5.

[143] L. M. Broche, F. H. Labeed, and M. P. Hughes, “Extraction of dielectric properties of multiple populations from dielectrophoretic collection spectrum data,” *Phys. Med. Biol.*, vol. 50, no. 10, pp. 2267–2274, 2005, doi: 10.1088/0031-9155/50/10/006.

[144] R. Pethig, L. M. Jakubek, R. H. Sanger, E. Heart, E. D. Corson, and P. J. S. Smith, “Electrokinetic measurements of membrane capacitance and conductance for pancreatic β-cells,” *IEE Proc. Nanobiotechnology*, vol. 152, no. 6, pp. 189–193, Dec. 2005, doi: 10.1049/ip-nbt:20050040.

[145] L. M. Broche, K. F. Hoettges, S. L. Ogin, G. E. N. Kass, and M. P. Hughes, “Rapid, automated measurement of dielectrophoretic forces using DEP-activated microwells,” *Electrophoresis*, vol. 32, no. 17, p. n/a-n/a, Jul. 2011, doi: 10.1002/elps.201100063.

[146] D. M. Vykoukal, P. R. C. Gascoyne, and J. Vykoukal, “Dielectric characterization of complete mononuclear and polymorphonuclear blood cell subpopulations for label-free discrimination,” *Integr. Biol.*, vol. 1, no. 7, pp. 477–484, 2009, doi: 10.1039/b906137a.

[147] H. Fricke and S. Morse, “The electric resistance and capacity of blood for frequencies between 800 and 41/2 million cycles,” *J. Gen. Physiol.*, vol. 9, no. 2, pp. 153–167, Nov. 1925, doi: 10.1085/jgp.9.2.153.

[148] H. P. SCHWAN, “Electrical properties of tissue and cell suspensions.,” *Adv. Biol. Med. Phys.*, vol. 5, pp. 147–209, 1957, doi: 10.1016/b978-1-4832-3111-2.50008-0.

[149] R. Pethig and D. B. Kell, “The passive electrical properties of biological systems: Their significance in physiology, biophysics and biotechnology,” *Phys. Med. Biol.*, vol. 32, no. 8, pp. 933–970, 1987, doi: 10.1088/0031-9155/32/8/001.

[150] K. R. Foster and H. P. Schwan, “Dielectric properties of tissues and biological materials: a critical review.,” *Crit. Rev. Biomed. Eng.*, vol. 17, no. 1, pp. 25–104, Jan. 1989, Accessed: Dec. 28, 2020. [Online]. Available: https://europepmc.org/article/med/2651001.

[151] W. Gu and Y. Zhao, “Cellular electrical impedance spectroscopy: An emerging technology of microscale biosensors,” *Expert Review of Medical Devices*, vol. 7, no. 6. Expert Rev Med Devices, pp. 767–779, Nov. 2010, doi: 10.1586/erd.10.47.

[152] C. Xiaoa and J. H. T. Luong, “A simple mathematical model for electric cell-substrate impedance sensing with extended applications,” *Biosens. Bioelectron.*, vol. 25, no. 7, pp. 1774–1780, Mar. 2010, doi: 10.1016/j.bios.2009.12.025.

[153] T. S. Hug, “Biophysical Methods for Monitoring Cell-Substrate Interactions in Drug Discovery,” *Assay and Drug Development Technologies*, vol. 1, no. 3. Mary Ann Liebert Inc., pp. 479–488, Jun. 01, 2003, doi: 10.1089/154065803322163795.

[154] A. R. A. Rahman, C. M. Lo, and S. Bhansali, “A detailed model for high-frequency impedance characterization of ovarian cancer epithelial cell layer using ECIS electrodes,” *IEEE Trans. Biomed. Eng.*, vol. 56, no. 2, pp. 485–492, Feb. 2009, doi: 10.1109/TBME.2008.2008488.

[155] L. L. Sohn, O. A. Saleh, G. R. Facer, A. J. Beavis, R. S. Allan, and D. A. Notterman, “Capacitance cytometry: Measuring biological cells one by one,” *Proc. Natl. Acad. Sci. U. S. A.*, vol. 97, no. 20, pp. 10687–10690, Sep. 2000, doi: 10.1073/pnas.200361297.

[156] T. Sun, N. G. Green, and H. Morgan, “Analytical and numerical modeling methods for impedance analysis of single cells on-chip,” *Nano*, vol. 3, no. 1, pp. 55–63, Feb. 2008, doi: 10.1142/S1793292008000800.

[157] L. Huang, P. Zhao, and W. Wang, “3D cell electrorotation and imaging for measuring multiple cellular biophysical properties,” *Lab Chip*, vol. 18, no. 16, pp. 2359–2368, 2018, doi: 10.1039/c8lc00407b.

[158] W. M. Arnold and U. Zimmermann, “Electro-rotation: development of a technique for dielectric measurements on individual cells and particles,” *J. Electrostat.*, vol. 21, no. 2–3, pp.

151–191, Sep. 1988, doi: 10.1016/0304-3886(88)90027-7.

[159] M. Bao, J. Xie, A. Piruska, and W. T. S. Huck, “3D microniches reveal the importance of cell size and shape,” *Nat. Commun.*, vol. 8, no. 1, Dec. 2017, doi: 10.1038/s41467-017-02163-2.

[160] X. B. Wang, Y. Huang, P. R. C. Gascoyne, F. F. Becker, R. Hölzel, and R. Pethig, “Changes in Friend murine erythroleukaemia cell membranes during induced differentiation determined by electrorotation,” *BBA - Biomembr.*, vol. 1193, no. 2, pp. 330–344, 1994, doi: 10.1016/0005-2736(94)90170-8.

[161] S. I. Han, Y. D. Joo, and K. H. Han, “An electrorotation technique for measuring the dielectric properties of cells with simultaneous use of negative quadrupolar dielectrophoresis and electrorotation,” *Analyst*, vol. 138, no. 5, pp. 1529–1537, 2013, doi: 10.1039/c3an36261b.

[162] J. Gimsa, P. Marszalek, U. Loewe, and T. Y. Tsong, “Dielectrophoresis and electrorotation of neurospora slime and murine myeloma cells,” *Biophys. J.*, vol. 60, no. 4, pp. 749–760, 1991, doi: 10.1016/S0006-3495(91)82109-9.

[163] J. Sudsiri, D. Wachner, J. Donath, and J. Gimsa, “Can molecular properties of human red blood cells be accessed by electrorotation?,” *J. Sci. Technol.*, pp. 785–789, 2002.

[164] J. Yang, Y. Huang, X. Wang, X.-B. Wang, F. F. Becker, and P. R. C. Gascoyne, “Dielectric Properties of Human Leukocyte Subpopulations Determined by Electrorotation as a Cell Separation Criterion,” 1999.

[165] G. De Gasperis, X. B. Wang, J. Yang, F. F. Becker, and P. R. C. Gascoyne, “Automated electrorotation: Dielectric characterization of living cells by real-time motion estimation,” *Meas. Sci. Technol.*, vol. 9, no. 3, pp. 518–529, 1998, doi: 10.1088/0957-0233/9/3/029.

[166] Y. Huang, X. B. Wang, P. R. C. Gascoyne, and F. F. Becker, “Membrane dielectric responses of human T-lymphocytes following mitogenic stimulation,” *Biochim. Biophys. Acta - Biomembr.*, vol. 1417, no. 1, pp. 51–62, 1999, doi: 10.1016/S0005-2736(98)00253-3.

[167] J. Bauer, V. Kachel, and K. Hannig, “The negative surface charge density is a maturation marker of human B lymphocytes,” *Cell. Immunol.*, vol. 111, no. 2, pp. 354–364, 1988, doi: 10.1016/0008-8749(88)90099-8.

[168] A. Ramos, A. González, A. Castellanos, N. G. Green, and H. Morgan, “Pumping of liquids with ac voltages applied to asymmetric pairs of microelectrodes,” *Phys. Rev. E - Stat. Physics, Plasmas, Fluids, Relat. Interdiscip. Top.*, vol. 67, no. 5, p. 11, May 2003, doi: 10.1103/PhysRevE.67.056302.

[169] J. Gimsa, T. Müller, T. Schnelle, and G. Fuhr, “Dielectric spectroscopy of single human erythrocytes at physiological ionic strength: Dispersion of the cytoplasm,” *Biophys. J.*, vol. 71, no. 1, pp. 495–506, 1996, doi: 10.1016/S0006-3495(96)79251-2.

[170] W. M. Arnold, U. Zim, and E. Ann, “Rotating-Field-Induced Rotation and Measurement of the Membrane Capacitance of Single Mesophyll Cells of A vena sativa Introduction Materials and Methods,” 1982.

[171] B. Prasad, S. Du, W. Badawy, and K. V. I. S. Kaler, “A real-time multiple-cell tracking platform for dielectrophoresis (DEP)-based cellular analysis,” *Meas. Sci. Technol.*, vol. 16, no. 4, pp. 909–924, 2005, doi: 10.1088/0957-0233/16/4/003.

[172] K. F. Hoettges, J. W. Dale, and M. P. Hughes, “Rapid determination of antibiotic resistance in E. coli using dielectrophoresis,” *Phys. Med. Biol.*, vol. 52, no. 19, pp. 6001–6009, 2007, doi: 10.1088/0031-9155/52/19/019.

[173] K. F. Hoettges, Y. Hübner, L. M. Broche, S. L. Ogin, G. E. N. Kass, and M. P. Hughes, “Dielectrophoresis-activated multiwell plate for label-free high-throughput drug assessment,” *Anal. Chem.*, vol. 80, no. 6, pp. 2063–2068, 2008, doi: 10.1021/ac702083g.

[174] Y. Hubner, K. F. Hoettges, G. E. N. Kass, S. L. Ogin, and M. P. Hughes, “Parallel measurements of drug actions on Erythrocytes by dielectrophoresis, using a three-dimensional electrode design.,” *IEE Proc. Nanobiotechnol.*, vol. 152, no. 4, pp. 150–154, Aug. 2005, doi: 10.1049/ip-nbt:20050011.

[175] E. A. Henslee *et al.*, “Rhythmic potassium transport regulates the circadian clock in human red blood cells,” *Nat. Commun.*, vol. 8, no. 1, 2017, doi: 10.1038/s41467-017-02161-4.

[176] S. Jacesko, J. K. Abraham, T. Ji, V. K. Varadan, M. Cole, and J. W. Gardner, “Investigations on an electronic tongue with polymer microfluidic cell for liquid sensing and identification,” in *Smart Materials and Structures*, Oct. 2005, vol. 14, no. 5, pp. 1010–1016, doi: 10.1088/0964-1726/14/5/039.

[177] N. G. Green, H. Morgan, and J. J. Milner, “Manipulation and trapping of sub-micron

bioparticles using dielectrophoresis," *J. Biochem. Biophys. Methods*, vol. 35, no. 2, pp. 89–102, 1997, doi: 10.1016/S0165-022X(97)00033-X.

[178] R. M. White and F. W. Voltmer, "Direct piezoelectric coupling to surface elastic waves," *Appl. Phys. Lett.*, vol. 7, no. 12, pp. 314–316, 1965, doi: 10.1063/1.1754276.

[179] Taiyo Yuden, "Working principles and Applications of SAW/FBAR Devices." Accessed: Dec. 12, 2020. [Online]. Available: https://docplayer.net/30770605-Working-principles-and-applications-of-saw-fbar-devices.html.

[180] J. Nam, H. Lim, and S. Shin, "Manipulation of microparticles using surface acoustic wave in microfluidic systems: A brief review," *Korea Australia Rheology Journal*, vol. 23, no. 4. pp. 255–267, Dec. 2011, doi: 10.1007/s13367-011-0031-5.

[181] Roditi, "Lithium tantalate properties." http://www.roditi.com/SingleCrystal/Lithium-Tantalate/LiTaO3-Properties.html (accessed Dec. 12, 2020).

[182] S. Datta, *Surface Acoustic Wave Devices*. Prentice-Hall, 1986.

[183] M. Washizu, "Precise calculation of dielectrophoretic force in arbitrary field," *J. Electrostat.*, vol. 29, no. 2, pp. 177–188, 1993, doi: 10.1016/0304-3886(93)90104-F.

[184] K. W. Wagner, "Erklärung der elektrischen nachwirkungsvorgänge auf grund Maxwellscher vorstellungen (Explanation of electric relaxation processes based on Maxwell's ideas)," *Arch. fur Elektrotechnik*, vol. 2, no. 9, pp. 371–387, 1914.

[185] G. Molinari and A. Viviani, "Analytical evaluation of the electro-dielectrophoretic forces acting on spherical impurity particles in dielectric fluids," *J. Electrostat.*, vol. 5, no. C, pp. 343–354, 1978, doi: 10.1016/0304-3886(78)90029-3.

[186] L. Benguigui and I. J. Lin, "More about the dielectrophoretic force," *J. Appl. Phys.*, vol. 53, no. 2, pp. 1141–1143, 1982, doi: 10.1063/1.329875.

[187] R. Pethig, *Dielectrophoresis: Theory, Methodology and Biological Applications*, First Edit. John Wiley & Sons, Ltd, 2017.

[188] M. Alshareef *et al.*, "Separation of tumor cells with dielectrophoresis-based microfluidic chip," *Biomicrofluidics*, vol. 7, no. 1, pp. 1–12, 2013, doi: 10.1063/1.4774312.

[189] R. Höber, "Eine Methode, die elektrische Leitfähigkeit im Innern von Zellen zu messen," *Pflügers Arch. Physiol. des Menschen und der Tiere*, vol. 133, pp. 237–253, 1910.

[190] Y. Huang, X. B. Wang, F. F. Becker, and P. R. C. Gascoyne, "Membrane changes associated with the temperature-sensitive P85gag-mos-dependent transformation of rat kidney cells as determined by dielectrophoresis and electrorotation," *Biochim. Biophys. Acta - Biomembr.*, vol. 1282, no. 1, pp. 76–84, 1996, doi: 10.1016/0005-2736(96)00047-8.

[191] A. Salmanzadeh, E. Elvington, S. P. C. Roberts, E. M. Schmelz, and R. V. Davalos, "Sphingolipid Metabolites Modulate Dielectric Characteristics of Cells in a Mouse Ovarian Cancer Progression Model," *Integr Biol (Camb).*, vol. 5, no. 6, pp. 843–852, 2013, doi: 10.1038/jid.2014.371.

[192] J. Gimsa and D. Wachner, "A unified resistor-capacitor model for impedance, dielectrophoresis, electrorotation, and induced transmembrane potential," *Biophys. J.*, vol. 75, no. 2, pp. 1107–1116, 1998, doi: 10.1016/S0006-3495(98)77600-3.

[193] M. Muratore, V. Srsen, M. Waterfall, A. Downes, and R. Pethig, "Biomarker-free dielectrophoretic sorting of differentiating myoblast multipotent progenitor cells and their membrane analysis by Raman spectroscopy," *Biomicrofluidics*, vol. 6, no. 3, pp. 1–16, 2012, doi: 10.1063/1.4746252.

[194] S. Shim, K. Stemke-Hale, A. M. Tsimberidou, J. Noshari, T. E. Anderson, and P. R. C. Gascoyne, "Antibody-independent isolation of circulating tumor cells by continuous-flow dielectrophoresis," *Biomicrofluidics*, vol. 7, no. 1, pp. 1–12, 2013, doi: 10.1063/1.4774304.

[195] P. Gascoyne, R. Pethig, J. Satayavivad, F. F. Becker, and M. Ruchirawat, "Dielectrophoretic detection of changes in erythrocyte membranes following malarial infection," *Biochim. Biophys. Acta - Biomembr.*, vol. 1323, no. 2, pp. 240–252, 1997, doi: 10.1016/S0005-2736(96)00191-5.

[196] P. R. C. Gascoyne, J. Noshari, T. J. Anderson, and F. F. Becker, "Isolation of Rare Cells from Cell Mixtures by Dielectrophoresis," *Electrophoresis*, vol. 30, no. 8, pp. 1388–1398, 2009, doi: 10.1038/jid.2014.371.

[197] C. Chung, M. Waterfall, S. Pells, A. Menachery, S. Smith, and R. Pethig, "Dielectrophoretic characterisation of mammalian cells above 100 MHz," *J. Electr. Bioimpedance*, vol. 2, no. 1, pp. 64–71, 2011, doi: 10.5617/jeb.196.

[198] “Eukaryotic cell (animal).” https://commons.wikimedia.org/wiki/File:Eukaryotic_Cell_(animal).jpg (accessed Dec. 12, 2020).

[199] W. Liang, Y. Zhao, L. Liu, Y. Wang, W. J. Li, and G. Bin Lee, “Determination of Cell Membrane Capacitance and Conductance via Optically Induced Electrokinetics,” *Biophys. J.*, vol. 113, no. 7, pp. 1531–1539, 2017, doi: 10.1016/j.bpj.2017.08.006.

[200] X. Wang, F. F. Becker, and P. R. C. Gascoyne, “Membrane dielectric changes indicate induced apoptosis in HL-60 cells more sensitively than surface phosphatidylserine expression or DNA fragmentation,” *Biochim Biophys Acta.*, vol. 2, no. 1564, pp. 412–420, 2002.

[201] A. Irimajiri, T. Hanai, and A. Inouye, “A dielectric theory of ‘multi-stratified shell’ model with its application to a lymphoma cell,” *J. Theor. Biol.*, vol. 78, no. 2, pp. 251–269, May 1979, doi: 10.1016/0022-5193(79)90268-6.

[202] A. Irimajiri, A., Doida, Y., Hanai, T. and Inouye, “Passive electrical properties of cultured marine lymphoblasts (L5178Y) with reference to its cytoplasmic membrane, nuclear-envelope and intracellular phases.,” *J. Membr. Biol.*, vol. 38, no. 3, pp. 209– 232, 1978.

[203] R. Pethig, “Review Article—Dielectrophoresis: Status of the theory, technology, and applications,” *Biomicrofluidics*, vol. 4, 2010.

[204] A. Irimajiri, K. Asami, T. Ichinowatari, and Y. Kinoshita, “Passive electrical properties of the membrane and cytoplasm of cultured rat basophil leukemia cells. I. Dielectric behavior of cell suspensions in 0.01-500 MHz and its simulation with a single-shell model,” *BBA - Biomembr.*, vol. 896, no. 2, pp. 203–213, 1987, doi: 10.1016/0005-2736(87)90181-7.

[205] H. Morgan and N. G. Green, *AC Electrokinetics: Colloids and Nanoparticles*. Wiley–Blackwell, 2001.

[206] N. G. Green, A. Ramos, and H. Morgan, “Numerical solution of the dielectrophoretic and travelling wave forces for interdigitated electrode arrays using the finite element method,” 2002.

[207] Y. Chen *et al.*, “Tunable nanowire patterning using standing surface acoustic waves,” *ACS Nano*, vol. 7, no. 4, pp. 3306–3314, Apr. 2013, doi: 10.1021/nn4000034.

[208] Kayaku advanced materials, “SU-8 Permanent Negative Epoxy Photoresist.” SU-8 Permanent Negative Epoxy Photoresist (accessed Dec. 26, 2020).

[209] E. O. Adekanmbi, A. T. Giduthuri, and S. K. Srivastava, “Dielectric characterization and separation optimization of infiltrating ductal adenocarcinoma via insulator-dielectrophoresis,” *Micromachines*, vol. 11, no. 4, Apr. 2020, doi: 10.3390/MI11040340.

[210] H. Moncada-Hernandez, J. L. Baylon-Cardiel, V. H. Pérez-González, and B. H. Lapizco-Encinas, “Insulator-based dielectrophoresis of microorganisms: Theoretical and experimental results,” *Electrophoresis*, vol. 32, no. 18, pp. 2502–2511, Sep. 2011, doi: 10.1002/elps.201100168.

[211] A. Gencoglu, D. Olney, A. Lalonde, K. S. Koppula, and B. H. Lapizco-Encinas, “Dynamic microparticle manipulation with an electroosmotic flow gradient in low-frequency alternating current dielectrophoresis,” *Electrophoresis*, vol. 35, no. 2–3, pp. 362–373, Feb. 2014, doi: 10.1002/elps.201300385.

[212] J. Oh, R. Hart, J. Capurro, and H. Noh, “Comprehensive analysis of particle motion under non-uniform AC electric fields in a microchannel,” *Lab Chip*, vol. 9, no. 1, pp. 62–78, 2009, doi: 10.1039/b801594e.

[213] S. D. Berger, N. E. McGruer, and G. G. Adams, “Simulation of dielectrophoretic assembly of carbon nanotubes using 3D finite element analysis,” *Nanotechnology*, vol. 26, no. 15, Apr. 2015, doi: 10.1088/0957-4484/26/15/155602.

[214] V. Gauthier, A. Bolopion, and M. Gauthier, “Analytical formulation of the electric field induced by electrode arrays: Towards automated dielectrophoretic cell sorting,” *Micromachines*, vol. 8, no. 8, 2017, doi: 10.3390/mi8080253.

[215] Y. Guan *et al.*, “Dielectrophoresis separation of platelets using a novel zigzag microchannel,” *Micromachines*, vol. 11, no. 10, Oct. 2020, doi: 10.3390/mi11100890.

[216] Y. Patel, G. Janusas, A. Palevicius, and A. Vilkauskas, “Development of nanoporous AAO membrane for nano filtration using the acoustophoresis method,” *Sensors (Switzerland)*, vol. 20, no. 14, pp. 1–26, Jul. 2020, doi: 10.3390/s20143833.

[217] U. C. Kaletta and C. Wenger, “FEM simulation of Rayleigh waves for CMOS compatible SAW

devices based on AlN/SiO2/Si(1 0 0)," *Ultrasonics*, vol. 54, no. 1, pp. 291–295, Jan. 2014, doi: 10.1016/j.ultras.2013.04.009.

[218] Z. Chen, Q. Zhang, S. Fu, X. Wang, X. Qiu, and H. Wu, "Hybrid full-wave analysis of surface acoustic wave devices for accuracy and fast performance prediction," *Micromachines*, vol. 12, no. 1, pp. 1–13, Jan. 2021, doi: 10.3390/mi12010005.

[219] X. Pang and Y. K. Yong, "Simulation of Nonlinear Resonance, Amplitude-Frequency, and Harmonic Generation Effects in SAW and BAW Devices," *IEEE Trans. Ultrason. Ferroelectr. Freq. Control*, vol. 67, no. 2, pp. 422–430, Feb. 2020, doi: 10.1109/TUFFC.2019.2945522.

[220] J. Schindelin *et al.*, "Fiji: An open-source platform for biological-image analysis," *Nature Methods*, vol. 9, no. 7. pp. 676–682, Jul. 2012, doi: 10.1038/nmeth.2019.

[221] Y. C. Kung, K. W. Huang, Y. J. Fan, and P. Y. Chiou, "Fabrication of 3D high aspect ratio PDMS microfluidic networks with a hybrid stamp," *Lab Chip*, vol. 15, no. 8, pp. 1861–1868, Apr. 2015, doi: 10.1039/c4lc01211a.

[222] M. A. Unger, H. P. Chou, T. Thorsen, A. Scherer, and S. R. Quake, "Monolithic microfabricated valves and pumps by multilayer soft lithography," *Science (80-.).*, vol. 288, no. 5463, pp. 113–116, Apr. 2000, doi: 10.1126/science.288.5463.113.

[223] M. A. Eddings, M. A. Johnson, and B. K. Gale, "Determining the optimal PDMS-PDMS bonding technique for microfluidic devices," *J. Micromechanics Microengineering*, vol. 18, no. 6, p. 67001, Jun. 2008, doi: 10.1088/0960-1317/18/6/067001.

[224] M. Chu, T. T. Nguyen, E. K. Lee, J. L. Morival, and M. Khine, "Plasma free reversible and irreversible microfluidic bonding," *Lab Chip*, vol. 17, no. 2, pp. 267–273, Jan. 2017, doi: 10.1039/C6LC01338D.

[225] Q. Q. Qiu, W. Q. Sun, and J. Connor, "Biocompatibility, Surface engineering, and Delivery of Drugs, Genes and Other Molecules," in *Comprehensive Biomaterials,* 1st ed., P. Duchevne, Ed. Amsterdam: Elsevier, 2011, pp. 127–144.

[226] T. G. Oyama, K. Oyama, and M. Taguchi, "A simple method for production of hydrophilic, rigid, and sterilized multi-layer 3D integrated polydimethylsiloxane microfluidic chips," *Lab Chip*, vol. 20, no. 13, pp. 2354–2363, Jul. 2020, doi: 10.1039/d0lc00316f.

[227] A. Chen and T. Pan, "Three-dimensional fit-to-flow microfluidic assembly," *Biomicrofluidics*, vol. 5, no. 4, p. 46505, 2011, doi: 10.1063/1.3670368.

[228] J. Jeong, K. Chun, J. Kim, and B. Lee, "Simple alignment technique for molding and transfer of 3D PDMS structure using the mechanical alignment jig," 2009, doi: 10.1109/AFRCON.2009.5308216.

[229] X. Li *et al.*, "Desktop aligner for fabrication of multilayer microfluidic devices," *Rev. Sci. Instrum.*, vol. 86, no. 7, p. 75008, Jul. 2015, doi: 10.1063/1.4927197.

[230] B. K. Gale *et al.*, "A review of current methods in microfluidic device fabrication and future commercialization prospects," *Inventions*, vol. 3, no. 3. MDPI Multidisciplinary Digital Publishing Institute, p. 60, Sep. 01, 2018, doi: 10.3390/inventions3030060.

[231] P. Nath, D. Fung, Y. A. Kunde, A. Zeytun, B. Branch, and G. Goddard, "Rapid prototyping of robust and versatile microfluidic components using adhesive transfer tapes," *Lab Chip*, vol. 10, no. 17, pp. 2286–2291, Sep. 2010, doi: 10.1039/c002457k.

[232] S. J. Morrison and D. T. Scadden, "The bone marrow niche for haematopoietic stem cells," *Nature*, vol. 505, no. 7483. NIH Public Access, pp. 327–334, 2014, doi: 10.1038/nature12984.

[233] M. Jagannathan-Bogdan and L. I. Zon, "Hematopoiesis," *Dev.*, vol. 140, no. 12, pp. 2463–2467, Jun. 2013, doi: 10.1242/dev.083147.

[234] P. C. Hermann *et al.*, "Concentration of bone marrow total nucleated cells by a point-of-care device provides a high yield and preserves their functional activity," *Cell Transplant.*, vol. 16, no. 10, pp. 1059–1069, 2008, doi: 10.3727/000000007783472363.

[235] J. B. Cowland and N. Borregaard, "Granulopoiesis and granules of human neutrophils," *Immunological Reviews*, vol. 273, no. 1. Blackwell Publishing Ltd, pp. 11–28, Sep. 01, 2016, doi: 10.1111/imr.12440.

[236] J. Prinyakupt and C. Pluempitiwiriyawej, "Segmentation of white blood cells and comparison of cell morphology by linear and naïve Bayes classifiers," *Biomed. Eng. Online*, vol. 14, no. 1, Jun. 2015, doi: 10.1186/s12938-015-0037-1.

[237] X. Hu, W. M. Arnold, and U. Zimmermann, "Alterations in the electrical properties of T and B lymphocyte membranes induced by mitogenic stimulation. Activation monitored by electro-

rotation of single cells," *BBA - Biomembr.*, vol. 1021, no. 2, pp. 191–200, Jan. 1990, doi: 10.1016/0005-2736(90)90033-K.

[238] K. Asami, "Dielectric properties of microvillous cells simulated by the three-dimensional finite-element method," *Bioelectrochemistry*, vol. 81, no. 1, pp. 28–33, 2011, doi: 10.1016/j.bioelechem.2011.01.002.

[239] T. Harayama and H. Riezman, "Understanding the diversity of membrane lipid composition," *Nature Reviews Molecular Cell Biology*, vol. 19, no. 5. Nature Publishing Group, pp. 281–296, May 01, 2018, doi: 10.1038/nrm.2017.138.

[240] M. Stoneman, A. Chaturvedi, D. B. Jansma, M. Kosempa, C. Zeng, and V. Raicu, "Protein influence on the plasma membrane dielectric properties: In vivo study utilizing dielectric spectroscopy and fluorescence microscopy," *Bioelectrochemistry*, vol. 70, no. 2, pp. 542–550, 2007, doi: 10.1016/j.bioelechem.2006.12.008.

[241] F. F. Becker, X. B. Wang, Y. Huang, R. Pethig, J. Vykoukal, and P. R. Gascoyne, "Separation of human breast cancer cells from blood by differential dielectric affinity.," *Proc. Natl. Acad. Sci. U. S. A.*, vol. 92, no. 3, pp. 860–4, Jan. 1995, [Online]. Available: http://www.ncbi.nlm.nih.gov/pubmed/7846067.

[242] H. Frusawa, "Frequency-Modulated Wave Dielectrophoresis of Vesicles And Cells: Periodic U-Turns at the Crossover Frequency," *Nanoscale Res. Lett.*, vol. 13, 2018, doi: 10.1186/s11671-018-2583-5.

[243] P. Gascoyne, J. Satayavivad, and M. Ruchirawat, "Microfluidic approaches to malaria detection," *Acta Trop.*, vol. 89, no. 3, pp. 357–369, 2004, doi: 10.1016/j.actatropica.2003.11.009.

[244] Y. Polevaya, I. Ermolina, M. Schlesinger, B. Z. Ginzburg, and Y. Feldman, "Time domain dielectric spectroscopy study of human cells II. Normal and malignant white blood cells," *Biochim. Biophys. Acta - Biomembr.*, vol. 1419, no. 2, pp. 257–271, 1999, doi: 10.1016/S0005-2736(99)00072-3.

[245] A. Surowiec, S. S. Stuchly, and C. Izaguirre, "Dielectric properties of human B and T lymphocytes at frequencies from 20 kHz to 100 MHz," *Phys. Med. Biol.*, vol. 31, no. 1, pp. 43–53, 1986, doi: 10.1088/0031-9155/31/1/004.

[246] P. R. C. Gascoyne, S. Shim, J. Noshari, F. F. Becker, and K. Stemke-Hale, "Correlations between the dielectric properties and exterior morphology of cells revealed by dielectrophoretic field-flow fractionation," *Electrophoresis*, vol. 34, no. 7, pp. 1042–1050, 2013, doi: 10.1002/elps.201200496.

[247] A. Ismail, M. P. Hughes, H. J. Mulhall, R. O. C. Oreffo, and Labeed, "Characterization of human skeletal stem and bone cell populations using dielectrophoresis," *J. Tissue Eng. Regen. Med.*, vol. 9, pp. 162–168, 2015.

[248] World Health Organization, "Best practices in phlebotomy," in *WHO Guidelines on Drawing Blood: Best Practices in Phlebotomy.*, World Health Organization, 2010.

[249] M. David *et al.*, "The dielectric spectroscopy of human red blood cells: The differentiation of old from fresh cells," *Physiol. Meas.*, vol. 38, no. 7, pp. 1335–1348, 2017, doi: 10.1088/1361-6579/aa707a.

[250] Invitrogen, "Cell concentrations in human and mouse samples," 2008. https://tools.thermofisher.com/content/sfs/brochures/I-076357 cell count table topp_WEB.pdf (accessed Sep. 11, 2019).

[251] J. Bocsi, S. Melzer, I. Dähnert, and A. Tárnok, "OMIP-023: 10-Color, 13 antibody panel for in-depth phenotyping of human peripheral blood leukocytes," *Cytom. Part A*, vol. 85, no. 9, pp. 781–784, Aug. 2014, doi: 10.1002/cyto.a.22505.

[252] et al. Alberts B, Johnson A, Lewis J, "Molecular Biology of the Cell," in *Molecular Biology of the Cell*, 4th editio., New York: Garland Science, 2002.

[253] E. Šimková and D. Staněk, "Probing nucleic acid interactions and pre-mRNA splicing by förster resonance energy transfer (FRET) microscopy," *International Journal of Molecular Sciences*, vol. 13, no. 11. MDPI AG, pp. 14929–14945, 2012, doi: 10.3390/ijms131114929.

[254] C. Le Roy, N. Varin-Blank, F. Ajchenbaum-Cymbalista, and R. Letestu, "Flow cytometry APC-tandem dyes are degraded through a cell-dependent mechanism," *Cytom. Part A*, vol. 75A, no. 10, pp. 882–890, Oct. 2009, doi: 10.1002/cyto.a.20774.

[255] W. R. Strohl and L. M. Strohl, "Antibody interactions with the immune system," in *Therapeutic Antibody Engineering*, Elsevier, 2012, pp. 131–595.

[256] J. E. Smith-Garvin, G. A. Koretzky, and M. S. Jordan, “T cell activation,” *Annual Review of Immunology*, vol. 27. NIH Public Access, pp. 591–619, 2009, doi: 10.1146/annurev.immunol.021908.132706.

[257] J. P. H. Burt, R. Pethig, P. R. C. Gascoyne, and F. F. Becker, “Dielectrophoretic characterisation of Friend murine erythroleukaemic cells as a measure of induced differentiation,” *BBA - Gen. Subj.*, vol. 1034, no. 1, pp. 93–101, 1990, doi: 10.1016/0304-4165(90)90158-S.

[258] V. L. Sukhorukov, W. M. Arnold, and U. Zimmermann, “Hypotonically induced changes in the plasma membrane of cultured mammalian cells,” *J. Membr. Biol.*, vol. 132, no. 1, pp. 27–40, 1993, doi: 10.1007/BF00233049.

[259] H. Z. Shi, A. Humbles, C. Gerard, Z. Jin, and P. F. Weller, “Lymph node trafficking and antigen presentation by endobronchial eosinophils,” *J. Clin. Invest.*, vol. 105, no. 7, pp. 945–953, 2000, doi: 10.1172/JCI8945.

[260] L. S. van Rijt, N. Vos, D. Hijdra, V. C. de Vries, H. C. Hoogsteden, and B. N. Lambrecht, “Airway Eosinophils Accumulate in the Mediastinal Lymph Nodes but Lack Antigen-Presenting Potential for Naive T Cells,” *J. Immunol.*, vol. 171, no. 7, pp. 3372–3378, 2003, doi: 10.4049/jimmunol.171.7.3372.

[261] F. H. Labeed, H. M. Coley, and M. P. Hughes, “Differences in the biophysical properties of membrane and cytoplasm of apoptotic cells revealed using dielectrophoresis,” *Biochim. Biophys. Acta - Gen. Subj.*, vol. 1760, no. 6, pp. 922–929, Jun. 2006, doi: 10.1016/j.bbagen.2006.01.018.

[262] R. C. Nordberg, J. Zhang, E. H. Griffith, M. W. Frank, B. Starly, and E. G. Loboa, “Electrical Cell-Substrate Impedance Spectroscopy Can Monitor Age-Grouped Human Adipose Stem Cell Variability During Osteogenic Differentiation,” *Stem Cells Transl. Med.*, vol. 6, pp. 502–511, 2017, doi: 10.5966/sctm.2014-0180.

[263] Y. H. K. Yang, C. R. Ogando, C. Wang See, T. Y. Chang, and G. A. Barabino, “Changes in phenotype and differentiation potential of human mesenchymal stem cells aging in vitro,” *Stem Cell Res. Ther.*, vol. 9, no. 1, p. 131, May 2018, doi: 10.1186/s13287-018-0876-3.

[264] S. Cho and H. Thielecke, “Electrical characterization of human mesenchymal stem cell growth on microelectrode,” *Microelectron. Eng.*, vol. 85, no. 5–6, pp. 1272–1274, 2008, doi: 10.1016/j.mee.2008.01.004.

[265] Z. Poon *et al.*, “Enabling Technologies for Cell-Based Clinical Translation Bone Marrow Regeneration Promoted by Biophysically Sorted Osteoprogenitors From Mesenchymal Stromal Cells,” *Stem Cells Transl. Med.*, vol. 4, pp. 56–65, 2015, doi: 10.5966/sctm.2014-0154.

[266] M. J. Whitfield, W. C. J. Lee, and K. J. Van Vliet, “Onset of heterogeneity in culture-expanded bone marrow stromal cells,” *Stem Cell Res.*, vol. 11, no. 3, pp. 1365–1377, 2013, doi: 10.1016/j.scr.2013.09.004.

[267] W. C. Lee *et al.*, “Multivariate biophysical markers predictive of mesenchymal stromal cell multipotency,” *Proc. Natl. Acad. Sci. U. S. A.*, vol. 111, no. 42, pp. E4409–E4418, 2014, doi: 10.1073/pnas.1402306111.

[268] M. Xavier *et al.*, “Mechanical phenotyping of primary human skeletal stem cells in heterogeneous populations by real-time deformability cytometry,” *Integr. Biol. (United Kingdom)*, vol. 8, no. 5, pp. 616–623, 2016, doi: 10.1039/c5ib00304k.

[269] J. M. Maloney *et al.*, “Mesenchymal stem cell mechanics from the attached to the suspended state,” *Biophys. J.*, vol. 99, no. 8, pp. 2479–2487, 2010, doi: 10.1016/j.bpj.2010.08.052.

[270] P. J. Simmons and B. Torok-Storb, “Identification of stromal cell precursors in human bone marrow by a novel monoclonal antibody, STRO-1,” *Blood*, vol. 78, no. 1, pp. 55–62, 1991.

[271] D. Gothard, K. Cheung, J. M. Kanczler, D. I. Wilson, and R. O. C. Oreffo, “Regionally-derived cell populations and skeletal stem cells from human foetal femora exhibit specific osteochondral and multi-lineage differentiation capacity in vitro and ex vivo,” *Stem Cell Res. Ther.*, vol. 6, no. 1, pp. 1–17, 2015, doi: 10.1186/s13287-015-0247-2.

[272] K. Stewart *et al.*, “Further characterization of cells expressing STRO-1 in cultures of adult human bone marrow stromal cells,” *J. Bone Miner. Res.*, vol. 14, no. 8, pp. 1345–1356, 1999, doi: 10.1359/jbmr.1999.14.8.1345.

[273] S. Halfon, N. Abramov, B. Grinblat, and I. Ginis, “Markers distinguishing mesenchymal stem cells from fibroblasts are downregulated with passaging.,” *Stem Cells Dev.*, vol. 20, no. 1, pp. 53–66, Jan. 2011, doi: 10.1089/scd.2010.0040.

[274] A. Banfi, A. Muraglia, B. Dozin, M. Mastrogiacomo, R. Cancedda, and R. Quarto, “Proliferation kinetics and differentiation potential of ex vivo expanded human bone marrow stromal cells: Implications for their use in cell therapy,” *Exp. Hematol.*, vol. 28, no. 6, pp. 707–715, 2000, doi: 10.1016/S0301-472X(00)00160-0.

[275] M. M. Bonab, K. Alimoghaddam, F. Talebian, S. H. Ghaffari, A. Ghavamzadeh, and B. Nikbin, “Aging of mesenchymal stem cell in vitro,” *BMC Cell Biol.*, vol. 7, pp. 1–7, 2006, doi: 10.1186/1471-2121-7-14.

[276] J. Lo Surdo and S. R. Bauer, “Quantitative approaches to detect donor and passage differences in adipogenic potential and clonogenicity in human bone marrow-derived mesenchymal stem cells,” *Tissue Eng. - Part C Methods*, vol. 18, no. 11, pp. 877–889, 2012, doi: 10.1089/ten.tec.2011.0736.

[277] J. Kim *et al.*, “Biological characterization of long-term cultured human mesenchymal stem cells,” *Arch. Pharm. Res.*, vol. 32, no. 1, pp. 117–126, 2009, doi: 10.1007/s12272-009-1125-1.

[278] J. Y. Rho, L. Kuhn-Spearing, and P. Zioupos, “Mechanical properties and the hierarchical structure of bone,” *Med. Eng. Phys.*, vol. 20, no. 2, pp. 92–102, Mar. 1998, doi: 10.1016/S1350-4533(98)00007-1.

[279] M. Sadat-Shojai, “Calcium Phosphate–Reinforced Polyester Nanocomposites for Bone Regeneration Applications,” in *Biodegradable Polymeric Nanocomposites*, CRC Press, 2015, pp. 1–34.

[280] L. C. Gerstenfeld *et al.*, “Three-dimensional reconstruction of fracture callus morphogenesis,” *J. Histochem. Cytochem.*, vol. 54, no. 11, pp. 1215–1228, Nov. 2006, doi: 10.1369/jhc.6A6959.2006.

[281] T. A. Einhorn, “The cell and molecular biology of fracture healing,” in *Clinical Orthopaedics and Related Research*, 1998, no. 355 SUPPL., doi: 10.1097/00003086-199810001-00003.

[282] G. G. Walmsley *et al.*, “Stem Cells in Bone Regeneration,” *Stem Cell Reviews and Reports*, vol. 12, no. 5. Humana Press Inc., pp. 524–529, Oct. 01, 2016, doi: 10.1007/s12015-016-9665-5.

[283] A. M. Phillips, “Overview of the fracture healing cascade.,” *Injury*, vol. 36 Suppl 3, 2005, doi: 10.1016/j.injury.2005.07.027.

[284] R. Marsell and T. A. Einhorn, “The biology of fracture healing,” *Injury*, vol. 42, no. 6, pp. 551–555, 2011, doi: 10.1016/j.injury.2011.03.031.

[285] E. Kon *et al.*, “Bone regeneration with mesenchymal stem cells.,” *Clin. Cases Miner. Bone Metab.*, vol. 9, no. 1, pp. 24–7, Jan. 2012, Accessed: Feb. 07, 2021. [Online]. Available: http://www.ncbi.nlm.nih.gov/pubmed/22783331.

[286] L. C. Gerstenfeld, D. M. Cullinane, G. L. Barnes, D. T. Graves, and T. A. Einhorn, “Fracture healing as a post-natal developmental process: Molecular, spatial, and temporal aspects of its regulation,” *J. Cell. Biochem.*, vol. 88, no. 5, pp. 873–884, Apr. 2003, doi: 10.1002/jcb.10435.

[287] S. Al-Maawi, A. Orlowska, R. Sader, C. James Kirkpatrick, and S. Ghanaati, “In vivo cellular reactions to different biomaterials—Physiological and pathological aspects and their consequences,” *Seminars in Immunology*, vol. 29. Academic Press, pp. 49–61, Feb. 01, 2017, doi: 10.1016/j.smim.2017.06.001.

[288] R. Dimitriou, E. Tsiridis, and P. V. Giannoudis, “Current concepts of molecular aspects of bone healing,” *Injury*, vol. 36, no. 12. pp. 1392–1404, Dec. 2005, doi: 10.1016/j.injury.2005.07.019.

[289] B. A. Rahn, “Bone healing: histologic and physiologic concepts,” *Bone Clin. Orthop.*, pp. 287–326, 2002.

[290] N. C. Keramaris, G. M. Calori, V. S. Nikolaou, E. H. Schemitsch, and P. V Giannoudis, “Fracture vascularity and bone healing: A systematic review of the role of VEGF,” 2008. [Online]. Available: www.elsevier.com/locate/injury.

[291] Z. S. Al-Aql, A. S. Alagl, D. T. Graves, L. C. Gerstenfeld, and T. A. Einhorn, “Molecular mechanisms controlling bone formation during fracture healing and distraction osteogenesis,” *Journal of Dental Research*, vol. 87, no. 2. J Dent Res, pp. 107–118, Feb. 2008, doi: 10.1177/154405910808700215.

[292] F. Granero-Moltó *et al.*, “Regenerative effects of transplanted mesenchymal stem cells in fracture healing,” *Stem Cells*, vol. 27, no. 8, pp. 1887–1898, Aug. 2009, doi: 10.1002/stem.103.

[293] T. Kitaori *et al.*, “Stromal cell-derived factor 1/CXCR4 signaling is critical for the recruitment of mesenchymal stem cells to the fracture site during skeletal repair in a mouse model,” *Arthritis Rheum.*, vol. 60, no. 3, pp. 813–823, Mar. 2009, doi: 10.1002/art.24330.

[294] A. Schindeler, M. M. McDonald, P. Bokko, and D. G. Little, “Bone remodeling during fracture repair: The cellular picture,” *Seminars in Cell and Developmental Biology*, vol. 19, no. 5. Elsevier Ltd, pp. 459–466, 2008, doi: 10.1016/j.semcdb.2008.07.004.

[295] G. J. Breur, B. A. Vanenkevort, " C E Farnum, and N. J. Wilsman, “Linear Relationship Between the Volume of Hypertrophic Chondrocytes and the Rate of Longitudinal Bone Growth in Growth Plates.”

[296] B. WENDEBERG, “Mineral metabolism of fractures of the tibia in man studied with external counting of Sr85,” *Acta Orthop. Scand. Suppl.*, vol. 52, pp. 1–79, 1961, doi: 10.3109/ort.1961.32.suppl-52.01.

[297] I. H. Kalfas, “Principles of bone healing,” *Neurosurg. Focus*, vol. 10, no. 4, pp. 1–4, 2001.

[298] M. Liebergall *et al.*, “Stem cell-based therapy for prevention of delayed fracture union: A randomized and prospective preliminary study,” *Mol. Ther.*, vol. 21, no. 8, pp. 1631–1638, 2013, doi: 10.1038/mt.2013.109.

[299] R. Vélez *et al.*, “Treatment of femoral head osteonecrosis with advanced cell therapy in sheep,” *Arch. Orthop. Trauma Surg.*, vol. 132, no. 11, pp. 1611–1618, Nov. 2012, doi: 10.1007/s00402-012-1584-6.

[300] I. Müller *et al.*, “Secretion of angiogenic proteins by human multipotent mesenchymal stromal cells and their clinical potential in the treatment of avascular osteonecrosis,” *Leukemia*, vol. 22, no. 11, pp. 2054–2061, 2008, doi: 10.1038/leu.2008.217.

[301] K. E. M. Benders, P. R. van Weeren, S. F. Badylak, D. B. F. Saris, W. J. A. Dhert, and J. Malda, “Extracellular matrix scaffolds for cartilage and bone regeneration,” *Trends in Biotechnology*, vol. 31, no. 3. Trends Biotechnol, pp. 169–176, Mar. 2013, doi: 10.1016/j.tibtech.2012.12.004.

[302] S. J. Hollister, “Porous scaffold design for tissue engineering,” 2005. [Online]. Available: www.nature.com/naturematerials.

[303] R. M. Boehler, J. G. Graham, and L. D. Shea, “Tissue engineering tools for modulation of the immune response,” *BioTechniques*, vol. 51, no. 4. pp. 239–254, Oct. 2011, doi: 10.2144/000113754.

[304] D. L. Worthley *et al.*, “Gremlin 1 identifies a skeletal stem cell with bone, cartilage, and reticular stromal potential,” *Cell*, vol. 160, no. 1–2, pp. 269–284, Jan. 2015, doi: 10.1016/j.cell.2014.11.042.

[305] A. L. Gamblin *et al.*, “Bone tissue formation with human mesenchymal stem cells and biphasic calcium phosphate ceramics: The local implication of osteoclasts and macrophages,” *Biomaterials*, vol. 35, no. 36, pp. 9660–9667, 2014, doi: 10.1016/j.biomaterials.2014.08.018.

[306] M. H. Mankani, S. A. Kuznetsov, R. M. Wolfe, G. W. Marshall, and P. G. Robey, “In Vivo Bone Formation by Human Bone Marrow Stromal Cells: Reconstruction of the Mouse Calvarium and Mandible,” *Stem Cells*, vol. 24, no. 9, pp. 2140–2149, Sep. 2006, doi: 10.1634/stemcells.2005-0567.

[307] M. A. Brennan *et al.*, “Pre-clinical studies of bone regeneration with human bone marrow stromal cells and biphasic calcium phosphate,” *Stem Cell Res. Ther.*, vol. 5, no. 6, Dec. 2014, doi: 10.1186/scrt504.

[308] R. Quarto *et al.*, “Repair of large bone defects with the use of autologous bone marrow stromal cells,” *New England Journal of Medicine*, vol. 344, no. 5. pp. 385–386, Feb. 01, 2001, doi: 10.1056/NEJM200102013440516.

[309] M. Marcacci *et al.*, “Stem cells associated with macroporous bioceramics for long bone repair: 6- To 7-year outcome of a pilot clinical study,” *Tissue Eng.*, vol. 13, no. 5, pp. 947–955, May 2007, doi: 10.1089/ten.2006.0271.

[310] R. Müller, “Hierarchical microimaging of bone structure and function,” *Nature Reviews Rheumatology*, vol. 5, no. 7. pp. 373–381, 2009, doi: 10.1038/nrrheum.2009.107.

[311] Y. Yang, B. Hallgrimsson, and E. E. Putnins, “Craniofacial defect regeneration using engineered bone marrow mesenchymal stromal cells,” *J. Biomed. Mater. Res. - Part A*, vol. 99 A, no. 1, pp. 74–85, Oct. 2011, doi: 10.1002/jbm.a.33155.

[312] S. S. Kim, M. Sun Park, O. Jeon, C. Yong Choi, and B. S. Kim, “Poly(lactide-co-

glycolide)/hydroxyapatite composite scaffolds for bone tissue engineering," *Biomaterials*, vol. 27, no. 8, pp. 1399–1409, Mar. 2006, doi: 10.1016/j.biomaterials.2005.08.016.

[313] M. P. Prabhakaran, J. Venugopal, and S. Ramakrishna, "Electrospun nanostructured scaffolds for bone tissue engineering," *Acta Biomater.*, vol. 5, no. 8, pp. 2884–2893, Oct. 2009, doi: 10.1016/j.actbio.2009.05.007.

[314] M. Igarashi, N. Kamiya, M. Hasegawa, T. Kasuya, T. Takahashi, and M. Takagi, "Inductive effects of dexamethasone on the gene expression of Cbfa1, Osterix and bone matrix proteins during differentiation of cultured primary rat osteoblasts," 2004.

[315] L. Legan, K. Retko, and P. Ropret, "Vibrational spectroscopic study on degradation of alizarin carmine," *Microchem. J.*, vol. 127, pp. 36–45, Jul. 2016, doi: 10.1016/j.microc.2016.02.002.

[316] Y. T. Tsao, Y. J. Huang, H. H. Wu, Y. A. Liu, Y. S. Liu, and O. K. Lee, "Osteocalcin mediates biomineralization during osteogenic maturation in human mesenchymal stromal cells," *Int. J. Mol. Sci.*, vol. 18, no. 1, Jan. 2017, doi: 10.3390/ijms18010159.

[317] H. Puchtler, S. N. Meloan, and M. S. Terry, "On the history and mechanism of alizarin and alizarin red S stains for calcium," *J. Histochem. Cytochem.*, vol. 17, no. 2, 1969.

[318] J. Bancroft and A. Stevens, *The Theory and Practice of Histological Techniques*, 2nd ed. Longman Group Limited, 1982.

[319] S. K. Doke and S. C. Dhawale, "Alternatives to animal testing: A review," *Saudi Pharmaceutical Journal*, vol. 23, no. 3. Elsevier, pp. 223–229, Jul. 01, 2015, doi: 10.1016/j.jsps.2013.11.002.

[320] "NC3Rs. The 3Rs." https://www.nc3rs.org.uk/the-3rs (accessed Jul. 11, 2020).

[321] P. P. Spicer, J. D. Kretlow, S. Young, J. A. Jansen, F. K. Kasper, and A. G. Mikos, "Evaluation of bone regeneration using the rat critical size calvarial defect," *Nat. Protoc.*, vol. 7, no. 10, pp. 1918–1929, Sep. 2012, doi: 10.1038/nprot.2012.113.

[322] R. Cancedda, P. Giannoni, and M. Mastrogiacomo, "A tissue engineering approach to bone repair in large animal models and in clinical practice," *Biomaterials*, vol. 28, no. 29. pp. 4240–4250, Oct. 2007, doi: 10.1016/j.biomaterials.2007.06.023.

[323] J. C. Reichert *et al.*, "Establishment of a preclinical ovine model for tibial segmental bone defect repair by applying bone tissue engineering strategies," *Tissue Engineering - Part B: Reviews*, vol. 16, no. 1. pp. 93–104, Feb. 01, 2010, doi: 10.1089/ten.teb.2009.0455.

[324] E. W. H. Bodde, P. H. M. Spauwen, A. G. Mikos, and J. A. Jansen, "Closing capacity of segmental radius defects in rabbits," *J. Biomed. Mater. Res. - Part A*, vol. 85, no. 1, pp. 206–217, Apr. 2008, doi: 10.1002/jbm.a.31549.

[325] A. I. Pearce, R. G. Richards, S. Milz, E. Schneider, and S. G. Pearce, "Animal models for implant biomaterial research in bone: A review," *European Cells and Materials*, vol. 13. AO Research Institute Davos, pp. 1–10, 2007, doi: 10.22203/eCM.v013a01.

[326] J. P. Schmitz and J. 0 Hollinger, "The Critical Size Defect as an Experimental Model for Craniomandibulofacial Nonunions." [Online]. Available: https://journals.lww.com/clinorthop.

[327] T. A. Einhorn, J. M. Lane, A. H. Burstein, C. R. Kopman, and V. J. Vigorita, "The healing of segmental bone defects induced by demineralized bone matrix. A radiographic and biomechanical study," *J. Bone Jt. Surg. - Ser. A*, vol. 66, no. 2, pp. 274–279, 1984, doi: 10.2106/00004623-198466020-00015.

[328] B. C. Jeffrey Wang, L. E. Kanim, S. Yoo, P. A. Campbell, A. J. Berk, and J. R. Lieberman, "Effect of Regional Gene Therapy with Bone Morphogenetic Protein-2-Producing Bone Marrow Cells on Spinal Fusion in Rats," 2003.

[329] H. Castano-Izquierdo, J. Álvarez-Barreto, J. Van Den Dolder, J. A. Jansen, A. G. Mikos, and V. I. Sikavitsas, "Pre-culture period of mesenchymal stem cells in osteogenic media influences their in vivo bone forming potential," *J. Biomed. Mater. Res. - Part A*, vol. 82, no. 1, pp. 129–138, Jul. 2007, doi: 10.1002/jbm.a.31082.

[330] C. Szpalski, J. Barr, M. Wetterau, P. B. Saadeh, and S. M. Warren, "Cranial bone defects: Current and future strategies," *Neurosurg. Focus*, vol. 29, no. 6, pp. 1–11, 2010, doi: 10.3171/2010.9.FOCUS10201.

[331] J. U. Umoh *et al.*, "In vivo micro-CT analysis of bone remodeling in a rat calvarial defect model," *Phys. Med. Biol.*, vol. 54, no. 7, pp. 2147–2161, 2009, doi: 10.1088/0031-9155/54/7/020.

[332] E. Freeman and R. S. Turnbull, "The value of osseous coagulum as a graft material," *J. periodont. Res.*, vol. 8, pp. 229–236, 1973.

[333] K. Takagi and M. R. Urist, “The Reaction of the Dura To Bone Morphogenetic Protein (BMP) in Repair of Skull Defects.”

[334] C. Bosch, B. Melsen, and K. Vargervik, “Importance of the critical-size bone defect in testing bone-regenerating materials,” *J. Craniofac. Surg.*, vol. 9, no. 4, pp. 310–316, 1998, doi: 10.1097/00001665-199807000-00004.

[335] A. Aybar Odstrcil, E. Territoriale, and L. Missana, “An experimental model in calvaria to evaluate bone therapies.,” *Acta Odontol. Latinoam.*, vol. 18, no. 2, pp. 63–67, Jan. 2005, Accessed: Feb. 07, 2021. [Online]. Available: https://europepmc.org/article/med/16673794.

[336] N. U. Zitzmann, R. Naef, and P. Schärer, “Resorbable versus nonresorbable membranes in combination with Bio-Oss for guided bone regeneration.,” *Int. J. Oral Maxillofac. Implants*, vol. 12, no. 6, pp. 844–52, Nov. 1997, Accessed: Feb. 07, 2021. [Online]. Available: http://www.ncbi.nlm.nih.gov/pubmed/9425767.

[337] A. K. Schlegel, H. Mijhler, F. Busch, and A. Mehli, “Preclinical and clinical studies of a collagen membrane (Bio-Gide@),” 1997.

[338] X. B. Yang, R. S. Bhatnagar, S. Li, and R. O. C. Oreffo, “Biomimetic collagen scaffolds for human bone cell growth and differentiation,” *Tissue Eng.*, vol. 10, no. 7–8, pp. 1148–1159, Jul. 2004, doi: 10.1089/ten.2004.10.1148.

[339] R. S. Bhatnagar, J. J. Qian, and C. A. Gough, “The role in cell binding of a β1-bend within the triple helical region in collagen αl(i) chain: Structural and biological evidence for conformational tautomerism on fiber surface,” *J. Biomol. Struct. Dyn.*, vol. 14, no. 5, pp. 547–560, 1997, doi: 10.1080/07391102.1997.10508155.

[340] H. Nguyen, J. J. Qian, R. S. Bhatnagar, and S. Li, “Enhanced cell attachment and osteoblastic activity by P-15 peptide-coated matrix in hydrogels,” *Biochem. Biophys. Res. Commun.*, vol. 311, no. 1, pp. 179–186, Nov. 2003, doi: 10.1016/j.bbrc.2003.09.192.

[341] R. S. Bhatnagar, J. J. Qian, A. Wedrychowska, M. Sadeghi, Y. M. Wu, and N. Smith, “Design of Biomimetic Habitats for Tissue Engineering with P-15, a Synthetic Peptide Analogue of Collagen,” *Tissue Eng.*, vol. 5, no. 1, pp. 53–65, Feb. 1999, doi: 10.1089/ten.1999.5.53.

[342] J. J. Qian and R. S. Bhatnagar+, “Enhanced cell attachment to anorganic bone mineral in the presence of a synthetic peptide related to collagen.”

[343] E. M. Lindley, F. A. Guerra, J. T. Krauser, S. M. Matos, E. L. Burger, and V. V. Patel, “Small peptide (P-15) bone substitute efficacy in a rabbit cancellous bone model,” *J. Biomed. Mater. Res. - Part B Appl. Biomater.*, vol. 94, no. 2, pp. 463–468, Aug. 2010, doi: 10.1002/jbm.b.31676.

[344] A. Kasaj, B. Röhrig, C. Reichert, and B. Willershausen, “Clinical evaluation of anorganic bovine-derived hydroxyapatite matrix/ cell-binding peptide (P-15) in the treatment of human infrabony defects,” *Clin. Oral Investig.*, vol. 12, no. 3, pp. 241–247, Sep. 2008, doi: 10.1007/s00784-008-0191-y.

[345] F. Gomar, R. Orozco, J. L. Villar, and F. Arrizabalaga, “P-15 small peptide bone graft substitute in the treatment of non-unions and delayed union. A pilot clinical trial,” *Int. Orthop.*, vol. 31, no. 1, pp. 93–99, Feb. 2007, doi: 10.1007/s00264-006-0087-x.

[346] R. A. Yukna *et al.*, “Multi-Center Clinical Evaluation of Combination Anorganic Bovine-Derived Hydroxyapatite Matrix (ABM)/Cell Binding Peptide (P-15) as a Bone Replacement Graft Material in Human Periodontal Osseous Defects. 6-Month Results,” *J. Periodontol.*, vol. 69, no. 6, pp. 655–663, Jun. 1998, doi: 10.1902/jop.1998.69.6.655.

[347] R. A. Yukna, J. T. Krauser, D. P. Callan, G. H. Evans, R. Cruz, and M. Martin, “Thirty-Six Month Follow-up of 25 Patients Treated With Combination Anorganic Bovine-Derived Hydroxyapatite Matrix (ABM)/Cell-Binding Peptide (P-15) Bone Replacement Grafts in Human Infrabony Defects. I. Clinical Findings,” *J. Periodontol.*, vol. 73, no. 1, pp. 123–128, Jan. 2002, doi: 10.1902/jop.2002.73.1.123.

[348] A. Kozlovsky *et al.*, “Bio-degradation of a resorbable collagen membrane (Bio-Gide ®) applied in a double-layer technique in rats,” *Clin. Oral Implants Res.*, vol. 20, no. 10, pp. 1116–1123, Oct. 2009, doi: 10.1111/j.1600-0501.2009.01740.x.

[349] J. D. Boerckel, D. E. Mason, A. M. Mcdermott, and E. Alsberg, “Microcomputed tomography: approaches and applications in bioengineering.” [Online]. Available: http://stemcellres.com/content/5/6/144.

[350] I. F. Cengiz, J. M. Oliveira, and R. L. Reis, “Micro-CT – a digital 3D microstructural voyage into scaffolds: a systematic review of the reported methods and results,” *Biomater. Res.*, vol. 22, no. 1, Dec. 2018, doi: 10.1186/s40824-018-0136-8.

[351] R. E. Guldberg *et al.*, “Analyzing Bone, Blood Vessels, and Biomaterials with Microcomputed Tomography,” *IEEE Engineering in Medicine and Biology Magazine*, vol. 22, no. 5. IEEE Eng Med Biol Mag, pp. 77–83, Sep. 2003, doi: 10.1109/MEMB.2003.1256276.

[352] P. F. M. Gielkens *et al.*, “A comparison of micro-CT, microradiography and histomorphometry in bone research,” *Arch. Oral Biol.*, vol. 53, no. 6, pp. 558–566, Jun. 2008, doi: 10.1016/j.archoralbio.2007.11.011.

[353] S. Young *et al.*, “Dose effect of dual delivery of vascular endothelial growth factor and bone morphogenetic protein-2 on bone regeneration in a rat critical-size defect model,” *Tissue Eng. - Part A*, vol. 15, no. 9, pp. 2347–2362, Sep. 2009, doi: 10.1089/ten.tea.2008.0510.

[354] E.-S. Kim *et al.*, “Improved Bone Healing by Angiogenic Factor-Enriched Platelet-Rich Plasma and Its Synergistic Enhancement by Bone Morphogenetic Protein-2 Eun-Jin Park, DDS [Postgraduate student in Advanced Graduate,” 2008.

[355] X. He, Y. Liu, X. Yuan, and L. Lu, “Enhanced healing of rat calvarial defects with MSCs loaded on BMP-2 releasing chitosan/alginate/hydroxyapatite scaffolds,” *PLoS One*, vol. 9, no. 8, Aug. 2014, doi: 10.1371/journal.pone.0104061.

[356] N. R. Parsons, M. D. Teare, and A. J. Sitch, “Unit of analysis issues in laboratory-based research,” *Elife*, vol. 7, Jan. 2018, doi: 10.7554/eLife.32486.

[357] H. Ehrlich, P. G. Koutsoukos, K. D. Demadis, and O. S. Pokrovsky, “Principles of demineralization: Modern strategies for the isolation of organic frameworks. Part I. Common definitions and history,” *Micron*, vol. 39, no. 8. pp. 1062–1091, Dec. 2008, doi: 10.1016/j.micron.2008.02.004.

[358] W. A. M. E. Schrijver *et al.*, “Influence of decalcification procedures on immunohistochemistry and molecular pathology in breast cancer,” *Mod. Pathol.*, vol. 29, no. 12, pp. 1460–1470, Dec. 2016, doi: 10.1038/modpathol.2016.116.

[359] W. Lan, H. Kwan, and I. Sunada, “Slicing technique for tooth specimens in histological preparation.,” *Bull. Tokyo Med. Dent. Univ.*, vol. 33, no. 4, pp. 129–136, 1986.

[360] J. dos S. Neves, N. F. Omar, E. A. O. Narvaes, J. R. Gomes, and P. D. Novaes, “Influence of different decalcifying agents on EGF and EGFR immunostaining,” *Acta Histochem.*, vol. 113, no. 4, pp. 484–488, Jul. 2011, doi: 10.1016/j.acthis.2010.04.006.

[361] M. Yoshioka *et al.*, “Adhesion/decalcification mechanisms of acid interactions with human hard tissues,” 2001.

[362] A. Morse, “Formic acid-sodium citrate decalcification and butyl alcohol dehydration of teeth and bones for sectioning in paraffin.”

[363] S. Gupta, “Qualitative Histological Evaluation of Hard and Soft Tissue Components of Human Permanent Teeth Using Various Decalcifying Agents - A Comparative Study,” *J. Clin. DIAGNOSTIC Res.*, 2014, doi: 10.7860/jcdr/2014/10195.4874.

[364] H. Liu *et al.*, “Evaluation of Decalcification Techniques for Rat Femurs Using HE and Immunohistochemical Staining,” *Biomed Res. Int.*, vol. 2017, 2017, doi: 10.1155/2017/9050754.

[365] M. Titford, “The long history of hematoxylin,” *Biotech. Histochem.*, vol. 80, no. 2, pp. 73–78, Mar. 2005, doi: 10.1080/10520290500138372.

[366] V. S. Constantine, “A combined tissue stain for the selective staining of collagen, elastic fibers and acidic carbohydrates.,” *J. Invest. Dermatol.*, vol. 52, no. 4, pp. 353–356, 1969, doi: 10.1038/jid.1969.60.

[367] G. GOMORI, “A rapid one-step trichrome stain.,” *Am. J. Clin. Pathol.*, vol. 20, no. 7, pp. 661–664, 1950, doi: 10.1093/ajcp/20.7_ts.661.

[368] J. A. Ramos-Vara and M. A. Miller, “When Tissue Antigens and Antibodies Get Along: Revisiting the Technical Aspects of Immunohistochemistry-The Red, Brown, and Blue Technique,” *Veterinary Pathology*, vol. 51, no. 1. pp. 42–87, Jan. 2014, doi: 10.1177/0300985813505879.

[369] C. P. Drew and W.-J. Shieh, “Current Laboratory Techniques in Rabies Diagnosis,” in *Research and Prevention*, Academic Press, 2015.

[370] A. H. Vermeulen, C. Vermeer, and F. T. Bosman, “Histochemical detection of osteocalcin in normal and pathological human bone.,” *J. Histochem. Cytochem.*, vol. 37, no. 10, pp. 1503–1508, Oct. 1989, doi: 10.1177/37.10.2789247.

[371] M. Camelo *et al.*, “Clinical, radiographic, and histologic evaluation of human periodontal defects treated with Bio-Oss and Bio-Gide.,” *Int. J. Periodontics Restorative Dent.*, vol. 18,

no. 4, pp. 321–31, 1998, doi: 10.11607/prd.00.0273.

[372] F. Braye *et al.*, “Resorption kinetics of osseous substitute: Natural coral and synthetic hydroxyapatite,” *Biomaterials*, vol. 17, no. 13, pp. 1345–1350, 1996, doi: 10.1016/0142-9612(96)88682-0.

[373] J. T. Koh, Z. Zhao, Z. Wang, I. S. Lewis, P. H. Krebsbach, and R. T. Franceschi, “Combinatorial gene therapy with BMP2/7 enhances cranial bone regeneration,” *J. Dent. Res.*, vol. 87, no. 9, pp. 845–849, Sep. 2008, doi: 10.1177/154405910808700906.

[374] J. H. Shin *et al.*, “Ex vivo bone morphogenetic protein-2 gene delivery using gingival fibroblasts promotes bone regeneration in rats,” *J. Clin. Periodontol.*, vol. 37, no. 3, pp. 305–311, Mar. 2010, doi: 10.1111/j.1600-051X.2009.01522.x.

[375] M. Thorwarth *et al.*, “Enhanced bone regeneration with a synthetic cell-binding peptide - In vivo results,” *Biochem. Biophys. Res. Commun.*, vol. 329, no. 2, pp. 789–795, Apr. 2005, doi: 10.1016/j.bbrc.2005.01.157.

[376] R. Hestehave Pedersen, M. Rasmussen, S. Overgaard, and M. Ding, “Effects of P-15 Peptide Coated Hydroxyapatite on Tibial Defect Repair in Vivo in Normal and Osteoporotic Rats,” *Biomed Res. Int.*, vol. 2015, 2015, doi: 10.1155/2015/253858.

[377] B. P. Sherman *et al.*, “Evaluation of ABM/P-15 versus autogenous bone in an ovine lumbar interbody fusion model,” *Eur. Spine J.*, vol. 19, no. 12, pp. 2156–2163, 2010, doi: 10.1007/s00586-010-1546-z.

[378] H. A. Alturkistani, F. M. Tashkandi, and Z. M. Mohammedsaleh, “Histological Stains: A Literature Review and Case Study,” *Glob. J. Health Sci.*, vol. 8, no. 3, pp. 72–79, 2015, doi: 10.5539/gjhs.v8n3p72.

[379] M. Titford, “Progress in the development of microscopical techniques for diagnostic pathology,” *J. Histotechnol.*, vol. 32, no. 1, pp. 9–19, 2009, doi: 10.1179/his.2009.32.1.9.

[380] J. Black, *Microbiology: Principles and exploration.* John Wiley & Sons, 2012.

[381] A. L. Mescher, *Junqueira’s Basic histology: Text and Atlas*, 15th ed. McGraw-Hill Education.

[382] S. M. Hasheminia, G. Feizi, S. M. Razavi, M. Feizianfard, N. Gutknecht, and M. Mir, “A comparative study of three treatment methods of direct pulp capping in canine teeth of cats: A histologic evaluation,” *Lasers Med. Sci.*, vol. 25, no. 1, pp. 9–15, 2010, doi: 10.1007/s10103-008-0584-9.

[383] M. Paknejad *et al.*, “Histologic evaluation of bone healing capacity following application of inorganic bovine bone and a new allograft material in rabbit calvaria.,” *J. Dent. (Tehran).*, vol. 12, no. 1, pp. 31–318, 2015.

[384] A. L. Boskey, F. H. Wians, and P. V. Hauschka, “The effect of osteocalcin on In vitro lipid-induced hydroxyapatite formation and seeded hydroxyapatite growth,” *Calcif. Tissue Int.*, vol. 37, no. 1, pp. 57–62, 1985, doi: 10.1007/BF02557680.

[385] T. A. Owen *et al.*, “Progressive development of the rat osteoblast phenotype in vitro: Reciprocal relationships in expression of genes associated with osteoblast proliferation and differentiation during formation of the bone extracellular matrix,” *J. Cell. Physiol.*, vol. 143, no. 3, pp. 420–430, 1990, doi: 10.1002/jcp.1041430304.

[386] G. S. Stein, J. B. Lian, and T. A. Owen, “Relationship of cell growth to the regulation of tissue-specific gene expression during osteoblast differentiation,” *FASEB J.*, vol. 4, no. 13, pp. 3111–3123, Oct. 1990, doi: 10.1096/fasebj.4.13.2210157.

[387] A. L. Boskey, S. Gadaleta, C. Gundberg, S. B. Doty, P. Ducy, and G. Karsenty, “Fourier transform infrared microspectroscopic analysis of bones of osteocalcin-deficient mice provides insight into the function of osteocalcin,” *Bone*, vol. 23, no. 3, pp. 187–196, 1998, doi: 10.1016/S8756-3282(98)00092-1.

[388] S. Bailey, G. Karsenty, C. Gundberg, and D. Vashishth, “Osteocalcin and osteopontin influence bone morphology and mechanical properties,” *Ann N Y Acad Sci*, vol. 1409, no. 1, pp. 79–84, 2017, doi: 10.1016/j.physbeh.2017.03.040.

[389] H. Assi, “Rodent Glioma Models: Intracranial Stereotactic Allografts and Xenografts,” in *Animal Models of Brain Tumors. Neuromethods*, R. Martínez Murillo and A. Martínez, Eds. Humana Press Inc., 2012.

[390] M. A. O’Reilly, A. Muller, and K. Hynynen, “Ultrasound Insertion Loss of Rat Parietal Bone Appears to Be Proportional to Animal Mass at Submegahertz Frequencies,” *Ultrasound Med. Biol.*, vol. 37, no. 11, pp. 1930–1937, Nov. 2011, doi: 10.1016/j.ultrasmedbio.2011.08.001.

[391] P. C. Hobar, J. A. Masson, R. Wilson, and J. Zerwekh, “The importance of the dura in craniofacial surgery,” *Plast. Reconstr. Surg.*, vol. 98, no. 2, pp. 217–225, Aug. 1996, doi: 10.1097/00006534-199608000-00003.

[392] G. M. Cooper, M. P. Mooney, A. K. Gosain, P. G. Campbell, J. E. Losee, and J. Huard, “Testing the critical size in calvarial bone defects: Revisiting the concept of a critical-size defect,” *Plast. Reconstr. Surg.*, vol. 125, no. 6, pp. 1685–1692, Jun. 2010, doi: 10.1097/PRS.0b013e3181cb63a3.

[393] P. Ducy, R. Zhang, V. Geoffroy, A. L. Ridall, and G. Karsenty, “Osf2/Cbfa1: A transcriptional activator of osteoblast differentiation,” *Cell*, vol. 89, no. 5, pp. 747–754, May 1997, doi: 10.1016/S0092-8674(00)80257-3.

[394] T. Komori *et al.*, “Targeted disruption of Cbfa1 results in a complete lack of bone formation owing to maturational arrest of osteoblasts,” *Cell*, vol. 89, no. 5, pp. 755–764, May 1997, doi: 10.1016/S0092-8674(00)80258-5.

[395] H. G. Schulze, S. O. Konorov, N. J. Caron, J. M. Piret, M. W. Blades, and R. F. B. Turner, “Assessing differentiation status of human embryonic stem cells noninvasively using raman microspectroscopy,” *Anal. Chem.*, vol. 82, no. 12, pp. 5020–5027, Jun. 2010, doi: 10.1021/ac902697q.

[396] P. I. Okagbare, D. Begun, M. Tecklenburg, A. Awonusi, S. A. Goldstein, and M. D. Morris, “ Noninvasive Raman spectroscopy of rat tibiae: approach to in vivo assessment of bone quality ,” *J. Biomed. Opt.*, vol. 17, no. 9, p. 905021, Sep. 2012, doi: 10.1117/1.jbo.17.9.090502.

[397] R. Mukherjee, P. Kanti Barman, P. Kumar Thatoi, R. Tripathy, B. Kumar Das, and B. Ravindran, “Non-Classical monocytes display inflammatory features: Validation in Sepsis and Systemic Lupus Erythematous,” *Sci. Rep.*, vol. 5, no. May, pp. 1–14, 2015, doi: 10.1038/srep13886.

Appendix A
Experimental DEP profiles for different channel heights and powers

Figure 0.1: Plots of experimentally measured profiles of the DEP force component driving alignment of 5 µm beads for different powers power in 24 µm high channel.

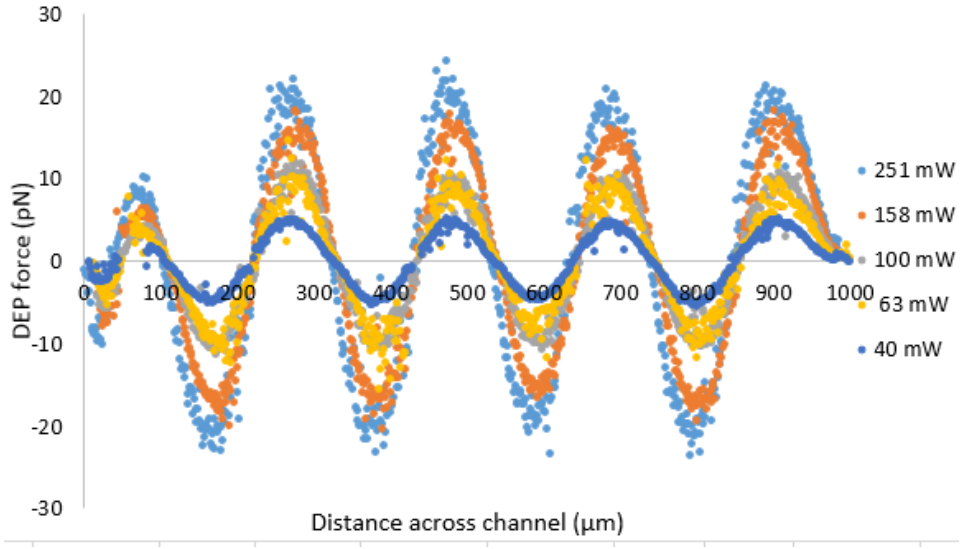

Figure 0.2: Plots of experimentally measured profiles of the DEP force component driving alignment of 5 µm beads for different powers power in 44 µm high channel.

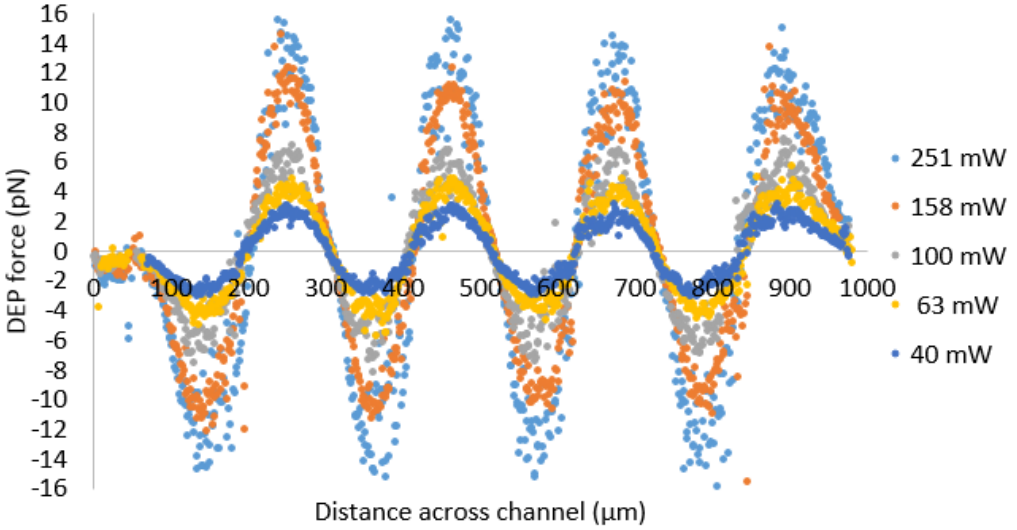

Figure 0.3: Plots of experimentally measured profiles of the DEP force component driving alignment of 5 µm beads for different powers power in 64 µm high channel.

Figure 0.4: Plots of experimentally measured profiles of the DEP force component driving alignment of 5 μm beads for different powers power in 84 μm high channel.

Appendix B
Spectral overlap of antibodies used in FACS multi-panel

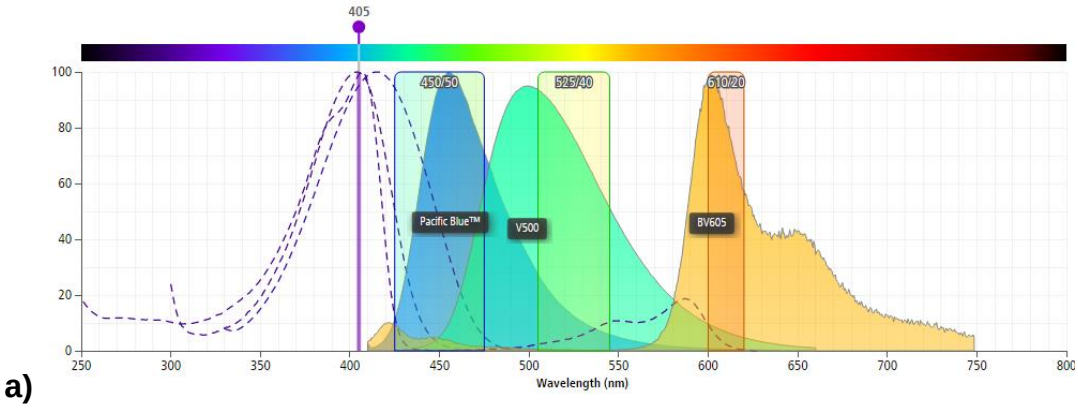

a)

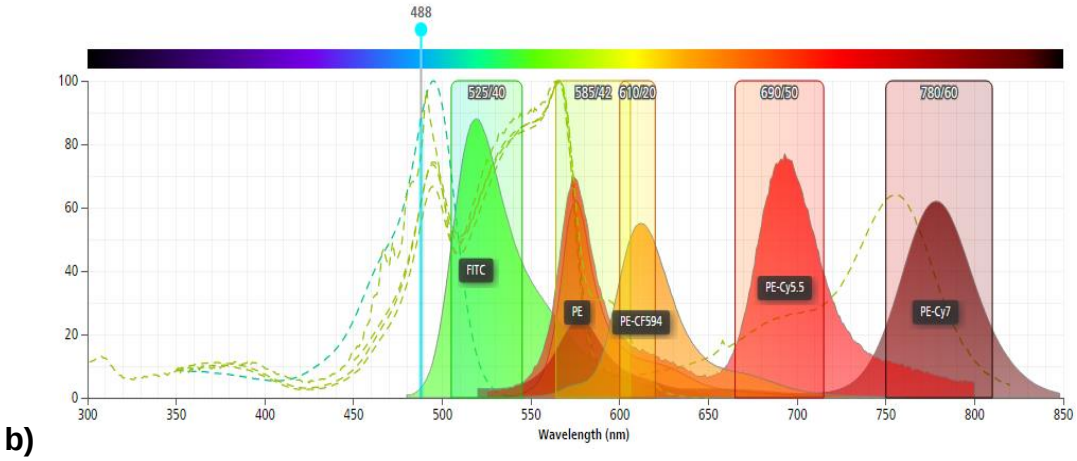

b)

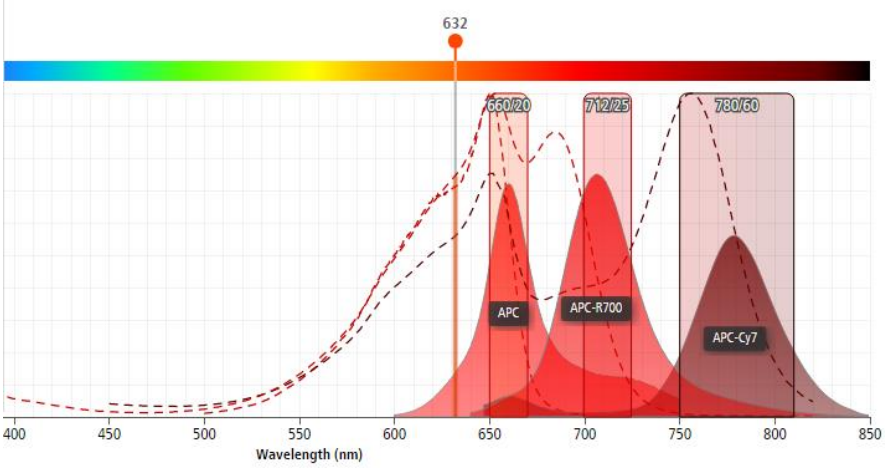

c)

Figure B.0.0.1: a) Spectral overlap of antibodies excited with the violet laser. b) Spectral overlap of antibodies excited with the blue laser. c) Spectral overlap of antibodies excited with the red laser. The excitation spectra are represented in dotted lines and the emission spectra are represented in coloured peaks. This figure was created using BD fluorescence spectrum viewer (BD biosciences). The filters used are represented as boxes around the passband.

Appendix C
Titration of antibodies used in FACS and FMO controls

C.1. Titration of antibodies used in FACS panel

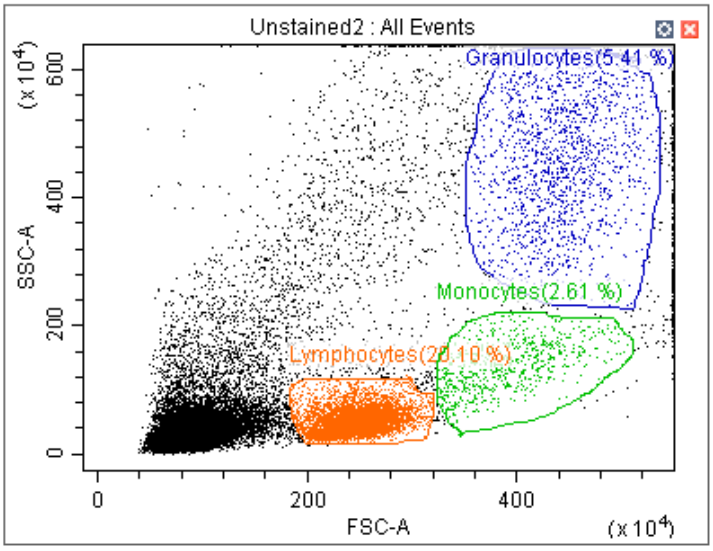

Figure C.0.1: Gates used for all antibody titrations.

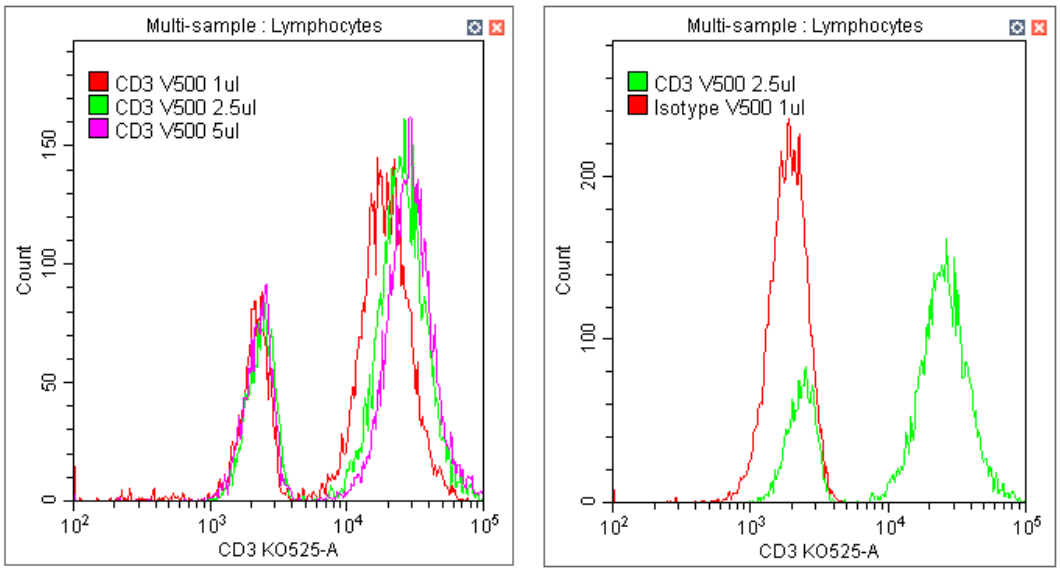

Figure C.0.2: Titration of CD3 antibody using the lymphocyte gate. a) Fluorescence of three volumes of CD3 V500. b) Comparison of CD3 antibody fluorescence with Isotype control.

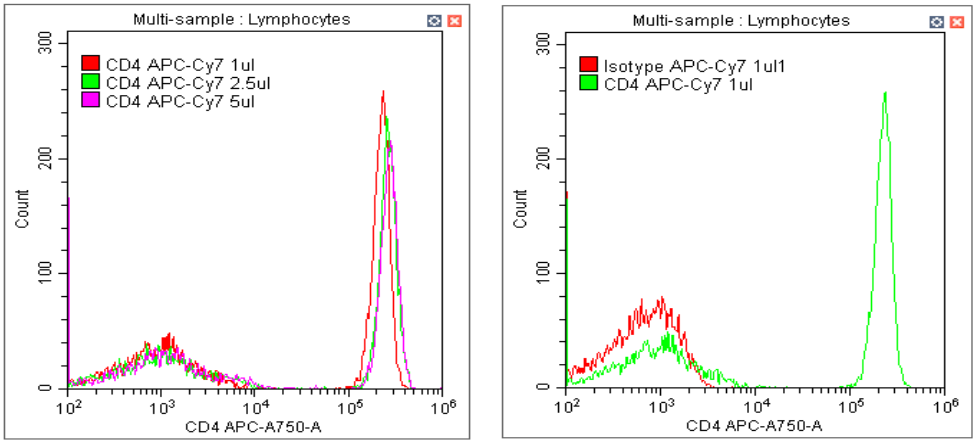

Figure C.0.3: Titration of CD4 antibody using the lymphocytes gate. a) Fluorescence of three volumes of CD4 APC-Cy7. b) Comparison of CD4 antibody fluorescence with Isotype control.

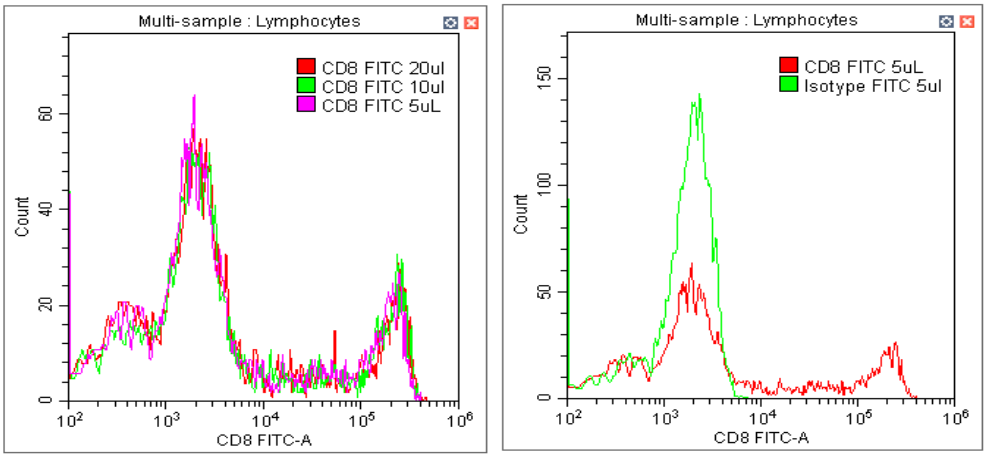

Figure C.0.4: Titration of CD8 antibody using the lymphocytes gate. a) Fluorescence of three volumes of CD8 FITC. b) Comparison of CD8 antibody fluorescence with Isotype control.

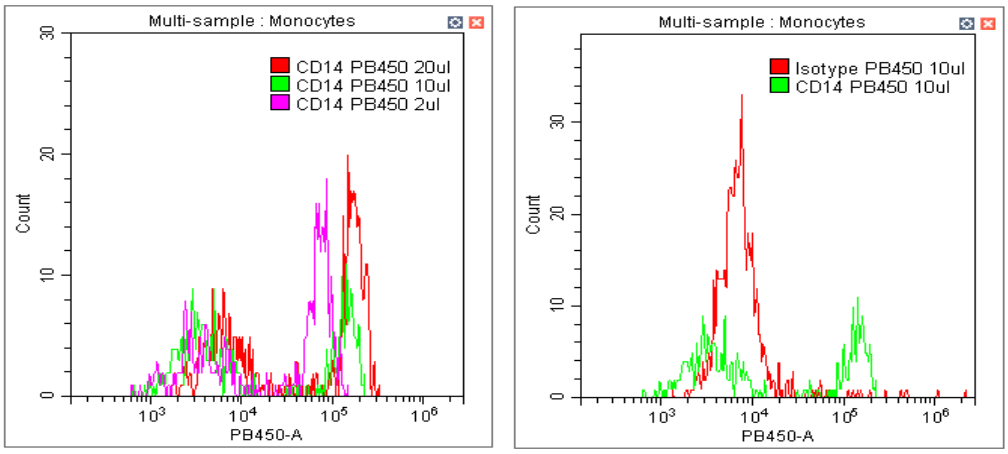

Figure C.0.5: Titration of CD14 antibody using the monocytes gate. a) Fluorescence of three volumes of CD14 PB450 gated. b) Comparison of CD14 antibody fluorescence with Isotype control.

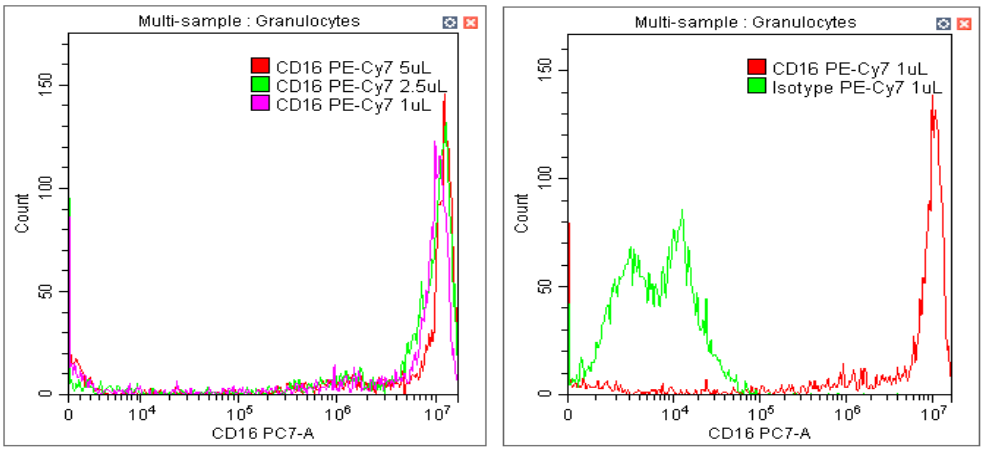

Figure C.0.6: Titration of CD16 antibody using the granulocytes gate. a) Fluorescence of three volumes of CD16 PE-Cy7. b) Comparison of CD16 antibody fluorescence with Isotype control.

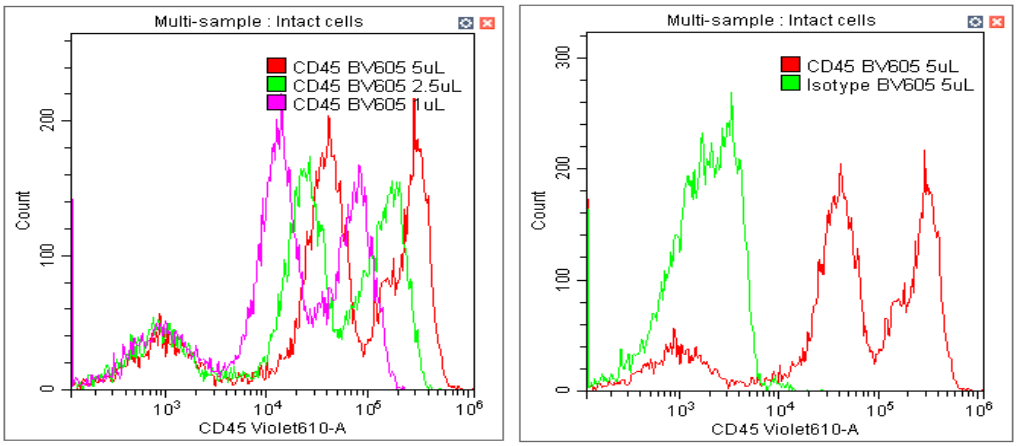

Figure C.0.7: Titration of CD45 antibody using the intact cells gate. a) Fluorescence of three volumes of CD45 BV605 . b) Comparison of CD45 antibody fluorescence with Isotype control.

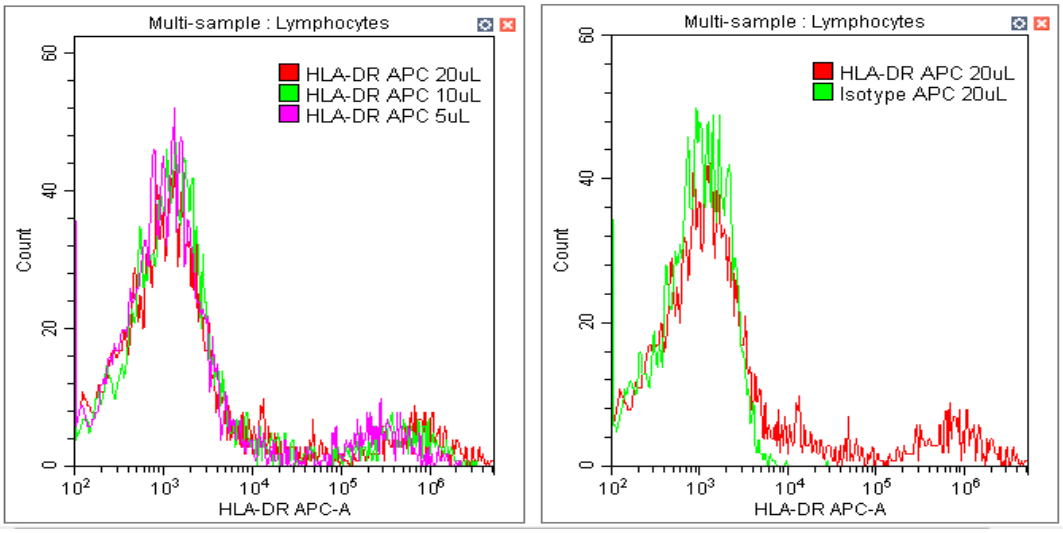

Figure C.0.8: Titration of HLA-DR antibody using the lymphocytes gate. a) Fluorescence of three volumes of HLA-DR APC. b) Comparison of CD45 antibody fluorescence with Isotype control.

C.2. FMO controls used in FACS panel

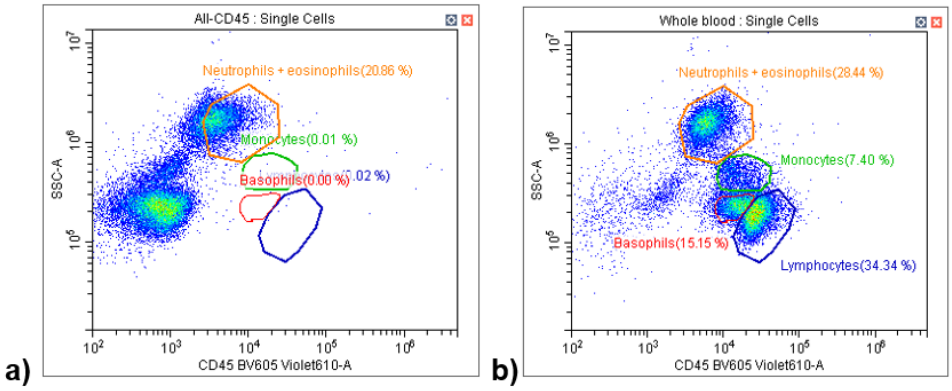

Figure C.0.9: Neutrophils, monocytes, and lymphocytes gating for sample containing all antibodies – CD45 (a) and a sample containing all antibodies (b).

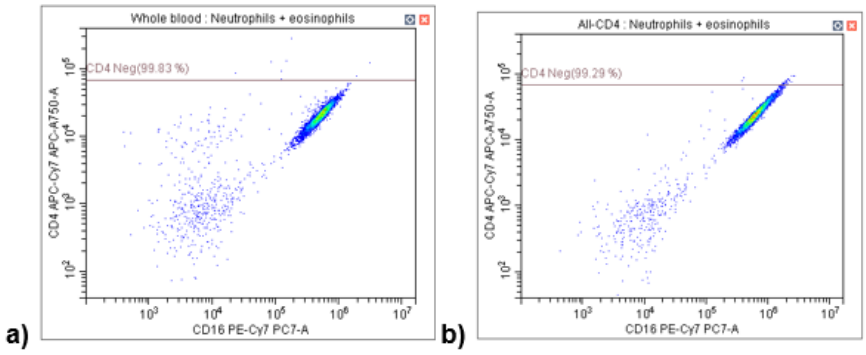

Figure C.0.10: Plot showing CD4-Cy7 fluorescence for a sample containing all antibodies – CD4 (a) and a sample containing all antibodies (b). The CD4- gate was placed using sample a).

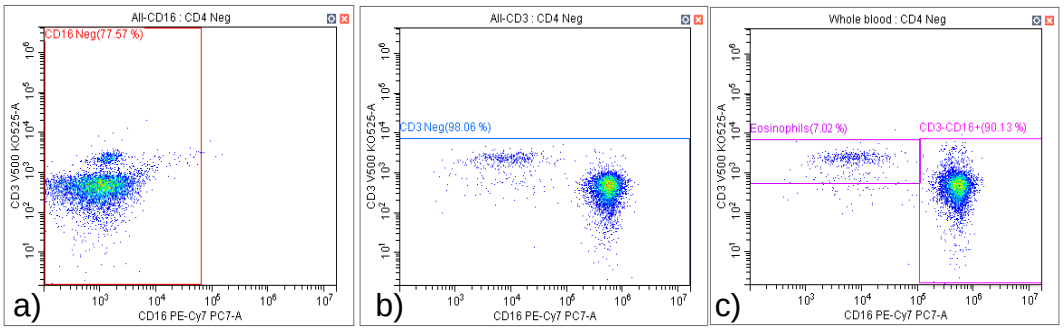

Figure C.0.11: Plots showing CD3-V500 fluorescence against CD16-PE-Cy7 for a sample containing all antibodies – CD16 (a), a sample containing all antibodies – CD3 (b) and a sample containing all antibodies (c). Plot a) was used to place the CD16- gate, plot b) was used to set the CD3- gate and plot c) shows the eosinophils gate (CD3-CD16-) and the CD3-CD16+ gate.

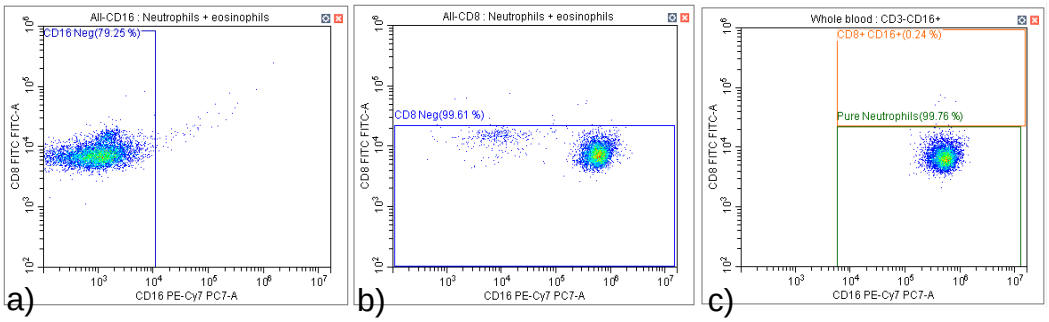

Figure C.0.12: Plots showing CD8-FITC fluorescence against CD16-PE-Cy7 for a sample containing all antibodies – CD16 (a), a sample containing all antibodies – CD8 (b) and a sample containing all antibodies (c). Plot a) was used to place the CD16- gate, plot b) was used to set the CD8- gate and plot c) shows the pure neutrophils gate (CD8- CD16+) and the CD3-CD16+ gate.

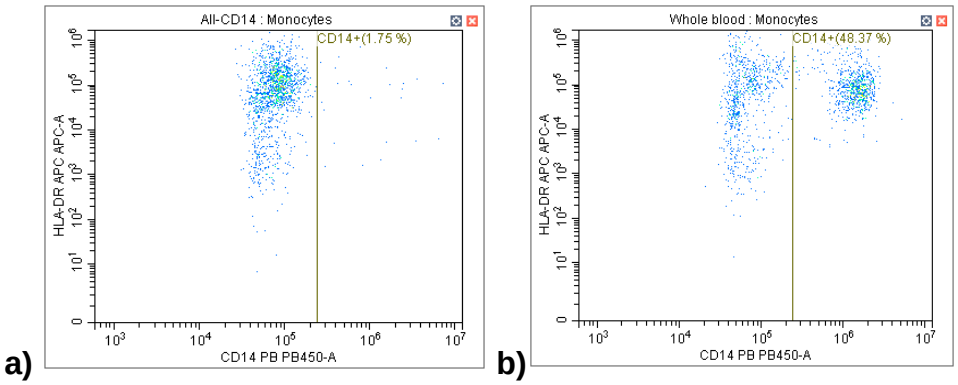

Figure C.0.13: Plot showing CD14-Pacific blue fluorescence for a sample containing all antibodies – CD14 (a) and a sample containing all antibodies (b). The CD14+gate was placed using sample a).

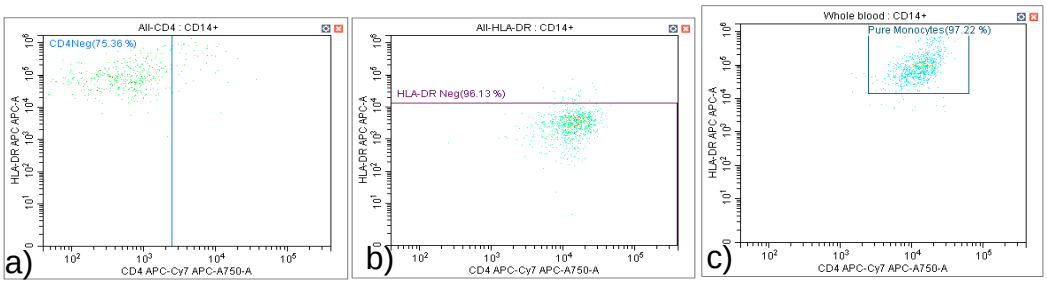

Figure C.0.14: Plots showing HLA-DR-APC fluorescence against CD4-APC-Cy7 for a sample containing all antibodies – CD14 (a), a sample containing all antibodies – HLA-DR (b) and a sample containing all antibodies (c). Plot a) was used to place the CD4- gate, plot b) was used to set the HLA-DR- gate and plot c) shows the pure monocytes gate (CD14+ HLA-DR+).

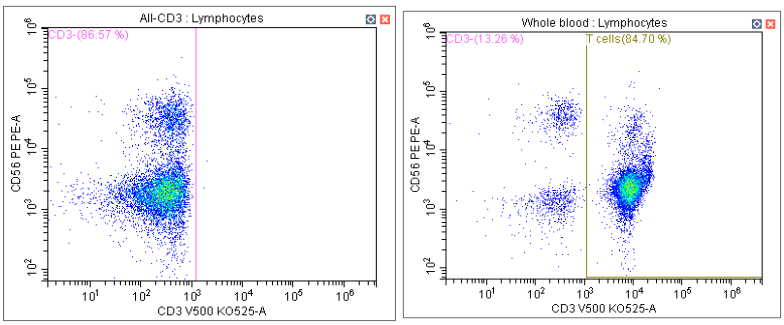

Figure C.0.15: Plot showing CD3-V500 fluorescence for a sample containing all antibodies – CD3 (a) and a sample containing all antibodies (b). The CD3- gate and T cells gate (CD3+) were placed using sample a).

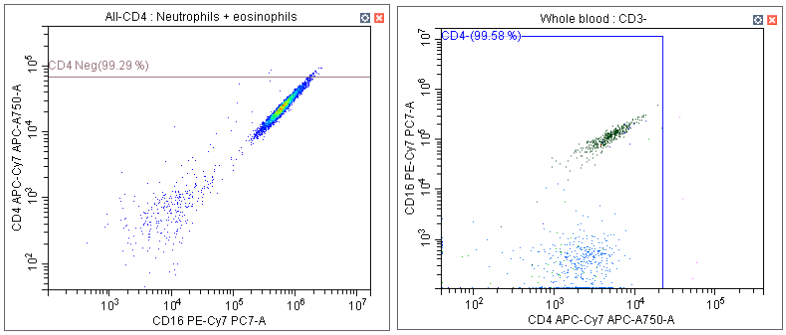

Figure C.0.16: Plot showing CD4-APC-Cy7 fluorescence for a sample containing all antibodies – CD4 (a) and a sample containing all antibodies (b). The CD4- gate was placed using sample a).

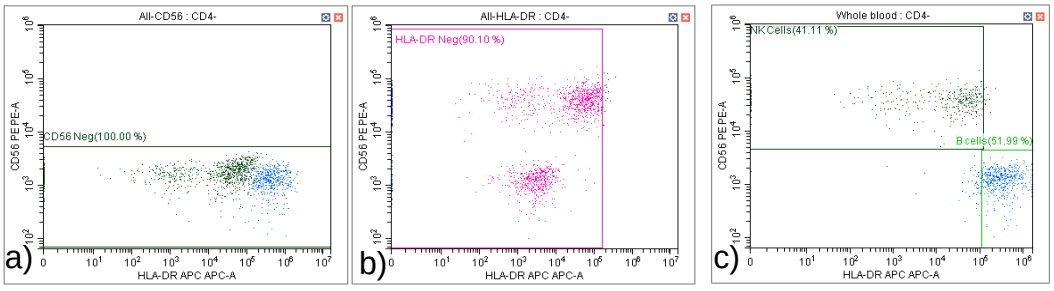

Figure C.0.17: Plots showing HLA-DR-APC fluorescence against CD56-PE for a sample containing all antibodies – CD4 (a), a sample containing all antibodies – HLA-DR (b) and a sample containing all antibodies (c). Plot a) was used to place the CD56- gate, plot b) was used to set the HLA-DR- gate and plot c) shows the NK cells gate (CD56+ HLA-DR-) and the B cells gate (CD56- HLA-DR+).

Appendix D
Determination of dielectric properties of cells

D.1. Dielectric properties of monocytes

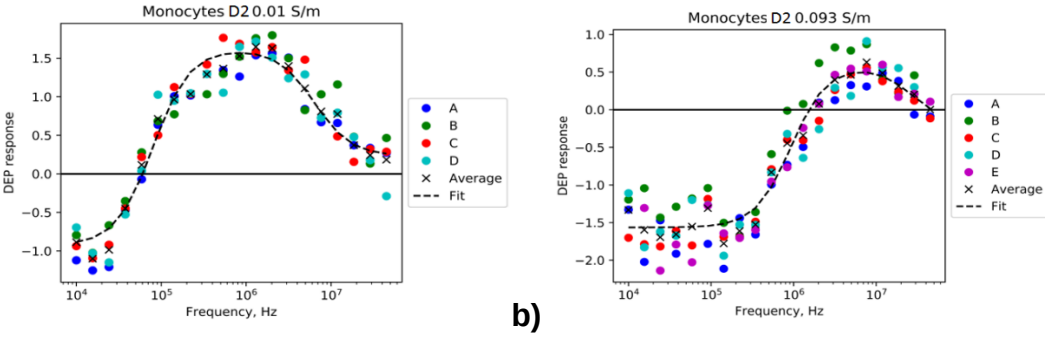

a) b)

Figure D.0.1: DEP spectra of monocytes from donor 2 at two buffer conductivities: 0.01 S/m (a) and 0.093 S/m (b) The dashed line represents the single-conductivity fit and the experimental DEP response obtained by 3DEP is shown by dots. The different replicates (A, B, C, D, E) are shown in different colours.

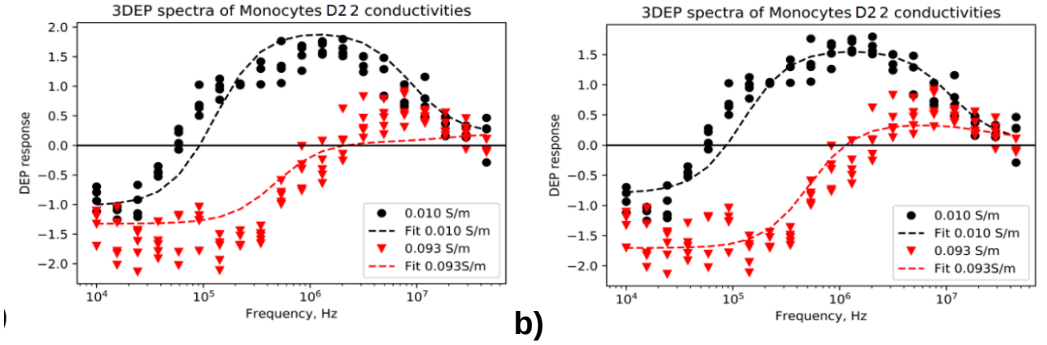

a) b)

Figure D.0.2: 3DEP spectra of monocytes from donor 2 using the two-conductivity model for a single common scaling factor (a) and two different scaling factors (b). The fitting curves are represented as dotted lines while the experimental data is shown by circles and triangles. For each conductivity, at least four replicates were considered.

	Conductivities used (S/m)			
	0.01	0.093	0.01 & 0.93 Same scale	0.01 & 0.93 different scale
Cell cadius	3.735 µm			
Membrane Conductance	500 S/m^2 (fixed)			
Reduced χ^2	0.055	0.081	0.16	0.10
Bayesian criteria	-215	-183	-304	-383
Membrane capacitance (mF/m^2)	9.1±0.5	3.9±0.3	6.0±0.4	6.3±0.3
Cytoplasm Permittivity	108±9	69±16	103±12	90±10
Cytoplasm Conductivity (S/m)	0.074±0.009	0.16±0.01	0.104±0.008	0.129±0.007
Scaling factor	2.5	3.2	2.7	2.1 & 3.5

Table D.1: Summary of dielectric properties of monocytes from a single donor (D2) derived using a triple conductivity fit (with the same of different scaling factors) of DEP spectra obtained for different medium conductivities.

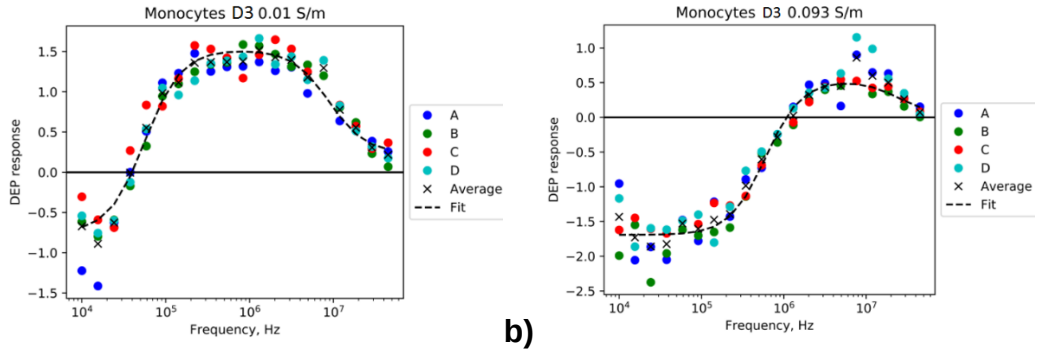

Figure D.0.3: DEP spectra of monocytes from donor 3 at two buffer conductivities: 0.01 S/m (a) and 0.093 S/m (b) The dashed line represents the single-conductivity fit and the experimental DEP response obtained by 3DEP is shown by dots. The different replicates (A, B, C, D, E) are shown in different colours.

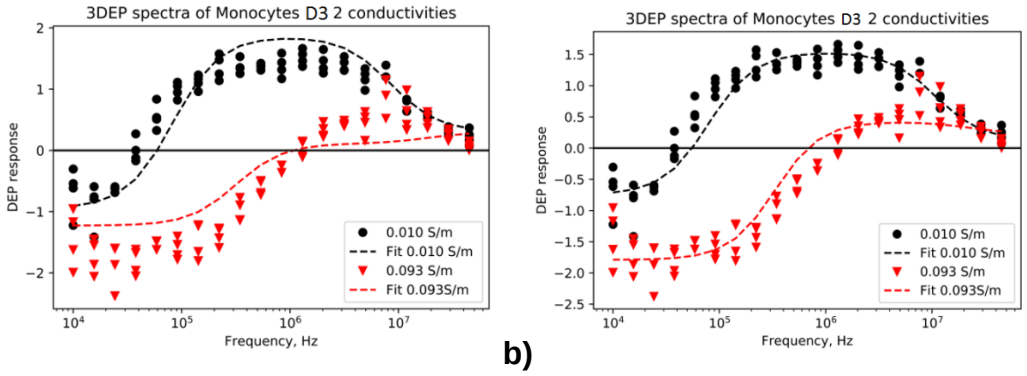

Figure D.0.4: 3DEP spectra of monocytes from donor 3 using the two-conductivity model for a single common scaling factor (a) and two different scaling factors (b). The fitting curves are represented as dotted lines while the experimental data is shown by circles and triangles. For each conductivity, at least four replicates were considered.

	Conductivities used (S/m)			
	0.01	0.093	0.01 & 0.93 Same scale	0.01 & 0.93 different scale
Radius (µm)	3.735			
Membrane Conductance (S/m^2)	500 (fixed)			
Reduced χ^2	0.045	0.050	0.16	0.076
Bayesian criteria	-168	-158	-264	-380
Membrane capacitance (mF/m^2)	14.0±0.9	5.9±0.5	9.3±0.7	10.0±0.5
Cytoplasm Permittivity	114±15	85±12	116±14	98±9
Cytoplasm Conductivity (S/m)	0.11±0.02	0.149±0.008	0.11±0.1	0.133±0.006
Scaling factor	2	3.5	2.5	2 & 3.7

Table D.2: Summary of dielectric properties of monocytes from a single donor (D3) derived using a triple conductivity fit (with the same of different scaling factors) of DEP spectra obtained for different medium conductivities.

D.2. Dielectric properties of neutrophils

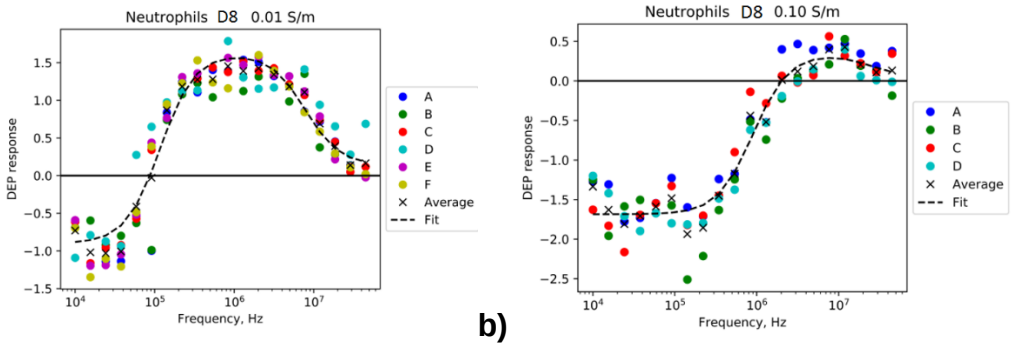

a) b)

Figure D.0.5: DEP spectra of neutrophils from donor 8 at two buffer conductivities: 0.01 S/m (a) and 0.10 S/m (b) The dashed line represents the single-conductivity fit and the experimental DEP response obtained by 3DEP is shown by dots. The different replicates (A, B, C, D, E) are shown in different colours.

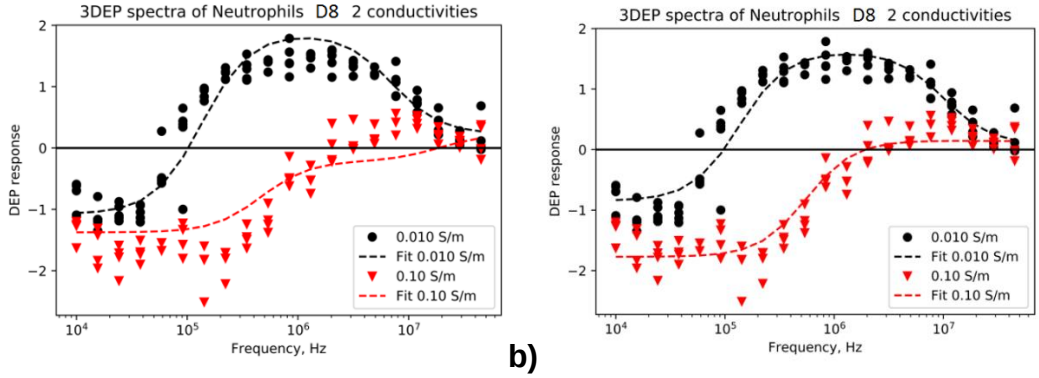

a) b)

Figure D.0.6: 3DEP spectra of neutrophils from donor 8 using the two-conductivity model for a single common scaling factor (a) and two different scaling factors (b). The fitting curves are represented as dotted lines while the experimental data is shown by circles and triangles. For each conductivity, at least four replicates were considered.

	Conductivities used (S/m)			
	0.01	0.10	0.01 & 0.10 Same scale	0.01 & 0.10 different scale
Fixed values	Radius: 3.52µm		Membrane Conductance: 500 S/m^2	
Reduced χ^2	0.081	0.067	0.13	0.085
Bayesian criteria	-269	-197	-372	-452
Membrane capacitance (mF/m^2)	6.7±0.4	4.1±0.3	5.7±0.3	6.0±0.3
Cytoplasm Permittivity	99±11	88±12	106±9	93±8
Cytoplasm Conductivity (S/m)	0.90±0.01	0.14±0.009	0.083±0.006	0.118±0.006
Scaling factor	2.4±0.1	3.46	2.8	2.2&3.6

Table D.3: Summary of dielectric properties of neutrophils from a single donor (D8) derived using a triple conductivity fit (with the same of different scaling factors) of DEP spectra obtained for different medium conductivities.

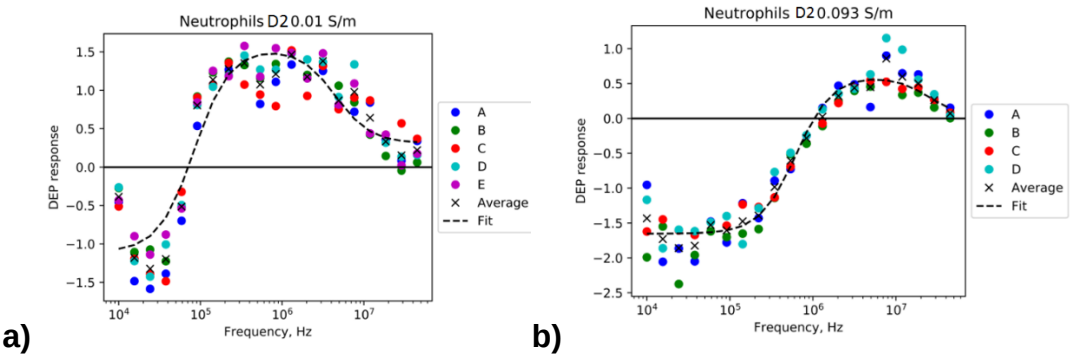

a) b)

Figure D.0.7: DEP spectra of neutrophils from donor 2 at two buffer conductivities: 0.01 S/m (a) and 0.093 S/m (b) The dashed line represents the single-conductivity fit and the experimental DEP response obtained by 3DEP is shown by dots. The different replicates (A, B, C, D, E) are shown in different colours.

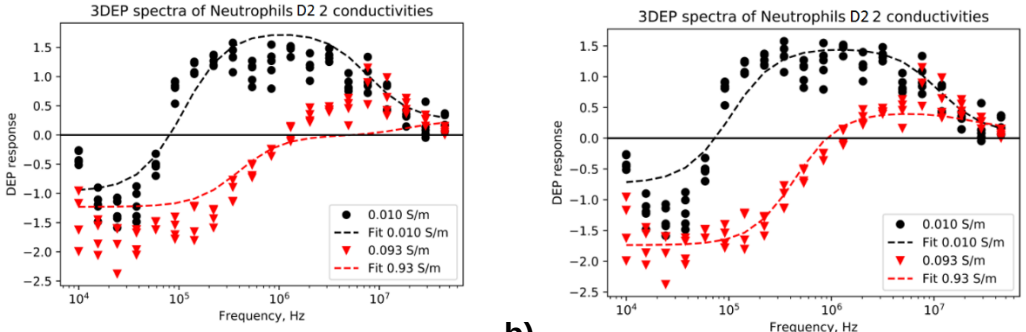

a) b)

Figure D.0.8: 3DEP spectra of neutrophils from donor 2 using the two-conductivity model for a single common scaling factor (a) and two different scaling factors (b). The fitting curves are represented as dotted lines while the experimental data is shown by circles and triangles. For each conductivity, at least four replicates were considered.

	Conductivities used (S/m)			
	0.01	0.093	0.01 & 0.93 Same scale	0.01 & 0.93 different scale
Fixed values	Radius: 3.52µm		Membrane Conductance: 500 S/m^2	
Reduced χ^2	0.12	0.056	0.19	0.11
Bayesian criteria	-192	-209	-278	-362
Membrane capacitance (mF/m^2)	8.3±0.6	6.2±0.4	7.2±0.6	8.0±0.5
Cytoplasm Permittivity	113±20	82±11	111±14	93±11
Cytoplasm Conductivity (S/m)	0.048±0.007	0.160±0.008	0.0956±0.009	0.135±0.008
Scaling factor	2.9	3.4	2.5	1.9 & 3.6

Table D.4: Summary of dielectric properties of neutrophils from a single donor (D2) derived using a triple conductivity fit (with the same of different scaling factors) of DEP spectra obtained for different medium conductivities.

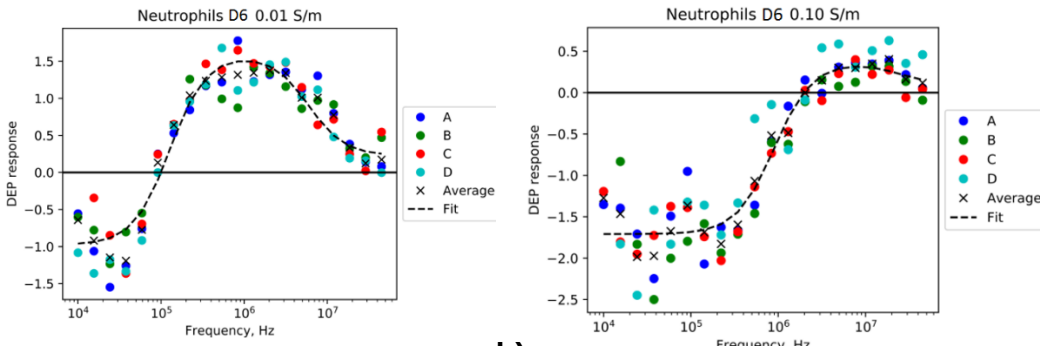

a) b)

Figure D.0.9: DEP spectra of neutrophils from donor 6 at two buffer conductivities: 0.01 S/m (a) and 0.1 S/m (b). The dashed line represents the single-conductivity fit and the experimental DEP response obtained by 3DEP is shown by dots. The different replicates (A, B, C, D, E) are shown in different colours.

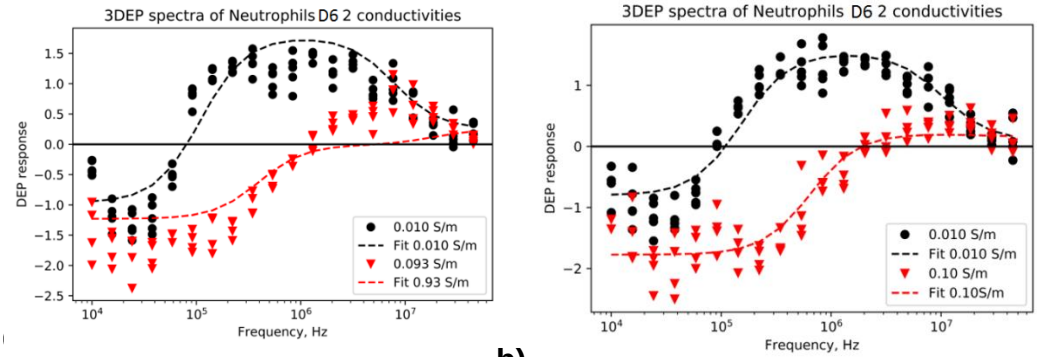

a) b)

Figure D.0.10: 3DEP spectra of neutrophils from donor 6 using the two-conductivity model for a single common scaling factor (a) and two different scaling factors (b). The fitting curves are represented as dotted lines while the experimental data is shown by circles and triangles. For each conductivity, at least four replicates were considered.

	Conductivities used (S/m)			
	0.01	0.10	0.01 & 0.10 Same scale	0.01 & 0.10 different scale
Fixed values	Radius: 3.52µm		Membrane Conductance: 500 S/m^2	
Reduced χ^2	0.080	0.098	0.16	0.098
Bayesian criteria	-228	-168	-305	-384
Membrane capacitance (mF/m^2)	5.9±0.4	4.1±0.4	4.8±0.03	5.3±0.3
Cytoplasm Permittivity	109±10	92±14	110±11	95±10
Cytoplasm Conductivity (S/m)	0.068±0.008	0.14±0.01	0.085±0.007	0.12±0.007
Scaling factor	2.6	3.5	2.8	2.6 &3.6

Table D.5: Summary of dielectric properties of neutrophils from a single donor (D6) derived using a triple conductivity fit (with the same of different scaling factors) of DEP spectra obtained for different medium conductivities.

D.3. Dielectric properties of eosinophils

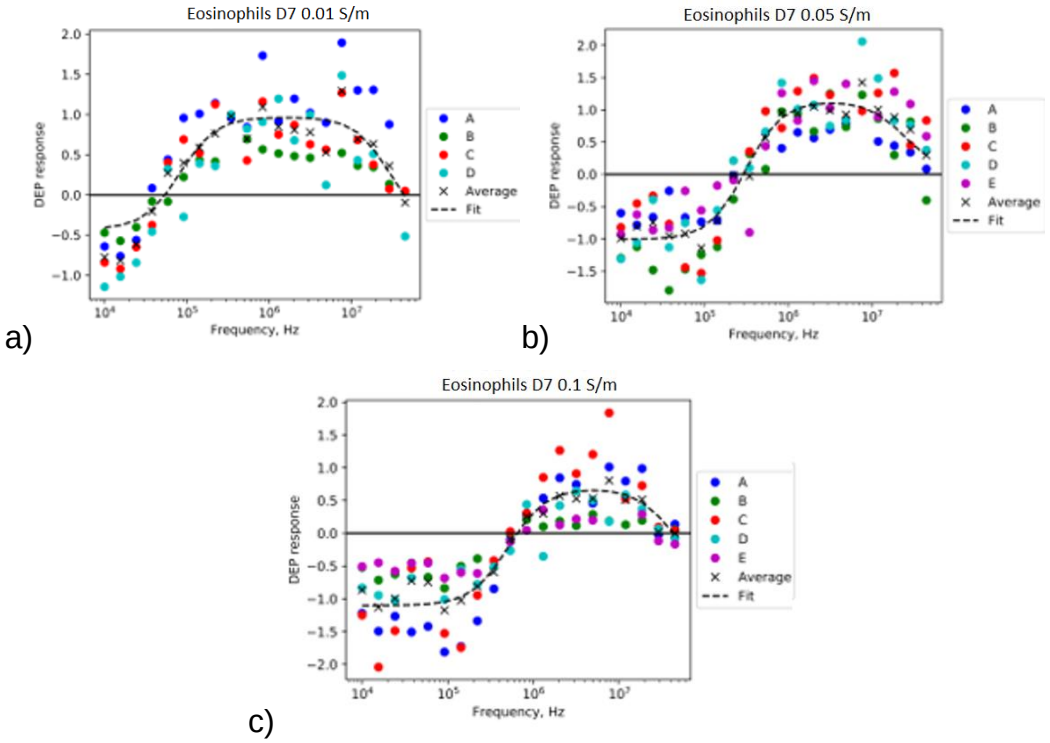

Figure D.0.11: DEP spectra of eosinophils from donor 7 at three buffer conductivities: 0.01 S/m (a) 0.05 S/m (b) and 0.1 S/m (c). The dashed line represents the single-conductivity fit and the experimental DEP response obtained by 3DEP is shown by dots. The different replicates (A, B, C, D, E) are shown in different colours.

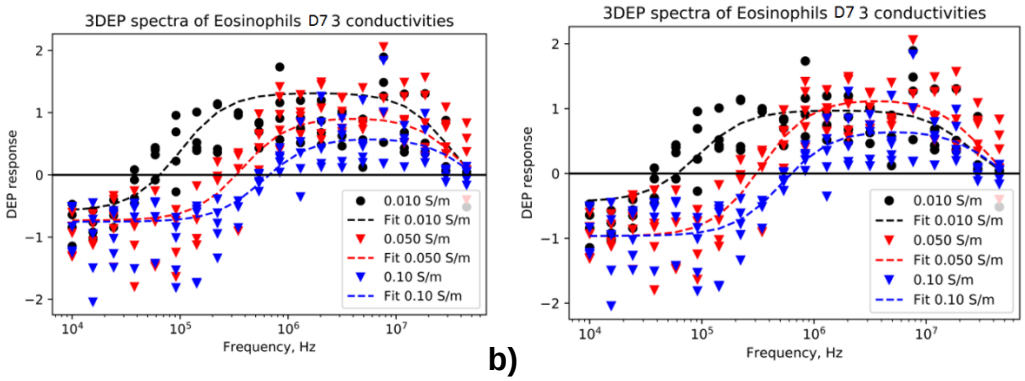

Figure D.0.12: 3DEP spectra of eosinophils from donor 7 using the three-conductivity model for a single common scaling factor (a) and three different scaling factors (b). The fitting curves are represented as dotted lines while the experimental data is shown by circles and triangles. For each conductivity, at least four replicates were considered.

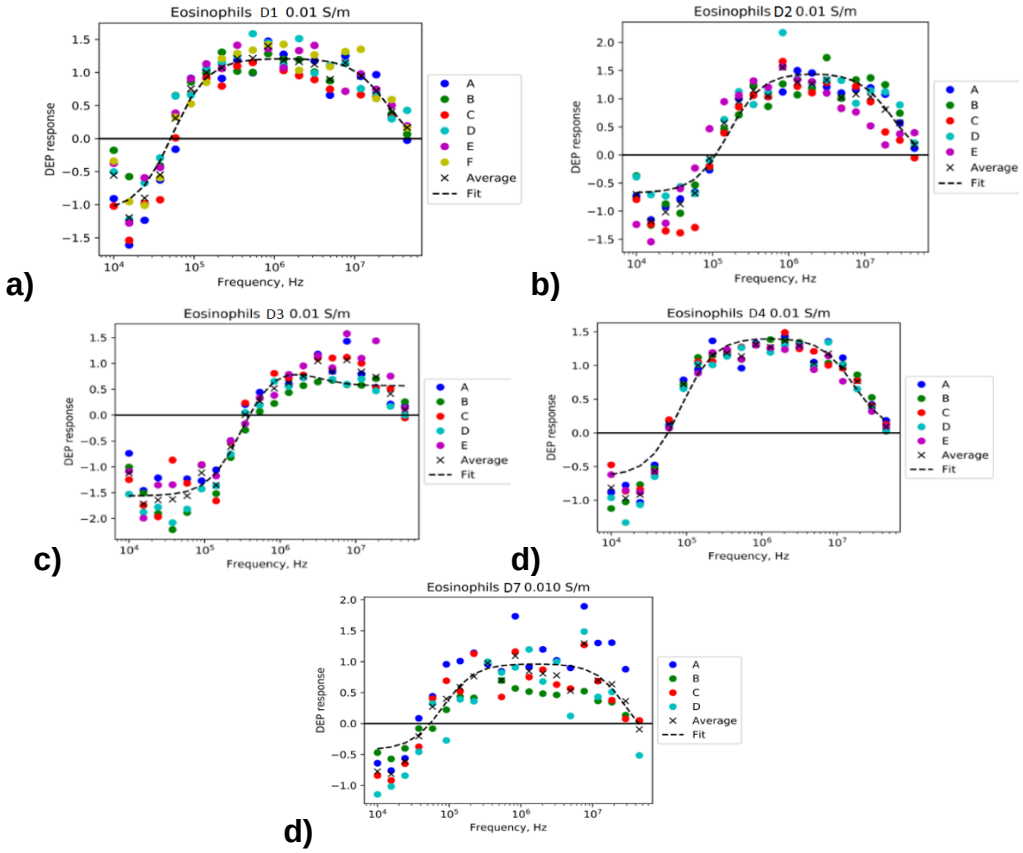

Figure D.0.13: DEP spectra of eosinophils from donors 1, 2, 3, 4 and 7 (a, b, c, d, e) at 0.01 S/m buffer conductivity. The dashed line represents the single-conductivity fit and the experimental DEP response obtained by 3DEP is shown by dots. The different replicates (A, B, C, D, E) are shown in different colours.

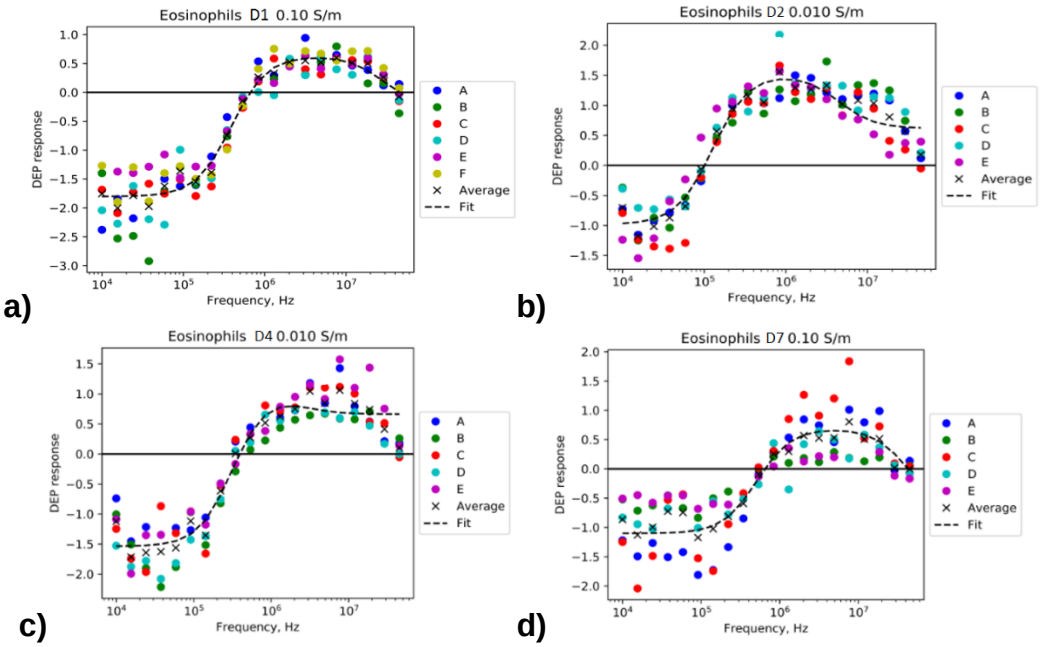

Figure D.0.14: DEP spectra of eosinophils from five different donors (a, b, c, d, e) at 0.1 S/m buffer conductivity. The dashed line represents the single-conductivity fit and the experimental DEP response obtained by 3DEP is shown by dots. The different replicates (A, B, C, D, E) are shown in different colours

D.4. Dielectric properties of BM-MSCs

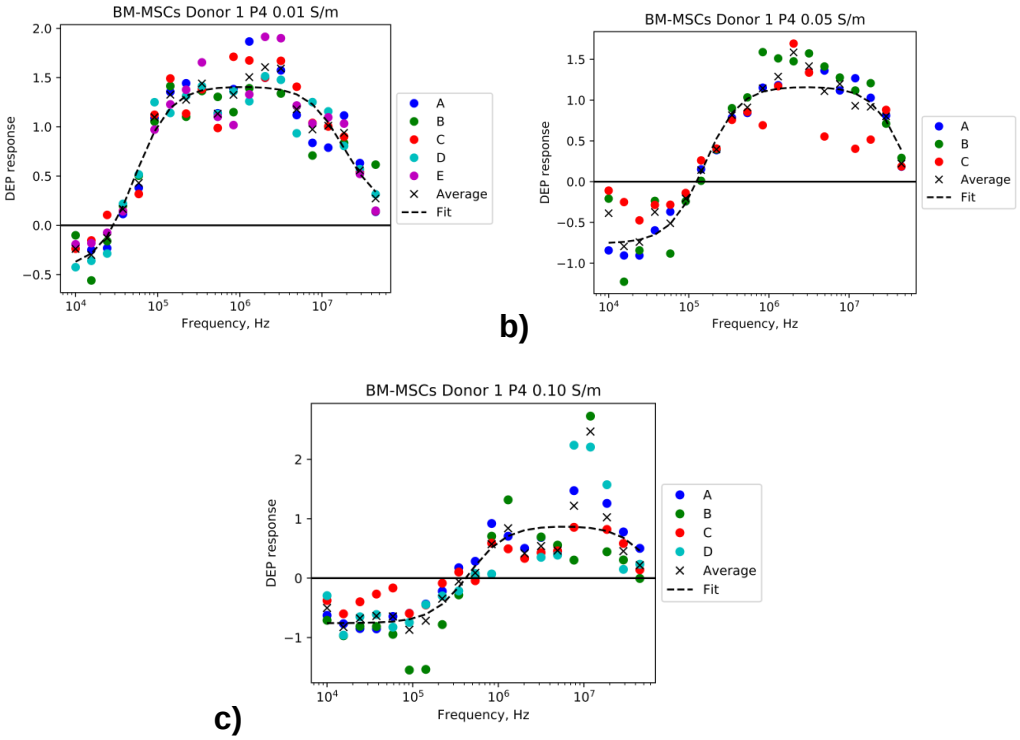

Figure D.0.15: DEP spectra of BM-MSCs from donor 1 passage 4 at three buffer conductivities: 0.01 S/m (a) 0.05 S/m (b) and 0.1 S/m (c). The dashed line represents the single-conductivity fit and the experimental DEP response obtained by 3DEP is shown by dots. The different replicates (A, B, C, D, E) are shown in different colours.

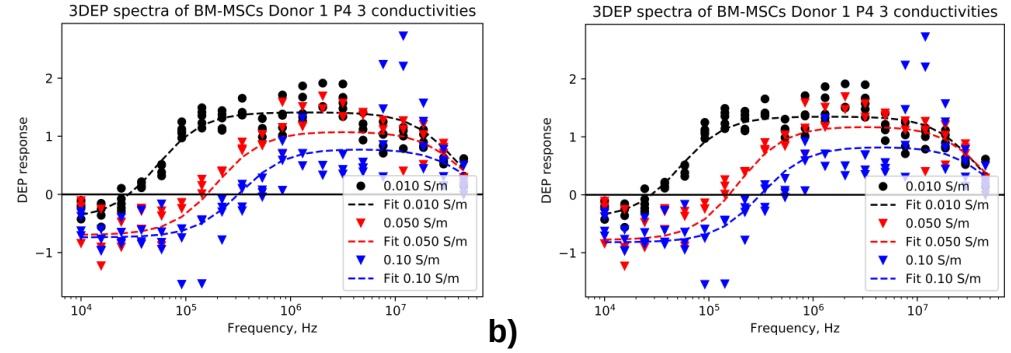

Figure D.0.16: 3DEP spectra of BM-MSCs from donor 1 passage 4 using the three-conductivity model for a single common scaling factor (a) and three different scaling factors (b). The fitting curves are represented as dotted lines while the experimental data is shown by circles and triangles. For each conductivity, at least four replicates were considered.

	0.01	0.05	0.1	0.01, 0.05 & 0.1 Same scale	0.01, 0.05 & 0.1 different scale
Fixed values	Radius: 7.5 µm			Membrane Conductance: 500 S/m^2	
Reduced χ^2	0.0425	0.085	0.22	0.12	0.12
Bayesian criteria	-289	-131	-100	-469	-466
Membrane capacitance (mF/m^2)	8.8±0.6	11.2±0.1	6.7±1	8.87±0.6	9.0±0.6
Cytoplasm Permittivity	106±26	1±13	1±164	44±76	30±68
Cytoplasm Conductivity (S/m)	0.25±0.03	0.40±0.06	0.48±0.1	0.41±0.04	0.38±0.03
Scaling factor	1.6	1.7	1.6	1.6	1.5, 1.7&1.7

Table D.6: Summary of dielectric properties of BM-MSCs from Donor 1 P4 derived using a single conductivity fit and the triple conductivity fit of DEP spectra obtained for different medium conductivities.

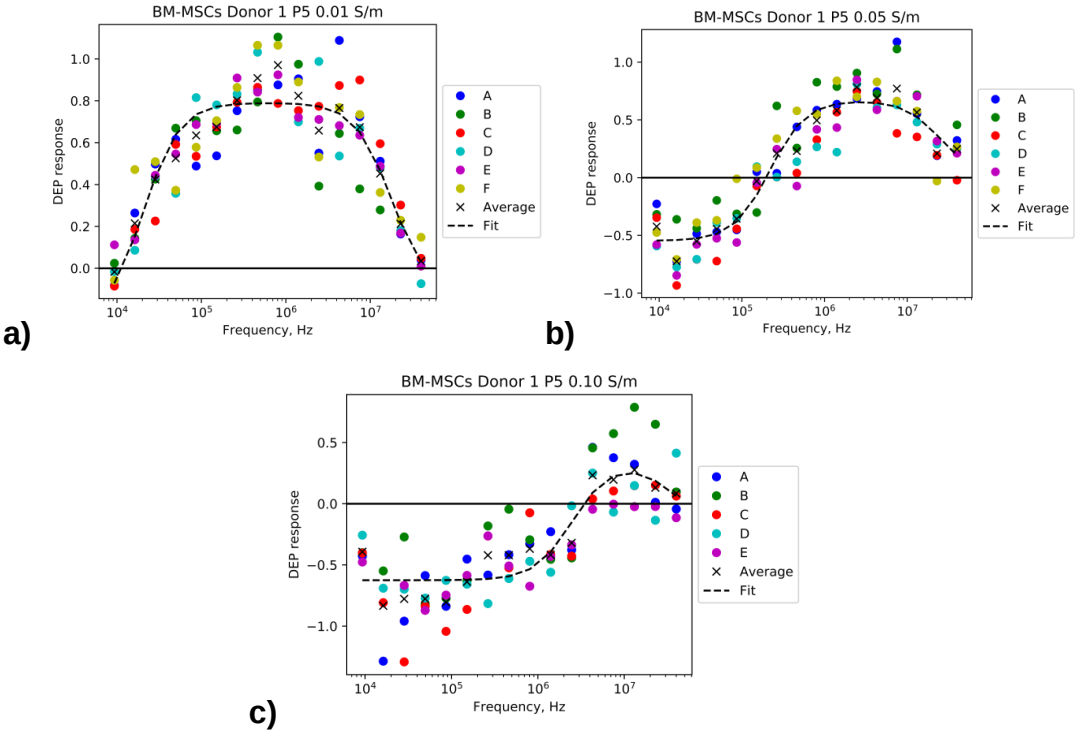

Figure D.0.17: DEP spectra of BM-MSCs from donor 1 passage 5 at three buffer conductivities: 0.01 S/m (a) 0.05 S/m (b) and 0.1 S/m (c). The dashed line represents the single-conductivity fit and the experimental DEP response obtained by 3DEP is shown by dots. The different replicates (A, B, C, D, E) are shown in different colours.

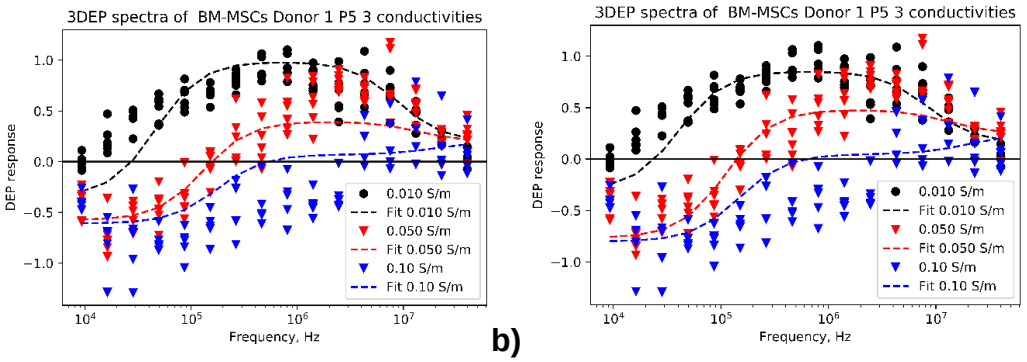

Figure D.0.18: 3DEP spectra of BM-MSCs from donor 1 passage 5 using the three-conductivity model for a single common scaling factor (a) and three different scaling factors (b). The fitting curves are represented as dotted lines while the experimental data is shown by circles and triangles. For each conductivity, at least four replicates were considered.

	BM-MSCs – Donor 1 P5 Conductivities used (S/m)				
	0.01	0.05	0.1	0.01, 0.05, 0.1 Same scale	0.01, 0.05, 0.1 different scale
Fixed values	Radius: 7.5 µm			Membrane Conductance: 500 S/m^2	
Reduced χ^2	0.021	0.043	0.067	0.080	0.071
Bayesian criteria	-353	-288	-200	-663	-687
Membrane capacitance (mF/m^2)	22±2	7.1±0.7	0.8±1	9.4±0.8	10.6±0.9
Cytoplasm Permittivity	53±23	81±38	60±66	125±17	121±13
Cytoplasm Conductivity (S/m)	0.19±0.02	0.24±0.03	0.23±0.04	0.12±0.01	0.110±0.007
Scaling factor	0.9	1.2	1.3	1.3	1.1, 1.7 & 1.7

Table D.7: Summary of dielectric properties of BM-MSCs from Donor 1 P5 derived using a single conductivity fit and the triple conductivity fit of DEP spectra obtained for different medium conductivities.

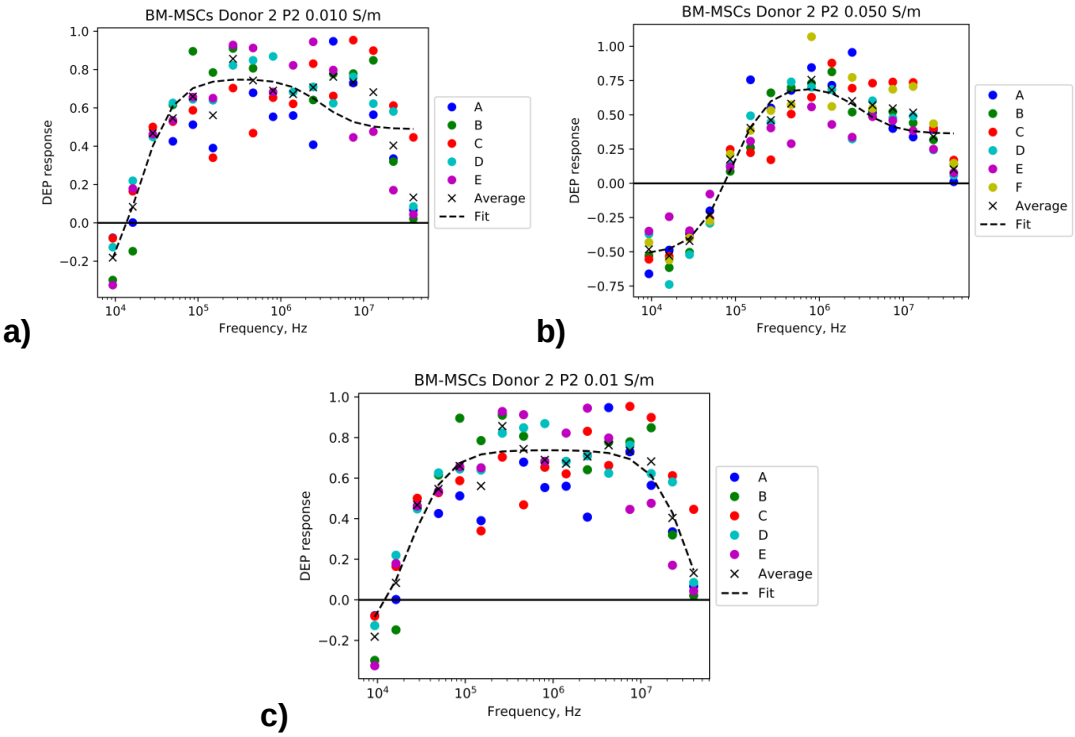

Figure D.0.19: DEP spectra of BM-MSCs from donor 2 passage 2 at three buffer conductivities: 0.01 S/m (a) 0.05 S/m (b) and 0.1 S/m (c). The dashed line represents the single-conductivity fit and the experimental DEP response obtained by 3DEP is shown by dots. The different replicates (A, B, C, D, E) are shown in different colours.

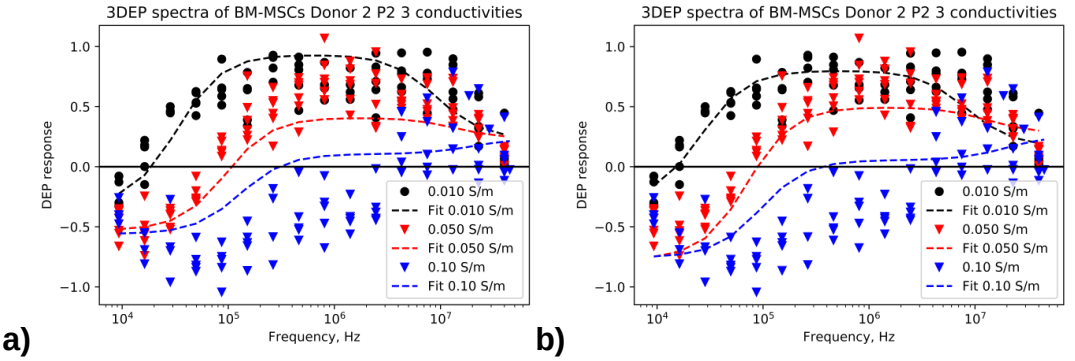

Figure D.0.20: 3DEP spectra of BM-MSCs from donor 2 passage 2 using the three-conductivity model for a single common scaling factor (a) and three different scaling factors (b). The fitting curves are represented as dotted lines while the experimental data is shown by circles and triangles. For each conductivity, at least four replicates were considered.

	BM-MSCs – Donor 2 P2 Conductivities used (S/m)				
	0.01	0.05	0.1	0.01, 0.05 & 0.1 Same scale	0.01, 0.05 & 0.1 different scale
Fixed values	Radius: 7.5 µm		Membrane Conductance: 500 S/m^2		
Reduced χ^2	0.025	0.029	0.056	0.081	0.072
Bayesian criteria	-272	-326	-217	-617	-638
Membrane capacitance (mF/m^2)	20±2	3.7±0.3	0.8±0.1	14±1	17±2
Cytoplasm Permittivity	10±71	146±10	34±84	141±20	128±13
Cytoplasm Conductivity (S/m)	0.32±0.03	0.031±0.003	0.26±0.04	0.13±0.01	0.112±0.007
Scaling factor	0.82	1.8	1.2	1.2	1,1.7 &1.6

Table D.8: Summary of dielectric properties of BM-MSCs from Donor 2 P2 derived using a single conductivity fit and the triple conductivity fit of DEP spectra obtained for different medium conductivities.

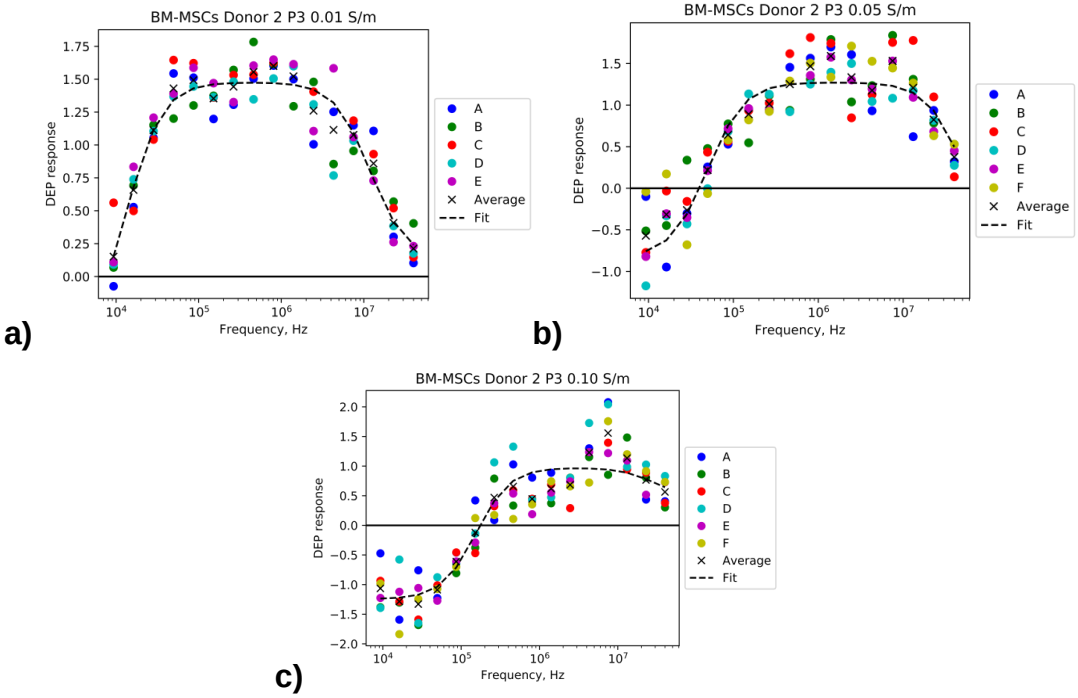

Figure D.0.21: DEP spectra of BM-MSCs from donor 2 passage 3 at three buffer conductivities: 0.01 S/m (a) 0.05 S/m (b) and 0.1 S/m (c). The dashed line represents the single-conductivity fit and the experimental DEP response obtained by 3DEP is shown by dots. The different replicates (A, B, C, D, E) are shown in different colours.

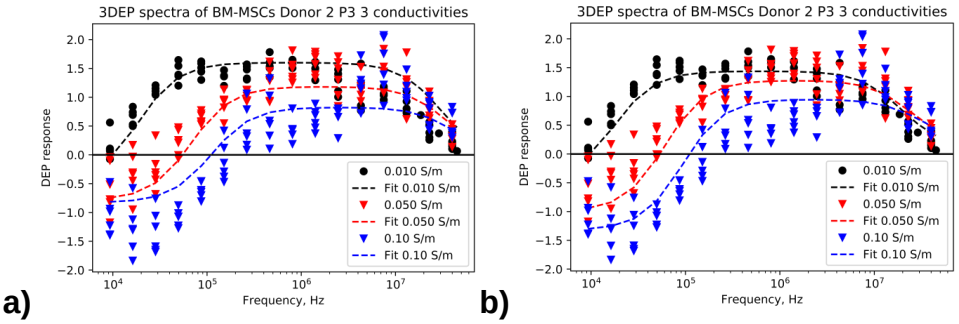

Figure D.0.22: 3DEP spectra of BM-MSCs from donor 2 passage 3 using the three-conductivity model for a single common scaling factor (a) and three different scaling factors (b). The fitting curves are represented as dotted lines while the experimental data is shown by circles and triangles. For each conductivity, at least four replicates were considered.

	BM-MSCs – Donor 2 P3 Conductivities used (S/m)				
	0.01	0.05	0.1	0.01, 0.05 & 0.1 Same scale	0.01, 0.05 & 0.1 different scale
Fixed values	Radius: 7.5 µm			Membrane Conductance: 500 S/m^2	
Reduced χ^2	0.030	0.094	0.149	0.15	0.12
Bayesian criteria	-262	-211	-169	-491	-546
Membrane capacitance (mF/m^2)	34±2	35±2	16±2	26±2	26±1
Cytoplasm Permittivity	99±14	8±152	132±38	80±58	99±21
Cytoplasm Conductivity (S/m)	0.15±0.02	0.38±0.05	0.28±0.03	0.37±0.03	0.26±0.02
Scaling factor	1.8	1.9	2.6	1.7	1.6, 2.2 & 2.8

Table D.9: Summary of dielectric properties of BM-MSCs from Donor 2 P3 derived using a single conductivity fit and the triple conductivity fit of DEP spectra obtained for different medium conductivities.

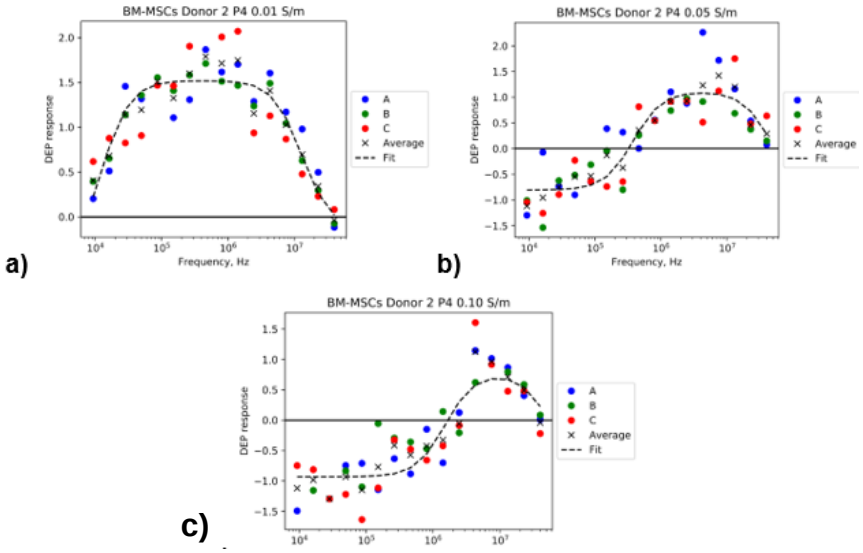

Figure D.0.23: DEP spectra of BM-MSCs from donor 2 passage 4 at three buffer conductivities: 0.01 S/m (a) 0.05 S/m (b) and 0.1 S/m (c). The dashed line represents the single-conductivity fit and the experimental DEP response obtained by 3DEP is shown by dots. The different replicates (A, B, C, D, E) are shown in different colours.

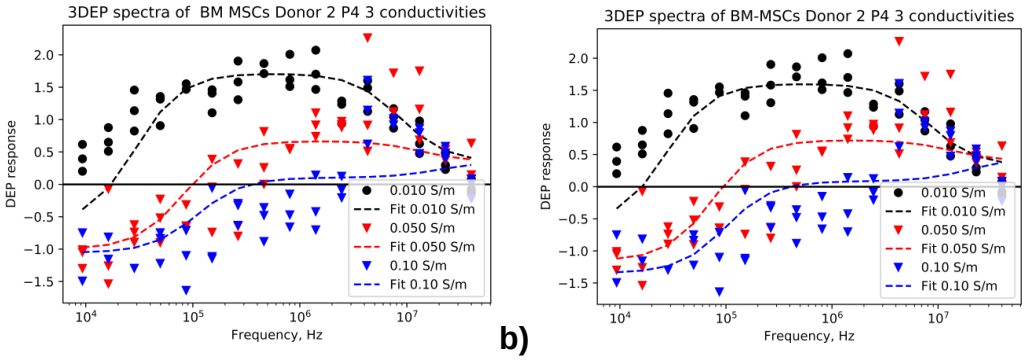

a) b)

Figure D.0.24: 3DEP spectra of BM-MSCs from donor 2 passage 4 using the three-conductivity model for a single common scaling factor (a) and three different scaling factors (b). The fitting curves are represented as dotted lines while the experimental data is shown by circles and triangles. For each conductivity, at least four replicates were considered.

	BM-MSCs – Donor 2 P4 Conductivities used (S/m)				
	0.01	0.05	0.1	0.01, 0.05 & 0.1 Same scale	0.01, 0.05 & 0.1 different scale
Fixed values	Radius: 7.5 µm Membrane Conductance: 500 S/m^2				
Reduced χ^2	0.064	0.19	0.16	0.28	0.27
Bayesian criteria	-115	-64	-69	-151	-155
Membrane capacitance (mF/m^2)	36±4	4.3±0.8	1.7±0.3	15	16±2
Cytoplasm Permittivity	64±21	9±202	1±100	126	126±21
Cytoplasm Conductivity (S/m)	0.14±0.02	0.31±0.06	0.31±0.06	0.12	0.11±0.01
Scaling factor	1.9	1.8	2	2.2	2,1, 2.6 & 2.8

Table D.10: Summary of dielectric properties of BM-MSCs from Donor 2 P4 derived using a single conductivity fit and the triple conductivity fit of DEP spectra obtained for different medium conductivities.

APPENDIX E
Python Scripts used to analyse DEP response curves

E.1. Single-conductivity script

```
import numpy
import matplotlib.pyplot as plt
import lmfit
import pandas
plt.rcParams[ 'axes.color_cycle' ] = [ 'm' , 'k' , "b", "g" ]
vacperm = 8.854e-12

def mamcell_cap_model(freq, radius , g_membrane , cap_membrane , perm_cyt ,
sigma_cyt, scale0) : #modify the conductivity here!!!

# General values
    scale = []
    sigma_medium = [0.01]
    scale.append(scale0)
    scale = numpy.asarray(scale)
    sigma_medium = numpy.asarray(sigma_medium)

    #sigma_membrane = 3e-6
    omega = 2*numpy.pi*freq
    e1 = perm_cyt*vacperm
    perm_medium = 80*vacperm
    #membrane thickess
    d=7e-9
    a=((radius+d)/radius)*((radius+d)/radius)*((radius+d)/radius)

# Complex permittivities .

   #ec1 Cytoplasm complex permittivity
    ec1 = numpy. vectorize (complex) (e1, sigma_cyt/omega)
    #ec2 Membrane complex permittivity
    ec2 = numpy.vectorize(complex) (cap_membrane*d , g_membrane*d/omega)
    #ec3 Medium complex permittivity
    ec3 = numpy.vectorize(complex) (perm_medium , sigma_medium/omega)

# Complex permittivity of the cell
    ec12= (ec1-ec2)/(ec1+2*ec2)
    ef2=ec2*(a+2*ec12)/(a-ec12)

# FCM calculation
    FCM = (ef2-ec3)/(ef2+2*ec3)
    return FCM.real*scale

# Makes a model/fit out of my previously defined mamcell_cap_model function
cellmodel = lmfit.Model(mamcell_cap_model)

# Declaring all parameters
params = cellmodel.make_params()
params.add('radius', value=6.5e-6, vary=False)
params.add('cap_membrane', value=0.01, min=1e-6, max=0.1)
params.add('perm_cyt', value=50, min=10, max=500)
```

```
params.add('sigma_cyt', value=0.1, min=1e-6, max=1)
params.add('g_membrane', value=500, vary=False)
params.add('scale0', value=1.6, min=0.5,max=5)

data0 = pandas.read_csv("C:/Users/DATA/ReplicateA.csv",sep=",")
data1 = pandas.read_csv("C:/Users/DATA/ReplicateB.csv",sep=",")
data2 = pandas.read_csv("C:/Users/DATA/ReplicateC.csv",sep=",")
data3 = pandas.read_csv("C:/Users/DATA/ReplicateD.csv",sep=",")
data4 = pandas.read_csv("C:/Users/DATA/ReplicateE.csv",sep=",")
average = pandas.read_csv("C:/Users/DATA/Average.csv",sep=",")

#Concatenates all data into the same columns
dataconcat = pandas.concat([data0,data1,data2,data3,data4],axis=0)
data=dataconcat.sort_values(by=['Frequency [Hz]'], ascending=True)

x = data["Frequency [Hz]"]
y = data["Value"]
x0 = data0["Frequency [Hz]"]
y0 = data0["Value"]
x1 = data1["Frequency [Hz]"]
y1 = data1["Value"]
x2 = data2["Frequency [Hz]"]
y2 = data2["Value"]
x3 = data3["Frequency [Hz]"]
y3 = data3["Value"]
x4 = data4["Frequency [Hz]"]
y4 = data4["Value"]
x7 = average["Frequency [Hz]"]
y7 = average["Value"]

result = cellmodel.fit(y, params, freq=x)
print(result.fit_report())

plt.figure(1)
plt.semilogx(x0,y0,"bo",label="A")
plt.semilogx(x1,y1,"go",label="B")
plt.semilogx(x2,y2,"ro",label="C")
plt.semilogx(x3,y3,"co",label="D")
plt.semilogx(x4,y4,"mo",label="E")
plt.semilogx(x7,y7,"kx",label="Average")
plt.semilogx(x,result.best_fit[0:len(x)],"k--",label="Fit")
plt.xlabel ('Frequency, Hz') # x axis name
plt.ylabel ('DEP response') # y axis name

ax = plt.subplot(111)
box = ax.get_position()
ax.set_position([box.x0, box.y0, box.width * 0.8, box.height])
ax.legend(loc='center left', bbox_to_anchor=(1, 0.5))
plt.axhline (0 , color = 'black')
plt.title ('DPSCs Donor 1 P3 0.010 S/m')
plt.savefig('DPSCs - Donor 1 - P3 - 0.010 Sm - all replicates.png', edgecolor='black',
dpi=1600, transparent=True)
```

E.2. Three-conductivity script

```
import numpy
import matplotlib.pyplot as plt
import lmfit
import pandas
plt.rcParams[ 'axes.color_cycle' ] = [ 'm' , 'k' , "b", "g" ]
vacperm = 8.854e-12

def mamcell_cap_model(Modfreq, radius , g_membrane , cap_membrane , perm_cyt , sigma_cyt, scale0,scale1,scale2) :

# General values
    conductivities = [0.01, 0.05, 0.10]
    condIndex = Modfreq // 100000000
    freq = Modfreq - condIndex * 100000000

# This allows for different scaling factor to be used for each conductivity

    scale = []
    sigma_medium = []

    for c in condIndex:
        if c == 0:
            scale.append(scale0)
            sigma_medium.append(conductivities[0])
        elif c == 1:
            scale.append(scale1) #for same scale, scale1 is replaced by scale0
            sigma_medium.append(conductivities[1])
        elif c == 2:
            scale.append(scale2) #for same scale, scale1 is replaced by scale0
            sigma_medium.append(conductivities[2])

    scale = numpy.asarray(scale)
    sigma_medium = numpy.asarray(sigma_medium)

    omega = 2*numpy.pi*freq
    e1 = perm_cyt*vacperm
    perm_medium = 80*vacperm
    d=7e-9  #membrane thickess
    a=((radius+d)/radius)*((radius+d)/radius)*((radius+d)/radius)

# Complex permittivities

    #ec1 Cytoplasm complex permittivity
    ec1 = numpy. vectorize (complex) (e1, sigma_cyt/omega)
    #ec2 Membrane complex permittivity
    ec2 = numpy.vectorize(complex) (cap_membrane*d , g_membrane*d/omega)
    #ec3 Medium complex permittivity
    ec3 = numpy.vectorize(complex) (perm_medium , sigma_medium/omega)

# Complex permittivity of the cell
    ec12= (ec1-ec2)/(ec1+2*ec2)
    ef2=ec2*(a+2*ec12)/(a-ec12)
```

```
# FCM calculation
    FCM = (ef2-ec3)/(ef2+2*ec3)
    return FCM.real*scale

# Makes a model/fit out of my previously defined mamcell_cap_model function
cellmodel = lmfit.Model(mamcell_cap_model)

# Declaring all parameters
params = cellmodel.make_params()
params.add('radius', value=7.5e-6, vary=False)
params.add('cap_membrane', value=0.01, min=1e-6, max=0.1)
params.add('perm_cyt', value=50, min=1, max=500)
params.add('sigma_cyt', value=0.1, min=1e-6, max=1)
params.add('g_membrane', value=500, vary=False)
params.add('scale0', value=1.7, min=0.5,max=5)
params.add('scale1', value=1, min=0.5,max=5)
params.add('scale2', value=1, min=0.5,max=5)

data00 = pandas.read_csv("C:/Users/Africa/DATA2/0.01.csv",sep=",")
data11 = pandas.read_csv("C:/Users/Africa/DATA2/0.05.csv",sep=",")
data22 = pandas.read_csv("C:/Users/Africa/DATA2/0.10.csv",sep=",")

data0=data00.sort_values(by=['Frequency [Hz]'], ascending=True)
data1=data11.sort_values(by=['Frequency [Hz]'], ascending=True)
data2=data22.sort_values(by=['Frequency [Hz]'], ascending=True)

data1["Frequency [Hz]"] = data1["Frequency [Hz]"] + 100000000
data2["Frequency [Hz]"] = data2["Frequency [Hz]"] + 200000000

data = pandas.concat([data0,data1,data2],axis=0)

x = data["Frequency [Hz]"]
y = data["Value"]
x0 = data0["Frequency [Hz]"]
y0 = data0["Value"]
x1 = data1["Frequency [Hz]"] - 100000000
y1 = data1["Value"]
x2 = data2["Frequency [Hz]"] - 200000000
y2 = data2["Value"]

result = cellmodel.fit(y, params, Modfreq=x)
print(result.fit_report())

plt.figure(1)
plt.semilogx(x0,y0,"ko",label="0.010 S/m")
plt.semilogx(x0,result.best_fit[0:len(x0)],"k--",label="Fit 0.010 S/m ")
plt.semilogx(x1,y1,"rv",label="0.050 S/m")
plt.semilogx(x1,result.best_fit[len(x0):len(x0)+len(x1)],"r--",label="Fit 0.050 S/m ")
plt.semilogx(x2,y2,"bv",label="0.10 S/m")
plt.semilogx(x2,result.best_fit[len(x0)+len(x1):len(x0)+len(x1)+len(x2)],"b--
",label="Fit 0.10 S/m ")
plt.xlabel ('Frequency, Hz')
plt.ylabel ('DEP response')

plt.axhline (0 , color = 'black')
plt.title ('3DEP spectra of  BM-MSCs Donor 1 P5 3 conductivities')
```

```
plt.savefig('BM-MSCs - Donor 1 P5 - 0.01, 0.05 & 0.10 - ALL - different scale.png',
edgecolor='black', dpi=1600, transparent=True)

# Generates plot for the first conductivity
plt.figure(2)
plt.semilogx(x0,y0,"ko",label="DATA")
plt.semilogx(x0,result.best_fit[0:len(x0)],"k--",label="Fit")
plt.xlabel ('Frequency, Hz')
plt.ylabel ('DEP response')
plt.axhline (0 , color = 'black')
plt.title ('3DEP spectra of BM-MSCs Donor 1 P5 0.01 S/m')
plt.savefig('BM-MSCs - Donor 1 P5 - 0.01, 0.05 & 0.10 - 0.01 - different scale.png',
edgecolor='black', dpi=1600, transparent=True)

# Generates plot for the second conductivity
plt.figure(3)
plt.semilogx(x1,y1,"rv",label="DATA")
plt.semilogx(x1,result.best_fit[len(x0):len(x0)+len(x1)],"r--",label="Fit")
plt.xlabel ('Frequency, Hz')
plt.ylabel ('DEP response')
plt.axhline (0 , color = 'black')
plt.title ('3DEP spectra of BM-MSCs Donor 1 P5 0.05 S/m')
plt.legend(loc=4)

plt.savefig('BM-MSCs - Donor 1 P5 - 0.01, 0.05 & 0.10 - 0.05 - different scale.png',
edgecolor='black', dpi=1600, transparent=True)

# Generates plot for the third conductivity
plt.figure(4)
plt.semilogx(x2,y2,"bv",label="DATA")
plt.semilogx(x2,result.best_fit[len(x0)+len(x1):len(x0)+len(x1)+len(x2)],"b--
",label="Fit")
plt.xlabel ('Frequency,  Hz')
plt.ylabel ('DEP response')
plt.axhline (0 , color = 'black')
plt.title ('3DEP spectra of BM-MSCs Donor 1 P5 0.10 S/m')
plt.legend(loc=4)

plt.savefig('BM-MSCs - Donor 1 P5 - 0.01, 0.05 & 0.10 - 0.10 - different scale.png',
edgecolor='black', dpi=1600, transparent=True)
```

E.3. DEP response of blood cells for varying frequencies

```
import numpy
import matplotlib.pyplot as plt
plt.rcParams[ 'axes.color_cycle' ] = [ 'm' , 'c' , 'k', "b", "g", "y" ]
vacperm = 8.854e-12

def mamcell_cap_model( cell_type , freq , sigma_medium , radius , membrane_thick
,cap_membrane , perm_cyt , sigma_cyt ) :

#General values
    sigma_membrane = 3e-6
    omega = 2*numpy.pi*freq
```

```
    e_cyt = perm_cyt*vacperm
    g_membrane = sigma_membrane/membrane_thick
    perm_medium = 80*vacperm

#Complex permittivities .
comcap_membrane=numpy.vectorize(complex)(cap_membrane,g_membrane/om
ega)
comperm_cyt = numpy. vectorize (complex) ( e_cyt , sigma_cyt/omega)

#Complex permittivity of the cell and medium
comperm_cell=(comcap_membrane*radius*comperm_cyt)/(comcap_membrane*ra
dius+comperm_cyt)
comperm_medium=numpy.vectorize(complex)(perm_medium,sigma_medium/ome
ga)

#FCM calculation
    FCM= (comperm_cell-comperm_medium)/(comperm_cell+2*comperm_medium)
    return FCM.real

xValues = numpy.arange (0.00100,0.4,0.001)

#Define cells
# Note, in this case we are checking the FCM at a range of values (xValues that we
had previously generated) of medium conductivity, the rest are all constants.
a = mamcell_cap_model ('B cells', 100e6, xValues, 3.1e-6 , 8e-9, 9.8e-3 , 93, 0.13)
b = mamcell_cap_model ('T cells', 100e6, xValues, 3.1e-6 , 8e-9, 11.7e-3, 57, 0.24)
c = mamcell_cap_model ('Monocytes', 100e6, xValues, 3.74e-6, 8e-9, 4.5e-3, 83, 0.10)
d = mamcell_cap_model ('Eosinophils', 100e6, xValues,3.65e-6, 8e-9, 9.1e-3, 80, 0.14)
e = mamcell_cap_model ('Neutrophils', 100e6, xValues, 3.51e-6,8e-9,7.1e-3,110, 0.05)
f = mamcell_cap_model ('BM-MSCs', 100e6, xValues, 7.5e-6, 8e-9, 17e-3, 128, 0.11)

plt.figure(1)
plt.xlabel ('Medium conductivity, S/m')
plt.ylabel ('DEP response')
plt.title ('Cells DEP response at 100 MHz')
plt.axhline (0 , color = 'black'
plt.legend ()
plt.savefig('Cells DEP response - Conductivities - 100 MHz.png', edgecolor='black',
dpi=1600, transparent=True)
```

E.4. Response of blood cells for varying medium conductivities

```
import numpy
import matplotlib.pyplot as plt
plt.rcParams[ 'axes.color_cycle' ] = [ 'm' , 'k' , "b", "g", "c", "y" ]
vacperm = 8.854e-12

def mamcell_cap_model( cell_type , freq , sigma_medium , radius , membrane_thick
,cap_membrane , perm_cyt , sigma_cyt ) :

#General values
    sigma_membrane = 3e-6
```

```
    g_membrane = sigma_membrane/membrane_thick
    omega = 2*numpy.pi*freq
    e_cyt = perm_cyt*vacperm
    perm_medium = 80*vacperm

#Complex permittivities .
comcap_membrane=numpy.vectorize(complex)(cap_membrane,
g_membrane/omega)
comperm_cyt = numpy. vectorize (complex) ( e_cyt , sigma_cyt/omega)

#Complex permittivity of the cell and medium
comperm_cell=(comcap_membrane*radius*comperm_cyt)/(comcap_membrane*ra
dius+comperm_cyt)
comperm_medium=numpy.vectorize(complex)(perm_medium,
sigma_medium/omega)

#FCM calculation
    FCM =(comperm_cell-comperm_medium)/(comperm_cell+2*comperm_medium)
    return FCM.real
freqs = numpy.logspace(7, 8, num=100, base=10)

# Define cells
# Note, in this case we are checking the FCM at a range of values (freqs) of
frequency
a = mamcell_cap_model ('B cells', freqs , 0.22 , 3.1e-6 , 8e-9, 9.8e-3 , 93, 0.13)
b = mamcell_cap_model ('T cells', freqs , 0.22 , 3.1e-6 , 8e-9, 11.7e-3, 57, 0.24)
c = mamcell_cap_model ('Monocytes', freqs , 0.22 , 3.74e-6, 8e-9, 4.5e-3 , 83, 0.10)
d = mamcell_cap_model ('Eosinophils', freqs , 0.22 , 3.65e-6, 8e-9, 9.1e-3, 80, 0.14)
e = mamcell_cap_model ('Neutrophils', freqs , 0.22 , 3.51e-6, 8e-9, 7.1e-3, 110,
0.05)
f = mamcell_cap_model ('BM-MSCs P2', freqs , 0.22 , 7.5e-6 , 8e-9, 17e-3 , 128,
0.11)

plt.semilogx(freqs, a, label='B cell')
plt.semilogx(freqs, b, label='T cell')
plt.semilogx(freqs, c, label='Monocytes')
plt.semilogx(freqs, d, label='Eosinophils')
plt.semilogx(freqs, e, label='Neutrophils')
plt.semilogx(freqs, f, label='BM-MSCs')
plt.xlabel ('Frequency, Hz')
plt.ylabel ('DEP response')
plt.title ('Cells DEP response for 0.22 S/m')
plt.axhline (0 , color = 'black')
plt.legend (loc=4)
plt.savefig('Cells DEP response - Frequencies - 0.22 Sm.png', edgecolor='black',
dpi=1600, transparent=True)
```

APPENDIX F
Preliminary *in vivo* histological sections

a) 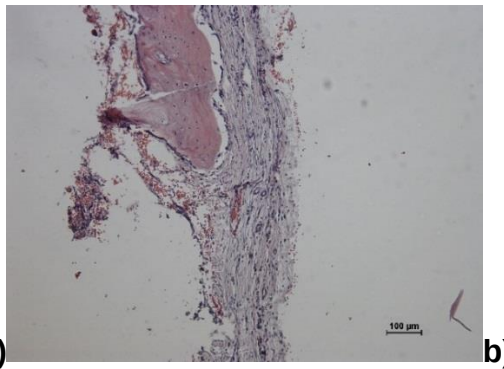 b) 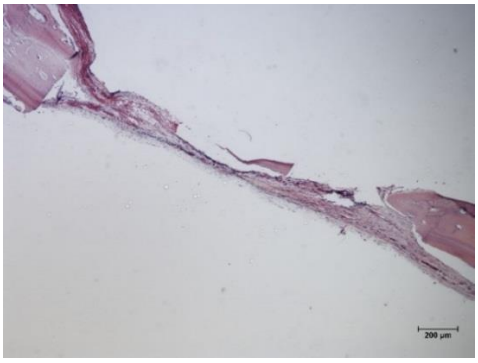

Figure F.0.1: Histological staining using H&E of defects 8L (a) and 9L (b) with no scaffold and no cells 1 month after implantation. Nuclei were stained blue by Haematoxylin whereas cytoplasm and collagen were stained pink by eosin. Old bone was stained in a darker shade of pink.

a) 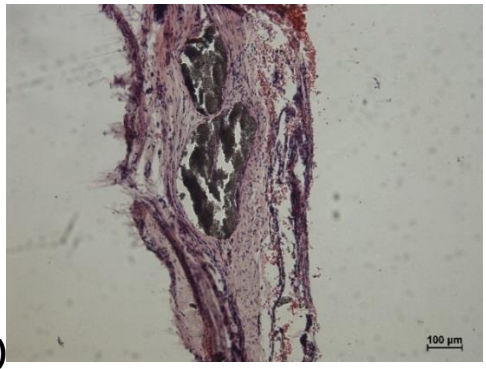 b) 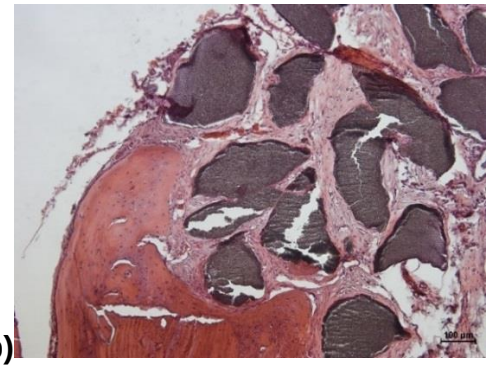

Figure F.0.2: Histological staining using H&E of defects 2L (a) and 8R (b) with ABM+P15 scaffold and no cells 1 month after implantation. Nuclei were stained blue by Haematoxylin whereas cytoplasm and collagen were stained pink by eosin. Old bone was stained in a darker shade of pink.

a) 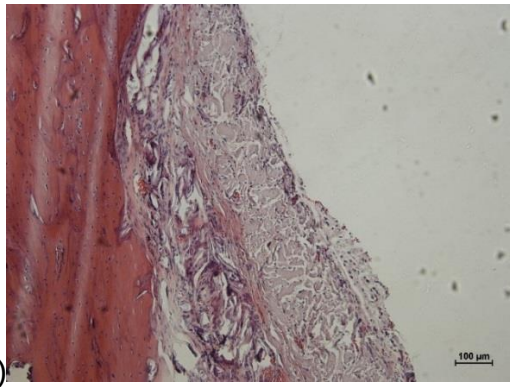 b) 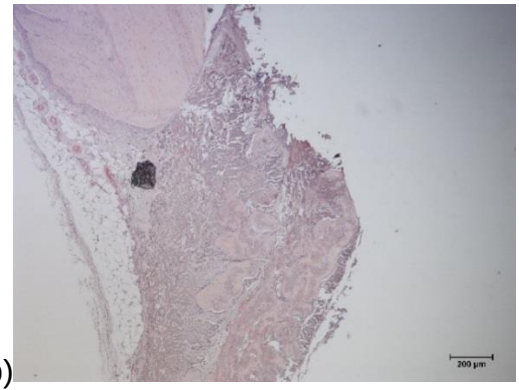

Figure F.0.3: Histological staining using H&E of defects 2R (a) and 10R (b) with Biogide scaffold and no cells 1 month after implantation. Nuclei were stained blue by Haematoxylin whereas cytoplasm and collagen were stained pink by eosin. Old bone was stained in a darker shade of pink.

a) 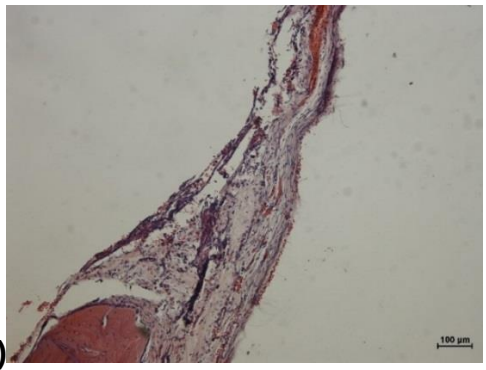 **b)** 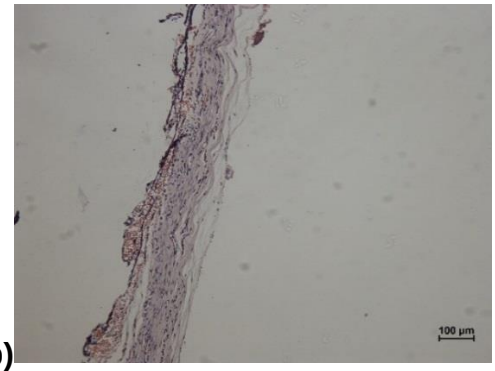

Figure F.0.4: Histological staining using H&E of defects 5L (a) and 7L (b) with no scaffold and cells exposed to SAW-DEP 1 month after implantation. Nuclei were stained blue by Haematoxylin whereas cytoplasm and collagen were stained pink by eosin. Old bone was stained in a darker shade of pink.

a) 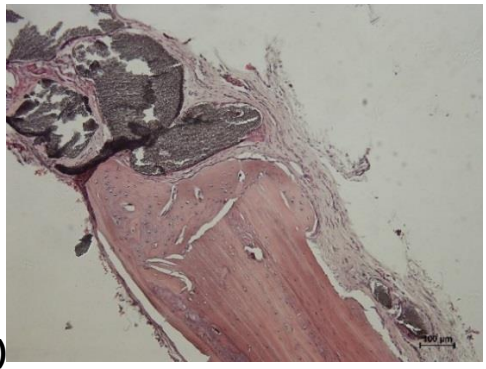 b) 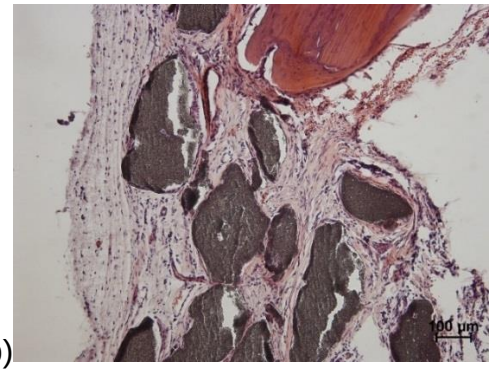

Figure F.0.5: Histological staining using H&E of defects 3L (a) and 7R (b) with ABM+P15 scaffold and cells exposed to SAW-DEP 1 month after implantation. Nuclei were stained blue by Haematoxylin whereas cytoplasm and collagen were stained pink by eosin. Old bone was stained in a darker shade of pink.

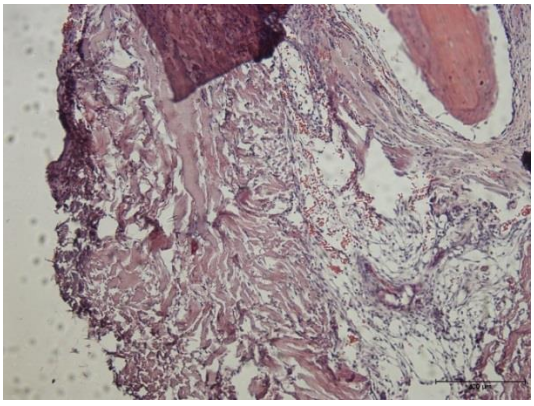

Figure F.0.6: Histological staining using H&E of defects 3R with Biogide scaffold and cells exposed to SAW-DEP 1 month after implantation. Nuclei were stained blue by Haematoxylin whereas cytoplasm and collagen were stained pink by eosin. Old bone was stained in a darker shade of pink.

Figure F.0.7: Histological staining using H&E of defects 6L (a) with no scaffold and control cells 1 month after implantation. Nuclei were stained blue by Haematoxylin whereas cytoplasm and collagen were stained pink by eosin. Old bone was stained in a darker shade of pink.

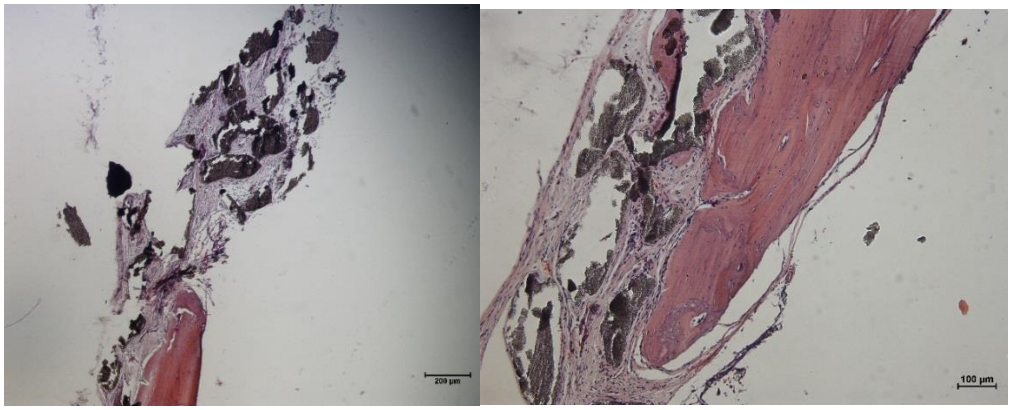

Figure F.0.8: Histological staining using H&E of defects 4L (a) with ABM+P15 scaffold and control cells 1 month after implantation. Nuclei were stained blue by Haematoxylin whereas cytoplasm and collagen were stained pink by eosin. Old bone was stained in a darker shade of pink.

a) 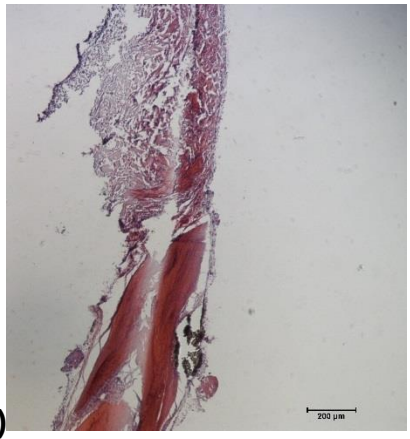 b) 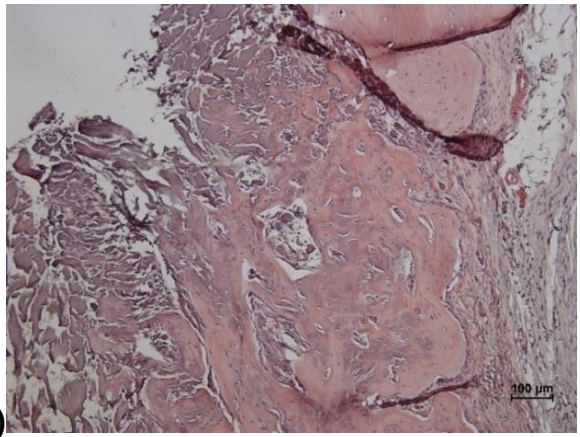

Figure F.0.9: Histological staining using H&E of defects 4R (a) and 9R (b) with Biogide scaffold and control cells 1 month after implantation. Nuclei were stained blue by Haematoxylin whereas cytoplasm and collagen were stained pink by eosin. Old bone was stained in a darker shade of pink.

APPENDIX G
Formal *in vivo* histological sections

G.1. Histological sections of samples with no scaffold no cells 1 month after implantation

a)

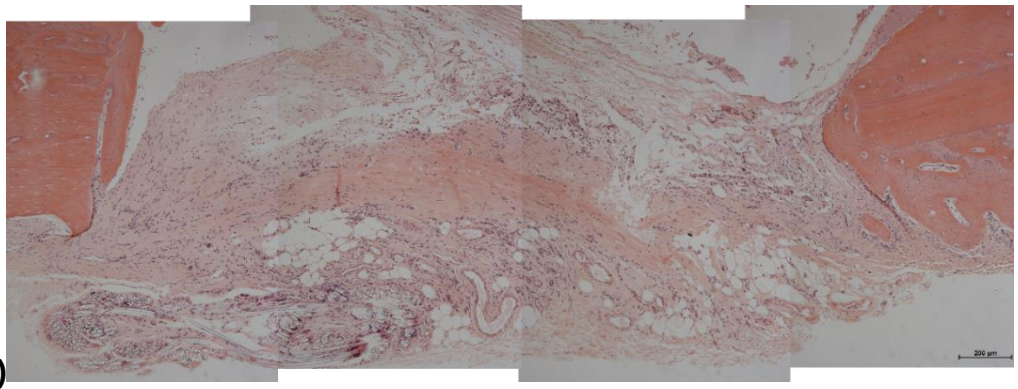

b)

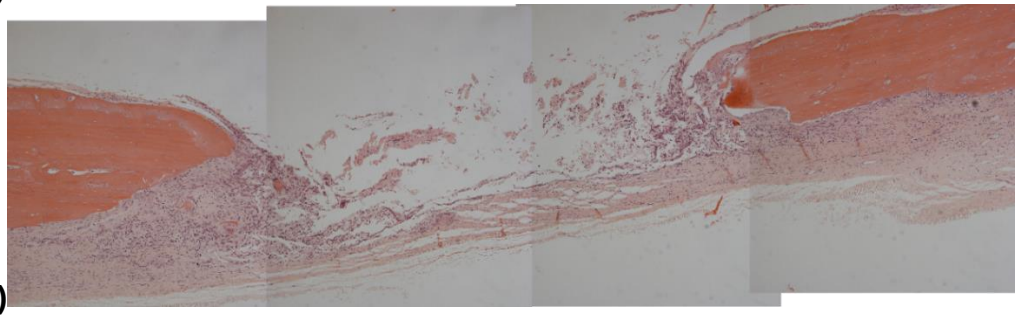

c)

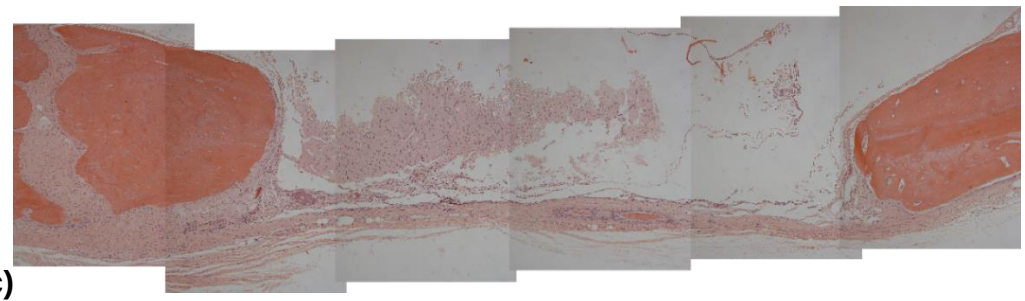

d)

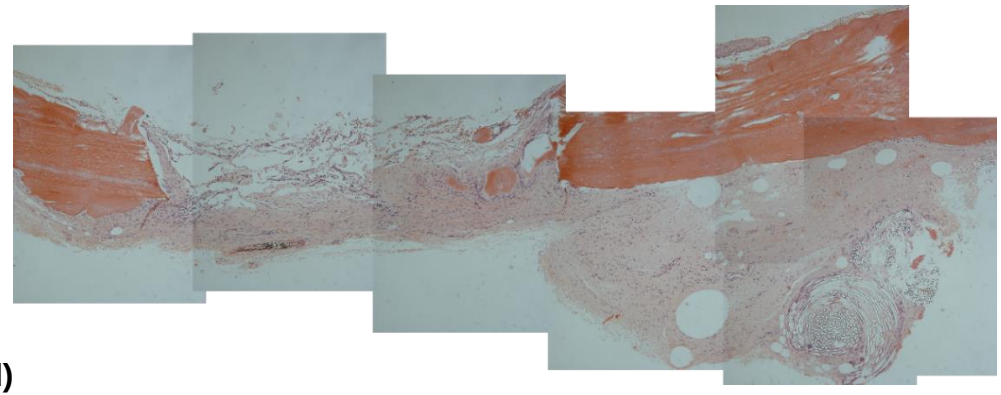

Figure G.0.1: Histological staining using H&E of defects 3N (a), 6N (b), 6R (c), 7L (d) with no scaffold and no cells 1 month after implantation. Nuclei were stained blue by Haematoxylin whereas cytoplasm and collagen were stained pink by eosin. Old bone was stained in a darker shade of pink.

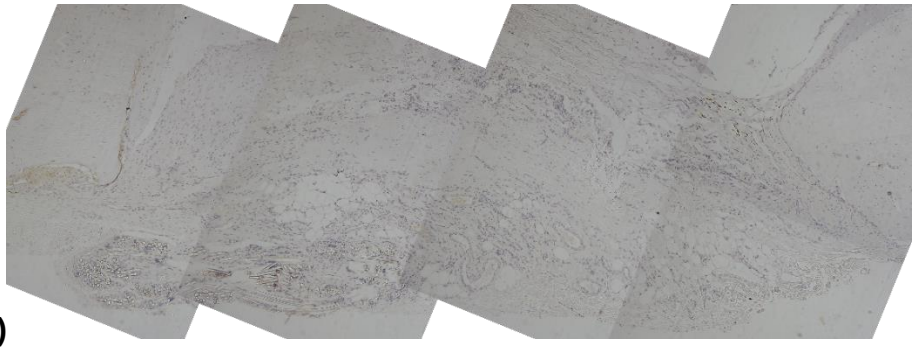

a)

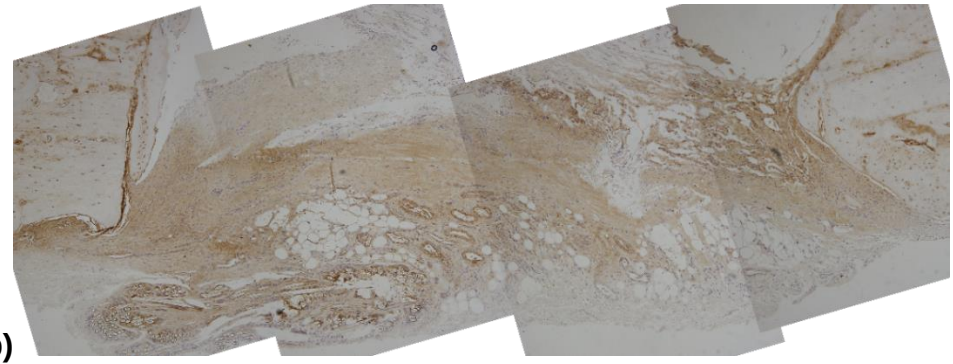

b)

Figure G.0.2: Histochemical staining of defect 3N with no scaffold and no cells 1 month after implantation. a) Negative control. b) Collagen type I antibody. c) Osteocalcin antibody.

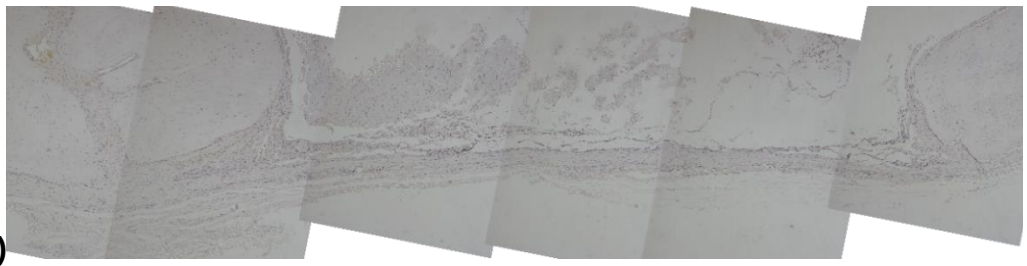

a)

b)

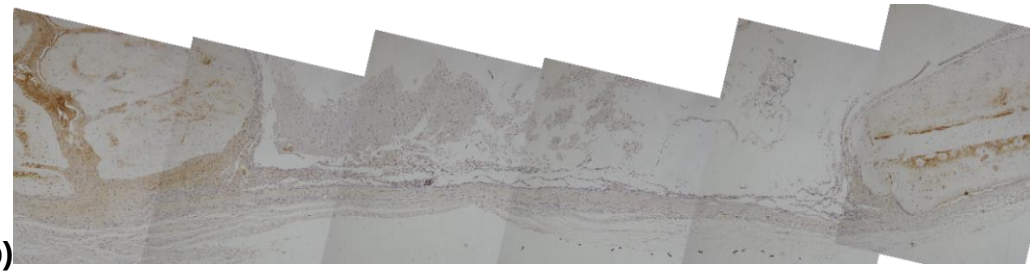

Figure G.0.3: Histochemical staining of defect 6R with no scaffold and no cells 1 month after implantation. a) Negative control. b) Collagen type I antibody.

a)

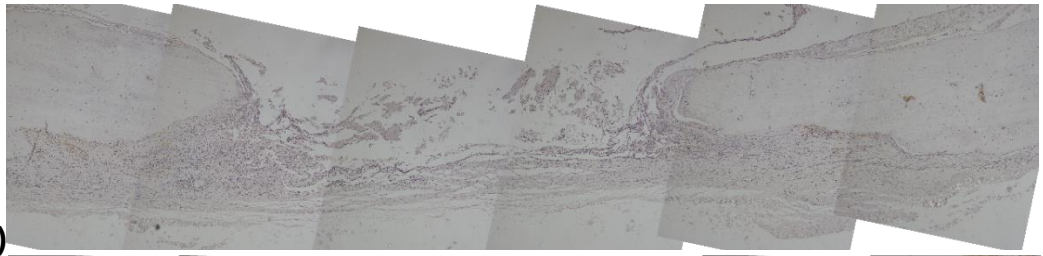

b)

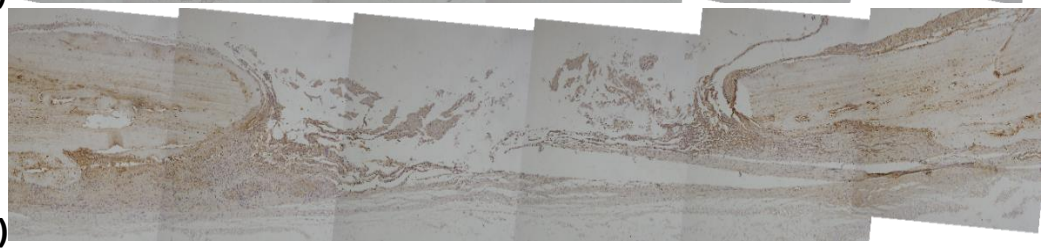

c)

Figure G.0.4: Histochemical staining of defect 6N with no scaffold and no cells 1 month after implantation. a) Negative control. b) Collagen type I antibody. c) Osteocalcin antibody.

a)

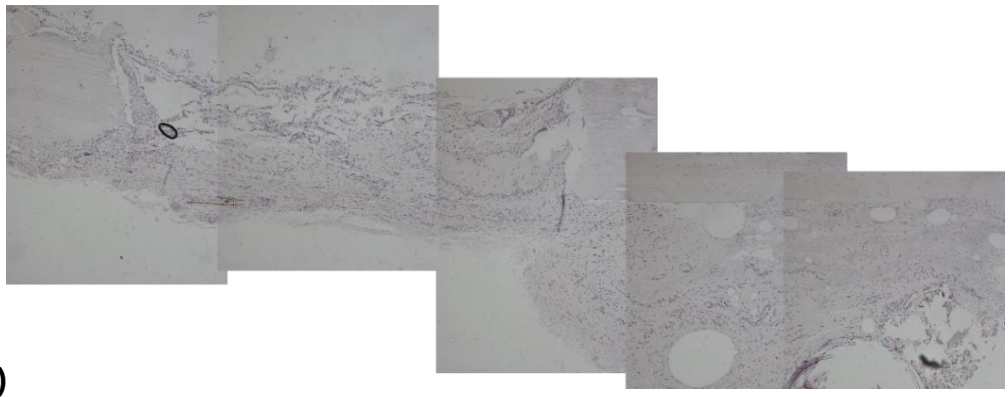

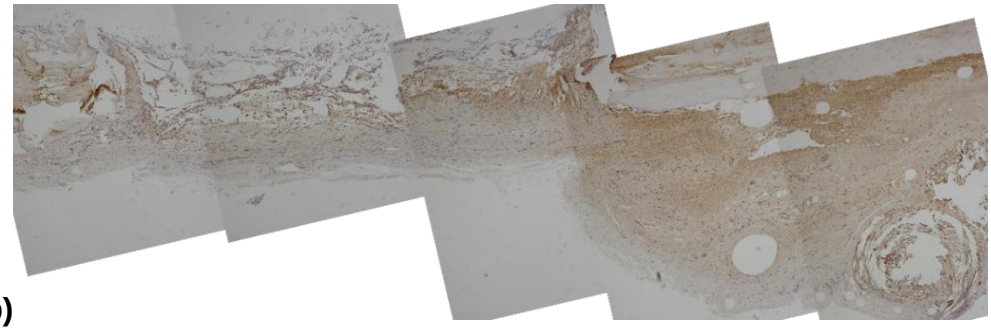

b)

Figure G.0.5: Histochemical staining of defect 7L with no scaffold and no cells 1 month after implantation. a) Negative control. b) Collagen type I antibody.

G.2. Histological sections of samples with no scaffold no cells 2 months after implantation

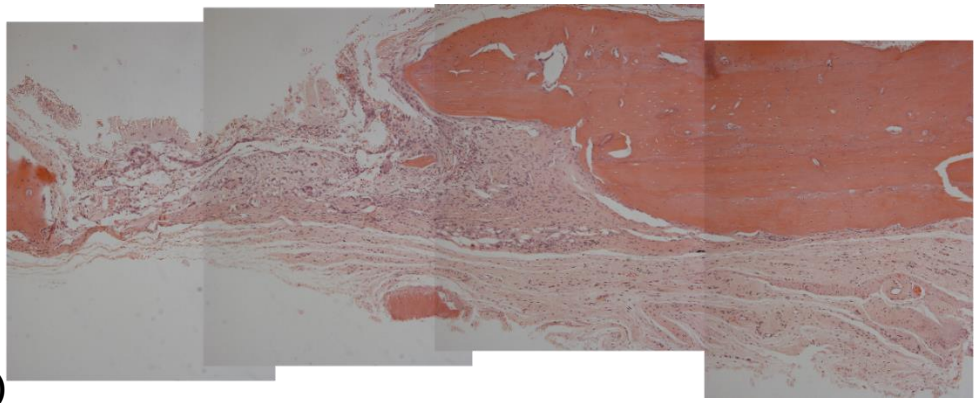

a)

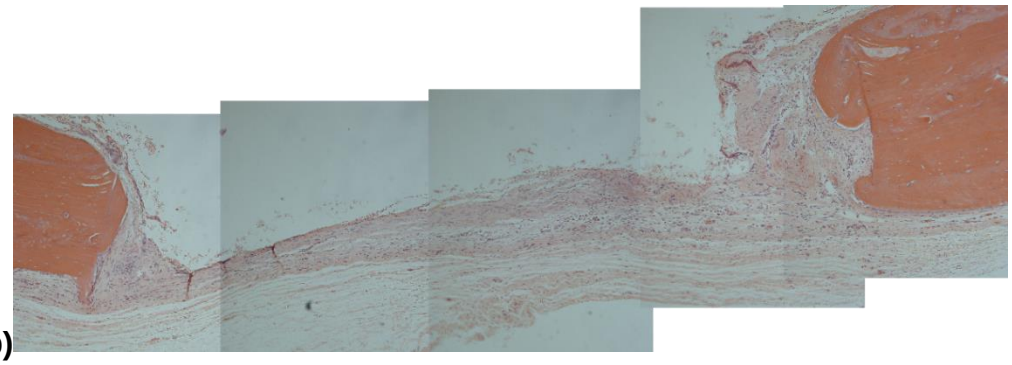

b)

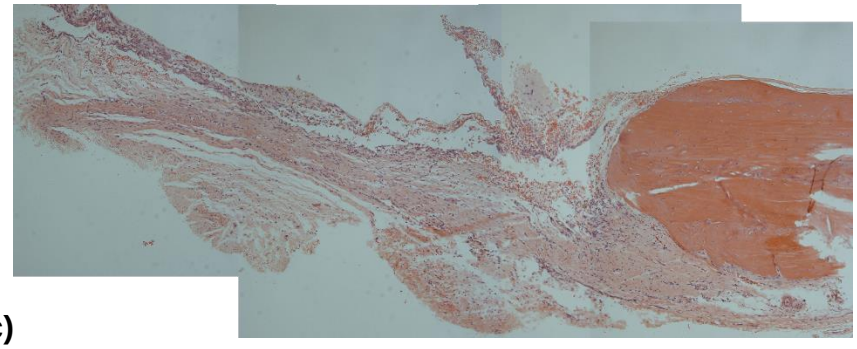

c)

Figure G.0.6: Histological staining using H&E of defects 2R (a), 8N (b), 8R (c) with no scaffold and no cells 2 months after implantation. Nuclei were stained blue by Haematoxylin whereas cytoplasm and collagen were stained pink by eosin. Old bone was stained in a darker shade of pink.

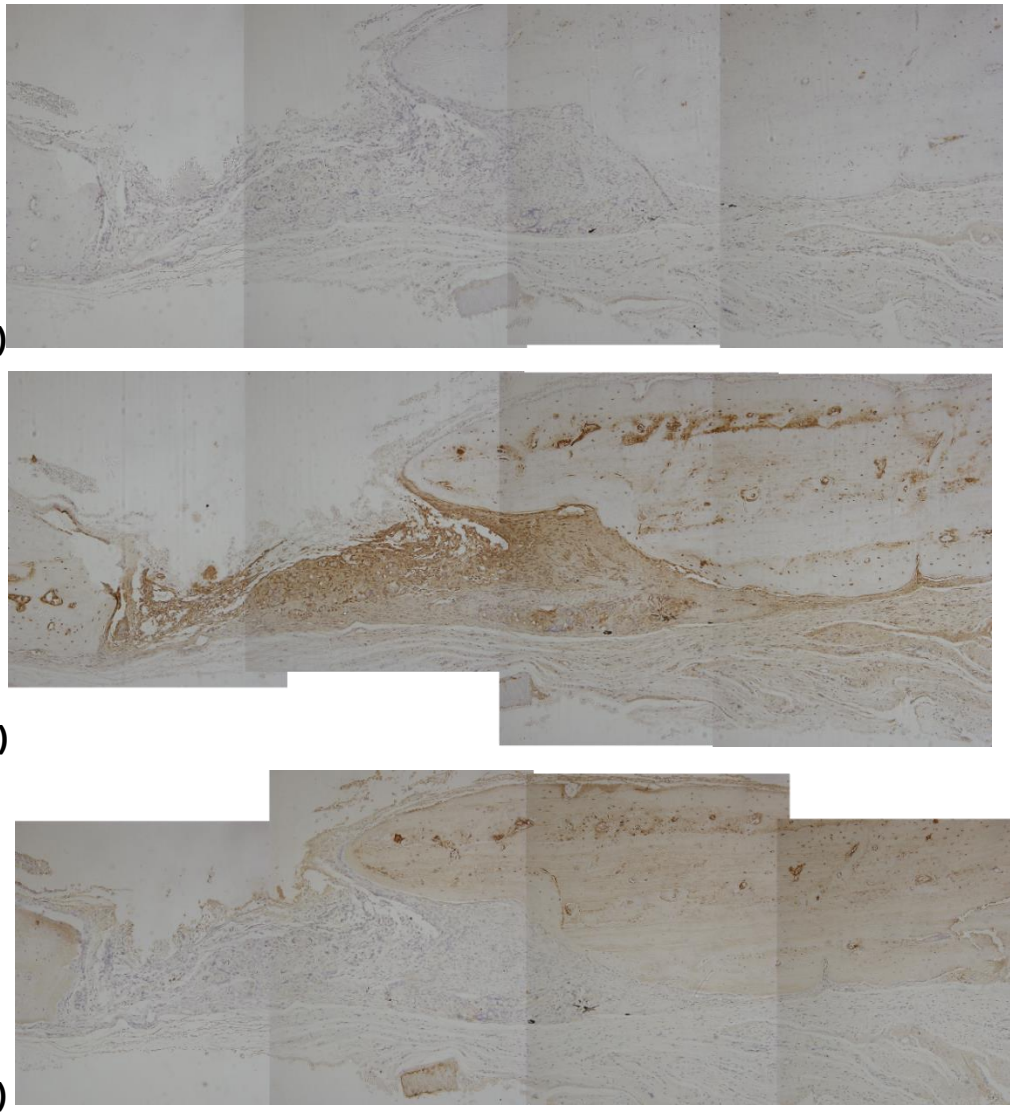

a)

b)

c)

Figure G.0.7: Histochemical staining of defect 2R with no scaffold and no cells 2 months after implantation. a) Negative control. b) Collagen type I antibody. c) Osteocalcin antibody.

a)

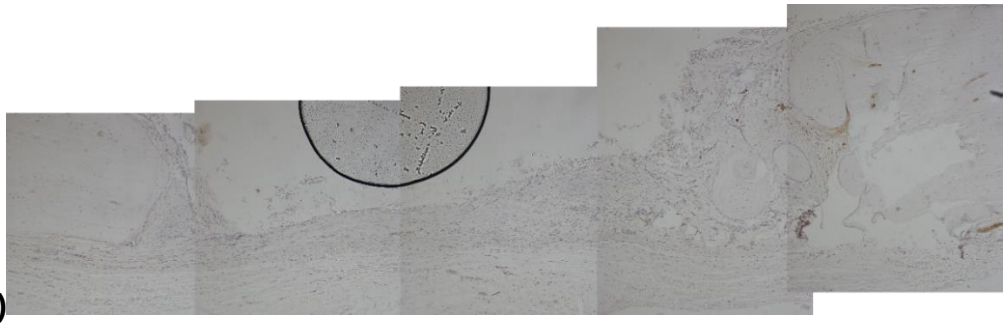

b)

Figure G.0.8: Histochemical staining of defect 8N with no scaffold and no cells 2 months after implantation. a) Negative control. b) Collagen type I antibody.

a)

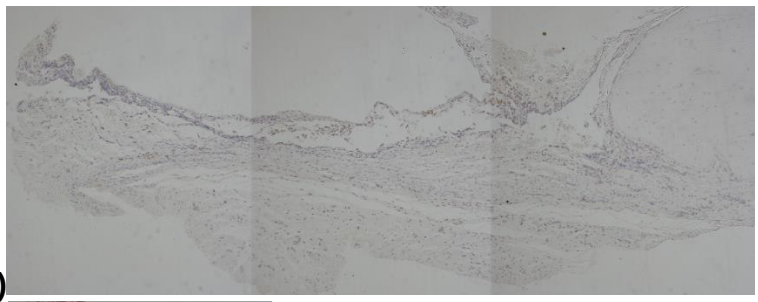

b)

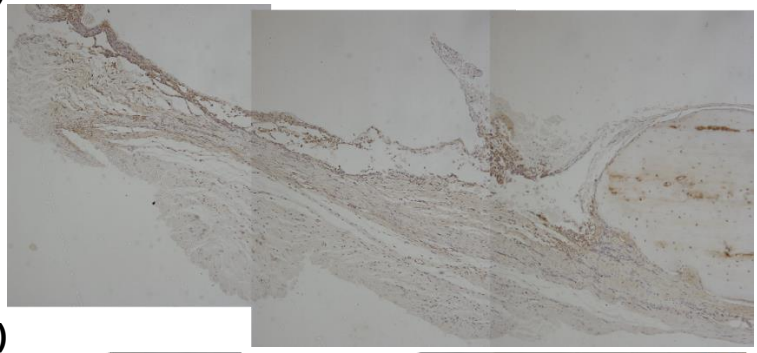

c)

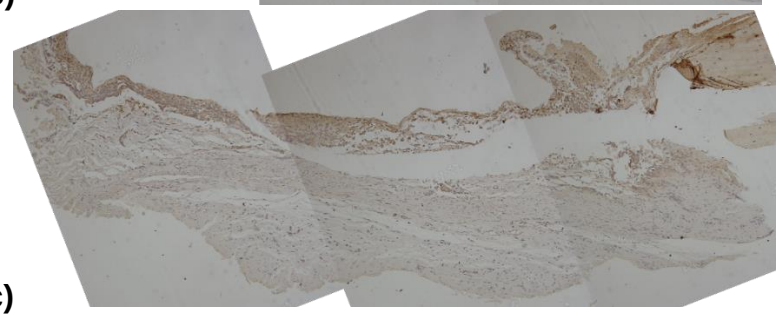

Figure G.0.9: Histochemical staining of defect 8R with no scaffold and no cells 2 months after implantation. a) Negative control. b) Collagen type I antibody. c) Osteocalcin antibody.

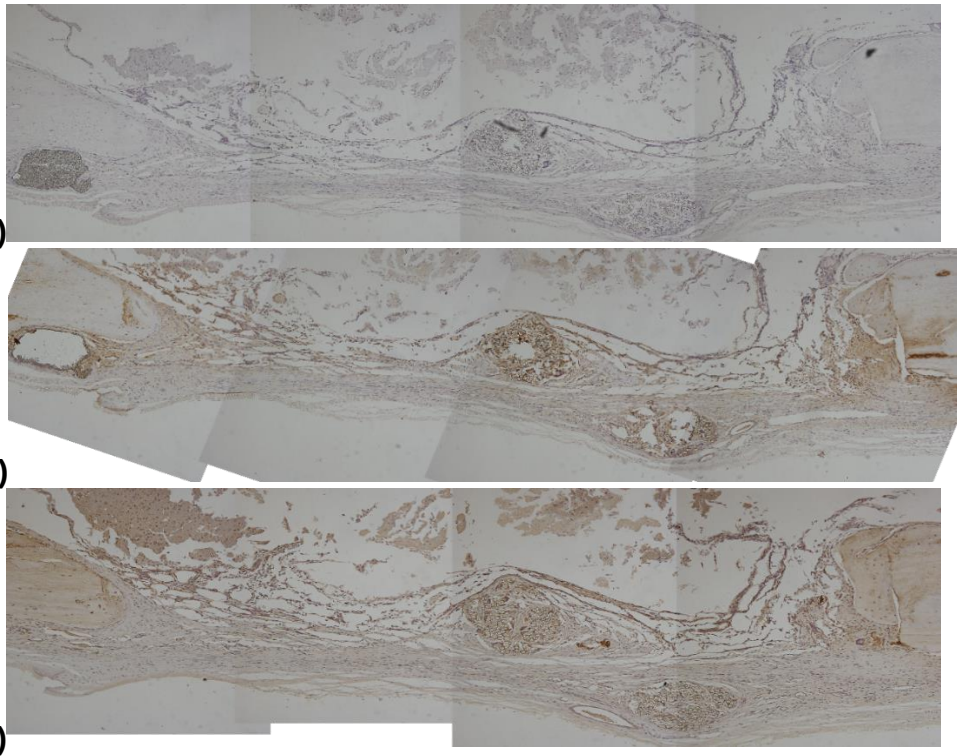

Figure G.0.10: Histochemical staining of defect with no scaffold and no cells 2 months after implantation. a) Negative control. b) Collagen type I antibody. c) Osteocalcin antibody.

G.3. Histological sections of samples with no scaffold and control cells 1 month after implantation

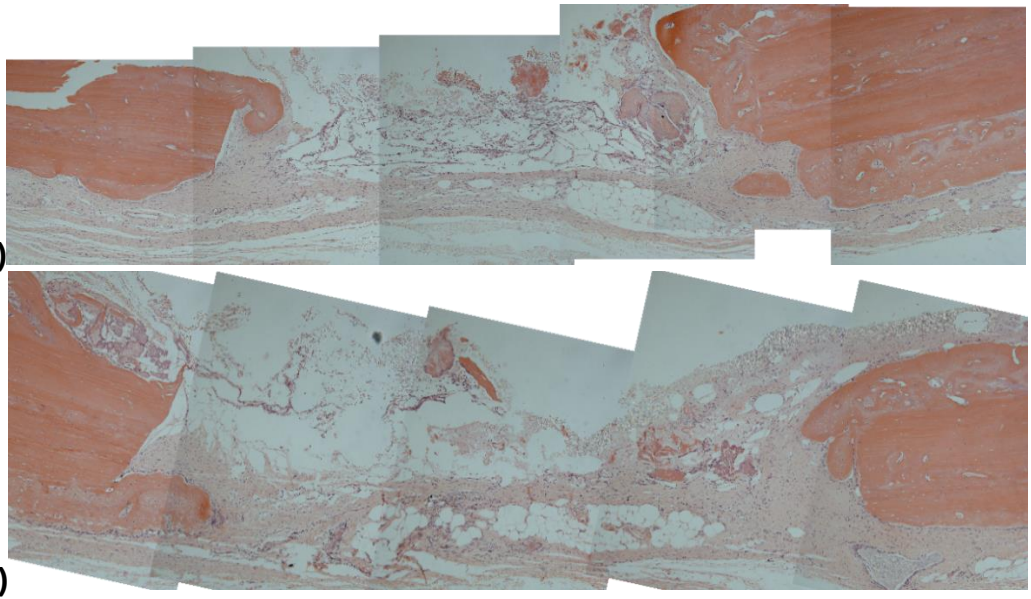

Figure G.0.11: Histological staining using H&E of defects 7N (a) and 7R (b) with no scaffold and control cells 1 month after implantation. Nuclei were stained blue by Haematoxylin whereas cytoplasm and collagen were stained pink by eosin. Old bone was stained in a darker shade of pink.

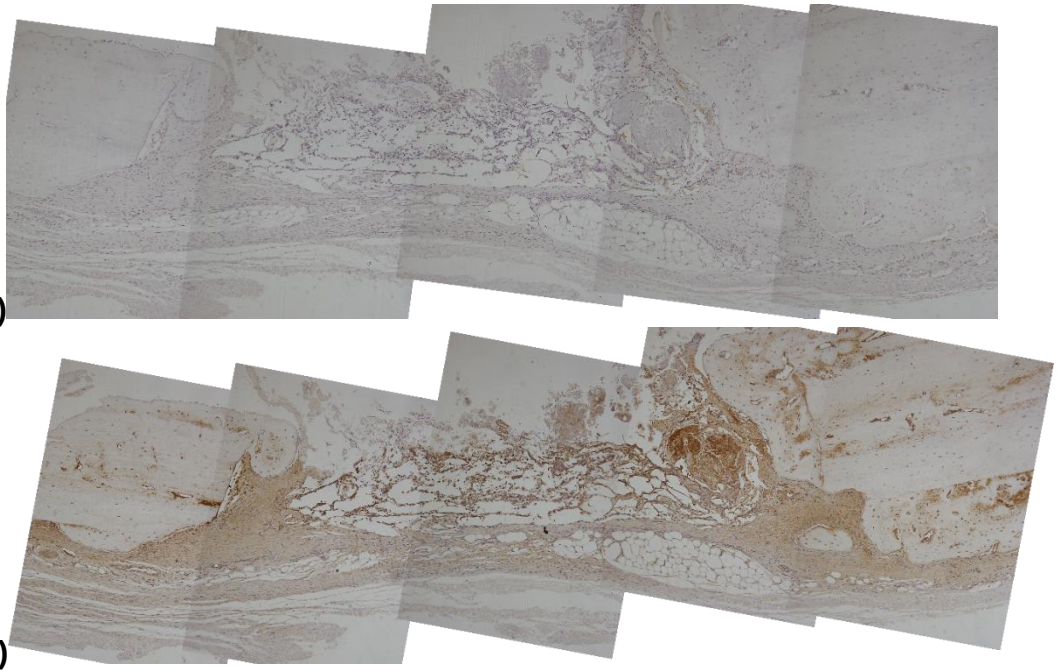

a)

b)

Figure G.0.12: Histochemical staining of defect 7N with no scaffold and control cells 1 month after implantation. a) Negative control. b) Collagen type I antibody.

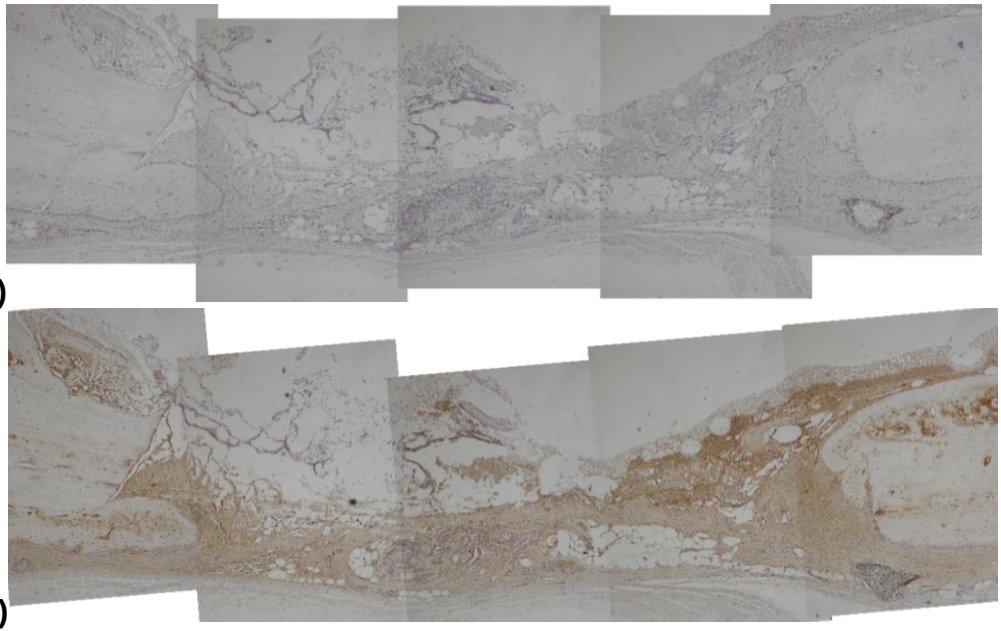

a)

b)

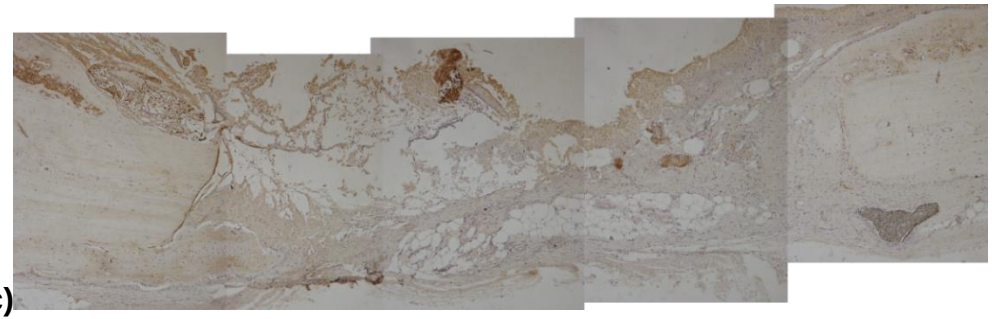

c)

Figure G.0.13: Histochemical staining of defect 7R with no scaffold and no cells 2 months after implantation. a) Negative control. b) Collagen type I antibody. c) Osteocalcin antibody.

G.4. Histological sections of samples with no scaffold and control cells 1 month after implantation

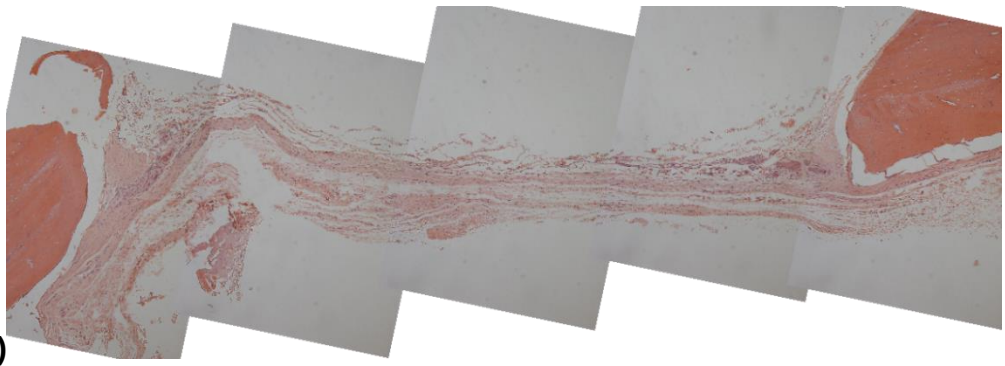

a)

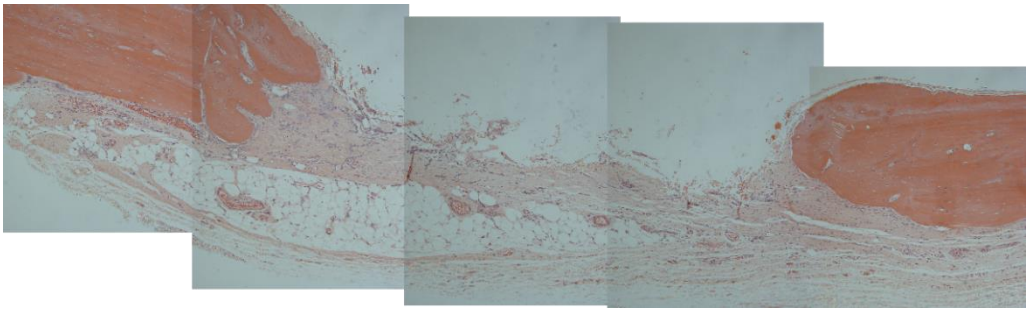

b)

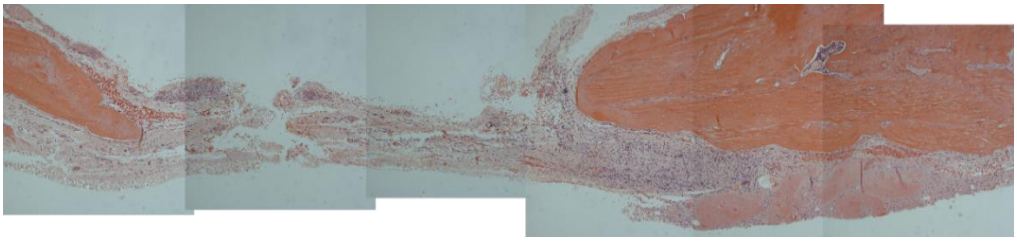

c)

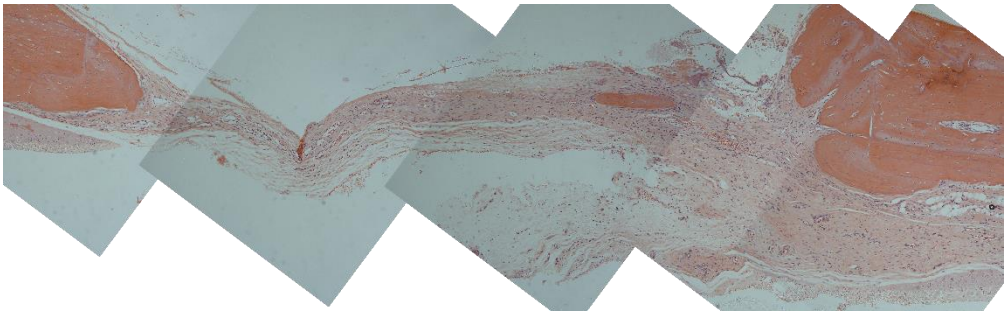

d)

Figure G.0.14: Histological staining using H&E of defects 2L (a), 7R (b), 9N (c), 9R (d) with no scaffold and control cells 1 month after implantation. Nuclei were stained blue by Haematoxylin whereas cytoplasm and collagen were stained pink by eosin. Old bone was stained in a darker shade of pink.

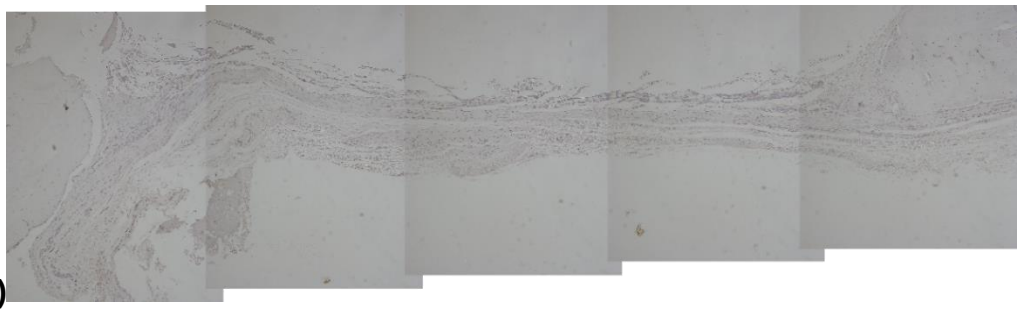

a)

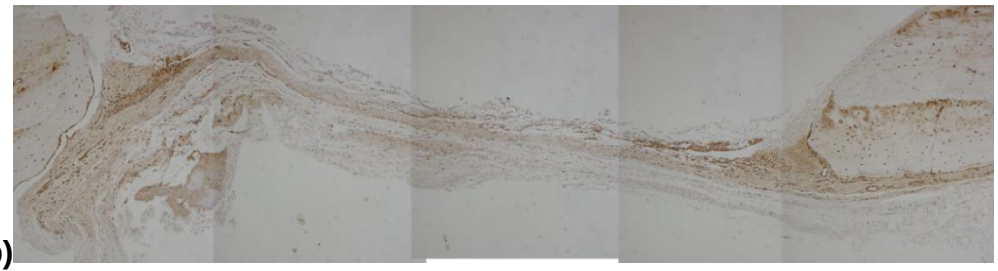

b)

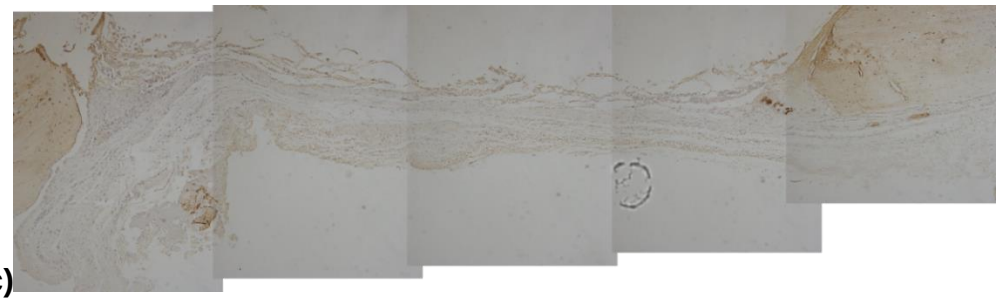

c)

Figure G.0.15: Histochemical staining of defect 2L with no scaffold and control cells 1 month after implantation. a) Negative control. b) Collagen type I antibody. c) Osteocalcin antibody.

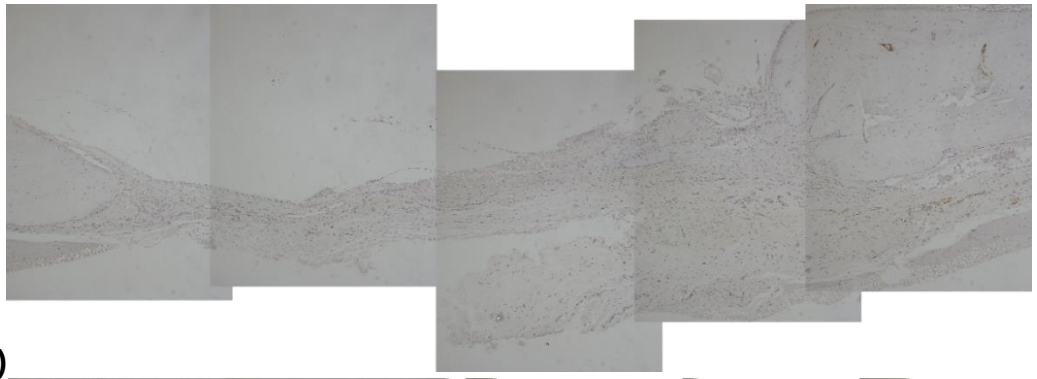

a)

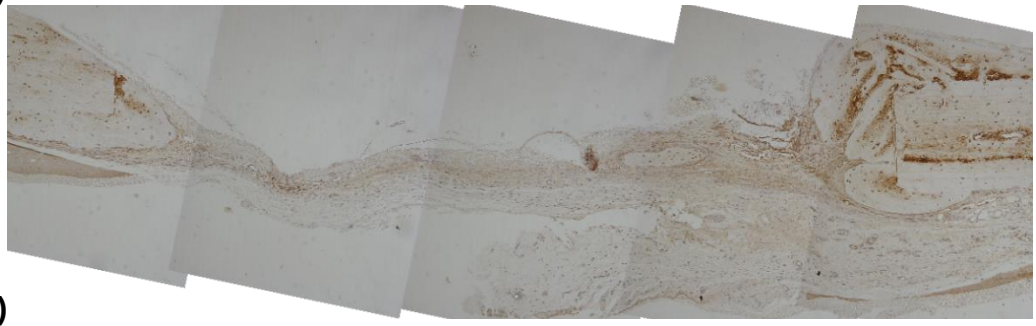

b)

Figure G.0.16: Histochemical staining of defect 9R with no scaffold and control cells 1 month after implantation. a) Negative control. b) Collagen type I antibody.

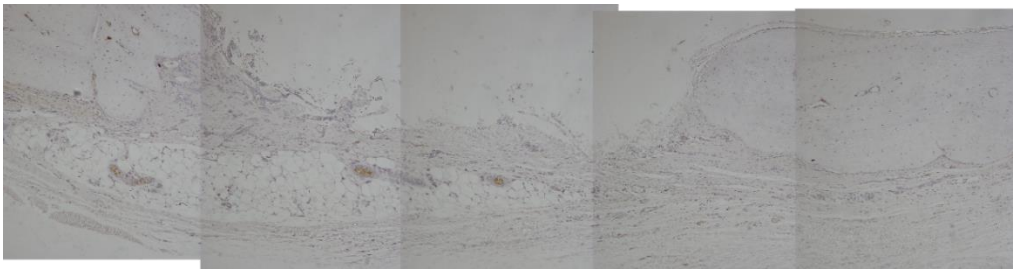

a)

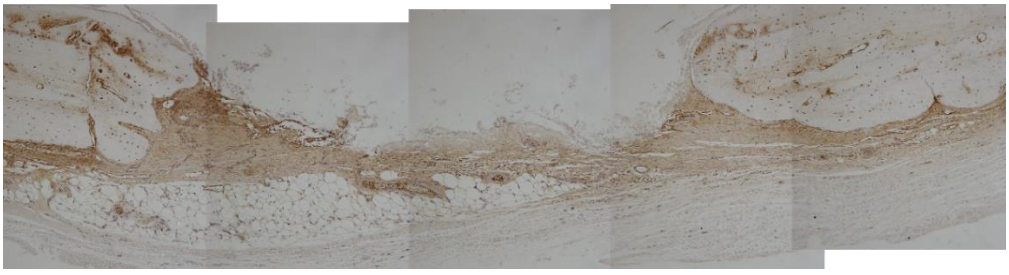

b)

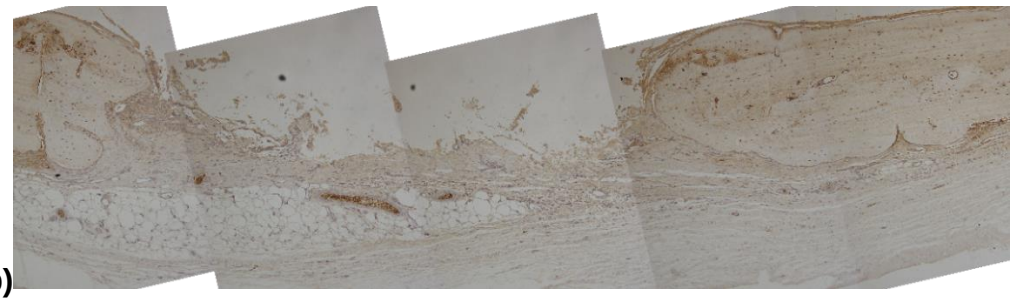

b)

Figure G.0.17: Histochemical staining of defect 8L with no scaffold and control cells 1 month after implantation. a) Negative control. b) Collagen type I antibody. c) Osteocalcin antibody.

a)

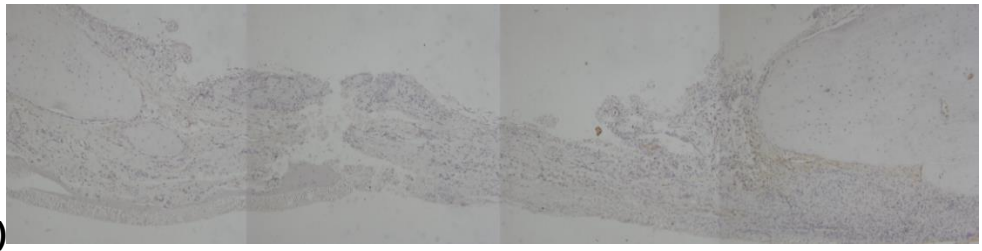

b)

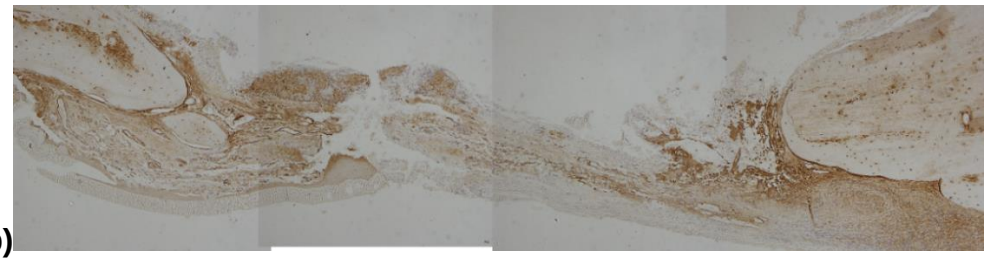

c)

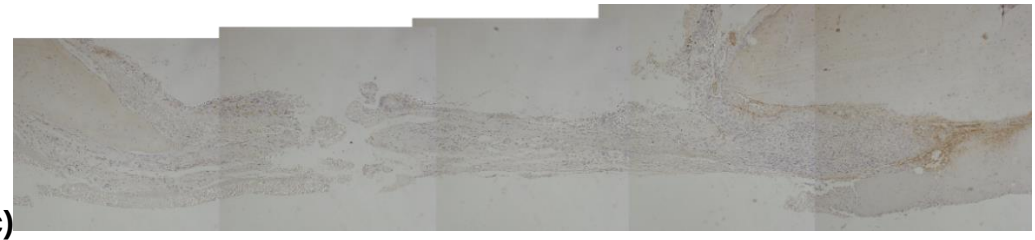

Figure G.0.18: Histochemical staining of defect 9N with no scaffold and control cells 1 month after implantation. a) Negative control. b) Collagen type I antibody. c) Osteocalcin antibody.

G.5. Histological sections of samples with no scaffold and cells exposed to SAW-DEP 1 month after implantation

a)

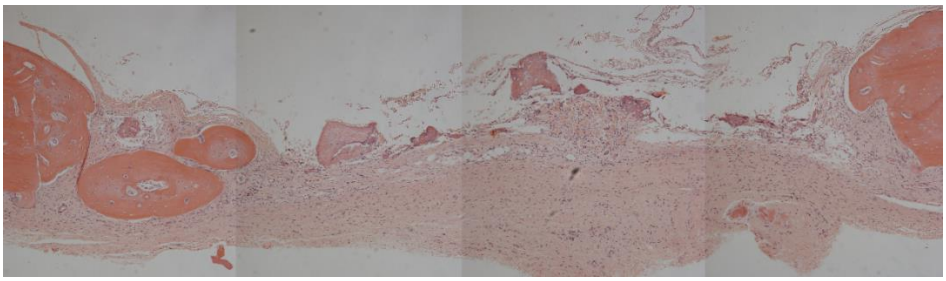

b)

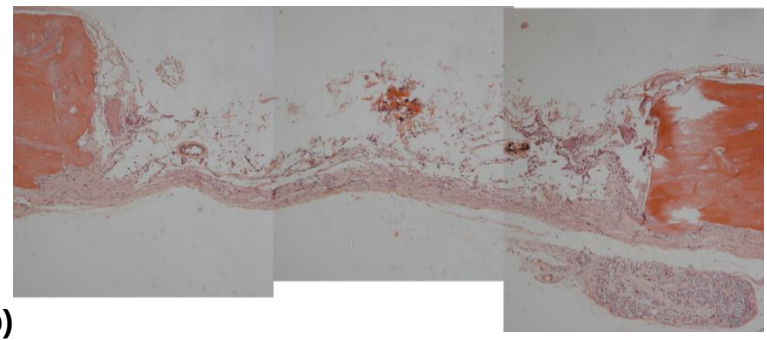

Figure G.0.19: Histological staining using H&E of defects 3R (a), 5L (b), with no scaffold and cells exposed to SAW-DEP 1 month after implantation. Nuclei were stained blue by Haematoxylin whereas cytoplasm and collagen were stained pink by eosin. Old bone was stained in a darker shade of pink.

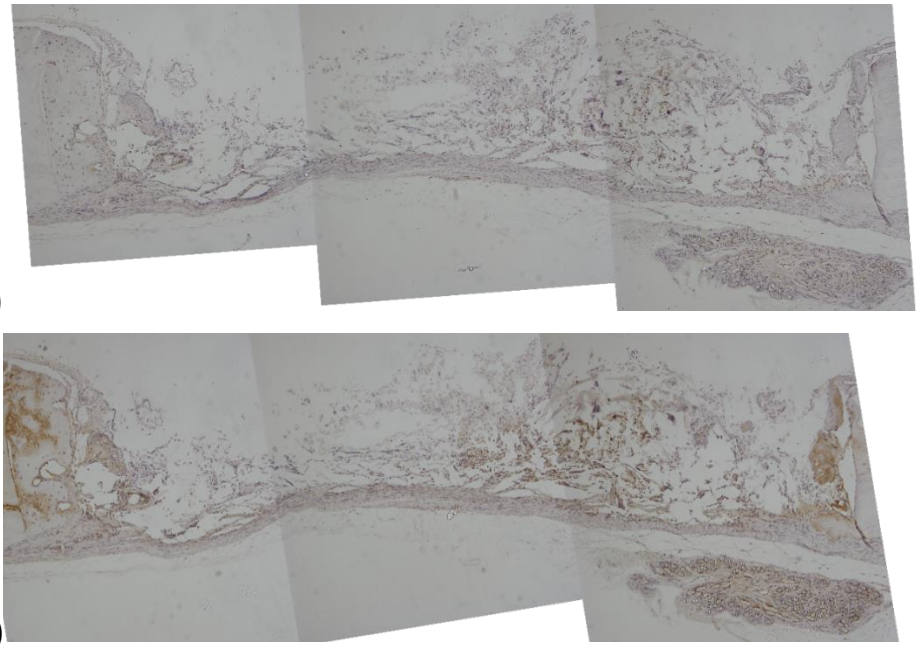

a)

b)

Figure G.0.20: Histochemical staining of defect 5L with no scaffold and cells exposed to SAW-DEP 1 month after implantation. a) Negative control. b) Collagen type I antibody.

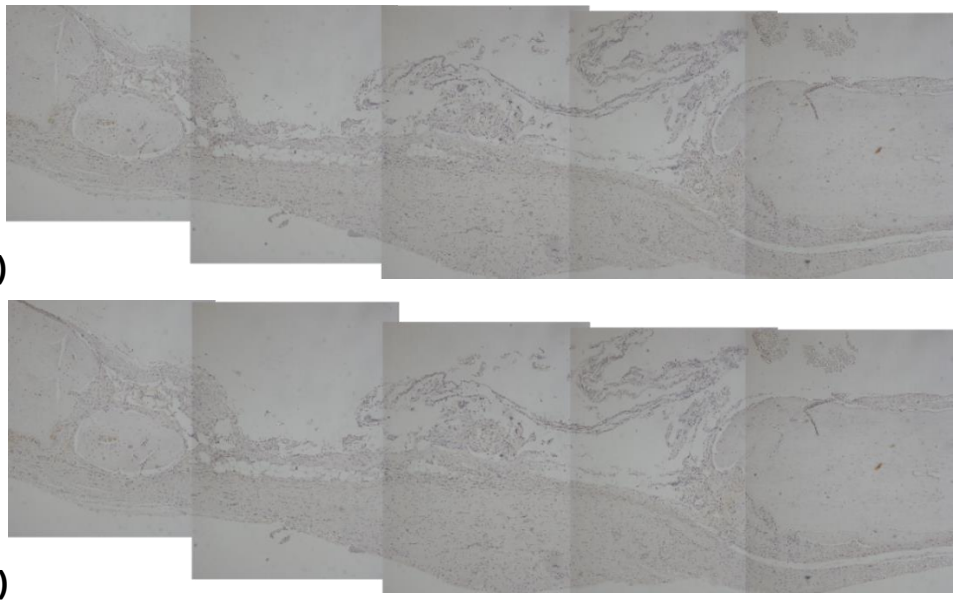

a)

b)

c) 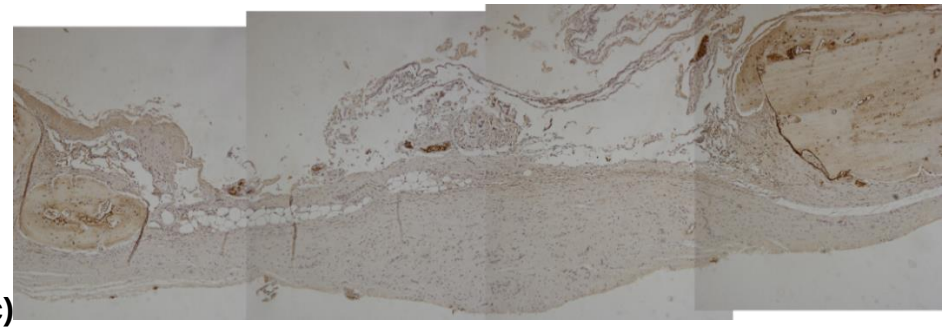

Figure G.0.21: Histochemical staining of defect 3R with no scaffold and cells exposed to SAW-DEP 1 month after implantation. a) Negative control. b) Collagen type I antibody. c) Osteocalcin antibody.

G.6. Histological sections of samples with no scaffold and cells exposed to SAW-DEP 2 months after implantation

a) 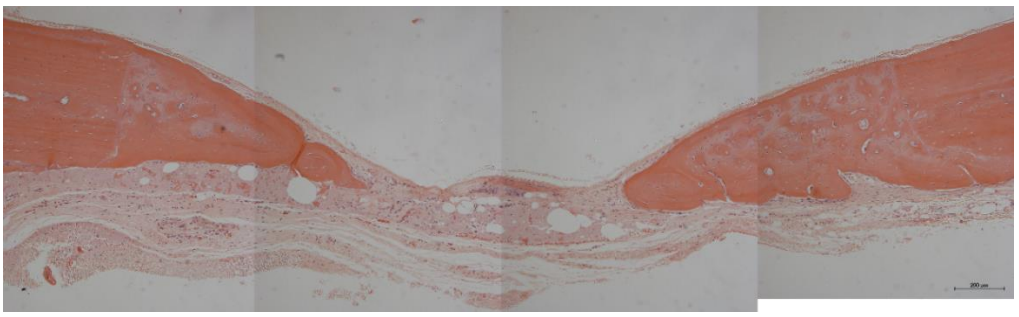

b)

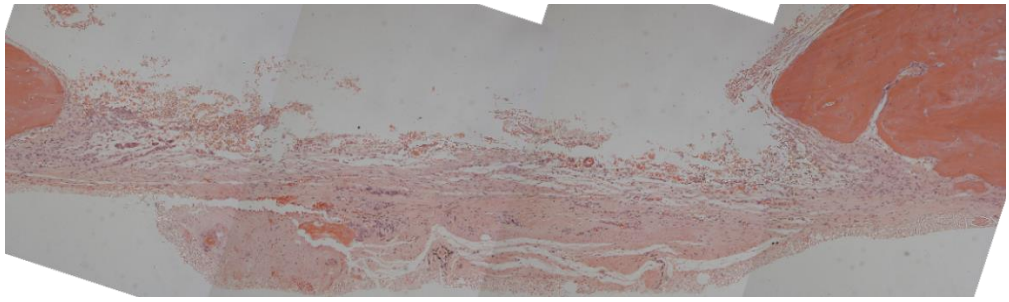

c)

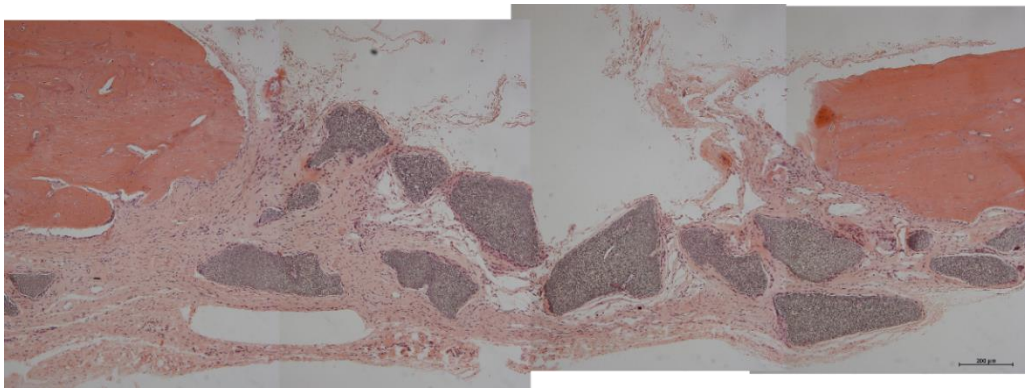

Figure G.0.22: Histological staining using H&E of defects 4R (a), 4N (b), 3N (c), with no scaffold and cells exposed to SAW-DEP 2 months after implantation. Nuclei were stained blue by Haematoxylin whereas cytoplasm and collagen were stained pink by eosin. Old bone was stained in a darker shade of pink.

a)

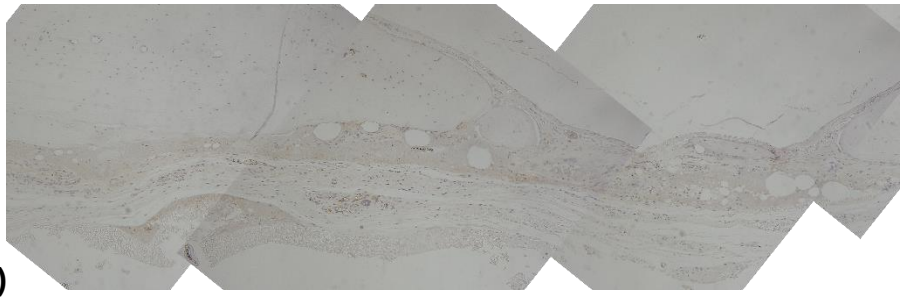

b)

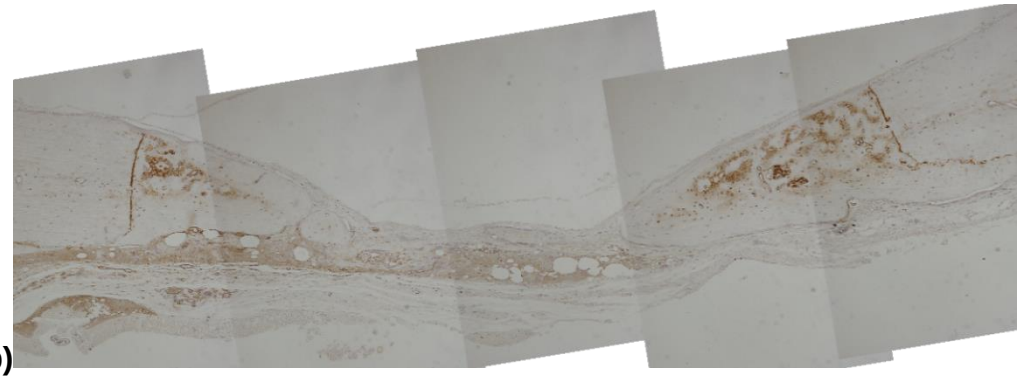

Figure G.0.23: Histochemical staining of defect 4R with no scaffold and cells exposed to SAW-DEP 2 months after implantation. a) Negative control. b) Collagen type I antibody.

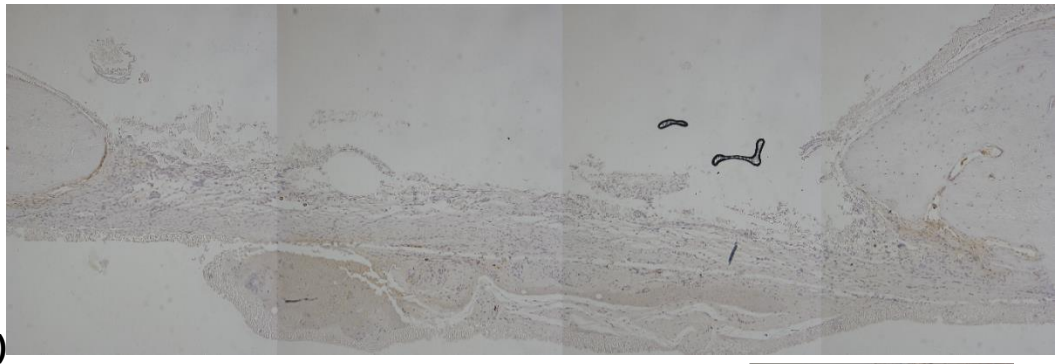

a)

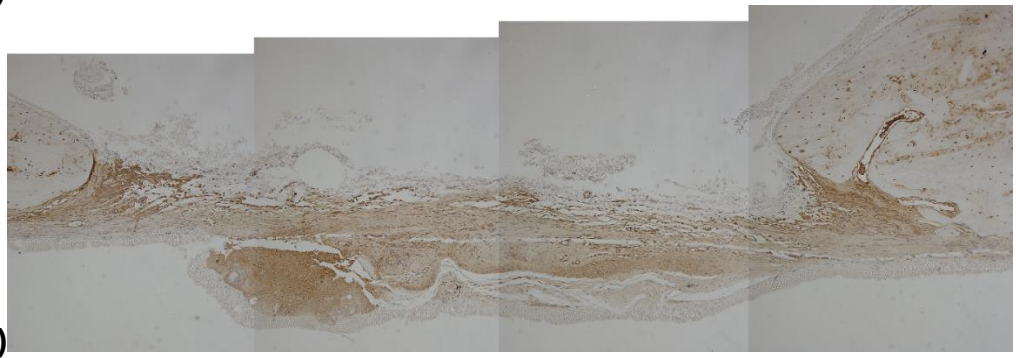

b)

Figure G.0.24: Histochemical staining of defect 4N with no scaffold and cells exposed to SAW-DEP 2 months after implantation. a) Negative control. b) Collagen type I antibody.

G.7. Histological sections of samples with ABM+P15 scaffold no cells 1 month after implantation

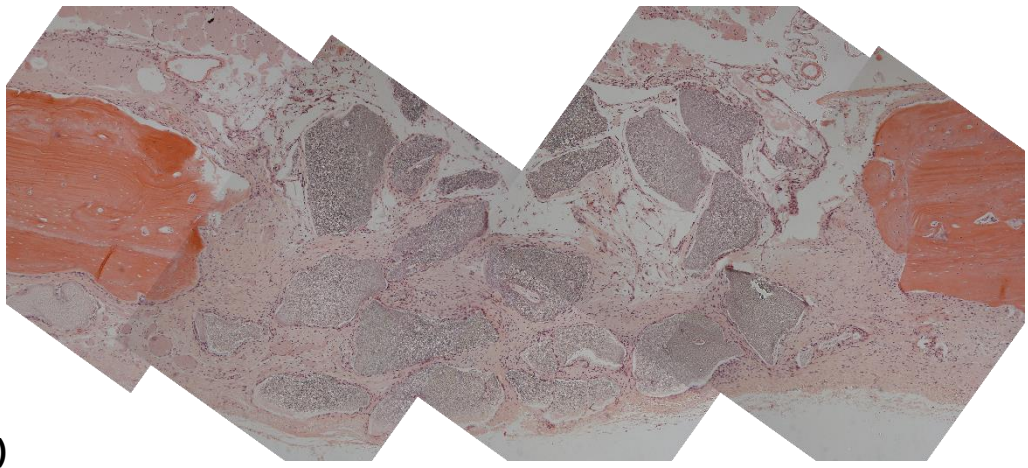

a)

b)

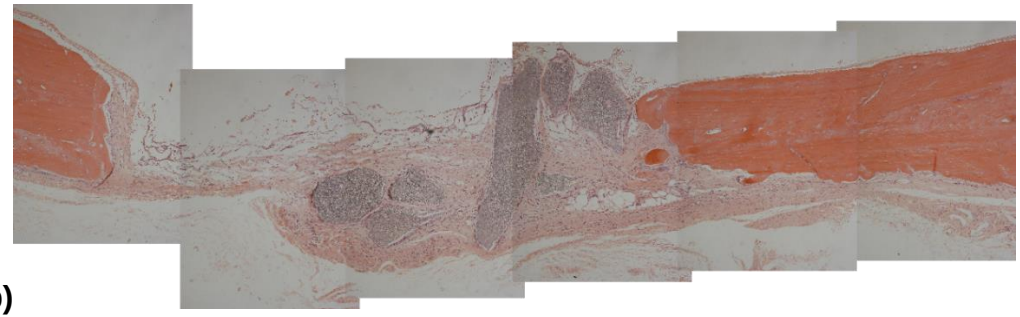

c)

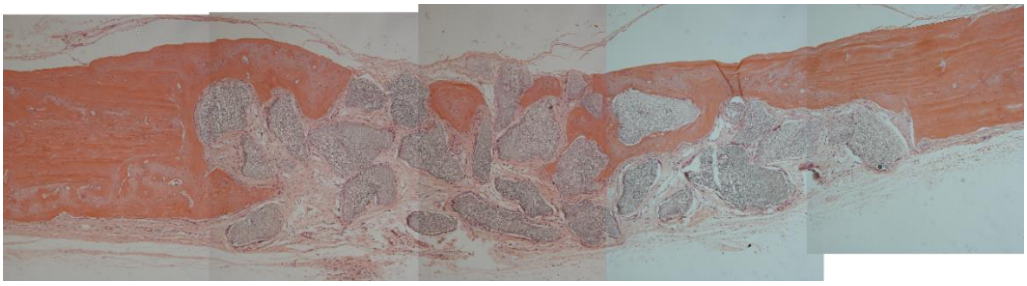

Figure G.0.25: Histological staining using H&E of defects 6N (a), 6R (b), 7L (c), with ABM+P15 scaffold and no cells 1 month after implantation. Nuclei were stained blue by Haematoxylin whereas cytoplasm and collagen were stained pink by eosin. Old bone was stained in a darker shade of pink.

a)

b)

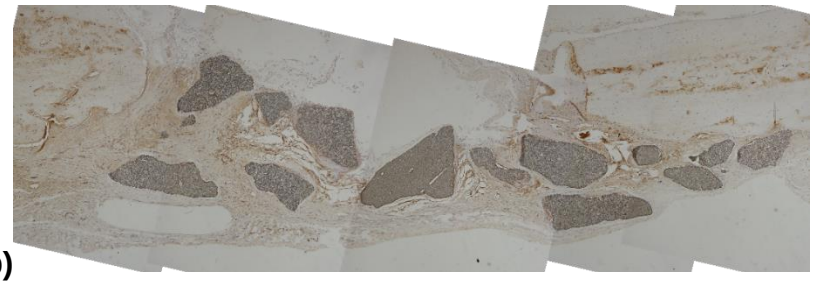

c)

Figure G.0.26: Histochemical staining of defect 3R with ABM+P15 scaffold and no cells 1 month after implantation. a) Negative control. b) Collagen type I antibody. c) Osteocalcin antibody.

a)

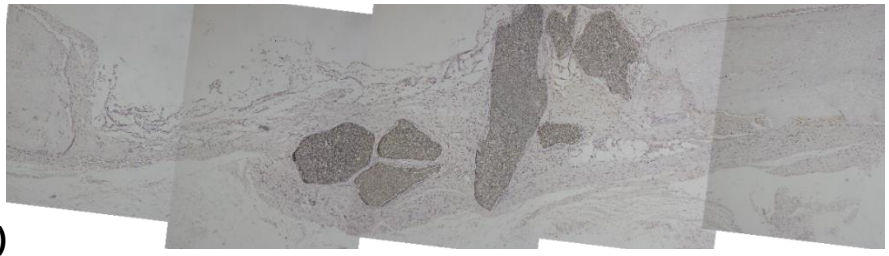

b)

c)

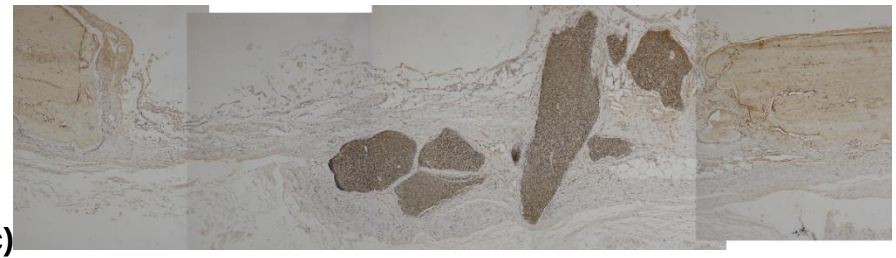

Figure G.0.27: Histochemical staining of defect 6R with ABM+P15 scaffold and no cells 1 month after implantation. a) Negative control. b) Collagen type I antibody. c) Osteocalcin antibody.

a)

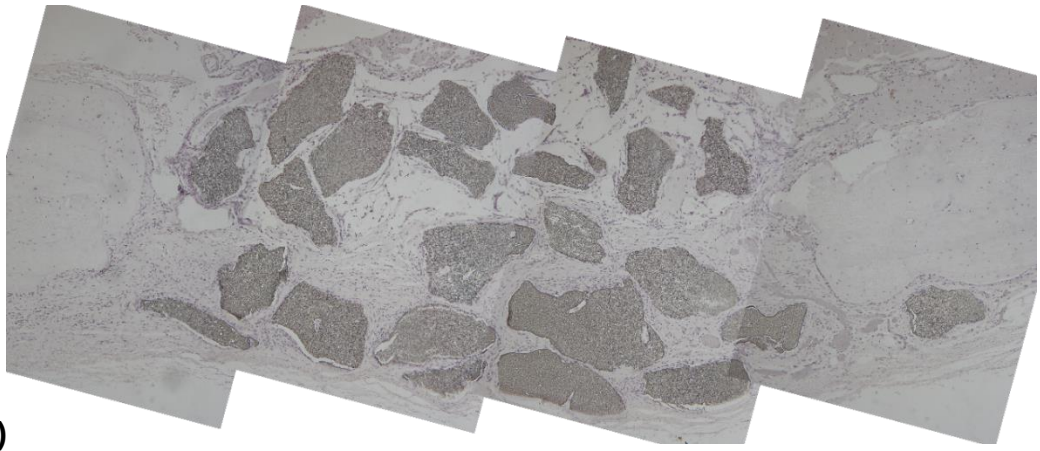

b)

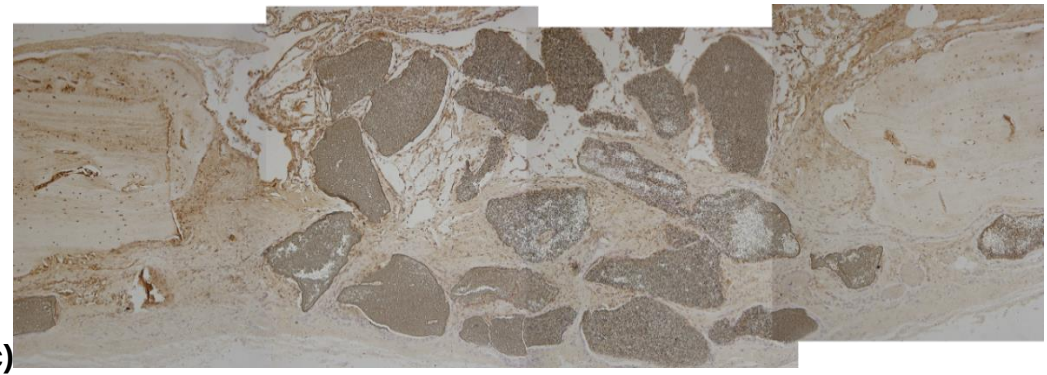

c)

Figure G.0.28: Histochemical staining of defect 6N with ABM+P15 scaffold and no cells 1 month after implantation. a) Negative control. b) Collagen type I antibody. c) Osteocalcin antibody.

a)

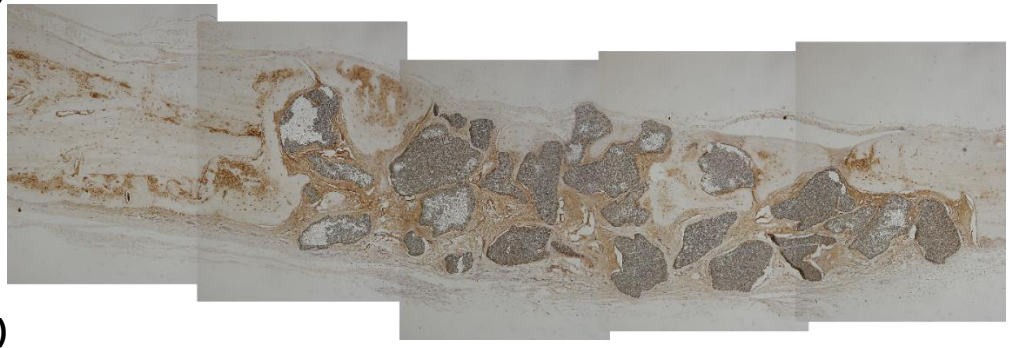

b)

c) 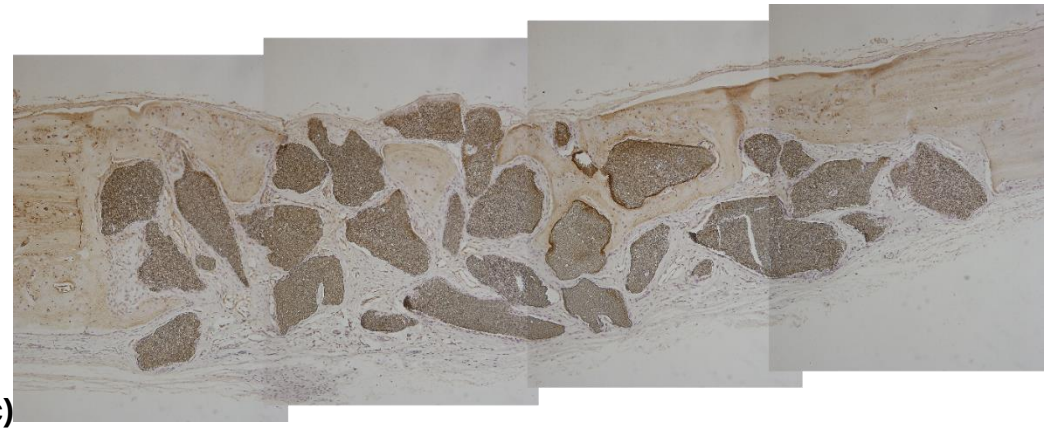

Figure G.0.29: Histochemical staining of defect 7L with ABM+P15 scaffold and no cells 1 month after implantation. a) Negative control. b) Collagen type I antibody. c) Osteocalcin antibody.

G.8. Histological sections of samples with ABM+P15 scaffold no cells 2 months after implantation

a) 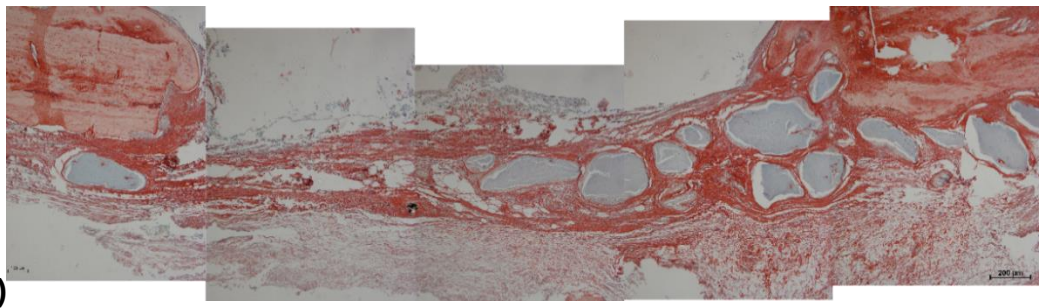

b)

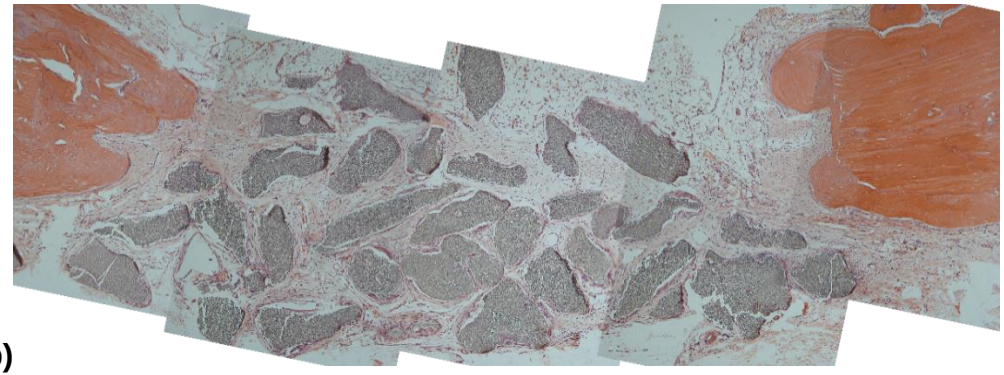

c)

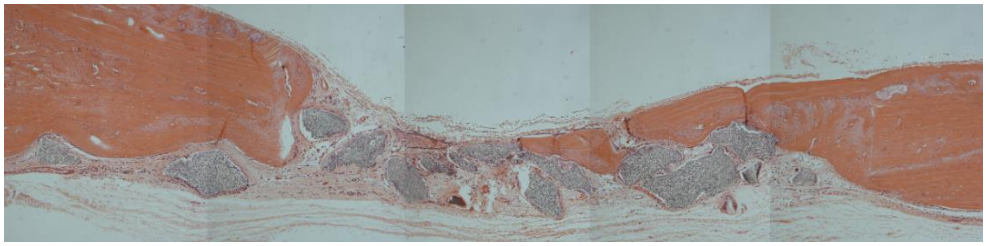

Figure G.0.30: Histological staining using H&E of defects 2R (a), 8N (b), 9L (c), with ABM+P15 scaffold and no cells 2 months after implantation. Nuclei were stained blue by Haematoxylin whereas cytoplasm and collagen were stained pink by eosin. Old bone was stained in a darker shade of pink.

a)

b)

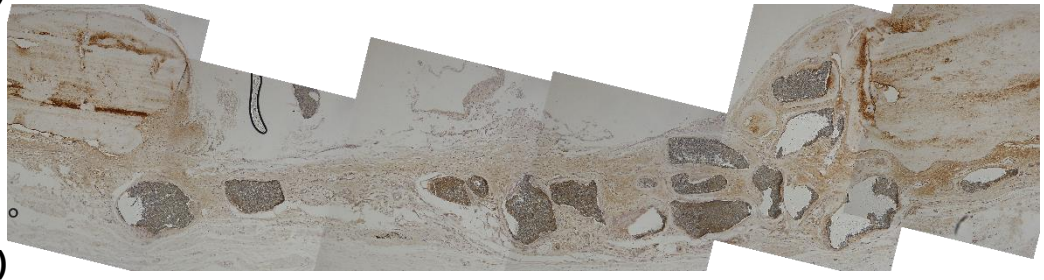

c)

Figure G.0.31: Histochemical staining of defect 2R with ABM+P15 scaffold and no cells 2 months after implantation. a) Negative control. b) Collagen type I antibody. c) Osteocalcin antibody.

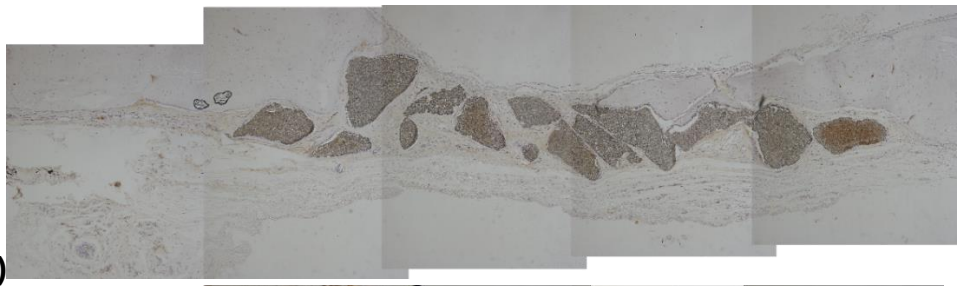

a)

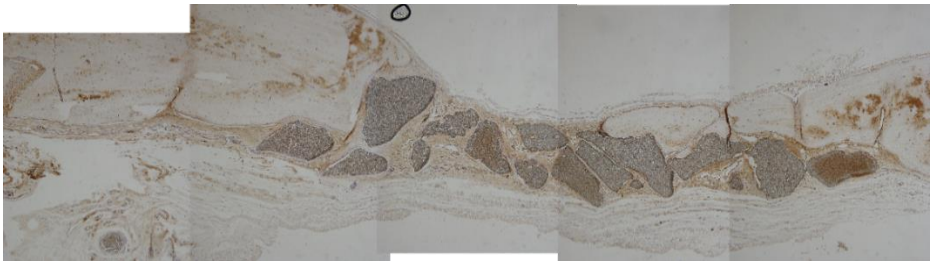

b)

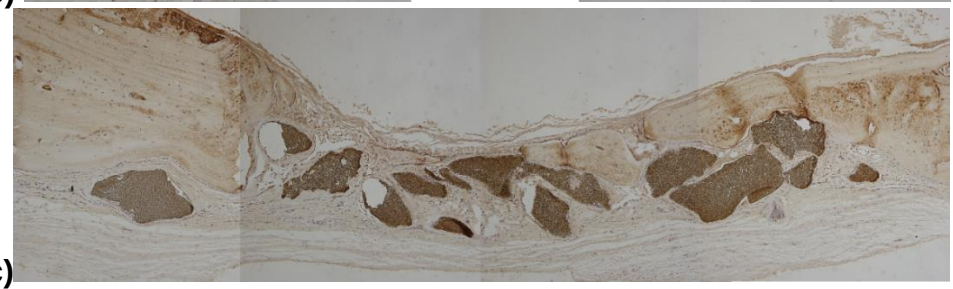

c)

Figure G.0.32: Histochemical staining of defect 9L with ABM+P15 scaffold and no cells 2 months after implantation. a) Negative control. b) Collagen type I antibody. c) Osteocalcin antibody.

a)

b)

c)

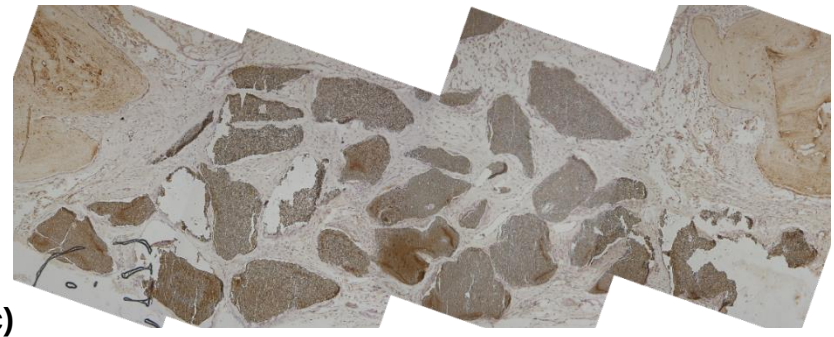

Figure G.0.33: Histochemical staining of defect 8N with ABM+P15 scaffold and no cells 2 months after implantation. a) Negative control. b) Collagen type I antibody. c) Osteocalcin antibody.

G.9. Histological sections of samples with ABM+P15 scaffold and control cells 1 month after implantation

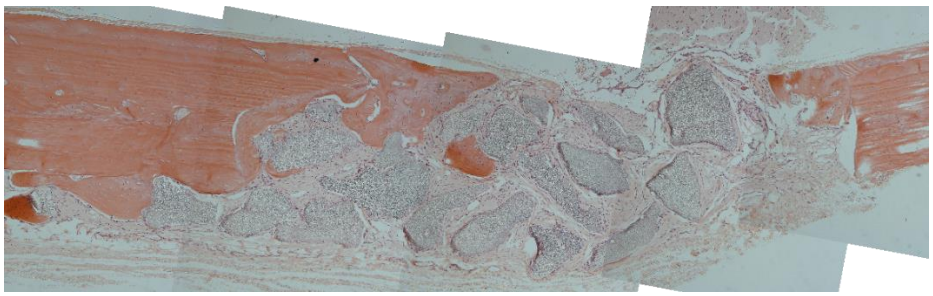

Figure G.0.34: Histological staining using H&E of defects 7N with ABM+P15 scaffold and control cells 1 month after implantation. Nuclei were stained blue by Haematoxylin whereas cytoplasm and collagen were stained pink by eosin. Old bone was stained in a darker shade of pink.

a)

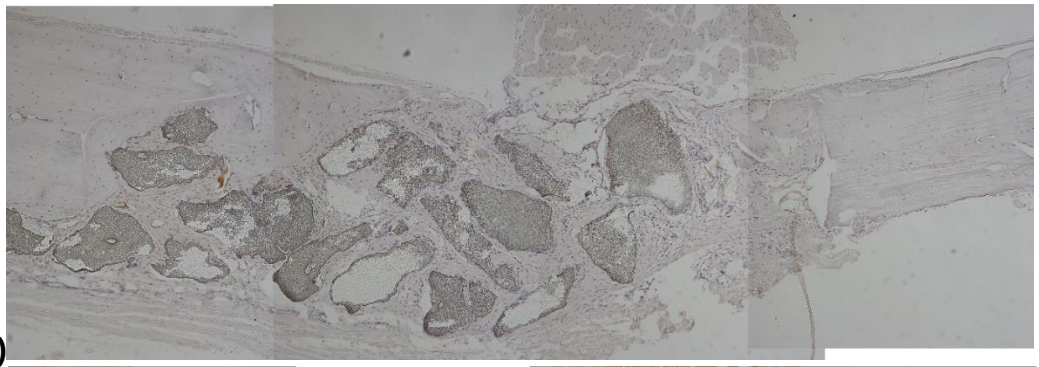

b)

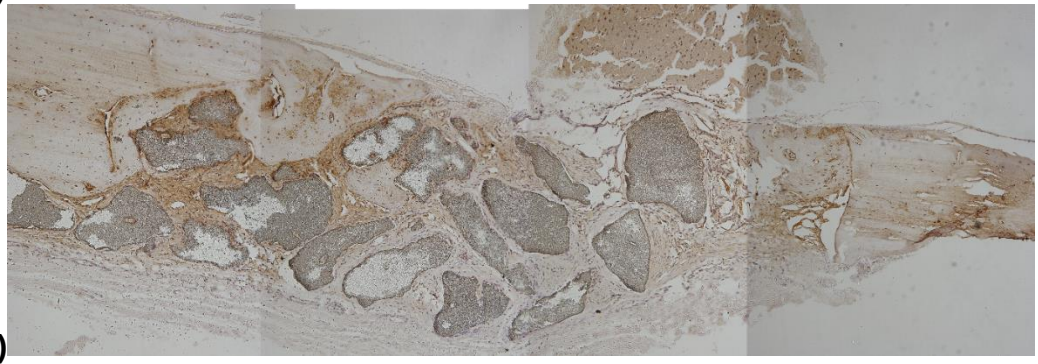

c)

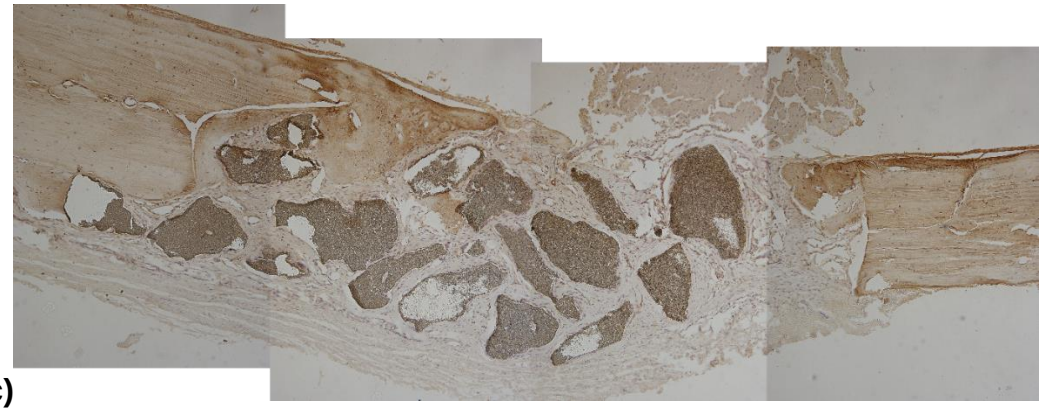

Figure G.0.35: Histochemical staining of defect 7N with ABM+P15 scaffold and control cells 1 month after implantation. a) Negative control. b) Collagen type I antibody. c) Osteocalcin antibody.

G.10. Histological sections of samples with ABM+P15 scaffold and control cells 2 months after implantation

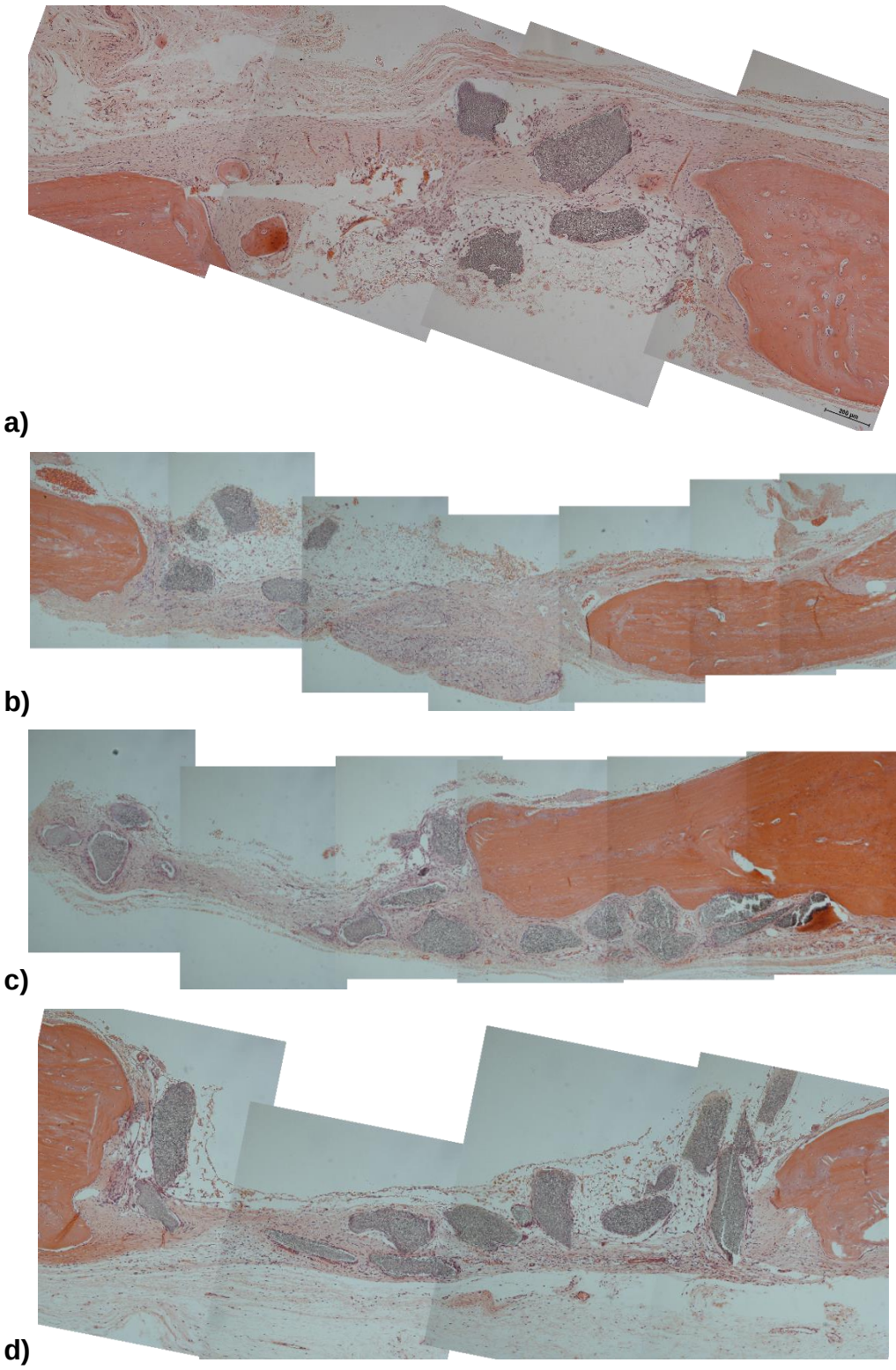

Figure G.0.36: Histological staining using H&E of defects 2L (a), 8L (b), 9N (c), 9R (d) with ABM+P15 scaffold and control cells 2 months after implantation. Nuclei were stained blue by Haematoxylin whereas cytoplasm and collagen were stained pink by eosin. Old bone was stained in a darker shade of pink.

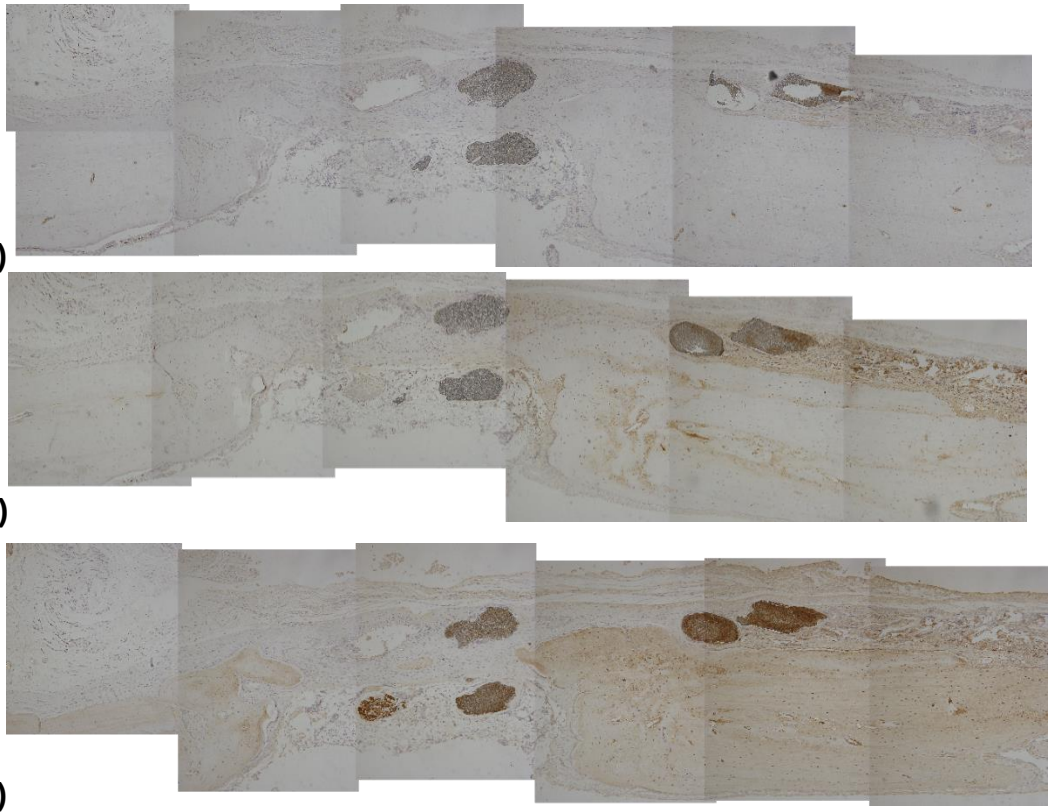

Figure G.0.37: Histochemical staining of defect 2L with ABM+P15 scaffold and control cells 2 months after implantation. a) Negative control. b) Collagen type I antibody. c) Osteocalcin antibody.

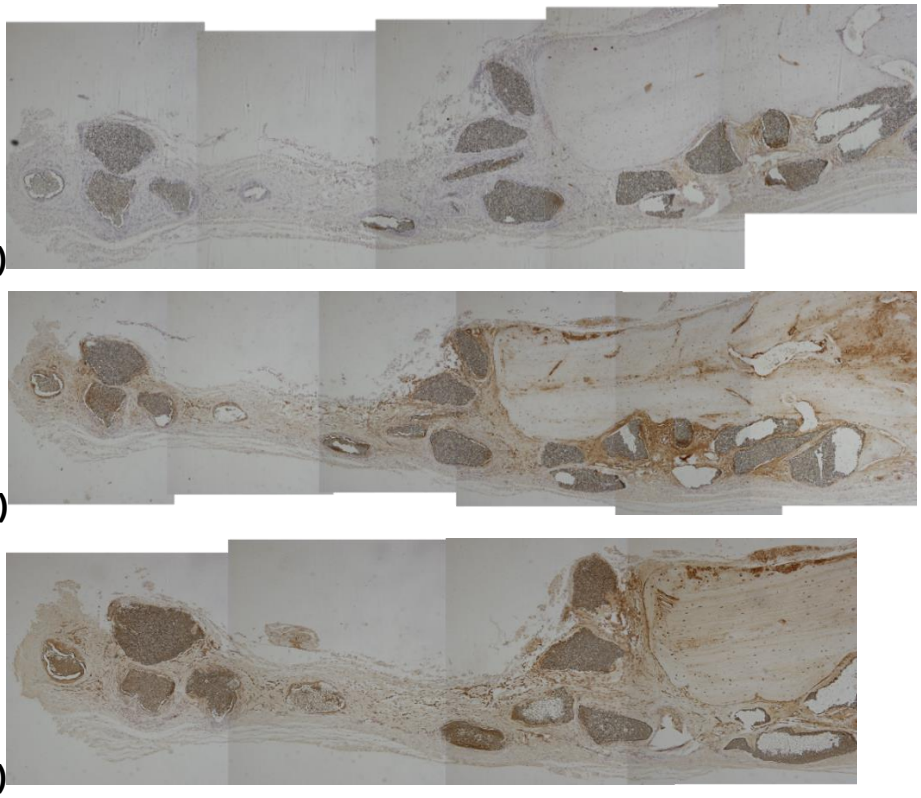

Figure G.0.38: Histochemical staining of defect 9N with ABM+P15 scaffold and control cells 2 months after implantation. a) Negative control. b) Collagen type I antibody. c) Osteocalcin antibody.

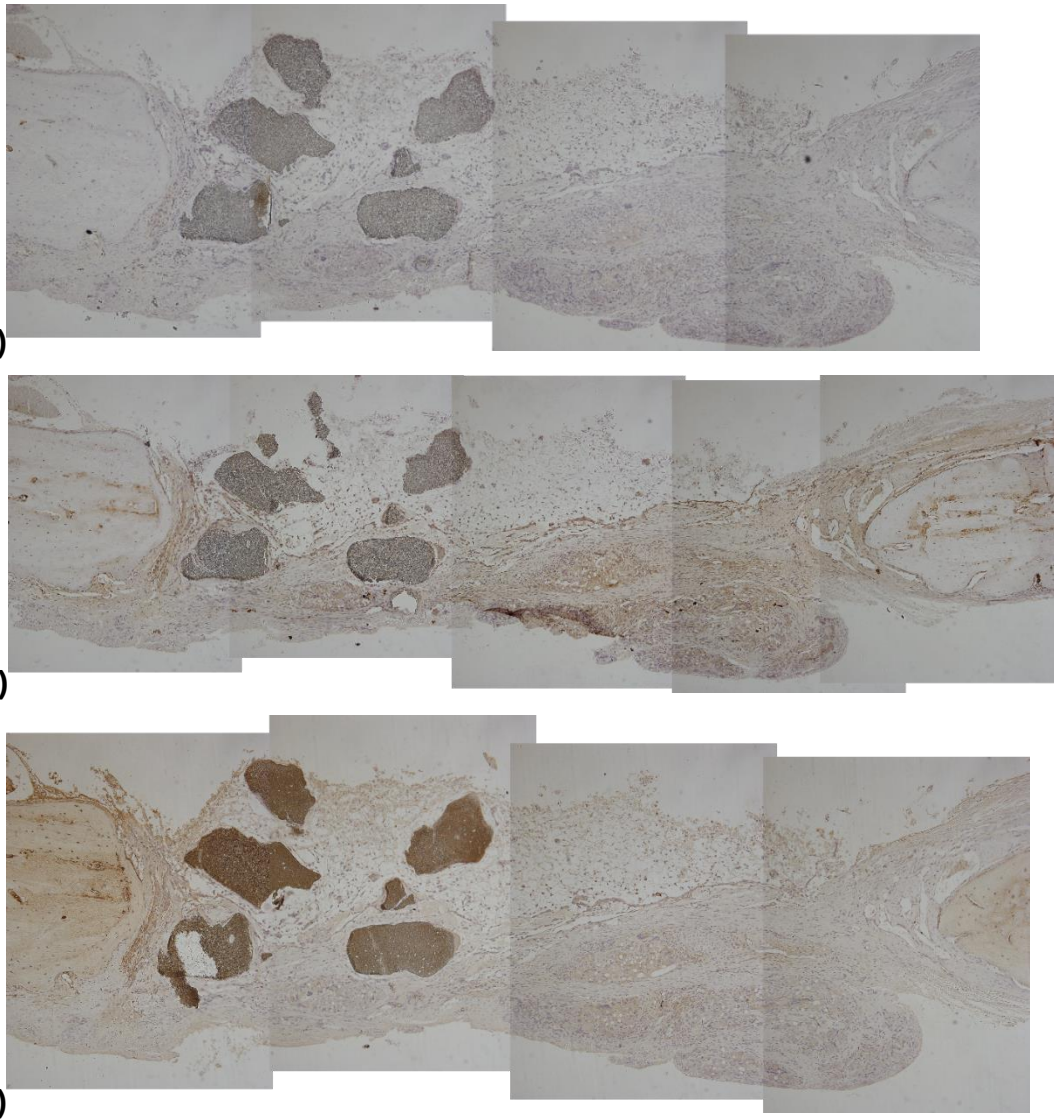

Figure G.0.39: Histochemical staining of defect 8L with ABM+P15 scaffold and control cells 2 months after implantation. a) Negative control. b) Collagen type I antibody. c) Osteocalcin antibody.

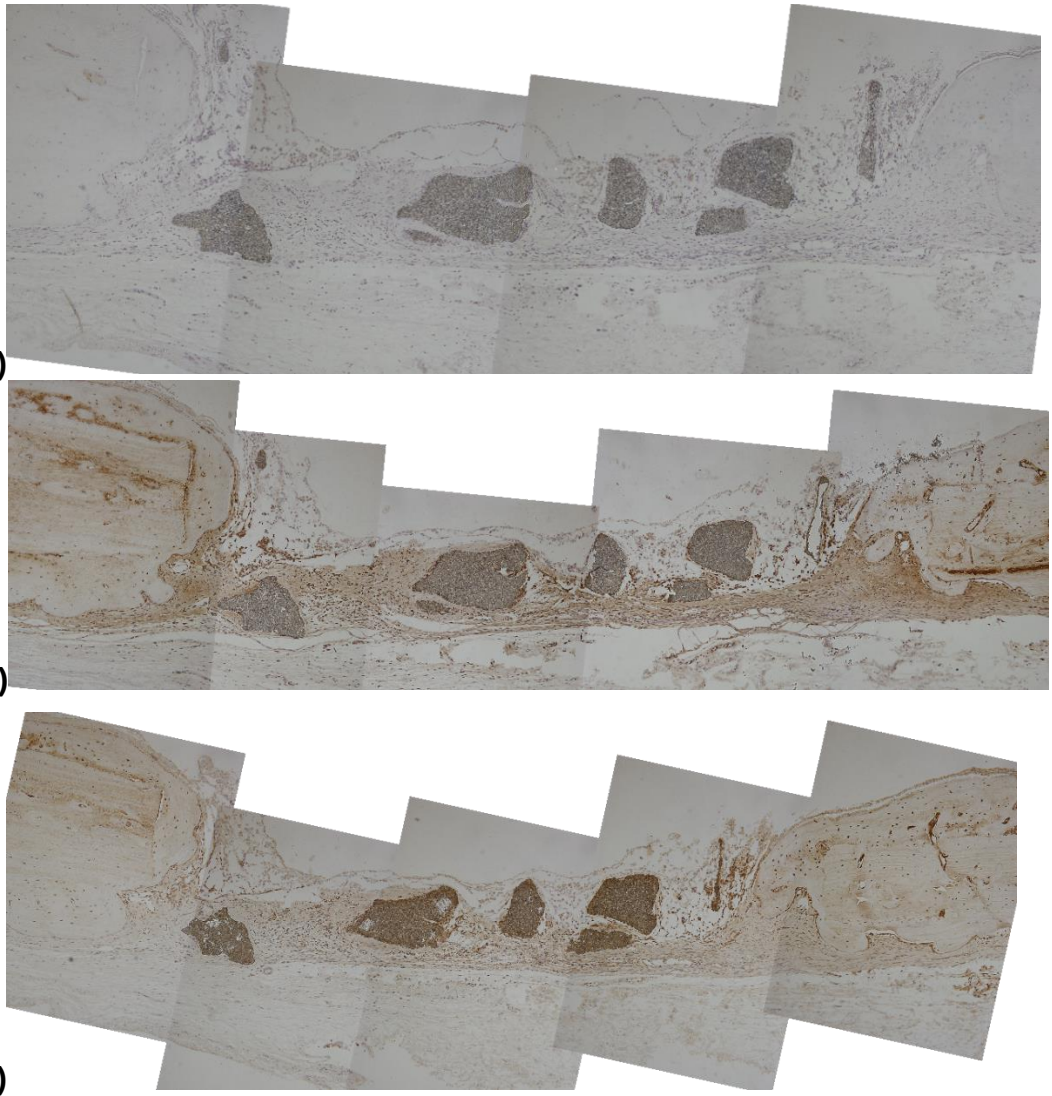

Figure G.0.40: Histochemical staining of defect 9R with ABM+P15 scaffold and control cells 2 months after implantation. a) Negative control. b) Collagen type I antibody. c) Osteocalcin antibody.

G.11. Histological sections of samples with ABM+P15 scaffold and cells exposed to SAW-DEP 1 month after implantation

a)

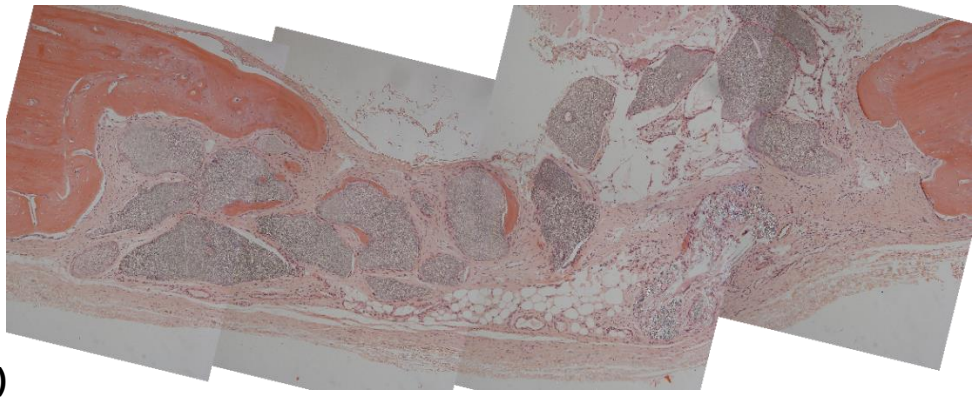

b)

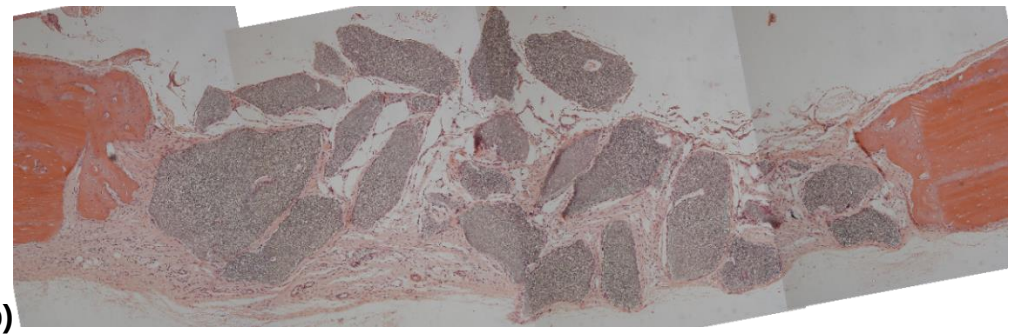

c)

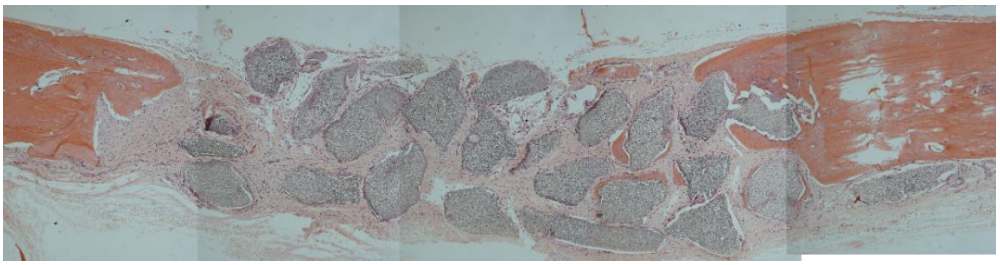

d)

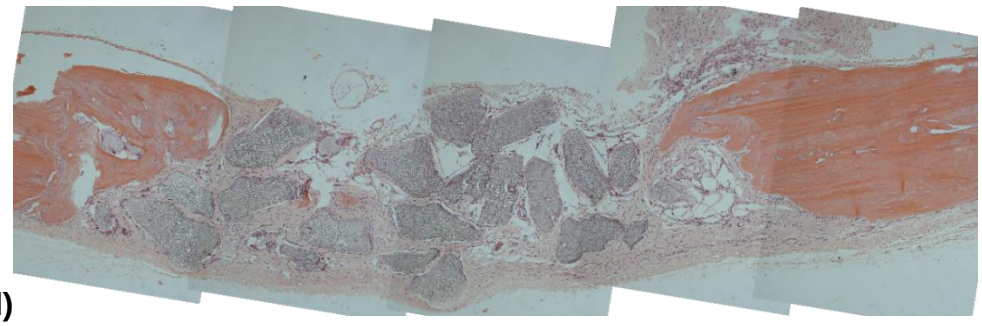

Figure G.0.41: Histological staining using H&E of defects 3R (a), 5L (b), 11R1 (c), 11R2 (d) with ABM+P15 scaffold and cells exposed to SAW-DEP 1 month after implantation. Nuclei were stained blue by Haematoxylin whereas cytoplasm and collagen were stained pink by eosin. Old bone was stained in a darker shade of pink.

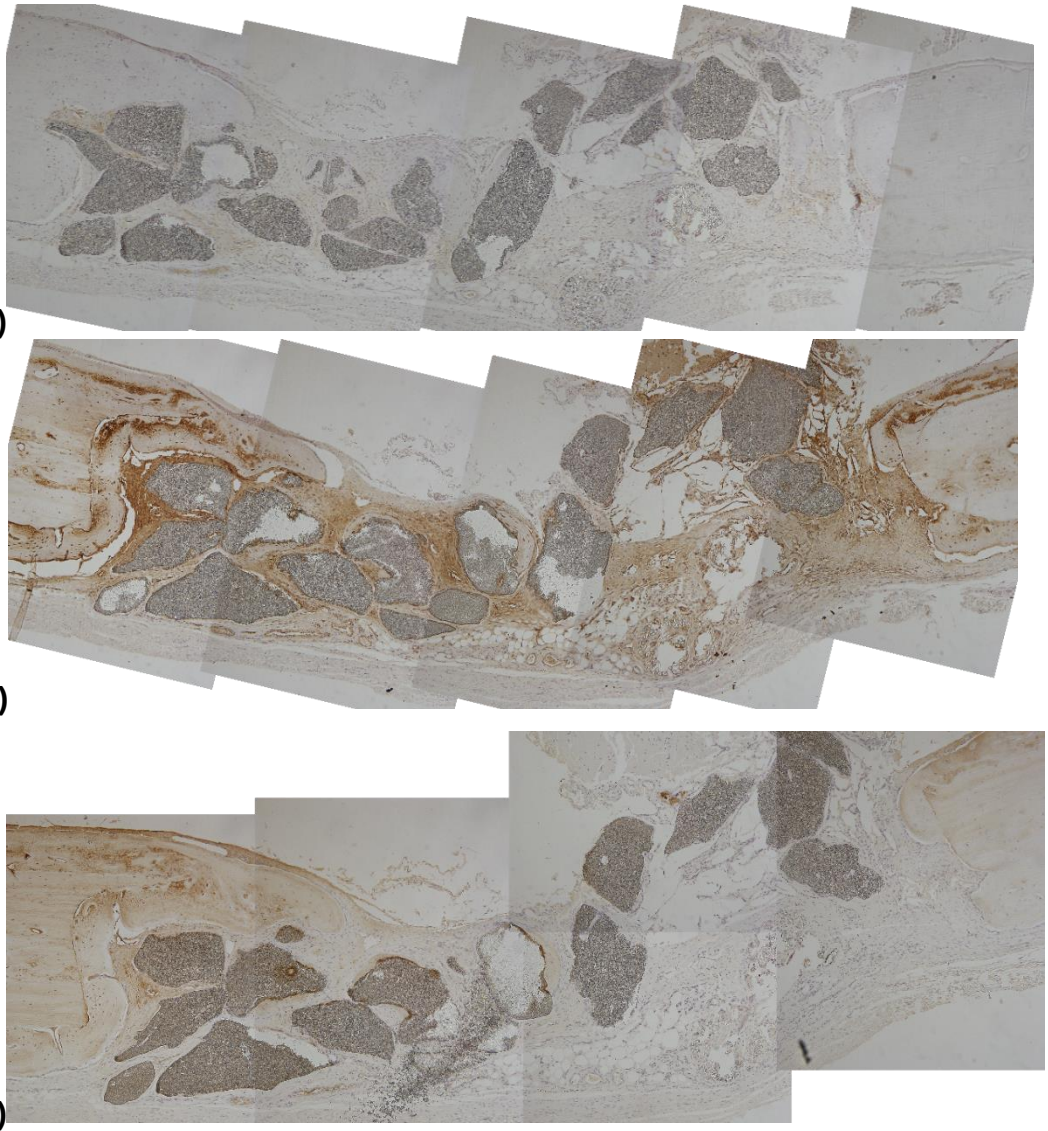

a)

b)

c)

Figure G.0.42: Histochemical staining of defect 3R with ABM+P15 scaffold and cells exposed to SAW-DEP 1 month after implantation. a) Negative control. b) Collagen type I antibody. c) Osteocalcin antibody.

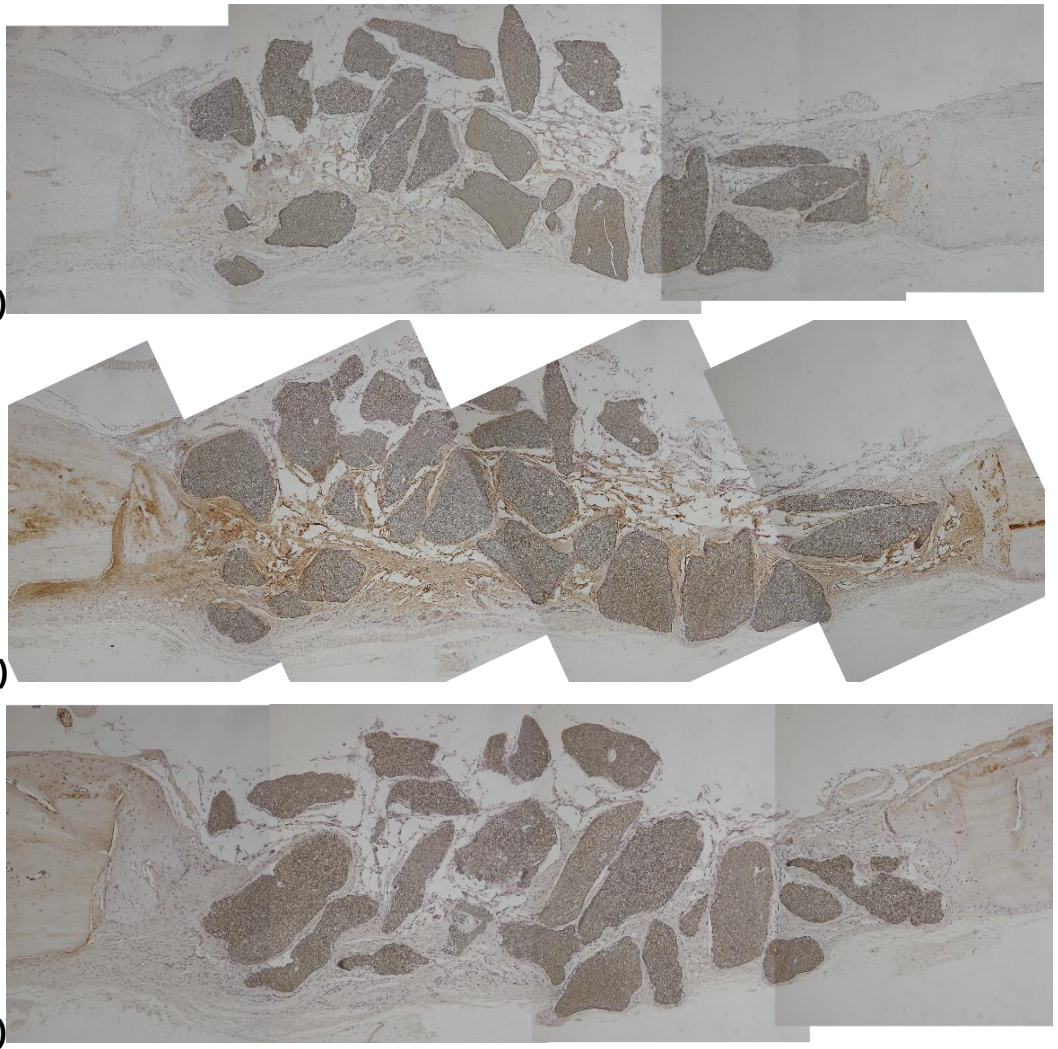

Figure G.0.43: Histochemical staining of defect 5L with ABM+P15 scaffold and cells exposed to SAW-DEP 1 month after implantation. a) Negative control. b) Collagen type I antibody. c) Osteocalcin antibody.

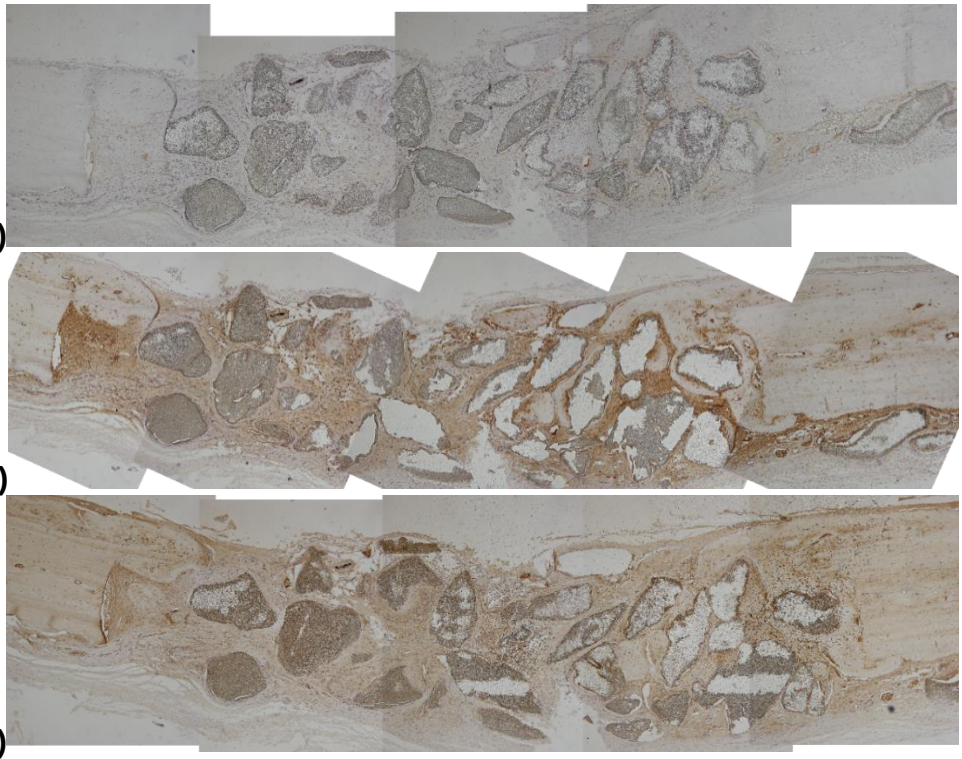

Figure G.0.44: Histochemical staining of defect 11R1 with ABM+P15 scaffold and cells exposed to SAW-DEP 1 month after implantation. a) Negative control. b) Collagen type I antibody. c) Osteocalcin antibody.

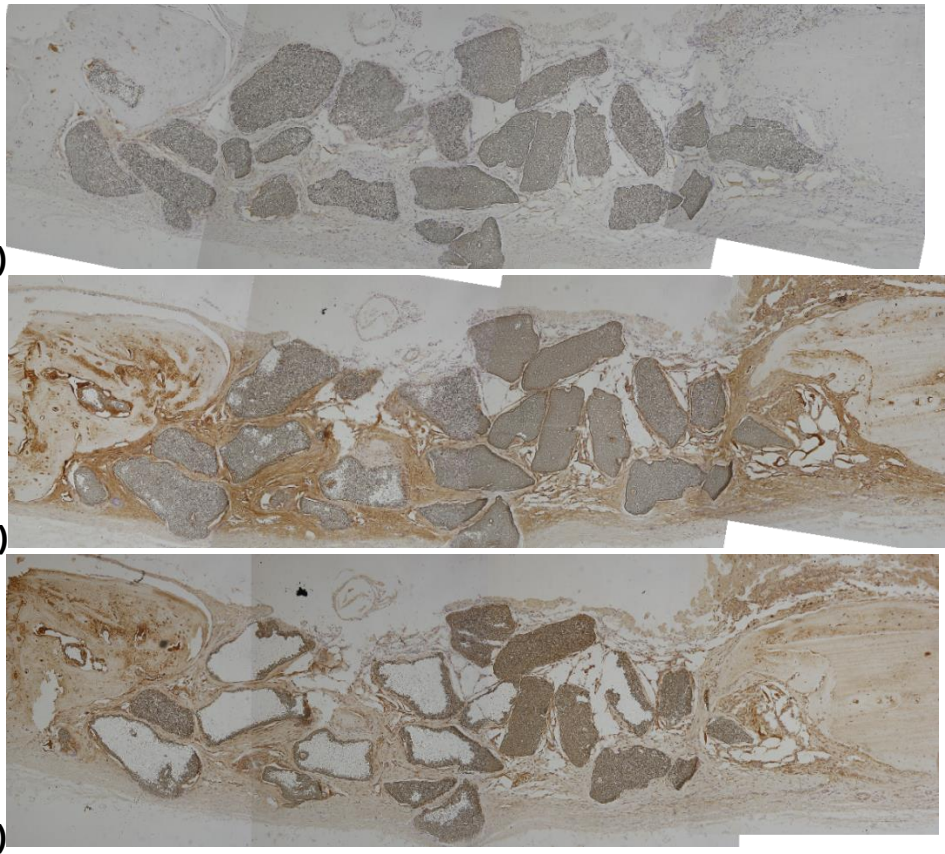

Figure G.0.45: Histochemical staining of defect 11R2 with ABM+P15 scaffold and cells exposed to SAW-DEP 1 month after implantation. a) Negative control. b) Collagen type I antibody. c) Osteocalcin antibody.

G.12. Histological sections of samples with ABM+P15 scaffold and cells exposed to SAW-DEP 2 months after implantation

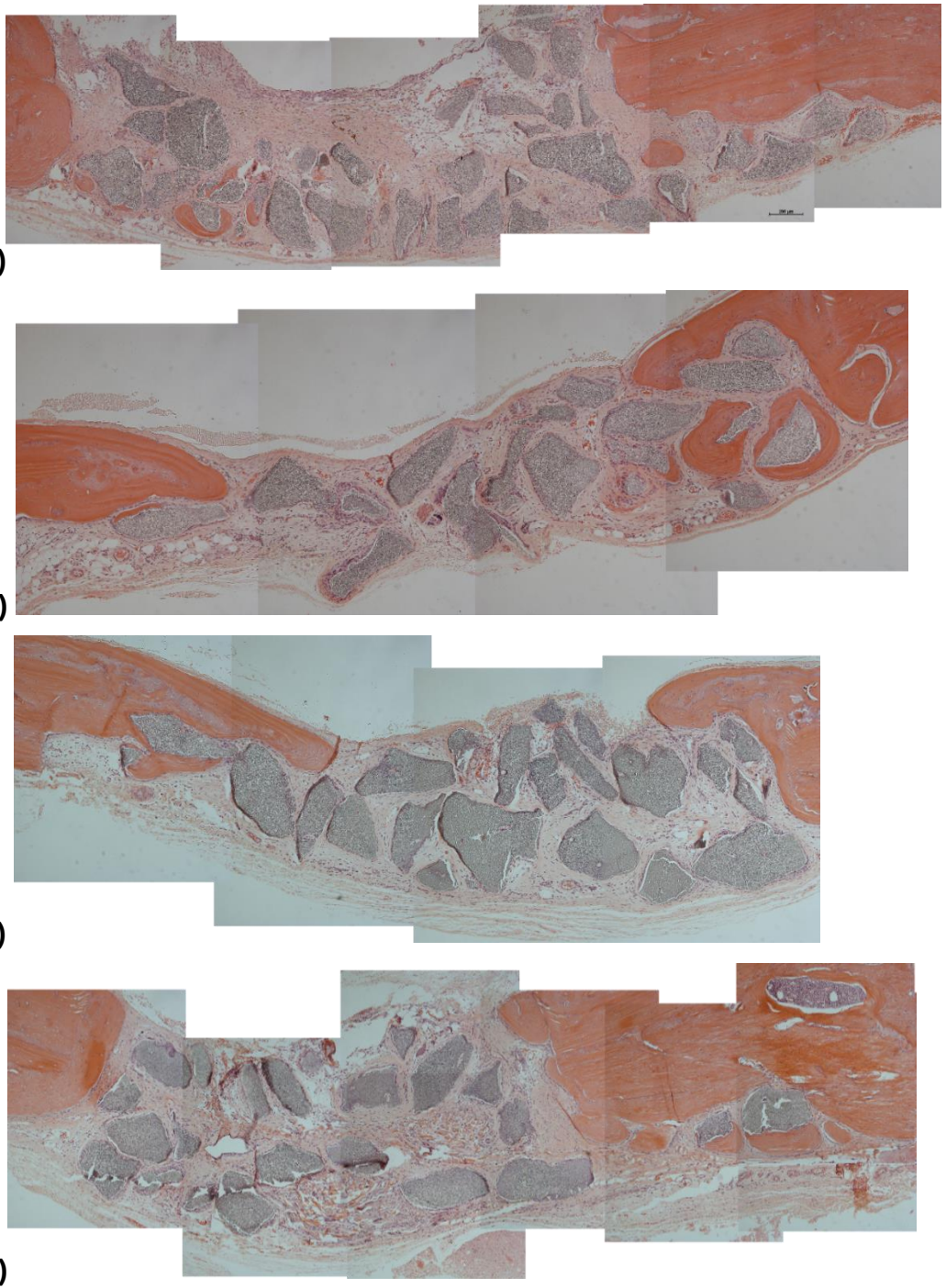

Figure G.0.46: Histological staining using H&E of defects 4R (a), 4N (b), 11N1 (c), 11N2 (d) with ABM+P15 scaffold and cells exposed to SAW-DEP 2 months after implantation. Nuclei were stained blue by Haematoxylin whereas cytoplasm and collagen were stained pink by eosin. Old bone was stained in a darker shade of pink.

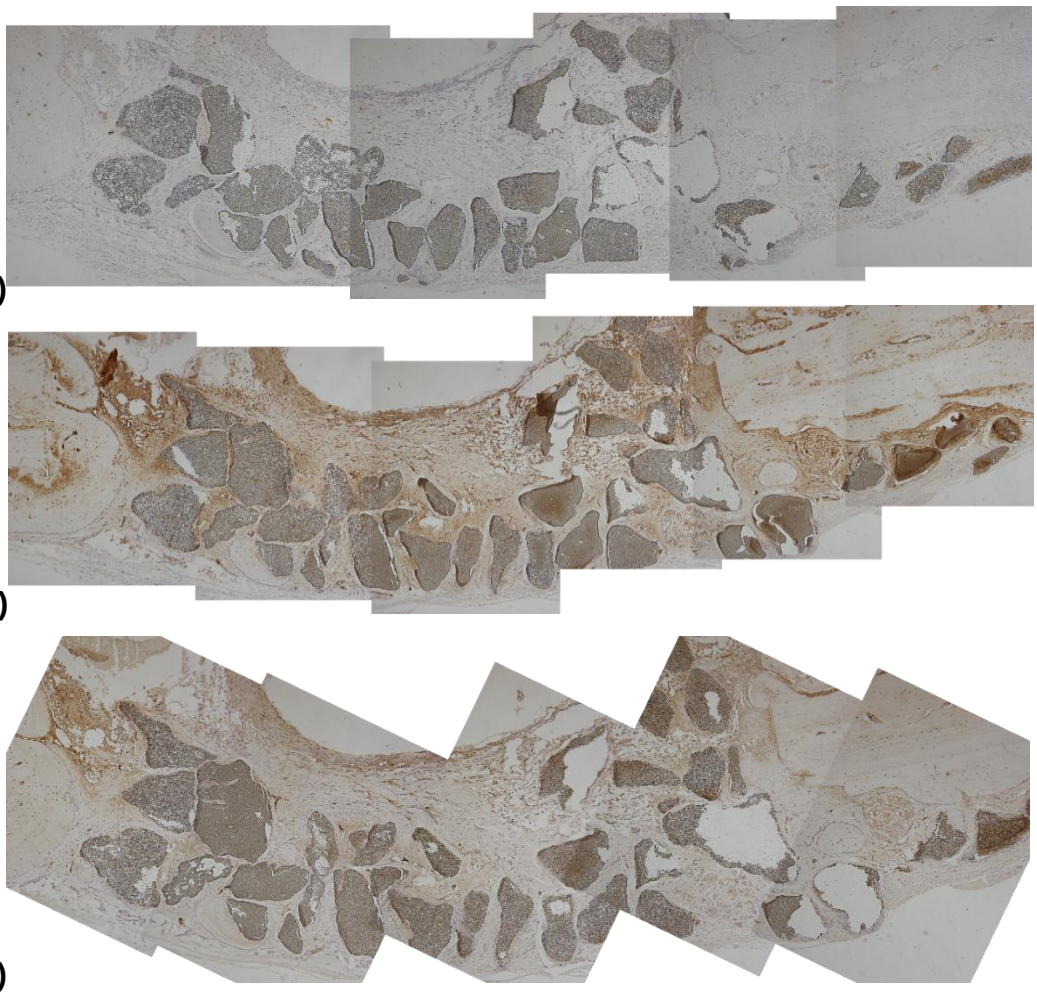

Figure G.0.47: Histochemical staining of defect 4N with ABM+P15 scaffold and cells exposed to SAW-DEP 2 months after implantation. a) Negative control. b) Collagen type I antibody. c) Osteocalcin antibody.

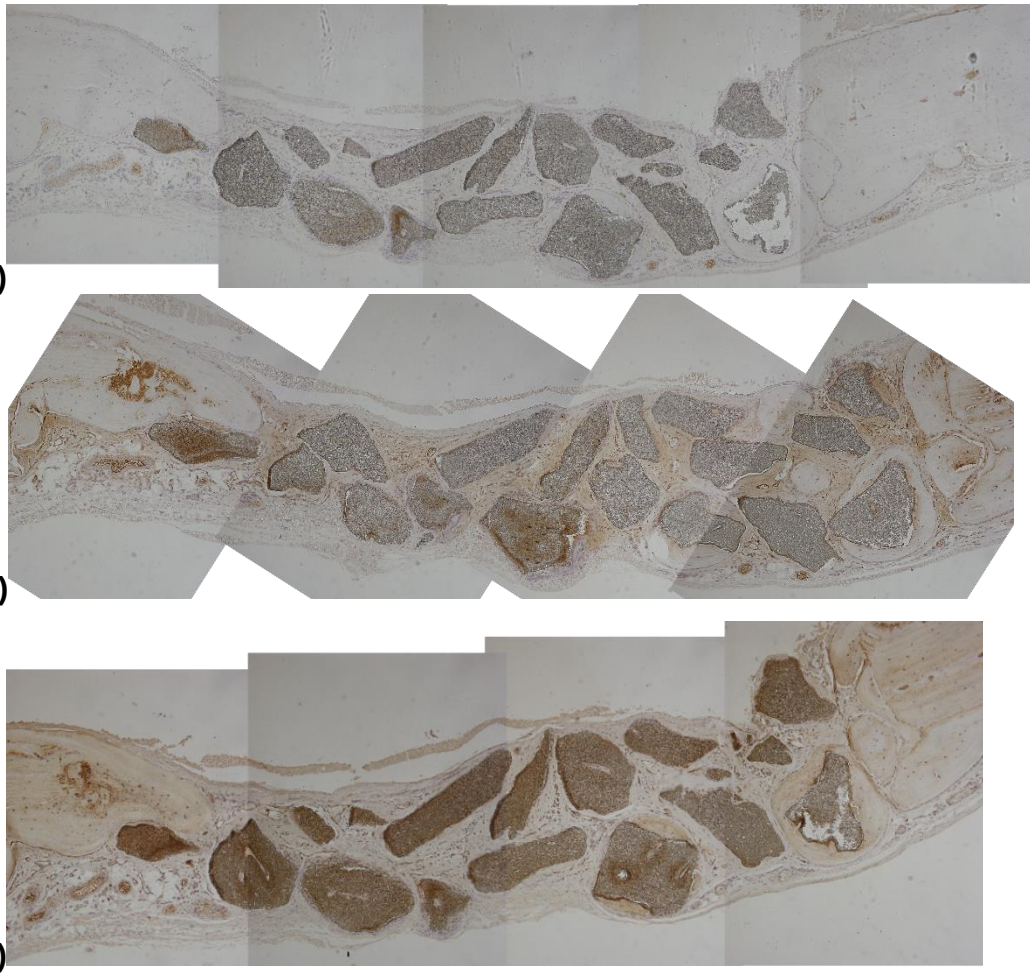

Figure G.0.48: Histochemical staining of defect 4N with ABM+P15 scaffold and cells exposed to SAW-DEP 2 months after implantation. a) Negative control. b) Collagen type I antibody. c) Osteocalcin antibody.

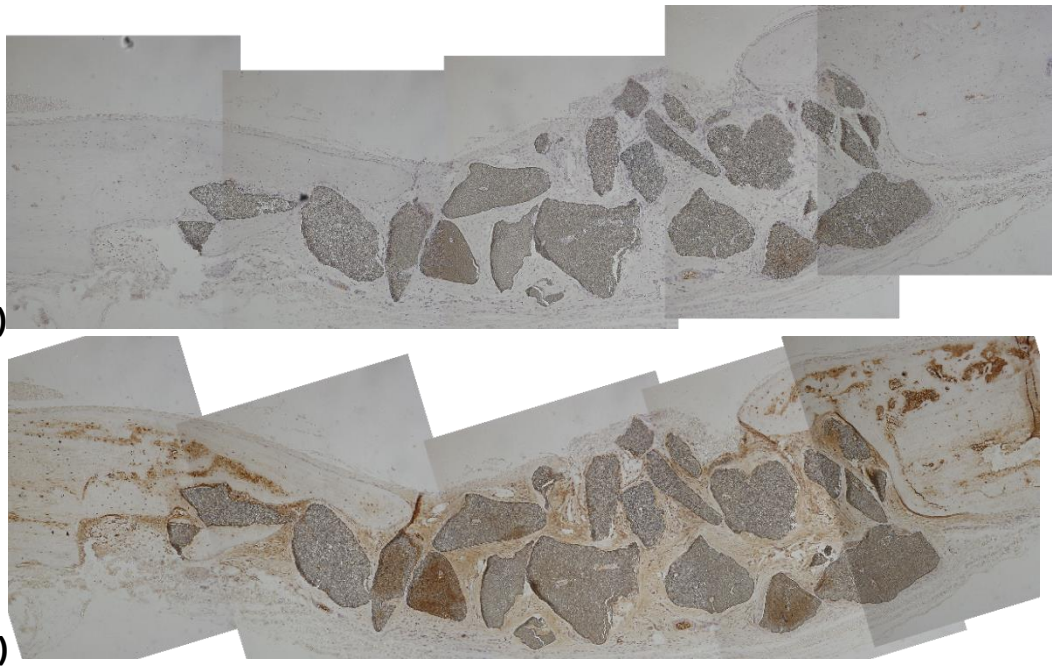

c)

Figure G.0.49: Histochemical staining of defect 11N1 with ABM+P15 scaffold and cells exposed to SAW-DEP 2 months after implantation. a) Negative control. b) Collagen type I antibody. c) Osteocalcin antibody.

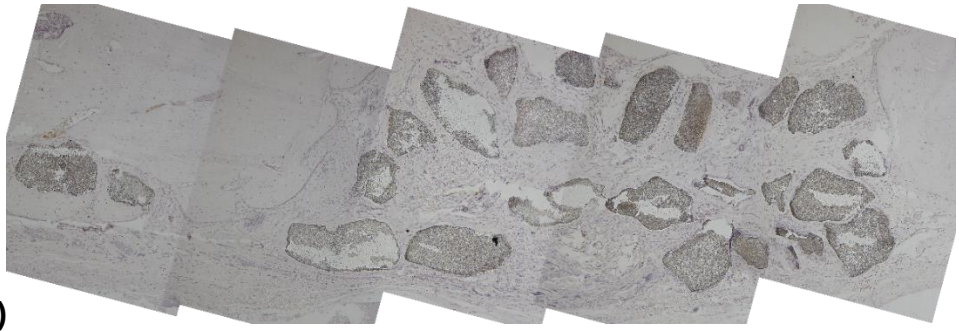

a)

b)

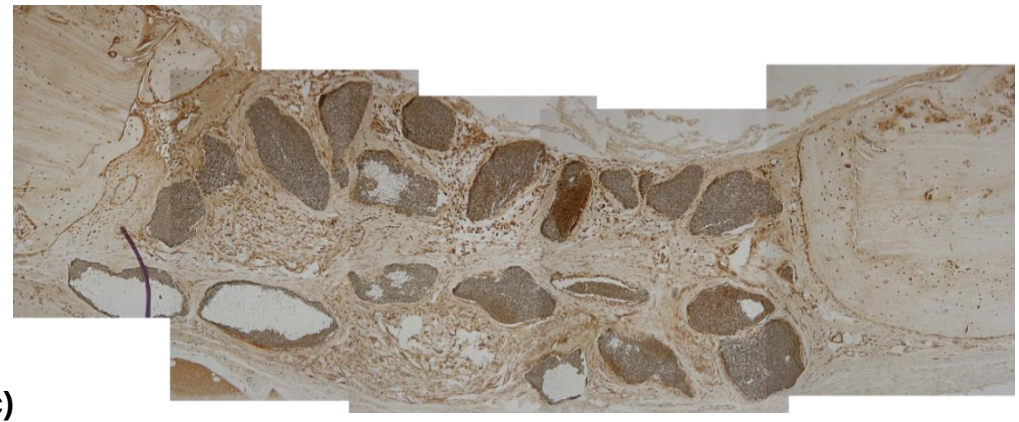

c)

Figure G.0.50: Histochemical staining of defect 11N2 with ABM+P15 scaffold and cells exposed to SAW-DEP 2 months after implantation. a) Negative control. b) Collagen type I antibody. c) Osteocalcin antibody.